I. R. IRAN

ISSN: 1728-144X
e-ISSN: 1735-9244

International Journal of Engineering

Journal Homepage: www.ije.ir

MERC

TRANSACTIONS B: APPLICATIONS

Volume 35, Number 08, June 2022

Materials and Energy Research Center

In the Name of God

INTERNATIONAL JOURNAL OF ENGINEERING
Transactions B: Applications

DISCLAIMER

The publication of papers in International Journal of Engineering does not imply that the editorial board, reviewers or publisher accept, approve or endorse the data and conclusions of authors.

International **J**ournal of **E**ngineering *Transactions A: Basics* (ISSN 1728-1431) (EISSN 1735-9244)
International **J**ournal of **E**ngineering *Transactions B: Applications* (ISSN 1728-144X) (EISSN 1735-9244)
International **J**ournal of **E**ngineering *Transactions C: Aspects* (ISSN 2423-7167) (EISSN 1735-9244)
Web Sites: www.ije.ir & www.ijeir.info E-mails: ije.editor8@gmail.com, Tel: (+9821) 88771578, Fax: (+9821) 88773352
Materials and Energy Research Center (MERC)

ISSN: 1728-144X, e-ISSN: 1735-9244

International Journal of Engineering, Volume 35, Number 08, June 2022

CONTENTS

Transactions B: Applications

ISSN: 1728-144X, e-ISSN: 1735-9244

International Journal of Engineering, Volume 35, Number 08, June 2022

IJE TRANSACTIONS B: Applications Vol. 35, No. 08, (August 2022) 1457-1467

International Journal of Engineering

Journal Homepage: www.ije.ir

New Dominant Color Descriptor Features Based on Weighting of More Informative Pixels using Suitable Masks for Content-Based Image Retrieval

S. Fadaei*

Department of Electrical Engineering, Faculty of Engineering, Yasouj University, Yasouj, Iran

PAPER INFO

Paper history:
Received 15 January 2022
Received in revised form 25 February 2022
Accepted 02 March 2022

Keywords:
Content-based Image Retrieval
Dominant Color Descriptor
Canny Edge Detector
Morphological Operations
Masking

ABSTRACT

Content-based image retrieval (CBIR) is a process of retrieving images based on their content in a dataset automatically. CBIR is a common solution to search images similar to a desired image among all images in dataset. To do this, many methods have been developed to extract images features. Here, a new Dominant Color Descriptor (DCD) method is proposed to improve CBIR accuracy. In the first step, Canny edges of images are extracted. In the next step, edges are widened by employing morphological operations. Finally, pixels that are not at the edges are weighted less than the pixels which are located at edges. Indeed, pixels in regions with low color variations are less weighted and more informative pixels are more weighted in providing DCD features. To show the effectiveness of the proposed method, experiments are performed on three datasets Corel-1k, Corel-10k and Caltech256. Results demonstrate that the proposed method outperforms competitive methods.

***doi**: 10.5829/ije.2022.35.08b.01*

1. INTRODUCTION

Due to mobile phones, digital cameras and other digital imaging equipments, image libraries have been greatly enlarged and managing these images is very tedious and, in some cases, is impossible for humans to handle. So, an automatic technique to search for a desired image from the huge dataset is necessary. Content-based image retrieval (CBIR) is a common solution for this problem. In CBIR, images are mapped to a feature vector and then retrieval process is done. It is tried to make feature vector containing a lot of information of the image. In the retrieval step, the feature vector of desired image (query) is compared with images in dataset and images with less distance to query are retrieved. The feature extraction is a vital step in CBIR and affects retrieval accuracy is significant [1, 2].

Color, texture and shape are the most important features of images. Among these features, color features are the most significant features which are robust agaist object rotation and translation [3]. Singha et al. [4]have used histogram as a color feature in images. A new method based on color coherence vector (CCV) was proposed by Pass and Zabih [5]. Similar to color histogram method, CCV is computed from color histogram by considering bins as incoherent or coherent. Chun et al. [6] have used color auto-correlograms of H and S components in HSV domain as color discriptors and combined with texture components as feature vector. DCD is another feature extraction method in which the image color space is partitioned into limited number of partitions [7].

Talib et al. [8] presented a new semantic feature extraction method named as weighted DCD in which each dominant color is weighted properly. The weighted DCD method diminishes the bad effect of backgrounds in images and highlights the foreground or object. To do this, three different weights Borther Weight of Dominant

*Corresponding Author Institutional Email: *s.fadaei@yu.ac.ir* (S. Fadaei)

Please cite this article as: S. Fadaei, New Dominant Color Descriptor Features Based on Weighting of More Informative Pixels using Suitable Masks for Content-Based Image Retrieval, ***International Journal of Engineering, Transactions B: Applications***, Vol. 35, No. 07, (2022) 1457-1467

Color (BWDC), Salient Object Weights (SOW) and Dominant Color Weights (DCW) are introduced and final dominant color weights are calculated using these weights. Also, a similarity measure based on Mutual Color Ratio (MCR) is modified to consider the defined weights. A new CBIR method by optimize combination of color and texture features is introduced by Fadaei et al. [9] to increase CBIR retrieval accuracy. A fast color quantization method with clusters merging is presented by Deng et al. [10] to achieve effective color features. Then some texture and shape features added to color features to increase the precision of CBIR system.

Wang et al. [11] proposed an efficient and compact color descriptor as well as a convenient similarity measure similar to the quadratic color histogram distance. As the original quadratic histogram similarity measure does not work well for DCDs in MPEG-7, a measure of similiraty between histograms is used by Po and Wong [12] to address drawbacks of quadratic histogram similarity measure. Mojsilovic et al. [13] obtained DCD features in Lab color space and a new similarity measure was defined to address the issue of how humans measure the similarity of images within the color domain. Speed of CBIR is improved by Fadaei and Rashno [14] based on integration of Zernike and wavelet components by PSO.

Drawbacks of DCD were addressed by Pavithra and Sharmila [1] while considereding first, middle and last points of values in color interval. Another efficient seed point selection method was presented by Pavithra and Sharmila [15] to drawbacks of DCD. Xie et al. [16] used the texton template to extract consistent area of the image and then DCD features are extracted from the pixels of the consistent area. By employing Convlutional Neural Network by Sezavar et al. [17], CBIR was implemented based on high-level features to increase the CBIR precision.

DCD provides compact and precise features and is easy and fast in implementation. In this research we focussed on these features and improved them to increase the CBIR precision. As mentioned before, statistical parameters of similar color clusters were considered as DCD features. It is obvious that the number of pixels in different partitions is not equal and for some partitions is high while it is very low for another. On the other hand, there are important and fundamental information of an image in its edges while regions of less color variations have no significant information. Therefore, here, a new procedure is proposed to assign low weight to pixels in regions with low color variations and emphasize on pixels placed on edges and their neighbors. To do this, edges of image are detected firstly and then edges width is widened. Finally, pixels that are on edges are weighted more than the pixels not located on edges.

The remained sections are organized as follows: The proposed method is presented in section 2. Experimental setup and results are reported in sections 3 and 4 and the paper is concluded in section 5.

2. PROPOSED DCD FEATURES

2. 1. DCD Feature Extraction Method DCD features have been widely used in previous researches because extracting of them is easier and faster than the other features. Providing a compact description of the color distribution of the image is another advantage of these features. As shown in Figure 1, the color space is firstly divided into several partitions in the DCD method. Each pixel of the image belongs to a partition. The mean color of the pixels and percentage of them in each partition are used as DCD features.

It is clear from Figure 2 that partitions 2 (Figure 2c), 4 (Figure 2e) and 6 (Figure 2g) have few pixles, so it is expected that the corresponding percentage of these partitions should be low. According to Figure 2k, the percentage of these partitions are 0.00048, 0.00014 and 0.00150, respectively.

2. 2. Proposed Method As mentioned before, pixels located on edges and their neighbors are more informative than the other pixels and in contrast, regions with less color variations have no significant information. If the number of pixels located in several partitions of the color space is very different, then the extracted DCD features will not perform well. To address this drawback, weighted DCD was proposed by Talib et al. [8] in which lower weights are assigned to the background section and higher weights are assigned to the object. Although it was tried to solve this problem in weighted DCD, but the weights have not been properly adjusted and does not work well.

To address this challenge, a new method is proposed here. The proposed method is inspired by this property that edeges contain significant information of images. Indeed, the colors of the edge pixels are given higher weight in the proposed method and pixels in regions with low color variations are given lower weight. Therefore, the edges of the image should be segmented and used to form DCD features.

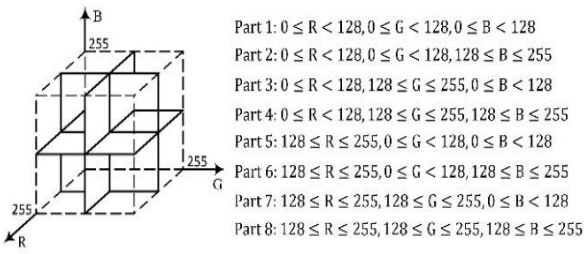

Figure 1. Dividing RGB into 8 partitions in DCD method

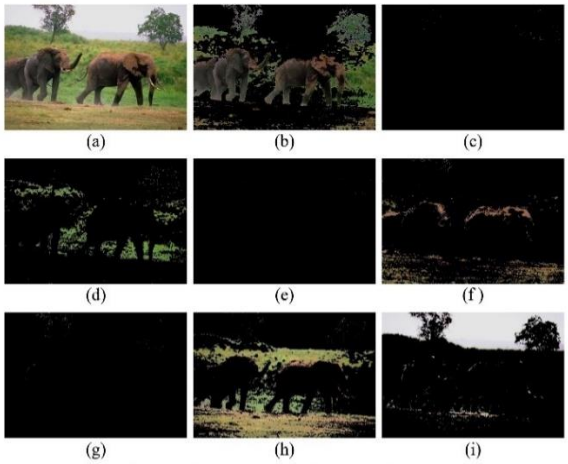

(j)

	R	G	B
C1	74.9	76.7	51.9
C2	124.1	120.7	131.0
C3	114.5	139.2	76.5
C4	125.2	133.9	131.4
C5	142.4	115.8	76.3
C6	134.8	123.5	133.7
C7	158.3	149.6	93.7
C8	214.3	212.3	213.1

(k)

	P
P1	0.38909
P2	0.00048
P3	0.06931
P4	0.00014
P5	0.06870
P6	0.00150
P7	0.26166
P8	0.20914

Figure 2. Implementation of DCD method on a sample image of the Corel-1k dataset; a) the original image, b-i) the pixels belonging to partitions 1 to 8, j) mean of pixels in each partition and k) percentage of pixels in each partition

Figure 3 illustrates the diagram of the proposed method. In this method, at first, the input image is transferred to gray-level domain and then the edges of the image are extracted. Since the edges of the image contain a lot of information, the purpose of this stage is to extract edges locations. The pixels around the edges also contain high color information, so, the morphological dilation is applied to edge image to widen the edges. According to Figure 3, location of the edges and their neighbors are determined in this step.

Output of this step is two binary images: The first image is 1 in locations with important information (edges and their neighbors) and is 0 in the others. The second image is the opposite of first image so that is 0 in edge locations and 1 in the others. In the next step, the binary images are used as mask and multiplied by the input image. Finally, two images are obtained which the DCD features are extracted from these images by suitable weighting.

The input image is shown by I with size $X \times Y$ and the color information of pixel (x, y) is indicated by $I(x, y)$. At first, the input image is transferred to gray-level domain:

$$G(x,y) = \frac{I_R(x,y)+I_G(x,y)+I_B(x,y)}{3} \quad (1)$$

where $I_R(x, y)$, $I_G(x, y)$ and $I_B(x, y)$ are red, green and blue components of the image and $G(x, y)$ is the gray-scale image. Edges of the gray image $G(x, y)$ are extracted using Canny edge detector in the next step. The edge image is indicated by $G_E(x, y)$ and is 1 on edge locations and 0 on the others.

In the next step, edge image is dilated by a disk-shaped structuring element with diameter D. The disk-shaped structuring element is indicated by S_D and the edges are thickened in proportion to the D:

$$M_{H,D} = G_E \oplus S_D = \{z|(\hat{S}_D)_z \cap G_E \neq \phi\} \quad (2)$$

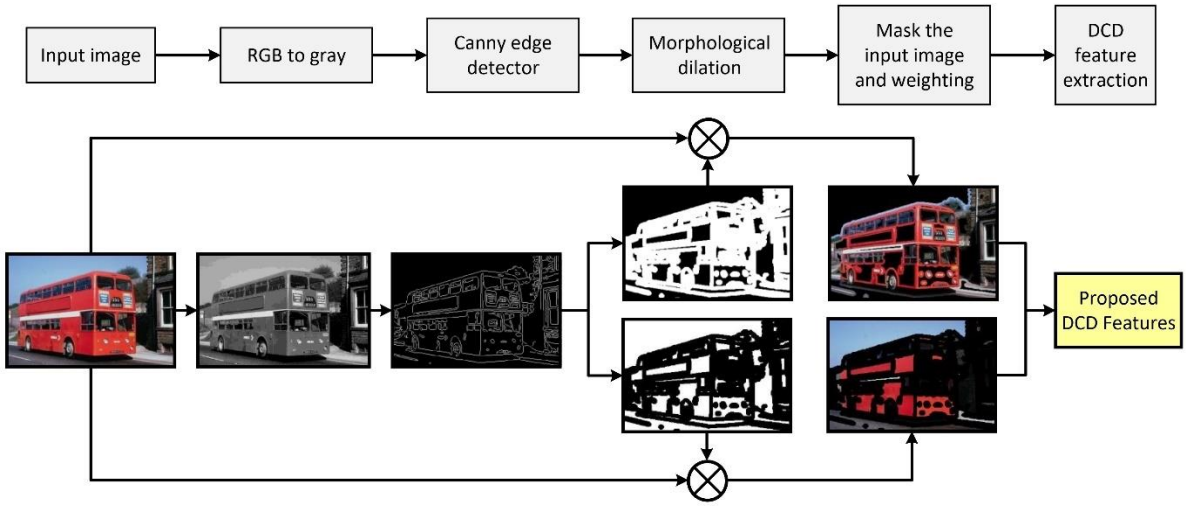

Figure 3. Flowchart of the proposed method

where $\oplus$ is dilation operator, $\hat{S}_D$ indicates the complement of S_D, $(\hat{S}_D)_z$ is the translation of $\hat{S}_D$ by z and $M_{H,D}$ is a binary image which is 1 on edges and their neighbors and 0 on other locations. Therefore $M_{H,D}$ is a mask that can be used to determine the pixels located at the edges which contain a lot of information. Based on mask $M_{H,D}$, mask $M_{L,D}$ is defined which is 1 in regions with low variations and 0 in other locations.

$$M_{L,D} = 1 - M_{H,D} \tag{3}$$

In the next step, the pixels with more and less information are determined:

$$I_{H,D}(x,y) = M_{H,D}(x,y) \times I(x,y) \tag{4}$$

$$I_{L,D}(x,y) = M_{L,D}(x,y) \times I(x,y) \tag{5}$$

In DCD method, the color space is partitioned to N partitions and pixels that are placed in each partition are identified. To do this, a mask is defined for each partition as follows:

$$M_{P,i}(x,y) = \begin{cases} 1, & \alpha_{a,i} \le I_R(x,y) < \alpha_{b,i} \text{ and} \\ & \beta_{a,i} \le I_G(x,y) < \beta_{b,i} \text{ and} \\ & \gamma_{a,i} \le I_B(x,y) < \gamma_{b,i} \\ 0, & \text{otherwise} \end{cases} \tag{6}$$

Where $M_{P,i}$ is the mask of ith partition and is 1 for pixels belong to that partition and 0 for the others. $\alpha_{a,i}$ and $\alpha_{b,i}$ are the low and high limit of the ith partition for the first component of color space, $\beta_{a,i}$ and $\beta_{b,i}$ are the low and high limits of the second component of partition i in color space and $\gamma_{a,i}$ and $\gamma_{b,i}$ are the low and high limits for the third component. In the next step the center and percentage of each partition is calculated as follows:

$$C_{R,i} = \frac{1}{|M_{P,i}|}\sum_{y=1}^{Y}\sum_{x=1}^{X} M_{P,i}(x,y) \times \left(k_H I^R_{H,D}(x,y) + k_L I^R_{L,D}(x,y)\right) = \frac{1}{|M_{P,i}|}\sum_{y=1}^{Y}\sum_{x=1}^{X} M_{P,i}(x,y) \times \left[k_H M_{H,D}(x,y) \times I_R(x,y) + k_L M_{L,D}(x,y) \times I_R(x,y)\right] \tag{7}$$

$$C_{G,i} = \frac{1}{|M_{P,i}|}\sum_{y=1}^{Y}\sum_{x=1}^{X} M_{P,i}(x,y) \times \left(k_H I^G_{H,D}(x,y) + k_L I^G_{L,D}(x,y)\right) = \frac{1}{|M_{P,i}|}\sum_{y=1}^{Y}\sum_{x=1}^{X} M_{P,i}(x,y) \times \left[k_H M_{H,D}(x,y) \times I_G(x,y) + k_L M_{L,D}(x,y) \times I_G(x,y)\right] \tag{8}$$

$$C_{B,i} = \frac{1}{|M_{P,i}|}\sum_{y=1}^{Y}\sum_{x=1}^{X} M_{P,i}(x,y) \times \left(k_H I^B_{H,D}(x,y) + k_L I^B_{L,D}(x,y)\right) = \frac{1}{|M_{P,i}|}\sum_{y=1}^{Y}\sum_{x=1}^{X} M_{P,i}(x,y) \times \left[k_H M_{H,D}(x,y) \times I_B(x,y) + k_L M_{L,D}(x,y) \times I_B(x,y)\right] \tag{9}$$

$$P_i = \frac{|M_{P,i}|}{X \times Y} \tag{10}$$

where k_H and k_L are assigned weights to more and less important pixels, respectively, and $|M_{P,i}|$ is defined as follows:

$$\left|M_{P,i}\right| = \sum_{y=1}^{Y}\sum_{x=1}^{X} M_{P,i}(x,y) \tag{11}$$

Finally, the proposed feature vector is formed by Equation (12), which is a vector of length 4*N*:

$$F = \{C_{R,1}, C_{G,1}, C_{B,1}, P_1, \dots, C_{R,N}, C_{G,N}, C_{B,N}, P_N\} \tag{12}$$

2. 3. Distance Measure Each CBIR system is working based on distance between query image and images in dataset. Since distance computation method proposed by Mojsilovic et al. [13] is used in this research, it is described in details as follows:

Suppose that images Q and DB are query and an image of dataset and their feature vectors are:

$$F_Q = \left\{\left(C_a^Q, P_a^Q\right), a = 1,2, \dots, N_Q\right\} \tag{13}$$

$$F_{DB} = \left\{\left(C_b^{DB}, P_b^{DB}\right), b = 1,2, \dots, N_{DB}\right\} \tag{14}$$

where, C and P are the dominant color and its percentage, respectively. At first, distance between Q and DB with respect to ith dominant color of image Q is defined as:

$$D(Q_i, DB) = \min_{b \in [1, N_{DB}]} d\left(\left(C_i^Q, P_i^Q\right), \left(C_b^{DB}, P_b^{DB}\right)\right) \tag{15}$$

$$d\left(\left(C_i^Q, P_i^Q\right), \left(C_b^{DB}, P_b^{DB}\right)\right) = \left|P_i^Q - P_b^{DB}\right| + \sqrt{\sum_{k=1}^{3}\left(C_{i,k}^Q - C_{b,k}^{DB}\right)^2} \tag{16}$$

where, $C_{i,k}^Q$ is the kth component of dominant color C_i^Q. In the next step, $D(Q_i, DB)$ and $D(DB_i, Q)$ are calculated for $i = 1,2,..N_Q$ and $i = 1,2,..N_{DB}$, respectively. Finally, distanse between two images Q and DB is defined as follows:

$$Distance(Q, DB) = \sum_{a=1}^{N_{DB}} D(Q_i, DB) + \sum_{a=1}^{N_Q} D(DB_i, Q) \tag{17}$$

3. EXPERIMENTAL SETUP

3. 1. Datasets Three datasets including Corel-1k, Corel-10k and Caltech256 are used for evaluation. As reported in Table 1, Corel-1k dataset consists of 10 classes, 100 images in each class and total number of images is 1000; Corel-10k consists of 100 classes, 100 images per class and total number of images is 10000; Caltech256 consists of 257 classes and 30607 images.

3. 2. Performance Evaluation Criteria Precision, Recall, P10, Average Retrieval Rate (ARR), Average Normalized Modified Retrieval Rank (ANMRR) and Mean Average Precision (MAP) are used as evaluation criteria.

TABLE 1. Details of datasets Corel-1k, Corel-10k and Caltech256

Dataset	Classes	Total images	Images per class		
			min	max	mean
Corel-1k	10	1000	100	100	100
Corel-10k	100	10000	100	100	100
Caltech256	257	30607	80	827	119

To obtain precision, one image of the dataset images is considered as query image. Then, the feature vectors are extracted for query image and all images in dataset. In the next step, the distance between the query image and other images in dataset are obtained using Equation (17). Finally, the first *T* images in dataset with the lower distance from the query image are considered as images similar to the query. From these *T* images, some of them (suppose *N*) are from the class of query image and the rest are not. Therefore, the precision and recall of this experiment are:

$$P = \frac{N}{T} = \frac{\text{Number of similar images retrieved}}{\text{Total number of images retrieved}} \quad (18)$$

Recall is defined as:

$$R = \frac{N}{K} = \frac{\text{Number of similar images retrieved}}{\text{Total number of similar images in dataset}} \quad (19)$$

where *N*, *T* and K are number of similar retrived images, total number of retrieved images, and total number of similar images in dataset, respectively.

P10 is the average precision of 10 retrieved images. Indeed, P10 is the precision for $T = 10$.

ARR is calculated as follows:

$$ARR = \frac{1}{N_q}\sum_{q=1}^{N_q} RR_q \quad (20)$$

where, N_q is the number of query images used in the test which is set to all images in the dataset (E.g. $N_q = 1000$ for Corel-1k) and RR_q is calculated as follows:

$$RR_q = \frac{NR_q(\alpha)}{NG_q} \quad (21)$$

NG_q is the total number of relevant images with query q in the dataset and $NR_q(\alpha)$ is the number of relevant images retrieved in the first αNG_q. Here, α is configured to 1.

ANMRR is introduced as follows:

$$ANMRR = \frac{1}{N_q}\sum_{q=1}^{N_q} NMRR_q \quad (22)$$

$$NMRR_q = \frac{2\times AVR_q - NG_q - 1}{2\times W_q - NG_q + 1} \quad (23)$$

$$AVR_q = \frac{1}{NG_q}\sum_{i=1}^{NG_q} Rank_i \quad (24)$$

where, $W_q = 2NG_q$ and $Rank_i$ is calculated as follows: *W* images are retrieved for query q. Then, the *i*th relevant image to the query q is considered, if it is among these *W* images the $Rank_i$ is adjusted according to the order of this image in the *W* retrieved images, otherwise, it set to $W + 1$. Note that the best and worst values of ANMRR are 0 and 1, respectively. Indeed, the lower value of ANMRR is equivalent with the higher retrieval performance.

MAP is calculated as follows:

$$MAP = \frac{1}{N_q}\sum_{q=1}^{N_q} AP_q \quad (25)$$

$$AP_q = \frac{1}{NG_q}\sum_{i=1}^{NG_q} P_i \quad (26)$$

To calculate P_i, the order of *i*th relevant image in the retrieved images is considered as the number of retrieved images and the precision is calculated as P_i. It is worth mentioning that MAP measures the retrieval precision among all relevant images in the dataset while ANMRR calculates the precision for a window *W*.

4. EXPERIMENTAL RESULTS

4. 1. Structuring Element Impact In the first experiment, the impact of SE size of morphological dilation on these datasets is evaluated. The structuring element is a disk. Here, the precision is considered for evaluation and $T = 20$. To obtain the precision for each SE size, precision of all images in dataset is calculated and then, the final precision is averaged over all precisions. Therefore, the reported values on the Corel-1k, Corel-10k and Caltech256 datasets are averaged over 1000, 10000 and 30607 experiments, respectively. Figure 4 shows precision of these datasets for different SE size. The Corel-1k dataset for SE size of 47 has achieved a maximum precision of 70.87% and the maximum precision in Corel-10k and Caltech256 datasets are 40.75% and 11.65%, respectively, for SE size of 25 and 15.

4. 2. Impact of Retrieved Images Number Number of retrieved images is varied from 5 to 40 and the precision and recall are calculated for each dataset in the best SE size. Precision and recall results are reported in Table 2, Figures 5 and 6 for Corel-1k, Corel-10k and Caltech256 datasets.

Based on Figure 5, precision is decreased by increment of retrieved images.

As the number of retrieved images increases, the recall increases which can be seen in Figure 6.

4. 3. Comparing the Proposed Method with Other Methods In this experiment, the precision and

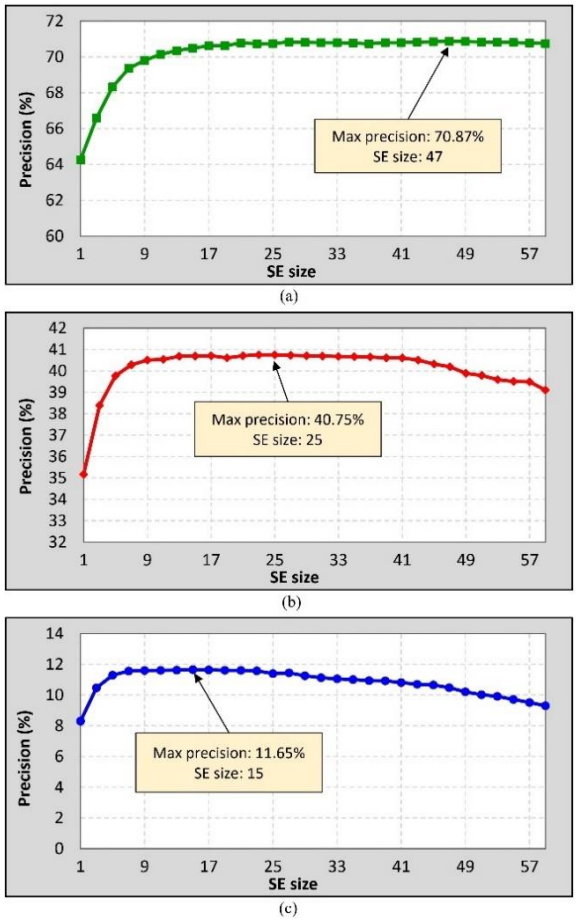

Figure 4. Precision results for SE size in a) Corel-1k, b) Corel-10k and c) Caltech256 datasets

TABLE 2. Precision and recall results of the proposed method for different number of retrieved images in Corel-1k, Corel-10k and Caltech256 datasets

T	Precision (%)			Recall (%)		
	Corel-1k	Corel-10k	Caltech256	Corel-1k	Corel-10k	Caltech256
5	83.28	61.35	27.06	4.16	3.07	1.14
10	77.15	50.06	16.61	7.72	5.01	1.40
15	73.66	44.37	12.94	11.05	6.66	1.63
20	70.87	40.75	11.65	14.17	8.15	1.96
25	68.57	37.94	9.85	17.14	9.49	2.07
30	66.59	35.70	9.02	19.98	10.71	2.27
35	64.79	33.85	8.42	22.68	11.85	2.48
40	63.13	32.25	7.95	25.25	12.90	2.67

recall of the proposed scheme are compared with previous methods on the Corel-1k, Corel-10k and Caltech256. Precision and recall of the proposed method and literature [8, 10-13,15] in Corel-1k dataset are shown in Tables 3 and 4. Figure 7 demonstrates the precision of the proposed method and other methods. In this experiment number of retrieved images is configured to $T = 20$.

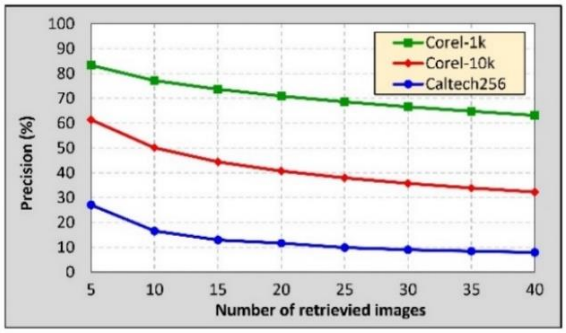

Figure 5. Precision results for different number of retrieved images (T) in Corel-1k, Corel-10k and Caltech256 datasets

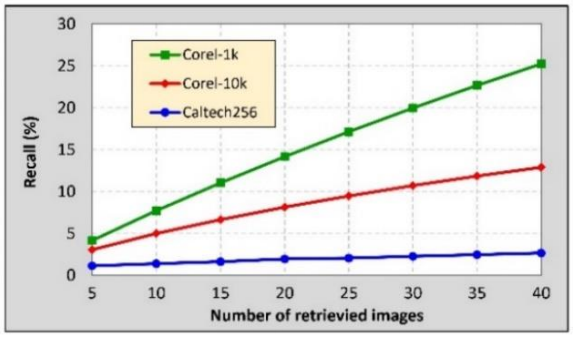

Figure 6. Recall results for different number of retrieved images (T) in Corel-1k, Corel-10k and Caltech256 datasets

TABLE 3. Precision of the proposed method and literature [8, 10-13,15] in Corel-1k dataset.

Class	Precision (%)						
	[11]	[8]	[10]	[12]	[13]	[15]	Proposed
Africa	53.50	51.25	58.35	64.10	65.65	69.27	**72.05**
Beach	39.50	39.60	41.35	43.10	44.65	**45.12**	36.85
Building	38.10	44.25	39.85	45.85	52.35	44.31	**74.00**
Bus	46.70	47.75	61.10	53.70	65.00	71.46	**77.10**
Dinosaur	99.70	79.45	99.25	99.95	**100.00**	96.36	97.20
Elephant	51.15	54.55	55.40	53.60	53.85	55.10	**58.20**
Flower	53.95	63.35	67.90	70.00	**94.40**	81.05	84.65
Horse	81.45	83.40	**94.05**	90.95	89.50	79.61	90.75
Mountain	30.35	36.60	32.80	39.50	44.10	**45.83**	43.10
Food	58.50	61.95	59.95	67.00	68.95	72.43	**74.80**
Win	**0**	**0**	**1**	**0**	**2**	**2**	**5**

TABLE 4. Recall of the proposed method and literature [8, 10-13, 15] in Corel-1k dataset

Class	Recall (%)						
	[11]	[8]	[10]	[12]	[13]	[15]	Proposed
Africa	10.70	10.25	11.67	12.82	13.13	13.85	**14.41**
Beach	7.90	7.92	8.27	8.62	8.93	**9.02**	7.37
Building	7.62	8.85	7.97	9.17	10.47	8.86	**14.80**
Bus	9.34	9.55	12.22	10.74	13.00	14.29	**15.42**
Dinosaur	19.94	15.89	19.85	19.99	**20.00**	19.27	19.44
Elephant	10.23	10.91	11.08	10.72	10.77	11.02	**11.64**
Flower	10.79	12.67	13.58	14.00	**18.88**	16.21	16.93
Horse	16.29	16.68	**18.81**	18.19	17.90	15.92	18.15
Mountain	6.07	7.32	6.56	7.90	8.82	**9.17**	8.62
Food	11.70	12.39	11.99	13.40	13.79	14.49	**14.96**
Win	**0**	**0**	**1**	**0**	**2**	**2**	**5**

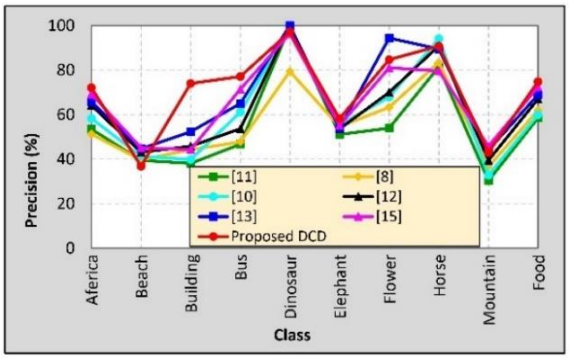

Figure 7. Precision of the proposed method and literature [8, 10-13,15] in Corel-1k dataset

Tables 3 and 4 indicate that the proposed method makes superior precision results in comparison with competetive methods in 5 classes out of 10 classes.

Table 5 and Figure 8 indicates the average precision over all classes in Corel-1k, Corel-10k and Caltech256 for all methods. It may be concluded that: 1) The proposed method outperforms literature [8, 10-13,15] by 14.66%, 9.87%, 15.58%, 8.10%, 3.02% and 4.82% with respect to average precision in Corel-1k; 2) The proposed method works better than [11] by 16.73%, [8] by 14.00%, [10] by 15.43%, [12] by 11.97%, [13] by 7.03% and [15] by 7.83% in terms of average precision in Corel-10k; 3) Although method by Mojsilovic et al. [13] has reached precision of 11.87% in Caltech256 and is the best method in this dataset, but the proposed method with precision 11.65% is very close to this method.

In the next experiment, to compare the proposed method with the other methods, the metrics P10, ARR, ANMRR and MAP for Corel-1k are considered. Tables

TABLE 5. Precision of the proposed method and literature [8, 10-13, 15] in three datasets Corel-1k, Corel-10k and Caltech256

Dataset	Precision (%)						
	[11]	[8]	[10]	[12]	[13]	[15]	Proposed
Corel-1k	55.29	56.21	61.00	62.77	67.85	66.05	**70.87**
Corel-10k	24.02	26.75	25.32	28.78	33.72	32.92	**40.75**
Caltech256	8.87	8.71	7.91	10.27	**11.87**	11.06	11.65

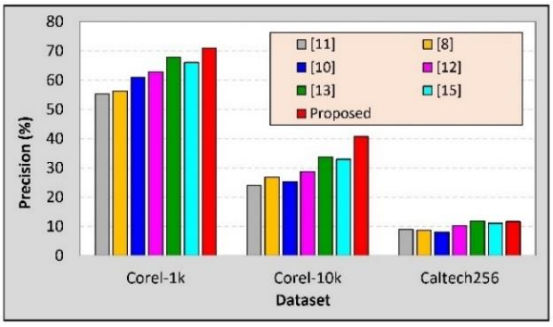

Figure 8. Precision of the proposed method and literature [8, 10-13,15] in three datasets Corel-1k, Corel-10k and Caltech256

6-9 report the P10, ARR, ANMRR and MAP of the proposed method and methods in literature [8, 10-13,15] on Corel-1k dataset.

It cab be concluded from Tables 6-9 that: 1) The proposed method outperforms methods in literature [8, 10-13, 15] in terms of P10, ARR, ANMRR and MAP; 2). The proposed method is the best method in 5, 4, 4 and 5 classes out of 10 classes in P10, ARR, ANMRR and MAP measures, respectively.

TABLE 6. P10 of the proposed method and literature [8, 10-13,15] in Corel-1k dataset.

Class	Method						
	[11]	[8]	[10]	[12]	[13]	[15]	Proposed
Africa	0.5910	0.4930	0.6446	0.7190	0.7120	0.7652	**0.7940**
Beach	0.4520	0.4360	0.4732	0.5960	0.3870	**0.5163**	0.4400
Building	0.4560	0.6220	0.4769	0.5330	0.7320	0.5303	**0.8070**
Bus	0.5270	0.4530	0.6895	0.5980	0.7000	0.7664	**0.8110**
Dinosaur	**0.9970**	0.8860	0.9925	0.9960	0.8400	0.9636	0.9930
Elephant	0.6190	0.5160	0.6804	0.6560	0.6340	0.6767	**0.7100**
Flower	0.6040	0.7040	0.7502	0.8410	**0.9140**	0.8955	0.9000
Horse	0.8760	0.9050	**1.0000**	0.8230	0.9860	0.8465	0.9600
Mountain	0.3620	0.4270	0.3782	0.4640	0.5160	**0.5285**	0.5040
Food	0.6610	0.6920	0.6774	0.6770	0.7910	0.7884	**0.7960**
Average	0.6145	0.6134	0.6763	0.6903	0.7212	0.7277	**0.7715**

TABLE 7. ARR of the proposed method and literature [8, 10-13, 15] in Corel-1k dataset

Class	Method						
	[11]	[8]	[10]	[12]	[13]	[15]	Proposed
Africa	0.3757	0.3328	0.4351	0.4171	0.3848	**0.5166**	0.4133
Beach	0.2649	0.2592	0.2813	0.3112	0.2584	**0.3169**	0.2343
Building	0.2536	0.3333	0.2556	0.2443	0.4520	0.3342	**0.5041**
Bus	0.3551	0.3271	0.4679	0.3359	0.4077	0.5001	**0.5022**
Dinosaur	0.9785	0.4291	0.4807	0.9815	0.5102	0.4867	**0.7566**
Elephant	0.3469	0.3525	**0.4948**	0.3576	0.3634	0.4922	0.3399
Flower	0.3143	0.3741	0.3786	0.4642	0.4095	0.4820	**0.6401**
Horse	0.4555	0.4299	0.4750	0.3919	**0.6522**	0.4321	0.5897
Mountain	0.2221	0.2648	0.2346	0.2202	**0.3590**	0.3277	0.2758
Food	0.3741	0.4017	0.4132	0.3483	**0.5434**	0.4809	0.4792
Average	0.3941	0.3505	0.3917	0.4072	0.4341	0.4369	**0.4735**

TABLE 8. ANMRR of the proposed method and literature [8, 10-13, 15] in Corel-1k dataset

Class	Method						
	[11]	[8]	[10]	[12]	[13]	[15]	Proposed
Africa	0.5416	0.5853	0.5207	0.5081	0.5390	0.6512	**0.5000**
Beach	0.6630	0.6673	0.6541	0.6272	0.6844	**0.5231**	0.7067
Building	0.6760	0.5815	0.6870	0.6829	0.4449	0.3884	**0.3839**
Bus	0.5527	0.5802	0.6731	0.5858	0.5158	0.7041	**0.4013**
Dinosaur	**0.0102**	0.4902	0.0302	0.0952	0.3873	0.2962	0.1422
Elephant	0.5662	0.5613	0.6024	0.5645	**0.5535**	0.5733	0.5735
Flower	0.6356	0.5504	0.7194	0.4590	0.5188	0.4148	**0.2663**
Horse	0.4549	0.4785	0.4393	0.5332	**0.2463**	0.4565	0.3110
Mountain	0.7124	0.6629	0.6044	0.7132	0.5618	**0.5468**	0.6503
Food	0.5278	0.5026	0.5109	0.5890	**0.3607**	0.5773	0.4192
Average	0.5340	0.5660	0.5441	0.5358	0.4812	0.4714	**0.4354**

Also, the precisions of the proposed CBIR scheme and methods reported in literature [18-25] in Corel-1k dataset are reported in Table 10. Here, the results were stated according to the highest 20 images [25]. It was noted that in these experiments, since 20 images are considered for precision and recal computation, these measures are increased sifnificantly in comparisaion with considering all images (Table 4).

From Table 6, the proposed method with precision 91.24% is the best method. On the other hand, the proposed method is the best method in 6 classes out of 10 classes.

TABLE 9. MAP of the proposed method and literature [8, 10-13, 15] in Corel-1k dataset

Class	Method						
	[11]	[8]	[10]	[12]	[13]	[15]	Proposed
Africa	0.3683	0.3180	0.4357	0.3819	0.4383	**0.5285**	0.4372
Beach	0.2753	0.2609	0.2831	0.3275	**0.3453**	0.3440	0.2236
Building	0.2488	0.3305	0.3034	0.2796	0.3188	0.3668	**0.5446**
Bus	0.3459	0.3223	0.4811	0.3642	0.4725	0.5304	**0.5447**
Dinosaur	0.9866	0.4689	0.5752	0.9906	**1.0000**	0.5449	0.8335
Elephant	0.3379	0.3375	0.4737	0.3754	0.4079	**0.4776**	0.3506
Flower	0.2946	0.3780	0.3825	0.4914	0.3646	0.5157	**0.6956**
Horse	0.4717	0.4704	0.5198	0.4027	0.5417	0.4750	**0.6398**
Mountain	0.2049	0.2554	0.2263	0.2597	0.2749	**0.3611**	0.2751
Food	0.3937	0.4284	0.4407	0.3141	0.4637	0.5130	**0.5188**
Average	0.3928	0.3570	0.4122	0.4187	0.4628	0.4657	**0.5064**

TABLE 10. Precision of the proposed method and literature [18-25] in Corel-1k dataset

Class	Precision (%)								
	[18]	[19]	[20]	[21]	[22]	[23]	[24]	[25]	Proposed
Africa	83.00	77.82	69.08	73.03	72.50	51.00	64.00	83.00	**99.40**
Beach	72.00	79.56	72.20	74.58	65.20	**90.00**	54.00	82.85	60.60
Building	86.00	80.75	84.85	80.24	70.60	58.00	53.00	82.00	**97.00**
Bus	**100.0**	95.74	95.75	95.84	89.20	78.00	94.00	**100.0**	99.80
Dinosaur	97.00	98.12	**100.0**	97.95	**100.0**	**100.0**	98.00	**100.0**	**100.0**
Elephant	82.00	89.54	89.99	87.64	70.50	84.00	78.00	**90.00**	88.00
Flower	86.00	86.87	94.01	85.13	94.80	**100.0**	71.00	95.00	**100.0**
Horse	82.00	89.41	86.38	86.29	91.80	**100.0**	93.00	91.80	**100.0**
Mountain	69.00	85.78	82.85	82.43	72.25	84.00	42.00	**86.87**	68.20
Food	90.00	84.92	85.88	78.96	78.80	38.00	50.00	90.00	**99.40**
Average	84.70	86.85	86.10	84.21	80.57	78.30	69.70	90.15	**91.24**

4. 4. Retrieval Results A graphical comparison between all methods are performed in this secretion. For this task, a query image is considered as input for all methods and the retrieved output images of each method are depicted. Figures 9-15 show the retrieval results for flower query image in Corel-1k dataset. In these figures, the top left image (in orange box) is the query and the others are retrieved images. Images in blue box are similar to query and images in red box are irrelevant to query.

As shown in Table 11, the proposed method with precision 95.00% outperforms the other methods.

Figure 9. Retrieval results of the method in literature [11]

Figure 10. Retrieval results of the method in literature [8]

Figure 11. Retrieval results of the method in literature [10]

Figure 12. Retrieval results of the method in literature [12]

Figure 13. Retrieval results of the method in literature [13]

Figure 14. Retrieval results of the method in [15]

Figure 15. Retrieval results of the proposed method

TABLE 11. Conclusion of Figures 9-15

Method	$T = 20$		
	Number of similar images	Number of irrelevant images	Precision
[11]	7	13	35.00%
[8]	13	7	65.00%
[10]	18	2	90.00%
[12]	17	3	85.00%
[13]	18	2	90.00%
[15]	16	4	80.00%
Proposed	**19**	**1**	**95.00%**

Retrieval results of Figures 9-15 are concluded in Table 11.

4. 5. Computational Complexity In this experiment, retrieval time of our CBIR system and CBIRs in literature [8, 10-13,15] are explored. Figure 16 reveals the comparison of the mean retrieval time in all CBIR systems applied to Corel-1k dataset. The proposed scheme is faster than methods in [12] and [15] and slower than the other methods.

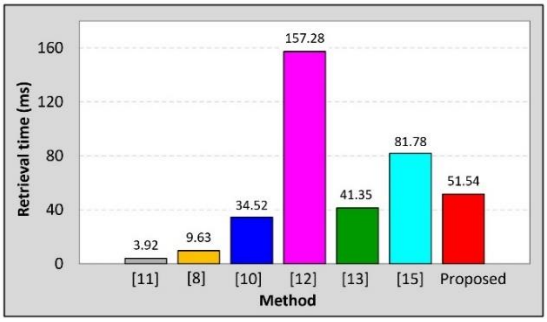

Figure 16. Retrieval time of the proposed method and literature [8, 10-13,15] in Corel-1k dataset

5. CONCLUSION

In this research, a new CBIR scheme was proposed. The proposed method focused on DCD features to improve

them. At first, the input image was transferred to gray-level image and then Canny edge detector was applied to image to determine image edges. In the next step, the morphological dilation was applied to edges to widen them. Finally, pixels that are located on the edges were assigned higher weight than the others. Corel-1k, Corel-10k and Caltech256 datasets were used for the evaluation and the experimental results indicated that the proposed CBIR method achieves better retrieval results in comparison with other competitive methods.

The limitation of the proposed DCD is that the SE size should be calculated for each dataset separately. For future work, precision of the proposed method can be checked on the different color spaces. Finally, determination of CBIR parameters using optimization algorithms such as particle swarm optimization (PSO) can be considered as another future work.

6. REFERENCES

1. Pavithra, L. K., and Sharmila, T. S., "Optimized feature integration and minimized search space in content based image retrieval", ***Procedia Computer Science***, Vol. 165, (2019), 691-700, doi: 10.1016/j.procs.2020.01.065.
2. Fadaei, S., Amirfattahi, R., and Ahmadzadeh, M. R., "Local derivative radial patterns: A new texture descriptor for content-based image retrieval", ***Signal Processing***, Vol. 137, (2017), 274-286, doi: 10.1016/j.sigpro.2017.02.013.
3. Dubey, S.R., Singh, S.K., and Singh, R.K., "Local neighbourhood-based robust colour occurrence descriptor for colour image retrieval", ***IET Image Processing***, Vol. 9, No. 7, (2015), 578-586, doi: 10.1049/iet-ipr.2014.0769.
4. Singha, M., Hemachandran, K., and Paul, A., "Content-based image retrieval using the combination of the fast wavelet transformation and the colour histogram", ***IET Image Processing***, Vol. 6, No. 9, (2012), 1221-1226, doi: 10.1049/iet-ipr.2011.0453
5. Pass, G. and Zabih, R., "Histogram refinement for content-based image retrieval", Proc. 3rd IEEE Workshop on Applications of Computer Vision (WACV'96), Sarasota, FL, (1996), 96-102, doi: 10.1109/ACV.1996.572008.
6. Chun, Y.D., Kim, N.C., and Jang, I.H., "Content-based image retrieval using multiresolution color and texture features", ***IEEE Transactions on Multimedia***, Vol. 10, No. 6, (2008), 1073-1084, doi: 10.1109/TMM.2008.2001357.
7. Wang, X.-Y., Yu, Y.-J., and Yang, H.-Y., "An effective image retrieval scheme using color, texture and shape features", ***Computer Standard Interfaces***, Vol. 33, No. 1, (2011), 59-68, doi: 10.1016/j.csi.2010.03.004.
8. Talib, A., Mahmuddin, M., Husni, H., and George, L. E., "A weighted dominant color descriptor for content-based image retrieval", ***Journal of Visual Communication and Image Representation***, Vol. 24, No. 3, (2013), 345-360, doi: 10.1016/j.jvcir.2013.01.007.
9. Fadaei, S., Amirfattahi, R., and Ahmadzadeh, M. R., "New content-based image retrieval system based on optimised integration of DCD, wavelet and curvelet features", ***IET Image Processing***, Vol. 11, No. 2, (2017), 89-98, doi: 10.1049/iet-ipr.2016.0542.
10. Deng, Y., Manjunath, B. S., Kenney, C., Moore, M. S., and Shin, H., "An efficient color representation for image retrieval", ***IEEE Transactions on Image Processing***, Vol. 10, No. 1, (2001) 140-147, doi: 10.1109/83.892450.
11. Wang, X. Y., Yu, Y. J., and Yang, H. Y., "An effective image retrieval scheme using color, texture and shape features", ***Computer Standards & Interfaces***, Vol. 33, No. 1, (2011), 59-68, doi: 10.1016/j.csi.2010.03.004.
12. Po, L. M., and Wong, K. M., "A new palette histogram similarity measure for MPEG-7 dominant color descriptor", In 2004 International Conference on Image Processing (ICIP'04), IEEE, (2004), 1533-1536, doi: 10.1109/ICIP.2004.1421357.
13. Mojsilovic, A., Kovacevic, J., Hu, J., Safranek, R. J., and Ganapathy, S. K., "Matching and retrieval based on the vocabulary and grammar of color patterns", ***IEEE Transactions on Image Processing***, Vol. 9, No. 1, (2000), 38-54, doi: 10.1109/83.817597.
14. Fadaei, S., and Rashno, A., "Content-based image retrieval speedup based on optimized combination of wavelet and zernike features using particle swarm optimization algorithm", ***International Journal of Engineering, Transactions B: Applications***, Vol. 33, No. 5, (2020), 1000-1009, doi: 10.5829/IJE.2020.33.05B.34.
15. Pavithra, L. K., and Sharmila, T. S., "An efficient seed points selection approach in dominant color descriptors (DCD)", ***Cluster Computing***, Vol. 22, No. 4, (2019), 1225-1240, doi: 10.1007/s10586-019-02907-3.
16. Xie, G., Baolong, G., Zhe, H., Yan, Z., and Yunyi Y., "Combination of dominant color descriptor and Hu moments in consistent zone for content-based image retrieval", ***IEEE Access***, Vol. 8, (2020), 146284-146299, doi: 10.1109/ACCESS.2020.3015285.
17. Sezavar, A., Farsi, H., and Mohamadzadeh, S., "A modified grasshopper optimization algorithm combined with cnn for content-based image retrieval", ***International Journal of Engineering, Transactions A: Basics***, Vol. 32, No. 7, (2019), 924-930, DOI: 10.5829/IJE.2019.32.07A.04.
18. Irtaza, A., Adnan, S. M., Ahmed, K. T., Jaffar, A., Khan, A., Javed, A., and Mahmood, M. T., "An ensemble based evolutionary approach to the class imbalance problem with applications in CBIR", ***Applied Sciences***, Vol. 8, No. 4, (2018), 495, doi: 10.3390/app8040495.
19. Mehmood, Z., Mahmood, T., and Javid, M. A., "Content-based image retrieval and semantic automatic image annotation based on the weighted average of triangular histograms using support vector machine", ***Applied Intelligence***, Vol. 48, No. 1, (2018), 166-181, doi: 10.1007/s10489-017-0957-5.
20. Ali, N., Bajwa, K. B., Sablatnig, R., and Mehmood, Z., "Image retrieval by addition of spatial information based on histograms of triangular regions", ***Computers & Electrical Engineering***, Vol. 54, (2016), 539-550, doi: 10.1016/j.compeleceng.2016.04.002.
21. Mehmood, Z., Anwar, S. M., Ali, N., Habib, H. A., and Rashid, M., "A novel image retrieval based on a combination of local and global histograms of visual words", ***Mathematical Problems in Engineering***, (2016), doi: 10.1155/2016/8217250.
22. Zeng, S., Huang, R., Wang, H., and Kang, Z., "Image retrieval using spatiograms of colors quantized by gaussian mixture models", ***Neurocomputing***, Vol. 171, (2016), 673-684, doi: 10.1016/j.neucom.2015.07.008.
23. Walia, E., and Pal, A., "Fusion framework for effective color image retrieval", ***Journal of Visual Communication and Image Representation***, Vol. 25, No. 6, (2014), 1335-1348, doi: 10.1016/j.jvcir.2014.05.005.
24. Wang, C., Zhang, B., Qin, Z., and Xiong, J., "Spatial weighting for bag-of-features based image retrieval", In International Symposium on Integrated Uncertainty in Knowledge Modelling

and Decision Making, Springer, Berlin, Heidelberg, (2013), 91-100, doi: 10.1007/978-3-642-39515-4_8.

25. Alsmadi, M. K., "Content-based image retrieval using color, shape and texture descriptors and features", ***Arabian Journal for Science and Engineering***, Vol. 45, No. 4, (2020), 3317-3330, doi: 10.1007/s13369-020-04384-y.

Persian Abstract

چکیده

بازیابی تصویر مبتنی بر محتوی یک فرایند برای بازیابی اتوماتیک تصاویر در یک پایگاه داده است. در حقیقت بازیابی تصویر مبتنی بر محتوی، یک راه‌حل برای جستجوی تصاویر مشابه با یک تصویر مطلوب (تصویر پرس وجو) در میان تمامی تصاویر پایگاه داده است. برای این منظور، روش‌های متعددی برای استخراج ویژگی‌های تصویر ارایه شده است. در این مقاله برای بهبود دقت بازیابی تصویر، یک روش جدید مبتنی بر ویژگی‌های DCD ارایه شده است. در روش پیشنهادی، ابتدا تصویر رنگی به تصویر خاکستری تبدیل شده سپس لبه‌های تصویر به کمک لبه‌یاب کَنی آشکارسازی می‌شود. در مرحله‌ی بعد لبه‌های تصویر توسط عملیات مورفولوژی عریض می‌شوند. در نهایت در تشکیل ویژگی‌های DCD، به پیکسل‌هایی که در مکان لبه‌ها قرار دارند وزن بالاتری نسبت به دیگر پیکسل‌ها داده می‌شود. در حقیقت، به پیکسل‌هایی که در نواحی با تغییرات روشنایی کم قرار دارند وزن کمتری اختصاص می‌یابد در حالیکه پیکسل‌های با اطلاعات بالاتر وزن بیشتری خواهند داشت. به منظور ارزیابی روش پیشنهادی، نتایج پیاده‌سازی روی سه پایگاه داده‌ی Corel-1k، Coler-10k و Caltech256 ارایه شده است. نتایج نشان می‌دهند که روش پیشنهادی قابل رقابت با دیگر روش‌ها است.

IJE TRANSACTIONS B: Applications Vol. 35, No. 08, (August 2022) 1468-1478

International Journal of Engineering

Journal Homepage: www.ije.ir

Generator Scheduling Optimization Involving Emission to Determine Emission Reduction Costs

K. M. D. Puspitasari, J. Raharjo*, A. S. Sastrosubroto, B. Rahmat

School of Electrical Engineering, Telkom University, Bandung, Indonesia

P A P E R I N F O

Paper history:
Received 21 February 2022
Received in revised form 11 March 2022
Accepted 14 March 2022

Keywords:
Generator Scheduling
Emission Costs
Simulated Annealing
Java-Bali Power System

A B S T R A C T

Climate change, greenhouse gases, and global warming are global issues today. Of course, this global issue cannot be separated from the issue of emissions. Various methods to solve generator scheduling problems by considering emissions or Economic Emission Dispatch (EED) have been published, but not to the extent of calculating the cost to reduce emissions. The main objective of this research is to determine the cost of reducing the emission of electricity generation in Indonesia through solving the EED problem. The method proposed to solve the EED problem is an annealing simulation algorithm and tested using an electrical system of eight generators, four different loads, and five combinations of cost and emission weights. This method is tested with various loads (conditions), and each condition is tested with various combinations of cost weights and emission weights. The obtained results were compared with the results of the calculation of the Cuckoo algorithm, and the whale optimization algorithm. The simulation results show that it costs US$258.81 to reduce 1 ton of emissions. This paper can be used as a material for further consideration for the government and generator providers in making policies related to the operation of power plants by considering emissions.

***doi**: 10.5829/ije.2022.35.08b.02*

NOMENCLATURE

ABC	Artificial bee colony	*MOMA*	Multi-objectivemetaheuristic algorithm
ANN	Artificial neural network	*MOPSO*	Multi-objective particle swarm optimization
BoMM	Bi-objective mathematical model	*MOO*	Multi-objective optimization
CA	Cuckoo algorithm	*MOOHE*	Multi-objective optimal heat exchange
CO2	Carbon dioxide	*MOSTES*	Multi-objective solar thermal energy storage
CSOA	Cuckoo search optimization algorithm	*MW*	Mega watt
DE	Differential evolution	*NN*	Neural network
DECQPSO	Differential evolution crossover Quantum particle swarm optimization	*NPGA*	Niched pareto genetic algotithm
ED	Economic dispatch	*NRGA*	Non-dominated ranked genetic algorithm
EED	Economic emission dispatch	*NSGA*	Non-dominated sorting genetic algorithm
EPS	Electric power system	*PSO*	Particle swarm optimization
EPSA	Enhanced particle swarm algorithm	*QPSO*	Quantum particel swarm optimization
FA	Firefly algorithm	*SA*	Simulated annealing
FO	Objective function of EED	*SAA*	Simulated annealing algorithm
GA	Genetic algorithm	*SOA*	Spiral optimization algorithm
GEP	Gene expression programming	*WOA*	Whale optimization algorithm
GHG	Greenhouse gases	a_i, b_i, c_i	Cost coefficient of the unit generator-i
GO	Global optimization	d_i, e_i, f_i	Emission coefficient of the unit generator-i
GSA	Gravitational search algorithm	FC_i	The cost function of generator-i
HMGOA	Hybrid modified grasshopper optimization algorithm	FE_i	Emission function of generator-i
IDR	Indonesian rupiah (Indonesian Currency)	P_D	Load demand
MA	Metaheuristic algorithm	P_i	The output power of generator-i
MAGO	Metaheuristic algorithm for global optimization	$P_{i,max}, P_{i,min}$	Maximum & minimum limit of generator output power-i
MBFA	Modified bacterial foraging algorithm	*P(t)*	The decrement power at time t

*Corresponding Author Institutional Email:
jangkungraharjo@telkomuniversity.ac.id (J. Raharjo)

Please cite this article as: K. M. D. Puspitasari, J. Raharjo, A. S. Sastrosubroto, B. Rahmat, Generator Scheduling Optimization Involving Emission to Determine Emission Reduction Costs, ***International Journal of Engineering, Transactions B: Applications***, Vol. 35, No. 08, (2022) 1468-1478

MHSA	Modified harmony search algorithm	w_C, w_S	Weight of cost, weight of emission
MODE	Multi-objective differential evolution	α	A constant close to 1
MOFA	Multi-objective firefly algorithm	β	A very small value

1. INTRODUCTION

Climate change, greenhouse gases, and global warming are global issues today. Climate change is the biggest problem facing humankind in recent decades, one of the main causes of GHG. To mitigate it, an international agreement has been proposed in Paris 2016, known as COP21 by some countries [1]. Climate change is also a major challenge in local markets with its potentially harmful effects on the agricultural sector [2]. Research on emissions related to oil consumption, energy use, and economic growth, such as those conducted and reported in the literature [3, 4], as well as emissions associated with power generation [5], have been published.

The issue of environmental sustainability has also become a strategic issue recently. Various activities carried out by the community have started to care about the environment. Likewise, many studies focused on the environment, such as Fasihia et al. [6] and Chouhan et al. [7]. Development of a BoMM for designing a closed loop fish supply [6].

The relationship between economic growth, oil consumption, and emissions in Thailand using ARDL and Granger causality approach has been studied [8] used in this study are annual data from 1971 to 2014. Higher incomes and economic growth can increase CO_2 emissions in the long term [4].

Conventionally, optimizing the fuel mixture for the EPS components does not involve emission costs in the electrical system [5], so it is necessary to involve the costs of greenhouse gas emissions into the fuel cost function for power flow optimization calculations. Meanwhile [8] developed a new hybrid metaheuristic algorithm called Hybrid of WOA and SA, called HWS based on WOA and SA to Solve the optimization problem of production-distribution network taking into account carbon emissions, where the result is better than using WOA alone or SA only.

Optimization of multi-objective problems was also carried out by Fard et al. [9] for modeling and MOOHE through the Tube Bank using NN and GA. Many artificial methods have been implemented in the area of the power system, such as the work done by Sadafi et al. [10] in optimizing MOSTES using hybrid PSO, multiple crossovers, and operator mutation.

As the fourth largest country globally in terms of the population[1], Indonesia requires electrical energy consumption that continues to increase significantly from year to year. Indonesia has enormous potential for renewable energy sources, but until now, the contribution of renewable energy sources is still low compared to fossil energy sources. So that most of the power plants in Indonesia are still dominated by fossil fuels.

Various efforts have been made, including, for a long time, Indonesia has had a ministry specifically dealing with energy and mineral resources, the establishment of a national energy council, the government has targeted the energy mix from renewable energy sources in 2025 and 2050 at 23 and 31%, respectively (The Presidential Regulation No.22/2017). On the other hand, many publications have been related to optimizing generator scheduling, which is to obtain the cheapest fuel costs and consider the resulting low emissions, known as EED. Many research results have been published to solve the EED problem, namely solving the multi-objective optimization problem between costs and emissions using various methods based on metaheuristic algorithms.

Metaheuristic algorithms are divided into four, namely: evolutionary algorithms, physics-based algorithms, herd-based algorithms, and human-based algorithms [11]. Research on solving EED problems based on evolutionary algorithms such as genetic algorithms has been studied [12, 13]. This multi-objective problem becomes more complex in large-scale power systems because it is difficult to find an optimal solution. After all, it is a non-smooth and non-convex function and contains several local optima [13]. Using a NRGA can overcome the problem of convergence in GA, which is still slow and computational complexity is higher in solving EED problems [14].

Physics-based algorithms, such as the GSA, have been reported by Radosavljević, [14] to solve the EED problem. The simulation results show that the GSA approach provides a high-quality solution that is effective and better or comparable to that obtained data using other techniques such as GA, NSGA, NPGA, differential evolution (DE), MODE, ABC, PSO, MOPSO, SOA, and MBFA.

The metaheuristic method is used in a wide field because it can solve optimization problems on differentiable and non-differentiable functions. Projectiles Optimization: A Novel MAGO [15]. The fruit fly algorithm was applied to the Multi-Objective Unload Scheduling [16].

The application of the EPSA for supporting structure modal optimization is carried out by Shijing et al. [17]. Application of HMGOA and GA to detect and prevent DDoS Attacks [18]. Optimizing the placement of Bank Voltage Regulators and Capacitors based on FSM and MMOPSO [19]. Optimization of the Rubber Compound

[1] https://www.statista.com/statistics/262879/countries-with-the larges-population

Design Process was conducted Using Artificial Neural Networks and Genetic Algorithms [20].

Modification of PSO-ANN and GEP to predict high-temperature oxidation behavior of Ni–Cr–W-Mo alloys [21]. Design of a multi-objective sustainable drug supply chain network using novel hybrid MOMA [22]. Parameter identification based on PSO applied to target tracking robot with flexible cation Isotherm Models for the Adsorption of H_2, N_2, CO, CH_4, and CO_2 Using the CSOA [23]. The MOO of Multi-vehicle Relief Logistics Considering Satisfaction Levels gone under Uncertainty [24].

Meanwhile, SA as a metaheuristic method has been widely used in solving optimization. SA is known as an effective single-point metaheuristic algorithm for finding global solutions in the presence of a large number of local optima. This concept evolved from the thermodynamics of the heating and cooling behavior of metals in which the metal is first heated to a certain temperature and cooled slowly. The implementation of this algorithm is very simple. Quests are based on random movement which is very similar to hill climbing. Initially, it was chosen a bad move instead of a good move. If the selected move fixes the solution, it is always accepted. Otherwise, the move will be considered based on a random probability of less than one to avoid falling into the local minimum.

Hybrid method between SA and other methods such as H-GASA, hybrid of GA with SA, H-KASA, hybrid of Keshtel Algorithm with SA, and H-RDASA, hybrid of Red Deer Algorithm with Simulated Annealing to handle the complexity of problems in sugarcane-based product supply chain network [25]. The application of SA to a sustainable sugarcane supply chain network taking into account the carbon tax on emissions from the industry was studied [7].

Solving the EED problem using a swarm-based algorithm such as PSO has also been proposed [26-28]. The MOPSO algorithm to solve the EED problem shows advantages in terms of the diversity of the Pareto optimal solutions obtained and produces high-quality non-dominant solutions [26]. Modulated PSO (MPSO) is a modification of conventional PSO by modulating particle velocity for better exploration and exploitation of search space, is proposed [28]. MPSO gives promising results for solving the EED problem compared to its comparison methods.

Meanwhile, the hybrid DE-CQPSO method resulted in fast convergence of the DE algorithm and the diversity of the genetic crossover algorithm operator particles. The parameter adaptive control method updates the crossover probability to get better optimization results. Moreover, the MOO problem is solved by introducing a penalty factor. The experimental results show that: the evaluation index and convergence speed of the DE-CQPSO algorithm is better than QPSO and other algorithms, be it single-objective optimization of fuel costs and emissions or multi-objective optimization considering both optimization objectives. A good compromise value was verified, which verifies the effectiveness and robustness of the DE-CQPSO algorithm in solving environmental, economic dispatch problems [29].

Planning and scheduling problems are the most significant problems in the world and have a major impact on increasing productivity [30]. Likewise, with optimization problems, especially applied in the field of power systems. The paper that introduced the theory of genetic algorithms into the control strategy used in the switching chain in wind turbines was studied [31], providing improved performance and efficiency. Hybrid GA for Integrated Production and Distribution Scheduling Problems with Allowed Outsourcing [32]. Such as the case is with optimizing power plant scheduling.

Research to reduce emissions has also been published such as the Emission Reduction Strategy for Small Single Cylinder Diesel Engines Using Valve Timing and Swirl Ratio [33]. The MHSA is a modification of the harmony search algorithm (HSA) as part of an artificial human-based algorithm proposed to solve the EED problem [34]. MHSA can provide a search for a more diverse solution space during the early stages of interim evolution and has been successfully applied to solve EEDs involving all constraints [35].

The solution of EED using a simulated annealing algorithm has been published [36], where the simulation results show a 20.14% reduction in the total fuel cost compared to the classical method of distributing power generation. This method assists the expert in preventive maintenance decision-making of machine downtime during multi-objective optimization, improving generation yields and emission reductions.

Solving the EED problem with the case of the electricity system in Indonesia has also been studied [37, 38]. Generator scheduling by considering emissions using MOPSO gives better results than the MOFA [37]. Meanwhile, the use of CA, FA and PSO algorithms for optimization of generator scheduling has been studied [38].

The main objective of this study is to determine the cost of reducing power generation emissions in Indonesia through solving the EED problem. The proposed method for solving the EED problem is a simulated annealing algorithm. The electrical system that is the test object is the 500 kV, 25 bus electrical system, Java-Bali, Indonesia. So far, many kinds of research on optimizing generator scheduling have only stopped at the EED results. On the other hand, the determination of the cost of reducing power plant emissions so far has not been through optimization of generator scheduling (EED). The novelty of this research is to determine the additional cost in reducing

emissions through optimization of power plant scheduling (EED).

This paper consists of 4 main parts. The first part discusses the scheduling of power plants by considering emissions or known as EED. The second section briefly discusses the proposed method. The third part presents the simulation results and discussion, and the last part presents the conclusions.

2. ECONOMIC EMISSION DISPATCH

The EED was an optimization problem with two objectives: minimizing the total cost of generation and considering emissions. The problem in this research is optimization with two objectives: minimizing the total cost of generation and considering low emissions by including the minimization of emission reduction costs. The simulation process uses the simulated annealing method by including generator scheduling and calculating emission reduction costs. Next, our process will be named X_EED.

The process diagram is shown in Figure 1 by the block diagram.

2. 1. Cost Function Fuel cost is the most dominant component in thermal power plants. The fuel cost curve is approximated by a quadratic function [34]. The first objective function in the EED problem is to minimize generation cost function in US$ per hour [36]. The fuel cost function is shown in Equation (1).

$$FC_i(P_i) = a_i + b_i P_i + c_i P_i^2 \quad (1)$$

where $FC_i(P_i)$ is a function of the cost of fuel of each generator (US$/Hours), and a_i, b_i, c_i is the cost coefficient of the unit generator i, is output power of generator i.

2. 2. Emission Function The second objective function minimizes each unit's emission function in grams per hour [20]. The emission function is shown in Equation (2).

$$FE_i(P_i) = d_i + e_i P_i + f_i P_i^2 \quad (2)$$

where $F_{Ei}(P_i)$ is the fuel emission of generator-i (grams), N is the number of generators, P_i is the active power output of the generator-i (MW), whereas d_i $[grams]$, e_i $[\frac{grams}{MW}]$, and f_i $[\frac{grams}{MW^2}]$ are the constants of input-output of generator-i.

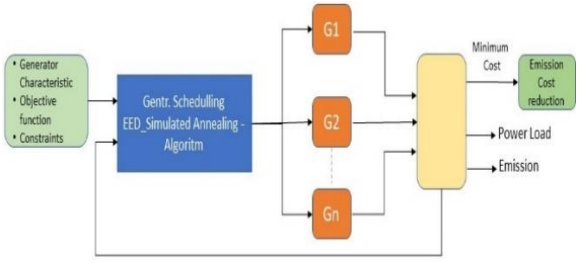

Figure 1. Generator Scheduling X_EED Simulated Annealing

2. 3. The Multi-objective Function Multi-objective optimization (MOO) consists of several goals that must be achieved simultaneously, so MOO is the process of reaching a compromise between various objective functions in a problem [37]. Because of the multi-objective function of simultaneously reducing the optimum operating emission for generating economic dispatch, these two objective functions must be combined to become the EED objective function, formulated in Equation (3).

$$FO = w_C . \sum_{i=1}^{n} FC_i(P_i) + w_S . \sum_{i=1}^{n} FE_i(P_i) \quad (3)$$

where w_C+ w_S=1 (must be worth 1) and the weighting value of w based on the priority scale to be achieved [38]. The FO is EED to minimize cost function and emission function with different weighting values.

2. 4. Constraints Economic Emissions Dispatch is inseparable from several limitations that must be complied with to stabilize the system. The power generated by the generators must be equal to the demand if the system losses are neglected, as shown in Equation (4).

$$\sum P_i = P_D \quad (4)$$

where the total supply must equal the power demand, and P_D is a request, and Pi represents the summation of power volume generated by units [39]. The generator operating limits for each generator are limited by the minimum and maximum limits, which are shown in Equation (5).

$$P_{i\,min} \le P_i \le P_{i\,max} \quad (5)$$

where Generator limit Constrains $\boldsymbol{P_i}$: Power generation unit I must be between the minimum and maximum limits. $\boldsymbol{P_{i\,min}}$ and $\boldsymbol{P_{i\,max}}$ are the minimum and maximum generation limits unit-i, respectively [36].

Ramp rate measures how fast the increase and decrease in electric power output that the generator can generate in one unit of time. This value needed to be considered because if at any time there was a peak load occurs, the ramp rate can bear the power jumps quickly. Equations (6) and (7) illustrate the ramp rate.

$$Max\,P_{min,i}, P_{i,t-1} - ramp \le P_{i,t-1} - ramp \le Min\,P_{min,i}, P_{i,t-1} + ramp \quad (6)$$

Ramp limit makes the first hour's generation automatic maximum and minimum, by Equation (7).

$$P_{min,i} = Max\big(P_{min,i}, P_{i,t-1} - ramp\big), for\ min.value$$
$$P_{max,i} = Max\big(P_{min,i}, P_{i,t-1} + ramp\big), for\ max.value \quad (7)$$

3. RESEARCH METHOD

The SAA was developed in 1980s. It was one of the first metaheuristic algorithms to be inspired by physical phenomena occurring in statistical mechanics and metallurgical engineering. A metaheuristic is a method for finding solutions that combine the interaction between local search procedures and higher-level strategies to create a process that can exit the local optimal point and search in the solution space to find the global optimal solution [40]. The SAA is an algorithmic and rhythmic word that was first revealed by Abu Ja'far Mohammed Ibn Musa al Khwarizmi (825 AD) in Al-Jabr Wa-al Muqabla. The algorithm is defined as an appropriate method consisting of a structured and written series systematically to solve a problem with the help of a computer.

Simulated Annealing is a random optimization algorithm used to simulate crystal annealing processes. The problem solution region is represented as the crystalline state of the particle. This method is very stochastic, so convergence speed is slow [41]. The SAA can also simulate, calculate, and find the optimal solution between electricity generation costs and carbon emissions [39]. Optimization of the SA method is very significant for power plant scheduling [42]. SA is a search method that utilizes probability theory to find the global minimum of a problem [36].

In the initial process of the algorithm, the initial power must be set at a higher value, to get more possibilities of acceptance for the solution to be optimized and too high initial power makes the algorithm slow and inefficient. When working with the SAA, the final power drop is generally set to zero. The SAA can take longer to run operations if the exponential power drop. Therefore, this algorithm needs a constraint that limits the iteration process of selecting the final solution. Since the initial and final powers have values defined by constraints, it is important to find the path of the change in power loss from the beginning to the end because the algorithm's success depends on it. The decrement of power at time 't'.

$$P(t) = {}^{d}/_{\log(t)} \tag{8}$$

where d is a positive constant.

$$P\ (t+1) = \alpha\ P(t) \tag{9}$$

α is a constant close to 1.

Algorithm efficiency can be increased by selecting the right number of iterations. Realization of only iterations for each power should occur at a very slow rate which can be denoted in Equation (10).

$$P(t) = {}^{t}/_{(1+\beta t)} \tag{10}$$

4. RESULTS AND DISCUSSION

4. 1. Java-Bali Electricity System The simulated annealing method was tested on the Java-Bali interconnection electrical system with four load variations. Record power data used for simulations on the Java-Bali Grid 500 kV generating system was taken on June 9, 2014, and divided into four times, namely at 18:00 with 13,096 MW, 19:00 with 13,108 MW, 20:00 with 12,863 MW, and 21:00 with 12,228 MW [34]. The analysis of the Economic Emission Dispatch simulation using the SA algorithm on the Java-Bali 500 kV electrical system based on the 2015-2024 RUPTL Objective Function, shows that the amount of power generated from the simulation process of each generating unit is very dependent on the objective cost function and objective emission function.

One-line diagram 500kV electrical system, Java-Bali, Indonesia consists of 25 buses, of which eight are generator buses. Of the eight generator buses, there are two hydroelectric power plants (PLTA) and the remaining six steam power plants (PLTU). The characteristics of generators are shown in Table 1, and the single line diagram of EPS is shown in Figure 2.

In EPS, generation must not exceed the ramp limit for each generator. The characteristic of each generator shown is Table 1.

TABLE 1. The Generators Characteristic

Generator	a_i	b_i	c_i	d_i	e_i	f_i	$P_{i,min}$ (MW)	$P_{i,max}$ (MW)	Ramp Rate (MW/h)
P_1	57,543,208.0	3,332,794.0	-400.0	34,251,909.8	1,983,806.2	-236.7	1,610.0	4,200.0	300
P_2	519,353,767.1	3,047,098.0	691.0	72,202,664.7	423.6	96.2	934.0	2,308.0	510
P_3	0.0	400.0	0.0	0.0	0.0	0.0	404.0	1,008.0	930
P_4	0.0	660.0	0.0	0.0	0.0	0.0	208.0	700.0	660
P_5	133,177,025.6	2,828,349.0	-80.0	93,654,729.7	1,988,993.9	-56.9	848.0	2,400.0	337
P_6	180,205,527.9	2,104,640.0	218.0	123,428,443.8	1,441,534.9	149.5	1,080.0	4,714.0	420
P_7	140,621,312.5	2,545,832.0	203.0	140,621,312.5	2,545,832.5	62.1	360.0	900.0	240
P_8	112,522,922.1	5,877,235.0	-73.0	24,146,549.8	1,261,209.3	-15.8	305.0	1,610.0	420

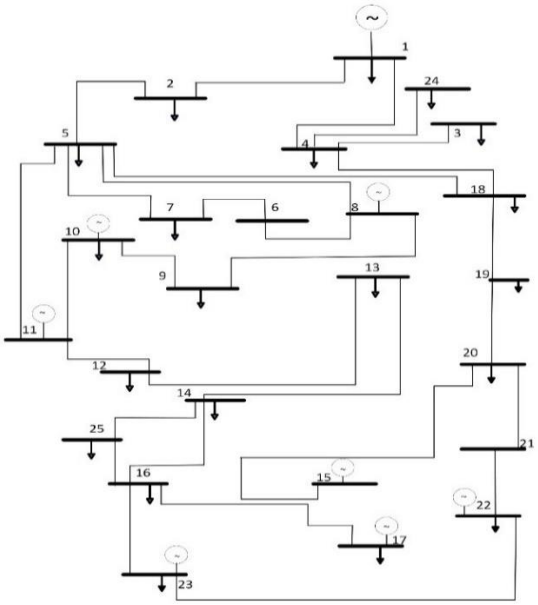

Figure 2. Java-Bali Electricity Systems

In each condition or at each load test, carried out with 5 variations of the combination of cost weight (w_C) and emission weight (w_S) as shown in Table 2.

4. 2. Economic Emission Dispatch Results The simulation was carried out using the MATLAB R2018b software. MATLAB R2018b software. The iteration process is shown in Figures 3 to 6.

TABLE 2. Weighted Value

Condition	w_C	w_S
I	1.00	0.00
II	0.75	0.25
III	0.50	0.50
IV	0.25	0.75
V	0.00	1.00

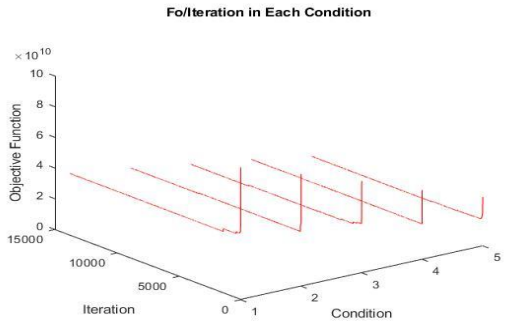

Figure 3. Iteration in each first-hour condition

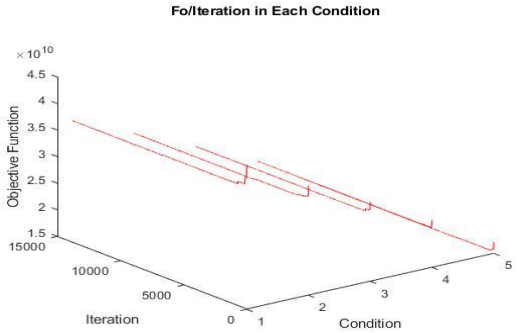

Figure 4. Iteration in each-second hour condition

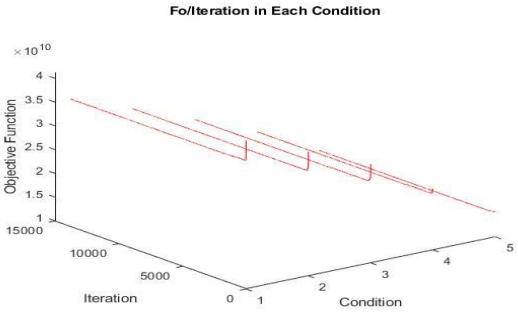

Figure 5. Iteration in each third-hour condition

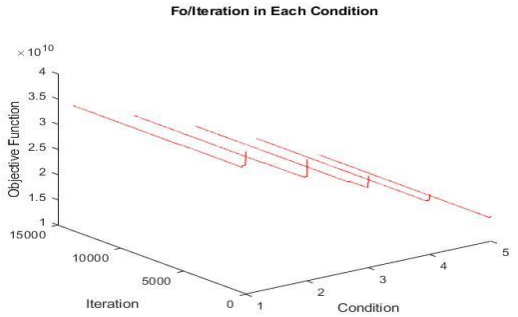

Figure 6. Iteration in each forth-hour condition

The total costs and emissions for various conditions and times are shown in Tables 3, 4, and 5. The results of the EED simulation using SA are shown in Table 3. The cost of power generation has been converted from Indonesian currency (IDR) to US$ (assuming an exchange rate of US$1=IDR 14385), on March 6, 2022. Table 3 power generated by each generator in optimal conditions. The power generated in supplying the load meets the limits of Equations (4) and (5), so that no generator operating limit is violated. Meanwhile, Table 4 shows the rate of change of power for each generator which is also appropriate with the constraints.

Table 5 shows additional costs required to reduce emissions. It costs US$ 255.81 to reduce 1 ton of

TABLE 3. Total Cost and Emission per Hour

Condition	Time	Load (MW)	Generator Power (MW)								Power (MW)	Cost (US$)	Emission (tons)
			P_1	P_2	P_3	P_4	P_5	P_6	P_7	P_8			
I	18:00	13096	3109	934	1008	700	2030	3823	900	592	13096	2,338,676	19,034
	19:00	13108	3099	934	1008	700	2031	3843	900	593	13108	2,343,912	19,084
	20:00	12863	3099	801	998	700	2013	3812	898	542	12863	2,272,440	18,881
	21:00	12228	3025	589	998	700	2013	3465	898	540	12228	2,118,992	17,933
Average												2,268,505	18,733
II	18:00	13096	3180	1008	1008	700	1831	3823	859	687	13096	2,360,357	18,740
	19:00	13108	3081	934	1008	700	2027	3865	900	593	13108	2,347,927	19,125
	20:00	12863	3082	801	998	700	2022	3810	900	550	12863	2,276,096	18,898
	21:00	12228	2998	571	998	700	2013	3465	898	585	12228	2,130,572	17,972
Average												2,278,738	18,684
III	18:00	13096	3168	1008	1008	700	1812	3812	831	757	13096	2,375,926	18,685
	19:00	13108	3080	917	1008	700	2026	3865	900	612	13108	2,350,227	19,143
	20:00	12863	3071	801	998	700	2022	3814	900	557	12863	2,279,298	18,911
	21:00	12228	2974	571	998	700	2019	3465	900	601	12228	2,136,887	17,994
Average												2,285,584	18,683
IV	18:00	13096	3110	1008	1008	700	1843	3823	839	765	13096	2,385,771	18,771
	19:00	13108	3080	902	1008	700	2018	3865	900	635	13108	2,353,597	19,155
	20:00	12863	3067	800	996	700	2017	3818	900	565	12863	2,282,165	18,921
	21:00	12228	3002	571	968	700	2019	3444	900	624	12228	2,142,704	17,986
Average												2,291,059	18,708
V	18:00	13096	3110	999	1008	700	1827	3815	839	798	13096	2,391,302	18,760
	19:00	13108	3054	887	1008	700	2005	3850	900	704	13108	2,369,050	19,162
	20:00	12863	3050	806	996	700	2012	3818	900	581	12863	2,288,425	18,924
	21:00	12228	2998	571	968	700	2003	3405	900	683	12228	2,153,616	17,933
Average												2,300,598	18,609

TABLE 4. Rate of Power Change

Gen	Rate of Power Change															Ramp rate (MW/h)
	Cond. I			Cond. II			Cond. III			Cond. IV			Cond. V			
	18:00 to 19:00	19:00 to 12:00	20:00 to 21:00	18:00 to 19:00	19:00 to 12:00	20:00 to 21:00	18:00 to 19:00	19:00 to 12:00	20:00 to 21:00	18:00 to 19:00	19:00 to 12:00	20:00 to 21:00	18:00 to 19:00	19:00 to 12:00	20:00 to 21:00	
P_1	10	0	74	0	-1	84	88	9	97	30	13	65	56	4	52	300
P_2	0	133	212	74	133	230	91	116	230	106	102	229	112	81	235	510
P_3	0	10	0	0	10	0	0	10	0	0	12	28	0	12	28	930
P_4	0	0	0	0	0	0	0	0	0	0	0	0	0	0	0	660
P_5	-1	18	0	-196	5	9	-214	4	3	-175	1	-2	-178	-7	-1	337
P_6	-20	31	147	-42	55	345	-53	51	349	-42	47	374	-35	32	413	420
P_7	0	2	96	-41	0	2	-69	0	0	-61	0	0	-61	0	0	240
P_8	-1	51	2	94	43	-35	145	55	-44	130	70	-59	94	123	-102	420

TABLE 5. Additional Cost to Reduce Emissions

Condition	w_C	w_S	Cost (US$)	Emission (tons)	Emission Reduction (tons)	Additional Cost (US$)	Additional cost/tons of emission reduction (US$)
I	1	0	2,268,505	18,733	-	-	-
II	0.75	0.25	2,278,738	18,684	49	10,233	208.84
III	0.5	0.5	2,285,584	18,683	50	17,079	341.58
IV	0.25	0.75	2,291,059	18,670	63	22,554	358.00
V	0	1	2,300,598	18,609	124	32,093	258.81

emissions. The execution time required for EED with eight generators is still under 1 minute. This is of course still quite feasible to be applied to the generator schedule for the next 1 hour, where generally the generator schedule is 1 hour ahead.

The simulation results of the SA method compared to other methods are shown in Table 6. In terms of generation costs, the SA method has the best performance compared to Cuckoo and WOA. Meanwhile, in terms of emissions, the WOA method has the best performance. Compared to the Cuckoo algorithm, SA is able to provide a cost-performance improvement of up to 10.568% and an emission performance improvement of up to 11.493%.

Meanwhile, when compared with WOA, SA provides a cost-performance improvement of up to 12.75%, but related to emission performance, WOA has better performance than SA as shown in Table 7.

TABLE 6. Comparison Results

Condition	Time	Load (MW)	SA		CA		WOA	
			Cost (US$)	Emission (tons)	Cost (US)	Emission (tons)	Cost (US$)	Emission (tons)
I	18:00	13096	2,338,676	19,034	2,394,530	19,791	2,341,963	17,632
	19:00	13108	2,343,912	19,084	2,471,776	20,173	2,341,963	17,544
	20:00	12863	2,272,440	18,881	2,506,295	22,502	2,336,913	17,338
	21:00	12228	2,118,992	17,933	2,339,840	21,079	2,247,200	16,494
Average			2,268,505	18,733	2,428,110	20,886	2,317,010	17,252
II	18:00	13096	2,360,357	18,740	2,457,356	19,205	2,507,661	17,865
	19:00	13108	2,347,927	19,125	2,369,426	19,470	2,342,943	17,114
	20:00	12863	2,276,096	18,898	2,267,626	17,906	2,302,329	16,775
	21:00	12228	2,130,572	17,972	2,224,815	18,163	2,282,456	16,603
Average			2,278,738	18,684	2,329,806	18,686	2,358,847	17,089
III	18:00	13096	2,375,926	18,685	2,561,731	19,779	2,633,410	16,897
	19:00	13108	2,350,227	19,143	2,477,518	21,519	2,350,769	15,893
	20:00	12863	2,279,298	18,911	2,432,040	19,571	2,308,521	15,462
	21:00	12228	2,136,887	17,994	2,277,238	18,085	2,298,513	15,373
Average			2,285,584	18,683	2,437,132	19,739	2,397,803	15,906
IV	18:00	13096	2,385,771	18,771	2,670,662	19,536	2,713,948	16,068
	19:00	13108	2,353,597	19,155	2,563,233	20,013	2,481,338	15,543
	20:00	12863	2,282,165	18,921	2,503,692	18,953	2,481,323	15,543
	21:00	12228	2,142,704	17,986	2,393,588	19,193	2,481,299	15,543
Average			2,291,059	18,670	2,532,794	19,424	2,539,477	15,674
V	18:00	13096	2,391,302	18,760	2,565,745	16,869	2,708,014	15,729
	19:00	13108	2,369,050	19,162	2,634,074	17,347	2,735,308	16,215
	20:00	12863	2,288,425	18,924	2,555,360	16,759	2,497,764	15,310
	21:00	12228	2,153,616	17,933	2,419,741	15,359	2,434,584	15,178
Average			2,300,598	18,609	2,543,730	16,584	2,593,917	15,608

TABLE 7. Performance Comparison

Con	Cost (US$)			Δ_{SA-CA}		Δ_{SA-WOA}		Emission (tons)			Δ_{SA-CA}		Δ_{SA-WOA}	
	SA	CA	WOA	US$	%	US$	%	SA	CA	WOA	tons	%	tons	%
I	2,268,505	2,428,110	2,317,010	-159,605	-7.036	-48,505	-2.138	18,733	20,886	17,252	-2,153	-11.493	1,481	7.906
II	2,278,738	2,329,806	2,358,847	-51,068	-2.241	-80,109	-3.515	18,884	18,686	17,089	198	1.049	1,795	9.505
III	2,285,887	2,437,132	2,397,803	-151,245	-6.616	-111,916	-4.896	18,683	19,739	15,906	-1,056	-5.652	2,777	14.864
IV	2,291,059	2,532,794	2,539,477	-241,735	-10.551	-248,418	-10.843	18,670	19,424	15,674	-754	-4.039	2,996	16.047
V	2,300,598	2,543,730	2,593,917	-243,132	-10.568	-293,319	-12.750	18,609	16,584	15,608	2,025	10.882	3,001	16.127

5. CONCLUSION AND FUTURE WORK

From the optimization of the generator scheduling by considering emissions, it can be calculated the additional costs needed to reduce emissions. This study proposes to calculate the cost of reducing emissions from the operation of a power plant through optimization of generator scheduling by considering emissions or optimization of EED using SA.

This method was tested on Java-Bali electricity system, Indonesia, and tested with 4 different loads where each load is calculated for various combinations of fuel costs and emissions. The simulation results and calculations were compared with other methods, the Cuckoo and WOA algorithms. From the simulation results and calculations, to reduce 1 ton of electricity generation emissions, an additional cost of US$258.81 is required. The results of this study can be considered in formulating policies related to emission restrictions in the operation of power plants. On the one hand, limiting generator emissions follows the international spirit of controlling the greenhouse effect. On the other hand, emission restrictions on the operation of power plants will certainly provoke protest reactions from generator providers. So, there needs to be a wise policy; for example, the government provides support to managers or providers of power plants that reduce emissions in the operation of their plants. Government support can be in the form of tax breaks, financial assistance, or other forms of incentives. For this reason, it is deemed necessary to have an academic text or policy text that examines the matter in more detail by taking into account the interests of stakeholders as a whole.

Future work can be explained as follows: this research is still limited to testing with four consecutive loading hours, involving eight generators, and five combinations of cost and emission weights. Further, this research needs to be applied to a large-scale electrical system, tested with more varied loads and more (for example daily load), with a combination of cost and emission weights with a smaller observation range, to get more accurate results. In addition, for better optimization results in the future, the SA algorithm was developed by applying the SA concept based on predictive control.

6. REFERENCES

1. Ramírez-Tovar, A., Moreno, R. and Carrillo-Rodríguez, L.A., "The colombian energy policy challenges in front of climate change", ***International Journal of Energy Economics and Policy***, Vol. 11, No. 6, (2021), 401, doi: 10.32479/ijeep.10517.
2. Mumuh, M.Z., Herlina, N., Falah, M., Saringendyanti, E., Sofianto, K. and Zin, N.M., "Impact of climate change on agriculture sector of malaysia", ***International Journal of Energy Economics and Policy***, Vol. 11, No. 6, (2021), 138, doi: 10.32479/ijeep.10939.
3. Bunnag, T., "The causal relationship among CO_2 emission, oil consumption and economic growth in thailand: Ardl bound testing approach", ***International Journal of Energy Economics and Policy***, Vol. 11, No. 6, (2021), 427, doi: 10.32479/ijeep.11811.
4. Shaari, M.S., "The impacts of rural population growth, energy use and economic growth on CO_2 emissions", ***670216917***, (2021), doi: 10.32479/ijeep.11566.
5. Mardiyanto, I.R., Zein, H. and Soeprijanto, A., "Combining parameters of fuel and greenhouse gas costs as single objective function for optimization of power flow", ***Telkomnika***, Vol. 15, No. 4, (2017), 1585-1600, doi: 10.12928/TELKOMNIKA.v15i4.5769.
6. Fasihi, M., Tavakkoli-Moghaddam, R., Najafi, S.E. and Hajiaghaei-Keshteli, M., "Developing a bi-objective mathematical model to design the fish closed-loop supply chain", ***International Journal of Engineering***, ***Transaction B: Applications,*** Vol. 34, No. 5, (2021), 1257-1268, doi: 10.5829/IJE.2021.34.05B.19.
7. Chouhan, V.K., Khan, S.H. and Hajiaghaei-Keshteli, M., "Sustainable planning and decision-making model for sugarcane mills considering environmental issues", ***Journal of Environmental Management***, Vol. 303, (2022), 114252, doi: 10.1016/j.jenvman.2021.114252.
8. Mehranfar, N., Hajiaghaei-Keshteli, M. and Fathollahi-Fard, A.M., "A novel hybrid whale optimization algorithm to solve a production-distribution network problem considering carbon emissions", ***International Journal of Engineering***, ***Transaction C: Aspects,*** Vol. 32, No. 12, (2019), 1781-1789, doi: 10.5829/ije.2019.32.12c.11.
9. Fard ,N.A., Hajiloo, A. and Tohidi, N., "Using neural network and genetic algorithm for modeling and multi-objective optimal heat exchange through a tube bank", doi: 10.5829/idosi.ije.2012.25.04c.07.

10. Sadafi, M., Hosseini, R., Safikhani, H., Bagheri, A. and Mahmoodabadi, M., "Multi-objective optimization of solar thermal energy storage using hybrid of particle swarm optimization and multiple crossover and mutation operator", (2011), doi: 10.5829/idosi.ije.2011.24.04b.07.
11. El-Henawy, I. and Abdelmegeed, N.A., "Meta-heuristics algorithms: A survey", ***International Journal of Computer Applications***, Vol. 179, No. 22, (2018), 45-54, doi: 10.5120/ijca2018916427.
12. Arthur, J.K., Frimpong, E.A. and Adjei, J.O., "Optimization algorithms for solving combined economic emission dispatch: A review", in Proceedings of the World Congress on Engineering and Computer Science. (2019), 22-24.
13. Gopalakrishnan, R. and Krishnan, A., "An advanced genetic optimization algorithm to solve combined economic and emission dispatch problem", ***Bonfring International Journal of Man Machine Interface***, Vol. 2, No. 1, (2012), 11-19.
14. Radosavljević, J., "Gravitational search algorithm for solving combined economic and emission dispatch", in Proc. XIV Int. Scientific-Professional Symposium Infoteh. (۲۰۱۵).
15. Kahrizi, M. and Kabudian, S., "Projectiles optimization: A novel metaheuristic algorithm for global optimization", ***International Journal of Engineering***, ***Transaction A: Basics,*** Vol ,۳۳ .No. 10, (2020), 1924-1938, doi: 10.5829/ije.2020.33.10a.11.
16. Yuan, G., Yang, Y., Tian, G. and Fathollahi-Fard, A.M., "Capacitated multi-objective disassembly scheduling with fuzzy processing time via a fruit fly optimization algorithm", ***Environmental Science and Pollution Research***, (2022), 1-18, doi: 10.1007/s11356-022-18883-y.
17. Shijing, D., Hongru, C., Xudong, W., Deshi, W. and Yongyong, Z., "Modal optimization design of supporting structure based on the improved particle swarm algorithm", ***International Journal of Engineering***, ***Transaction A: Basics,*** Vol. 35, No. 4, (2022), 740-749, doi: 10.5829/ije.2022.35.04a.14.
18. Mohammadi, S. and Babagoli, M., "A hybrid modified grasshopper optimization algorithm and genetic algorithm to detect and prevent ddos attacks", ***International Journal of Engineering***, ***Transaction A: Basics,*** Vol. 34, No. 4, (2021), 811-824, doi: 10.5829/ije.2021.34.04a.07.
19. Shafiee, M., Amirahmadi, M., Farzinfar, M. and Lapthorn, A., "Voltage stability improvement in optimal placement of voltage regulators and capacitor banks based on fsm and mmopso approach", ***International Journal of Engineering***, ***Transaction A: Basics,*** Vol. 34, No. 4, (2021), 881-890, doi: 10.5829/ije.2021.34.04a.14.
20. Ghaffarian, N. and Hamedi, M., "Optimization of rubber compound design process using artificial neural network and genetic algorithm", ***International Journal of Engineering***, ***Transaction B: Applications,*** Vol. 33, No. 11, (2020), 2319-2326, doi: 10.5829/ije.2020.33.11b.22.
21. Hasibi, H., Mahmoudian, A. and Khayati, G., "Modified particle swarm optimization-artificial neural network and gene expression programing for predicting high temperature oxidation behavior of Ni–Cr–W-MO alloys", ***International Journal of Engineering***, ***Transaction B: Applications,*** Vol. 33, No. 11, (2020), 2327-2338, doi: 10.5829/IJE.2020.33.11B.23.
22. Goodarzian, F., Hosseini-Nasab, H. and Fakhrzad, M., "A multi-objective sustainable medicine supply chain network design using a novel hybrid multi-objective metaheuristic algorithm", ***International Journal of Engineering***, ***Transaction A: Basics,*** Vol. 33, No. 10, (2020), 1986-1995, doi: 10.5829/IJE.2020۳۳,۱۰.A.17.
23. Esfandian, H., Esfandian, N. and Rezazadeh, M., "Modeling and comparison of optimized isotherm models for H_2, N_2, CO, CH_4 and CO_2 adsorption using cuckoo search optimization algorithm", ***International Journal of Engineering***, ***Transaction B: Applications,*** Vol. 33, No. 5, (2020), 712-719, doi: 10.5829/IJE.2020.33.05B.01.
24. Beiki, H., Seyedhosseini, S., Ghezavati, V. and Seyedaliakbar, S., "Multi-objective optimization of multi-vehicle relief logistics considering satisfaction levels under uncertainty", ***International Journal of Engineering***, ***Transaction B: Applications,*** Vol. 33, No. 5, (2020), 814-824, doi: 10.5829/ije.2020.33.05b.13.
25. Chouhan, V.K., Khan, S.H. and Hajiaghaei-Keshteli, M., "Metaheuristic approaches to design and address multi-echelon sugarcane closed-loop supply chain network ,"***Soft Computing***, Vol. 25, No. 16, (2021), 11377-11404, doi: 10.1007/s00500-021-05943-7.
26. Abido, M., "Multiobjective particle swarm optimization for environmental/economic dispatch problem", ***Electric Power Systems Research***, Vol. 79, No. 7, (2009), 1 ,۱۱۱۳-۱۰۵doi: 10.1016/j.epsr.2009.02.005.
27. Xin-gang, Z., Ji, L., Jin, M. and Ying, Z., "An improved quantum particle swarm optimization algorithm for environmental economic dispatch", ***Expert Systems with Applications***, Vol. 152, (2020), 113370 ,doi: 10.1016/j.eswa.2020.113370.
28. Jadoun, V.K., Gupta, N., Niazi, K. and Swarnkar, A., "Modulated particle swarm optimization for economic emission dispatch", ***International Journal of Electrical Power & Energy Systems***, Vol. 73, (2015), 80-88, doi: 10.1016/j.ijepes.2015.04.004.
29. Maghzi, P., Mohammadi, M., Pasandideh, S. and Naderi, B., "Operating room scheduling optimization based on a fuzzy uncertainty approach and metaheuristic algorithms", ***International Journal of Engineering***, ***Transaction B: Applications,*** Vol. 35, (2022), 275-258, doi: 10.5829/IJE.2022.35.02B.01.
30. Izadi, L., Ahmadizar, F. and Arkat, J., "A hybrid genetic algorithm for integrated production and distribution scheduling problem with outsourcing allowed", ***International Journal of Engineering***, ***Transaction B: Applications,*** Vol. 33, No. 11, (2020), 2285-2298, doi: 10.5829/ije.2020.33.11b.19.
31. Jain, A., Porpatham, E. and Thipse, S., "Emission reduction strategies for small single cylinder diesel engine using valve timing and swirl ratio", ***International Journal of Engineering***, ***Transaction B: Applications,*** Vol. 33, No. 8, (2020), 1608-1619, doi: 10.5829/ije.2020.33.08b.19 .
32. Jeddi, B. and Vahidinasab, V., "A modified harmony search method for environmental/economic load dispatch of real-world power systems", ***Energy Conversion and Management***, Vol. 78, (2014), 661-675, doi: 10.1016/j.enconman.2013.11.027 .
33. Júnior, J.d.A.B., Nunes, M.V.A., Nascimento, M.H.R., Rodríguez, J.L.M. and Leite, J.C., "Solution to economic emission load dispatch by simulated annealing: Case study", ***Electrical Engineering***, Vol. 100, No. 2, (2018), 749-761, doi: 10.1007/s00202-017-0544-0 .
34. Eliezer, I., "Dynamic economic emission dispatch pada sistem transmisi jawa-bali 500 kv berdasarkan ruptl tahun 2015-2024 menggunakan metode multi-objective particle swarm optimization (MOPSO)", Institut Teknologi Sepuluh Nopember Surabaya ,(۲۰۱٦) .
35. Rahmatullah, A.D., "Pendekatan dengan cuckoo optimization algorithm untuk solusi permasalahan economic emission dispatch", Institut Teknologi Sepuluh Nopember ,(۲۰۱۷)
36. Ziane, I., Benhamida, F. and Graa, A., "Simulated annealing optimization for multi-objective economic dispatch solution", ***Leonardo Journal of Sciences***, Vol. 13, No. 25, (2014), 43-56
37. Phommixay, S., Doumbia, M.L. and Lupien St-Pierre, D., "Review on the cost optimization of microgrids via particle swarm optimization", ***International Journal of Energy and Environmental Engineering***, Vol. 11, No. 1, (2020), 73-89, doi: 10.1007/s40095-019-00332-1.

38. Daqaq, F., Ouassaid, M. and Ellaia, R., "Wind thermal economic emission dispatch solution using multi-objective backtracking search algorithm", in 2017 International Renewable and Sustainable Energy Conference (IRSEC), IEEE., (2017), 1-6.
39. Kuo, M.-T., Lu, S.-D. and Tsou, M.-C., "Considering carbon emissions in economic dispatch planning for isolated power systems: A case study of the taiwan power system", ***IEEE Transactions on Industry Applications***, Vol. 54, No. 2, (2017), 987-997, doi: 10.1109/TIA.2017.2771338.
40. Muhaddad, R.A" ,.Pengembangan algoritma simulated annealing untuk penyelesaian permasalahan alokasi pada closed loop supply chain (CLSC)", Institut Technology Sepuluh Nopember ,(٢٠١٤)
41. Lu, S.-D., Wang, M.-H., Kuo, M.-T., Tsou, M.-C. and Liao, R.-M., "Optimal unit commitment by considering high penetration of renewable energy and ramp rate of thermal units-a case study in taiwan", ***Applied Sciences***, Vol. 9, No. 3, (2019), 421, doi: 10.3390/app9030421 .
42. Wicaksono, B., Abdullah, A. and Saputra, W., "Coordination hydrothermal interconnection java-bali using simulated annealing", in IOP Conference Series: Materials Science and Engineering, IOP Publishing. Vol. 128, (2016), 012005.

Persian Abstract

چکیده

تغییرات اقلیمی، گازهای گلخانه ای و گرم شدن زمین از مسائل جهانی امروز هستند. البته این موضوع جهانی را نمی توان از بحث انتشار گازهای گلخانه ای جدا کرد. روش‌های مختلفی برای حل مشکلات زمان‌بندی ژنراتور با در نظر گرفتن انتشار گازهای گلخانه‌ای یا توزیع انتشار اقتصادی (EED) منتشر شده است، اما نه در حد محاسبه هزینه برای کاهش انتشار. هدف اصلی این تحقیق تعیین هزینه کاهش انتشار تولید برق در اندونزی از طریق حل مشکل EED است. روش پیشنهادی برای حل مشکل EED یک الگوریتم شبیه‌سازی بازپخت است و با استفاده از یک سیستم الکتریکی از هشت ژنراتور، چهار بار مختلف و پنج ترکیب وزن هزینه و انتشار آزمایش شده است. این روش با بارها (شرایط) مختلف آزمایش می شود و هر شرایط با ترکیب های مختلف وزن هزینه و وزن انتشار آزمایش می شود. نتایج به‌دست‌آمده با نتایج محاسبه الگوریتم فاخته و الگوریتم بهینه‌سازی نهنگ مقایسه شد. نتایج شبیه سازی نشان می دهد که برای کاهش ۱ تن آلاینده ها ۲۵۸.۸۱ دلار آمریکا هزینه دارد. این مقاله می تواند به عنوان ماده ای برای بررسی بیشتر برای دولت و ارائه دهندگان ژنراتور در اتخاذ سیاست های مربوط به بهره برداری از نیروگاه ها با در نظر گرفتن انتشار گازهای گلخانه ای مورد استفاده قرار گیرد.

IJE TRANSACTIONS B: Applications Vol. 35, No. 08, (August 2022) 1479-1487

International Journal of Engineering

Journal Homepage: www.ije.ir

Experimental Modal Analysis of Radiator Fan Module to Predict its Influence of Structural Characteristics on Vibration and Noise Contribution

K. Venugopal, P. Halder, V. Susarla, S. Palanivelu*

Vehicle Dynamics Laboratory, Department of Automotive Engineering, School of Mechanical Engineering, Vellore Institute of Technology, Vellore, India

PAPER INFO

Paper history:
Received 24 December 2021
Received in revised form 14 March 2022
Accepted 15 March 2022

Keywords:
Radiator Fan Module
Modal Analysis
Spectral Test
Signature Test
Sound Pressure Level

ABSTRACT

Among many accessories of a passenger car, engine cooling Radiator Fan Module (RFM) is an important source of noise and vibration. Modal parameters provide the basis for the noise generation mechanism and noise propagation phenomena. The objective of the current research work is to characterize RFM through its modal behavior to investigate the contribution of structural vibration to noise radiation during its operating state. Hence, the experimental modal analysis and the noise measurement of RFM were carried out. Additionally a finite element modal analysis of RFM was performed to validate the finite element model that can be used for vibro-acoustic and computational fluid dynamic studies. Below 500 Hz total of eight critical modal frequencies, three for fan and five for shroud are determined and between 500 Hz to 2000Hz seven modes for fan and fifteen modes for shroud were dedermined. From the correlation study, it is witnessed that the contribution of modal behaviour for noise radiation is observed with 20 dB(A) variation below 500 Hz, along the diagonal grid points whereas beyond 500 Hz the variation was negligible. Importantly, blade passing frequencies corresponding to the fan speeds between 500 to 3000 rpm were compared with resonance frequencies obtained and they do not conicide with modal frequencies.

doi: *10.5829/ije.2022.35.08b.03*

1. INTRODUCTION

Automotive Noise Vibration Harshness (NVH) is the main focus rendered by automotive industries due to tight market competition in attracting and retaining the coustomers. There are many sources of noise and vibration such as power train and transmission, tire road interaction and wind during high speeds. However, these are pronounced during mid or high speeds. During slow speed or waiting in the traffic signals, the important sources are accessories of the vehicle. Though these accessories are masked by other predominent sources one can not neglect during aforementioned situations. Among all the accessories of car, engine cooling RFM is one important system that takes care of preventing engine from over heating by pushing or pulling the air through the radiator. During its functioning, it creates tonal and braod band noise that increases with increasing speed of the fan. Air flow dynamics over the fan shroud and blades of the fan is the reason for vibro-acoustic phenomina and that forms the basis for the noise generation mechanism. Hence it is motivated to investigate structural energy transfer characteristics of RFM to identify its contribution considering it as an important noise source.

Zhu et al. [1] adopted hybrid procedure based on computational fluid dynamics and computational aero acoustics numerically to investigate automotive cooling fan sound. They considered the role of fan shroud for sound propagation followed by boundary element method to determine aerodynamic noise field of the cooling fan module. Modal behavior forms the basis to characterize structural vibrational behavior in terms of modal parameters which is essential for vibro-acoustic analysis. Liu et al. [2] investigated with the help of six

*Corresponding Author Institutional Email: psakthivel@vit.ac.in (S. Palanivelu)

Please cite this article as: K. Venugopal, P. Halder, V. Susarla, S. Palanivelu, Experimental Modal Analysis of Radiator Fan Module to Predict its Influence of Structural Characteristics on Vibration and Noise Contribution, ***International Journal of Engineering, Transactions B: Applications***, Vol. 35, No. 08, (2022) 1479-1487

degree of freedom model of an automotive condenser radiator fan module for its vibration and noise issues and concluded that the mount stiffness and natural frequencies influence the same. Baniasadi et al. [3] carried out computational aerodynamics study on cooling fan of an engine and concluded that the pressure loss depends on blockage distances and vehicle speed. The article published by Lim et al. [4] presents the importance of mass unbalance of a radiator cooling fan for its vibration during vehicle idling condition. Vibration signals of the fan blades were experimentally measured both with and without an added mass in their study. Kumar et al. [5] correlated the vehicle body vibration with radiator fan module vibration and have proved that the radiator fan module structural vibration and their modal behavior play an important role in vehicle NVH. Arefin and Islam [6] considered noise radiation characteristics as one of the validating factor for a proposed micro gas turbine for an electric truck. Rajabi et al. [7] examine the effects of blade design of an axial flow fan used for cooling electronic devices.

Wang et al. [8] and Suzuki et al. [9] proposed on noise control methods for cooling fan of a simple computer and automotive radiator fan respectively. There are many challenges to understand the noise radiation mechanisms and predication of structural behavior of the components. Jayachandran et al. [10] carried out component level simulations and testing to predict contact between fan motors mounted on fan shroud and radiator; then proposed as a requirement in designing a fan shroud to eliminate damage due to inertial movement of fan motors in low speed impacts. At certain frequencies the fan shroud assembly will resonate, and these resonating frequencies indicate the higher amplitude noise. From modal analysis, the modal frequencies, and mode shapes describe the dynamic behavior of the radiator fan and form the basis for noise generation mechanism. Hence there is a need to understand the mode shapes of the radiator fan and shroud. Authors of this paper motivated to read and understand the theory and application of modal testing from the classical text book written by Ewins [11]. Subsequently the experimenental modal analysis procedure is understood from the work published by Nijmeijer, et al. [12], Patil et al. [13], and Vervoort et al. [14] on tire modal anlaysis. There were no specific papers on experimental modal anslysis on RFM. The experimental procedure learnt from tire modal analysis is employed on RFM in the current work. Tare et al. [15] used computational fluid dynamics approach to propose an effective noise management technique for radiator cooling fan module of a passenger vehicle.

Three different setups of noise measurement were carried out, namely free space, wallmounted, and in vehicle measurement by Lu [16] in his very recent experimental research studies on installation effects on cooling fan noise. With the help of spectral decomposition technique the source strength and the energy propagation effect of the fan vibration is quantified and reported the modal behavior forms the basis of energy transfer. Application of analytical methods for the solution of free vibration study is possible theoritically. Bakhshi Khaniki and Hosseini Hashemi [17] carried out free vibration analysis of non uniform microbeams based on modifed couple stress theroy. Effect of material and geometrical parameters on natural vibration of sandwich beams were predicted for various boundary conditions by Bensahal and Nadir Amrane [18] by analytical approach. Euler-Bernoulli beam theory is used by Rezaiee-Pajand et al. [19] to predict the modal behaviour of a generalied frame for its variation in the structural properties, such as joint angles, springs' stiffness and flexural rigidity of members.

Though, this article study structural behaviour of RFM module that used in a vehicle to cool the engine on one hand, on the other hand for a whole vehicle is concern the comfort depands on not only with less noise and vibrations also depends on conditioning of the cabin. Particularly thermal energy management in electric vehicle batteries is vital and appropriate HVAC system is essential. Verma et al. [20] studied combined single effect Vapour compression system and tc-CO_2 compression refregertion system based on thermodynamic analysis. Enhanced occupant comfort and safety, lightweight materials with enhanced thermal insulation properties, and optimised vehicle energy management are important and their achivements through HVAC modelling for an electric vehicle investicated by Kapeller et al. [21]. Peng et al. [22] have applied modulation principles on both rotor and stator of the cooling fan module to control the tonal noise.

In the current project work, spectral test has been carried out on the radiator fan module to determine frequency response functions and further used to evaluate the mode shapes and corresponding natural frequencies using LMS Test Lab software. From the litereature it is understood carrying out analytical appraoch on a complex contour RFM is not viable. Hence, it is proposed to provide a finite element model of RFM for its computational fluid dynamic study. In the current work a finite element model of RFM is develpoed and validated through its modal behavior.

Numerical modal analysis has also been carried out on the RFM using ANSYS. An important objective of this work is to investigate the mode shapes of the RFM by both experimental and numerical method. The signature test has also been done on the radiator fan to predict the actual noise radiated.

2. METHODOLOGY

This work has been divided into two parts such as spectral test and the signature test. The first part is the spectral test used for experimental modal analysis and is performed to obtain the modal parameters of a radiator fan module. The mode shapes of the radiator fan obtained from FE modal analysis is validated by the experimental modal analysis. The second part is the signature test used for predicting the noise radiated from the radiator fan in near field. The methedology is presented in Figure 1. On one hand spectral test carried out to determine the modal parameters experimentally and the same has been used to validate the FE (finite element) model. On the other hand singature test carried out to measure near field noise measurement using microphone indexing procedure with rectanguler array field points. Finally, a correlation study has been carried out from inference of results to conclude the influence of force transfer charcteristics over noise radiation of RFM.

The following Figure 2a shows the fan and shroud assembly of the RFM for experimental modal analysis and its CAD model shown in Figure 2b is used for Finite Element (FE) modal analysis.

3. EXPERIMENTAL MODAL ANALYSIS

A dynamic characteristic refers to modal parameters such as natural frequencies, damping factors, and mode shapes that are required to formulate mathematical model for NVH studies of any mechanical components or components forming the system. With the help of experimental modal analysis, it is possible to convert the vibration signals of excitation given and responses measured at discrete points on a complex structure, into a set of modal parameters. This section describes the experimental set up and the procedure followed to obtain the modal parameters such as resonance frequencies and mode shapes of RFM. Figure 2 presents the measurement system that includes LMS Scadas Mobile data acquisition system, instrumented hammer and LMS Test Lab software for spectral test. There were four channels used for this experiment. First channel is reference signal channel for instrumented hammer and the other three channels used for measuring acceleration responses from various points marked on the RFM. Channel set up, Acquisition set up and Test run set up all were carefully defined. The software and the hardware communication were done with the help of LAN cord.

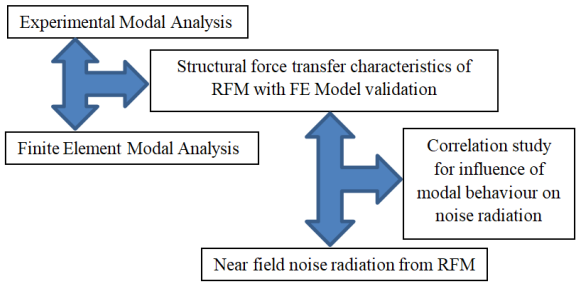

Figure 1. Methodology

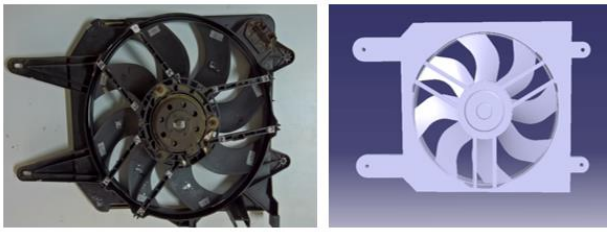

(a) Actual RFM (b) RFM CAD model

Figure 2. RFM assembly and its CAD model

3. 1. Experimental Setup for Spectral Test

The primary objective of this spectral test is to do experimental modal analysis to determine the modal parameters of the radiator fan and shroud during free vibration and is tested in a free condition. This means that the RFM is not attached to the any structure or fixed support at any of its coordinates. In practice it is not possible to make a completely free support, but it is possible to provide a system which closely relates to the free condition. The Radiator fan and shroud assembly is hung with the help of light elastic bungee cords as shown in Figure 3. ISO coordinate system of the vehicle is followed. Hence x direction is considered to be coinciding with axis of the fan and other two directions are in transverse direction to the axis as per the right hand rule. There are 51 response points marked on the radiator fan and shroud which includes the 2 excitation points, one (point 51) is on the component fan and other is (point 1) on the shroud, this is because there is no rigid connection between the fan and the shroud and fan is freely rotating and the shroud which is stationary. For each and every response point of the fan and shroud the excitation is given with the help of instrumented hammer at one point (point 1) on the shroud and other point on the fan (point 51) in all three directions.

Figure 3. Experimental setup for spectral test

However, modal analysis is performed independently for fan and shroud considering respective FRFs of the components.

Figures 4 and 5 are the graphs that shows the variation of amplitude of frequency response function and the corresponding drive point coherence function as function of frequency of both excitation points. The peaks in the FRFs refer to the resonance frequencies of the component. It is observed the good coherence exists upto 800 Hz for axial direction drive points for both fan and shroud excitation compared to that of other two direction. Beyond 800 Hz the abservation is that good coherence for the drive point exciation in transverse direction is observed for shroud point excitation compared to that of fan spindle exciation. Drive points of the shroud do have better coherence for the input compared to that of fan spindle drive points. However coherence corresponding to the peaks in frequency response function is good. This single point FRFs give the idea of resonance frequencies at just one excitation but are not sufficient to get mode shapes. All the response points FRFs are superposed to get overall FRF sum. The stabilization curve fit of the overall FRF sum is used to get modal frequencies and mode shapes using popular PolyMax algorithm. Figures 6 and 7 gives the corresponding stabilization curves.

The stabilisation diagram can be interpretated as that provides a set of poles and corresponding participation factors. Futher the mode shapes are determined from pole-redude model represented by Equation (1).

$$[H(\omega)] = \sum_{i=1}^{n} \left\{ \frac{\{v_i\}\langle l_i^T \rangle}{j\omega - \lambda_i} + \frac{\{v_i^*\}\langle l_i^H \rangle}{j\omega - \lambda_i^*} - \frac{LR}{\omega^2} + UR \right\} \quad \text{.....(1)}$$

where, n is the number of modes; v_i^* is the complex conjugate of a matrix; are the mode shapes; are the modal participation factors and are the poles, which are essentially a part of complex conjugated pairs and are relaated to the eigenfrequencies and damping ratios as given by Equation (2).

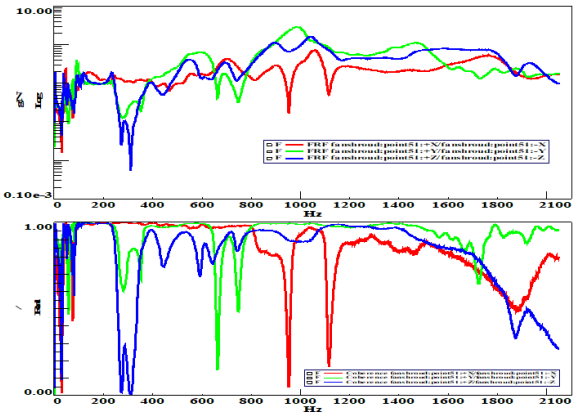

Figure 4. Variation of FRFs and Coherence Function for excitation at fan spindle

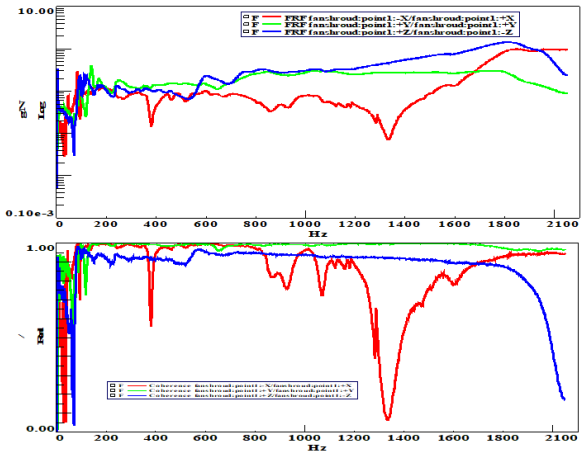

Figure 5. Variation of FRFs and Coherence Function for excitation at shroud

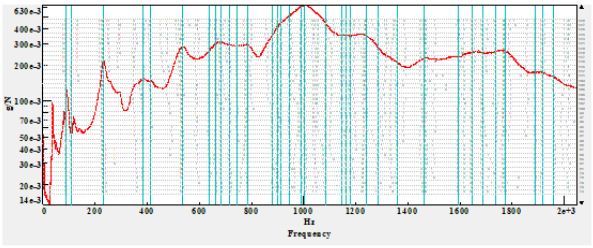

Figure 6. Stabilization curve for radiator fan for modal extraction

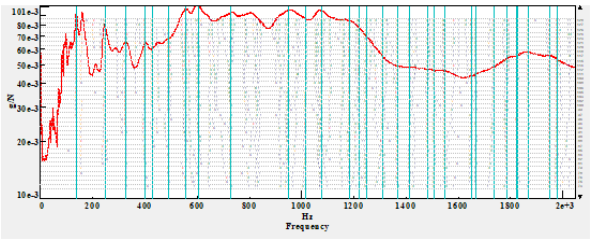

Figure 7. Stabilization curve for shroud for modal extraction

$$\lambda_i, \lambda_i^* = -\xi_i \omega_i \pm j\sqrt{1 - \xi_i^2 \omega_i} \quad \text{.....(2)}$$

LR, UR are respectively the lower and upper residuals represents the out of band moeds in the considered frequecy band. A complete theoritical aspects of PolyMax is presented by Peeters et al. [23].

The stabilization curve is very important in modal analysis which brings in the complete characteristic nature of the component tested. The model size of the curve decides the number of poles. Due to the curve fit of all FRFs there are many mathematical poles along with actual physical poles. The PolyMax algorithm along with automatic modal parameter selection picks the physical poles alone which is further verified with

modal assurance criteria and synthesized overall FRF sum. The vertical lines on the graphs are corresponding to the poles and each pole indicate the resonating frequencies of the fan and shroud respectively in the stabilization curve. Finally for all the stabilized poles the corresponding mode shapes are identified. The synthesized FRFs from the obtained modes are validating the complete experimental procedure followed. Figure 8 compares the estimated overall FRF sum obtained through impulse excitation test, with one which is synthesized from the modes obtained. This validate the experimental procedure.

3. 2. Experimental Setup for Signature Test

The signature test has been carried out in the night time when influence of environmental noise is almost negligible compared to the radiator fan noise. The fan along with the shroud is hung freely using bungee cords as shown in Figure 8. The minimum distance from the ground is maintained as 1m. A grid is prepared to position microphone to measure radiated noise in the near field. The microphone grid is placed 1.6 m from the ground and 1m in front of the fan. The motor is powered to rotate the fan and the measurement of noise is made for the rated rotational speed of the fan fixed at the speed of 3000 rpm. The noise measurements were made using single microphone method. LMS Test Lab software and the data acquition system is connected with the help of LAN cord and in turn the sensor indexed in the grid is connected to the data acquition system through BNC cables. Singature test module is used for measurement. Before the start of the measurement the ranging of sensor is carried out to decide the optimum power voltage to the active channel. The Free run option of measurement is chosen for 10 seconds and subsequently the sound pressure level time history has been recorded.

A rectangular array of grid size of 6 rows x 7 columns with 42 grid points is used to index the microphone using a tripod shown in Figure 9, which was positioned at 1 m distance from the radiator fan.

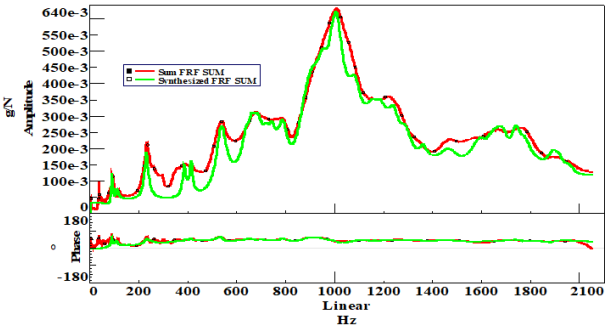

Figure 8. Comparison of synthesized overall FRF with estimated FRFs

Figure 9. Experimental setup for signature test for noise measurement

Sound field at the source plane was computed from the measured data. For 10 seconds for at all these grid point location the overall sound pressure level is obtained sequentially indexing the microphone and the Figure 10 presents the variation of the same for six diagonal points. The difference in sound pressure level between the extreme diagonal points is more compared to the of other points. The variation is observed to be between 60 to 95 dB sound pressure level. However, the overall sound pressure level obtained with A weighting is found out to be around 60 dB (A).

4. FINITE ELEMENT MODAL ANALYSIS

Numerical modal analysis is performed using ANSYS finite element software. The CAD model shown in Figure 2b is used for the same. The material definition and boundary condition were defined. Polymeric plastic material has been defined for shroud where as fan is made of aluminium. Table 1 below provide the material properties used to define the RFM. The shroud vertex are fixed, fan spindle is free to rotate in its axis. The FE model has been created with fine turning mesh size until the convergence criterion is met. Thus the prepared FE model is used further for modal analysis. The modal results were compared with experimental results.

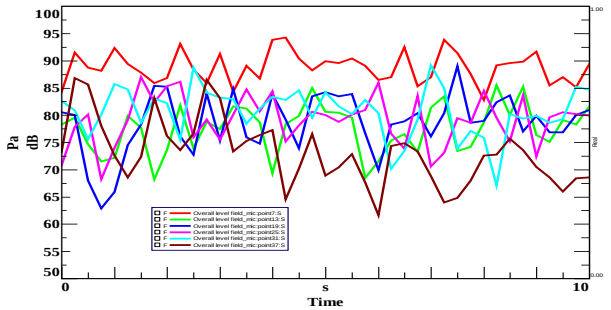

Figure 10. Variation of sound pressure level time histroy along the diagonal points

Figures 11 and 12 present and compare the modal frequencies and the corresponding mode shapes of the RFM obtained through numerically with experimental one for fan component.

Figures 13 and 14 present and compare the same for shroud. It is to be noted that though the mode shape compared in both the cases closer to the resonance

TABLE 1. Material properties

Component	Material	Density (kg/m^3)	Young's Modulus (N/m^2)	Poison ratio
Fan	Aluminium	2550	7×10^{10}	0.33
Shroud	Plastic	1200	2×10^{10}	0.15

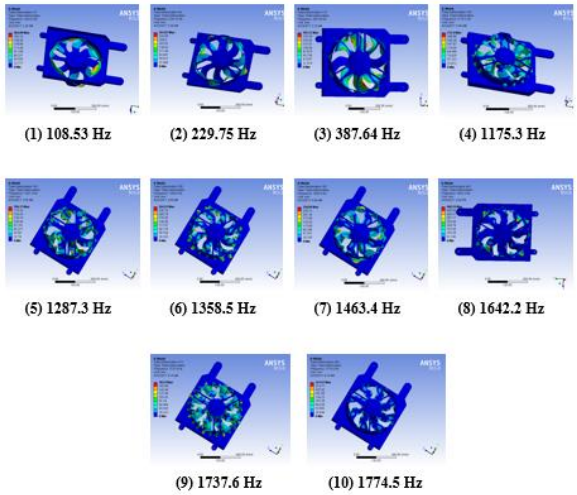

Figure 11. Modal parameters obtained from finite element modal analysis of radiator fan

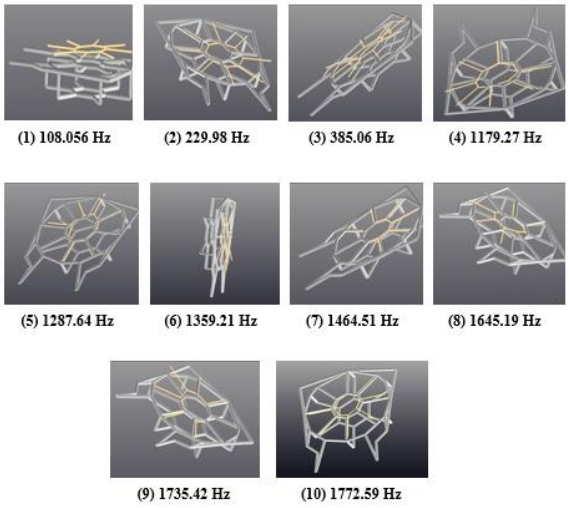

Figure 12. Modal parameters obtained from experimental modal analysis of radiator fan

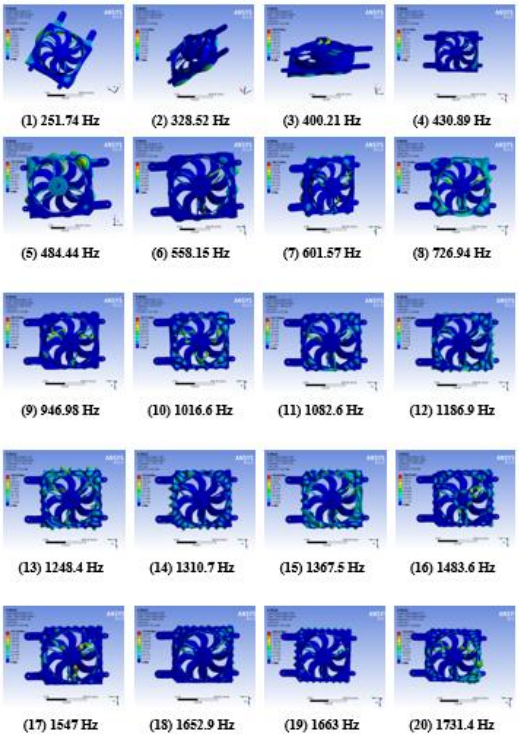

Figure 13. Modal parameters obtained from finite element analysis of shroud

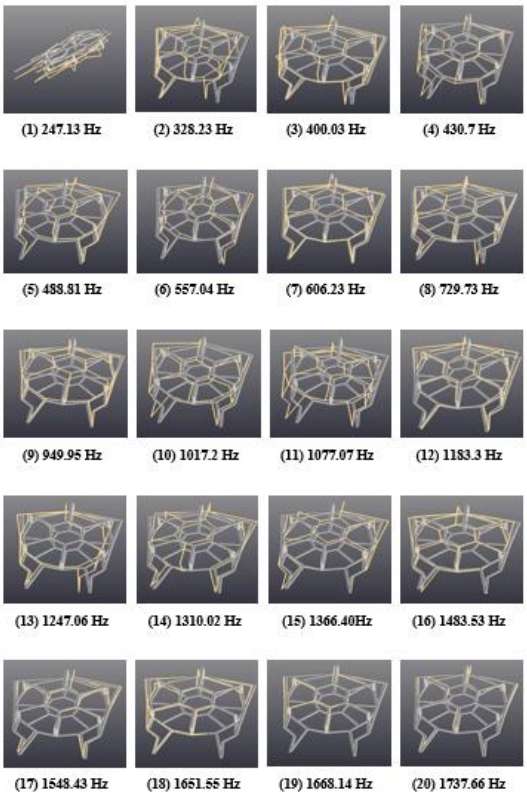

Figure 14. Modal parameters obtained from experimental modal analysis of shroud

frequencies the deflection shape obtained is not exact with numerical results. This is due to the reason that the number of measurement points in the experiment is limited. Finite number of discrete points are marked on the actual RFM as shown in Figure 2a for the response measurements during spectral test when impulse excitation is given with the help of instrumented hammer.

5. RESULTS AND DISCUSSION

Tables 2 and 3 summaries the natural frequencies of the fan and shroud components of RFM obtained from experimental and numerical modal analysis. The observed deviation is insignificant except at higher frequencies and the finite element model thus validated and proposed as an entension work to carry out vibro-acoustic and aero-acoustic simulation study. The resonance frequencies obtained and the speed of the fan need to confirm the design requirements. Figure 15 shows the variation of A weighted 1/3 rd octave band sound pressure level for the diagonal points (points 7, 13, 19, 25, 31 and 37) in the grid. Except grid point 7 rest of the points in the diagonal sound pressure level is below 50 dB(A) for the entire frequency range that include all the resonance frequencies. It is observed from the graph that the central frequencies between the bounds 561.2 to 2244.9 Hz for all the diagonal points negligible variation as compared to the frequency bound range up to 561.2 Hz.

Importantly,blade passing frequencies corresponding to the fan speeds between 500 to 3000 rpm are compared with resonance frequencies of listed in Table2 as well as in Table 3. They do not coincide with any of the modes. That ensures the optimum design consideration of structural noise contribution of the chosen automotive RFM.

TABLE 2. Resonance frequencies of radiator fan in Hz

Modes	Experiemntal Modal Analysis	Finite Element Modal Analysis
Mode 1	108.06	108.53
Mode 2	229.98	229.75
Mode 3	385.06	387.64
Mode 4	1179.27	1175.3
Mode 5	1287.64	1287.3
Mode 6	1359.21	1358.5
Mode 7	1464.51	1463.4
Mode 8	1645.19	1642.2
Mode 9	1735.42	1737.6
Mode 10	1772.59	1774.5

TABLE 3. Resonance frequencies of shroud in Hz

Modes	Experiemntal Modal Analysis	Finite Element Modal Analysis
Mode 1	247.13	251.74
Mode 2	328.23	328.52
Mode 3	400.03	400.21
Mode 4	430.70	430.89
Mode 5	488.81	484.44
Mode 6	557.04	558.15
Mode 7	606.23	601.57
Mode 8	729.73	726.94
Mode 9	949.95	946.98
Mode 10	1017.20	1016.6
Mode 11	1077.07	1082.60
Mode 12	1183.30	1186.90
Mode 13	1247.06	1248.40
Mode 14	1310.02	1310.70
Mode 15	1366.40	1367.50
Mode 16	1483.53	1483.60
Mode 17	1548.43	1547.00
Mode 18	1651.55	1652.90
Mode 19	1668.14	1663.00
Mode 20	1737.66	1731.40

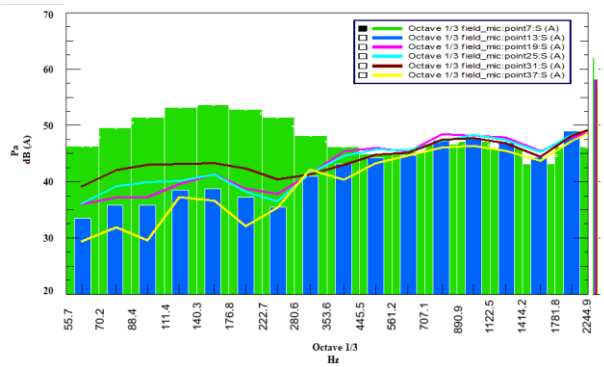

Figure 15. Variation of sound pressure level along the diagonal points

The difference in sound pressure level is significant upto 500 Hz bound frequency and the variation between the extreme diagonal points is arround 20 dB(A). This is becouse of structural resonance modes amplitudes are much pronounced till 500 Hz for both fan as well as shroud. The frequency corresponding to the speed of the fan is 314 Hz is the exciation and only the top right diagonal point captured the higher sound pressure level than the other points. At this frequency arround 8 dB(A)

difference is observed between microphone location at point 7 and the rest of the diagonal points. Also it is evedent from the modal analysis that structural mode is not at 314 Hz hence it can be concluded it is due to speed of the fan the noise is contributed.

6. CONCLUSION

Modal parameters of radiator fan and shroud assembly was determined by carrying out spectral test. Sufficient number of FRFs is calculated to get appropriate overall curve fit of FRF sum. The drive point coherence and synthesized overall FRFs were obtained to ensure the quality and validity of the experimental modal analysis. Further the experimental results were used to compare the numerical modal results to validate the FE modal model and hence the FE model can be proposed for parametric study for product development which is not a scope of current work. The validated FE model is also proposed for extension work of vibro-acoustic and aero-acoustic simulation. There are only three critical modal frequencies for fan and five critical modal frequencies for shroud below 500 Hz are obtained. Whereas above 500 Hz to 2000Hz frequency range there were seven for fan and fifteen for shroud are obtained. And interestingly no coincident resonance frequencies of both fan and shroud as well as no conincidence of blade passing frequencies from 500 rpm to 3000 rpm with the incremental speed of 500 rpm are observed which an important design requirement. The signature test was also performed and the overall sound pressure level of 60 dB (A) is observed in the near field at a distance of 1 m from RFM which would be a permissible value. Important conclusion to correlate the modal behaviour with noise radiation can be observed in the two ranges of frequencies. Up to 500 Hz the sound pressure level has shown variation on the diagonal grid points whereas above 500 Hz the variation is negligible.

7. ACKNOWLEDGMENT

Authors convey their sincere thanks to Vehicle Dynamics Laboratory, Vellore Institute of Technology, Vellore for providing the testing facility to carry out the necessary experiments for the current research work.

8. REFERENCES

1. Zhu, M., Wang, K., Zhang, P. and Li, Z., "Numerical and experimental investigation of aerodynamic noise from automotive cooling fan module", ***Journal of Vibroengineering***, Vol. 17, No. 2, (2015), 967-977.
2. Liu, X.-A., Zhu, X., Shangguan, W., Wang, T., Wang, X.-L. and Chen, Y., "A study on design methods for condenser radiator fan module mounting system", ***International Journal of Heavy Vehicle Systems***, Vol. 26, No. 2, (2019), 119-135.
3. Baniasadi, E., Aydin, M., Dincer, I. and Naterer, G., "Computational aerodynamic study of automotive cooling fan in blocked conditions", ***Engineering Applications of Computational Fluid Mechanics***, Vol. 7, No. 1, (2013), 66-73, doi: org.10.1080/19942060.2013.11015454
4. Lim, J., Sim, W., Yun, S., Lee, D. and Chung, J., "Reduction of vibration forces transmitted from a radiator cooling fan to a vehicle body", ***Journal of Sound and Vibration***, Vol. 419, (2018), 183-199, doi: org/10.1016/j.jsv.2018.01.016
5. Kumar, S. and Talwar, H., *Optimization of radiator fan for nvh improvement*. 2017, SAE Technical Paper.
6. Wang, J., Huang, L. and Cheng, L., "A study of active tonal noise control for a small axial flow fan", ***The Journal of the Acoustical Society of America***, Vol. 117, No. 2, (2005), 734-743, https://asa.scitation.org/doi/10.1121/1.1848072
7. Arefin, A. and Islam, R., "Investigation of different validation parameters of micro gas turbine for range extender electric truck", ***International Journal of Engineering***, ***Transactions A: Basics,*** Vol. 31, No. 10, (2018), 1782-1788, doi: 10.5829/ije.2018.31.10a.22.
8. Rajabi, N., Rafee, R. and Farzam-Alipour, S., "Effect of blade design parameters on air flow through an axial fan", ***International Journal of Engineering***, ***Transactions A: Basics,*** Vol. 30, No. 10, (2017), 1583-1591, doi: 10.5829/ije.2017.30.10a.20.
9. Suzuki, A., Tominaga, T., Eguchi, T., Kudo, T. and Takada, T., "Study on the fun noise reduction for automotive radiator cooling fans", ***Mitsubishi Heavy Industries Technical Review***, Vol. 43, No. 3, (2006), 23-30.
10. Jayachandran, R., Alavandi, B., Niesluchowski, M., Low, E., Miao, Y. and Zhang, Y., *Fan shroud design for low speed damageability*. 2017.
11. Ewins, D.J., "Modal testing: Theory, practice and application, John Wiley & Sons, (2009).
12. Pieters, R., "Experimental modal analysis of an automobile tire under static load", ***DCT Rapporten***, Vol. 112, (2007), 1-24.
13. Patil, K., Baqersad, J. and Behroozi, M., "Experimental modal analysis on a tyre–lessons learned", ***International Journal of Vehicle Noise and Vibration***, Vol. 13, No. 3-4, (2017), 200-215, doi: 10.1504/IJVNV.2017.10010555.
14. Vervoort, J., "Experimental modal analysis of an automobile tire", Bachelor final project report No, DCT, (2007).
15. Tare, K., Mukherjee, U. and Vaidya, R.J., *Design optimization of automotive radiator cooling module fan of passenger vehicle for effective noise management using cfd technique*. 2017, SAE Technical Paper.
16. Lu, Y.-Y., *Experimental study of installation effects on cooling fan noise*. 2021.
17. Hosseini Hashemi, S. and Bakhshi Khaniki, H., "Free vibration analysis of nonuniform microbeams based on modified couple stress theory: An analytical solution", ***International Journal of Engineering***, ***Transactions B: Applications,*** Vol. 30, No. 2, (2017), 311-320, doi: 10.5829/idosi.ije.2017.30.02b.19.
18. Amrane, M.N. and Bensahal, D., "Effects of material and geometrical parameters on the free vibration of sandwich beams", ***International Journal of Engineering***, ***Transactions B: Applications,*** Vol. 29, No. 2, (2016), 222-228, doi: 10.5829/idosi.ije.2016.29.02b.11.
19. Rezaiee-Pajand, M., Aftabi Sani, A. and Hozhabrossadati, S.M., "Free vibration of a generalized plane frame", ***International Journal of Engineering***, ***Transactions A: Basics,*** Vol. 31, No. 4, (2018), 538-547, doi: 10.5829/ije.2018.31.04a.04.

20. Verma, A., Kaushik, S. and Tyagi, S., "Thermodynamic analysis of a combined single effect vapour absorption system and tc-CO_2 compression refrigeration system", ***HighTech and Innovation Journal***, Vol. 2, No. 2, (2021), 87-98.
21. Kapeller, H., Dvorak, D. and Šimić, D., "Improvement and investigation of the requirements for electric vehicles by the use of hvac modeling", ***HighTech and Innovation Journal***, Vol. 2, No. 1, (2021), 67-76.
22. Peng, Z., Ouyang, H., Wu, Y. and Tian, J., "Tonal noise control of cooling fan module by using modulation principles on both rotor and stator", in Turbo Expo: Power for Land, Sea, and Air, American Society of Mechanical Engineers. Vol. 50985, (2018), V001T009A007.
23. Peeters, B., Van der Auweraer, H., Guillaume, P. and Leuridan, J., "The polymax frequency-domain method: A new standard for modal parameter estimation?", ***Shock and Vibration***, Vol. 11, No. 3-4, (2004), 395-409.

Persian Abstract

چکیده

در میان بسیاری از لوازم جانبی خودروهای سواری، ماژول فن رادیاتور خنک کننده موتور (RFM)منبع مهم صدا و لرزش است. پارامترهای مودال اساس مکانیسم تولید نویز و پدیده انتشار نویز را فراهم می کنند. هدف کار تحقیقاتی فعلی، توصیف RFM از طریق رفتار مودال آن برای بررسی سهم ارتعاش ساختاری در تشعشعات نویز در طول حالت عملکرد آن است. از این رو، تجزیه و تحلیل مودال تجربی و اندازه‌گیری نویز RFM انجام شد. علاوه بر این، یک تحلیل مودال المان محدود از RFM برای اعتبارسنجی مدل المان محدود که می‌تواند برای مطالعات دینامیک سیالات ارتعاشی-آکوستیک و محاسباتی استفاده شود، انجام شد. زیر ۵۰۰ هرتز در مجموع هشت فرکانس مودال بحرانی، سه فرکانس برای فن و پنج فرکانس برای shroud تعیین شده است و بین ۵۰۰ هرتز تا ۲۰۰۰ هرتز هفت حالت برای فن و پانزده حالت برای shroud حذف شده است. از مطالعه همبستگی، مشاهده می‌شود که سهم رفتار مودال برای تابش نویز با تغییرات ۲۰ دسی‌بل (A)زیر ۵۰۰ هرتز، در امتداد نقاط شبکه مورب مشاهده می‌شود، در حالی که این تغییرات فراتر از ۵۰۰ هرتز ناچیز بود. نکته مهم این است که فرکانس‌های عبور تیغه مربوط به سرعت فن بین ۵۰۰ تا ۳۰۰۰ دور در دقیقه با فرکانس‌های تشدید به‌دست‌آمده مقایسه شد و با فرکانس‌های مدال همخوانی ندارند.

IJE TRANSACTIONS B: Applications Vol. 35, No. 08, (August 2022) 1488-1493

International Journal of Engineering

Journal Homepage: www.ije.ir

RESEARCH NOTE

Development and Control of an upper Limb Rehabilitation Robot via Ant Colony Optimization -PID and Fuzzy-PID Controllers

N. Mirrashid[a], E. Alibeiki*[a], S. M. Rakhtala[b]

[a] *Department of Electrical Engineering, Aliabad Katoul Branch, Islamic Azad University, Aliabad Katoul, Iran*
[b] *Faculty of Engineering, Department of Electrical Engineering, Golestan University, Gorgan, Iran*

PAPER INFO

Paper history:
Received 17 August 2021
Received in revised form 11 March 2022
Accepted 15 March 2022

Keywords:
Rehabilitation Robot
Ant Colony Optimization Algorithm
Fuzzy-PID Controller
Ziegler-Nichols Method
PID Tuning

ABSTRACT

The control of movement rehabilitation robots is necessary for the recovery of physically disabled patients and is an interesting open problem. This paper presents a mathematical model of the upper limb rehabilitation robot using Euler-Lagrange approach. Since the PID controller is one of the most popular feedback controllers in the control strategy due to its simplicity, we proposed an ACO-PID controller for an upper limb rehabilitation robot. The main part of designing the PID controller is determining the gains of the controller. For this purpose, we used Ant Colony Optimization Algorithm (ACO) to tune the coefficients. To evaluate the validity of the proposed controller, we have compared it to Fuzzy-PID controller and the PID controller adjusted with the Ziegler-Nichols method (ZN-PID). The results showed that the performance of the ACO-PID controller is better than the others. Also, the adaptive PID controllers (ACO-PID and Fuzzy-PID) ensure accurate tracking, finite-time convergence, and stability. The results showed that the mean absolute error and normalized root mean square (NRMS) of tracking error using the ACO-PID are less than that using the Fuzzy-PID and ZN-PID controller.

***doi**: 10.5829/ije.2022.35.08b.04*

1. INTRODUCTION

Today, the increasing number of stroke patients has increased the need for rehabilitation. A simple definition of rehabilitation is an increase in the ability of human muscles by doing certain movements frequently [1]. The traditional rehabilitation method is not effective due to the lack of hospital resources and trained therapist. Robots, as a new method, are useful tools to help patients in need of rehabilitation. Accurate tracking of desired motion by the robot requires a good control strategy [2]. One of the most popular controllers is the PID controller, which is used widely in various applications due to its simplicity and convenient operation. Piltan et al. [3] have used a feedback linearization compensator (FLC) to assist the PID controller performance in the presence of system uncertainty and concluded that the above compensator improves the performance of the classic PID controller. Widhiada et al. [4] have designed an advanced PID control with automatic adjustment for the multi-fingered robot hand. The purpose of the design was to achieve a fast steady-state response and reduce convergence time. They also showed that the system has a stable response under different inputs using a designed controller. A PID controller, using the PSO algorithm and the cuckoo search algorithm, has been tuned by Ayas et al. [5]. The proposed controller has been used to control the performance of the ankle rehabilitation robot with 2-degree of freedom. The results showed that the adjusted PID controller by intelligent algorithms has lesser tracking error than the classical PID. Ayas et al. [6] have compared a fuzzy logic controller with a PID controller to control the movement of an ankle rehabilitation robot. The boundary scales of the fuzzy controller membership functions are adjusted using the cuckoo search algorithm. Experimental results showed that the proposed fuzzy controller has about 50% less tracking error than the PID controller. A PID controller

*Corresponding Author Institutional Email: esmail_alibeiki@aliabadiau.ac.ir. (E. Alibeiki)

Please cite this article as: N. Mirrashid, E. Alibeikia, S. M. Rakhtala, Development and Control of an upper Limb Rehabilitation Robot via Ant Colony Optimization -PID and Fuzzy-PID Controllers, ***International Journal of Engineering, Transactions B: Applications***, Vol. 35, No. 07, (2022) 1488-1493

has been proposed to control the performance of the lower limb rehabilitation robot by Mohanta et al. [7], which have showed good accuracy in tracking the desired path. Cheng et al. [8] have developed a rehabilitation robot to perform flexion exercises of fingers with nine degrees of freedom. They have evaluated the performance of their rehabilitation robot with a PID controller and a combined controller of the active disturbance rejection control (ADRC) and the iterative learning control (ILC) and have achieved satisfactory results. Due to the highly nonlinear nature of the walking robot, Aldair et al. [9] have proposed a robust adaptive Fuzzy-ACO controller. Also, the stability of the proposed controller has been examined by the Lyapunov algorithm. Jiang et al. [10] have provided a Fuzzy-PID controller for precise tracking by the lower limb rehabilitation robot. The suggested controller test has shown high accuracy, smooth operation, and limited-time convergence. To some applications of the PID controller to control the rehabilitation robots, interested readers may refer to literature [11-16], to name a few. Other applications of fuzzy logic and optimization algorithms can be found in literature [17-21].

Dorigo et al. [22], using the behavior of ants to find food, have introduced the ant algorithm. For a comprehensive study about the ACO algorithm, we refer to literature [23, 24]. Now, by considering the non-linear nature of the upper limb rehabilitation robot system and the conditions of uncertainty and disturbances, the coefficients of the classic PID controller should be adjusted to ensure system stability and high tracking accuracy. In this paper, we use the ACO algorithm and fuzzy logic to adjust the coefficients of the adaptive PID controller. The organization of the paper is as follows. Section 2 is devoted to the dynamic modeling of a rehabilitation robot. In section 3, the controller is designed. Section 4 explains the ACO algorithm. The simulation results are given in Section 5. Finally, section 6 concludes the paper.

2. SYSTEM MODELING

By considering the Euler-Lagrange method [25], we know:

$$\frac{d}{dt}\left(\frac{\partial L(\delta,\dot{\delta})}{\partial \dot{\delta}}\right) - \frac{\partial L(\delta,\dot{\delta})}{\partial \delta} = \tau\,, \tag{1}$$

where δ is a joint position, $\dot{\delta}$ is time derivative of the position, τ is the driving torque from the servo motor, L represents lagrangian, and:

$$L(\delta(t),\dot{\delta}(t)) = K(\delta(t),\dot{\delta}(t)) - U(\delta(t)) \tag{2}$$

where K is kinetic energy and equal to $\frac{1}{2}m||v||^2 + \frac{1}{2}I\delta^2$, $U = mgh$ is potential energy, m is the mass, ν is the angular velocity vector, and I is the inertia. The structure of an upper limb robot is shown in Figure . For the upper limb rehabilitation robot, we have:

$$X = \begin{bmatrix} x \\ y \end{bmatrix} = \begin{bmatrix} l_1\sin(\vartheta) + l_2\sin(\vartheta+\delta) \\ -l_1\cos(\vartheta) - l_2\cos(\vartheta+\delta) \end{bmatrix},$$

where X is a position vector, ϑ is a constant angle and $\delta \in \mathbb{R}$ is the position angle for the vertical axis, l_1 and l_2 are the lengths of link 1 and link 2, respectively. According to Equation (1), we developed the following expression:

$$(m_2 l_2^2)\ddot{\delta} + m_2 I_2 g\sin(\vartheta+\delta) = \tau - F_{ext}, \tag{3}$$

where $F_{ext}(\delta,\dot{\delta},t) \in \mathbb{R}$ is external forces as friction or disturbances:and considered as follow

$$\mathrm{F_{ext}}(\delta,\dot{\delta},\mathrm{t}) = \mathrm{f_c sign}(\dot{\delta}) + \mathrm{f_v}\dot{\delta}\,, \tag{4}$$

where f_c is the coulomb-friction constant and f_v is the viscous friction coefficient. On the other hand, the actuator dynamics are equal to:

$$J_m\ddot{\delta} + \frac{1}{r}f_m(r\dot{\delta}) + \frac{K_aK_b}{R_a}\dot{\delta} + \frac{\tau}{r^2} = \frac{K_a}{rR_a}v\,, \tag{5}$$

where $J_m, f_m(r\dot{\delta}), K_a, K_b, R_a, r$ and$v(t)$ are, the inertia of the rotor, the friction between the rotor and its bearing, the motor-torque constant, the back emf constant, the armature resistance, the gears reduction ratio, the armature voltage and control input, respectively. Thus, the dynamic model of rehabilitation upper limb robot will be equal to [26]:

$$\left[\frac{1}{r^2}(m_2l_2^2 + I_2) + J_m\right]\ddot{\delta} + \frac{1}{r}f_m(r\dot{\delta}) + \frac{m_2l_2g}{r^2}sin(\vartheta+\delta) + \left[\frac{K_aK_b}{R_a} + \frac{F_v}{r^2}\right]\dot{\delta} + \frac{F_c}{r^2}sign(\dot{\delta}) = \frac{K_a}{rR_a}v\,. \tag{6}$$

3. TRAJECTORY TRACKING CONTROL FOR THE UPPER LIMB REHABILITATION ROBOT

3. 1. The ZN-PID Controller Design The block diagram of the PID controller is shown in Figure 2 and it presents the following equation:

$$U(t) = K_p e(t) + K_i\int_0^t e(\tau)\partial\tau + K_d\frac{de(\tau)}{d\tau} \tag{7}$$

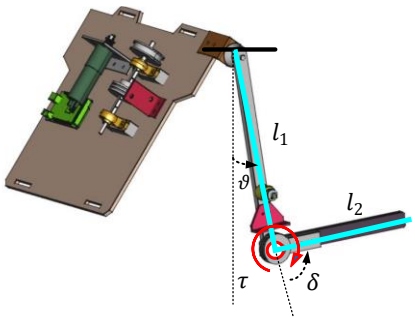

Figure 1. Structure of an upper limb robot

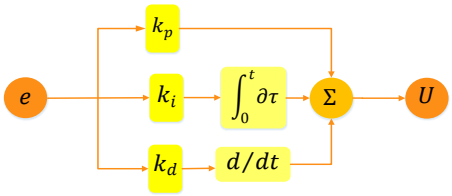

Figure 2. Structure of PID controller

where $U(t)$ is control input, K_p is proportional parameter, K_i delegates integral gain, K_d is derivative constant, and $e(t)$ is the tracking error as $e = \delta_d - \delta$. To tune the coefficients of ZN-PID, one can use the Ziegler-Nichols formula as follows [27]:

$$K_p = 0.6K_u\ ,\ K_i = \frac{2K_p}{T_u}\ ,\ K_d = \frac{K_pT_u}{8} \quad (8)$$

where K_u and T_u are the Critical gain and the oscillation period, respectively.

3. 2. The Fuzzy-PID Controller Design In this section, the gains of the Fuzzy-PID controller are adapted based on the fuzzy rules. Figure 1 depicts the block diagram of the Fuzzy-PID controller.

Suppose $[K_{p,min}, K_{p,max}]$ and $[K_{d,min}, K_{d,max}]$ are the bounds of $K_p$and K_d, respectively [27]; and

$$K_{p,min} = 0.32K_u,\quad K_{p,max} = 0.6K_u,\quad K_{d,min} = 0.08K_uT_u,\ K_{d,max} = 0.15K_uT_u$$

The coefficients of Fuzzy-PID controller are

$$K_p = K_{p,min} + K'_p(K_{p,max} - K_{p,min}) \quad (9)$$

$$K_d = K_{d,min} + K'_d(K_{d,max} - K_{d,min}) \quad (10)$$

$$K_i = {K_p}^2/\alpha K_d, \quad (11)$$

where $K'_p, K'_d \in [0,1]$, and $\alpha \in [2,5]$ are obtained outputs from fuzzy logic controller by the fuzzy rules with following form [27]:
if $e(k)$ is A_i and $\Delta e(k)$ is B_i, then K'_p is C_i, K'_p is D_i , and $\alpha = \alpha_i$, where $i = 1, 2, \dots, m$.

The fuzzy sets A_i and B_i are depicted in Figure 2 (a), and the fuzzy sets C_i and D_i are shown in Figure 2 (b) and α_i is constant (Figure 2 (c)). Where ZO, S, M, B, N, and P are zero, small, medium, big, and negative, positive, respectively.

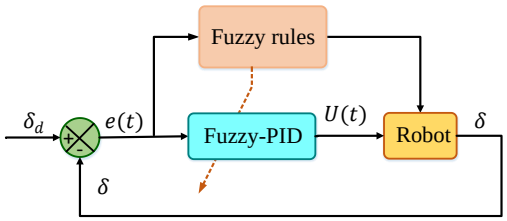

Figure 1. Block diagram of the closed-loop system for Fuzzy-PID

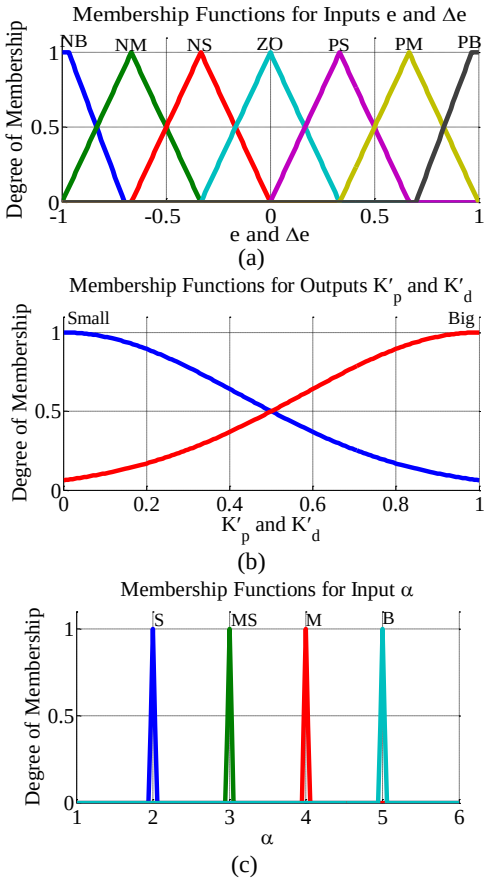

Figure 2. Membership functions of: (a) Inputs (e and Δe), (b) Outputs (K'_p and K'_d), (c) output (α)

3. 3. The ACO-PID Controller Design We use the ACO algorithm to find the optimal values of the PID controller gains. Figure shows the block diagram of the closed-loop system for the ACO-PID.

The flow chart of the ACO algorithm follows from Figure . The ant algorithm optimization method is as follows:

1. First, we consider some ants. Then for each ant, a path that lacks a pheromone is randomly assigned to look for food. The intersections of the trajectories are also determined.
2. Ants mark the path to food by pheromone on the way back to the nest. Each intersection that has more pheromones (more ants have passed through it) attracts more ants.
3. The shortest path to food has more pheromones due to the faster return of ants to the nest and movement in the previous path. At the same time, the pheromones of the other pathways evaporate over time, and eventually, large numbers of ants converge toward the shorter pathway.
4. One can calculate the concentration of pheromone at time t by $\emptyset(t) = \emptyset_0 e^{-\gamma t}$, where $\emptyset_0$ and γ are the initial

focus of the pheromone and constant rate of pheromone evaporation. This amount is updated in the next iterations as $\emptyset_{ij}^{t+1} = (1-\gamma)\emptyset_{ij}^{t} + \alpha\emptyset_{ij}^{t}$ (if there is no ant left in the path, the amount of pheromone will be zero), where $\alpha\emptyset_{ij}^{t}$ is the amount of pheromone stored in time t for the i to j path.

The cost function (C_F) is defined as integral time absolute error (ITAE):

C_F=$\int_0^{\infty} t|e(t)|dt$,

where $e(t) = \delta_d - \delta$.

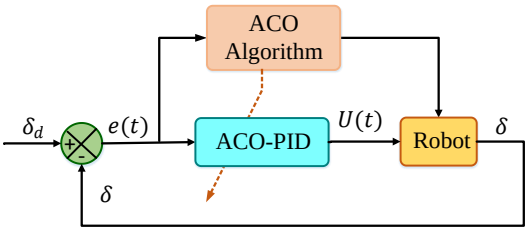

Figure 5. Block diagram of the closed-loop system for ACO-PID

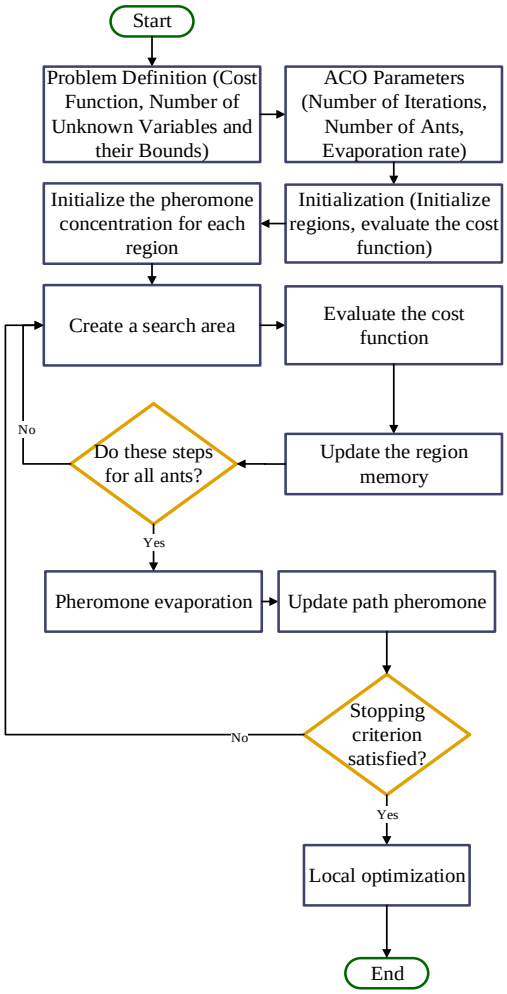

Figure 6. The flow chart of the ACO algorithm

4. RESULT AND DISCUSSION

The relationship for the desired path and velocity of tracking are given as follows.

$$\delta_d = sin(2\pi ft) + 1 \quad (12)$$

$$\dot{\delta}_d = 2\pi f cos(2\pi ft) \quad (13)$$

System velocity and acceleration ranges are [28]:

$-2\frac{rad}{s} < \dot{\delta}_d < 2\frac{rad}{s}$, $-10\frac{\text{rad}}{\text{s}^2} < \ddot{\delta}_{\text{d}} < 10\frac{rad}{s^2}$

Figures 7 and 8 show the desired and measured position (δ) trajectories and the measured velocity ($\dot{\delta}$) by applying the controllers, respectively. One can see from Figures 7 and 8, the adjusted gains using the fuzzy logic cause a good performance for the PID controller. The tracking is accurate, and the tracking error is small. Also, the convergence time for the Fuzzy-PID controller is shorter than the others. The position error in radians is illustrated in Figure 9.The convergence rate for the ACO-PID cost function shows in Figure 10. It is clear from the figure the best value of the cost function is 1.78 which is happened in iteration 47.

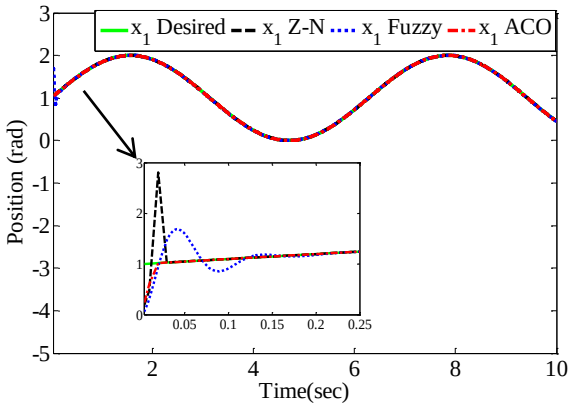

Figure 3. The measured and the desired elbow position trajectories

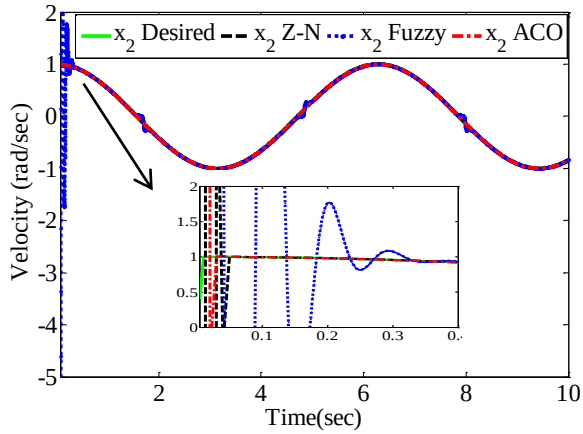

Figure 4. The measured and the desired elbow velocity trajectories

Some statistical indices corresponding to the error, such as mean absolute error (MAE), root mean square error (RMS), and normalized root mean square error (NRMS), are summarized in TABLE as follows:

$$\text{MAE(rad)} = \frac{\sum_{i=1}^{n}|e_i|}{n} \quad (14)$$

$$\text{RMS(rad)} = \sqrt{\frac{\sum_{i=1}^{n}|e_i|}{n}} \quad (15)$$

$$\text{NRMS(\%)} = \frac{RMS}{\max(\delta_d)-\min(\delta_d)} \quad (16)$$

In the case of uncertainty, we change the system parameters values between 5 and 10%.

TABLE 1. RMS, NRMS, and MAE of controllers

Nominal conditions			
	ZN-PID	**Fuzzy-PID**	**ACO-PID**
MAE(rad)	0.0033	0.0021	0.0014
RMS(rad)	0.0668	0.0447	0.0341
NRMS(%)	3.3387	2.2366	1.7036
Uncertainties			
	ZN-PID	**Fuzzy-PID**	**ACO-PID**
MAE(rad)	0.0034	0.0023	0.0015
RMS(rad)	0.0687	0.0452	0.0357
NRMS(%)	3.4259	2.2604	1.7847

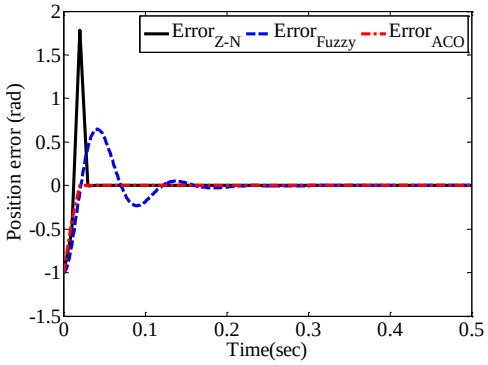

Figure 5. The position error

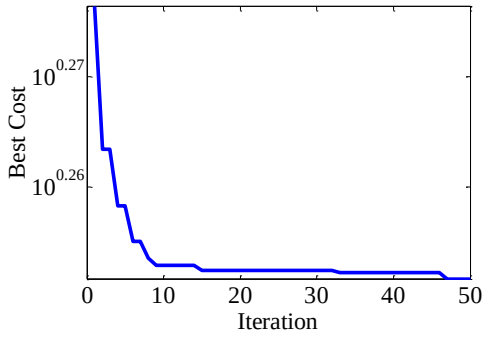

Figure 10. The convergence rate for ACO-PID cost function

5. CONCLUSION

In this paper, three controllers, ACO-PID, Fuzzy-PID, and ZN-PID, were designed to control the movement of the arm rehabilitation robot. The simulation results showed that the PID controller adjusted by the Ziegler-Nichols method, in addition to slowing down the convergence, has lower detection accuracy than the adaptive controllers (ACO-PID and Fuzzy-PID). Also, the ACO-PID controller converged to the desired path earlier than the other controllers and had higher tracking accuracy. To better evaluate the proposed controllers, the statistical comparison indices such as MAE, RMS, and NRMS reported. By analyzing the results, one can conclude that an adaptive PID controller (ACO-PID and Fuzzy-PID), while simple, can accurately track the movement of the upper limb rehabilitation robot.

6. REFERENCES

1. Zhang, K., "The design and realization of a gait rehabilitation training robot with body supporting mechanism", ***International Journal of Engineering, Transactions C: Aspects***, Vol. 29, No. 9, (2016), 1314-1318, doi: 10.5829/idosi.ije.2016.29.09c.18.
2. Zawawi, M.Z.F.B.M., Elamvazuthi, I., Aziz, A.B.A. and Daud, S.A., "Comparison of pid and fuzzy logic controller for dc servo motor in the development of lower extremity exoskeleton for rehabilitation", in 2017 IEEE 3rd International Symposium in Robotics and Manufacturing Automation (ROMA), IEEE. (2017), 1-6, doi: 10.1109/ROMA.2017.8231822.
3. Piltan, F., Emamzadeh, S., Heidari, S., Zahmatkesh, S. and Heidari, K., "Design artificial intelligent parallel feedback linearization of pid control with application to continuum robot", ***International Journal of Engineering and Manufacturing***, Vol. 3, No. 2, (2013), 51-72, doi: 10.5815/ijem.2013.02.04.
4. Widhiada, W., Nindhia, T. and Budiarsa, N., "Robust control for the motion five fingered robot gripper", ***International Journal of Mechanical Engineering and Robotics Research***, Vol. 4, No. 3, (2015), 226, doi: 10.18178/ijmerr.4.3.226-232.
5. Ayas, M.S., Altas, I.H. and Sahin, E., "Fractional order based trajectory tracking control of an ankle rehabilitation robot", ***Transactions of the Institute of Measurement and Control***, Vol. 40, No. 2, (2018), 550-564, doi: 10.1177/0142331216667810.
6. Ayas, M.S. and Altas, I.H., "Fuzzy logic based adaptive admittance control of a redundantly actuated ankle rehabilitation robot", ***Control Engineering Practice***, Vol. 59, (2017), 44-54, doi: 10.1016/j.conengprac.2016.11.015.
7. Mohanta, J.K., Mohan, S., Deepasundar, P. and Kiruba-Shankar, R., "Development and control of a new sitting-type lower limb rehabilitation robot", ***Computers & Electrical Engineering***, Vol. 67, (2018), 330-347, doi: 10.1016/j.compeleceng.2017.09.015.
8. Cheng, L., Chen, M. and Li, Z., "Design and control of a wearable hand rehabilitation robot", ***IEEE Access***, Vol. 6, (2018), 74039-74050, doi: 10.1109/ACCESS.2018.2884451.
9. Aldair, A.A., Rashid, A.T., Rashid, M.T. and Alsaedee, E.B., "Adaptive fuzzy control applied to seven-link biped robot using ant colony optimization algorithm", ***Iranian Journal of Science and Technology, Transactions of Electrical Engineering***, Vol. 43, No. 4, (2019), 797-811, doi: 10.1007/s40998-019-00201-x.
10. Jiang, D., Shi, G., Pang, Z., Li, S. and Tian, Y., "Control of a new cycling rehabilitation robot based on fuzzy pid", in Journal of

Physics: Conference Series, IOP Publishing. Vol. 1622, (2020), 012119, doi:10.1088/1742-6596/1622/1/012119.

11. Awouda, A. and Mamat, R., "New pid tuning rule using itae criteria", ***International Journal of Engineering***, Vol. 3, No. 6, (2008), 597-608, doi: 10.1109/ICCAE.2010.5451484.
12. Kang, H.-B. and Wang, J.-H., "Adaptive robust control of 5 dof upper-limb exoskeleton robot", ***International Journal of Control, Automation and Systems***, Vol. 13, No. 3, (2015), 733-741, doi: 10.1007/s12555-013-0389-x.
13. Pastor, S., Rivera, C., Avilés, O. and Mauledoux, M., "A real-time motion tracking wireless system for upper limb exosuit based on inertial measurement units and flex sensors", ***International Journal of Engineering, Transactions C: Aspects***, Vol. 32, No. 6, (2019), 820-827, doi: 10.5829/ije.2019.32.06c.04.
14. Saadat, M. and Garmsiri, N., "A new intelligent approach to patient-cooperative control of rehabilitation robots", ***International Journal of Engineering, Transactions C: Aspects***, Vol. 27, No. 3, (2014), 467-474, doi: 10.5829/idosi.ije.2014.27.03c.15.
15. Shen, Z., Zhuang, Y., Zhou, J., Gao, J. and Song, R., "Design and test of admittance control with inner adaptive robust position control for a lower limb rehabilitation robot", ***International Journal of Control, Automation and Systems***, Vol. 18, No. 1, (2020), 134-142, doi: 10.1007/s12555-018-0477-z.
16. Wang, S., Yin, X., Li, P., Zhang, M. and Wang, X., "Trajectory tracking control for mobile robots using reinforcement learning and pid", ***Iranian Journal of Science and Technology, Transactions of Electrical Engineering***, Vol. 44, No. 3, (2020), 1059-1068, doi: 10.1007/s40998-019-00286-4.
17. Maurya, R.K. and Bhowmick, B., "Review of finfet devices and perspective on circuit design challenges", ***Silicon***, (2021), 1-9, doi: 10.1007/s12633-021-01366-z.
18. Qazani, M.R.C., Asadi, H., Khoo, S. and Nahavandi, S., "A linear time-varying model predictive control-based motion cueing algorithm for hexapod simulation-based motion platform", ***IEEE Transactions on Systems, Man, and Cybernetics: Systems***, Vol. 51, No. 10, (2019), 6096-6110, doi: 10.1109/TSMC.2019.2958062.
19. Qazani, M.R.C., Asadi, H., Mohamed, S., Lim, C.P. and Nahavandi, S., "An optimal washout filter for motion platform using neural network and fuzzy logic", ***Engineering Applications of Artificial Intelligence***, Vol. 108, No., (2022), doi: 104564, 10.1016/j.engappai.2021.104564.
20. Shaik, S., "A coplanar wave guide fed compact antenna for navigational applications", ***National Journal Of Antennas and Propagation***, Vol. 2, No. 1, (2020), 7-12, doi: 10.31838/NJAP/02.01.02.
21. Srinivasareddy, D.S., Narayana, D.Y. And Krishna, D.D., "Sector beam synthesis in linear antenna arrays using social group optimization algorithm", ***National Journal of Antennas And Propagation***, Vol. 3, No. 2, (2021), 6-9, doi: 10.31838/NJAP/03.02.02.
22. Colorni, A., Dorigo, M. and Maniezzo, V., "An investigation of some properties of an" ant algorithm"", in Ppsn. Vol. 92, (1992), doi: 10.1109/3477.484436.
23. De Oliveira, S.M., Bezerra, L.C., Stützle, T., Dorigo, M., Wanner, E.F. and de Souza, S.R., "A computational study on ant colony optimization for the traveling salesman problem with dynamic demands", ***Computers & Operations Research***, (2021), 105359, doi: 10.1016/j.cor.2021.105359.
24. Fidanova, S. and Fidanova, S., "Ant colony optimization", ***Ant Colony Optimization and Applications***, (2021), 3-8, doi: 10.1007/978-3-030-67380-2_2.
25. Rosales, Y., Lopez, R., Rosales, I., Salazar, S. and Lozano, R., "Design and modeling of an upper limb exoskeleton", in 2015 19th International Conference on System Theory, Control and Computing (ICSTCC), IEEE. (2015), 266-272, doi: 10.1109/ICSTCC.2015.7321304.
26. Mirrashid, N., Alibeiki, E. and Rakhtala, S.M., "Nonlinear robust controller design for an upper limb rehabilitation robot via variable gain super twisting sliding mode", ***International Journal of Dynamics and Control***, (2022), doi: 10.1007/s40435-021-00902-4.
27. Hang, C.C., Åström, K.J. and Ho, W.K., "Refinements of the ziegler–nichols tuning formula", in IEE Proceedings D (Control Theory and Applications), IET. Vol. 138, (1991), 111-118, doi: 10.1049/ip-d.1991.0015.
28. Mefoued, S., "A second order sliding mode control and a neural network to drive a knee joint actuated orthosis", ***Neurocomputing***, Vol. 155, (2015), 71-79, doi: 10.1016/j.neucom.2014.12.047.

Persian Abstract

چکیده

کنترل حرکت ربات‌های توانبخشی برای بهبود بیماران ناتوان جسمی ضروری و یک مسئله مورد علاقه است. در این مقاله یک مدل ریاضی از ربات توانبخشی اندام فوقانی با استفاده از رویکرد اویلر–لاگرانژ ارائه شده است. از آنجا که کنترل‌کننده PID به دلیل سادگی یکی از محبوب‌ترین کنترل‌کننده‌های بازخورد در استراتژی کنترل است، یک کنترل‌کننده ACO-PID برای کنترل ربات توانبخشی اندام فوقانی پیشنهاد می‌کنیم. بخش اصلی طراحی کنترل‌کننده PID تعیین بهره‌های کنترل‌کننده است. برای این منظور، از الگوریتم بهینه سازی کلونی مورچه‌ها (ACO) برای تنظیم ضرایب استفاده می‌کنیم. اعتبار کنترل‌کننده پیشنهادی با مقایسه آن با کنترل‌کننده ACO-PID و کنترل‌کننده PID تنظیم شده با روش زیگلر–نیکولز (ZN-PID) ارزیابی می‌شود. نتایج نشان می‌دهد که عملکرد کنترل‌کننده ACO-PID بهتر از کنترل‌کننده Fuzzy-PID و کنترل‌کننده ZN-PID است. همچنین، کنترل‌کننده‌های تطبیقی PID (Fuzzy-PID وACO-PID) ردیابی دقیق، همگرایی زمان محدود و ثبات را تضمین می‌کنند. نتایج نشان می‌دهد که میانگین مربع نرمال خطای ردیابی (NRMS) با استفاده از ACO-PID کمتر از حالتی است که از کنترل‌کننده Fuzzy-PID و ZN-PID استفاده می‌شود.

International Journal of Engineering

Journal Homepage: www.ije.ir

RESEARCH NOTE

Sustainable Use of Polypropylene Fibers as a Cement Mortar Reinforcement

H. S. Jawad[a], I. S. Al-Haydari*[b]

[a] *Civil Engineering Department, Al-Nahrain University, Baghdad, Iraq*
[b] *Highway and Transportation, College of Engineering, Mustansiriyah University, Baghdad, Iraq*

PAPER INFO

Paper history:
Received 02 February 2022
Received in revised form 13 March 2022
Accepted 24 March 2022

Keywords:
Polypropylene Fibers
Recycled Fibers
Sustainability
Cement Mortar
Mechanical Properties
T-test

ABSTRACT

Reinforcing cement mortars with fibers is an essential step to enhance their flexural strength. This study compares the fresh properties and mechanical characteristics of cement mortars reinforced with polypropylene fibers and recycled polypropylene fibers. The reinforcing fibers ratio were (0, 0.5,1, and 1.5) % by weight of cement mortar for both types of fibers. The casted samples were tested by means of flow test for fresh mortar, compressive strength, flexural strength, and toughness for hardened mortars. The results from this experimental program showed that both types of fibers caused a reduction in the mortar flow and enhanced its mechanical characteristics. The results were statistically tested to measure the significance of the difference. The cement mortar reinforced with recycled fibers exhibited approximately similar results as compared to the mixtures containing raw polypropylene fibers at 95% confidence level. However, it shows a significant increase in flexural strength when comparing to the mixtures with new polypropylene fibers that may be attributed to the fiber shape and cross section area.

***doi**: 10.5829/ije.2022.35.08b.05*

1. INTRODUCTION

The cementitious materials as cement mortar or cement concrete exhibit strong resistance to compression [1] whereas show weak performance in bending and tension [2]. The need for concrete elements with higher tensile or flexural strength spur researchers and engineers' effort to strengthen these properties. Different techniques have been adopted to eliminate this drawback in concrete. The most widely used method is fiber reinforcement [3]. Bio-fibers as palm fibers [4, 5] sheep wool [6], jute, coconuts, and kelp fibers [7], and hemp fibers [8] have been used as a reinforcing material since ancient ages. It acts as a controller of plastic shrinkage cracking in addition to enhancement of tensile and fatigue resistance.

The development of building materials over the last years leads to the development of synthetic fibers. Many fibers have been introduced and used successfully as nylon fibers [9], steel fibers [10, 11], glass fibers [12], chopped carbon fibers [13] and polypropylene fibers [14-18]. The use of polypropylene fibers has many advantages since it is very effective in reducing the plastic shrinkage cracks and post-cracking [19] that limit the cracks formation, thereby, extending the concrete service life. It also showed higher flexural and tensile strength.

On the other side, these developments in building materials and industry resulted in accumulation of waste materials. These synthetic materials are non-biodegradable [20] that means it will accumulate over the land and cause land and marine pollution. Fortunately, these waste materials can be recycled and used as concrete fibers. Examples of these recycled fibers are nylon fibers recycled from fishing nets [21-23], recycled brass fiber [24], carbon fibers [25, 26] textile, acrylic, and waste glass fibers [27], etc. Previous works showed that the recycled fibers are also effective in a similar way of the new fibers.

In Iraq, the country's ability for waste management is 4000 tons daily, which comprise approximately 13% of daily trash [28]. This deficiency in waste management requires more attentions and implementing strategies to overcome the anticipated environmental crisis. The most common type of the waste materials is plastic. Different

*Corresponding Author Institutional Email: israasaeed@uomustansiriyah.edu.iq (I. S. Al-Haydari)

Please cite this article as: H. S. Jawad, I. S. Al-Haydari, Sustainable Use of Polypropylene Fibers as a Cement Mortar Reinforcement, ***International Journal of Engineering, Transactions B: Applications***, Vol. 35, No. 08, (2022) 1494-1500

polymers as polypropylene, polyethylene, polystyrene, and polyethylene terephthalate form plastic materials. This study deals with recycling plastic materials made from polypropylene. Since, there is relatively few studies to compare the cement mortars reinforced with new fibers and recycled fibers. This work focus on comparing the experimantal test results of cement mortar to determine the applicability of utilizing the recycled fiber instead of the new one to achive sustainability, reduce pollution, and conserve natural resources.

2. MATERIALDS AND METHODS

2. 1. Materials The materials used for the reinforced cement mortars were tab water, cement, and sand, in addition to PPF either raw or recycled RPPF. The descriptions of each material are:

2. 1. 1. Cement an ordinary Portland cement, brought from Almass company was used in this work.

2. 1. 2. Sand the natural river sand is used as a fine aggregate.

2. 1. 3. Raw Polypropylene Fibers the physical properties are summarized in Table 1.

2. 1. 4. Recycled Polypropylene Fibers plastic bags, used for packaging pantry supplies, were used in this study. These bags, made from ribbons of polypropylene material, were shredded to a length similar to that of PPF, which is 19 mm, and used as mortar reinforcement.

Both types of fibers are shown in Figure 1.

A total of seven set of mixtures has been prepared with the mix design stated in Table 2 for the reference mix and three dosage rates for each fiber type. The essential materials for cement mortar production (cement: sand) were kept constant as (1:3) with 0.5 of water/cement ratio. Whereas, the two types of fibers were used in different proportions (0, 0.5, 1.5) % of weight of the total mix.

TABLE 1. Physical properties of polypropylene fibers (PPF)

Form	Virgin Polypropylene Fiber
Specific gravity	0.91
Air entrainment	Air content of concrete will not be significantly increased
Young modulus	(5500-7000) MPa
Tensile strength	350 MPa
Melting point	160 ºC
Fiber length	19 mm

(a) (b)

Figure 1. (a) Polypropylene Fibers and (b) Recycled Polypropylene Fibers

TABLE 2. Nomination of cement mortars reinforced with fibers

Mix code	Fiber type	Fiber content
R	None	0
PP0.5	Raw PP	0.5%
PP1	Raw PP	1.0%
PP1.5	Raw PP	1.5%
RPP0.5	Recycled PP	0.5%
RPP1	Recycled PP	1.0%
RPP1.5	Recycled PP	1.5%

2. 2. Specimens Preparation Initially, the mix design for the cement mortars were set as (1: 3) for cement: sand which is the common mortar mixtures prepared in Iraq. These ratios are kept constant for both reference and the reinforced mixes. The only difference of the fiber-reinforced mixes was the inclusion of the three proportions (0.5%, 1%, and 1.5%) of the fiber (either PP or RPP) as a percentage from the mixture weight. The proportion of PP fibers are limited to 1.5 % as recommended by Sohaib et al. [29] because this ratio was found as the optimum ratio that achieves higher strength as compared to other ratios. Increasing this ratio would result in a negative impact on strength properties. The water-cement ratio was designed as 0.5 for all the mixtures. When the materials were prepared and carefully weighted, the dry cement and sand were mixed together in the mixer for 1-2 minutes. Then, the specified amount of water was poured gradually and stirred with the mixture for another 2 minutes, until a homogeneous mixture would appear. These steps are set for the reference mixture. Regarding the fiber-reinforced mixtures, the same procedure was adopted, and the specified quantities of the fibers were added gradually to the mixture and mixed thoroughly to maintain homogeneity. Afterward, the mixtures of fresh mortar were divided into sections, the first one was tested for workability, and others were poured into different molds 50×50×50 mm cubes and 40×40×160mm prisms for

compressive strength and flexural strength tests, respectively. Then, these molds were subjected to vibration for 10 seconds at a frequency of 300Hz, to ensure homogenous consistency. The molds were sealed by plastic sheets and kept under ambient laboratory temperature for 24 h. Then, mixtures were de-molded and cured by submerging in a water bath of 20-24 ℃ for 28 days (the testing age).

2. 3. Testing Program

2. 3. 1. Fresh Mortar Properties The consistency of the fresh mortar was measured by flow value consistency test to investigate the influence of fibers on the workability of cement mortar. This test was conducted in accordance with ASTM C1437 [30].

2. 3. 2. Physical Properties of the Hardened Mortar In order to determine the effect of PP fibers type and content on the physical properties of cement mortars, the ASTM C 642-13 standard was utilized. The average results of three cubes with 28 days age was used to measure the bulk density and water absorption.

2. 3. 3. Mechanical Properties of the Hardened Mortar In order to evaluate the mechanical properties of the cement mortars, the compressive strength and the flexural strength were tested. The compressive strength of cement mortar was conducted in accordance with ASTM C 109 [31]. The cement mortar cubes were subjected to a load increment of 0.5 KN/s until failure. Whereas, the flexural strength test was performed in accopmliance with ASTM C348 [32]. The cement mortar prisms were subjected to a displacement of 0.5 mm/minute until failure.

2. 4. Statistical Analysis The t-test was used for testing the significance difference between two data set. This test is applicable for comparing the means of two samples that having a small data points. Equation (1) explains the t-test.

$$t = \frac{\bar{x}_1 - \bar{x}_2}{\sqrt{\frac{{S_1}^2}{n_1}} + \sqrt{\frac{{S_2}^2}{n_2}}} \quad (1)$$

where :

$\bar{x}_1$, and $\bar{x}_2$ are the mean of the tested property for PP, and recycled PP-fiber reinforced mortar, respectively.

S_1, and S_2 are the standard deviation of the tested property for PP, and recycled PP- fiber reinforced mortar, respectively.

n_1, and n_2 are the total number of the tested property for PP and recycled PP-fiber reinforced mortar, respectively.

3. RESULTS AND DISCUSSION

The test results for the fresh and hardened PPF-reinforced cement mortar are summarized as:

3. 1. Flow Test The flow value of the PPF and RPPF reinforced cement mortars were tested, and results are presented in Figure 2. This figure shows that there is a slight decrease in the workability of the fiber-reinforced cement mortar. The presence of fibers tends to hinder the mortar flow, thereby reduce workability. The reduction in workability with the RPP reinforced mortar is found to be more that than observed with the raw fibers. This behavior may be attributed to the dimension of the fiber. The flow value decrease by approximately 16%, 16%, and 22% for the raw PP fiber content of 0.5, 1, 1.5% by weight, respectively. Whereas, the percent reduction of recycled PP cement mortar is found as 19%, 25%, and 31%, for the same aforementioned ratios, respectively.

3. 2. Bulk Density The unit weight and bulk density is one of the physical parameters that have to be checked for cementitious mixtures. The density of PP and RPP fibers reinforced mortars have been tested and results are presented in Figure 3. It is clear to notice that the inclusion of PP fibers resulted in density reduction, except for RPP0.5. This may be attributed to the lower unit weight of fibers as compared to the cement mortar.

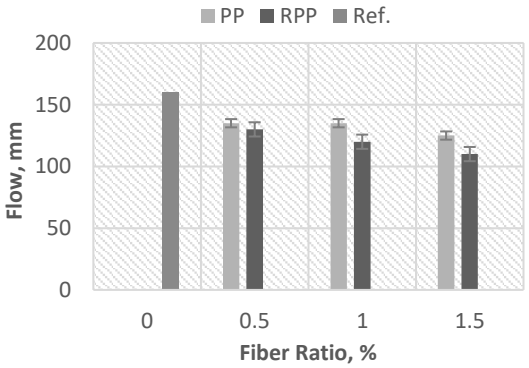

Figure 2. Effect of fiber type and proportion on the workability of the PP fiber-reinforced mortar

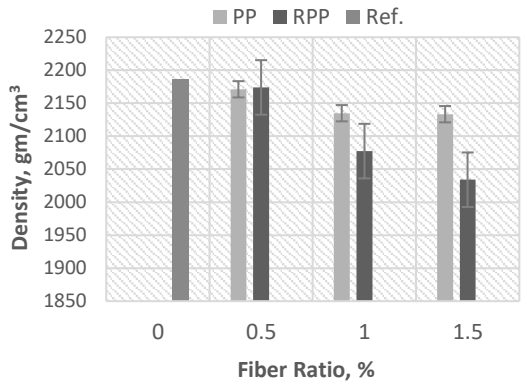

Figure 3. Effect of fiber type and proportion on the density of the PP fiber-reinforced mortar

Comparing the density of reinforced mortars with PP and RPP fibers, there is slight difference, not significance at 95% confidence level, in bulk density for cement mortar reinforced with PP or RPP fibers with the same dosage rate.

3. 3. Water Absorption The absorption rate of cementitious material is another important criterion that needs to be investigated. It is an indicator of material durability. Lower absorption rate means lesser ability of water and other liquid materials to infiltrate through cement mortar and thereby the adjacent structure. The water absorption for the cube mortars were tested and results are presented in Figure 4. It is clear to notice that the addition of fibers reduces water absorption ability. The presence of fibers in cement mortars block continues voids thereby reducing water absorption. The fiber geometry also impacts this property. The reduction of recycled PP fibers is higher than mixtures having raw PP fibers.

3. 4. Compressive Strength The compressive strength of the cubic cement mortars were tested and presented in Figure 5 as an average value for three samples as a function of fiber type and content. The compressive strength of PP-reinforced cement mortar increase with increasing the PP fiber content no matter the fiber type and the dosage rate. The percent of the increase is 3, 8, and 68% for 0.5, 1, and 1.5% of the raw PP fiber reinforced mortars, respectively, considering the non-reinforced mortar as a reference mix. Similarly, the compressive strength of the RPPF mortars also enhances with the fiber addition, especially, at high proportions. The percent enhancement is found as 32, 52, and 61% for 0.5, 1, and 1.5% of fiber content, respectively. This improvement in compressive strength of fiber-reinforced cement mortar may be attributed to the fibers that interlocking the cement mortar matrix. This can be noticed in Figure 6 that shows the failure mode of PPF and RPPF mixes.

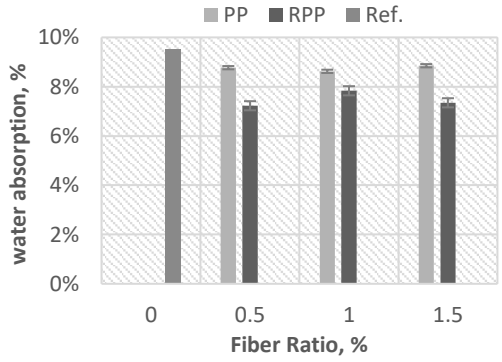

Figure 4. Effect of fiber type and proportion on the water absorption of the PP fiber-reinforced mortar

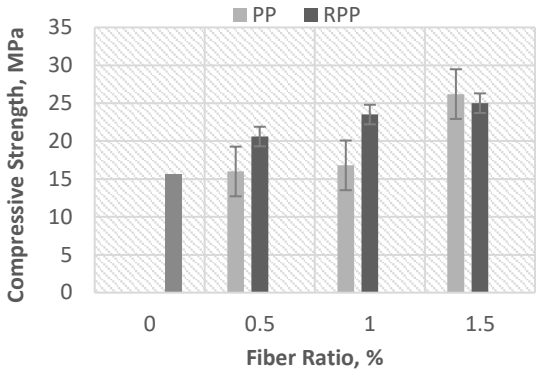

Figure 5. Effect of fiber type and proportion on the compressive strength of PP fiber-reinforced mortar

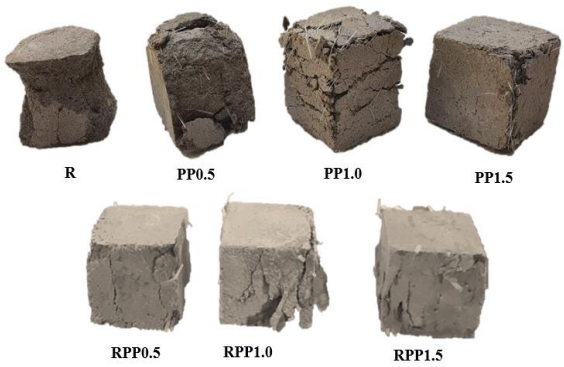

Figure 6. Mode of failure of PP and RPP- reinforced cement mortar

3. 5. Flexural Strength Regarding flexural strength, the beam samples were tested and presented in Figure 7 to show the average values for the different mixes. Even though the PPF 0.5 mix has higher flexural strength compared to the reference mix, there is a slight decrease in the flexural strength of the raw PPF mortars PPF1 and PPF 1.5. This behavior may be attributed to the geometry of PP fiber. The fibers shape of new PP is a combination of tiny hairlines that are connected together. These hairlines entrain air bubbles inside. These voids represent weak points in the mixture besides weaker bonds within the cement – sand- fiber matrix. Thereby, reinforcing cement mortar with 0.5 % of PPF can be used as the optimum dosage rate. In contrast, the cement mortars reinforced with RPPF exhibits higher flexural strength to double fold as compared to the reference mixture. This may be attributed to the fiber's ability to bridge the cracks at high level of strain [33]. In addition, the RPPF has larger cross- sectioal area, therby sustain more stress, beside it higher brittleness as compared to the new PP fibers. Figure 7 shows specimens containing PPF and RPPF after testing. So, there is a significant enhancement in the modulus of rupture for the RPPF mixtures s compared to PPF-mixes.

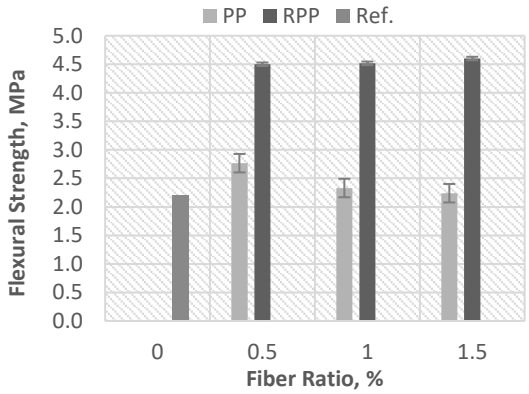

Figure 7. Effect of fiber type and proportion on the flexural strength of PP fiber-reinforced mortar

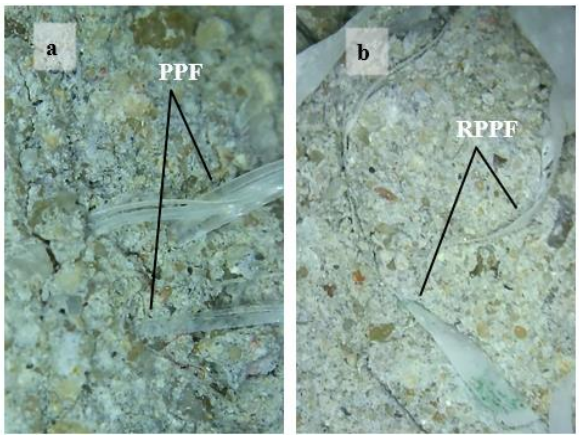

Figure 8. Cement mortar reinforced with (a) Polypropylene Fibers and (b) Recycled Polypropylene Fibers

3. 6. Toughness The ratio of compressive to flexural strength of mortar is an important indicator for mortar toughness [34]. The values for fiber-reinforced cement mortars are presented in Figure 9. It is clear to notice that the PP- mortars have higher toughness as compared to the RPP- mortars. However, mixtures contain RPP fibers tend to have lower toughness when compared to reference mixtures. The variation in toughness between PP-mortars and RPP- mortars is insignificant.

3. 7. Statistical Test Results The experimental results for each test were fed into STATISTICA v. 12 software for comparision. The output results of the t-test are summarizred in Table 3.

The test results in this table reveal that the workabilility, bulk density, and toughness for cement

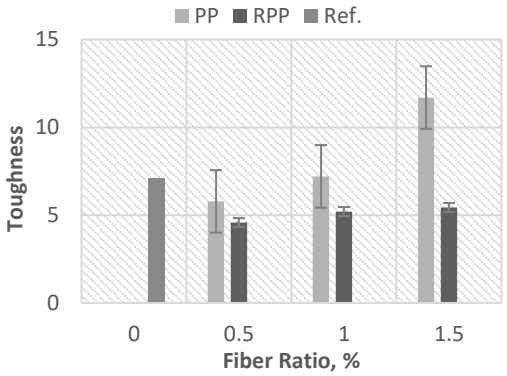

Figure 9. Effect of fiber type and proportion on the toughness of PP fiber-reinforced mortar

TABLE 3. Statistical Test for differences in properties of the PP and recycled PP fiber-reinforced mortar

Property	Variables	mean	Std. Dv.	Difference	Std. Dv. Dif.	t	P	Significance
Workability	PPF	131.667	5.773	11.667	5.773	3.50	0.073	No
	RPPF	120.000	10.00					
Bulk Density	PPF	2143.3	16.03	41.15	67.76	1.05	0.403	No
	RPPF	2102.2	83.34					
Water absorption	PPF	0.0875	0.0012	0.0128	0.004	5.214	0.035	**Yes**
	RPPF	0.0747	0.0032					
Compressive strength	PPF	19.663	5.676	-3.37	4.094	-1.426	0.29	No
	RPPF	23.033	2.237					
Flexural strength	PPF	2.446	0.281	-2.093	0.323	-11.224	0.007	**Yes**
	RPPF	4.539	0.054					
Toughness	PPF	8.228	3.087	3.156	2.719	2.010	0.182	No
	RPPF	5.072	0.443					

mortars reinforced either by PP or recycled PPF are approximetaly the same, with slight difference towards the PP-fiber reinforced mortars. However, this difference is not significant at 95% confidence level. Whereas, the compressive strength of the RPP fibers cement mortars are slightly higher than those mixes reinforced with new PP fibers. However, it is still insiginificant within 95% confidence level. From this test, it can be conclud that the recycled fibers made from PP can be used efficiently for renforcing since it provides approximately the same results as the new ones. This behavior may be attributed to the same inherent properties of the fibers that made from the same polymer type.

Moreover, there are significant differences in water absorption, and flexural strength. The water absorption of cement mortars with PPF is higher than thos with RPPF by about 13.7%. In addition, the flexural strength of cement mortars reinforced with RPPF is found to be higher than those reinforced with raw PPF by about 85.5% which can be considered as a great enhancement. The mean difference is significant at 95% confidence level. This finding may be atrributed to the fiber shape and cross section area.

Thereby, it can be concluded that the RPPF not only give similar results as new PPF when it used as reinforcing material with cement paste, but also give better results with two main properties which are water absorption and flexural strength. This serve as a sustainable solution to overcome the anticipataed environmental crisis.

4. CONCLUSIONS

This study compares the fresh properties and mechanical characteristics of cement mortars reinforced with polypropylene and recycled polypropylene fibers. The fibers` dosage was limited to 1.5% of mixture weight. The experimental and statistical test results reveal:

1. The flow values, density, and water absorption rate reduced with the addition of PP fibers either recycled or new. The reduction is higher with RPPF-reinforced mortars.
2. The mechanical properties like compressive and flexural strength increased with the inclusion of PPF and RPPF. The rate of an increase in is higher with the recycled fibers.
3. Some properties as the workability, bulk density, and toughness for cement mortars reinforced either by PP or recycled PPF are approximately the same, with slight difference towards the PP-fiber reinforced mortars.
4. The water absorption, and flexural strength test reveal a significant difference between PPF and RPPF mixtures.
5. The water absorption of cement mortars with PPF is higher than those with RPPF by about 13.7%.
6. The flexural strength of cement mortars reinforced with RPPF is higher than mixtures with raw PPF by about 85.5%

Thereby, this work shows the efficiency of using the recycled fiber since it provide similar strength as compared to new fibers. Moreover, cement mortars reinforced with recycled fibers exhibit better flexural strength than cement mortars reinforced with new PP fibers. The reinforcement tends to be effective at each dosage rate with optimum at 1.5%. This confirm the feasibility of using waste PP as a sustainable practice in addition to their desired characteristics for cementitious material reinforcement.

5. REFERENCES

1. Al-Haidari, H.S.J. and Al-Haydari, I.S., "Artificial intelligence-based compressive strength prediction of medium to high strength concrete", ***Iranian Journal of Science and Technology, Transactions of Civil Engineering***, (2021), 1-14, doi: 10.1007/S40996-021-00717-5.
2. Abid, S.R., Shamkhi, M.S., Mahdi, N.S. and Daek, Y.H., "Mechanical properties of pp-based engineered cementitious composites", in 2018 International Conference on Advance of Sustainable Engineering and its Application (ICASEA), IEEE., (2018), 142-146.
3. Choi, S.Y., Park, Y.H. and Jung, W.T., "Evaluation of the flexural performance of fiber reinforced mortar with low fiber content", in Advanced Materials Research, Trans Tech Publ. Vol. 639, (2013), 319-324.
4. Dawood, E.T., "The incorporations of wood ash and palm fibers for the production of high performance mortar", ***Journal of Techniques***, Vol. 29, No. 1, https://www.iasj.net/iasj/article/136598
5. Hassan, M.S. and Salih, W.M., "Mechanical performance of co2 and autoclave cured date palm fiber reinforced eco-mortar composites", ***Engineering and Technology Journal***, Vol. 34, No. 14 Part (A) Engineering, (2016), https://www.iasj.net/iasj/article/123731
6. De Fazio, P. and Feo, A., "Thermal and mechanical characterization of panels made by cement mortar and sheep's wool fibres", in 50th AiCARR International Congress on Beyond NZEB Buildings, Elsevier Ltd. Vol. 140, (2017).
7. Kesikidou, F. and Stefanidou, M., "Natural fiber-reinforced mortars", ***Journal of Building Engineering***, Vol. 25, (2019), 100786, doi: 10.1016/j.jobe.2019.100786.
8. Çomak, B., Bideci, A. and Bideci, Ö.S., "Effects of hemp fibers on characteristics of cement based mortar", ***Construction and Building Materials***, Vol. 169, (2018), 794-799, doi: 10.1016/j.conbuildmat.2018.03.029.
9. Song, P., Hwang, S. and Sheu, B., "Strength properties of nylon- and polypropylene-fiber-reinforced concretes", ***Cement and Concrete Research***, Vol. 35, No. 8, (2005), 1546-1550, doi: 10.1016/j.cemconres.2004.06.033.
10. Nguyen, T., Toumi, A. and Turatsinze, A., "Mechanical properties of steel fibre reinforced and rubberised cement-based mortars", ***Materials & Design***, Vol. 31, No. 1, (2010), 641-647, doi: 10.1016/J.MATDES.2009.05.006.

11. Al-Ridha, A.S., Ibrahim, A.K., Al-Taweel, H.M. and Dheyab, L.S., "Effect of steel fiber on ultrasonic pulse velocity and mechanical properties of self-compact light weight concrete", in IOP Conference Series: Materials Science and Engineering, IOP Publishing. Vol. 518, (2019), 022017.
12. Mahdi, R.S., "Experimental study effect of using glass fiber on cement mortar", ***Journal of Babylon University/Engineering Sciences***, Vol. 22, No. 1, (2014), 162-181, doi. https://www.iasj.net/iasj/article/85718
13. Elaiwi, E.H., Al-Chalabi, S.F., Al-Asadi, L.S., Abbood, A.A. and AL-Ridha, A.S., "Evaluating the performance of fibrous cement mortar containing chopped carbon fiber (CCF)", in IOP Conference Series: Materials Science and Engineering, IOP Publishing. Vol. 988, (2020), 012041.
14. Zaman, A.B., Shahzada, K. and Tayyab, N.M., "Mechanical properties of polypropylene fibers mixed cement-sand mortar", ***Journal of Applied Engineering Science***, Vol. 17, No. 2, (2019), 116-125, doi: 10.5937/jaes17-19092.
15. Mohseni, E., Khotbehsara, M., Naseri, F., Monazami, M. and Sarker, P., "Polypropylene fibre reinforced cement mortars containing rice husk ash and nano-alumina", ***Construction and Building Materials***, Vol. 111, (2016), 429-439, doi: 10.1016/j.conbuildmat.2016.02.124.
16. Salih, S.A. and Al-Azaawee, M.E., "Effect of polypropylene fibers on properties of mortar containing crushed bricks as aggregate", ***Eng Technol***, Vol. 26, No. 12, (2008), 1508-1513.
17. Abou Kheir, S., Wakim, J. and Awwad, E., "Flexural resistance of the polypropylene fibres reinforced cement mixes with waste material", in MATEC Web of Conferences, EDP Sciences. Vol. 281, (2019), 01010.
18. Xie, X., Hui, T., Luo, Y., Li, H., Li, G. and Wang, Z., "Research on the properties of low temperature and anti-uv of asphalt with nano-zno/nano-tio2/copolymer sbs composite modified in high-altitude areas", ***Advances in Materials Science and Engineering***, Vol. 2020, (2020), doi: 10.1155/2020/4752841.
19. Blazy, J. and Blazy, R., "Polypropylene fiber reinforced concrete and its application in creating architectural forms of public spaces", ***Case Studies in Construction Materials***, Vol. 14, (2021), e00549, doi: 10.1016/j.cscm.2021.e00549.
20. Al-Haydari, I.S. and Jawad, H.S., "Durability and aging characteristics of sustainable paving mixture", ***International Journal of Engineering***, ***Transactions B: Applications,*** Vol. 34, No. 8, (2021), doi: 10.5829/ije.2021.34.08b.07.
21. Park, J.K., Kim, M.O. and Kim, D.J., "Pullout behavior of recycled waste fishing net fibers embedded in cement mortar", ***Materials***, Vol. 13, No. 18, (2020), 4195, doi: 10.3390/MA13184195.
22. Spadea, S., Farina, I., Carrafiello, A. and Fraternali, F., "Recycled nylon fibers as cement mortar reinforcement", ***Construction and Building Materials***, Vol. 80, (2015), 200-209, doi: 10.1016/j.conbuildmat.2015.01.075.
23. Shanya, O., Daiki, U., Hiroshi, Y. and Katsufumi, H., "Effectiveness of recycled nylon fibers as reinforcing material in mortar", ***Journal of Asian Concrete Federation***, Vol. 2, No. 2, (2016), 102-109, doi: 10.18702/acf.2016.12.2.2.102.
24. Borinaga-Treviño, R., Orbe, A., Canales, J. and Norambuena-Contreras, J., "Experimental evaluation of cement mortars with recycled brass fibres from the electrical discharge machining process", ***Construction and Building Materials***, Vol. 246, (2020), 118522, doi: 10.1016/j.conbuildmat.2020.118522.
25. Nguyen, H., Carvelli, V., Fujii, T. and Okubo, K., "Cement mortar reinforced with reclaimed carbon fibres, cfrp waste or prepreg carbon waste", ***Construction and Building Materials***, Vol. 126, (2016), 321-331, doi: 10.1016/j.conbuildmat.2016.09.044.
26. Wang, Y., Zhang, S., Luo, D. and Shi, X., "Effect of chemically modified recycled carbon fiber composite on the mechanical properties of cementitious mortar", ***Composites Part B: Engineering***, Vol. 173, (2019), 106853, doi: 10.1016/j.compositesb.2019.05.064.
27. Farinha, C.B., de Brito, J. and Veiga, R., "Incorporation of high contents of textile, acrylic and glass waste fibres in cement-based mortars. Influence on mortars' fresh, mechanical and deformability behaviour", ***Construction and Building Materials***, Vol. 303, (2021), 124424, doi: 10.1016/J.conbuildmat.2021.124424.
28. Caliendo, H., "City in iraq opens its first recycling, production plant", ***Recycled Materials***, (2016), doi.
29. Sohaib, N., Seemab, F., Sana, G. and Mamoon, R., "Using polypropylene fibers in concrete to achieve maximum strength", in Proc. of the Eighth International Conference on Advances in Civil and Structural Engineering., (2018), 36-42.
30. ASTM, C., "Standard test method for flow of hydraulic cement mortar", ***C1437***, (2007).
31. C109/C109M-16a, A., "Standard test method for compressive strength of hydraulic cement mortars (using 2-in. Or [50-mm] cube specimens)", ***West Conshohocken: ASTM International***, (2016).
32. Materials, A.S.f.T., *Standard test method for flexural strength of hydraulic-cement mortars*. 2014, ASTM International West Conshohocken, PA, USA.
33. Oktay, D., Aktürk, B. And Kabay, N., "Properties of cement mortars reinforced with polypropylene fibers", ***Sigma Journal of Engineering and Natural Sciences***, Vol. 32, No. 2, (2014), 164-175.
34. Ali, A.S., Jawad, H.S. and Majeed, I.S., "Improvement the properties of cement mortar by using styrene butadiene rubber polymer", ***Journal of Engineering and Development***, Vol. 16, No. 3, (2012), 61-72.

Persian Abstract

چکیده

تقویت ملات سیمان با الیاف یک مرحله ضروری برای افزایش مقاومت خمشی آنها است. این مطالعه به مقایسه خواص تازه و ویژگی‌های مکانیکی ملات سیمانی تقویت‌شده با الیاف پلی‌پروپیلن و الیاف پلی‌پروپیلن بازیافتی می‌پردازد. نسبت الیاف تقویت کننده (۰، ۰.۵، ۱، و ۱.۵) درصد وزن ملات سیمان برای هر دو نوع الیاف بود. نمونه‌های ریخته‌گری شده با استفاده از آزمایش جریان برای ملات تازه، مقاومت فشاری، مقاومت خمشی و چقرمگی برای ملات‌های سخت شده آزمایش شدند. نتایج حاصل از این برنامه آزمایشی نشان می‌دهد که هر دو نوع الیاف باعث کاهش جریان ملات و افزایش ویژگی‌های مکانیکی آن می‌شوند. نتایج از نظر آماری برای اندازه‌گیری معنی‌داری تفاوت مورد آزمایش قرار گرفتند. ملات سیمانی تقویت شده با الیاف بازیافتی نتایج تقریباً مشابهی را در مقایسه با مخلوط‌های حاوی الیاف پلی پروپیلن خام در سطح اطمینان ۹۵٪ نشان داد. با این حال، در مقایسه با مخلوط‌های با الیاف پلی‌پروپیلن جدید که ممکن است به شکل الیاف و سطح مقطع نسبت داده شود، افزایش قابل‌توجهی در استحکام خمشی نشان می‌دهد.

International Journal of Engineering

Journal Homepage: www.ije.ir

Effect of Active Flux on Aluminum 6061 and its Mechanical Properties by Gas Tungsten Arc Welding Process

R. Ajezi-Sardroud[a], A. Mostafapour[a], F. Ajezi-Sardroud*[b], M. A. Mohtadi-Bonab[b]

[a] *Department of Mechanical Engineering, University of Tabriz, Tabriz, Iran*
[b] *Department of Mechanical Engineering, University of Bonab, Bonab, Iran*

PAPER INFO

Paper history:
Received 16 Febraury 2022
Received in revised form 16 March 2022
Accepted 19 March 2022

Keywords:
Tungsten Inert gas
Aluminum Alloy
Mechanical Properties
Active Flux
Titanium Oxide
Silicon Oxide

ABSTRACT

The current research was carried out with the aim of increasing the penetration depth and improving the mechanical properties of weld region by addition of active fluxes of titanium oxide (TiO_2) and silicon oxide (SiO_2). Tungsten inert gas (TIG) welding is applied on Aluminum 6061 alloy and active fluxes including SiO_2 and TiO_2 with 2.5, 7.5, and 10 wt% were incorporated. Up to now, TIG welding on aluminum 6061 with SiO_2 and TiO_2 fluxes has not been carried out. Mechanical properties were determined using tensile and Vickers micro-hardness experiments. The results showed that the highest tensile strength corresponds to the base metal and in welded specimens was related to 10% TiO_2 active flux. The ratio of tensile strength using titanium active flux and without flux mode is 90%. The use of both active titanium oxide and silicon oxide flux make the welded specimen granular and increases its strength. The effect of addition of titanium oxide is more noticeable than that of the silicon oxide flux since titanium oxide plays a key role on the granularity than the silicon oxide.

***doi**: 10.5829/ije.2022.35.08b.06*

1. INTRODUCTION

Aluminum 6061 has a great weldability feature in which thin parts are welded by tungsten arc welding technique while thick parts are welded by electric arc welding method [1]. The strength of this alloy is reduced after the welding process [2]. In 1920's, a great effort was designated to improve the quality of welding using arc protection and molten puddle in front of the atmosphere. One of the most important methods is the use of active flux in TIG welding process, which is known as active TIG. Tungsten is a hard metal with a melting point temperature of about 3800 °C [3]. The base metal molten puddle is protected from atmospheric elements by inert gas especially against combining with oxygen since inert gas does not mix with any of affinity elements. As soon as, the inert gas flows, the oxygen and air in the welding zone are pushed aside [4]. The protective gas passes through the tungsten electrode by a torch which is partly effective for cooling of the tungsten. Inert gas is mostly argon, but helium and nitrogen are also used in some cases depending on the type of application. The helium is used since it causes an increase in arc power and due to this, the speed of welding can be raised. This phenomenon also causes a better gas emissions from the weld zone [5]. It is worth mentioning that AC and DC currents are used in TIG welding [6]. Since welding rate in TIG method is relatively low, such method is used in welding of thick sheets for welding first pass (root pass). The welding cost is inversely proportional with welding time [7]. Kulkarni et al. [8] used P91 and P22 steel plates of 8 mm thickness, activating fluxes and TIG welding method. In their study, the effect of various fluxes such as silicon dioxide, titanium dioxide, chromium oxide, molybdenum oxide and copper oxide on the weld bead shape were investigated. Ramkumar et al. [9] studied the ferritic stainless steel (AISI 430) ability of welding using with and without activating fluxes. Two types of fluxes such as silicon dioxide and iron oxide have been used for analyzing mechanical properties of weld beads of

*Corresponding Author Email: razzaghajezi@gmail.com (F. Ajezi-Sardroud)

Please cite this article as: R. Ajezi-Sardroud, A. Mostafapour, F. Ajezi-Sardroud, M. A. Mohtadi-Bonab, Effect of Active Flux on Aluminum 6061 and its Mechanical Properties by Gas Tungsten Arc Welding Process, ***International Journal of Engineering, Transactions B: Applications***, Vol. 35, No. 08, (2022) 1501-1508

AISI430. The studies showed the existence of two kinds of phase structures including ferrite-intergranular martensite and precipitate-free zone surrounding the grain boundary martensite. Venukumar et al. [10] studied the welding parameters on inconel 718 alloy welded by TIG welding method. The post-world heat treatment performed at 750°C/8h furnace and the cooling rate was at 650°C/8h/air on weld beads. The results showed that welded specimens had better mechanical properties. In another study, Ramkumar et al. [11] investigated the effect of heat treatment on microstructure and mechanical properties in inconel 750 at fusion zone welded by A-TIG method. The tensile strength in post weld heat treated was higher than the as-weld condition, while the toughness value of as-weld specimens was higher than post weld heat treated specimen. Babbar et al. [12] studied TIG welding on different thicknesses of SS-304 steel. According to results, the welded specimens had higher tensile strength. Xie et al. [13] carried out a process using AZ31 magnesium alloy as base metal, Nano particles strengthening activating flux tungsten inert gas (NSA-TIG) as welding method and compound of titanium dioxide and nano-silicon carbide as coating fluxes. The results showed that compound of nano-particles as coating activating fluxes increased the microhardness in fusion zone and tensile strength of the joints. Ezazi et al. [14] have carried out research on two types of materials named stainless steel 3041 and aluminum alloy 5083. In their study, different activating fluxes were used such as titanium dioxide and calcium fluoride. The results showed that calcium fluoride increased strength more than titanium dioxide. Khoshroyan and Darvazi [15] conducted a research on distribution of heat and residual stress in Illinois aluminum 6061-T6 by ANSYS software in which MIG welding method was applied. In this study, the fluxes were not used and the affecting factors were only speed and currents of welding. Pk et al. [16] concentrated on improving the mechanical properties of aluminum 6061-SiC composite welded by TIG method. Also, in this research, the fluxes were homogenized and aged at 100, 150 and 200°C. The results showed that the aged and homogenized specimen in laboratory conditions had optimal hardness and minimum tensile strength.

The activated TIG can increase productivity by using TiO_2 and SiO_2 fluxes. It has been reported that activating fluxes such as TiO_2 and SiO_2 increased the maximum weld penetration [17]. However, an increase in the mechanisms of penetration in the activated flux TIG welding process is not fully understood [18]. It is worth-mentioning that two mechanisms can be considered on the activating flux on weld penetration. The first one is the arc constriction in which the activating flux may induce arc constriction during TIG welding [19, 20]. In this mechanism, the heat density has increased by the activating flux at the anode root area. As a result, the activating flux increases the penetration depth. The second mechanism is the reversal of surface tension gradient showing that surface active elements including sulfur and oxygen decomposed from the flux during welding change the fluid flow direction in the weld pool [21]. The purpose of this research in gas tungsten arc welding (GTAW) was to use active flux to increase the penetration depth and improve mechanical properties of weld region. It is expected that the use of active flux in TIG welding increases the weld depth and D/w. Also, active flux causes granularity in the weld zone leading to increase of tensile strength and microhardness. For the first time in this study, Al 6061 as a base metal and SiO_2 and TiO_2 as active fluxes were used and investigated.

2. EXPERIMENTAL PROCEDURE

The primary material used in this article is aluminum 6061-T6. Chemical composition of the used metal (for GTAW process) is summarized in Table 1. For specimen preparation, first a sheet with the thickness of 6 mm of the alloy was cut with dimensions of 100 mm x 50 mm by wire cut.

The active flux powders of TiO_2 and SiO_2 powders are used in this study. In aluminum welding by activating flux, first, the specimen is covered with a thin layer of TiO_2 or SiO_2 which is mixed with acetone. For this purpose, first, the specimens are weighted and then two pieces are stuck with the glue tape with the distance of 1 cm. After weighting, each specimen is covered with related oxide.

The schematic of active flux application is shown in Figure 1. The TIG welding machine used in this study had an automatic steady-speed with the speed of 15 mm/min. The specimens were fixed by a clamp and the electricity arc was determined by a filler with 2 mm thickness.

After welding process, the apparent quality of all welded specimens was evaluated. The apparent quality of the welded specimens like excessive reinforcement, under cut and spatter were evaluated and from each of the welded specimens, one with the best quality was chosen, see Figure 2. According to Figure 2, specimens of AL6061 were welded by two different types of active

TABLE 1. Chemical composition of aluminum 6061-T6 alloy (%) [22]

Al 6061-T6	Al	Si	Mn	Mg	Cr	Zn	Ti	Cu
----	Balance	0.68	0.32	0.85	0.06	0.07	0.05	0.22

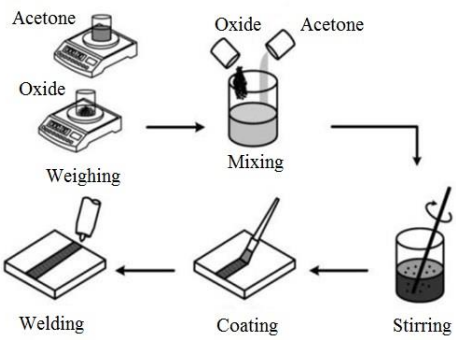

Figure 1. Schematic view of the flux application on specimens [23]

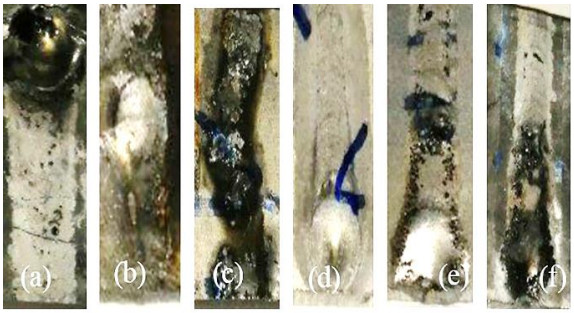

Figure 2. Physical appearance of welded specimens by (a) SiO_2 2.5% (b) SiO_2 7.5% (c) SiO_2 10% (d) TiO_2 2.5% (e) TiO_2 7.5% and (f) TiO2 10%

fluxes with different percentages of 2.5 and 7.5 and 10. Then, as shown in Figure 3, the specimens were subjected to the tensile testing.

According to Figure 4, tensile testes specimens were cut by the JIS Z2201 standard [24]. They were cut by wire cut in order to weld on their center. The specimens were under tensile test with 10 mm/min in order to examine their tensile strength and flexibility.

Vickers micro hardness testing was carried out with 200 g weight for 27 s. These 15 micro hardness experiments were carried out on each specimen which covered and evaluated the whole welding zone including the base metal, HAZ zone and weld pool.

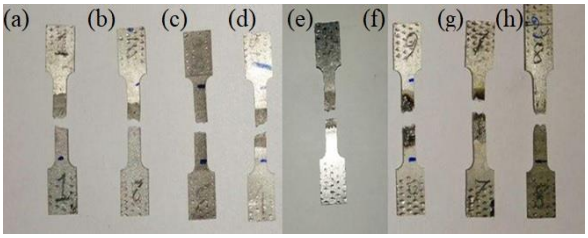

Figure 3. Tensile and micro hardness tested specimens welded by (a) without flux (b) SiO_2 2.5% (c) SiO_2 7.5% (d) SiO_2 10% (e) TiO_2 2.5% (f) TiO_2 7.5% (g) TiO_2 10% and (h) raw specimen

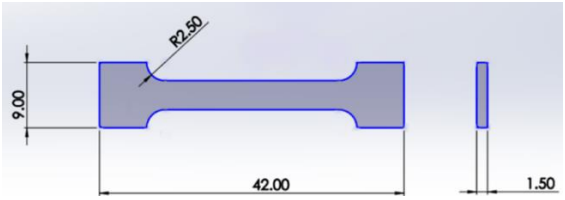

Figure 4. Dimensions of tensile tested specimens based on JIS Z2201 standard [24]

3. RESULTS AND DISCUSSION

The results of the depth-to-width ratio (D/W) measurement in welded specimens are shown in Table 2. As seen in this table, at the same inlet heat, the ratio of depth to weld width increases with increasing the percentage of activating fluxes. The reason for the increase in penetration depth is the reverse of the Marangoni flow rate of the weld pool. As is clear, elements such as oxygen, which have a high surface activity, reverse the direction of the Marangoni force and increase the depth. On the other hand, in the active mode of active flux, by decomposing the welding flux, oxygen gas escapes from the welding site and surrounds the arc. The presence of this gas prevents heat loss and narrows the arc, which ultimately increases the intensity of the flow and weld depth. As a result of the application of activating fluxes on the welding of specimens, the results show the high positive effects of surface activator flux on the depth-to-width ratio in the present study. As mentioned earlier, the main reason for the increase in penetration depth is the reversal of Marangoni displacement of the weld pool fluid, which is possible despite the elements with high surface activity [25]. The next factor affecting the depth of penetration of the weld is the increase of the temperature of the arc plasma due to the decomposition and even evaporation of the surface activating flux. By decomposing the active flux elements, the oxide molecules join the free electron ring around the arc and surround the arc [26]. The presence of this cloud layer of oxide elements around the arc prevents heat loss and arc contraction and increases the plasma flow density as well [27, 28]

The results of the ratio of depth to weld width are presented in Figure 5 and Table 2 with TiO_2 and SiO_2 active fluxes with different percentages of 2.5%, 7.5% and 10%. The results show that the ratio of depth to weld width increases with the increase of active flux. As seen in 10% of TiO_2 specimen, the highest ratio is 0.92 which is 2.68 times higher than the non-flux welded specimen.

Microstructure of specimens tested by metallographic method are shown in Figures 6(a)-6(h) and also crystal grain sizes are presented in Table 3. As seen in this figure, the application of their active flux increases the nucleation centers and, as a result, causes the smelting area to shrink

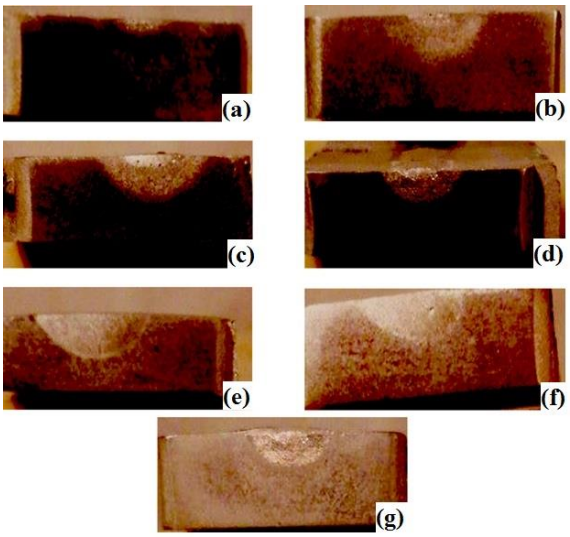

Figure 5. Penetration depth of welded specimens (a) welded without flux, (b) SiO_2 2.5%, (c) SiO_2 7.5%, (d) SiO_2 10%, (e) TiO_2 2.5%, (f) TiO_2 7.5%, and (g) TiO_2 10%

TABLE 2. Depth to width ratio of welded specimens

Specimen No.	Name	Width (W)	Depth (D)	Ratio of (D/W)
1	Welded Without Flux	6	1.5	0.25
2	SiO_2 2.5%	6	2	0.33
3	SiO_2 7.5%	6	3.5	0.58
4	SiO_2 10%	5	3	0.6
5	TiO_2 2.5%	8	6	0.75
6	TiO_2 7.5%	5	4	0.8
7	TiO_2 10%	7	6.5	0.92

[29, 30]. There are some sediments shown in the images in which the source of these sediments is the evaporation of magnesium oxide which is visible among sediments by black dots called inclusion. Figures 6(a) and 6(b) show the microstructure of raw material and welded without flux. In the raw material, there is no inclusion and precipitate; however, there are few precipitates and inclusions in welded material without flux. The precipitates and inclusions are shown with black spots. Moreover, many elongated grains are observed in both figures. Figures 6(c)-6(e) show the HAZ zone microstructures of welded specimens by adding SiO_2 2.5%, SiO_2 7.5%, and SiO_2 10%, respectively. As clearly, one can see that there are many black spots in these specimens showing that the density of precipitates and inclusions are increased with the SiO_2 addition. One can also see the elongated grains in these figures show that full recrystallization was not achieved in these grains. Figures 6(f)-6(h) show HAZ zone microstructures of welded specimens by addition of TiO_2 2.5%, TiO_2 7.5%,

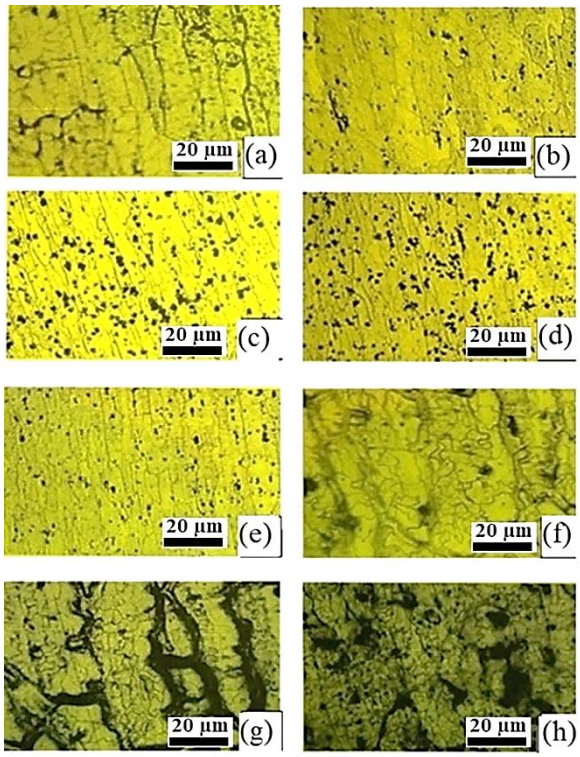

Figure 6. HAZ zone microstructures of welded specimens in 100x (a) raw material (b) welded without flux (c) SiO_2 2.5% (d) SiO_2 7.5% (e) SiO_2 10% (f) TiO_2 2.5% (g) TiO_2 7.5%, and (h) TiO_2 10%

and TiO_2 10%, respectively. In these figures, the size of black spots is significantly increased and some subgrains are formed during welding process. More importantly, when the amount of TiO_2 increased, some big cracks are formed in the HAZ zone. As stated in Table 3, the decrease in grain size improves the mechanical properties.

According to Table 4, it is observed that the active flux of SiO_2 and TiO_2 is active based on the ratio of Hall-Petch and finer than active granulation without flux.

TABLE 3. Crystal grain medium sizes

Specimen No.	Name	Average grain size (µm)
1	Welded Without Flux	26
2	SiO_2 2.5%	20
3	SiO_2 7.5%	15
4	SiO_2 10%	13
5	TiO_2 2.5%	16
6	TiO_2 7.5%	14
7	TiO_2 10%	10
8	Raw specimen	23

TABLE 4. Average value of Vickers micro hardness of specimens

Specimen No.	Name	Vickers Micro Hardness (HV)
1	Welded Without Flux	66±2
2	SiO_2 2.5%	70±1
3	SiO_2 7.5%	77±3
4	SiO_2 10%	87±2
5	TiO_2 2.5%	68±2
6	TiO_2 7.5%	72±1
7	TiO_2 10%	96±3
8	Raw specimen	106±3

Therefore, the hardness of activated flux welds is higher than that of without active flux [31].

As shown in Figures 7(a) and 7(b), as the concentration of active flux increases, the melted area becomes finer which increases the hardness. The base metal, due to rolling process, increases its stiffness and hardness called work-hardening creating a cast-like structure during welding. Molten metal loses its hardening properties and due to recrystallization, the hardness of the welded parts decreases.

The results of the tensile test are summarized in Table 5. In all welded specimens, there is a correlation between the maximum elongation and the tensile strength. It is worth-mentioning that the raw specimen has the highest tensile strength and maximum elongation. A comparison with welded specimens by A-TIG method shows that the active fluxes percentage has a considerable effect on the tensile strength and strain of the tested specimen. Finer the microstructure, the better mechanical properties are achieved. For this reason, the tensile strength in specimen 7 is the highest.

By comparing the tensile test results of the specimens in Figures 8(a)-8(h), it is concluded that active flux welding has a more tensile strength than active flax-free welding. However, in the welded active flux, the welding is divided into two groups with active SiO_2 and TiO_2. In SiO_2, specimen 4 has the maximum tensile strength, including 10% SiO_2. In TiO_2, specimen 7 has the maximum tensile strength including 10% TiO_2. This indicates that in both types of activated fluxes, the tensile strength increases with increasing flux percentage. However, in general, addition of TiO_2 has achieved better results than that of the SiO_2.

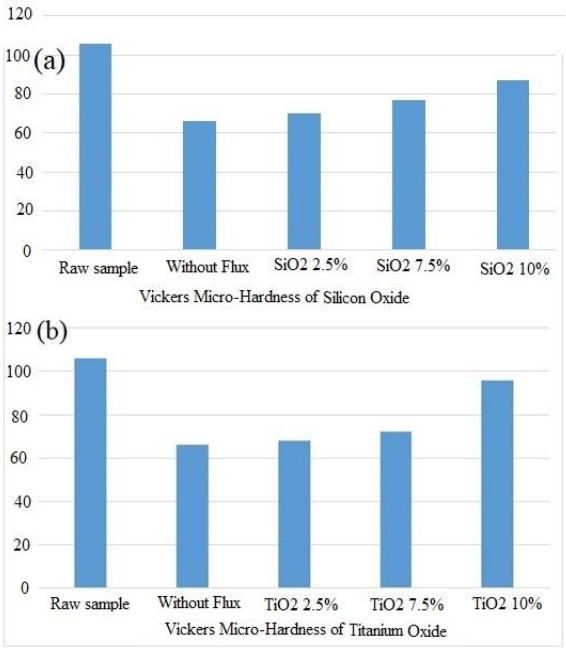

Figure 7. Vickers micro hardness of (a) SiO_2 and (b) TiO_2

TABLE 5. Tensile strength and Strain of welded specimens

Specimen No.	Name	Tensile Strength (MPa)	Max. Elongation (%)	Elasticity Modulus (GPa)
1	Welded Without Flux	80±5	3	90.2±2
2	SiO_2 2.5%	126±6	6	79.7±2
3	SiO_2 7.5%	129±4	6	83.1±3
4	SiO_2 10%	138+4	4	120.9±4
5	TiO_2 2.5%	137±6	16	43.8±2
6	TiO_2 7.5%	144±5	12	63.1±4
7	TiO_2 10%	152±5	5	100.4±3
8	Raw specimen	274±6	8	151.5 ±4

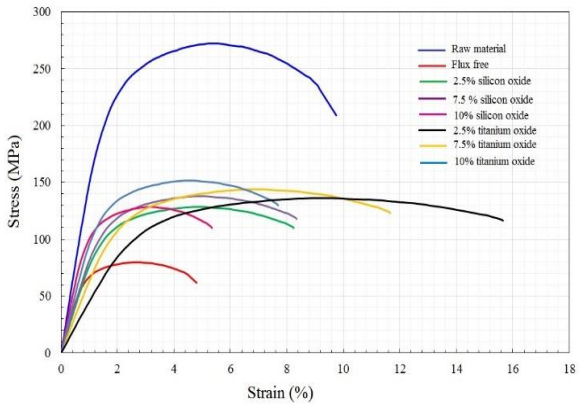

Figure 8. Stress- strain curve for (a) raw material (b) flux-free welded specimen (c) 2.5% SiO_2 active flux welded specimen, (d) 7.5% SiO_2 active flux welded specimen, (e) 10% SiO_2 active flux welded specimen, (f) 2.5% TiO_2 active flux welded specimen, (g) 7.5% TiO_2 active flux welded specimen, (h) 10% TiO_2 active flux welded specimen

Due to its eutectic state, silicon and aluminum reduce the melting temperature and an increase in the speed of melting operations and welding at the same time. In addition, all the components of silicon and aluminum melt in the solution and simultaneously begin to crystallize, which reduces stress when the welding area cools [32]. Silicon improves welding operations and reduces the percentage of gas absorption and facilitates shell freezing. Due to the reduction of the melting point and the decrease in the percentage of contraction during freezing of the weld zone, silicon has caused this to be a factor in reducing the stress when the melt area cools. The active SiO_2 flux during Al 6061 is not sensitive to hot cracking and scattered shrinkage welding due to its eutectic properties [33]. In comparison, titanium causes granularity and has a special effect on nucleation, granulation, oxidation and quality of the operations. As mentioned earlier, the reason for the granularity in the active titanium flux is its acting as non-uniform cores in freezing. Moreover, an increase in the number of cores causes the crystal lattice of the weld zone to become smaller and more uniform. Titanium makes the weld region granular, which is due to an increase in grain boundary length and strength. On the other hand, this granularity increases the flexibility. Granularity also prevents large shrinkage cavities in the weld region increasing the quality of the weld. Using active flux, no matter what type they are, both of them create granularity in the base weld metal. These active fluxes decompose due to welding heat and release oxygen. Some of oxygen atoms emit gas around the plasma channel and prevent the plasma channel from expanding. However, the narrowing of the plasma canal reduces the width of the weld and increases the depth. Also, the presence of oxygen in the melt changes the shape of the metal impurities in the composition of the elements. This phenomenon acts as granulation centers and the welding metal becomes finer. In comparison of SiO_2 and TiO_2, the presence of titanium and its oxide in the melt increases the nuclearization centers and the weld metal becomes finer. More importantly, titanium and TiO_2 nucleation role is higher than silicon and SiO_2.

Figures 9(a)-9(d) show SEM images of fracture surfaces for tensile tested specimens. As shown in Figures 9(a) and 9(b), in the fracture surfaces of raw and flux-free welded specimens, there are a lot of dimples which are considered a sign of ductile fracture. Figures 9(c)-9(e) also show the fracture surfaces of 2.5% and 7.5% and 10% SiO_2 active flux welded specimens. One can clearly see that the type of fracture is ductile due to the presence of many dimples in the fracture surfaces of these specimens. Interestingly, the fracture surface of 2.5% TiO_2 active flux welded specimen show that when TiO_2 is added to the weld part, the number of dimples is significantly reduced and the surface becomes flat. The flat surface proves that the nature of fracture transfers from ductile to brittle. If one looks at the Figures 9h and 9g, 7.5% and 10% TiO_2 active flux welded specimens, the fracture surfaces are completely flat showing that the fracture nature has become brittle. Moreover, some cracks are also observed in the fracture surfaces of 7.5% and 10% TiO_2 active flux welded specimens. The characteristics of both regions were quasi-cleavage with some secondary cracks.

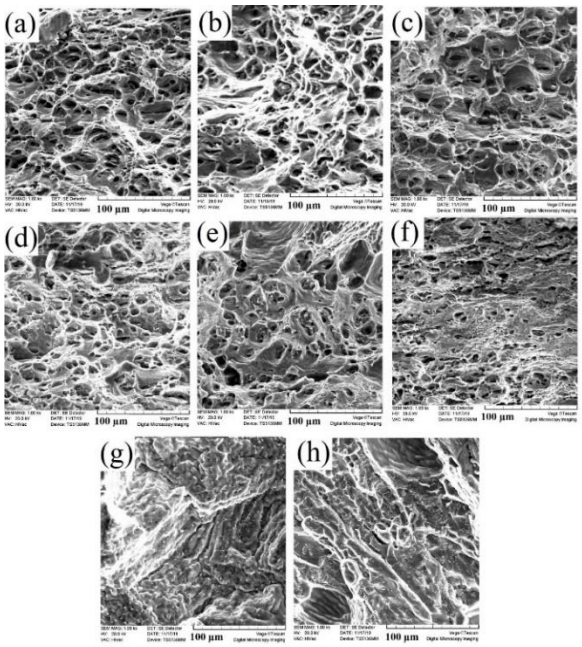

Figure 9. SEM micrographs of fracture surfaces for tensile tested (a) raw material (b) flux-free welded specimen (c) 2.5% SiO2 active flux welded specimen, (d) 7.5% SiO2active flux welded specimen, (e) 10% SiO2active flux welded specimen, (f) 2.5% TiO_2 active flux welded specimen, (g) 7.5% TiO_2 active flux welded specimen, (h) 10% TiO_2 active flux welded specimens

4. CONCLUSIONS

This research was carried in order to increase the penetration depth and improve the mechanical properties of weld region by addition of the active fluxes of TiO_2 and SiO_2. Therefore, the effect of these active fluxes was investigated on microstructure properties of aluminum 6061 welded by TIG method. The following conclusions were obtained based on experimental results:

1) The stiffness and hardness of the base metal are increased due to the work-hardening occurred by creating a cast-like structure during welding. Therefore, the highest strength was related to the base metal. However, the strength of the base metal is also reduced by the loss of work hardening during the welding process.

2) The addition of active flux increased granularity in the weld zone leading to increase of tensile strength and

microhardness. Moreover, they decreased the grain size and increased the strength.

3) The highest tensile strength in SiO_2 added specimens was occurred in 10% SiO_2 added specimen with the amount of 138 MPa. The ratio of tensile strength in 10% SiO_2 added specimen to welded specimen without using flux was72%.

4) The highest tensile strength in TiO_2 added specimen was occurred in 10% TiO_2 added specimen with the amount of 152 MPa. The ratio of tensile strength in 10% TiO_2 added specimen to the specimen without using flux was 90%.

5) The effect of addition of TiO_2 flux was more considerable than that of SiO_2, because the TiO_2 had more nucleation effect than the SiO_2.

5. REFERENCES

1. Choudhary, S., Choudhary, S., Vaish, S., Upadhyay, A. K., Singla, A. and Singh, Y., "Effect of Welding Parameters on Microstructure and Mechanical Properties of Friction Stir Welded Al 6061 Aluminum Alloy Joints", ***Materials Today: Proceedings***, Vol. 25, No. 4, (2020), 563-569. doi: 10.1016/j.matpr.2019.05.466
2. Ahmad Fauzi, M. N., Uday M. B., Zuhailawati, H. and Ismail, A. B., "Microstructure and Mechanical Properties of Alumina-6061 Aluminum Alloy Joined by Friction Welding", ***Materials & Design***, Vol. 31, No. 2, (2010), 670-676. doi: 10.1016/j.matdes.2009.08.019
3. Wang, W., Fan, D., Huang, J. and Huang, Y., "Numerical Simulation of Arc Plasma and Weld Pool in Double Electrodes Tungsten Inert Gas Welding", ***International Journal of Heat and Mass Transfer***, Vol. 85, (2015), 924-934. doi: 10.1016/j.ijheatmasstransfer.2015.01.132
4. Singh, G., Kang, A. S., Singh, K. and Singh, J., "Experimental Comparison of Friction Stir Welding Process and TIG Welding Process for 6082-T6 Aluminum Alloy", ***Materials Today: Proceedings***, Vol. 4, No. 2, (2017), 3590-3600. doi: 10.1016/j.matpr.2017.02.251
5. Mishra, D. and Dakkili, M., "Gas Tungsten and Shielded Metal Arc Welding of Stainless Steel 310 and 304 Grades over Single and Double 'V' Butt Joints", ***Materials Today: Proceedings***, Vol. 27, No. 2, (2020), 772-776. doi: 10.1016/j.matpr.2019.12.189
6. Dong, B., Cai, X., Ni, Z., Lin, S., Fan, C. and Yang, C., "Numerical Simulation of Arc Characteristics in Narrow Gap TIG Welding", ***International Journal of Mechanical Sciences***, Vol. 161-162, (2019), 105031. doi: 10.1016/j.ijmecsci.2019.105031
7. Liu, Z., Fang, Y., Cui, S., Yi, S., Qiu, J., Jiang, Q., Liu, W. and Luo, Z., "Keyhole Thermal Behavior in GTAW Welding Process", ***International Journal of Thermal Sciences***, Vol. 114 (2017), 352-362. DOI: 10.1016/j.ijthermalsci.2017.01.005
8. Kulkarni, A., Dwivedi, D. K. and Vasudevan, M., "Study of Mechanism, Microstructure and Mechanical Properties of Activated Flux TIG Welded P91 Steel-P22 Steel Dissimilar Metal Joint", ***Materials Science and Engineering: A***, Vol. 731, (2018), 309-323. doi: 10.1016/j.msea.2018.06.054
9. Ramkumar, K. D., Chandrasekhar, A., Singh, A. K., Ahuja, S., Agarwal, A., Arivazhagan, N. and Rabel, A. M., "Comparative Studies on the Weldability, Microstructure and Tensile Properties of Autogeneous TIG Welded AISI 430 Ferritic Stainless Steel with and without Flux", ***Journal of Manufacturing Processes***, Vol. 20, No. 1, (2015), 54-69. doi: 10.1016/j.jmapro.2015.09.008
10. Venukumar, S., Sarkar, P., Sashank, J. S., Sampath, P. and Saikiran, K., "Microstructural and Mechanical Properties of Inconel 718 TIG Weldments", ***Materials Today: Proceedings***, Vol. 5, No. 2, (2018), 8480-8485. doi: 10.1016/j.matpr.2017.11.544
11. Ramkumar, K. D., Ramanand, R., Ameer, A., Simon, K. A. and Arivazhagan, N., "Effect of Post Weld Heat Treatment on the Microstructure and Tensile Properties of Activated Flux TIG Welds of Inconel X750", ***Materials Science and Engineering: A***, Vol. 658, (2016), 326-338. doi: 10.1016/j.msea.2016.02.022
12. Babbar, A., Kumar, A., Jain, V. and Gupta, D., "Enhancement of Activated Tungsten Inert Gas (A-TIG) Welding Using Multi-Component TiO_2-SiO_2-Al_2O_3 Hybrid Flux", ***Measurement***, Vol. 148, (2019), 106912. doi: 10.1016/j.measurement.2019.106912
13. Xie X., Shen, J., Cheng, L., Li, Y. and Pu, Y., "Effects of Nano-Particles Strengthening Activating Flux on the Microstructures and Mechanical Properties of TIG Welded AZ31 Magnesium Alloy Joints", ***Materials & Design***, Vol. 81, (2015), 31-38. doi: 10.1016/j.matdes.2015.05.024
14. Ezazi, M. A., Yusof, F., Sarhan, A. A. D., Shukor, M. H. A. and Fadzil, M., "Employment of Fiber Laser Technology to Weld Austenitic Stainless Steel 304l with Aluminum Alloy 5083 Using Pre-Placed Activating Flux", ***Materials & Design***, Vol. 87, (2015), 105-123. doi: 10.1016/j.matdes.2015.08.014
15. Khoshroyan, A. and Darvazi, A. R., "Effects of Welding Parameters and Welding Sequence on Residual Stress and Distortion in Al6061-T6 Aluminum Alloy for T-Shaped Welded Joint", ***Transactions of Nonferrous Metals Society of china***, Vol. 30, No. 1, (2020), 76-89. DOI: 10.1016/j.matdes.2015.08.014
16. Pk, J., Mc, G., Sharma, S., Shetty, R., Shettar, M. and Hiremath, P., "Influence of Homogenization and Aging on Tensile Strength and Fracture Behavior of TIG Welded Al6061-Sic Composites", ***Journal of Materials Research and Technology***, Vol. 9, No. 3, (2020), 3598-3613. doi: 10.1016/j.jmrt.2020.01.098
17. Surendran, N., Luhar, K., Mistry, D., Teacher, M. and Srivastav, S., "Effect of TiO_2 Flux and SiO_2 Flux Coating on Weld Penetration by A-TIG", ***SSRG International Journal of Mechanical Engineering***, Vol. 4, No. 4, (2018), 14-21. doi: 10.14445/23488360/IJME-V5I4P104
18. Li, C., Shi, Y., Gu, Y., Fan, D. and Zhu, M., "Effects of Different Activating Fluxes on the Surface Tension of Moltenmetal in Gas Tungsten Arc Welding", ***Journal of Manufacturing Processes***, Vol. 32, (2018), 395-402. doi: 10.1016/j.jmapro.2018.03.001
19. Morisada, Y., Fujii, H. and Xukun, W., "Development of Simplified Active Fluxtungsten Inert Gas Welding for Deep Penetration", ***Materials & Design***, Vol. 54, (2014), 526-530. DOI: 10.1016/j.matdes.2013.08.081
20. Savitskii, M., "The Mechanism of the Effects of Electrically-Negative Elements on the Penetrating Power of an Arc with a Tungsten Cathode", ***Avt. Svarka***, Vol. 9, (1980), 17-22.
21. Heiple, C. R. and Poper, J. R., "Mechanism for Minor Element Effect on GTA Fusion Zone Geometry***", Welding Journal***, Vol. 61, (1982), 975-1025.
22. Aruri, D., Adepu, K., Adepu, K. and Bazavada, K., "Wear and Mechanical Properties of 6061-T6 Aluminum Alloy Surface Hybrid Composites [(Sic+Gr) And (Sic+Al_2O_3)] Fabricated by Friction Stir Processing", ***Journal of Materials Research and Technology***, Vol. 2, No. 4, (2013), 362-369. doi: 10.1016/j.jmrt.2013.10.004
23. Sanket Bodkhe, D. R. D., "Effects of Flux Coated Tungsten Inert Gas Welding on 304L Austenitic Stainless Steel", ***IACSIT International Journal of Engineering and Technology***, Vol. 6, No. 3, (2014), 177-181. doi: 10.7763/IJET.2014.V6.691
24. JIS, J., "2201, Test pieces for tensile test for metallic material" Japanese Standards Association, (1998).

25. Zhang, T., Shen, J., LÜ, L., Wang, C., J.X. Sang, J. X. and D. Wu, D., "Effects of Graphene Nanoplates on Microstructures and Mechanical Properties of NSA-TIG Welded AZ31 Magnesium Alloy Joints", ***Transactions of Nonferrous Metals Society of China***, Vol. 27, (2017), 1285-1293. doi: 10.1016/s1003-6326(17)60149-3

26. Satputaley, S. S., Waware, Y., Ksheersagar, K., Jichkar, Y. and Khonde, K., "Experimental Investigation on Effect of TIG Welding Process on Chromoly 4130 And Aluminum 7075-T6", ***Materials Today: Proceedings***, Vol. 41, No. 5, (2021), 991-994. doi: 10.1016/j.matpr.2020.05.733

27. Zaretsky, E. B., N. Frage, N. and Kalabukhov, S., "Shock Wave Determination of the Strengthening of Commercial Aluminum Alloy 6061 by Point Defects", ***Materials Science and Engineering: A***, Vol. 761, (2019), 138066. doi: 10.1016/j.msea.2019.138066

28. Verma, J. and Taiwade, R. V., "Effect of Welding Processes and Conditions on the Microstructure, Mechanical Properties and Corrosion Resistance of Duplex Stainless-Steel Weldments-A Review", ***Journal of Manufacturing Processes***, Vol. 25, (2017), 134-152. doi: 10.1016/j.jmapro.2016.11.003

29. Ajezi-Sardroud, R., Mostafapour, A., Ajezi-Sardroud, F. and Mohtadi-Bonab, M.A., "Effect of activating flux on aluminum 6061 and its mechanical properties by gas tungsten arc welding process", ***International Journal of Engineering***, ***Transactions B: Applications,*** Vol. 35, No. 8, (2022), doi: 10.5829/IJE.2022.35.08B.06.

30. Jayakrishnan, S. and Chakravarthy, P., "Flux Bounded Tungsten Inert Gas Welding for Enhanced Weld Performance-A Review", ***Journal of Manufacturing Processes***, Vol. 28, No. 1, (2017), 116-130. doi: 10.1016/j.jmapro.2017.05.023

31. Li, C., Shi, Y., Gu, Y., Fan, D. and Zhu, M., "Effects of Different Activating Fluxes on the Surface Tension of Molten Metal in Gas Tungsten Arc Welding", ***Journal of Manufacturing Processes***, Vol. 32, (2018), 395-402. doi: 10.1016/j.jmapro.2018.03.001

32. Kulkarni, A. Dwivedi, D. K. and Vasudevan, M., "Effect of Oxide Fluxes on Activated TIG Welding of AISI 316l Austenitic Stainless Steel", ***Materials Today: Proceedings***, Vol. 18, (2019), 4695-4702. doi: 10.1016/j.matpr.2019.07.455

33. Xu, W. and Dávila, L. P., "Tensile Nanomechanics and the Hall-Petch Effect in Nanocrystalline Aluminum", ***Materials Science and Engineering: A***, Vol. 710, (2018), 413-418. doi: 10.1016/j.msea.2017.10.021

Persian Abstract

چکیده

تحقیق حاضر با هدف افزایش عمق نفوذ و بهبود خواص مکانیکی ناحیه جوش با افزودن فلاکس های فعال اکسید تیتانیوم و اکسید سیلیکون انجام یافت. جوشکاری گاز بی اثر تنگستن روی آلیاژ آلومینیوم ٦٠٦١ اعمال شد و فلاکس های فعال اکسید تینانیوم و اکسید سیلیکون با ۲.۵، ۷.۵ و ۱۰ درصد وزنی اضافه شد. تاکنون جوشکاری گاز بی اثر تنگستن روی آلومینیوم ٦٠٦١ با فلاکس های فعال اکسید تینانیوم و اکید سیلیکون انجام نشده است. در این تحقیق، خواص مکانیکی با استفاده از آزمایشات کششی و میکروسختی ویکرز تعیین شد. نتایج نشان می دهد که بیشترین مقاومت کششی مربوط به فلز پایه و در نمونه های جوش داده شده مربوط به فلاکس فعال اکسید تیتانیوم ۱۰درصد است. نسبت استحکام کششی با استفاده از فلاکس فعال تیتانیوم و بدون فلاکس ۹۰ درصد است. استفاده از هر دو فلاکس اکسید تیتانیوم فعال و اکسید سیلیکون، نمونه جوش داده شده را دانه بندی کرده و استحکام آن را افزایش می دهد. اثر افزودن فلاکس اکسید تیتانیوم بیشتر از فلاکس اکسید سیلیکون است زیرا اکسید تیتانیوم نقش کلیدی در دانه بندی نسبت به اکسید سیلیکون دارد.

International Journal of Engineering

Journal Homepage: www.ije.ir

RESEARCH NOTE

Behavior of Raft Foundation Built on Layered Soil under Different Earthquake Excitation

A. H. Ali, H. O. Abbas*, S. H. Abed-Awn

Department of Civil Engineering, University of Diyala, Diyala, Iraq

PAPER INFO

Paper history:
Received 20 February 2022
Received in revised form 21 March 2022
Accepted30 March 2022

Keywords:
Earthquake
Raft
Layered Soil
Numerical

ABSTRACT

Achieving the stability of buildings and facilities against any external influence, such as winds, storms, or earthquakes, depends primarily on the foundations supporting them, which are responsible for transferring those loads to the soil layers beneath them. Accordingly, the design of the foundations to be safe withstand these static and dynamic loads without causing dangers or failures on these structures has recently become the focus of the attention of many researchers. The task of this paper is to predict the behavior of shallow raft foundations supporting loads of structures under the influence of earthquakes in Baquba city and what results from them from downfall and displacement risks. To simulate the soil-foundation model for the study, numerical modeling was used depending finite element approach. Different thickness of raft foundation under different earthquake acceleration-time records that simulate with a Linear Elastic model (LE) built on layered soil represented by Mohr-Coulomb model (MC). The results from this analysis showed properties of soil are used for this study play a vital role in the ground response to the propagation waves. Also observed from the results that an increase in both lateral and vertical displacement as the duration of earthquake increases and raft thickness decreases, but these displacements decreased when the thickness of raft foundation increased from 0.8m to 1.6m are about 9% and 68%, respectively.

doi: *10.5829/ije.2022.35.08b.07*

1. INTRODUCTION

Studying the behavior of shallow foundations under earthquake excitation, especially in active seismic areas has attracted the attention of several researchers in the last years. The phenomenon of earthquakes is considered one of the most dangerous natural disasters, that occurs without warning and causes the damage of any building or structure through settlement, ground cracking, and loss bearing capacity of soil-foundation. In comparison to the static case, the design of foundations in seismic areas necessitates special considerations. Seismic risk mitigation is one of the most difficult challenges in civil engineering, and geotechnical earthquake engineering can make an important contribution to this challenge [1]. The earthquake-related ground motion can have several effects on the shallow foundation: (i) During an earthquake, cyclic loss of soil strength could lead to bearing capacity collapse; (ii) The foundation may break due to a large horizontal inertial force caused by an earthquake, resulting in sliding or overturning; significant settlement and tilting; (iii) After an earthquake, the ground softens or fails due to pore water pressure redistribution, which might compromise the foundation's post-seismic stability [2]. In today's design practice, the geotechnical earthquake engineer is frequently in charge of delivering acceptable design ground motions to the structural engineer [3]. As a result, foundation engineers must keep abreast of technological advancements in these domains, or be well informed in these fields, to achieve cost-effective and safe designs. There is still a lot of work to be done in developing methodologies to evaluate seismic bearing capacity and earthquake-induced permanent displacements in shallow and deep foundations [4].

Many academic researchers have been interested in studying the real behavior of different types of foundations, raft foundations subjected to different

* Corresponding Author Email: temimi71@yahoo.com (H. O. Abbas)

Please cite this article as: A. H. Ali, H. O. Abbas, S. H. Abed-Awn, Behavior of Raft Foundation Built on Layered Soil under Different Earthquake Excitation, ***International Journal of Engineering, Transactions B: Applications***, Vol. 35, No. 08, (2022) 1509-1515

earthquake values to evaluate and interpret their performance using various methods. Conducted research by Roy [5] on strength considerations, which essentially entails ensuring that foundation loads remain well below those dictated by the allowable bearing capacity under seismic conditions, and serviceability is ensured by designing the substructure for the estimated permanent ground deformation. Uncomplicated procedures are presented for assessment bearing capacity and permanent ground deformation below earthquake conditions. Numerical simulation performed by Vali [6] to assess the settlement and safety factor of a reinforced marine soil-footing system on marine soft soil layers on Qeshm Island in the presence of a water table with finite element method used for this study, because of the erratic fluctuations in the water table on such poor soils; it was found the settlement was reduced while the safety factor of the soil-footing system was increased by lowering the water table. Numerical analysis by finite element was conducted by Shafiqu and Abdulrasool [7] to predict the behavior of raft foundation during different excitation of earthquakes, taking into consideration the influence of some parameters, such as raft stiffness and thickness, the maximum lateral displacement of soil under the foundation, vertical settlement, and influence the earthquake acceleration-time records. Plaxis 3d computer program is used in this study. The results of the parametric study for all sites showed that the settlement caused by the earthquake can be decreased by about 72% by increasing the thickness from 0.5 m to 1.5m. Also, it was founded that the value of the maximum lateral displacement and vertical settlement depends on the magnitude of the seismic wave and the peak ground acceleration of the earthquake. Another study was conducted by Al-Ameri et al. [8] to explain the effect of the earthquake (California, El-Centro earthquake is used) on the vertical and lateral displacement of the foundation numerically using the finite element analysis Abaqus program. The thickness of the foundation was studied in three different values which were (0.5, 1, and 2 m), as well as the depth of the soil layer under the foundation was taken (10, 20, and 40 m), and the soil stiffness ratio studied too. They concluded that as the earthquake's duration increases, so does the vertical displacement. In addition, as the depth of the soil layer beneath the foundation increases, both vertical and horizontal displacements diminish. They also discovered that increasing the foundation thickness minimizes lateral movement while having no discernible effect on vertical displacement. The reason for this is that the earthquake force is directed perpendicular to the foundation's base, and this displacement diminishes as the earthquake force increases. Increasing the distance between the wave's beginning point and the base is due to an increase in the influence of soil damping on earthquake forces. Srilakshmi and Rekha [9] investigated the MAT foundation. However, theoretical studies on the MAT foundation are relatively scarce. Furthermore, traditional methods for analyzing MAT foundations, such as the rigid method and the flexible method, are cumbersome and time-consuming. To overcome these limitations, the authors of these papers attempted to analyze the MAT foundation using the Finite Element Method. When compared to all other methods, FEM is the most efficient for complex boundaries and nonlinear material properties. ANSYS finite element software was used to analyze the MAT foundation in this work. The scope of this paper is limited to 2-D axisymmetric nonlinear analysis in medium sand concerning geometric features such as MAT foundation size and thickness under compression. While the MAT is treated as linear, the soil and soil-mat interface is treated as nonlinear, with the Drucker-Prager constitutive model used for the soil. The nonlinear analysis is a mixed method that is incremental and iterative, resulting in greater accuracy. The findings of this analysis will continue to pique the interest of MAT foundation designers. Bearing capacity's behavior and the resulting settlement for the rectangular, circular, and square shallow footing foundation were studied by Lwti et al. [10]. In addition, It is used in this study three modes of (D/B) ratios (0, 1/3, and 2/3) with three cases of footing depth (rested on the ground surface, below the ground surface with 0.5 and 1m) under earthquake loading by the numerical simulation using finite element analysis. The results indicate that the square shape was less settlement and high bearing than other shapes of footings, a linear relationship between the depth of footing and settlement under the effect of earthquake loading, and the magnitude of dynamic bearing capacity and settlement has been affected by the footing shape.As Iraq's seismicity has increased in a general and discernible way from south to north and West to East [11]. After a major 7.3 magnitude earthquake struck the Iraq-Iran border in November 2017, killing more people and injuring thousands more [12]. Accordingly, it became necessary to investigate the behavior of the soil-foundation system under these seismic activities due to a direct and destructive effect on the foundations of the buildings.Therefore, the objective of this paper is to predict the behavior of the raft foundation on silty soil subjected to different waves of earthquakes, considering the effect of raft thickness on the maximum settlement of the foundation, PLAXIS 3D 2020 finite element has been used for this axisymmetric simulation in Baquba city, Iraq [13].

2. FINITE ELEMENT ANALYSIS FOR CASE STUDY

A three-dimensional analysis for a soil-foundation system of a four-multi-story building located in Baquba city in the Diyala governorate in Iraq, Northeast of

Baghdad. All the geotechnical reports, data, and important properties were available and listed in PLAXIS 3D Manual [13]. The geometry model for this study consists of raft foundation with square shape is suggested for analysis with dimensions (18.5x18.5x0.8 m) embedded in a (40x40x30 m) soil media is used as a type of shallow foundation to evaluate the behavior of shallow foundation under earthquakes in Baquba soils. A common geometry of the model, soil layers together with raft foundation, surface loads (dead and live load) 70 $kN/m^{2,}$ and multiplier loading of the earthquake as shown in Figure1.

2. 1. Constitutive Models For Simulating Material

In general, the model of this study includes two parts of material soil and raft foundation. soil domain with square two layers represented by an elastic perfectly plastic (Mohr-Coulomb model). The failure envelope demonstrates that the points of stress under the line represent elastic behavior, and when the stress circles contact the failure line, the soil behavior changes from elastic to plastic. Mohr-Coulomb is commonly used for mostly geotechnical problems than other models as considered simple, easily used, and computations are relatively quick [14, 15]. Another part of the concrete foundation is molded by (thelinear elastic model), based on isotropic elasticity Hook's law. The flow is fed by several cases. The deformation analysis in PLAXIS software, the soil drained response of long time analysis, the soil undrained response of short term without considering the development of pore pressure, as the change of stress (the loading and unloading), excess pore water pressure will generate as a combination with time. As water level lies 1.5m below the ground surface, which can be represented in plaxis software of clay soil with short-term behavior (undrained A) in which the properties ineffective state and sand soil with long-term behavior (drained) high permeability. The properties for the foundation materials and soils are summarized Tables 1 and 2.

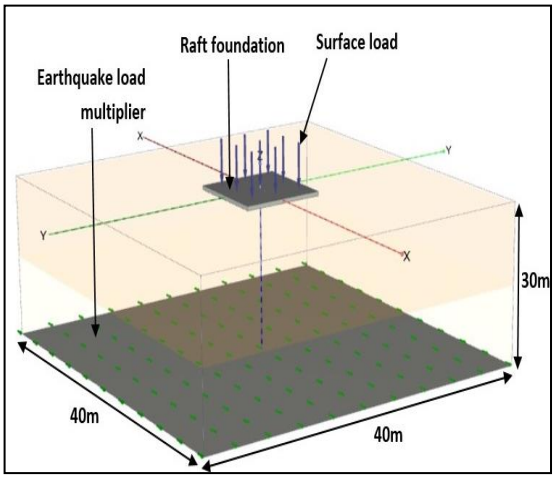

Figure 1. Geometry model with embedded raft foundation, surface load, and load multiplier of the earthquake

2. 2. Elements and Meshing

After completing the geometry model, PLAXIS 3D allows for a fully automatic to generate mesh, that is a collection of the finite element by dividing the model into volume elements taking full account soil stratigraphy, all structural objects, loads, and even boundary conditions. There is more than one selection of degree mesh start from very coarse to very fine, it is used in this study tetrahedral elements with 10 nodes, according to PLAXIS 3D Manual [13] strain is constant in the element and for accuracy results used with very fine mesh, but to avoid lengthy calculations time used medium-mesh as demonstrated in Figure 2. The relationship between the foundation and soil surrounding is rigid that delineates soil-foundation interaction, which means there is no relative displacement between these two materials. Raft

TABLE 1. Properties of the concrete foundation

Property	Unit	Value
Elastic Modulus	($kN\backslash m^2$)	$3x10^7$
Unit Weight	($kN\backslash m^3$)	34
Poisson's Ratio	-	0.15

TABLE 2. Properties of soil layers.

Type of soil	Soft clay	Silty sand
Interface	Rigid	Rigid
Elastic Modulus(kN/m^2)	7000	49000
UnitWeight of Soil(kN/m^3)	20	19
Poisson's Ratio	0.4	0.3
The angle of internal friction	-	40
Cohesion(kN/m^2)	28	-

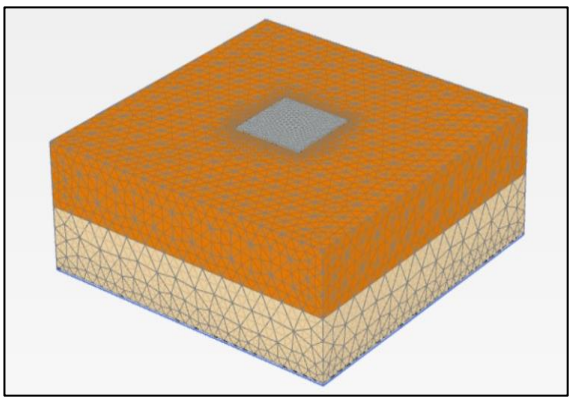

Figure 2. Medium mesh of raft footing and soils

foundation elements in full contact with soil elements [13]. Therefore, the interface element used has zero thickness.

2. 3. Definition of Earthquake and Boundary Condition The input motion used in this study is defined as dynamic surface load (load multipliers) at the bedrock level of the model as illustrated in Figure 3. The acceleration time history for three earthquakes selection in this search EL-Centro, Ali-Gharib, and Halabja that applied along the X-direction at the bottom boundary of the 3-D model in m/s^2 and s, respectively. In reality, the seismic waves propagate to infinity within the soil, according to this fact, and to prevent the sudden reflection of these waves on the model boundaries. Absorbent boundaries (viscous boundaries) are defined in Xmax, Xmin, and Zmin of the soil domain to absorb the incoming wave energy and a free move in all directions of the ground surface.

3. RESULTS AND DISCUSSION

The results of the numerical analysis of the model after completing all calculations of stage construction including excavation, raft construction, static and dynamic loads, that developed for this paper using the finite element method. The analysis is conducted to predict the behavior of raft foundation lateral displacement and vertical settlement under different distractive earthquakes: the first one is the EL-Centro earthquake 1940 with a local magnitude of 6.9, other earthquakes, 2017 Halabja earthquake with ML=7.3 was a record on Richter scale in the north of Iraq and Ali Al-Gharbi earthquake with ML=4.8 in the south of Iraq. In addition, the effect of raft thickness with (0.8m,1m,1.2m,1.4m and 1.6m), that discussion in the following section:

3. 1. Free Vibration of Soil The results of the free field analysis or as known free vibration of the soil deposits under the input earthquake motion as illustrated in Figure 4. This analysis describes the distribution and propagation of the seismic waves from bedrock to the surface soil, to get the response of soil layers of the model without any structure on or within it. It can be noted from the figure, the maximum lateral displacement occurs at the end of each one of the applied earthquakes and the minimum value at the start of wave propagation, this reason is related to the geophysical and mechanical properties of the soil layers under the foundation, that means the soil layers are silty sand (SH) to upper layers lean clay (CL) soft clay make the values of shear (V_s) and compression waves (V_p) lower than sandy soils. The second reason is when the duration of an earthquake increases the lateral displacement of soil increases with a reduction of the bearing capacity of those soil.

3. 2. Earthquake Loading The earthquake loading was applied to the raft foundation set above two layers of soil. Three situations of the earthquake were studied: the first one, the El-Centro earthquake (PGA) of intensity 0.35g was applied horizontally to the soil model while the foundation was subjected to surface load; and in the second situation, the Halabja earthquake (PGA) of intensity 0.1g; in the final situation, Ali AL-Gharbi (PGA) also of intensity 0.1g. Figure 5 shows the amount of lateral displacement resulting from EL-Centro load is higher than both of Halabja and Ali Al-Gharbi

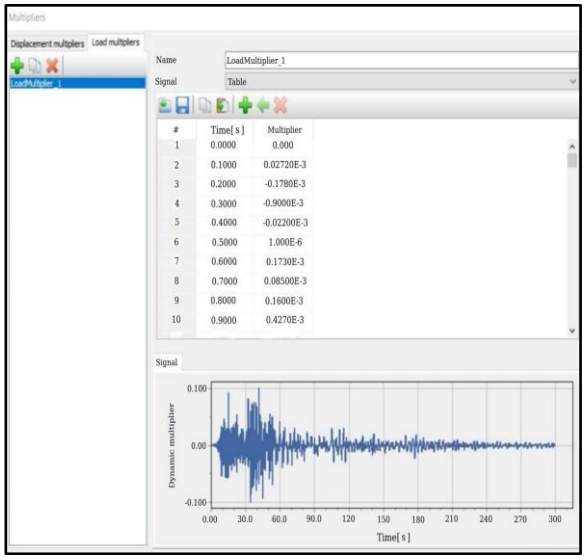

Figure 3. Acceleration –time history of Halabja earthquake

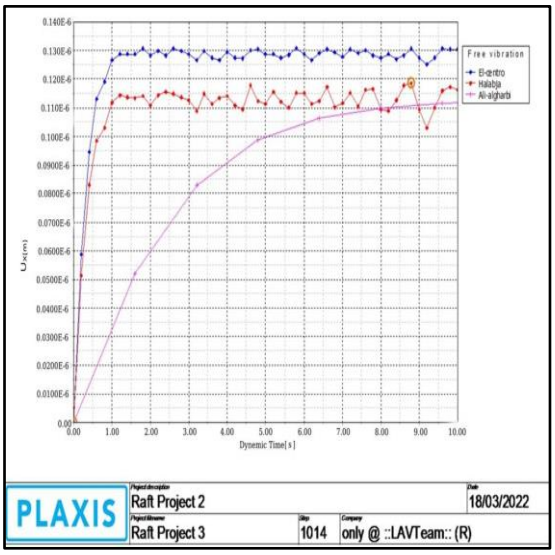

Figure 4. Lateral displacement of soil with time under different earthquakes

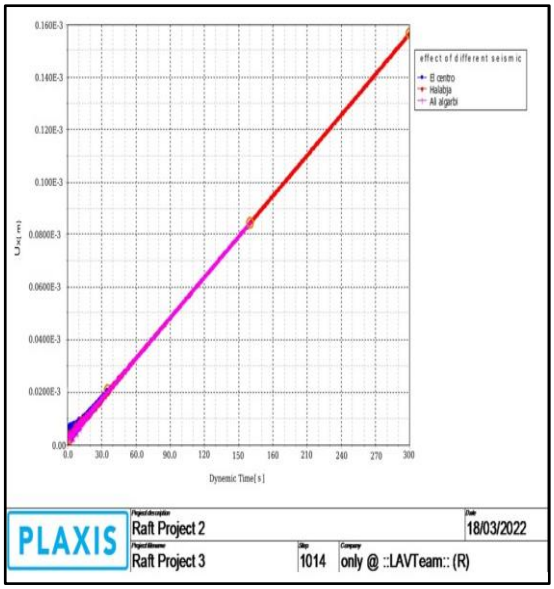

Figure 5. Dynamic time versus lateral displacement on foundation under different earthquakes

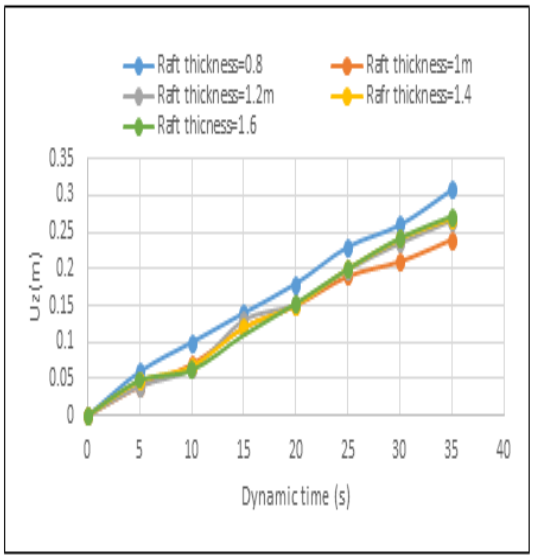

Figure 6. Vertical settlement versus dynamic time with different thicknesses placed on soil layers under El-Centro earthquake

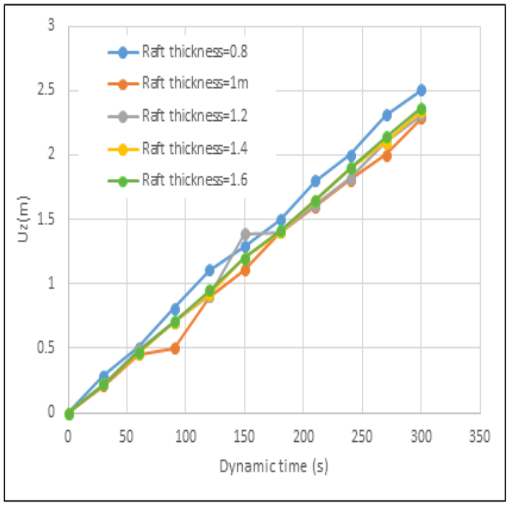

Figure 7. Vertical settlement versus dynamic time with different thicknesses placed on soil layers under Halabja earthquake

earthquakes at the beginning of loading, after the end of the EL-Centro earthquake period the oscillation of displacement with time is constant for values and start to increase with time acceleration of the other earthquakes to values about 5% from the previous increase. This may be to the displacement depending on the duration of the seismic waves and magnitude [16], in addition to the peak ground acceleration of the earthquake.

3. 3. Effect of Raft Foundation on Displacement

The influence of different raft thicknesses (i.e., T=0.8, 1, 1.2, 1.4 and 1.6m) which is embedded in soil models with two layers of soil lean clay and silty sand, concerning the vertical settlement and lateral displacement under different earthquake excitation is studied. In general, it can be noticed from the results, the maximum value of vertical settlement occurred in the lowest thickness of foundation (0.8m) under the Halabja earthquake is about 89% more than the value that occurred under the El-Centro earthquake and more than that under the Ali Al-Gharbi about 47%. As shown in Figures 6 to 8, the vertical settlement represents the highest values with 0.8m thickness for all earthquakes loading and being to reduce to 9% when gradually, the thickness of raft foundation increases even (1.6m). Also with every increase of raft thickness, the settlement was been at lower values with the beginning of the earthquake and increases with time of it, this response was generated due to an increases in the duration of an earthquake application on the model of study, an increase in the displacement foundation and, in addition to the state of soil layer beneath the foundation as soft clay soil that means has low strength properties to resist the application of earthquake loading. The lateral displacement of soil under the foundation has the same behavior pattern as vertical displacement because affected by changing the multiplier of the input motion of earthquakes, but the lateral displacement decreased by more than vertical, which is about 68% when the thickness of the raft foundation changed from (0.8 m) to (1.6m). From the above literature survey and the findings obtained are that there is a good agreement with data reported by Shafiqu and Abdulrasool [7] and Al-Ameri et al. [8] in different proportions due to the nature of each study that was

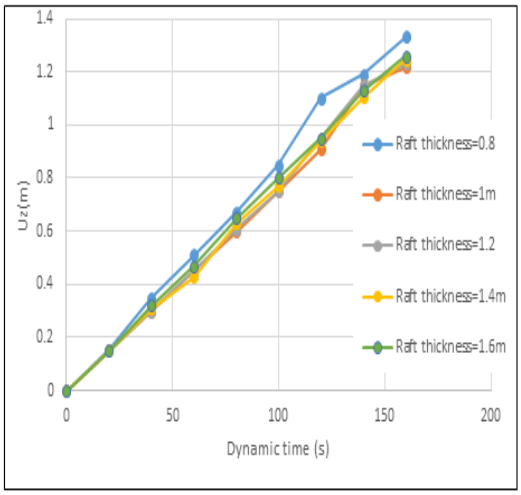

Figure 8. Vertical settlement versus dynamic time with different thicknesses placed on soil layers under the Ali Al-Gharbi earthquake

conducted according to different criteria. This agreement concluded that changing the thickness of the foundation under the same study conditions towards higher values than 0.8m reduces the displacement, and when PGA increases the displacement increases.

4. CONCLUSIONS

In this paper, three-dimensional numerical simulations were carried out for the dynamic behavior of the raft foundation on layered soil under different earthquake excitation. The most important observations from this simulation are the following points that can be derived from the study's findings.

1. The geotechnical and geophysical properties of soil are used with constitutive MC model for this study play a vital role in the ground response to the propagation waves.
2. The maximum and minimum lateral displacement of the raft foundation is 3mm and 0.35mm, respectively. The values are found under the influence of the Halabja earthquake, at 0.8m thickness, the higher value and 1m thickness the less value.
3. The vertical and lateral displacement of the foundation increases as the duration of the earthquake increase, and decrease when the thickness of the foundation increases. The vertical decreased about 9%, but the lateral displacement decreased by more than vertical is about 68% when the thickness of the raft foundation changed from (0.8 m) to (1.6m).
4. It can be noticed that the results of the vertical displacement from the Halabja earthquake applied with local magnitude (7.3) are greater is about 89% than from the El-Centro with (6.9ML), and 47% than Ali Al-Gharbi earthquake with (4.8ML).

5. REFERENCES

1. Kulkarni, P.R. and Sambre, T.R., "Literature review on effects of/.,m87 lateral forces on shallow foundations", ***International Journal of Emerging Science and Engineering***, Vol. 3, No. 10, (2015), 10-14. ISSN: 2319–6378.
2. Puri, V.K. and Prakash, S., "Shallow foundations for seismic loads: Design considerations", In International Conference on Case Histories in Geotechnical Engineering, (2013), 1-16.
3. Hair, J.F., Black, W., Babin, B., Anderson, R. and Tatham, R., "Pearson new international edition: Multivariate data analysis", ***Exploratory Data Analysis in Business and Economics***, (2014), 23-60.
4. Fattah, M., Karim, H. and Al-Recaby, M., "Dynamic behavior of pile group model in two-layer sandy soil subjected to lateral earthquake excitation", ***Global Journal of Engineering Science and Research Management***, Vol. 3, No. 8, (2016), 57-80.
5. Roy, D., "Design of shallow and deep foundations for earthquakes", ***Journal of Geotechnical Earthquake Engineering***, (2013), 1-8.
6. Vali, R., "Water table effects on the behaviors of the reinforced marine soil-footing system", ***Journal of Human, Earth, and Future***, Vol. 2, No. 3, (2021), 296-305.
7. Shafiqu, Q.S.M. and Abdulrasool, M.A., "Finite element analysis of raft foundation on various soil types under earthquake loading", ***International Journal of Architectural and Environmental Engineering***, Vol. 12, No. 9, (2018), 799-809. https://doi.org/10.5281/zenodo.1474315
8. Al-Ameri, A., Jawad, F. and Fattah, M., "Vertical and lateral displacement response of foundation to earthquake loading", ***International Journal of Engineering***, ***Transactions A: Basics,*** Vol. 33, No. 10, (2020), 1864-1871. doi: 10.5829/IJE.2020.33.10A.05.
9. Srilakshmi, G. and Rekha, B., "Analysis of mat foundation using finite element method", ***International Journal of Earth Sciences and Engineering***, Vol. 4, No. 6, (2011), 113-115.
10. Lwti, N.K., Al-Hamdani, D.A., Abbas, M.F. and Albusoda, B.S., "Numerical studies of shallow footing subjected to earthquake loading", in AIP Conference Proceedings, AIP Publishing LLC. Vol. 2404, (2021), 080019. https://doi.org/10.1063/5.0070651
11. Abd Alridha, N. and Mohammed, H.J., "Seismicity study of khanaqin area", ***Iraqi Journal of Science***, Vol. 56, No. 1A, (2015).
12. Al-Taie, A.J. and Albusoda, B.S., "Earthquake hazard on iraqi soil: Halabjah earthquake as a case study", ***Geodesy and Geodynamics***, Vol. 10, No. 3, (2019), 196-204. https://doi.org/10.1016/j.geog.2019.03.004
13. Manual, T., "Plaxis 3d", Delt University of Technology &PLAXIS, Netherland, (2016).
14. Waheed, M. and Asmsil, N., "Study simulation of shallow foundation behavior using different finite element models", ***Journal of Advanced Civil Engineering Practice and Research***, Vol. 8, (2019), 4-9.
15. Lancellotta, R., "Geotechnical engineering, CRC Press, (2008).
16. Toh, J. and Pender, M., "Earthquake performance and permanent displacements of shallow foundations", in Proceedings of New Zealand National Society for Earthquake Engineering Annual Conference, Citeseer. (2008).

Persian Abstract

چکیده

دستیابی به پایداری ساختمان ها و تأسیسات در برابر هر گونه تأثیر خارجی مانند باد، طوفان یا زلزله، در درجه اول به پایه های نگهدارنده آنها بستگی دارد که وظیفه انتقال آن بارها به لایه های خاک زیر آنها را بر عهده دارند. بر این اساس، طراحی پی برای ایمن بودن در برابر این بارهای استاتیکی و دینامیکی بدون ایجاد خطر یا خرابی بر روی این سازه ها اخیراً مورد توجه بسیاری از محققین قرار گرفته است. وظیفه این مقاله پیش‌بینی رفتار پی‌های رافت کم عمقی است که بارهای سازه‌ها را تحت تأثیر زلزله در شهر بعقوبه نگه می‌دارند و آنچه که در نتیجه آنها از خطرات ریزش و جابجایی حاصل می‌شود. برای شبیه‌سازی مدل خاک–پی برای مطالعه، از مدل‌سازی عددی بسته به رویکرد اجزای محدود استفاده شد. ضخامت های مختلف پایه قایق تحت رکوردهای مختلف شتاب–زمان زلزله که با یک مدل الاستیک خطی (***LE***) ساخته شده بر روی خاک لایه ای شبیه سازی شده توسط مدل ***MC)Mohr-Coulomb*** شبیه سازی شده است. نتایج حاصل از این تجزیه و تحلیل نشان داد که خواص خاک برای این مطالعه استفاده شده است، نقش حیاتی در پاسخ زمین به امواج انتشار دارد. همچنین از نتایج مشاهده شد که با افزایش مدت زلزله و کاهش ضخامت کلک، افزایش جابجایی جانبی و عمودی افزایش می یابد، اما این جابجایی ها با افزایش ضخامت پی رافت از ۰.۸ متر به ۱.٦ متر، به ترتیب حدود ۹٪ و ٦۸٪ کاهش یافته است.

IJE TRANSACTIONS B: Applications Vol. 35, No. 08, (August 2022) 1516-1523

International Journal of Engineering

Journal Homepage: www.ije.ir

Multi-label Text Categorization using Error-correcting Output Coding with Weighted Probability

V. Balamurugan[a*], V. Vedanarayanan[a], A. Sahaya Anselin Nisha[a], R. Narmadha[a], T. M. Amirthalakshmi[b]

[a] *Department of ECE, Sathyabama Institute of Science and Technology, Oldmamallapuram Road, Chennai, India*
[b] *Department of Electronics and Communication Engineering, SRM Institute of Technology, Ramapuram, Chennai, India*

PAPER INFO

Paper history:
Received 07 September 2021
Received in revised form 25 March 2022
Accepted 27 March 2022

Keywords:
Text Categorization
Multi-label Classification
Multi-label Text Categorization
Error Correcting Output Coding
Posterior Probability

ABSTRACT

In several real-world categorization problems, labeled data is generally hard to acquire when there is a huge number of unlabeled data. Hence, it is very important to devise a novel approaches to solve these problems, thereby choosing the most valuable instances for labeling and creating a superior classifier. Several existing techniques are devised for the binary categorization issues, only a limited number of algorithms are designed for handling the multi-label cases. The multi-label classification problem turns out to be more complex when the sample belongs to multiple labels from the group of accessible classes. In World Wide Web, text data is generally present nowadays, and is an obvious example for such type of tasks. This paper develops a novel technique to perform the multi-label text categorization by modifying the Error-Correcting Output Coding (ECOC) approach. Here, a cluster of binary complimentary classifiers are employed to facilitate the ECOC more effective for the multi-class problems. In addition, a weighted posterior probability is computed to enhance the multi-label text classification performance more effectively. Moreover, the performance of the proposed ECOC with weighted probability is analyzed using the performance metrics, like precision, recall, and f-measure with maximal precision of 0.897, higher recall value of 0.896, and maximum f-measure of 0.895.

***doi**: 10.5829/ije.2022.35.08b.08*

1. INTRODUCTION

Text categorization, also named as document categorization, play a vital part in various applications based on the Natural Language Processing (NLP) and Information Retrieval (IR)-based systems. Text categorization is fundamental and classical problem in NLP areas in which it has been used for a variety of applications, like pattern recognition, statistics, and machine learning. In text classification applications are grouped into automatic indexing for Boolean IR systems, hierarchical classification of web pages, word sense disambiguation, document filtering and arrangement [1-3]. The internet contains infinite number of text documents. This massive quantity of data poses a key challenge yet for simpler jobs, like IR. A feasible way is to organize textual data into various groups. Automatic document categorization is applied for discovering the fundamental document information in an automatic manner [4, 5], thereby saving human attempts and computational time. In addition, the documents are assigned to the pre-determined category groups with respect to the contents [6]. Text categorization divides the texts into various categories with respect to its content, topic, and attributes, and has been remains as a major issue. Moreover, multi-label text categorization is to assign multiple category labels to every text, and this technique is commonly employed in applications, such as information retrieval, sentiment analysis, news subject organization, and spam recognition [7-9].

Multi-class categorization is the process of classifying the unknown objects into numerous pre-determined classes. In general, multi-class categorization techniques are categorized into two different groups. The

*Corresponding Author Institutional Email: balamurugan.ece@sathyabama.ac.in (V. Balamurugan)

Please cite this article as: V. Balamurugan, V. Vedanarayanan, A. Sahaya Anselin Nisha, R. Narmadha, T. M. Amirthalakshmi, Multi-label Text Categorization using Error-Correcting Output Coding with Weighted Probability, ***International Journal of Engineering, Transactions B: Applications***, Vol. 35, No. 08, (2022) 1516-1523

first group is the direct multi-class categorization technique, which contains approaches, namely Multi-class Support Vector Machine (SVM), Neural Network, k-Nearest Neighbors (kNN), Naive Bayes (NB), Classification and Regression Trees (CART), Convolutional Neural Network (CNN) [9-12], and so on. On the other hand, the second one is the indirect technique, where the multi-class problem is decomposed into a cluster of binary sub-problems [13-16]. There are two different techniques utilized to perform the multi-label categorization. The first one is the problem transformation techniques where the multi-label problems are transformed into several single-label problems, whereas the second one is the algorithm adaptation techniques for handling the multi-label processing directly. Nowadays, multi-class classification remains as a major challenge because of the class imbalance problems and class overlapping problems [17]. ECOC has been utilized in the multi-label learning, and has shown an efficient performance [18]. ECOC algorithm includes two main phases, such as encoding and decoding. The encoding procedure decomposes the multiclass problem into a cluster of binary problems such that decomposition mechanisms are recorded as a code matrix with every column indicating a binary problem [19, 20]. Using ECOC, multiclass problem is partitioned into multiple binary class problems in such way that the binary class problem re-labels the original classes to either positive or negative groups, signifies by a column [21].

The major objective of this research is to devise an ECOC framework with the weighted posterior probability function. Here, the ECOC is utilized to generate the soft labels for each data, which can either categorize the data through the threshold label directly or to rank every label for each data. With respect to the soft labels after categorization, the diversity and the uncertainty of every data is obtained. In addition, the posterior probability computation makes the multi-label classification tasks more reliable. Proposed ECOC with weighted probability: An effective multi-label text categorization approach is devised using proposed ECOC with weighted probability. Here, the ECOC is used for incorporating multiple binary classifiers, thereby handling the multi-class classification problems. Furthermore, weighted posterior probability is computed for every class to enhance the categorization performance.

The structure of the research paper is designed as follows. The literature survey of several existing ECOC techniques is reviewed in section 2. Section 3 portrays the developed ECOC with weighted probability for the multi-label text categorization. The results and discussion of developed method is portrayed in section 4, and the paper is concluded in section 5

2. MOTIVATION

The existing ECOC techniques are illustrated in this section along with the merits and demerits. In addition, the challenges faced by the ECOC techniques during multi-label text categorization are also described as follows.

2. 1. Literature Review This section reviews the various existing ECOC approaches along with their drawbacks. Kajdanowicz et al. [1] developed an Extension of the ECOC algorithm named ML-ECOC for the multi-label text categorization. This method utilized a set of binary complimentary classifiers in order to handle the multi-class issues. This technique effectively reduced the computational cost and complexity, but this method failed to obtain accurate text categorization. Shan et al. [2] developed a Randomized Multi-Label Sub problems Concatenation (RMSC) technique for the multi-label classification problems. Using this method, the imbalance issues were tackled in such a way that the diversity between the classifiers was enhanced. In this technique, time complexity was very much reduced, but the data subsets utilized in automatic web page classification tasks are more challenging to learn.

Jin et al. [3] introduced an Image-driven wafer map defect pattern classification method (WMDPC). This technique was comprised with two various phases, such as feature extraction and classification. This method obtained better generalization ability. However, this method failed to improve the performance of the system. Gu et al. [4] devised a Multi-class active learning algorithm for the multi-class classification problems. Here, a codeword was created for every class, and then a test code was created for the labeled instances for addressing the multi-class cases. This algorithm effectively reduced the computation complexities, thereby enhanced the classification accuracy, but the overall training time was high in this technique.

2. 2. Challenges The challenges faced by different existing ECOC techniques for the text categorization are illustrated as follows,

The RMSC model was developed by Shan et al. [2] for the multi-label classification problems, but this method failed to learn the binary classifiers with their relationships together for enhancing the performance diversity.

WMDPC method was introduced by Bui et al. [11] for multi-class classification. However, the major challenge lies in utilizing various decomposition mechanisms, and other types of binary classifiers for improving the classification accuracy.

Nazari et al. [21], Multi-class active learning algorithm is devised for addressing multi-class classification problems. However, this approach failed to

consider batch mode active learning for incorporating the sample diversity standards, and the classifier uncertainty for enhancing the performance.

Multi-label active learning was introduced by Qin et al. [22] for determining the label instances on every class by hybridizing the multiple classifiers, but the main challenge lies in incorporating the Revisiting ECOC (RECOC) classification with other active learning mechanisms for improved performance results.

3. PROPOSED ECOC WITH WEIGHTED PROBABILITY

This section illustrates the proposed ECOC with weighted probability for the multi-label categorization tasks. The major steps involved in the process of text categorization are elucidated as follows: Here, the modification is carried out in the coding and the decoding steps of the standard ECOC algorithm in such a way that the process is more appropriate for multi-label classification issues. This modification involves creating novel rules in the steps of coding and decoding order to eliminate the inconsistency issues, while managing the multi-label data. Moreover, ECOC is the classifier-driven ensemble approach [1], which is encouraged by the transmission of signals based on information theory. It is utilized for transmitting and receiving the data in a safe and effective way. A set of binary complimentary classifiers were used in such a way that ECOC applications are considered to be more effective for solving the multi-class problems. Furthermore, a posterior probability of every class is computed with respect to the weighted function for the efficient labeling process.

3. 1. Error-Correcting Output Coding ECOC is a classifier ensemble technique motivated by the transmission of the signals in the information theory, which is utilized for transmitting and receiving the data. The error-correcting ability is used for recovering the errors occurred in every categorization level of sub problems. In addition, ECOC has the advantage of decomposing the multi-class problems into binary sub-problems, called dichotomies in the concept-based on machine learning. Here, all sub-problem is solved by the dichotomizer, such that the final solution necessary for multi-class problem is obtained by incorporating the outcomes obtained by the dichotomizers based on the divide-and-conquer rule. Moreover, ECOC executes well mainly on the inconvenience with several classes, whereas the other kinds of classifiers generally have complications.

Let us consider the categorization problem with M_k classes where the ECOC is utilized for generating a binary and ternary code for every class. The code matrix N is used for organizing the code words in the form of matrix rows, where $\mathrm{N} \in \{-1,0,+1\}^{\mathrm{M_k} \times C}$, and C represents the length of the code (coding step). Based on the learning perspective, N signifies M_k classes for training C dichotomizers, $g_1 \cdots g_C$. The training of the classifier g_c is performed with respect to the column $N(.,c)$. If $N(j,c)=+1$, then the instances of the class j are positive, whereas if $N(j,c)=-1$, then every instances are negative supper-class. If $N(j,c)=0$, then no instances of class j participate in order to train g_c.

Let $\bar{x}=[x_1 \ldots x_C], xc \in \{-1,+1\}$ be considered as the vector output of the C classifier ensemble for the input y. In the step of decoding, the output class maximizes similarity measure S among $\bar{x}$ and row $N(i,.)$ is chosen,

$$ClassLabel = ArgMax S(\bar{x}, N(i,.)) \quad (1)$$

The matrix of ECOC codifies the class labels for obtaining different class partitions measured by every dichotomizer. The strategy for coding can be partitioned into problem-dependent and problem-independent. The most common pre-defined constructions of the problem-independent codeword meet the requirements based on high separabaility among the columns and rows for improving the error-correcting ability, and the diversity among the dichotomies.

3. 2. Multi-label ECOC for Text ECOC decomposes multi-class problems into some binary sub-class problems [1]. The ECOC approach generally consists of three main steps, namely coding, binary classifier learning, and decoding. The encoding step maps all the class to the codeword, which includes the results of the decomposed binary problems on that class. After that, the set of binary classifiers are trained using the several partitions of the original data with respect to every column of coding matrix [23]. Once binary classifier learning is performed, a new instance is assigned for the classes using decoding on the basis of the trained binary classifier outputs, and the code matrix rows. In order to perform the encoding process, various binary coding designs, and the ternary coding designs are devised. In the binary coding design, the code words are $+1$ and -1, whereas in ternary coding design, the code words are +1, 0, and -1. A classifier is defined based on every column of the multi-label matrix, which is utilized for computing the membership degree of *d* into super-class, which consists of numerous categories. The dichotomizing procedure with some inconsistencies is eliminated by defining only neutral set and positive class, which does not containsany type of area for overlapping.

3. 3. Proposed ECOC with Weighted Posterior Probability Let us consider a predicted codeword $\bar{x}_d = [\bar{x}_1 ... \bar{x}_C], 0 \le \bar{x}_c \le +1\}$, and it is a string assigned for the document d where each bit signifies the output of the classifier, that is $P_c(+1|d)$. The posterior probability of every class is computed as follows:

$$P(k_M|d) = \frac{1}{|N(M,.)|} \sum_{c=1}^{C} P_c(+1|d) N(M,c) \frac{E_c}{n} \quad (2)$$

where, E_c signifies mean square error of training algorithm of classifier, n represents normalizing factor. For every document, ECOC arranges class by score and assigns YES to every t top-ranking categories. t is an integer ranging from 1 to the number of categories.

4. RESULTS AND DISCUSSION

The results and discussion of developed ECOC with weighted probability by considering the various performance metrics is illustrated in this subsection.

4. 1. Experimental Setup The implementation of developed ECOC with weighted probability is done in MATLAB tool using Reuters database [24] and rcv1data[2].

4. 2. Dataset Description Reuters database [20] is a text Categorization collection data set donated by David D. Lewis. Here, the documents are structured and indexed based on their categories. In this database,the total number of instances is 21578 with five attributes. The total number of webhits -obtained by the dataset is 163417.

4. 3. Performance Evaluation Metrics This section illustrates the various evaluation metrics, namely as precision, recall, and f-measure utilized for performing the assessment of the technique

Precision: It is a measure used for defining the fraction of appropriately classified texts, and the equation is formulated as follows:

$$P = \frac{|T_r \cap T_c|}{T_c} \quad (3)$$

Here, T_r signifies relevant texts, and T_c signifies the categorized texts.

Recall: It is measure of relevant texts present in classified texts that is related to text data.

$$R = \frac{|T_r \cap T_c|}{T_r} \quad (4)$$

F-measure: It computes the mean difference among the precision and the recall measure and is given as follows:

$$FM = 2 * \left(\frac{P * R}{P + R} \right) \quad (5)$$

4. 4. Comparative Techniques The various techniques, such as ML-ECOC [1], RMSC [19], WMDPC [25], dynamic semantic representation model and deep neural network (DSRM-DNN) [8], and Multi-relation Message Passing (MrMP) [24] are utilized for performing the comparative analysis of the developed ECOC with weighted probability.

4. 5. Comparative Analysis The comparative assessment of developed ECOC with weighted probability based on the evaluation metrics, like precision, recall, and f-measure with respect to Reuters database and rcv1 data is explained in this section.

4. 5. 1. Analysis using Reuter Database

4. 5. 1. 1. Analysis using Training Data Figure 1 illustrates the analysis using training da data with respect to precision, recall, and f-measure. The assessment using precision measure is portrayed in Figure 1(a). By considering the training data as 50%, the precision value achieved by the developed ECOC with weighted probability is 0.832, whereas the existing techniques, such as ML-ECOC, RMSC, WMDPC, DSRM-DNN, and MrMP achieved a precision value of 0.742, 0.716, 0.755, 0.760, and 0.792, respectively. Figure 1(b) presents the assessment using recall metric. The recall value obtained by the ML-ECOC is 0.742, RMSC is 0.775, WMDPC is 0.795, DSRM-DNN is 0.810, MrMP is 0.822, and the developed ECOC with weighted probability is 0.845 for the training data 70%. Figure 1(c) shows the analysis using f-measure. When the training data is 60%, the developed ECOC with weighted probability measured an f-measure value of 0.832, whereas the f-measure value obtained by the existing techniques ML-ECOC is 0.737, RMSC is 0.734, WMDPC is 0.761, DSRM-DNN is 0.783, and MrMP is 0.799.

4. 5. 1. 2. Analysis using K-fold The k-fold analysis for the developed approach with respect to precision, recall, and f-measure is presented in Figure 2. Figure 2(a) presents the analysis using precision metric. For the k-fold value 5, the developed ECOC with

[2] https://www.kaggle.com/kerneler/starter-rcv1data-1c5d94f9-d/data

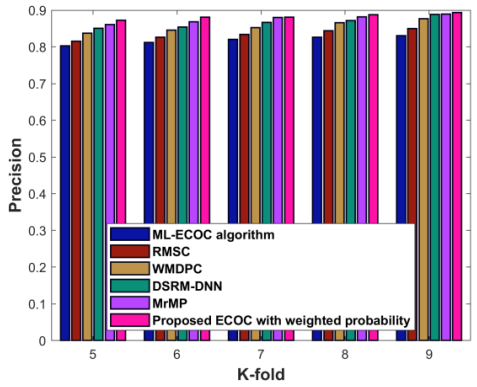

(a)

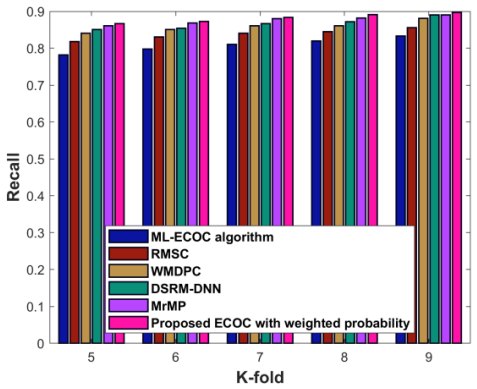

(b)

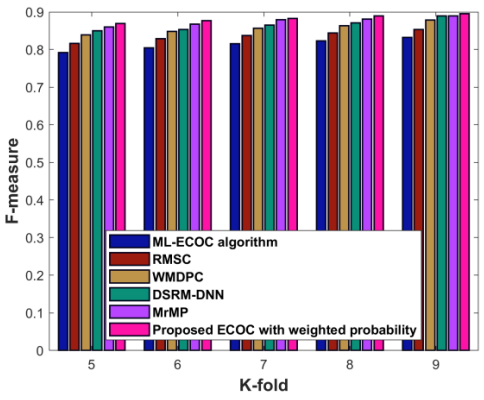

(c)

Figure 1. Analysis of the developed technique using a) Precision b) Recall c) F-measure

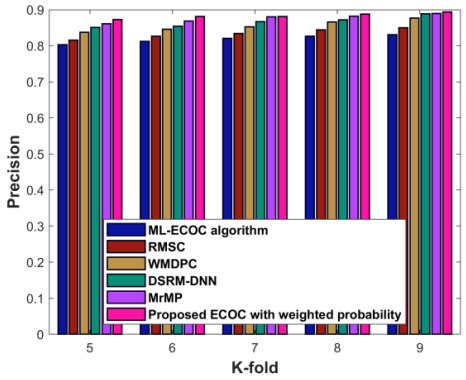

(a)

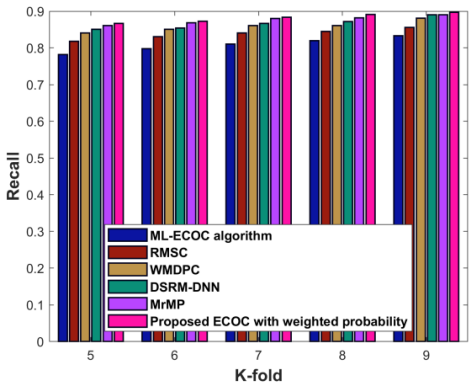

(b)

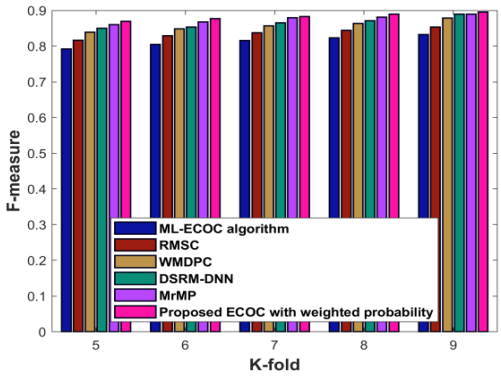

(c)

Figure 2. Analysis of the developed technique using a) Precision b) Recall c) F-measure

weighted probability obtained a precision value of 0.872, while the existing techniques such as ML-ECOC, RMSC, WMDPC, DSRM-DNN, MrMP achieved a precision value of 0.803, 0.816, 0.837, 0.851, and 0.861, respectively. The assessment using recall metric is portrayed in Figure 2(b). The recall value obtained by the ML-ECOC is 0.811, RMSC is 0.841, WMDPC is 0.861, DSRM-DNN is 0.866, MrMP is 0.880, and the developed ECOC with weighted probability is 0.884 for the k-fold value 7. The f-measure analysis is depicted in Figure 2(c).

By considering the k-fold value as 8, the f-measure value achieved by the developed ECOC with weighted probability is 0.889, whereas the f-measure value measured by the existing ML-ECOC is 0.823, RMSC is 0.844, WMDPC is 0.863, DSRM-DNN is 0.871, and MrMP is 0.881.

4. 5. 2. Analysis using Rcv1data

4. 5. 2. 1. Analysis using Training Data Figure 3 illustrates the analysis using training data using rcv1

data. The assessment using precision measure is portrayed in Figure 3(a). By considering the training data as 50%, the precision value achieved by the developed ECOC with weighted probability is 0.827, whereas the existing techniques, such as ML-ECOC, RMSC, WMDPC, DSRM-DNN, and MrMP achieved a precision value of 0.736, 0.710, 0.749, 0.754, and 0.786, respectively. Figure 3(b) presents the assessment using recall metric. The recall value obtained by the ML-ECOC is 0.737, RMSC is 0.770, WMDPC is 0.790, DSRM-DNN is 0.804, MrMP is 0.817, and the developed ECOC with weighted probability is 0.839 for the training data 70%. Figure 3(c) shows the analysis using f-measure. When the training data is 60%, the developed ECOC with weighted probability measured an f-measure value of 0.827, whereas the f-measure value obtained by the existing techniques ML-ECOC is 0.732, RMSC is 0.729, WMDPC is 0.756, DSRM-DNN is 0.777, and MrMP is 0.794.

4. 5. 2. 2. Analysis using K-fold The k-fold analysis for the developed approach using rcv1 data is presented in Figure 4. Figure 4(a) presents the analysis using precision metric. For the k-fold value 5, the developed ECOC with weighted probability obtained a precision value of 0.867, while the existing techniques such as ML-ECOC, RMSC, WMDPC, DSRM-DNN,

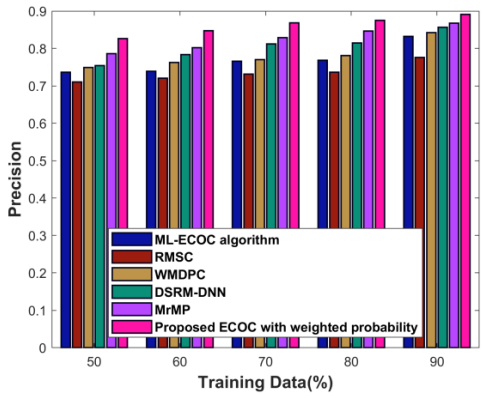

(a)

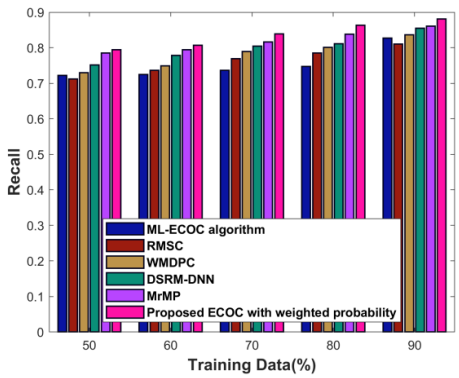

(b)

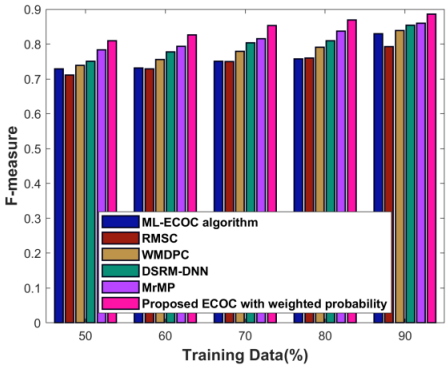

(c)

Figure 3. Analysis of the developed technique using a) Precision b) Recall c) F-measure

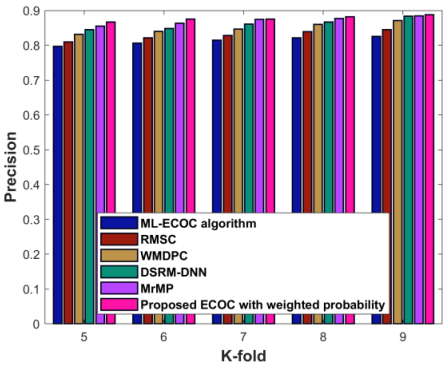

(a)

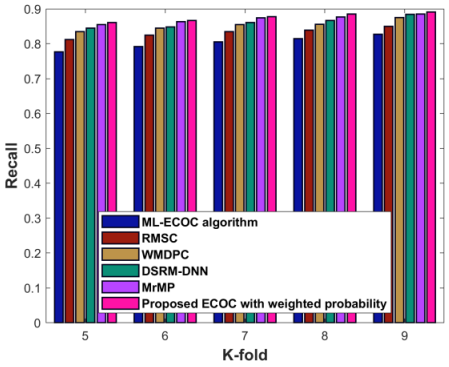

(b)

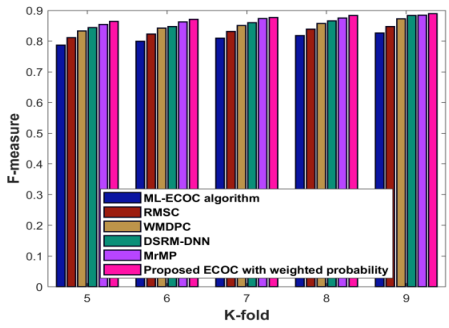

(c)

Figure 4. Analysis of the developed technique using a) Precision b) Recall c) F-measure

MrMP achieved a precision value of 0.797, 0.810, 0.832, 0.845, and 0.855, respectively. The assessment using recall metric is portrayed in Figure 4(b). The recall value obtained by the ML-ECOC is 0.805, RMSC is 0.835, WMDPC is 0.855, DSRM-DNN is 0.861, MrMP is 0.875, and the developed ECOC with weighted probability is 0.878 for the k-fold value 7. The f-measure analysis is depicted in Figure 4(c). By considering the k-fold value as 8, the f-measure value achieved by the developed ECOC with weighted probability is 0.884, whereas the f-measure value measured by the existing ML-ECOC is 0.818, RMSC is 0.839, WMDPC is 0.858, DSRM-DNN is 0.866, and MrMP is 0.876.

4. 6. Comparative Discussion This section illustrates comparative discussion of developed ECOC with weighted probability in comparison with various existing techniques, such as ML-ECOC, RMSC, and WMDPC with respect to the performance metrics, namely precision, recall, and f-measure. Table 1 portrays the assessment of developed approach with respect to the training value 90%, and k-fold value 9. The precision value achieved by the developed ECOC with weighted probability is 0.897, whereas the existing techniques, such as ML-ECOC, RMSC, WMDPC, DSRM-DNN, and MrMP achieved a precision value of 0.837, 0.781, 0.847, 0.863, and 0.873. The recall value measured by the ML-ECOC is 0.833, RMSC is 0.855, WMDPC is 0.880, DSRM-DNN is 0.860, and MrMP is 0.866, while the developed techniques ECOC with weighted probability measured a recall value of 0.896. The developed ECOC with weighted probability measured an f-measure value of 0.895, whereas the existing techniques, such as ML-ECOC, RMSC, WMDPC, DSRM-DNN, and MrMP achieved an f-measure value of 0.832, 0.852, 0.878, 0.889, and 0.89. From the table it is clearly shown that, the developed ECOC with weighted probability achieved a maximal precision of 0.897 using training data, higher recall of 0.896 using k-fold, and maximum f-measure of 0.895 using k-fold.

TABLE 1. Strouhal number for different geometric cases

	Metrics	ML-ECOC	RMSC	WMDPC	Proposed ECOC with weighted probability
Using training data (%)	***Precision***	0.837	0.781	0.847	**0.897**
	Recall	0.832	0.816	0.842	**0.886**
	F-measure	0.835	0.798	0.845	**0.891**
Using K-fold	***Precision***	0.831	0.850	0.876	**0.893**
	Recall	0.833	0.855	0.880	**0.896**
	F-measure	0.832	0.852	0.878	**0.895**

5. CONCLUSION

This research work designs a multi-label text categorization technique, combining a robust ECOC classification technique with a posterior probability computation. Here, the inconsistency in the coding phase is eliminated by utilizing the proposed ECOC as this approach decomposes the various multi-class problems into a few balancing one-class sub problems. In addition, the multi-label association is considered in the phase of testing by utilizing the decoding mechanism implemented for the ECOC algorithm. Finally, the posterior probability is computed as a weighted function for improving the performance efficiently. The advanced performance of the developed technique is demonstrated by the experiments performed using the Reuters database. The proposed ECOC with weighted probability outperforms the various existing multi-label text classification techniques by considering the various evaluation metrics, namely precision, recall, and f-measure. However, the developed ECOC with weighted probability achieved efficient performance with the maximum precision value of 0.897, higher recall value of 0.896, and maximum f-measure value of 0.895. The future work would be the concern of developing more novel classifiers to enhance the performance effectiveness of multi-label text categorization.

6. REFERENCES

1. Kajdanowicz, T. and Kazienko, P., "Multi-label classification using error correcting output codes", ***International Journal of Applied Mathematics and Computer Science***, Vol. 22, No. 4, (2012), 829-840.
2. Shan, J., Hou, C., Tao, H., Zhuge, W. and Yi, D., "Randomized multi-label subproblems concatenation via error correcting output codes", ***Neurocomputing***, Vol. 410, (2020), 317-327, doi: 10.1016/j.neucom.2020.06.035.
3. Jin, C.H., Kim, H.-J., Piao, Y., Li, M. and Piao, M., "Wafer map defect pattern classification based on convolutional neural network features and error-correcting output codes", ***Journal of Intelligent Manufacturing***, Vol. 31, No. 8, (2020), 1861-1875, doi: 10.1007/s10845-020-01540-x.
4. Gu, S., Cai, Y., Shan, J. and Hou, C., "Active learning with error-correcting output codes", ***Neurocomputing***, Vol. 364, (2019), 182-191, doi: 10.1016/j.neucom.2019.06.064.
5. Sun, N., Shan, J. and Hou, C., "Multi-label active learning with error correcting output codes", in Pacific-Asia Conference on Knowledge Discovery and Data Mining, Springer., (2019), 331-342.
6. Zhang, Y.-P., Ye, X.-N., Liu, K.-H. and Yao, J.-F., "A novel multi-objective genetic algorithm based error correcting output codes", ***Swarm and Evolutionary Computation***, Vol. 57, (2020), 100709, doi: 10.1016/j.swevo.2020.100709.
7. Almuzaini, H.A. and Azmi, A.M., "Impact of stemming and word embedding on deep learning-based arabic text categorization", ***IEEE Access***, Vol. 8, (2020), 127913-127928, doi: 10.1109/ACCESS.2020.3009217.

8. Wang, T., Liu, L., Liu, N., Zhang, H., Zhang, L. and Feng, S., "A multi-label text classification method via dynamic semantic representation model and deep neural network", ***Applied Intelligence***, Vol. 50, No. 8, (2020), 2339-2351, doi: 10.1007/s10489-020-01680-w.
9. Kimura, K., Kudo, M., Sun, L. and Koujaku, S., "Fast random k-labelsets for large-scale multi-label classification", in 2016 23rd International Conference on Pattern Recognition (ICPR), IEEE., (2016), 438-443.
10. Sebastiani, F., "Machine learning in automated text categorization", ***ACM Computing Surveys (CSUR)***, Vol. 34, No. 1, (2002), 1-47.
11. Bui, D.D.A., Del Fiol, G. and Jonnalagadda, S., "Pdf text classification to leverage information extraction from publication reports", ***Journal of Biomedical Informatics***, Vol. 61, (2016), 141-148, doi: 10.1016/j.jbi.2016.03.026.
12. Yu, B. and Xu, Z.-b., "A comparative study for content-based dynamic spam classification using four machine learning algorithms", ***Knowledge-Based Systems***, Vol. 21, No. 4, (2008), 355-362, doi: 10.1016/j.knosys.2008.01.001.
13. Loh, W.Y., "Classification and regression trees", ***Wiley Interdisciplinary Reviews: Data Mining and Knowledge Discovery***, Vol. 1, No. 1, (2011), 14-23, doi: 10.1002/widm.8.
14. Zhong, G., Huang, K. and Liu, C.-L., "Joint learning of error-correcting output codes and dichotomizers from data", ***Neural Computing and Applications***, Vol. 21, No. 4, (2012), 715-724, doi: 10.1007/s00521-011-0653-z.
15. Kyeong, K. and Kim, H., "Classification of mixed-type defect patterns in wafer bin maps using convolutional neural networks", ***IEEE Transactions on Semiconductor Manufacturing***, Vol. 31, No. 3, (2018), 395-402, doi: 10.1109/TSM.2018.2841416.
16. Krizhevsky, A., Sutskever, I. and Hinton, G.E., "Imagenet classification with deep convolutional neural networks", ***Advances in Neural Information Processing Systems***, Vol. 25, (2012), doi: 10.1145/3065386.
17. Krawczyk, B., Galar, M., Woźniak, M., Bustince, H. and Herrera, F., "Dynamic ensemble selection for multi-class classification with one-class classifiers", ***Pattern Recognition***, Vol. 83, (2018), 34-51.
18. Feng, K.-J., Liong, S.-T. and Liu, K.-H., "The design of variable-length coding matrix for improving error correcting output codes", ***Information Sciences***, Vol. 534, (2020), 192-217, doi: 10.1016/j.ins.2020.04.021.
19. Li, K.-S., Wang, H.-R. and Liu, K.-H., "A novel error-correcting output codes algorithm based on genetic programming", ***Swarm and Evolutionary Computation***, Vol. 50, (2019), 100564, doi: 10.1016/j.swevo.2019.100564.
20. Baró, X., Escalera, S., Vitria, J., Pujol, O. and Radeva, P., "Traffic sign recognition using evolutionary adaboost detection and forest-ecoc classification", ***IEEE Transactions on Intelligent Transportation Systems***, Vol. 10, No. 1, (2009), 113-126, doi.
21. Nazari, S., Moin, M.-S. and Kanan, H.R., "Securing templates in a face recognition system using error-correcting output code and chaos theory", ***Computers & Electrical Engineering***, Vol. 72, (2018), 644-659, doi: 10.1016/j.compeleceng.2018.01.029.
22. Qin, J., Liu, L., Shao, L., Shen, F., Ni, B., Chen, J. and Wang, Y., "Zero-shot action recognition with error-correcting output codes", in Proceedings of the IEEE Conference on Computer Vision and Pattern Recognition., (2017), 2833-2842.
23. Sadjadi, S., Mashayekhi, H. and Hassanpour, H., "A two-level semi-supervised clustering technique for news articles", ***International Journal of Engineering***, ***Transactions C: Aspects,*** Vol. 34, No. 12, (2021), 2648-2657, doi: 10.5829/IJE.2021.34.12C.10.
24. Vidyadhari, C., Sandhya, N. and Premchand, P., "A semantic word processing using enhanced cat swarm optimization algorithm for automatic text clustering", ***Multimedia Research***, Vol. 2, No. 4, (2019), 23-32, doi: 10.46253/j.mr.v2i4.a3.
25. Lee, Y., Kim, E., Kim, Y. and Seol, D., "Effective message authentication method for performing a swarm flight of drones", ***Emergency***, Vol. 3, No. 4, (2015), 95-97, doi: 10.2991/eers-15.2015.23.

Persian Abstract

چکیده

در چندین مشکل طبقه‌بندی در دنیای واقعی، وقتی تعداد زیادی داده بدون برچسب وجود دارد، معمولاً به‌دست آوردن داده‌های برچسب‌دار سخت است. از این رو، ابداع رویکردهای جدید برای حل این مشکلات بسیار مهم است و در نتیجه ارزشمندترین نمونه ها برای برچسب گذاری و ایجاد یک طبقه بندی برتر انتخاب می شود. چندین تکنیک موجود برای مسائل دسته‌بندی باینری ابداع شده‌اند، تنها تعداد محدودی الگوریتم برای رسیدگی به موارد چند برچسبی طراحی شده‌اند. مشکل طبقه‌بندی چند برچسبی زمانی پیچیده‌تر می‌شود که نمونه متعلق به چندین برچسب از گروه کلاس‌های قابل دسترس باشد. امروزه در وب جهانی، داده های متنی به طور کلی وجود دارد و نمونه بارز این نوع وظایف است. این مقاله یک تکنیک جدید را برای انجام دسته‌بندی متن چند برچسبی با اصلاح رویکرد کدگذاری خروجی تصحیح خطا (ECOC)ایجاد می‌کند. در اینجا، خوشه‌ای از طبقه‌بندی‌کننده‌های مکمل دودویی برای تسهیل ECOC برای مشکلات چند کلاسه مؤثرتر استفاده می‌شوند. علاوه بر این، یک احتمال پسین وزنی محاسبه می‌شود تا عملکرد طبقه‌بندی متن چند برچسبی را به طور مؤثرتری افزایش دهد. علاوه بر این، عملکرد ECOC پیشنهادی با احتمال وزن‌دار با استفاده از معیارهای عملکرد، مانند دقت، فراخوان و اندازه‌گیری f با حداکثر دقت ۰.۸۹۷، ارزش فراخوان بالاتر ۰.۸۹۶ و حداکثر اندازه‌گیری 0.895 f تجزیه و تحلیل می‌شود.

International Journal of Engineering

Journal Homepage: www.ije.ir

Experimental Study on Bonding CFRP to Fiber Concrete Beam Considering the Effect of using Nanographene Oxide in Improving the Mechanical Properties of Polyamine Resin

M. R. Halvaeyfar[a], S. M. Mirhosseini[a]*, E. Zeighami[a], A. Hassani Joshaghani[b]

[a] *Department of Civil Engineering, Arak Branch, Islamic Azad University, Arak, Iran*
[b] *Department of Chemical Engineering, Arak Branch, Islamic Azad University, Arak, Iran*

PAPER INFO

Paper history:
Received 09 February 2022
Received in revised form 21 March 2022
Accepted 31 March 2022

Keywords:
Graphene Oxide
Carbon Fiber
Fiber Concrete Beams
Strengthening
Retrofitting
Epoxy Resin

ABSTRACT

This research examined the effect of nanographene oxide in enhancing the mechanical properties of polyamine resin for better adhesion of carbon-fiber-reinforced polymer (CFRP) to a fiber-reinforced concrete beam. To this purpose, 33 fiber-reinforced concrete beams retrofitted with CFRP of lengths 50 cm, 35 cm, and 20 cm and widths 3 cm, 6 cm, and 10 cm were experimentally studied. Graphene oxide weight percentages of 1, 2, and 3 percent were considered, and the corresponding cases were compared with the case of a retrofitted beam without graphene oxide. According to the results of experiments on 12 of the beams, as the nanomaterial in the adhesive increases from 1 to 2 and 3%, the values of maximum load-carrying capacity, maximum mid-span deflection, beam stiffness, and beam toughness exhibited 46,19, 27, and 5 %, respectively, relative to the case of the beam reinforced with CFRP and without graphene oxide. Subsequently, given the close results of the beams reinforced with 2 and 3% graphene oxide. The 2% graphene oxide was used in the rest of the samples to investigate the effect changes in the number of layers, length, and width of the CFRP on the mechanical properties of the concrete beam. The results indicated that an increase in the number of layers, length, and width of CFRP results in an increase in the load-carrying capacity and deformability of the fiber-reinforced concrete beam

***doi**: 10.5829/ije.2022.35.08b.09*

1. INTRODUCTION

The increasing trend in the demand for structural reinforcement and strengthening can be due to a failure to follow regulations during construction, weakness of the structure against lateral forces, exposure to corrosion, changes in regulations, changes in usage, and old age, among other factors. In general, structural retrofitting and strengthening can be defined as an intelligent modification of structural properties of a building aimed at improving future seismic performance. Various strengthening methods have been considered suitable for reinforced concrete structures. Steel binding, increasing the cross-sectional area via concreting and adding rebars, strengthening via steel plates, epoxy injection, integration with prestressed cables, employing seismic techniques, and using fiber-reinforcement polymer (FRP) are examples of these methods. Among composites, the carbon-fiber-reinforced type is used more frequently than other types for concrete structures due to its higher strength, higher stiffness-to-weight ratio, better corrosion resistance, shorter construction time, and better durability [1-6]. Numerous studies have been conducted in recent years on the strengthening of reinforced concrete members, such as beams [7-10], slabs, columns [11], beam-to-column [12], connections, and other members [13]. Providing the debonding of carbon-fiber-reinforced polymer (CFRP) from the concrete surface is limited, this product may be considered to possess all the parameters required to strengthen reinforced concrete structures [14]. Various methods have been introduced to maximize the utility of the tensile capacity of CFRP under loading

*Corresponding Author Institutional Email: m-mirhoseini@iau-arak.ac.ir (S. M. Mirhosseini)

Please cite this article as: M. R. Halvaeyfar, S. M. Mirhosseini, E. Zeighami, A. Hassani Joshaghani, Experimental Study on Bonding CFRP to Fiber Concrete Beam Considering the Effect of using Nanographene Oxide in Improving the Mechanical Properties of Polyamine Resin, ***International Journal of Engineering, Transactions B: Applications***, Vol. 35, No. 08, (2022) 1524-1532

while preventing debonding between the CFRP and the reinforced concrete [15-17]. Most of these methods attempt to prevent debonding by using CFRP, steel plates, bolts, or a combination of these at the end of the connection between CFRP and concrete. In recent years, some research has been conducted on limiting fiber-concrete debonding by using nanomaterials to strengthen resins. Due to their large specific area, these materials have improved the mechanical properties of resins. An example of these materials is carbon nanotube (CNT) particles, which have been extensively studied by researchers [18-20]. These particles have been reported to increase the tensile strength, flexural strength, toughness, strain, and modulus of elasticity [21-24]. Another example of nanomaterials is graphene oxide, which is layered. Most studies have investigated the chemical effect of this material on the mechanical capacity of resins [25-28]. Little research has addressed the application of nanographene oxide in enhancing the properties of resins and in the strengthening of reinforced concrete structures. Acar et al. [29] carried out studies on the mechanical properties of monolayer prepreg (MP) and graphene-reinforced monolayer prepreg (GMP) composites aimed at improving resin properties to reinforce a concrete beam. The results indicated that adding graphene improved the mechanical properties of the resin and increased the tensile strength of the system. In another study, Wang et al. [30] demonstrated that participation by nanographene in epoxy resin improves the tensile strength and maximum strain of composite beams and significantly affects their abrasion properties and long-term durability. The present work experimentally researches the influence of nanographene oxide on improving the mechanical properties of polyamine resin in strengthening a fiber-reinforced concrete beam using CFRP. For this purpose, 33 fiber-reinforced concrete beams were prepared and subjected to four-point loading. Moreover, the influence of changing the number of layers and the length and width of the CFRP on the increase in the load-carrying capacity and deformability of the fiber-reinforced concrete beam was studied.

2. MATERIALS AND EXPERIMENTAL SETUP

In this research, an experimental setup was defined to determine the load-carrying capacity of the fiber-reinforced concrete beam strengthened using CFRP. The epoxy adhesive used to attach the CFRP to the tensile region of the fiber-reinforced concrete was polyamine resin with nanographene oxide. The fiber-reinforced concrete beam samples were 50 cm in length with cross-sectional dimensions of 10×10 cm and contained 1% Volumetric steel fibers. 3 samples were made for each type and their average was considered.

The specifications of the CFRP, number of CFRP layers, percentage of nanographene oxide, and number of identical test samples are displayed in Table 1. In this table, the letters Le, W, and L represent the length, width, and the number of layers of the CFRP, respectively, and the letter G denotes the weight percent of nanographene oxide used in the polyamine resin. For instance, the sample Le50-W3-L1-G2 is reinforced with one layer CFRP with a length of 50 cm, a width of 3 cm, and 2 wt% of nanographene oxide in the resin.

2. 1. Materials Unidirectional CFRP with a weight of 180 g/m^2 was used in this research to reinforce the beams. The specifications of the CFRP used are shown in Table 2. Concrete with an average compressive strength of 32.8 Mpa and a slump of 48 mm was used to prepare the beams. The cement used was of Type-5 with silica used in 5 different particle size ranges to maintain gradation continuity. The largest grain size was 5 mm, and microsilica was used to fill the space between the

TABLE 1. Specifications of fiber concrete samples

Number of similar samples	Nano weight percentage	Specifications of CFRP			Sample	Number
		No. of layers	Length(cm)	Wide(cm)		
3	___	___	50	___	No CFRP	1
3	___	1	50	10	Le50-W10-L1-G0	2
3	1	1	50	10	Le50-W10-L1-G1	3
3	2	1	50	10	Le50-W10-L1-G2	4
3	3	1	50	10	Le50-W10-L1-G3	5
3	2	2	50	10	Le50-W10-L2-G2	6
3	2	3	50	10	Le50-W10-L3-G2	7
3	2	1	20	10	Le20-W10-L1-G2	8
3	2	1	35	10	Le35-W10-L1-G2	9
3	2	1	50	3	Le50-W3-L1-G2	10
3	2	1	50	6	Le50-W6-L1-G2	11

TABLE 2. Mechanical specifications of CFRP

Modulus of elasticity (Gpa)	Tensile strength (Mpa)	Weight (g/m^2)	Thickness (mm)	
230	3800-4000	180	0.3	quantity

grains. Furthermore, a lubricant was used to improve the performance of concrete. The details of the concrete mix design according to ASTM C33 are displayed in Table 3.

Drinking water with a water-to-cement ratio of 0.35 was used in the mix design. The fibers in the concrete were made of metal and had a length of 3 cm and a diameter of 0.8 mm with hooks at the ends (Figure 1). The yield strength of the fibers was 385 MPa.

Epoxy resin based on a polyamine chemical radical with a specific weight of 1 g/cm^3 and tensile strength of 14 Mpa was used in the present research. Nanographene oxide was utilized to modify the mechanical properties of the epoxy resin. The nanographene oxide had a particle thickness of 3.7-4 nm and a purity of 99%. The chemical radical of the nanographene oxide used was in the range of 6-10 layers. For better mixing of the nanographene oxide in the adhesive, a solvent consisting of Xylene, MEK, and N. Butanol with volume fractions of 70, 15, and 15 percent, respectively. First, the solvent was solved in Part A of the resin, and the nanographene oxide was added. Then, the mixture was shaken for 5 minutes and placed in the ultrasonic device for 30 minutes for the nanoparticles to be dispersed. Ultimately, the hardener (part B) of the resin was added to the adhesive several minutes before use. The solvent possessed 10% of the total weight of the resin.

2. 2. Test schedule In order to prepare the fiber-reinforced concrete beam samples, first, the dry aggregates were mixed in the mixer. In the meanwhile, micro silica, metal fibers, water, and lubricant were added in that order. Mixing was allowed to continue for 10 minutes. Subsequently, horizontal metal molds were filled with the mixture in three steps, and the mixture was compacted for 3 minutes on a vibration table in each step.

After 24 hours, the samples were demolded and were then kept for 28 days in a curing tank according to ASTM C156 (see Figure 2).

At the end of the 28 days, the weak concrete coating on the surface of the samples was removed, and the samples were repaired using restorative materials. After the surfaces were prepared, the CFRP was bonded to the tensile region of the beam using the liquid adhesive prepared beforehand. For full adhesion between the concrete beam and the CFRP, the air trapped under the CFRP was forced out via rolling. Then, the strengthened samples were maintained at room temperature for one week before loading (Figure 3). After the carbon-fiber-reinforced samples were prepared, they were subjected to four-point loading using a 250 kN STM 250 jack with a loading rate of 0.1 mm/min according to ASTM C78, as shown in Figure 4, and the deflection of the beam span was measured using a linear variable differential transformer (LVDT) gage.

3. EXPERIMENTAL RESULTS

In this section, the results of four-point loading on the fiber-reinforced concrete beam with a length of 50 cm and cross-sectional dimensions of 10×10 cm reinforced with CFRP are presented. The load was applied by the jack at a constant rate of 0.1 mm/min, and the displacement midspan of the beam was measured by the strain gauge. The maximum load, midspan deflection at

TABLE 3. Weight values of materials used in fiber concrete mixing design

Aggregate (mm)					Superplasticizer	Micro silica	Fiber	Water	Cement	Materials
0-0.3	0.3-1	1-2	2-3	3-5						
180.8	259.2	235	192.9	337.5	4.6	191	80	267	763	Quantity(kg/m^3)

Figure 1. Synthetic metal fibers

Figure 2. Curing stage of fiber concrete beams

Figure 3. Step of removing trapped air under the CFRP using the roller method

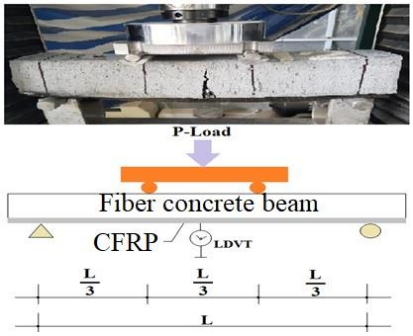

Figure 4. Preparation of reinforced fiber concrete beams for 4-point loading operations

the maximum load, initial stiffness (slope of the initial part of the force-deflection graph), and the toughness (area under the force-deflection graph), which were obtained automatically from the loading machine, are displayed in Table 4. This table draws a comparison between the strengthened fiber-reinforced concrete beam with various numbers of layers, lengths, and widths of CFRP and different weight percentages of nanographene oxide in the epoxy adhesive. Several instances of the tests performed on the fiber-reinforced beam strengthened at the tensile region using CFRP are displayed in Figure 5.

3. 1. Effect of Weight Percent of Nanographene Oxide This section addresses the effect of the weight percentage of nanographene oxide in the epoxy adhesive for improving the adhesive properties given the experimental results for the maximum load-carrying capacity, maximum deflection, initial stiffness, and toughness. The results pertaining to the maximum load-carrying capacity, maximum deflection, initial stiffness, and toughness with respect to changes in nanographene oxide are shown in Table 5.

TABLE 4. The results read from the 4-point jack machine on the reinforced fiber concrete beam

Toughness (N.m)	Initial Stiffness (kN/m)	Maximum Deflection Δ (mm)	Ultimate load Pu (KN)	Sample	Number
28.6	7361	1.44	10.6	No CFRP	1
36.3	8312	1.59	13.3	Le50-W10-L1-G0	2
36.6	9212	1.65	15.2	Le50-W10-L1-G1	3
36.7	9255	1.88	17.4	Le50-W10-L1-G2	4
38.1	10543	1.89	19.4	Le50-W10-L1-G3	5
44.4	11627	2.58	30	Le50-W10-L2-G2	6
60.1	14485	2.72	39.4	Le50-W10-L3-G2	7
36.4	8717	1.60	13.5	Le20-W10-L1-G2	8
36.5	9880	1.67	16.5	Le35-W10-L1-G2	9
36.0	9127	1.64	14.9	Le50-W3-L1-G2	10
36.3	9223	1.7	16.7	Le50-W6-L1-G2	11

Figure 5. A few examples of fiber reinforced concrete beams reinforced with CFRP

As seen in the table, a comparison of Le50W10L1G0, Le50W10L1G1, Le50W10L1G2, and Le50W10L1G3 with equal lengths, widths, and numbers of layers of CFRP and a change in the weight of graphene oxide from 0 to 1, 2, and 3 percent shows an increase in the ratio of the maximum load exerted on the beam from 1.14 to 1.31 and 1.46, respectively.

Similarly, the midspan deflection ratio increased from 1.037 to 1.18 and 1.19, respectively, the initial stiffness ratio increased from 1.11 to 1.12 and 1.27, respectively, and the toughness ratio increased from 1.003 to 1.01 and 1.05, respectively. These results indicate that a rise in the

TABLE 5. Influence of graphene oxide content on polyamine resin in mechanical properties of fiber concrete beams

$\frac{T}{T}$ No Graphen	$\frac{K_{int}}{K_{int}}$ No Graphen	$\frac{\Delta_{max}}{\Delta_{max}}$ No Graphen	$\frac{P_U}{P_U}$ No Graphen	$\frac{\Delta_{max}}{\Delta_{max}}$ No CFRP	$\frac{P_U}{P_U}$ NO CFRP	Toughness (N.m)	Initial Stiffness (Kn/m)	Maximum Deflection Δ (mm)	Ultimate load Pu (Kn)	Sample
0.78	0.88	0.91	0.79	1	1	28.6	7361	1.44	10.6	No CFRP
1	1	1	1	1.1	1.25	36.3	8312	1.59	13.3	Le50-W10-L1-G0
1.003	1.11	1.037	1.14	1.14	1.44	36.6	9212	1.65	15.2	Le50-W10-L1-G1
1.01	1.12	1.18	1.31	1.30	1.64	36.7	9255	1.88	17.4	Le50-W10-L1-G2
1.05	1.27	1.19	1.46	1.31	1.83	38.1	10543	1.89	19.4	Le50-W10-L1-G3

weight of graphene oxide has improved the adhesion between the epoxy adhesive and concrete. However, the above data show that the results corresponding to the use of 2 and 3% nanographene oxide were very close. Hence, the 2 wt% was used for the rest of the work in the research. It was also observed that the maximum load endured by the fiber-reinforced beam strengthened with CFRP and graphene oxide weight percentages of 0, 1, 2, and 3% were higher than those of the non-strengthened fiber-reinforced concrete beam by 25, 44, 64, and 83%, respectively. These increases were respectively 10, 14, 30, and 31% for the midspan deflection. The results corresponding to the effect of the weight percentage of graphene oxide are shown in Figure 6.

3. 2. Effect of Number of Layers of CFRP on the Results This section addresses the influence of the number of layers of the CFRP with a length of 50 cm and a width of 10 cm considering 2 wt% of nanographene oxide in the epoxy adhesive. As seen in Table 6, a comparison of Le50W10L1G2, Le50W10L2G2, and Le50W10L3G2 with constant lengths and widths of CFRP, 2 wt% of graphene oxide, and a change in the number of layers of CFRP from 1 to 2 and 3 shows an increase in the maximum load exerted on the beam from17.4 to 30 and 39.4 kN, respectively. Similarly, the midspan deflection increased from 1.88 to 2.58 and 2.72 mm, respectively, the initial stiffness increased from 9255 to 11627 and 14485 kN/m, respectively, and the toughness increased from 36.7 to 44.4 and 60.1 Nm, respectively. These results indicate that an increase in the number of layers of CFRP improves the load-carrying capacity and flexibility of the fiber-reinforced concrete beam. Moreover, Figure 7 indicates a downward jump in force at the maximum load point. This jump becomes more severe as the number of layers increases. This occurs due to a tear in the CFRP and its inability to withstand force any longer. The fracture of the concrete beam occurs immediately after the fracture of the CFRP.

3. 3. Effect of a Change in the Length of CFRP on the Results This section investigated the influence of a change in the length of the CFRP from 50 to 35 and 20 cm with a width of 10 cm, a single layer of CFRP, and 2

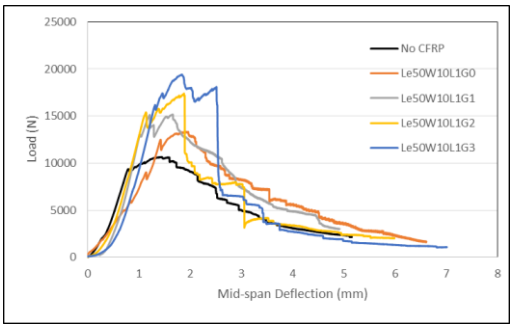

Figure 6. Effect of weight percentage of graphene oxide material used in the epoxy adhesive on the load-displacement diagram of fiber reinforced concrete beams reinforced with CFRP

TABLE 6. Influence of the number of layers of CFRP on the mechanical properties of fiber concrete beams

$\frac{T}{T}$ No Graphen	$\frac{K_{int}}{K_{int}}$ No Graphen	$\frac{\Delta_{max}}{\Delta_{max}}$ No Graphen	$\frac{P_U}{P_U}$ No Graphen	$\frac{\Delta_{max}}{\Delta_{max}}$ No CFRP	$\frac{P_U}{P_U}$ NO CFRP	Toughness(N.m)	Initial Stiffness (kN/m)	Maximum Deflection Δ (mm)	Ultimate load Pu (kN)	Sample
1.01	1.12	1.18	1.31	1.30	1.64	36.7	9255	1.88	17.4	Le50-W10-L1-G2
1.22	1.4	1.62	2.25	1.79	2.83	44.4	11627	2.58	30	Le50-W10-L2-G2
1.65	1.74	1.71	2.96	1.89	3.72	60.1	14485	2.72	39.4	Le50-W10-L3-G2

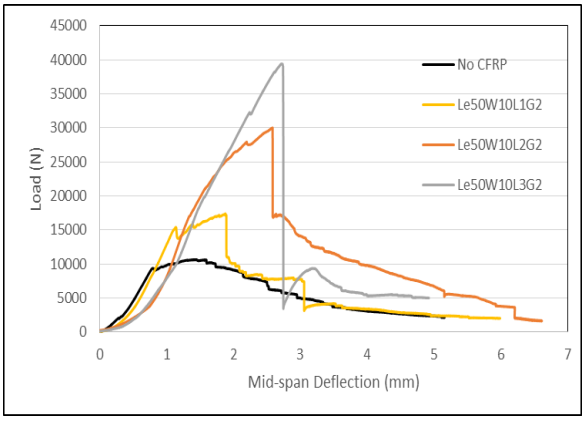

Figure 7. Effect of the number of layers of CFRP used to reinforce the fiber beam in the load-displacement diagram of the beam by considering two weight percent of the amount of graphene nano oxide in epoxy adhesive

wt% of nanographene oxide in the adhesive. As summarized in Table 7, a comparison of Le50W10L1G2, Le35W10L1G2, no CFRP, and Le20W10L1G2 with equal widths, one layer of CFRP, 2 wt% of graphene oxide, and with a change in the length of CFRP from 50 to 35 and 20 cm showed increases of 64, 55 and 27% in the maximum applied load compared to the beam sample without CFRP. Similarly, the midspan deflection increased from 30 to 16 and 11%, respectively. In addition, the results indicated that the toughness of the beam increases from 27.2 to 27.6 and 28.3% with an increase in the CFRP length from 20 to 35 and 50 cm. These results, displayed in Figure 8, demonstrate an improvement in the load-carrying capacity and flexibility of the strengthened fiber-reinforced beam given the use of the whole surface area of the tensile region of the concrete for strengthening. Furthermore, Figure 8 shows that the overall shapes of the load-deflection graphs of the three samples are almost identical. Initially, the load-carrying increases with a gentle slope, followed by a downward jump due to the formation of microcracks.

Subsequently, as the fibers come into play, the load-carrying capacity begins to rise again, followed by a strong decrease as the CFRP fractures.

3. 4. Effect of a Change in the Width of CFRP on the Results This section investigated the impact of a change in the width of the CFRP from 10 to 6 and 3 cm with a constant length of 50 cm, a single layer of CFRP, and 2 wt% of nanographene oxide in the resin. As stated in Table 8, a comparison of Le50W10L1G2, Le35W6L1G2, no CFRP, and Le20W3L1G2 with equal lengths, one layer of CFRP, 2 wt% of graphene oxide, and with a change in the width of CFRP from 10 to 6 and 3 cm showed increases of 64, 57, and 40% in the maximum load applied to the beam compared to the beam sample without CFRP. Similarly, the midspan deflection increased from 30 to 18 and 14%, respectively. In addition, the results indicated that the toughness of the beam decreases from 28.3 to 26.9 and 25.8% with an increase in the CFRP width from 10 to 6 and 3 cm. These results are also displayed in Figure 9.

TABLE 7. Influence length of CFRP on the mechanical properties of fiber concrete beams

$\frac{T}{T}$ *No CFRP*	$\frac{\Delta_{max}}{\Delta_{max}}$ *No CFRP*	$\frac{P_U}{P_U}$ *No CFRP*	Toughness(N.m)	Maximum Deflection Δ (mm)	Ultimate load Pu(kN)	Sample
1	1	1	28.6	1.44	10.6	No CFRP
1.28	1.30	1.64	36.7	1.88	17.4	Le50-W10-L1-G2
1.27	1.16	1.55	36.5	1.67	16.5	Le35-W10-L1-G2
1.27	1.11	1.27	36.4	1.60	13.5	Le20-W10-L1-G2

TABLE 8. Influence width of CFRP on the mechanical properties of fiber concrete beams

$\frac{T}{T}$ *No CFRP*	$\frac{\Delta_{max}}{\Delta_{max}}$ *No* CFRP	$\frac{P_U}{P_U}$ NO CFRP	Toughness (N.m)	Maximum Deflection Δ (mm)	Ultimate load Pu (kN)	Sample
1	1	1	28.6	1.44	10.6	No CFRP
1.28	1.30	1.64	36.7	1.88	17.4	Le50-W10-L1-G2
1.26	1.18	1.57	36.3	1.70	16.7	Le50-W6-L1-G2
1.25	1.14	1.4	36.0	1.64	14.9	Le50-W3-L1-G2

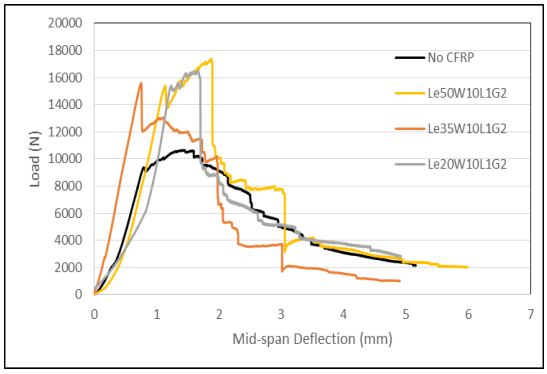

Figure 8. Effect of changing the length of carbon fiber used to strengthen the fiber beam in the load-displacement diagram of the beam by considering a layer of carbon fiber and 2% by weight of graphene nano oxide in epoxy resin

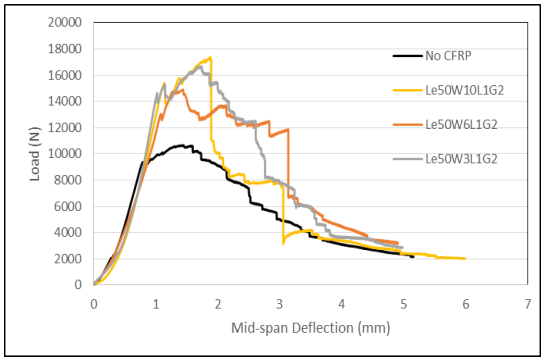

Figure 9. Effect of changing the width of carbon fiber used to strengthen the fiber beam in the load-displacement diagram of the beam by considering a layer of carbon fiber and 2% by weight of graphene nano oxide in epoxy resin

4. CONCLUSION

This research demonstrated that an increase in nanographene oxide in epoxy adhesive and the number of layers, length, and width of CFRP improve the load-carrying capacity and deformability of fiber-reinforced concrete beams. The following conclusions are drawn:

- As the weight percentage of nanographene oxide increased from 1 to 2 and 3% in the epoxy adhesive, the ultimate load-carrying capacity of a fiber-reinforced beam strengthened with a layer of CFRP with a length of 50 cm and width of 10 cm increased by 14, 31, and 46%, respectively, compared to a similar reinforced beam without nanographene oxide (Le50W10L1G0) and with an ultimate load-carrying capacity of 13.3 kN. Moreover, the results indicated a 3.7, 18, and 19% increase in the maximum midspan deflection for the strengthened beam, respectively, compared to the 1.59 maximum midspan deflection of the fiber-reinforced beam sample (Le50W10L1G0). In addition, as the weight of the nanographene oxide increased from 1 to 2 and 3% in epoxy adhesive, increases of 1.11, 1.12, and 1.27, respectively, in initial stiffness and 1.003, 1.01, and 1.04, respectively, in toughness were observed compared to the beam sample Le50W10L1G0.
- With a constant nanographene oxide weight of 2% in polyamine resin, an increase in the number of layers of CFRP from 1 to 2 and 3 was seen to increase the ultimate load-carrying capacity of the beam to respectively 1.64 to 2.83 and 3.72 times that of the non-strengthened case. Similarly, increases of 30, 79, and 89%, respectively, in the midspan deflection of the beam were observed. An increase in the number of layers of CFRP increased the initial stiffness from 9255 to 11627 and 14485 kN/m, respectively, and the toughness from 36.7 to 44.4 and 60.1 N.m.
- As the length of the CFRP increased from 20 to 35 and 50 cm, the maximum load-carrying capacity increased by 27, 55, and 64%, respectively. In addition, increases of 11, 16, and 30% were obtained from the maximum midspan deflection and 27.2, 27.6 and 28.3% for the toughness of the materials. In this case, 2% nanographene oxide was used in the polyamine resin.
- With an increase in the width of the CFRP from 3 to 6 and 10 cm, the ultimate load-carrying capacity was observed to increase by 40, 57 and 64%, respectively. The corresponding increases in the maximum midspan deflection were 14, 18, and 30%, respectively, and those in the toughness were 25.8, 26.9, and 28.3%, respectively.
- Using the results obtained in this study, due to the high resistance created in the resin, the full capacity of CFRP can be used, which is the result of significant progress in civil engineering.

5. REFERENCES

1. M. Shadmand, A. Hedayatnasab, and O. Kohnehpooshi, "Strengthening of RC beams using steel plate-fiber concrete composite jackets: Finite element simulation and experimental investigation," ***International Journal of Engineering, Transactions A: Basics***, Vol. 35, No. 1, (2022), 73-92, doi: 10.5829/ije.2022.35.01a.07.
2. S. B. Rahimi, A. Jalali, S. M. Mirhosseini, and E. Zeighami, "Comparative experimental study of different types of fiber-reinforced polymer wrapping in repairing of reinforced concrete deep beams with circular openings," ***International Journal of Engineering, Transactions B: Applications***, Vol. 34, No. 8, (2021), 1961-1973, doi: 10.5829/ije.2021.34.08b.17.
3. S. A. Abbas, I. F. Ali, and A. A. Abdulridha, "Behavior and strength of steel fiber reinforced self-compacting concrete columns wrapped by carbon fiber reinforced polymers strips," ***International Journal of Engineering, Transactions B: Applications***, Vol. 34, No. 2, (2021), 382-392, doi:

10.5829/IJE.2021.34.02B.10.

4. S. Yousefi Khatuni and H. Showkati, "Buckling behavior of semi-scale steel tank with carbon fiber reinforced polymer ring subjected to lateral uniform pressure loading," ***International Journal of Engineering, Transactions A: Basics***, Vol. 32, No. 10, (2019), 1407-1415, doi: 10.5829/ije.2019.32.10a.10.
5. M. B. S. Alferjani, A. A. A. Samad, B. S. Elrawaff, and N. Mohamad, "Experimental and Theoretical Investigation on Shear Strengthening of RC Precraced Continuous T-beams Using CFRP Strips," ***International Journal of Engineering***,, ***Transactions B: Applications,*** Vol. 28, No. 5, (2015), 671-676. doi: 10.5829/idosi.ije.2015.28.05b.04
6. A. A. Maghsudi and D. Y. Askari, "Ultimate unbonded tendon stress in CFRP strengthened post-tensioned indeterminate I-beams cast with HSCs," ***International Journal of Engineering, Transactions A: Basics***, Vol. 28, No. 3, (2015), 350-359, doi: 10.5829/idosi.ije.2015.28.03c.03.
7. M. Shadmand, A. Hedayatnasab, and O. Kohnehpooshi, "Retrofitting of Reinforced Concrete Beams with Steel Fiber Reinforced Composite Jackets," ***International Journal of Engineering***, ***Transactions B: Applications,*** Vol. 33, No. 5, (2020), 770-783, doi: 10.5829/ije.2020.33.05b.08
8. H. Dehghani and M. J. Fadaee, "Reliabilty-based Torsional Design of Reinforced Concrete Beams Strengthened with," ***International Journal of Engineering***, ***Transactions A: Basics,*** Vol. 26, No. 10, (2013), 1103-1110, doi: 10.5829/idosi.ije.2013.26.10a.01.
9. S. H. Hashemi, "Flexural Testing of High Strength Reinforced Concrete Beams Strengthened," ***International Journal of Engineering***, ***Transactions B: Applications,*** Vol. 22, No. 2, (2009), 131-146.
10. M. Riyazi, M. R. Esfahani, and H. Mohammadi, "Behavior of Coupling Beams Strengthened With Carbon Fiber Reinforced Polymer Sheets," ***International Journal of Engineering***, ***Transactions B: Applications,*** Vol. 20, No. 1, (2007), 49-58.
11. A. Agbossou, L. Michel, M. Lagache, and P. Hamelin, "Strengthening slabs using externally-bonded strip composites: Analysis of concrete covers on the strengthening," ***Composites Part B: Engineering***, Vol. 39, No. 7-8, (2008), 1125-1135, doi: 10.1016/j.compositesb.2008.04.002.
12. M. H. Mahmoud, H. M. Afefy, N. M. Kassem, and T. M. Fawzy, "Strengthening of defected beam-column joints using CFRP," ***Journal of Advanced Research***, Vol. 5, No. 1, (2014), 67-77, doi: 10.1016/j.jare.2012.11.007.
13. R. V. S. Ramakrishna Ravindra, V., "Experimental Investigation on Rehabilitation of Reinforced Cement Concrete Interior Beam-Column Joints Using CFRP and GFRP Sheets," ***International Journal of Engineering Science and Technology***, Vol. 4, No. 3, (2012), 874-881.
14. M. Hussain, A. Sharif, I. A. B. M. H. Baluch, and G. J. Al-Sulaimani, "Flexural behavior of precracked reinforced concrete beams strengthened externally by steel plates," ***Structural Journal***, Vol. 92, No. 1, (1995), 14-23.
15. M. Z. Jumaat and M. A. Alam, "Behaviour of U and L shaped end anchored steel plate strengthened reinforced concrete beams," ***European Journal of Scientific Research***, Vol. 22, No. 2, (2008), 184-196.
16. M. Amir, C. Omar, B. Brahim, and N. Kenneth, "Performance of End-Anchorage Systems for RC Beams Strengthened in Shear with Epoxy-Bonded FRP," ***Journal of Composites for Construction***, Vol. 16, No. 3, (2012), 322-331, doi: 10.1061/(ASCE)CC.1943-5614.0000263.
17. J.-W. Shi, W.-H. Cao, and B.-L. Xu, "Effect of liquid rubber modification on the bond behavior of externally bonded FRP laminate-concrete interface under dynamic loading," ***Journal of Building Engineering***, Vol. 32, No. 2, (2020), doi: 10.1016/j.jobe.2020.101533.
18. M. R. Irshidat and M. H. Al-Saleh, "Effect of using carbon nanotube modified epoxy on bond-slip behavior between concrete and FRP sheets," ***Construction and Building Materials***, Vol. 105, No. 2, (2016), 511-518, doi: https://doi.org/10.1016/j.conbuildmat.2015.12.183.
19. X. Yao, X. Gao, J. Jiang, C. Xu, C. Deng, and J. Wang, "Comparison of carbon nanotubes and graphene oxide coated carbon fiber for improving the interfacial properties of carbon fiber/epoxy composites," ***Composites Part B: Engineering***, Vol. 132, No. 3, (2018), 170-177, doi: https://doi.org/10.1016/j.compositesb.2017.09.012.
20. M. R. Irshidat, N. Al-Nuaimi, and M. Rabie, "Influence of carbon nanotubes on phase composition, thermal and post-heating behavior of cementitious composites," ***Molecules***, Vol. 26, No. 4, (2021).
21. E. Soliman, U. F. Kandil, and M. R. Taha, "Limiting shear creep of epoxy adhesive at the FRP-concrete interface using multi-walled carbon nanotubes," ***International Journal of Adhesion and Adhesives***, Vol. 33, No. 4, (2012), 36-44.
22. S. R. Abdullah, F. N. Rosli, N. Ali, N. A. Abd Hamid, and N. Salleh, "Modified Epoxy for Fibre Reinforced Polymer Strengthening of Concrete Structures," ***International Journal of Integrated Engineering***, Vol. 12, No. 9, (2020), 103-113.
23. M. R. Irshidat and M. H. Al-Saleh, "Flexural strength recovery of heat-damaged RC beams using carbon nanotubes modified CFRP," ***Construction and Building Materials***, Vol. 145, No. 6, (2017), 474-482.
24. M. R. Irshidat, M. H. Al-Saleh, and H. Almashagbeh, "Effect of carbon nanotubes on strengthening of RC beams retrofitted with carbon fiber/epoxy composites," ***Materials & Design***, Vol. 89, No. 1, (2016), 225-234.
25. H. Xu *et al.*, "Evolution of properties and enhancement mechanism of large-scale three-dimensional graphene oxide-carbon nanotube aerogel/polystyrene nanocomposites," ***Polymer Testing***, Vol. 97, No. 2, (2021), doi: https://doi.org/10.1016/j.polymertesting.2021.107158.
26. A. Sheikhmohammadi *et al.*, "Application of graphene oxide modified with 8-hydroxyquinoline for the adsorption of Cr (VI) from wastewater: Optimization, kinetic, thermodynamic and equilibrium studies," ***Journal of Molecular Liquids***, Vol. 233, No. 3, (2017), 75-88, doi: https://doi.org/10.1016/j.molliq.2017.02.101.
27. L. Wei, X. Liu, Y. Gao, X. Lv, N. Hu, and M. Chen, "Synergistic strengthening effect of titanium matrix composites reinforced by graphene oxide and carbon nanotubes," ***Materials & Design***, Vol. 197, No. 4, (2021), doi: https://doi.org/10.1016/j.matdes.2020.109261.
28. H. Ashassi-Sorkhabi, B. Rezaei-Moghadam, E. Asghari, R. Bagheri, and R. Kabiri, "Sonoelectrosynthesized polypyrrole-graphene oxide nanocomposite modified by carbon nanotube and Cu2O nanoparticles on copper electrode for electrocatalytic oxidation of methanol," ***Journal of the Taiwan Institute of Chemical Engineers***, Vol. 69, No. 5, (2016), 118-130, doi: https://doi.org/10.1016/j.jtice.2016.08.026.
29. V. Acar, F. Cakir, H. Uysal, M. O. Seydibeyoglu, H. Akbulut, and K. M. Mosalam, "Strengthening of concrete beams by monolayer prepreg composites with and without graphene reinforcement," ***Construction and Building Materials***, Vol. 151, No. 2, (2017), 866-880, doi: https://doi.org/10.1016/j.conbuildmat.2017.06.150.
30. X. Wang, F. Tang, X. Qi, and Z. Lin, "Mechanical, electrochemical, and durability behavior of graphene nano-platelet loaded epoxy-resin composite coatings," ***Composites Part B: Engineering***, Vol. 176, (2019), doi: 10.1016/j.compositesb.2019.107103.

Persian Abstract

چکیده

در این پژوهش، تاثیر ماده‌ی نانو اکسیدگرافن در بهبود خواص مکانیکی رزین پلی‌آمین جهت بهبود در چسبندگی پارچه کربنی به تیر بتن‌الیافی مورد بررسی قرار گرفت. برای این منظور در یک کار آزمایشگاهی تعداد ۳۳ تیر بتن الیافی با استفاده از پارچه‌ی کربنی به طول مختلف ۵۰، ۳۵و۲۰ سانتی‌متر و عرض مختلف ۳، ٦ و ۱۰ سانتی‌متر مقاوم‌سازی شده‌اند، مورد بررسی قرار گرفت. مقادیر وزنی اکسید گرافن در رزین به ترتیب ۱،۲و۳ درصد بوده که با حالت تیر مقاوم‌سازی شده بدون اکسیدگرافن مقایسه شد. نتایج کار ابتدا بر روی ۱۲ تیر نشان داد که با افزایش مقدار ماده‌ی نانو در چسب از ۱به۲و۳درصد، مقادیرحداکثر ظرفیت باربری، خیز حداکثر وسط دهانه، سختی تیرو طاقت آن به ترتیب ٤٦،١٩،٢٧و۵ درصد افزایش نسبت به حالت تیر مقاوم‌سازی شده باپارچه کربنی وبدون اکسید گرافن داشت. در ادامه با توجه به نزدیک بودن نتایج تیرهای مقاوم‌سازی شده با ۲ و۳ درصد ماده‌ی اکسید گرافن، از دودرصد اکسید گرافن در بقیه نمونه‌ها استفاده شده و تاثیر تغییر در تعداد نوار، طول و عرض پارچه کربنی در مشخصات مکانیکی تیر بتنی بررسی شد. نتایج نشان داد که با افزایش تعداد نوارهای پارچه‌کربنی و همچنین طول و عرض آنها ظرفیت باربری و شکل‌پذیری تیر بتن‌الیافی افزایش می‌یابد.

IJE TRANSACTIONS B: Applications Vol. 35, No. 08, (August 2022) 1533-1546

International Journal of Engineering

Journal Homepage: www.ije.ir

An Analytical Model for Confronting the Omicron Variant During COVID-19 Pandemic: A System Dynamic Approach

M. Akbari, N. Safaie*, Z. Jahani, M. R. Saadatmand

Department of Industrial Engineering, K. N. Toosi University of Technology, Tehran, Iran

PAPER INFO

Paper history:
Received 09 February 2022
Received in revised form 11 MArch 2022
Accepted 12 March 2022

Keywords:
Corona Virus
Pandemic
Vaccination
System Dynamic
Quarantine
Omicron

ABSTRACT

The global outbreak of COVID-19 began in December 2019 in Wuhan, China, and affected the entire world in a short time. Over time, the emergence of new species of the disease, the pace of response to it has also strongly affected, and with the emergence of the newest species called Omicron. Knowing and reviewing the system and publishing publications in the community is essential for sound policies. It is necessary to investigate the spread of COVID-19 to make proper policies. System dynamic can be adopted as an approach to the behavior evaluation of the COVID-19 pandemic. The present study introduces a system dynamic model to explore the effects of different factors on the pandemic and therapeutic and non-therapeutic modalities. Vaccination is evaluated as the main approach to prevent the disease. The influential factors of pandemic prevention and control are examined based on the SEIR model and policies such as vaccination. The safest way to prevent this epidemic is vaccination. Therefore, a policy that benefits the entire population and will be necessary is producing and purchasing vaccines. From 19 July 2021, the rate of vaccine imports to Iran has increased significantly, and therefore it is predicted that by the end of 2022, Iran's general vaccination will end, after which the number of cases and mortality rates will decline. Vaccines are the ultimate solution to contagious diseases to control disease spread and provide safety to deal with the infection. The results suggested that the fatality rate of the susceptible population was reduced by vaccination and protective protocols. Thus, this paper aims to analyze factors influencing the spread of COVID-19 and prevent the disease.

doi: *10.5829/ije.2022.35.08b.10*

1. INTRODUCTION

A total of six human corona virus types were detected during 1960-2019, including HCoV-229, OC43, HKU1, and NL63 [1]. A large number of severe pneumonia cases were detected in December 2019 in Wuhan, China. They were the first infected people in Wuhan. Then, the seventh type of corona virus was identified and announced as SARS-CoV-2 (also known as COVID-19) [1]. Initial epidemiological research showed that the disease was rapidly spreading. As can be seen in Figure 1, COVID-19 spread throughout China in January and February 2019 and affected some other countries [2].

Flights between China, the United States, Europe, and some other parts of the world transmitted the virus to Asian countries and then to the other continents [3]. As SARS-CoV-2 spread in Wuhan, the Ministry of Health and Medical Education began to check passengers arriving from China in Iran. As of July 15, 2020, a total of 13,119,239 confirmed cases were reported in at least 213 countries, with a total of 573,752 deaths. The first SARS-CoV-2 death case was reported in Qom, Central Iran, in February 2020 [4, 5]. World Health Organization (WHO) announced the disease as the COVID-19 pandemic and requested all countries to enhance control attempts concerning the largest global health emergency condition in the modern era [6][1].

WHO stated that early diagnosis and treatment were crucial and effective factors to control the spread of the pandemic. Today, most studies focus on the clinical characteristics, epidemiology, nucleic acid diagnosis methods, gene sequencing, medication effectiveness, and

*Corresponding Author Institutional Email: nsafaie@kntu.ac.ir (N. Safaie)

[1] https://www.who.int/en/activities/tracking-SARS-CoV-2-variants

Please cite this article as: M. Akbari, N. Safaie, Z. Jahani, M. R. Saadatmand, An Analytical Model for Confronting the Omicron Variant During COVID-19 Pandemic: A System Dynamic Approach, ***International Journal of Engineering, Transactions B: Applications***, Vol. 35, No. 08, (2022) 1533-1546

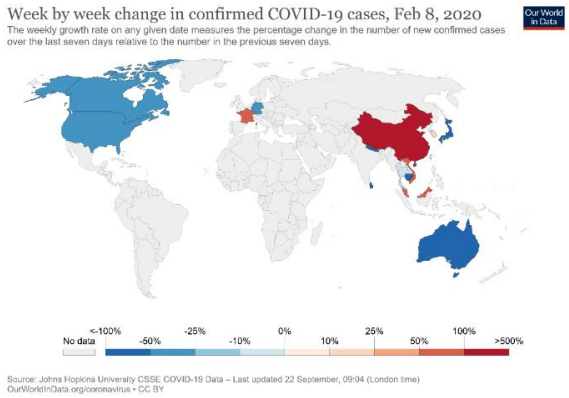

Figure 1. The first countries to be affected by the COVID-19 pandemic on February 8, 2020

other aspects of COVID-19 patients. However, there still is a need for the in-depth discussion of early diagnosis, early screening, early treatment, and early isolation and improvement concerning COVID-19 [7]. Thus, the present study seeks to evaluate factors influencing the spread of COVID-19 and prevent it by analyzing the data of COVID-19 infection and fatality rates.

COVID-19 is transmitted by breathing and touching, and its symptoms include fever, coughing, sore throat, tiredness, and digestive symptoms such as diarrhea, vomiting, and stomach ache. Digestive symptoms may appear earlier than respiratory symptoms [8]. The virus can be transmitted in different ways, depending on its type. In some cases, the virus is transmitted between humans through coughing and sneezing, as similar to flue virus. However, the probability of virus transmission is very small outdoors. The human-to-human transmission of COVID-19 has been found to occur in indoor places with long exposure to infected individuals (such as those who are in close contact with patients at hospitals). To cope with the COVID-19 pandemic, many countries have implemented preventive measures, such as isolation and social distancing, mainly to prevent the rate of hospitalization and reduce stress and pressure imposed on the healthcare workers. It also remains a crucial concern to protect healthcare workers from injections.

These measures, however, have resulted in the isolation of public life and induced many problems. The incomes of the population are a significant economic challenge imposed by the pandemic and have caused an economic gap between countries [9]. Thus, it is essential to shorten quarantine period[3].

The policy response of Iran to the COVID-19 pandemic indicates how countries that already have challenges deal with severe crises. The Iranian government had already been weakened economically by U.S. sanctions and had to consider short-term exchanges of public health and social stability with unemployment and food insecurity, which is used to justify a policy from economic decline to economic lasting. It has been revealed that explanations for the initially inefficient response of Iran to the COVID-19 pandemic included poor economic policies, a lack of public health coordination, treatment priority over prevention, and insufficient healthcare facilities.

At the beginning of the pandemic, a lack of vaccines led to a set of political interventions, such as travel bans, border restrictions, mandatory quarantine, screening protocols, mask regulations, and social distancing measures [10]. However, Iran experienced several waves of the COVID-19 pandemic as public protective protocols were not efficiently implemented. Although vaccination began on February 8, 2021, Iran underwent new waves of the pandemic due to the significantly slow rate of vaccination, as shown in Figure 2. Thus, the fatality and infection rates of COVID-19 did not decline in Iran.

The COVID-19 pandemic is a global crisis with adverse health, commercial, and social impacts. Vaccination is a safe, simple, and effective approach to diminish COVID-19 fatality [10]. Figure 3 depicts the shares of vaccinated populations until November 21, 2021, in different countries. As can be seen, more than 69% of the population was fully vaccinated in the UK and Germany, while 61% of the US population received full vaccination. Also, 47.6% of the world's population had been fully vaccinated. In the Middle East, 59.2% of the Iranian population was fully vaccinated. As shown in Figure 4 until December 19, 2021, over 100 million people received at least one vaccine dose in Iran.

Several vaccines have been developed and approved for emergency use since COVID-19 emerged. The current vaccines have shown effectiveness with a slight risk of side effects. However, some new variants of COVID-19 (such as the delta and lambda variants) may

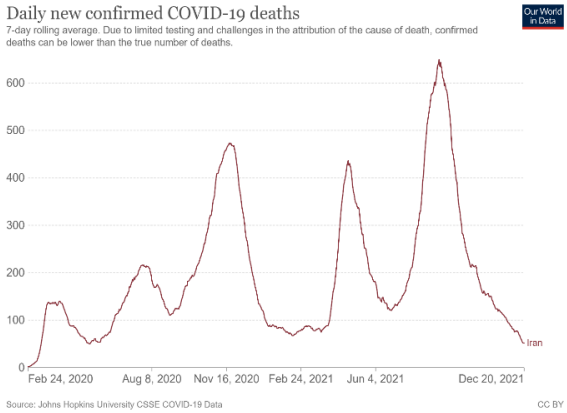

Figure 2. COVID-19 fatality and waves in Iran

[3] http://joc.kntu.ac.ir/article-1-824-en.html

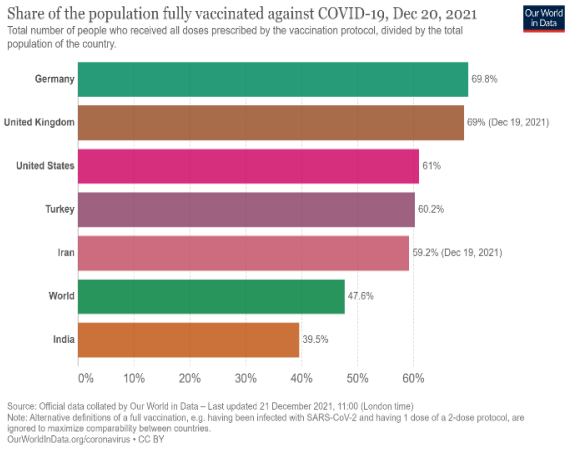

Figure 3. COVID-19 vaccination rates on November 21, 2021

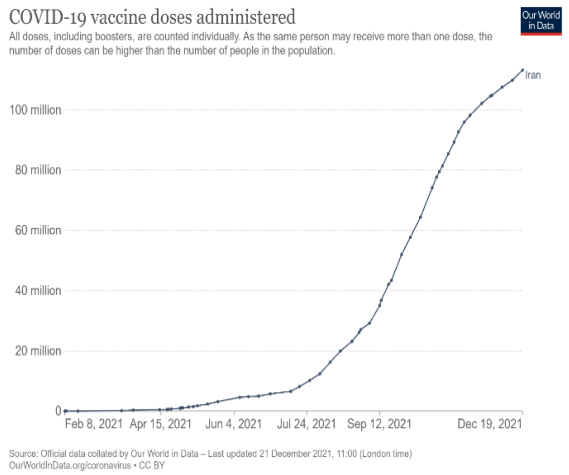

Figure 4. Vaccination in Iran

escape immunity extracted by the vaccines [10]. Having been one and a half years since the emergence of the pandemic, the mutations significantly facilitated the transmission of the disease compared to the initial virus detected in Wuhan in late 2019.

The delta variant of COVID-19 was recently detected in India and has been reported to be much more likely to be transmitted to individuals than its previous mutations. The delta variant infects a much larger number of individuals and increases the transmission chain. As a result, the fatality rate rises at a large rate compared to other viruses.

Researchers are still focused on the delta variant as the dominant COVID-19 variant in the world with increasing infected cases. Research has shown that the delta variant is more infectious than the alpha variant reported in the UK, representing the most transmittable variant of SARS-CoV-2 [11]. This has reduced the effectiveness of two doses of the Pfizer vaccine to 64%. Many countries have significant unvaccinated populations, and the delta variant has proved to infect a larger portion of the vaccinated population than the previous variants. WHO classifies the delta variant as a variant of concern (VOC); that has proved to increase transmutability, causing severer diseases or reducing the advantages of vaccines and treatments.

A more recent variant of COVID-19 was detected as the lambda variant in Peru. Infections with the lambda variant were reported in December 2020. The lambda variant has been considered to be a potential threat. However, some infectious disease specialists claimed that the lambda variant may be weakening as the number of lambda-infected cases reported to the GISAID database has been declining. The previous variant (Alpha, Beta, Gamma and Delta) resulted in a new wave of pandemic and thousands of deaths in more than one country and area, and even across the whole world[4]. On November 26, 2021, a new variant named Omicron immediately raised global concerns [12]. The present study proposes a system dynamic (SD) model to explore the effects of different factors on the spread of COVID-19 and therapeutic and non-therapeutic modalities and policies adopted to reduce the spread of the pandemic.

Dynamic modeling of the system has been used to study infectious diseases, such as human immunodeficiency virus (HIV) transmission [13, 14]. This environment is also used to study the disease on the economy [15] and the policy of migrant workers on the growth of the country under the influence of the COVID-19 epidemic [16]. In addition, dynamic system modeling has been simulated to explain the social effectiveness of COVID-19 laws in selected areas of Japan [17] and the spread of COVID-19 in Italy, India, South Korea and Iran [18]. Another study proposed a SEIR model to demonstrate the dynamic behavior of the disease at the regional level [19] and to model possible pathways resulting from Quid 19 and non-pharmacological interventions in the United States [20]. Due to the acceptable and low system dynamics, this study develops dynamic system modeling based on a model designed by Tom Fidaman to evaluate the various policies of the Iranian government.

2. LITERATURE REVIEW

A large number of studies have been conducted on cultural, economic, and medical aspects of the COVID-19 pandemic to prevent and mitigate it since late 2019. Researchers recently reported COVID-19 simulation models, such as SD for COVID-19, and the outcomes of possible interventions.

[4] https://www.who.int/en/activities/tracking-SARS-CoV-2 variants

Geier and Geier [21] in 2020 studied respiratory conditions of COVID-19. They proposed alternative treatments using the existing clinical methods, e.g., hyperbaric oxygen therapy, packed red blood cells, and anthroponosis stimulator treatment [21]. Ali and Alharbi [22] in 2020 investigated COVID-19 and its management, treatment, and social impacts. They suggested that the combined use of antiviral medications, hydroxychloroquine, and azithromycin as the most effective alternative to treat patients [22]. Bastos and Cajueiro [23] in 2020 predicted the primary evolution model of the pandemic using data from February 25 to March 30, 2020, in Brazil. They employed two susceptible-infected-recovered (SIR) models and simulated a parameter involving social measures. The SIR model divided the population in disease spread into three groups: (1) susceptible are those who are healthy but can be infected, (2) infected are those who are infected, and (3) recovered refers to people that have been recovered from the disease. They estimated the SIR model using the existing parameters and data [23].

Chanu and Singh [24] in 2020 studied public data of Indian COVID-19 patients and analyzed the possible impacts of quarantine and social distancing under the susceptible-exposed-quarantine-infected-recovered (SEQIR) to represent control policies. The SEQIR model divides the population into five groups: susceptible, exposed, and infected while not being test-detected, quarantined, hospitalized/reported/quarantined infected, and recovered people along with those who live in secured zones free of the pandemic. Pruyt and Hamarat [25] in 2020 developed an SD model of COVID-19 spread. The stringent age-structured model endogenously received disease transmission paths and significantly extended from the standard susceptible-exposed-infected-recovered (SEIR) model. The model was customized for India using a suitable population pyramid, contact matrix, foreign arrival, and some other calibration fractions based on the reported Indian COVID-19 cases. Through time-variant pyramids, they explicitly modeled the effects of testing, contact tracking, positive COVID-19 patients, quarantine, masks, and social distancing by reducing contact in certain places (e.g., home and workplace).

Ghaffarzadegan and Rahmandad [26] in 2020 proposed a dynamic, simple model of the epidemic in Iran to represent a more reliable image of the disease based on the existing data. They employed the SEIR model and incorporated behavioral and logistic considerations. First, they reported endogenous variations in contact (contact with people) as higher fatality. As a result, the number of reproductions endogenously changed in the model. Second, they distinguished the reported and real cases by simple formulations to detect only a fraction of the cases and how the fraction would change in response to epidemic progress. Sy et al. [27] in 2020 proposed policy recommendations through an SD approach. The developed model captured relationships, feedback, and delays in the disease transmission system. The dynamism of several policies was analyzed based on effectiveness in reducing infection and consequent economic pressure. Indeed, they are important to respond to the disease. Relationships were established between these factors in the SD framework and then were simulated as stock and flows. However, it is worth mentioning that SD values are not predictions. Instead, SD is used to represent the trends of variables with time under the existing feedback in the system.

Gkini [28] in 2020 examined the population-level coupled dynamics of COVID-19 infection and behavioral response in Norway. They developed an SD model that proposed alternations in the epidemiologic models of classical differential equations for more efficient use in the case of COVID-19. They sought to gather health behavior theories on individual responses to environmental well-being threats. The two components of the model were studied individually and collectively and were found to accurately replicate COVID-19 spread in Norway with rational assumptions. In particular, they constructed a simulation model capturing many common components in health behavior theories within a composite framework that could enable tests under various assumptions. Zia and Farooq [29] in 2020 simulated an SD model of epidemic progress that represented the mode dynamics of COVID-19 spread and handled population and mobility data. The model was calibrated based on epidemic data and particular incidents in Pakistan and could be generalized. The simulations produced disturbing results and revealed that the pandemic would significantly spread for a long time (even longer than a year), even under social distancing and testing strategies. In a specific scenario, they imitated 95% of the isolation of infected patients with symptoms. The 5% probability of infecting others was really lower (only 2.5%). Asymptomatic patients could infect people with a probability of 5% only due to the lockdown. The results indicated that 40% of the population was infected rather than being similar to cases in the previous group.

Hadiwibowo et al. [30] in 2020 analyzed the COVID-19 prediction peak by selecting scenarios. System dynamics prediction was enhanced by selecting scenarios to observe the prediction. Thus, the probability of COVID-19 cases in business could be typically found (including typical control, optimistic, and even uncontrolled situations). Medium conditions with precautious contact, implementing protective protocols (such as the healthy life movement), social distancing, disinfection, sufficient medical equipment and healthcare facilities, home settlement, and working at home could smoothly reduce the rate of infection.

Fathollahifard et al. [31] in 2021 examined the Home Health Care Supply Chain (HHCSC). This paper develops a bi-level programming model as a static Stalkberg game between nurses and patients within the HHCSC framework. From HHCSC's point of view, pharmacy location, nurses' scheduling and routing, and drug delivery rate have always been important issues, so this model considers the possibility of outsourcing demand and applies to emergencies such as the COVID-19 pandemic outbreak. In this situation, the demand for HHC services has increased and is beyond the capacity of the centers. In this regard, the proposed model can be used and outsourcing can be provided. In coronary conditions, vaccination is one of the most important factors to consider, for example, in order to expedite vaccination in Canada, vaccination services were provided in both pharmacies and hospitals [21]. In another paper, Fathollahifard et al. [32] in 2022, in this paper present a model for robust multi-objective optimization for a routing optimization problem and scheduling for the use of a home health care logistics network. The benefits of an efficient design are critical to responding to or responding to epidemics such as COVID-19. Due to the need for social distance during COVID-19, these services are very useful for reducing epidemic growth [32]. Due to the prevalence of COVID-19, Mosallanejad et al. [33] in 2021 have simultaneously developed a multi-objective, multi-product and multi-period model for the needs of personal protective equipment with the aim of optimizing total cost and scarcity.

Reviewing the literature on this subject, it was found that there are research gaps such as the lack of simultaneous study of the impact of quarantine and vaccination on the pandemic system using the systems dynamics approach. Therefore, this study investigates the effect of various factors on the prevalence of COVID-19 disease and ways to control or reduce its incidence and finally a system dynamics model is presented. The data required in this study to analyze the model are taken from official sources, the Ministry of Health of Iran, the World Health Organization and other articles presented in this field as Table 1.

TABLE 1. Research in the field of COVID-19

#	Authors	Year	Title	Approach	Case Study	Vaccine	Quarantine
1	Geier and Geier [21]	2020	Respiratory Conditions in Corona virus Disease 2019 (COVID-19): Important Considerations Regarding Novel Treatment Strategies to Reduce Mortaliy.				
2	Ali and Alharbi [22]	2020	COVID-19: Disease,Management, Treatment, and Social Impact.				✓
3	Bastos and Cajueiro [23]	2020	Modeling and forecasting the early evolution of the COVID-19 pandemic in Brazil.	Susceptible, Infected, Recovered (SIR)model	Brazil		
4	Chanu and Singh [24]	2020	Stochastic approach to study control strategies of COVID-19 pandemic in India.	Susceptible, Exposed, Quarantine, Infected, Recovered (SEQIR)model	India		✓
5	Pruyt and Hamarat [25]	2020	The Influenza A(H1N1) Pandemic: An Exploratory System Dynamics Approach.	Exploratory System Dynamics model	India	✓	
6	Ghaffarzadegan and Rahmandad [26]	2020	Simulation-based Estimation of the Spread of COVID-19 in Iran.	Susceptible, Exposed, Infected, Recovered (SEIR)model	Iran		
7	Sy et al. [27]	2020	Policy Development for Pandemic Response Using System Dynamics: a Case Study on COVID-19.	Susceptible, Infected, Recovered (SIR)model			✓
8	Gkini [28]	2020	Health Behaviour Theories and The Norwegian Response to COVID-19: A System Dynamics Modeling Approach.	SEIR model	Norway	✓	
9	Zia and Farooq [29]	2021	COVID-19 Outbreak in Pakistan: Model-Driven Impact Analysis and Guidelines.	Susceptible, Exposed, Infected, Recovered (SEIR)model	Pakistan		✓

10	Hadiwibowo et al. [30]	2021	A Policy Strategy Evaluation for Covid Pandemic in the City of Surabaya Using Vensim Ventana Dynamic System Simulation.	Susceptible, Exposed, Infected, Recovered (SEIR)model	Indonesia		
11	Fathollahi-Fard et al. [31]	2021	Sustainable and Robust Home Healthcare Logistics: A Response to the COVID-19 Pandemic,	multi-objective optimization model	Austria		
12	Mosallanezhad et al. [33]	2021	Disaster relief supply chain design for personal protection equipment during the COVID-19 pandemic,	multi-objective, multi-product, and multi-period model	Iran		
13	Fathollahi-Fard et al. [32]	2022	Bi-level programming for home health care supply chain considering outsourcing.	bi-level programming model	Iran		
14	Muniyappan et al. [34]	2022	Stability and Numerical Solutions of Second Wave Mathematical Modeling on COVID-19 and Omicron Outbreak Strategy of Pandemic: Analytical and Error Analysis of Approximate Series Solutions by Using HPM	homotopy perturbation method	India		
15	Present research	Under review	An analytical model for confronting the Omicron variant during COVID-19 pandemic: A system dynamic approach	System Dynamic, Susceptible, Exposed, Infected, Recovered (SEIR)model	Iran	✓	✓

The second part of this research reviews the literature and research background in this field, then in the third part, the method is explained, and in the fourth part, the result. The fifth part reviews Discussions and managerial insights and in the sixth part, conclusion is presented.

3. METHODS

The research method for developing prototypes and scenarios is dynamic system-based simulation with Vensim Ventana software. Dynamic systems simulation is a method used to transform real phenomena into clearer models whose systems will change over time. According to this method, this section is divided into 7 subsections, which first define the problem and provide a general explanation related to the simulation of dynamic systems, and then the data collection methods in this research are reviewed. In the continuation of this section, the existing initial model is developed and finally validation is performed.

3. 1. Problem Statement Contagious diseases pose essential impacts on the economy and physical and mental health of people. Many societies need to identify system behavior and disease spread to plan and cope with diseases. It is important to realize the behavior dynamic of disease spread to enhance healthcare systems and health workers. SD is a well-known, efficient approach to studying system behavior in the spread of diseases.

Infectious disease specialists view population composition, society culture, environment, and government responsiveness as the four major factors that potentially influence the spread of COVID-19 in a region. Also, personal protective measures, such as wearing a mask, consistently washing hands, and avoiding human crowds, can play a key role in preventing the spread of COVID-19[5]. The responsiveness of governments also plays an important role in COVID-19 spread, and countries that rapidly responded to the COVID-19 pandemic by implementing quarantine and social distancing experienced lower causalities.

The present study develops a model of vaccination based on the existing research gaps and a base model. To obtain a more realistic model, constant or auxiliary parameters were derived from the databases of the WHO and the Ministry of Health and Medical Education, drawing the stock-flow diagram of the key variables and reference behaviors and formulating the epidemic simulation model. The model was validated, and the sensitivity of the model to parameters, initial conditions, and boundaries was analyzed.

3. 2. System Dynamic System Dynamic (SD) is an aspect of systems theory and is used to understand dynamic and continuous behavior in complex systems. It is a methodology of simulation to determine frameworks and understand and discuss complex management, industrial, social, and even medical factors [33].

Due to the COVID-19 pandemic, researchers seek to realize how simulation instruments can help decision-

[5] https://www.who.int/en/activities/tracking-SARS-CoV-2 variants

makers deal with this very complex crisis [12]. Introduced by Foster, SD helps understand the relationships between the components of a system and represents dynamic behaviors through several feedback loops [34]. In particular, it is very beneficial as it enables policy-makers to accurately implement policies and detect their complex relationships, revealing the potential effects of alternative policies to make more efficient decisions [35].

In general, systematic mathematical models are an efficient framework to mitigate and control COVID-19, as with other contagious diseases. The spread of contagious diseases is very complicated and involves interconnected systems with feedback loops, delays, and nonlinear relationships. It is difficult to predict the behavior of such systems. Detailed modeling methods, such as SD, can be employed to illustrate spread dynamics and simulate spread behavior. Also, public health workers believe that systematic approaches such as SD are valuable in the design of effective policies [36]. The present study aims to develop an SD model and analyze the effects of factors on the spread of COVID-19 and therapeutic and non-therapeutic modalities and policies for the reduction of the pandemic.

3. 3. Data Collection Data from the onset of the pandemic in Iran to February 20, 2020, was introduced to the developed model. To obtain consistently varying data, such as disease progression rate, recovery rate, and fatality rate along with vaccination rate, the WHO database was utilized. It should be noted that the COVID-19-infected patients initially have no symptoms but gradually show symptoms. COVID-19 has an incubation period of 2-14 days (5 days on average). Furthermore, the rate of transmission in the incubation period is low. Recovery periods of 1-3 weeks have been reported. Research has shown that COVID-19 patients recover within 14 days on average [37].

3. 4. Modeling A SD simulation approach was adopted to develop the model and policy scenarios in Vensim. SD simulation is used to translate real phenomena into more explicit models of time-variant systems. The model was constructed for Iran based on the basic SEIR model and the framework of Hadiwibowo et al. [30] model. To obtain more realistic outputs, the vaccination rate and the effectiveness of government policies were incorporated into the model.

Modeling was implemented in the form of a causal loop diagram and then a stock-flow diagram. Once the causal loop diagram had been plotted, the stock-flow diagram was developed by applying formulations in Vensim. Figure 5 illustrates the causal loop diagram., whereas

3. 5. Base Model The SEIR model was employed as the base model to implement the SD analysis of COVID-19 spread. It is a well-known framework for investigating the spread of diseases. Figure 6 shows the SEIR framework. As can be seen, SEIR involves susceptible, exposed, infected, and recovered individuals [38]. The components of the SERI are described as:

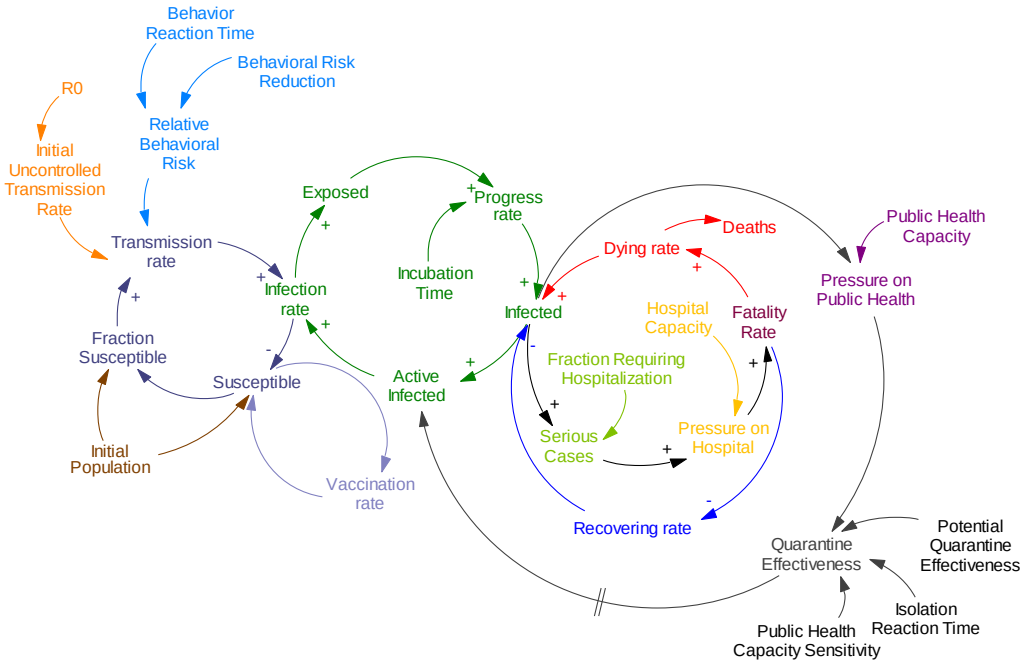

Figure 5. Causal loop diagram

Susceptible: Considering the nature of COVID-19, the initial population (the total Iranian population) was assumed to be susceptible. The infection rate in the base model was deducted from the susceptible population. Also, contact rate and infectivity influence the spread of COVID-19.

- Exposed: It refers to the accumulated rate of exposed people. However, the number of infected people is subtracted from the exposed people through the disease progression rate.
- Infected: It is the accumulated rate of infected arrivals into the country and progression rate. However, the recovery and fatality rates are subtracted from the infected people.

Recovered: It is the accumulated rate of patients recovering from the disease.

Figure 7 depicts the stock-flow diagram.

3. 6. Proposal Model As mentioned, the model introduced by Atun et al. [39] was utilized as the base model. Its major components include: 1-susceptible, a healthy population that is likely to be infected, 2-asymptomatic infected, infected people who show no symptoms of the disease, 3-symptomatic infected, those who are confirmed with COVID-19, 4-recovered, those who have recovered from the disease (either at home or treated by the healthcare system), and 5-fatality, those who die from the disease.

The loop of the transmission rate, fatality rate, and carriers was added to the SEIR model. Also, factors such as imported infections and behavior risk (e.g., protective protocols and social distancing) were incorporated into

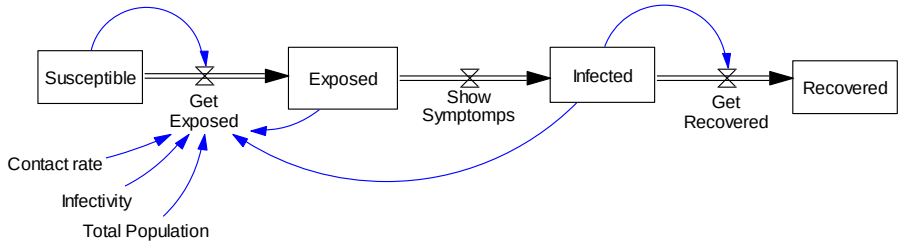

Figure 6. SEIR model

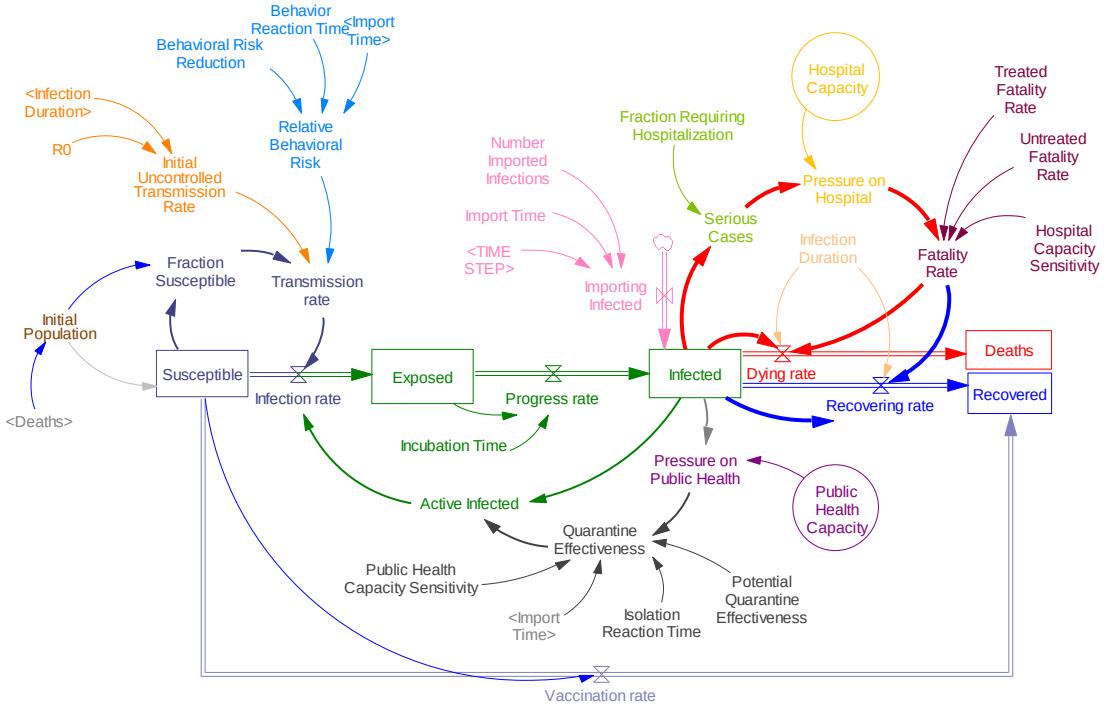

Figure 7. Proposed model

the base model. As it has a strong effect on COVID-19 spread, a quarantine loop was included in the model. The fatality rate consists of two components: 1-patients who were hospitalized and received sufficient healthcare services and 2-those who received no healthcare services. Also, the public healthcare system has a certain capacity that should be considered. Figure 7 depicts the proposed model.

The COVID-19 pandemic has become a huge challenge. To cope with the pandemic, it is required to make different policies, such as public vaccination. Therefore, the model was updated using Tom Fiddaman's model and Iran's requirements and measures, applying a number of such policies. The model was executed by introducing inputs and setting parameters based on the associated data of Iran. To obtain a more realistic model, parameters such as vaccination, hospital capacity, government policies, and personal protective protocols, were incorporated into the model.

Vaccination began in countries as some vaccines were developed. The susceptible population and even those who were infected and recovered should be vaccinated. However, only a small fraction of the population was initially vaccinated since the vaccines were limited, and the vaccination rate has been increasing. Thus, the vaccination loop and its effects were added to the proposed model, as shown in Figure 7.

3. 7. Validation The structural and behavioral validity of the model was verified using different tests. A variety of references, such as papers and reports on COVID-19, were used to determine the input parameters. A period of almost one year was selected for the spread of COVID-19, and a reliable view of the disease in education and health was obtained by using the existing data and evaluating the number of the infected, recovered, and dismissed individuals under different policies. The data and parameters formulated in Vensim were used as inputs, and the model was constructed based on the real, calibrated available data. A lack of real data-imposed limitations on data-based calibration. However, the model is based on real input parameters and some validation tests to measure its efficiency and effectiveness.

The present work employed the initial output of the SEIR model and earlier works on Iranian citizens. Once the model is properly simulated, it should be validated. Validation is carried out by comparing the simulations results to ground-truth observations. Comparisons were performed for the early period of the COVID-19 pandemic, when the virus spread in the city on February 20, 2020. The comparison was implemented by two validation measures, i.e., mean and percentage error variance. Table 2 shows the means and percentage error variances. The model was validated using the real rates of COVID-19 infection and fatality in Iran and the model estimations.

TABLE 2. Model validation results

Variable	Actual value	Estimate	E_1	Actual value	Estimate	E_2
Infection rate	5442232	6585100	21%	5442232	5605498	3%
Fatality rate	117526	130453	11%	117526	172763	47%

Mean

A model is assumed to be valid based on the mean measure when E1≤5%.

$$E_1 = \frac{|\bar{S} - \bar{A}|}{\bar{A}} \quad (1)$$

where $\bar{S}$ is the average estimate, whereas $\bar{A}$ is the ground-truth quantity [31, 40].

Percentage error variance

A model is assumed to be valid based on the percentage error variance when E_2≤30%.

$$E_2 = \frac{|S_s - S_a|}{S_a} \quad (2)$$

where S_s is the standard deviation of the estimates, while S_a is the standard deviation of the ground-truth data [31, 41].

4. RESULTS

Policies and scenarios were examined based on the proposed COVID-19 spread model. The increased infection and fatality rates imposed heavy pressure on the healthcare sector due to a lack of adherence to protective protocols and social distancing in holidays, e.g., the Persian New Year, religious ceremonies, and inter-city travels. This decreased the effectiveness of quarantine from 80% to 40%. Thus, the government has to adopt policies to control the spread of COVID-19.

A comparison of government behavior in the "onset of spread," "pandemic," and "control" stages indicates that differences in the fatality rate between countries arise from the policies and policy implementation time; i.e., not only policies but also their implementation time and strictness determine the effectiveness of COVID-19 policy effectiveness.

4. 1. The Policy of Quarantine and Vaccination Although almost all countries in the world, except for a few ones, banned social gatherings above ten in March 2020 (even earlier in some countries), there was no gathering ban in Iran until May 2020. Also, staying at home (or quarantine) has been a major control measure for the pandemic in countries. The policy of quarantine

was implemented at different levels, depending on the pandemic intensity [14, 42], in most countries. Although most countries adopted this policy at the peak of the pandemic (i.e., early April 2020), Iran was among the few countries that refused to strictly implement quarantine, despite a high fatality rate. However, the government finally decided to implement quarantine due to significant pandemic waves and numerous death cases.

To put an end to the COVID-19 pandemic, a large fraction of the global population should be immune to the virus. Vaccines are the most reliable solution. Thus, governments began to develop COVID-19 vaccines. Iran adopted a vaccine development approach while importing vaccines. The government should realize the particular conditions may strongly expose individuals to COVID-19 [43-45]. Therefore, some groups of people, e.g., pregnant and breastfeeding women, autoimmunity and immunodeficiency patients, diabetic patients, and people with respiratory and cardiovascular conditions, are in desperate need of vaccination [44]. The present study examined scenarios to realize how different scenarios, including early vaccination, could have influenced the infection and fatality rates. Different vaccination rates were applied, and the effectiveness of quarantine was evaluated in the form of different scenarios.

4. 1. 1. Scenario 1: Quarantine The COVID-19 virus was completely novel and had no effective treatment or medication for almost one year. Governments could reduce the infection and fatality rates only by policies such as quarantine and protective protocols. At the same time, researchers began to develop vaccines. The Iranian government was able to somewhat reduce the rate of infection by quarantine; however, quarantine was not consistently implemented in Iran, mainly due to the poor economic status of Iran. Thus, the government refused to strictly adopt public quarantine policies. Figure 8 defines quarantine conditions for the model and the output. The results suggest that quarantine would decrease the susceptible population over time.

4. 1. 2. Scenario 2: Beginning of Vaccination Iranian researchers were able to develop COVID-19 vaccines. These vaccines underwent clinical trials and were approved by the Ministry of Health and Medical Education. The government decided to vaccinate a majority of the Iranian population using domestic vaccines. Thus, the imports of vaccines were reduced, leading to a decreased rate of vaccination in Iran. As a result, Scenario 2 assumes a vaccination rate of 9% in a certain period (with vaccination being begun at a low rate after one year). According to Figure 9, vaccination diminished the infection rate and susceptible population, with the recovery rate increasing.

4. 1. 3. Scenario 3: Middle of Vaccination As mentioned, vaccination is the most efficient solution to prevent the pandemic. Despite vaccination in Iran, the spread of COVID-19 was not prevented in Iran, and the infection rate continued to rise, leading to new COVID-19 waves. This can be attributed to the slow vaccination rate and a lack of public adherence to protective protocols. Thus, the Iranian government began to import more vaccines to mitigate the pandemic. The vaccination rate began to rise on July 19, 2021, reaching 41%. These data were introduced to the model for a period until the end of 2021. The results indicated that the rise in the vaccination rate would more rapidly reduce the infection rate and susceptible population, as shown in Figure 10.

5. DISCUSSION AND MANAGERIAL INSIGHT

The present study developed an SD model to identify the factors influencing the COVID-19 epidemic. It was found that vaccination was the most reliable solution to prevent the epidemic. The fatality rate increasingly rose.

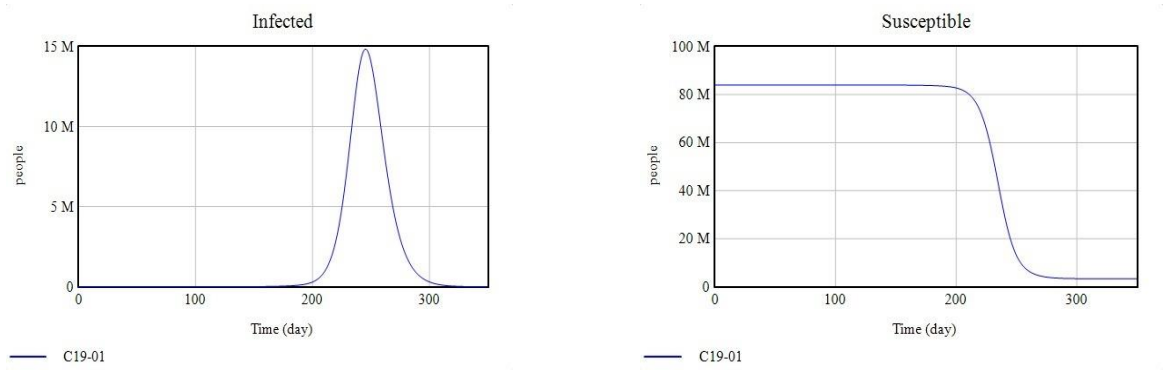

Figure 8. Quarantine scenario

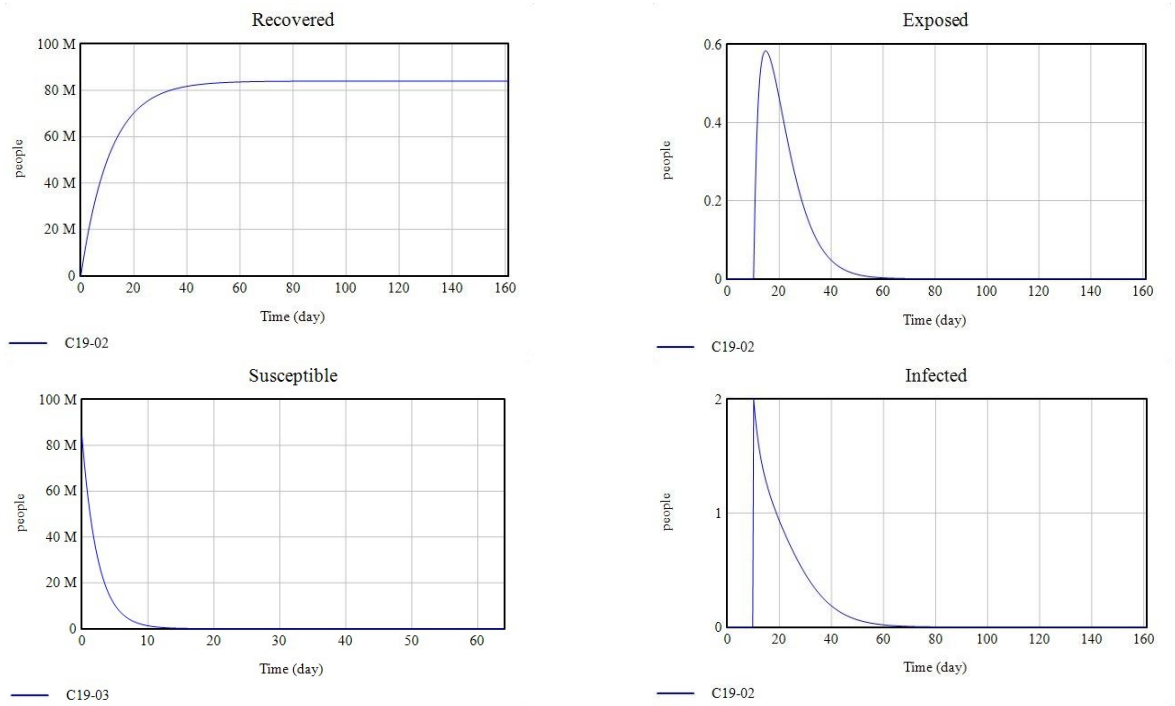

Figure 9. Vaccination scenario

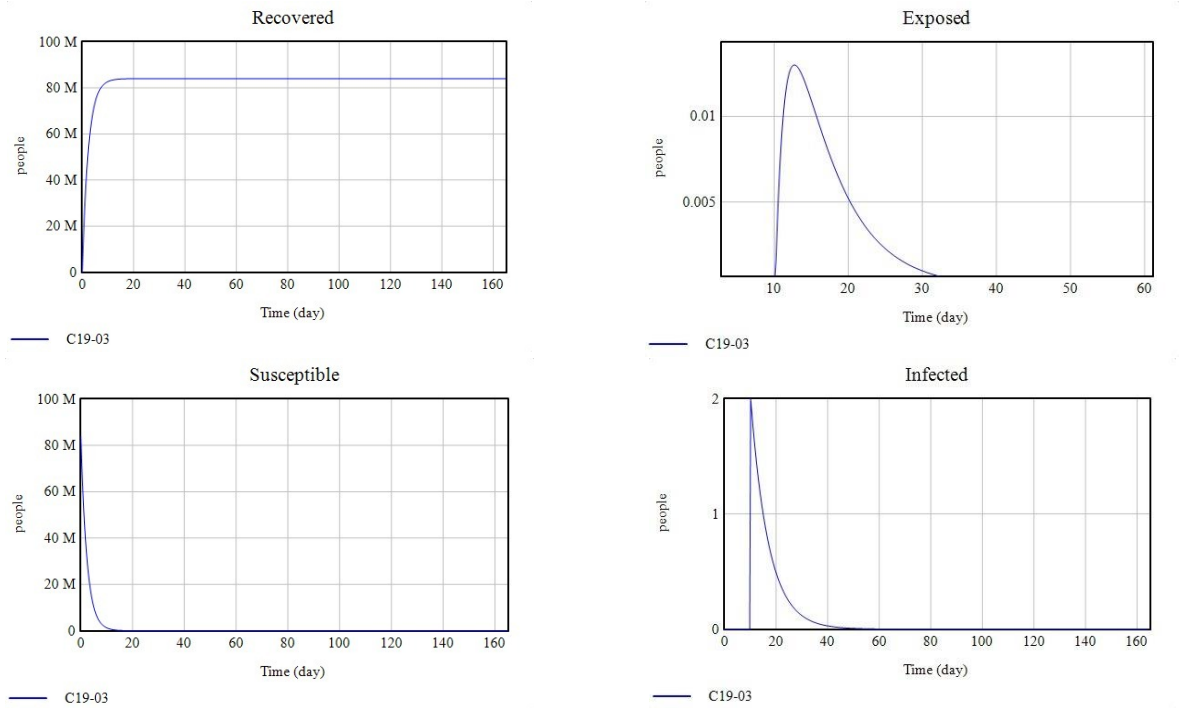

Figure 10. Vaccination scenario

However, the SD model predictions suggested that the rise in the vaccination rate would reduce the infection and fatality rates. Therefore, it is necessary to use domestic and imported vaccines to vaccinate the Iranian population. The people and the government must work together to prevent the next wave, as well as to control the disease. Today, the government has a significant role in controlling the disease by focusing on vaccinating

individuals, which will vaccinate all members of the community as soon as possible by increasing access to vaccines. The imports of COVID-19 vaccines significantly increased since July 19, 2021. Thus, public vaccination is estimated to be completed by the end of 2021, leading to reduced rates of infection and fatality.

The present work focuses on governmental decisions and their outcomes. It has also been observed in the community that some people refuse to be vaccinated for unscientific reasons; Therefore, it is necessary for the national media, with the help of trusted and specialized people in the Ministry of Health, to increase public trust and proper awareness, and to encourage people to be vaccinated. Also, according to the data and results of sensitivity analysis and different scenarios, to control and reduce corona virus disease, it is necessary to focus on quarantine and vaccination. The government should continue to work to maximize injections of more vaccines and encourage people to follow health advice. Because the use of a vaccine is the shortest way to recovery, the vaccine can be considered a temporary solution. Therefore, encouraging the implementation of health recommendations can be considered as a basic solution, and finally, the two solutions should be considered as a complement to each other.

The SD methodology is of great importance in research since it helps analyze data, visualize outcomes through diagrams, and understand the behavior of systems. It also enables developing simulation models for future system planning. To enhance the COVID-19 spread model, future works can include further variables, such as economic impacts, government policies, and demographic characteristics (e.g., age) as auxiliary variables. Although this would increase the complexity of the dynamic model, more accurate and reliable results could be obtained. Moreover, the proposed model can be implemented in other countries or at the provincial scale.

Since the government has announced that an intelligent quarantine scheme and reduction of restrictions for vaccinated people will be implemented shortly, it is suggested that future research of this program be considered in the face of new mutations in the COVID-19 virus that have a higher transmission rate. Consider several coping policies and adopt the best policy by designing different scenarios and analyzing them.

6. CONCLUSION

The COVID-19 epidemic has plunged the world into a crisis in health and the economy, a crisis that is perhaps unprecedented in the world since 1918, when the Spanish flu spread. The virus was first detected in Wuhan, China in late 2019, and spread with multiple mutations around the world, turning COVID-19 disease into a pandemic.The COVID-19 pandemic has become increasingly rampant in Iran. To determine municipal government policies to be right on target, policy scenarios are simulated first with a dynamic system simulation. This study examines the factors affecting the spread and control of COVID-19 pandemic by developing the basic SEIR model and considering interventions and policies such as vaccination and quarantine. The developed model was simulated using Vensim software. The desired parameters and variables were formulated according to previous research. Based on different conditions, three scenarios were designed and implemented. According to the results, the most important factor in reducing the prevalence of this disease is the increase in vaccination and quarantine. Vaccines are the ultimate solution to contagious diseases to control disease spread and provide safety to deal with the infection. The results suggested that the fatality rate of the susceptible population was reduced by vaccination and protective protocols. Due to the fact that the Corona virus is changing, the information is constantly being updated, so obtaining information about COVID-19 is one of the Limitations. Also, in face of the Omicron variant, it remains a question, the transmission capacity, and the immune-escape potential of the variant. The continuous emergence of new SARS-CoV-2 variants has made it much harder to control the COVID-19 pandemic.Fortunately, we have accumulated a lot of experiences and methods to deal with the novel corona virus. Thus, this paper aims to analyze factors influencing the spread of COVID-19 and prevent the disease. However, for policies to be implemented properly, contributions from all society elements are required. This paper examined quarantine and vaccination factor, so for future research other policies can be added to the model.

Limitations of this article include changes in statistics and data due to the speed of change of variants and the prevalence of the disease and access to some databases. Also, by the system dynamic, the category of prediction can be done in the future. In connection with Covid 19, it is possible to use this method to use the prevalence and control of the disease in different dimensions in future research.

7. REFERENCES

1. Yavarian, J., Shafiei-Jandaghi, N.-Z., Sadeghi, K., Malekshahi, S.S., Salimi, V., Nejati, A., Aja-Minejad, F., Ghavvami, N., Saadatmand, F. and Mahfouzi, S., "First cases of sars-cov-2 in iran, 2020: Case series report", ***Iranian Journal of Public Health***, Vol. 49, No. 8, (2020), 1564, doi: 10.18502/ijph.v49i8.3903.
2. Miller, M., "2019 novel coronavirus covid-19 (2019-ncov) data repository: Johns hopkins university center for systems science and engineering", ***Bulletin-Association of Canadian Map Libraries and Archives***, No. 164, (2020), 47-51. https://github.com/CSSEGISandData/COVID-19

3. Chen, N., Zhou, M., Dong, X., Qu, J., Gong, F., Han, Y., Qiu, Y., Wang, J., Liu, Y. and Wei, Y., "Epidemiological and clinical characteristics of 99 cases of 2019 novel coronavirus pneumonia in wuhan, china: A descriptive study", ***The lancet***, Vol. 395, No. 10223, (2020), 507-513, doi: 10.1016/S0140-6736(20)30211-7.
4. Adekunle, I.A., Onanuga, A.T., Akinola, O.O. and Ogunbanjo, O.W., "Modelling spatial variations of coronavirus disease (covid-19) in africa", ***Science of the Total Environment***, Vol. 729, (2020), 138998, doi: 10.1016/j.scitotenv.2020.138998.
5. Bora, A. and Bezboruah, T., "Evaluating the reliability of pwcov: A loosely coupled software as a service for covid-19 data processing system", ***International Journal of Engineering, Transactions C: Aspects,*** Vol. 33, No. 12, (2020), 2496-2502, doi: 10.5829/IJE.2020.33.12C.09.
6. Nozari, H., Tavakkoli-Moghaddam, R. and Gharemani-Nahr, J., "A neutrosophic fuzzy programming method to solve a multi-depot vehicle routing model under uncertainty during the covid-19 pandemic", ***International Journal of Engineering, Transactions B: Applications***, Vol. 35, No. 2, (2022), 360-371, doi: 10.5829/IJE.2022.35.02B.12.
7. Qingjie, Y., Wei, F., Chunhui, L., Huaming, M., Jinglong, L., Suxin, W., Lian, G., Yilin, W., Huawen, L. and Qing, X., "“Five-early” model: The magic weapon against covid-19", ***Iranian Journal of Public Health***, Vol. 49, No. Suppl 1, (2020), 82, doi: 10.18502/ijph.v49iS1.3673.
8. Pirnia, B., Pirnia, K., Malekanmehr, P. and Zahiroddin, A., "Challenges of differential diagnosis, symptoms of coronavirus disease 2019 (covid-19) or cannabinoid hyperemesis syndrome (chs)? A rare case report", ***Iranian Journal of Public Health***, Vol. 49, No. Suppl 1, (2020), 109, doi: 10.18502/ijph.v49iS1.3677.
9. Safaie, N., "Analysis of the effects of covid-19 virus on the import, export and labor in iran using system dynamic approach", ***Journal of Control***, Vol. 14, No. 5, (2021), 107-120, doi: 10.52547/joc.14.5.107.
10. Sajadi, H. and Hartley, K., "Covid-19 pandemic response in iran: A dynamic perspective on policy capacity", ***Journal of Asian Public Policy***, (2021), 1-22, doi: 10.1080/17516234.2021.1930682.
11. Mahase, E., "Covid-19: How many variants are there, and what do we know about them?", ***Bmj***, Vol. 374, No., (2021), doi.
12. He, X., Hong, W., Pan, X., Lu, G. and Wei, X., "Sars-cov-2 omicron variant: Characteristics and prevention", ***MedComm***, (2021), doi: 10.1002/mco2.110.
13. Batchelder, A., Gonzalez, J., Palma, A., Schoenbaum, E. and Lounsbury, D.W., "A social ecological model of syndemic risk affecting women with and at-risk for hiv in impoverished urban communities", ***American Journal of Community Psychology***, Vol. 56, No. 3, (2015), 229-240, doi: 10.1007/s10464-015-9750-y.
14. Weeks, M.R., Li, J., Lounsbury, D., Green, H.D., Abbott, M., Berman, M., Rohena, L., Gonzalez, R., Lang, S. and Mosher, H., "Using participatory system dynamics modeling to examine the local hiv test and treatment care continuum in order to reduce community viral load", ***American Journal of Community Psychology***, Vol. 60, No. 3-4, (2017), 584-598, doi: 10.1002/ajcp.12204.
15. Sihombing, L.B., Malczynski, L., Jacobson, J., Soeparto, H.G. and Saptodewo, D.T., "An analysis of the spread of covid-19 and its effects on indonesia’s economy: A dynamic simulation estimation", Available at SSRN 3597004, (2020).
16. Kozlovskyi, S., Bilenko, D., Kuzheliev, M., Lavrov, R., Kozlovskyi, V., Mazur, H. and Taranych, A., "The system dynamic model of the labor migrant policy in economic growth affected by covid-19", ***Global Journal of Environmental Science and Management***, Vol. 6, No. Special Issue (Covid-19), (2020), 95-106, https://www.sid.ir/en/journal/ViewPaper.aspx?id=735308
17. Niwa, M., Hara, Y., Sengoku, S. and Kodama, K., "Effectiveness of social measures against covid-19 outbreaks in selected japanese regions analyzed by system dynamic modeling", ***International Journal of Environmental Research and Public Health***, Vol. 17, No. 17, (2020), 6238, doi: 10.3390/ijerph17176238.
18. Cooper, I., Mondal, A. and Antonopoulos, C.G., "Dynamic tracking with model-based forecasting for the spread of the covid-19 pandemic", ***Chaos, Solitons & Fractals***, Vol. 139, (2020), 110298, doi: 10.1016/j.chaos.2020.110298.
19. Engbert, R., Rabe, M.M., Kliegl, R. and Reich, S., "Sequential data assimilation of the stochastic seir epidemic model for regional covid-19 dynamics", ***Bulletin of mathematical biology***, Vol. 83, No. 1, (2021), 1-16, doi. https://doi.org/10.1101/2020.04.13.20063768
20. COVID, I., Team, F. and Hay, S.I., "Covid-19 scenarios for the united states", ***MedRxiv***, (2020), doi: 10.1038/s41591-020-1132-9.
21. Geier, M.R. and Geier, D.A., "Respiratory conditions in coronavirus disease 2019 (covid-19): Important considerations regarding novel treatment strategies to reduce mortality", ***Medical Hypotheses***, Vol. 140, (2020), 109760, doi: 10.1016/j.mehy.2020.109760.
22. Ali, I. and Alharbi, O.M., "Covid-19: Disease, management, treatment, and social impact", ***Science of the Total Environment***, Vol. 728, (2020), 138861, doi: 10.1016/j.scitotenv.2020.138861.
23. Bastos, S.B. and Cajueiro, D.O., "Modeling and forecasting the early evolution of the covid-19 pandemic in brazil", ***Scientific Reports***, Vol. 10, No. 1, (2020), 1-10, doi: doi:10.1038/s41598-020-76257-1.
24. Chanu, A.L. and Singh, R.B., "Stochastic approach to study control strategies of covid-19 pandemic in india", ***Epidemiology & Infection***, Vol. 148, (2020), doi: 10.1017/S0950268820001946.
25. Pruyt, E. and Hamarat, C., "The influenza a (h1n1) v pandemic: An exploratory system dynamics approach", in Proceedings of the 28th International Conference of the System Dynamics Society, Seoul, Korea, 2 System Dynamics Society. (2010).
26. Ghaffarzadegan, N. and Rahmandad, H., "Simulation-based estimation of the early spread of covid-19 in iran: Actual versus confirmed cases", ***System Dynamics Review***, Vol. 36, No. 1, (2020), 101-129, https://doi.org/10.1101/2020.03.22.20040956
27. Sy, C., Bernardo, E., Miguel, A., San Juan, J.L., Mayol, A.P., Ching, P.M., Culaba, A., Ubando, A. and Mutuc, J.E., "Policy development for pandemic response using system dynamics: A case study on covid-19", ***Process Integration and Optimization for Sustainability***, Vol. 4, No. 4, (2020), 497-501, doi: 10.1007/s41660-020-00130-x.
28. Gkini, C., "Health behaviour theories and the norwegian response to covid-19: A system dynamics modeling approach", The University of Bergen, (2020),
29. Zia, K. and Farooq, U., "Covid-19 outbreak in pakistan: Model-driven impact analysis and guidelines", arXiv preprint arXiv:2004.00056, (2020), doi. https://doi.org/10.1101/2020.04.02.20050666
30. Hadiwibowo, J.C., Halim, S., Yahya, B.N., Agustin, K. and Sahputra, I.H., "A policy strategy evaluation for covid-19 pandemic in the city of surabaya using vensim ventana dynamic system simulation", in 2021 3rd East Indonesia Conference on Computer and Information Technology (EIConCIT), IEEE., (2021), 215-221.
31. Fathollahi-Fard, A.M., Hajiaghaei-Keshteli, M., Tavakkoli-Moghaddam, R. and Smith, N.R., "Bi-level programming for

home health care supply chain considering outsourcing", ***Journal of Industrial Information Integration***, Vol. 25, (2022), 100246, doi: 10.1016/j.jii.2021.100246.

32. Fathollahi-Fard, A.M., Ahmadi, A. and Karimi, B., "Sustainable and robust home healthcare logistics: A response to the covid-19 pandemic", ***Symmetry***, Vol. 14, No. 2, (2022), 193, doi. https://doi.org/10.3390/sym14020193
33. Mosallanezhad, B., Chouhan, V.K., Paydar, M.M. and Hajiaghaei-Keshteli, M., "Disaster relief supply chain design for personal protection equipment during the covid-19 pandemic", ***Applied Soft Computing***, Vol. 112, (2021), 107809, doi. https://doi.org/10.1016/j.asoc.2021.107809
34. Muniyappan, A., Sundarappan, B., Manoharan, P., Hamdi, M., Raahemifar, K., Bourouis, S. and Varadarajan, V., "Stability and numerical solutions of second wave mathematical modeling on covid-19 and omicron outbreak strategy of pandemic: Analytical and error analysis of approximate series solutions by using hpm", ***Mathematics***, Vol. 10, No. 3, (2022), 343, doi. https://doi.org/10.3390/math10030343
35. Azizi, B. and Seifi, A., "A system dynamics model of covid-19 epidemic in iran and controlling policies", ***Razi Journal of Medical Sciences***, Vol. 27, No. 8, (2020), http://rjms.iums.ac.ir/article-1-6268-en.html
36. Currie, C.S., Fowler, J.W., Kotiadis, K., Monks, T., Onggo, B.S., Robertson, D.A. and Tako, A.A., "How simulation modelling can help reduce the impact of covid-19", ***Journal of Simulation***, Vol. 14, No. 2, (2020), 83-97, doi: 10.1080/17477778.2020.1751570.
37. Sterman, J., "System dynamics: Systems thinking and modeling for a complex world", (2002).
38. Bruzzone, A.G., Frascio, M., Longo, F., Chiurco, A., Zanoni, S., Zavanella, L., Fadda, P., Fancello, G., Falcone, D. and De Felice, F., "Disaster and emergency management simulation in industrial plants", in Proc. 26th Eur. Model. Simul. Symp. (2014), 649.
39. Atun, R.A., Lebcir, R.M., McKee, M., Habicht, J. and Coker, R.J., "Impact of joined-up hiv harm reduction and multidrug resistant tuberculosis control programmes in estonia: System dynamics simulation model", ***Health Policy***, Vol. 81, No. 2-3, (2007), 207-217, doi: 10.1016/j.healthpol.2006.05.021.
40. Junapudi, S.S., Junapudi, S., Ega, K. and Chidipi, B., "Major cardiac concerns in therapy and vaccinations for covid-19", ***Metabolism Open***, Vol. 11, (2021), 100102, doi: 10.1016/j.metop.2021.100102.
41. Abta, A., Kaddar, A. and Alaoui, H.T., "Global stability for delay sir and seir epidemic models with saturated incidence rates", ***Electronic Journal of Differential Equations***, Vol. 2012, No. 23, (2012), 1-13, http://ejde.math.unt.eduftp ejde.math.txstate.edu
42. Allahi, F., Fateh, A., Revetria, R. and Cianci, R., "The covid-19 epidemic and evaluating the corresponding responses to crisis management in refugees: A system dynamic approach", ***Journal of Humanitarian Logistics and Supply Chain Management***, (2021), https://doi.org/10.1108/JHLSCM-09-2020-0077
43. Satrio, P. and Suryani, E., "Penerapan model sistem dinamik untuk melakukan pemeliharaan operasional aset unit transmisi dan visualisasi luaran model dengan menggunakan dashboard (studi kasus: Pt. Pln (persero) app semarang)", ***Jurnal Teknik ITS***, Vol. 6, No. 2, (2017), A325-A330.
44. Mirzaei, F., Khodadadi, I., Majdoub, N., Vafaei, S.A., Tayebinia, H. and Abbasi-Oshaghi, E., "Role of glucagon-like peptide-1 (glp-1) agonists in the management of diabetic patients with or without covid-19", ***The Open Medicinal Chemistry Journal***, Vol. 15, No. 1, (2021), doi: 10.1016/j.metop.2021.100122.
45. Kennedy, D.M., Zambrano, G.J., Wang, Y. and Neto, O.P., "Modeling the effects of intervention strategies on covid-19 transmission dynamics", ***Journal of Clinical Virology***, Vol. 128, (2020), 104440, doi: 10.2139/ssrn.3595898.

Persian Abstract

چکیده

شیوع جهانی COVID-19 در دسامبر ۲۰۱۹ در ووهان چین آغاز شد و در مدت کوتاهی کل جهان را تحت تاثیر قرار داد. به مرور زمان ظهور گونه های جدید بیماری، آهنگ مقابله با آن را نیز به شدت تحت تأثیر خود قرار داده و با ظهور جدیدترین گونه با نام امیکرون، شناخت و بررسی سیستم و انتشار نشریات در جامعه برای سیاست های صحیح ضروری است. بررسی شیوع COVID-19 برای اتخاذ سیاست های مناسب ضروری است. پویایی سیستم (SD) را می توان به عنوان رویکردی برای ارزیابی رفتار بیماری همه گیر COVID-19 اتخاذ کرد. مطالعه حاضر یک مدل SD را برای بررسی اثرات عوامل مختلف بر بیماری همه گیر و روش های درمانی و غیر درمانی معرفی می کند. واکسیناسیون به عنوان رویکرد اصلی برای پیشگیری از بیماری ارزیابی می شود. عوامل مؤثر در پیشگیری و کنترل همه‌گیری بر اساس مدل SEIR و سیاست‌هایی مانند واکسیناسیون بررسی می‌شوند. مطمئن ترین راه برای جلوگیری از این بیماری همه گیر، واکسیناسیون است. بنابراین، سیاستی که به نفع کل جمعیت است و ضروری خواهد بود، تولید و خرید واکسن است. از ۱۹ جولای ۲۰۲۱ میزان واردات واکسن به ایران افزایش چشمگیری داشته است و از این رو پیش بینی می شود تا پایان سال ۲۰۲۲ واکسیناسیون عمومی ایران پایان یابد و پس از آن تعداد موارد و مرگ و میر کاهش یابد. واکسن ها راه حل نهایی برای بیماری های مسری برای کنترل شیوع بیماری و ایجاد ایمنی برای مقابله با عفونت هستند. نتایج نشان داد که میزان مرگ و میر جمعیت مستعد با واکسیناسیون و پروتکل های حفاظتی کاهش یافته است. بنابراین، این مقاله با هدف تجزیه و تحلیل عوامل موثر بر گسترش COVID-19 و پیشگیری از این بیماری است.

IJE TRANSACTIONS B: Applications Vol. 35, No. 08, (August 2022) 1547-1557

International Journal of Engineering

Journal Homepage: www.ije.ir

A Modified Benders Decomposition Algorithm for a Last-mile Network with Flexible Delivery Options

A. Zahedi-Anaraki[a], R. Tavakkoli-Moghaddam*[b], R. Sadeghian[a]

[a] *Department of Engineering, Payame Noor University (PNU), Tehran, Iran*
[b] *School of Industrial Engineering, College of Engineering, University of Tehran, Tehran, Iran*

P A P E R I N F O

Paper history:
Received 16 December 2021
Received in revised form 06 April 2022
Accepted 07 April 2022

Keywords:
Transportation
Last-mile Network
Parcel Locker
Benders Decomposition
Variable Neighborhood Search
Local Branching

A B S T R A C T

The purpose of this paper is to introduce an integrated and specialized approach to tackling a challenging issue, known as "Last-mile Transportation". This issue, which is classified in terms of the decision-making level at the tactical level, is a model of the operational and application processes of prominent businesses in online commerce in developed countries, while it has attracted little attention from an operation-research aspect. This is a single-echelon network that includes a central distributor, parcel lockers, and customers, allowing customers to take advantage of three flexible product delivery options after purchasing the product. In the first option, the parcels are delivered at the door and in the time window specified by the customer. In the second option, customers pick up the parcels from the desired lockers with a discount, and in the third option, customers leave the choice of delivery type to the company under gaining an attractive discount. Offering online targeted discounts based on a selected option to encourage as many customers as possible for cooperation with the company and the guarantee of gradual development of the parcel-locker network by a management lever are other innovations of this study. To solve this model, a Benders decomposition algorithm has been modified by variable neighborhood search and local branching strategies. The results obtained from the analysis of parameters related to problem innovations indicate the efficiency and validity of this presented model in different scenarios and the proposed solution algorithm in large-sized instances.

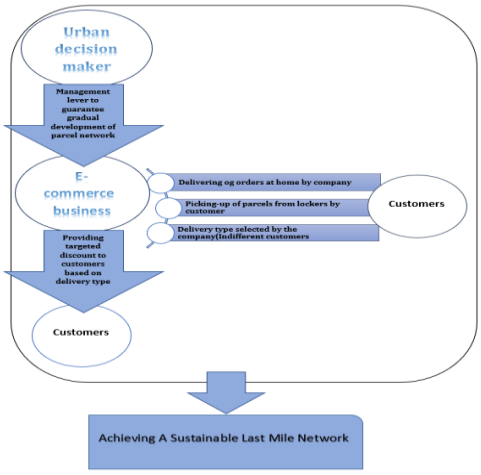

***doi**: 10.5829/ije.2022.35.08b.11*

* Corresponding Author's Email: *tavakoli@ut.ac.ir*
(R. Tavakkoli-Moghaddam)

Please cite this article as: A. Zahedi-Anaraki, R. Tavakkoli-Moghaddam, R. Sadeghian, A Modified Benders Decomposition Algorithm for a Last-mile Network with Flexible Delivery Options, ***International Journal of Engineering, Transactions B: Applications***, Vol. 35, No. 08, (2022), 1547-1557.

NOMENCLATURE

$G=(N,A)$	A non-directional graph	pc_j	Operational and rental cost for each parcel lockers $j \in N_{PL}$ (\$)
$N=N\bigcup N_C \bigcup N_{PL}$	Set of network nodes	ω	Transportation cost per kilometers (\$)
$N_{CPL}=N_C \bigcup N_{PL}$	Set of network nodes except central distributors	cv_k	Capacity of vehicle $k \in K$
N_C	Nodes related to the customers	cp_j	Capacity of parcel lockers $j \in N_{PL}$
N_{PL}	Nodes related to the lockers	τ	Sales price of product (\$)
K	Set of homogeneous vehicles	t_{ij}	Access time from node i to $j \in N$ (h)
M^1, M^2	A very large number	Θ_i	Binary parameter equals 1 if a customer $j \in N$ selects the option of a door-to-door delivery; 0, otherwise (option 1).
c_{ij}	Distance between two nodes $i, j \in N$	$x_{ijk} \in \{0,1\}$	Binary variable equals 1 if vehicle $k \in K$ immediately moves from the node i to $j \in N_C$; 0, otherwise.
pc_j	Operational and rental costs for each parcel lockers $j \in N_{PL}$ (\$)	$y_{ij} \in \{0,1\}$	Binary variable equals 1 if customer $i \in N_C$ is assigned to lockers j; 0, otherwise
d_i	Demand of cutomer $i \in N_C$	$h_i \in \{0,1\}$	Binary variable equals 1 if customer $i \in N_C$ is provided in the first-option manner (doo- to-door); 0, otherwise
a_i	Lower bound of customer i's time window.	$l_i \in \{0,1\}$	Binary variable equals 1 if customer $i \in N_C$ is provided in the second-option manner (parcel locker); 0, otherwise
b_i	Upper bound of customer i's time window	$z_{uj} \in \{0,1\}$	Binary variable equals 1 if the customer $i \in N_C$ or the parcel locker $j \in N_{PL}$ is provided by the central distributor (depot) $u \in N_u$; 0, otherwise
V_i	Upper bound of customer i's time window	$st_{uk} \geq 0$	Continuous variable indicates when vehicle k leaves the central distributor $u \in N_u$
$ls_{ij} \in \{0,1\}$	Maximum capacity of the central distributor (depot) $u \in N_u$	$ft_k \geq 0$	Continuous variable indicates when a vehicle $k \in K$ arrives at the last customer
Ψ	Binary parameter equals 1 if a customer $i \in N_C$ adds locker j to his/her favorite list; 0, otherwise	$dp_{jk} \geq 0$	Continuous variable that indicates amounts of parcels delivered to locker $j \in N_{PL}$ by vehicle $k \in K$
Υ_i	Binary parameter equals 1 if a customer $i \in N_C$ selects the delivery option of picking up from parcel lockers; 0, otherwise (option 2)	$s_{ik} \geq 0$	Continuous variable indicates when vehicle $k \in K$ starts service to node $i \in N_C$
Γ_i	Binary parameter equals 1 1f a customer $i \in N_C$ allows the company to select delivery option type; 0, otherwise (option 3)		

1. INTRODUCTION

The road transport sector is known as one of the largest producers of greenhouse gases [1, 2]. Automated parcel lockers enabling consumers to pick up e-purchased merchandise from allocated 24-hour Locker locations are rising while they suggest the promising better-quality accessibility to merchandise and declined travel of customers and firm vehicles [3]. Since similar to many new emerging technologies, parcel lockers have competitive advantages as well as social and implementation challenges, seeking efficient solutions to create a managerial perspective is a challenging issue for parcel-locker investors as economical beneficiaries and urban policymakers as beneficiaries of managerial urban issues. How and when to deploy and integrate this new technology into the existing traditional network, which on the one hand causes companies to flourish in a competitive global market and on the other hand on a horizon time results in the establishment of the sustainable urban last-mile delivery network, is its main strategic challenges. González-Varona et al. [3] introduced delivery of a last-mile parcel in their model that employs the current newspaper stands as parcel lockers.

In terms of a conceptual model of the parcel-lockers network, Iwan et al. [4] concentrated on the study of the serviceability and the productivity of the parcel lockers for Polish InPost Company and forecasted the efficient utilization of this sort of solution. Lemke et al. [5] studied on evaluation of this machine's serviceability according to the InPost system's instances. Gatta et al. [6] aimed to estimate the customers' willingness and the service providers to employ an alternative delivering/ picking-up option (e.g., a parcel locker) and to consequently forecast the demand amounts resulting from this willingness in the last-mile B2C e-commerce condition. Tang et al. [7] defined the service quality of the parcel lockers in five

cases named service price, service reliability, accessibility, the ability of fault handling, and service diversity. Based on these cases, they surveyed lockers via the service-quality theory and gained the satisfaction of the customer. Maximally motivating the customers both economically and socially to travel to locker positions and thoroughly exploiting the operational potentials of all these facilities, which not only result in not wasting the public and urban resources but also promotes the service level to citizens, are other challenging factors in a tactical level, clearly not observed in mentioned studies at least in terms of an operations research (OR) approach.

In terms of the mathematical model of a parcel-lockers system, Deutsch and Golany [8] for the first time developed a parcel locker system as a promising contribution for the last-mile concept while simultaneously maximizing the revenue resulting from product sales and minimizing costs driven by discounts on the delivery for customers traveling to pick up their packages, facilities' fixed and operational costs and the loss of potential consumers not eager to pick up. Although they considered a discount for customers picking up their parcels from parcel lockers, this discount lacked the necessary flexibility to gradually encourage customers. Lin et al. [9] proposed a parcel locker location problem, in which the company intends to present the locker service under locating locker facilities to attract clienteles. Maximizing the profit (i.e., calculating the revenue and the cost of facilities) is the objective, under the interaction of other delivery modes. To approximate the income, they used the threshold Luce's model. Pan et al. [10] offered a model for designing combined delivery networks in urban zones under applying parcel lockers. The model solved by a hybrid algorithm deals with a two-level structure. the lower level is a multi-depot capacitated vehicle routing problem and the upper level is a parcel network flow problem.

Unlike the previous studies that customers prefer to collect their packages from a predetermined locker, Orenstein et al. [11] presented a logistic model for the delivery of small parcels to a set of parcel lockers so that customers can collect their packages from a parcel locker or a set of ones having the same preference. To minimize operating costs, properties of mobile lockers named the location and the route are combined as a model being non-linear integer by Anderluh et al. [12]. A modified genetic algorithm (GA) is presented to determine optimal distributor locations, the number of lockers required by each distributor, and mobile lockers' scheduling and routing at the same time. Zhou et al. [13] provided a location-routing problem being a bi-level multi-sided terminal under customer's pickup services and a real-time home delivery solved by a hybrid GA and simulated annealing (SA) method, named self-adaptive SGA. Considering time constraints that incorporates important aspect related to same-day delivery logistics, Voccia et al. [14] provided a pickup and delivery problem being multi-vehicle dynamic. To decide more knowledgeably, their solution approach merges information about future demand into decisions of routing. Also, they analyzed the outcome that examines when it is useful for a fleet to wait in a warehouse. Based on issues of postal transportation, Sitek and Wikarek [15] presented a hybrid approach on pick-up and alternative delivery point combined with the capacitated vehicle routing problem while providing innovations such as time window, the distinction of delivery point types about their capacity, and probability of collecting the things for the period of the carrying out of delivery routes.

Based on the mentioned literature of the Last-mile area and the best of our knowledge, the research gaps are identified as follows:

- Despite the potential of exact solution algorithms to achieve optimal solutions, due to complexity and lack of timely convergence in many problems with specific structures, these approaches are not attracted enough researchers' attention in urban logistics issues. Therefore, in the literature related to the parcel lockers network, exact algorithms developed by an efficient strategy to reduce the convergence time of the master problem are not observed.
- Via the parcel locker, proposing a single delivery option can make customers feel that their right about free choice is ignored. So, a flexible delivery system with multiple options, which gradually conduct customers toward parcel lockers or other similar ones by its natural potentials (e.g., discount and 24-hour accessibly) can enable company managers gradually to reach the ultimate last-mile delivery network while following their customer-orientation policy. Despite the importance of this issue, implementing this philosophy in the last-mile delivery concept is not comprehensively observed in the academic literature.
- For the consistency and durability of a last-mile delivery network, discounts can be one of the most effective tools in creating a desire and motivation in customers to accept social responsibility. The proportion between the discounts of the delivery options offered to the customer has a significant impact on the network's customer orientations. Therefore, a lack of this proportion can lead to significant deviations from the goals for a long time. Despite conceptual studies, researches based on a mathematical framework under an integrative perspective in the literature are very rare.

In this paper, a Last-mile network with flexible delivery options (LNFDO) is specially and practically surveyed and modeled. The proposed model could be a good platform for leading businesses in online commerce as well as urban policymakers who want to not only promote the level of online customer service but also in a gradual process, increase customers' social

responsibility sense to pick up their parcels from lockers. In the following, section 2 is dedicated to defining the problem concept and model. Section 3 proposes a solution approach based on the modified Benders decomposition to obtain optimal solutions. Section 4 illustrates numerical results achieved from the presented model and proposed solution approach. Finally, Section 5 is relevant to research conclusions.

2. PROBLEM DEFINITION

2. 1. Network Description The considered LNFDO is a development of a vehicle routing problem with a time window. An outstanding difference between the two is to offer three types of delivery options to customers to achieve a gradual evolution from a traditional network to a modern urban logistic network. According to Figure 1, after completing the purchase process that is a simulated environment of an assumptive business application to clarify our contributions, customers can choose one of the three options to receive the product.

Based on an option selected and other subsequent details, the company offers the customer online and dynamically a discount (i.e., the maximum of which belongs to the third option and the minimum to the first option). In the first option, customers want to receive their parcels in front of their home, in which they must enter their desired time window, which is a continuous sub-period of the company office hours. The larger the interval, the greater the discount since companies can make more flexible planning. In the second option, customers announce the company to pick up the orders from parcel-locker positions, in which they must select the desired positions where lockers are located. The

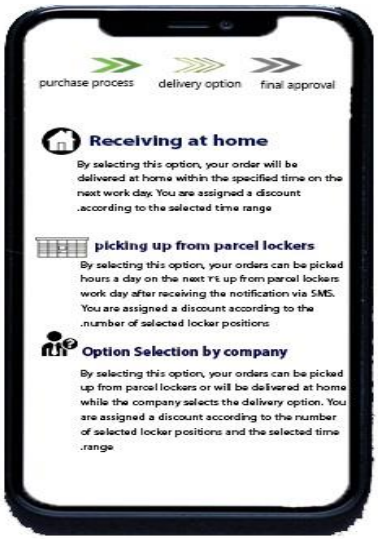

Figure 1. Simulated environment of a business application

greater the number of the selected positions, the more discount is allocated to a customer, and in option three, the customer is indifferent to the first two options and allows the company to choose how to deliver the parcels such a way that gaining the most discount. The model assumtions are as follows:

- It is a single period.
- It is a single product.
- It is a single echelon.
- It is a single sourcing.
- It is a homogeneous vehicle fleet.
- It is deterministic.
- The order of all customers must be met.

2. 2. Modelling of Customer's Discount Parameters α, β $(\alpha < \beta)$ are maximum discounts on delivery cost, which a customer can gain, receiving goods in front of their home and from designated parcel lockers respectively. Parameters η_k, μ_k, ζ_k which are discounts offered online to customers by a company on their webpages are relevant to delivery options 1 to 3 calculated by respectively:

$$\mu_k = \frac{b_k - a_k}{\varphi - \phi} \times \alpha \tag{1}$$

$$\eta_k = \frac{|\Lambda_k|}{\chi} \times \beta \tag{2}$$

$$\chi = \frac{|N_C|}{|N_{PL}|} \tag{3}$$

$$\xi_k = \theta \times \max\{\eta_k, \mu_k\} \tag{4}$$

Equation (1) indicates the amount of discount offered to customer k selecting the door-to-door delivery option under upper and lower bounds of a time window (a_k and b_k). Interval [ϕ, φ] is related to the company's working hours. Equations (2) and (3) indicate the amount of discount offered to customer k selecting the picking-up option (parcel lockers), which Λ_k is a set of desired positions of lockers. N_C and N_{PL} are a customer set and set of all parcel-locker positions, respectively. Equation (4) indicates the amount of discount offered to customer k selecting option 3, in which the company chooses how to take delivery of goods (θ), is a factor in the range of 1 and 1.1 to encourage customers to cooperate with the company as far as possible.

2. 3. Mathematical Model

$$(LNFDO)$$

$$Min\ TC(\{p\}) = \begin{bmatrix} \sum_{k\in K}\sum_{i\in N}\sum_{j\in N} \omega\, c_{ij}\, x_{ijk} + pc \sum_{j\in N}\sum_{k\in K} dp_{jk} \\ +(\sum_{i\in N_C} \mu_i d_i + \sum_{i\in N_C} \eta_i d_i + \sum_{i\in N_C} \xi_i d_i) \times \tau \end{bmatrix} \tag{5}$$

$$Max\ CP(\{p\}) = \Psi \tag{6}$$

$$\sum_{k\in K}\sum_{j\in N} x_{ijk} = h_i \qquad \forall i \in N_C \tag{7}$$

$$\sum_{k\in K}\sum_{j\in N} x_{ijk} \geq inl_i \qquad \forall i \in N_{PL} \tag{8}$$

$$\sum_{i\in N_C} y_{ij} \leq M_1 \times inl_j \qquad \forall j \in N_{PL} \tag{9}$$

$$\sum_{j\in N_{CPL}} x_{0jk} \leq 1 \qquad \forall k \in K \tag{10}$$

$$\sum_{j\in N_{CPL}} x_{i0k} \leq 1 \qquad \forall k \in K \tag{11}$$

$$\sum_{\substack{j\in N\\ i\neq j}} x_{ijk} = \sum_{\substack{j\in N\\ i\neq j}} x_{jik} \qquad \forall k \in K, i \in N \tag{12}$$

$$h_i + l_i = 1 \qquad \forall i \in N_C \tag{13}$$

$$h_i \geq 1-(1-\mu_i)\times M \qquad \forall i \in N_C \tag{14}$$

$$l_i \geq 1-(1-\eta_k)\times M \qquad \forall i \in N_C \tag{15}$$

$$\sum_{j\in PL} ls_{ij} y_{ij} = l_i \qquad \forall i \in N_C \tag{16}$$

$$\sum_{k\in K} dp_{jk} = \sum_{i\in N_C} y_{ij}\, d_i \qquad \forall j \in N_{PL} \tag{17}$$

$$\sum_{i\in N} d_i \sum_{\substack{j\in N\\ i\neq j}} x_{ijk} + \sum_{i\in N}\sum_{\substack{j\in N_{LC}\\ i\neq j}} dp_{jk} x_{ijk} \leq cv_k \qquad \forall k \in K \tag{18}$$

$$\sum_{k\in K} dp_{jk} \leq cp_j \qquad \forall j \in N_{PL} \tag{19}$$

$$st_k + t_{0j} - M_{0j}^2(1-x_{0jk}) \leq s_{jk} \qquad \forall k \in K,\ j \in N_C \tag{20}$$

$$s_{ik} + t_{ij} - M_{ij}^2(1-x_{ijk}) \leq s_{jk} \qquad \forall i, j \in N_C, k \in K \tag{21}$$

$$s_{i0} + t_{i0} - M_{i0}^2(1-x_{i0k}) \leq ft_k \qquad \forall k \in K, i \in N_C \tag{22}$$

$$a_i h_i \leq s_{ik} \leq b_i h_i \qquad \forall k \in K, i \in N_C \tag{23}$$

$$\frac{\sum_{k\in K}\sum_{i\in N_c} \xi_i\, y_{ij}\, d_i}{\sum_{k\in K}\sum_{j\in PL} dp_{jk}} \geq \Psi \tag{24}$$

$$x_{ijk}, y_{ij}, h_i, l_i \in \{0,1\} \qquad s_{ik}, st_k, ft_k \geq 0 \tag{25}$$

The first objective (5) is to minimize the total network cost. This cost consists of three terms, in which the first one is the transportation cost of vehicles and the second term is the operational cost plus the rent of lockers valued by players and the third term is discounts assigned to customers based on delivery options selected. The second objective (6) is to maximize the exploitation of lockers as far as possible for customers selecting the third delivery option. Constraint set (7) states that vehicles must visit exactly once a node related to a customer selecting either the first delivery option or the third delivery option that company does the delivery of their goods in front of customers. Constraint set (8) indicates that vehicles must visit exactly once a node related to a parcel locker in either the second or third delivery option in which the company puts goods in a locker. Constraint set (9) determines whether a locker on the time horizon is used or not. Constraint sets (10)-(12) guarantee flow equilibrium in the network. Constraint sets (13)-(16) convert the conceptual nature of the three delivery options into the mathematical nature. In the third option, the order must be either taken to the customer's home or delivered to the customer by a locker. Constraint set (17) shows that the total inventory of each locker equals the total parcel assigned to this locker. Constraint set (18) confirms that vehicle capacity limitation is met. Constraint set (19) warrants that a locker capacity limitation is met. Constraint sets (20) -(23) guarantees that vehicles arrive at the customer's home in a predetermined time window. The constraint set (24) controls amounts of the demands covered by parcel lockers via the third delivery option (push lever for gradual development parcel-locker). Constraint set (25) represents the model variables.

3. SOLUTION APPROACH

In this paper, to solve the proposed model, a modified Benders decomposition algorithm enhanced by three well-known strategies is proposed. The Benders decomposition algorithm [16] is a classic approach to combinatorial optimization problems based on the idea of partitioning and gradually producing constraints. This algorithm decomposes an original problem into two simpler sub-model called master and sub-problems. The master problem is a limited model of the original one only consisting of complicated variables and the relevant constraints while the sub-problem is the same original model, whose complicated variables are fixed. This algorithm relies on exchanging solutions obtained between master and sub-problems until achieving an optimized provable solution for the original program. A solution to the master problem provides a gradual development for the dual problem and Benders bounds. Then, these variables are fixed into the dual sub-problem, whose optimal solutions result in cuts of the master problem. These cuts are called optimality cuts if the

solution of the master problem becomes feasible for the sub-problem and feasibility cut if not. This process is continued until the gap value between master and dual problems converges on a predefined certain amount. To avoid further elaboration, the interested readers in the details of this algorithm are referred to the study of Benders [16]. The flowchart of the proposed solution approach is demonstrated in Figure 2. To reduce the overall running time of the Benders algorithm, the VNS algorithm and the local branching strategy are used in the first iterations when the solution of the master problem (MP) is not yet of the sufficient quality. The local branching strategy limits the exchange range of the binary variables and the VNS algorithm achieves efficient solutions for the master problem.

The MP is an integer model as shown below. An optimality cut (i.e., Constraint (26)) aims to produce the high quality for the next iteration. The feasibility cut (i.e., Constraint (27)) aims to generate cuts that keep the algorithm in the feasibility space for subsequent iterations.

$$Max\ Z^{Master}$$

s.t.

$$\begin{aligned} Z^{Master} \le & \Big[\sum_{\forall k \in K_{[\Gamma_m]}} (-cv_k + \sum_{i \in N} d_i \sum_{\substack{j \in N \\ i \ne j}} x_{ijk}) \overline{B}_k - \sum_{\forall k \in K} \sum_{i \in N_c} b_i h_i \overline{I}_{ik} \\ & - \sum M^3 (1 - x_{ijk}) \overline{D}_{ijk} - cp \sum_{j \in N} \overline{E}_j + \sum_{\forall k \in K} \sum_{i \in N_c} a_i h_i \overline{J}_{ik} \\ & + \sum_{j \in N_c} \sum_{\forall k \in K} (t_{0j} - M_{0j}^2 (1 - x_{0jk})) \overline{F}_{jk} + \sum_{k \in K} \sum_{i \in N} \sum_{j \in N} \omega c_{ij} x_{ijk} \\ & + \sum_{\forall k \in K} \sum_{j \in N_c} \sum_{i \in N_c} (t_{ij} - M_{ij}^2 (1 - x_{ijk})) \overline{G}_{ijk} + \sum_{j \in N_{\in [\Gamma_m]}} \sum_{i \in N_{\in [\Gamma_m]}} d_i y_{ij} \overline{A}_j \\ & + \sum_{\forall k \in K} \sum_{i \in N_c} (t_{i0} - M_{i0}^2 (1 - x_{i0k})) \overline{H}_{ik} \Big] \end{aligned} \quad (26)$$

$$\begin{aligned} & \Big[\sum_{\forall k \in K_{[\Gamma_m]}} (-cv_k + \sum_{i \in N} d_i \sum_{\substack{j \in N \\ i \ne j}} x_{ijk}) \overline{B}_k + \sum_{j \in N_{\in [\Gamma_m]}} \sum_{i \in N_{\in [\Gamma_m]}} d_i y_{ij} \overline{A}_j \\ & + \sum_{j \in N_c} \sum_{\forall k \in K} (t_{0j} - M_{0j}^2 (1 - x_{0jk})) \overline{F}_{jk} + \sum_{k \in K} \sum_{i \in N} \sum_{j \in N} \omega c_{ij} x_{ijk} \\ & - \sum M^3 (1 - x_{ijk}) \overline{D}_{ijk} - cp \sum_{j \in N} \overline{E}_j + \sum_{\forall k \in K} \sum_{i \in N_c} a_i h_i \overline{J}_{ik} \\ & + \sum_{\forall k \in K} \sum_{i \in N_c} (t_{i0} - M_{i0}^2 (1 - x_{i0k})) \overline{H}_{ik} - \sum_{\forall k \in K} \sum_{i \in N_c} b_i h_i \overline{I}_{ik} \\ & + \sum_{\forall k \in K} \sum_{j \in N_c} \sum_{i \in N_c} (t_{ij} - M_{ij}^2 (1 - x_{ijk})) \overline{G}_{ijk} \Big] \le 0 \end{aligned} \quad (27)$$

Equatons (7) - (16) (28)

3. 1. Variable Neighborhood Search In this paper these cuts are modified by the variable neighborhood search (VNS) algorithm successful on Vehicles routing problems. When a solution is found, this strategy can be used to obtain a higher-quality solution. As shown before, these new solutions can be used to generate new cuts for the master problem. neighborhood solutions (even with lower quality) may help to generate quality cuts in initial Benders iterations. To implement this strategy, a well-known local search algorithm, called variable neighborhood search [17], is used. This algorithm can be used in Finding an efficient and feasible solution to the master sub-problem.

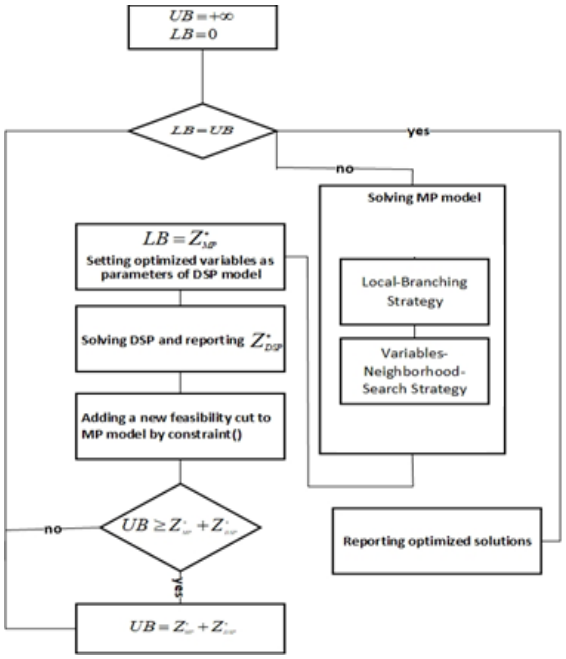

Figure 2. Proposed modified Benders decomposition flowchart

The VNS algorithm is used in the first iterations when the solution of the MP is not yet of the sufficient quality to reduce the total running time of the Benders algorithm. Therefore, the solution space of this algorithm is the space of the MP.

Defining symbols of *D*, *C*, and *L* as distributors, customers, and parcel lockers, respectively, Figure 3 shows a solution representation of the VNS algorithm, indicating how to assign customers to vehicles and lockers. Figures 4 to 7 show the VNS operators and the associated sequences for moving from one neighbourhood to another, referred to as the node-entering, node-swapping, edge-swapping, and block-swapping operators, respectively.

3. 2. Local-branching Strategy The main idea of this strategy is that when the Master problem is solved, a certain number of variables that in the last iteration were equal to 1 are allowed to exchange their value to 0 [18]. Assuming that there is an initial feasible solution to the Master problem (MP), the set $\overline{S} := \{ j \in \beta : x_j = 1 \}$ is

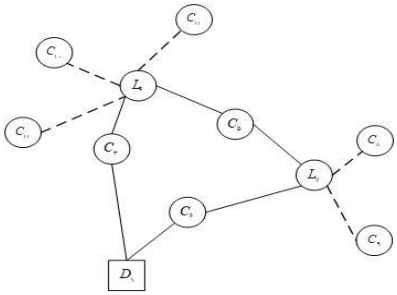

Figure 3. Customers allocation to lockers and vehicles

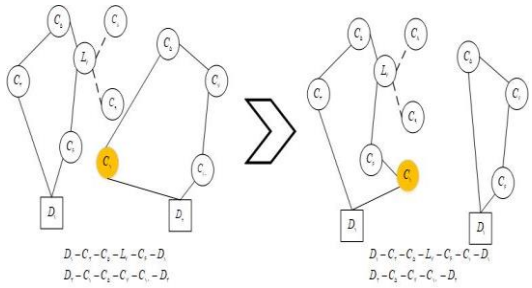

Figure 4. Example of a node-entering operator

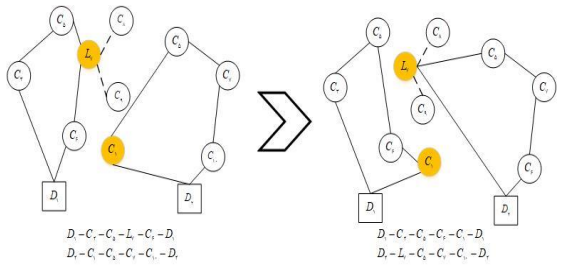

Figure 5. Example of a node-swapping operator

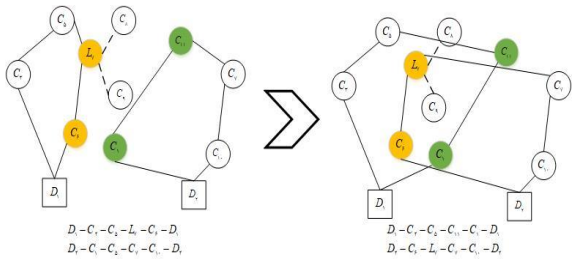

Figure 6. Example of an edge-swapping operator

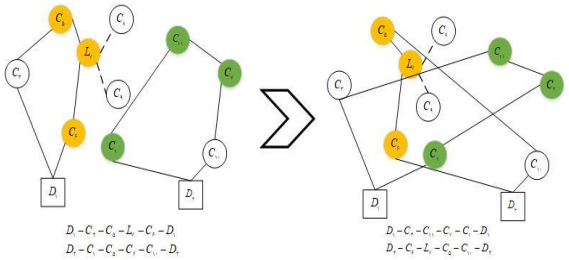

Figure 7. Example of a block-swapping operator

defined as variables being equal to 1. setting the certain positive integer number k in the range of 10 to 20, the neighborhood $k-opt$ of the variable $\bar{x}$, shown by $\Gamma(\bar{x},k)$, is defined as solutions satisfying Constraint (29).

$$\Delta(x,\bar{x})=\sum_{j\in S}(1-x_j)+\sum_{j\in\beta\setminus S}x_j\le k \tag{29}$$

Constraint (29) limits the sum of the variables exchanging their values from zero to one and one to zero. Local-branching constraints can be used as a benchmark within a counting scheme for MP. In other words, according to the current solution, the solution space associated with the current node can be separated by the new left and right-branch node of the local-branching method. The parameter of the neighborhood size (k) that can be produced as the largest radius of local searching for two new nodes, named right- and left-handed problem that is probably much easier to solve than its parent problem. According to Figure 8, this idea resulted from the fact that the neighborhood associated with the left and right branches $\Gamma(\bar{x},k),\Gamma(\bar{x},k+1)$ must be small enough to optimize in a short time, and large enough to achieve a better solution. We consider the mentioned manners, such as Constraint (29) for all binary variables of the proposed model ($x_{ijk}, y_{ij}, h_i, l_i$).

4. RESULTS

4. 1. Results Driven by the Proposed Model To solve the proposed models, the parameters are generated based on uniform distribution [19], as shown in Table 1. To demonstrate the efficiency of the proposed model, a network is considered consisting of 2 parcel-lockers and 8, 6, and 5 customers, who have selected the first, second, and third delivery options, respectively. The Pareto solutions to this problem are first shown in Figure 9. As

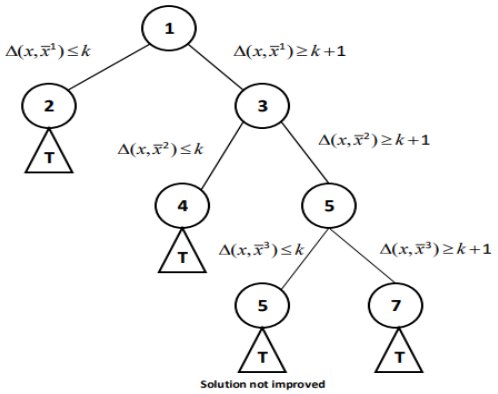

Figure 8. Local branching algorithm

TABLE 1. Generated parameters

Parameters	Value	Parameters	Value
d_i	Uniform(1, 6)	a_i	Uniform(8,12)
c_{ij}	Uniform(10, 50)	b_i	Uniform(9,16)
V_i	Uniform(50,100)	cv_k	Uniform(20,100)
pc_j	Uniform(10,15)	τ	Uniform(100,140)

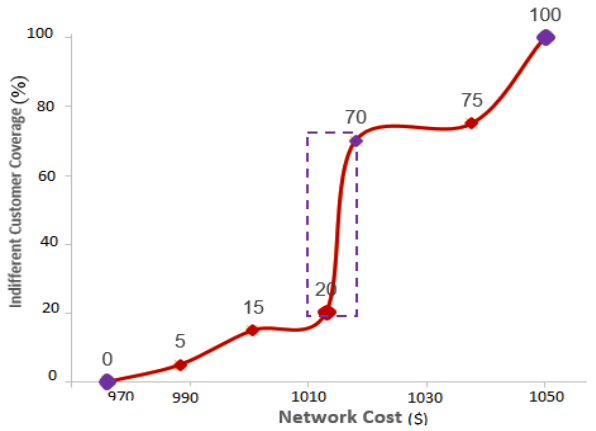

Figure 9. Pareto solution

can be seen, the two axes conflict with each other meaning that the costs of the network are increased and vice versa to increase the coverage of more indifferent customers. By increasing the coverage of indifferent customers from 20 to 70, a deeper gap compared to neighboring solutions is seen. It indicates that in this situation, with a low cost, a large increase in coverage of indifferent customers is created.

Figure 10 corresponds to a Pareto solution from Figure 9 with a cost of 1050 and 100% coverage. In this solution, all indifferent customers are assigned by the company to parcel lockers based on their selections. In this network, to achieve 100% coverage, an 8% increase in network costs is observed. By cpmparision with experts' opinion, the feasiblity of the proposed model is confirmed.

As previously explained, the applied discount of the indifferent customers is calculated from $\zeta_k=\theta\times\max\{\mu_k$ and $\eta_k\}$, where μ_k and η_k are the reference discount for the selection of the first and second delivery options, and by default, θ is between 1 and 1.1. In Figure 11, the current value is considered as the evaluation index, which is indicated by θ=1 and θ=1.1 means a ten percent increase in the discount coefficient, and θ=0.9 represents a ten percent decrease, and so on for other values. This sensitivity analysis is performed for five coefficients of the discount with values of 0.8, 0.9, 1, 1.1, and 1.2. As it

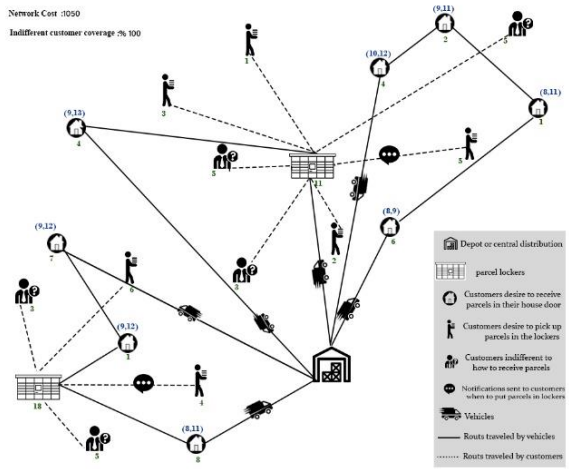

Figure 10. Network structure for a cost of 1050 and 100% coverage

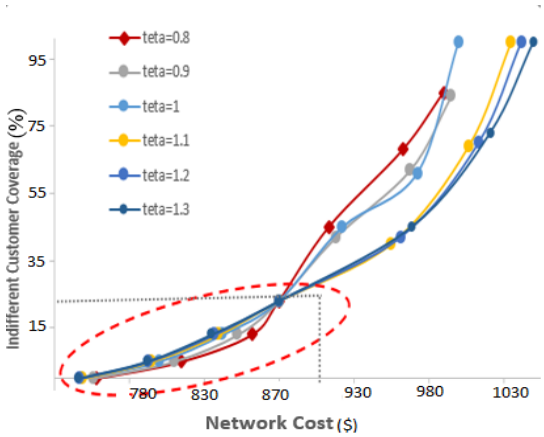

Figure 11. Sensitivity analysis based on a discount coefficient

is obvious, these five graphs can be classified into two classes of behavior, which are the coefficients (1.1, 1.2) in one class and the coefficients (0.8, 0.9, 1) in the other class. The important point is that with up to 20% coverage, all graphs are approximately tangent to each other, which means that cost imposed on the network due to discounts offered to the customer is balanced by saving cost resulting from the elimination of shipping operations. According to this, by increasing this coefficient, although it increases the cost of the network, it increases the potential of the network to cover more indifferent customers by parcel lockers.

4. 2. Results Derived by the Proposed Solution Method In this subsection, the computational examination is reported in such a way that the proposed solution approach is analyzed by emphasizing and examining the computational efficiency and effectiveness of the outputs. Initially, the impacts of

algorithmic enrichments upon the general methodology to solving LNFDO via the Benders decomposition algorithm is surveyed. The codes are written in Python. The master problem and dual sub-problems are solved by the CPLEX library of Python on a Laptop computer under properties of a 2.8-GHz Intel-Core processor and 16-GB RAM. To test the computational improvements of this algorithm, 18 instances are generated.

Table 2 shows the computational outcomes of different instants. The gap percentage of each instance is calculated as (*UB*-*LB*)/*LB*. A gap of 100% implies that a feasible solution is not obtained at the end. the term "Time" is a run-time algorithm displayed in an hour unit. The maximum of the allowed run time to continue iterations is 6 hours, and then, the Benders algorithm is terminated. In the following, after varying the problem size, the efficiency of the enhanced algorithms and the quality of the solutions are evaluated. Given the complexity of the problem, as summarized in Table 2, the performance of the modified algorithm is very promising in terms of the quality of the solution and the computational time obtained. In the class of medium sizes, ILOG CPLEX Optimization Studio is superior to the proposed algorithms; however, in the class of large sizes, all the combinations of the proposed strategies have a relative and absolute advantage, so that the modified Benders decomposition guarantees to obtain an efficient solution close to optimum and optimality gap less than 3.

Figure 12 illustrates how to converge between lower and upper bounds in the manners of classic and modified Benders decomposition algorithm. Regarding the lower bound, up to iteration 9, their growth is almost the same, but after that, the modified algorithm shows more growth than the classic one, and regarding the upper bound, from the beginning of the modified algorithm starts with a significantly lower value than classic one and decreases this value gradually and regularly.

TABLE 2. Properties of the proposed modified Benders decomposition

		CPLEX solver	Classic Benders		Modified Benders		
		Time (h)	Gap (%)	Time (h)	Gap (%)	Time (h)	Gap (%)
Medium	1	0.31	0	0.41	<8	0.29	0
	2	0.38	0	0.45	<7	0.27	0
	3	1.31	0	1.9	<6	0.59	<0.8
	4	1.98	0	2.13	<8	1.11	0
	5	2.56	0	3.1	<5	2.12	0
	6	3.22	0	3.5	<8	2.36	<0.5
	7	2.83	<1	3.1	<9	1.86	0
	8	3.45	<1	3.48	<11	2.86	0
	9	4.98	<3	3.96	<13	3.76	0
	10	5.89	<3	4.45	<10	4.23	0
large	11	>6	>15	4.9	<11	4.46	<1
	12	-	**100**	5.3	<12	5.12	<2
	13	>6	>15	5.6	<14	4.32	<1
	14	>6	>15	5.7	<12	4.11	<1
	15	>6	>15	5.2	<13	4.44	<3
	16	-	**100**	>6	<16	5.23	<3
	17	-	**100**	>6	<12	5.42	<3
	18	-	**100**	>6	<14	5.61	<3

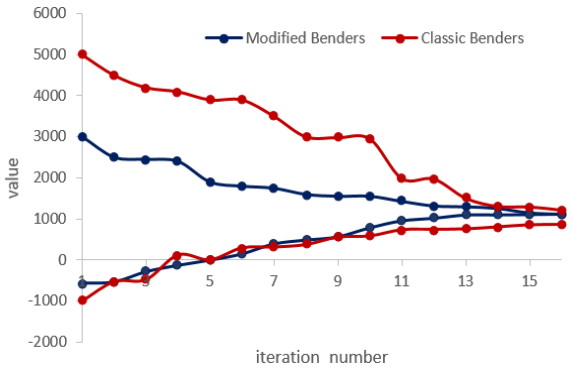

Figure 12. Convergence of the proposed algorithm

4. 3. Discussion and Managerial Insights As mentioned before, the proposed model has two objective functions. The first one is the network cost consisting of transportation costs, operational costs of parcel lockers, and discounts that the company provides to customers who accept to pick up their product from lockers. The second one is covering indifferent customers by locker facilities.

The companies encourage indifferent customers to pick up their products from the lockers by increasing the discounts, but the total cost of this discount and the operational locker cost should not be significantly greater than the cost of shipping goods in the at-the-door option. A relationship between company's costs and the covering of indifferent customers is not necessarily a linear one. As it is obvious in Figure 9, with only 20% more costs, 50% growth in coverage is gained which from the aspect of the operations research (OR) view can result from significantly expanding of solution space, because of releasing of restrictions such as time windows of vehicles. Given the significant impact of increasing company costs on covering more indifferent customers, the decision-makers should consider these Pareto solutions when determining their strategy and long-term policies in a competitive market and analyze the sensitivity of the model in the adopted policies and its neighborhood to know how to control sudden changes in cost and indifferent customer coverage.

The discounts offered to indifferent customers play an important role in gradually encouraging them to progressively cooperate with the last-mile network. Discounts should be commensurate with the option selected and its parameters specified by the customer. Low discount does not create the necessary motivation and unnecessary discount eliminates the effects of long-term targeted incentives. According to Figure 11, at low percentages of an indifferent customer coverage, the Pareto front for the incremental and decremental discount coefficients is almost tangent to each other, showing the sensitivity of the indifferent customer to the attractiveness of the discounts. In the solutions that the company adopts the cost reduction policy, indifferent customers in all discount coefficients tend not to participate in the cooperation of locker network and instead receive the product at home and in the ones that the company adopts the cost increase policy to develop the network of parcel lockers, a significant non-linear increase in changing of indifferent customers' attitude is obvious. As result, unlike cost-cutting policies, the nonlinear effects of the discount coefficient are more tangible in policies based on the development of a parcel-locker network and the encouragement of more indifferent customers. Thus, in the policy that the company intends to develop a locker network, the sensitivity analysis of discount coefficients to find out the attractiveness of indifferent customers' threshold and control total cost under locker network development is necessary.

In a class of large sizes, all the combinations of the proposed strategies had a relative and absolute advantage, so the modified Benders decomposition algorithm guaranteed to obtain an efficient solution close to an optimum and optimality gap of less than 3%. In the class of large sizes, ILOG CPLEX Optimization Studio even could not get a feasible solution in the four instances during the given run time. Thus, because real-world problem dimensions are almost large, the proposed solution approach is suitable for achieving global solutions or very close to it.

5. CONCLUSION

Focusing on parcel-locker systems emerging as a hopeful technology to accelerate the Last-mile logistics in recent years, this study has addressed a Last-mile network with flexible delivery options. Surveying the role of lockers in an integrated network, making this theoretical concept closer to the more practical one, defining management tools to encourage customers to cooperate more with the locker network, and ensuring the gradual development of locker network are the challenges of this investigation. Thus, the multiple delivery options, push lever for the gradual development of the parcel-locker network, online flexible discount to parcel lockers network are the innovations of this study, which have been presented for the first time according to the best of our knowledge. This paper introduces a single-echelon network that includes a central distributor, parcel lockers, and customers, allowing customers to take advantage of three flexible product delivery options after purchasing the product. In the first option, the parcels are delivered at the door and in the time window specified by the customer; In the second option, customers pick up the parcels from the desired lockers with a discount, and in the third option, customers leave the choice of delivery type to the company under gaining an attractive discount. The proposed model could be a good platform for leading businesses in online commerce as well as urban policymakers who want to not only promote the level of online customer service but also in a gradual process, increase customers' social responsibility sense to pick up their parcels from lockers.

To solve this problem, a modified Benders decomposition algorithm enhanced by two efficient strategies (i.e., local branching and variable-neighborhood-search) are presented. The variable-neighborhood-search strategy is used in finding an efficient and feasible solution to the master sub-problem and getting an efficient solution in the local branching problem. In the class of large sizes, all the combinations of the proposed strategies had a relative and absolute advantage, so the modified Benders decomposition algorithm guaranteed to obtain an efficient solution close to an optimum and optimality gap of less than 3%. In the class of large sizes, ILOG CPLEX Optimization Studio even could not get a feasible solution in the four instances during the given run time.

In terms of sensitivity analysis of the model, the relationship between company's costs and coverage of indifferent customers is not necessarily a linear one. According to Figure 9, with only 20% more costs, 50% growth in coverage is gained which from the aspect of operation research view, can result from significantly expanding of solution space, because of releasing of restrictions such as time windows of vehicles. Given the significant impact of increasing company costs on covering more indifferent customers, the decision-makers should consider these Pareto solutions when determining their strategy and long-term policies in a competitive market and analyze the sensitivity of the model in the adopted policies and its neighborhood to know how to control sudden changes in cost and indifferent customer coverage. According to Figure 11, unlike cost-cutting policies, the nonlinear effects of the discount coefficient are more tangible in policies based on the development of a parcel-locker network and the encouragement of more indifferent customers. Thus, in the policy that the company intends to develop a locker network, the sensitivity analysis of discount coefficients

to find out the attractiveness of indifferent customers' threshold and control total cost under locker network development is necessary.

For future research, we suggest a simulation-optimization approach to develop this paper based on an online sales company's case study in Iran. Considering the limitations of parcel lockers in this model such as the multi-product, dynamic, robustness, modality and mobility can be a challenging and useful concept to make that more practical.

6. REFERENCES

1. Fallah, M., Tavakkoli-Moghaddam, R., Salamatbakhsh-Varjovi, A. and Alinaghian, M., "A green competitive vehicle routing problem under uncertainty solved by an improved differential evolution algorithm", ***International Journal of Engineering, Transactions A: Basics***, Vol. 32, No. 7, (2019), 976-981, doi: 10.5829/ije.2019.32.07a.10.
2. Esmaili M. and Sahraeian, R., "A new bi-objective model for a two-echelon capacitated vehicle routing problem for perishable products with the environmental factor", ***International Journal of Engineering, Transactions A: Basics***, Vol. 30, No. 4, (2017), 523-531, doi: 10.5829/idosi.ije.2017.30.04a.10.
3. González-Varona, J. M., Villafáñez, F., Acebes, F., Redondo, A., and Poza, D., "Reusing Newspaper Kiosks for Last-Mile Delivery in Urban Areas" , ***Sustainability*** , Vol. 12, No. 22, (2020), 9770, doi: 10.3390/su12229770.
4. Iwan, S., Kijewska, K. and Lemke, J., "Analysis of parcel lockers' efficiency as the last mile delivery solution-the results of the research in Poland", ***Transportation Research Procedia***, Vol. 12, (2016), 644-655, doi:10.1016/j.trpro.2016.02.018.
5. Lemke, J., Iwan , S., and Korczak, J., "Usability of the parcel lockers from the customer perspective-the research in Polish Cities", ***Transportation Research Procedia***, Vol. 16, (2016), 272-287, doi:10.1016/j.trpro.2016.11.027.
6. Gatta , V., Marcucci, E., Nigro, M., and Serafini, S., "Sustainable urban freight transport adopting public transport-based crowdshipping for B2C deliveries", ***European Transport Research Review***, Vol. 11, No. 1, (2019), 1-14, doi: 10.1186/s12544-019-0352-x.
7. Tang, Y. M., Chau, K. Y., Xu, D., and Liu, X., "Consumer perceptions to support IoT based smart parcel locker logistics in China," ***Journal of Retailing and Consumer Services***, Vol. 62, (2021), 102659, doi: 10.1016/j.jretconser.2021.102659.
8. Deutsch, Y. and Golany , B., "A parcel locker network as a solution to the logistics last mile problem" ***International Journal of Production Research***, Vol. 56, No. 1-2, (2018), 251-261, doi: 10.1080/00207543.2017.1395490.
9. Lin, Y., Wang, Y., Lee, L. H., and Chew E. P., "Profit-maximizing parcel locker location problem under threshold Luce model", ***Transportation Research Part E: Logistics and Transportation***, Vol. 157, (2022), 10254, doi: 10.1016/ j.tre.2021.102541.
10. Pan, S., Zhang, L., Thompson R.G., and Ghaderi H., "A parcel network flow approach for joint delivery networks using parcel lockers", ***International Journal of Production Research,*** Vol. 59, No. 7, (2021), 2090-2115, doi:10.1080/00207543.2020.1856440.
11. Orenstein, I., Raviv, T. and Sadan, E., "Flexible parcel delivery to automated parcel lockers: models, solution methods and analysis", ***EURO Journal on Transportation and Logistics***, Vol. 8, No. 5, (2019), 683-711, doi:10.1007/s13676-019-00144-7.
12. Anderluh, A., Nolz, P. C., Hemmelmayr, V. C. and Crainic, T. G., "Multi-objective optimization of a two-echelon vehicle routing problem with vehicle synchronization and 'grey zone'customers arising in urban logistics", ***European Journal of Operational Researc*h**, Vol. 289, No. 3, (2021), 940-958, doi: 10.1016/j.ejor.2019.07.049.
13. Zhou, L. , Lin, Y., Wang, X. and Zhou, F., "Model and algorithm for bilevel multisized terminal location-routing problem for the last mile delivery", ***International Transactions in Operational Research***, Vol. 26, No. 1, (2019), 131-156, doi: 10.1111/itor.12399.
14. Voccia, S. A., M. Campbell, A. and Thomas, B. W., "The same-day delivery problem for online purchases", ***Transportation Science***, Vol. 53, No. 1, (2019), 167-184, doi: 10.1287/trsc.2016.0732.
15. Sitek, P. and Wikarek, J., "Capacitated vehicle routing problem with pick-up and alternative delivery (CVRPPAD): model and implementation using hybrid approach", ***Annals of Operations Research***, Vol. 273, No. 1, (2019) , 257-277, doi: 10.1007/s10479-017-2722-x.
16. Benders, J. F., "Partitioning procedures for solving mixed-variables programming problems", ***Numerische Mathematik***, Vol. 4, No. 1, (1962), 238-252, doi: 10.1007/BF01386316.
17. Mladenović, N. and Hansen, P., "Variable neighborhood search", ***Computers & Operations Research***, Vol. 24, No. 11, (1997), 1097-1100, doi: 10.1016/S0305-0548(97)00031-2.
18. Fischetti M., and Lodi, A., "Local branching", *Math. Program.*, Vol. 98, Vo. 1, (2003), 23-47, doi: 10.1007/s10107-003-0395-5, doi: 10.1007/s10107-003-0395-5.
19. Dethloff, J., "Vehicle routing and reverse logistics: the vehicle routing problem with simultaneous delivery and pick-up", ***OR-Spektrum***, Vol. 23, No. 1, (2001), 79-96, doi: 10.1007/PL00013346.

Persian Abstract

چکیده

هدف از ارائه این مقاله معرفی رویکردی یکپارچه و تخصصی برای مواجه‌شدن با مسئله‌ای چالش‌برانگیز معروف به «شبکه آخرین گام از توزیع محصول» است. این مسئله که از منظر سطح تصمیم‌گیری در سطح تاکتیکال طبقه‌بندی می‌گردد، یک مدل‌سازی از فرآیندهای عملیاتی و کاربردیِ کسب و کارهای مطرحِ اینترنتیِ کشورهای توسعه‌یافته می‌باشد درحالی‌که از جنبه تحقیق درعملیات مورد توجه زیادی واقع نشده است. این مسئله یک شبک یک سطحی است که دربردارنده توزیع‌کننده مرکزی، کمدهای خودکار تحویل کالا و مشتریان بوده و در آن به مشتریان امکان بهره جستن از سه گزینه منعطف دریافت محصول را پس از خرید محصول، داده می‌شود. در گزینه اول تحویل محصول در درب منزل و در پنجره زمانی تعیین شده توسط مشتری انجام شده؛ در گزینه دوم برداشت محصول توسط مشتریان از کمدهای خودکار مطلوب به همراه تخفیف صورت پذیرفته و در گزینه سوم مشتریان انتخاب نوع تحویل را با کسب تخفیف جذاب به شرکت واگذار می‌نمایند. پیشنهاد تخفیفات آنلاین متناسب با گزینه انتخابی بمنظور تشویق هرچه بیشتر مشتریان در همکاری با شرکت و تضمین توسعه تدریجی شبکه کمدهای خودکار توسط یک اهرم مدیریتی از دیگر نوآوری‌های این مدل می‌باشد. برای حل مدل پیشنهادی، یک الگوریتم تجزیه بندرز توسط یک الگوریتم فراابتکاری جستجو با شعاع متغیر شاخه‌زنی محلی اصلاح شده است. نتایج کسب‌شده از تحلیل حساسیت پارامترهای مرتبط با نوآوری‌های مسئله، بیان‌گر کارآمدی و صحّه مدل در سناریوهای مختلف و الگوریتم حل پیشنهادی در مسائلی با ابعاد بزرگ می‌باشد.

IJE TRANSACTIONS B: Applications Vol. 35, No. 08, (August 2022) 1558-1570

International Journal of Engineering

Journal Homepage: www.ije.ir

A State-of-the-art Model of Location, Inventory, and Pricing Problem in the Closed-loop Supply Chain Network

P. Haghshenas[a], R. Sahraeian*[a], A. M. Golmohammadi[b]

[a] *Department of Industrial Engineering, College of Engineering, Shahed University, Tehran, Iran*
[b] *Department of Industrial Engineering, Arak University, Arak, Iran*

PAPER INFO

Paper history:
Received 24 January 2022
Received in revised form 05 April 2022
Accepted 08 April 2022

Keywords:
Closed-Loop Supply Chain
Location
Pricing
Inventory & Carrying Policy
Metaheuristic Genetic Algorithms
Particle Swarm Optimization

ABSTRACT

The main objective of designing the supply chain is to increase profitability. For this reason, a state-of-the-art model of a three-echelon closed-loop supply chain is proposed that consists of the manufacturer, retailer, and collection centers. For the first time, a new separate and autonomous channel is considered in this model for the sale of Reman products aiming at increasing the manufacturer's profitability. In this model, location, inventory, and pricing of the product are also taken into consideration. Lingo software is utilized to solve nonlinear objective functions at a small scale, and metaheuristic genetic algorithms and particle swarm optimization were utilized to solve at a large scale. The research results depict that the state-of-the-art model design of the closed-loop supply chain network is credible and the optimal location of supply chain components, optimal response of product flow, and product price are determined in a proper manner. As a result, the profitability of the whole closed-loop supply chain network increased. Sensitivity analysis of mathematical model depicts that this model shows higher sensitivity to retailer replacement factor, price and purchasing power of collection centers. Also, the genetic algorithm shows better performance on a large scale in terms of response quality. On the other hand, the time required by particle swarm optimization to reach a response is far better than the genetic algorithm. Ultimately, practical suggestions for the managers are presented considering the state-of-the-art model design of a closed-loop supply chain network.

doi: *10.5829/ije.2022.35.08b.12*

1. INTRODUCTION

The subject of supply chain and its profitability in different fields are among the highly-focused research subjects in numerous articles. The main focus of this article is to design and propose a state-of-the-art model of a three-echelon closed-loop supply chain (CLSC). The advantages of closed-loop supply chain network design include reduced pollution, increased customer satisfaction, reduced costs, and increased profitability.

Considering the importance of supply chain design and location significance in it, a three-echelon closed-loop supply chain is designed that consists of the manufacturer, retailer, and collection centers. The manufacturer sells economic order quantity to the retailer at an optimal price and then, the retailer sells the products to the customers at his/her optimal prices. When the commodity has no use for the customers, the customer sells them to the collection centers at an optimal price designated by the collection centers. Afterwards, the economic quantity of collected commodities are sold to the manufacturers for salvage at an optimal price of the manufacturer and after this option, Reman products are sold to the customers in a direct manner at the manufacturer's optimal selling price for the Reman products. Such process for resale of the commodity is presented for the first time in the proposed supply chain model. Figure 1 gives an overall view of the proposed closed-loop supply chain.

At each stage/phase, the optimal prices were separately calculated. The economic quantity of order and delivery was determined considering the cost

* Corresponding Author Institutional Email: Sahraeian@shahed.ac.ir (R. Sahraeian)

Please cite this article as: P. Haghshenas, R. Sahraeian, A.M. Golmohammadi, A State-of-the-art Model of Location, Inventory, and Pricing Problem in the Closed-loop Supply Chain Network, ***International Journal of Engineering, Transactions B: Applications***, Vol. 35, No. 08, (2022), 1558-1570

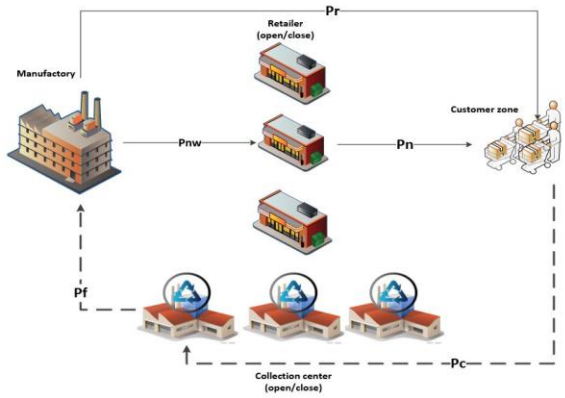

Figure 1. Overall view of proposed CLSC

function of retailers and collection centers. Customer demand is deterministic and depends on prices determined by the retailers and by manufacturers for Reman products. Following the determination of optimal prices and using a mathematical model for the manufacturer, the location of retailers and collection centers is determined in this model. In this problem, inventory costs of retailers and collection centers are also taken into consideration.

2. LITERATURE REVIEW

The closed-loop supply chain is one of the crucial and state-of-the-art subjects in supply chain literature. The main objective of each supply chain is to increase profitability. In this article, therefore, three main topics are taken into consideration for closed-loop supply chain modelling for the first time. These topics include:

- Pricing, inventory, and location
- A separate sales channel for the manufacturer
- The distance-sensitive location between each construct/component

Previous literature has not investigated the above topics simultaneously. However, we intend to investigate their impact on the closed-loop supply chain by applying them simultaneously. In the next section, the previous literature is reviewed.

Pricing of a three-echelon closed-loop supply chain was conducted for perishable products in a research and the echelons of this supply chain consist of the manufacturer, retailer, and customer [1]. In this research, the manufacturer has two options, to either sell the product to customers directly or to sell the product to the retailer. Related to the second option, the return policy is designed in a way that returned product is acquired by the retailer from the customer and then, sold to the manufacturer. In this article, we consider a separate channel for selling manufacturers' products to the customer in a direct manner, with a difference that there is no sale limit. Based on the pricing, the manufacturer can sell a percentage of the product to the retailer and another to the customer. The return policy of both channels is through collection channels.

Researchers investigated the pricing of a single-product closed-loop supply chain that includes retailers, customers, and collection centers [2]. This research considers a direct channel for product sale through the manufacturer to the customer. The supply chain and demand functions in our article are designed similar to this research. The difference is that the present research has investigated the subject of location and inventory and carrying costs. Moreover, the problem is solved for a multi-product scenario.

It was investigated the pricing of a two-echelon supply chain that consists of suppliers and retailers. In the proposed model, there is a direct channel from the supplier to the customer [3]. To solve the problem, the profit function of supplier and retailer is written for both channels and inventory costs are calculated for 6 situations and then, they are compared. However, we propose a three-echelon supply chain where there is a separate channel for product sale to the customer in a direct manner. Moreover, carrying costs are calculated using a single method.

It was investigated the optimal location and price for the retailers [4]. First, they proposed a separate price function in order to achieve the final price for the retailer and calculated the least possible price. Then, the price of commodities is changed randomly and the amount of profit is calculated in each change. After achieving the optimal price, the value is placed in the objective function and the problem is solved for optimal placement and determining the optimal location. Here, pricing and placement/location are also investigated with a difference that the optimal price is calculated for each component of the supply chain and pricing is carried out for the retailer and collection centers with the aid of derivative of the dependent function with respect to the demand. Next, the manufacturer price is calculated with the aid of a mathematical model by taking the profit of supply chain components into consideration. Regarding placement, the optimal location is determined considering the distance from customer to retailer and collection centers.

In an other paper, it was investigated the location of chain and pricing components in a five-echelon closed-loop supply chain [5]. The modelling objective in this problem is to maximize total supply chain profit considering the optimal location of supply chain components and optimal commodity sale price. Similar to our article, this research investigated the location and pricing, with a difference that our research not only investigates the optimal sale price but also the optimal purchase price of supply chain components. The location of components was determined considering the distance between the customer and components and the carrying

and inventory costs are taken into consideration in modelling .

Researchers investigated the pricing for a three-echelon closed-loop supply chain that consists of the manufacturer, supplier, and customer [6]. The chain is designed so that manufacturer can acquire the used product from the customer after selling a new product to the customer and can employ different approaches for the acquired product. In this article, the manufacturer also acquires used products from the customer through an intermediary. However, different approaches are not considered for the manufacturer and the acquired products can be only salvaged and re-supplied to the supply chain.

In 2017, two researchers have been considered the pricing for a two-echelon supply chain that consists of one manufacturer and several retailers [7]. The cost is assumed as a price-sensitive function in which carrying costs and prices, retailer shortage and inventory carrying cost for the manufacturer are taken into account. Two methods namely particle swarm optimization and binary quantum-behaved particle swarm optimization algorithm are utilized for solving the problem. In this article, we also investigated the pricing and inventory, with a difference that carrying costs are only calculated for the retailer and collection centers, and shortage costs are not among the problem premises.

It has been reviewed the pricing of multi-period and multi-product problems in which demand is assumed as price and advertisement sensitive function [8]. Inventory carrying costs are also taken into consideration in the proposed model. Here, however, we have investigated the pricing and inventory matter in a multi-product supply chain and the demand function of supply chain components depends on optimal purchase price, and carrying and location optimal costs. However, advertisement is not taken into consideration in this model.

It investigated the inventory costs in a non-deterministic and multi-product supply chain with the aim of maximizing the chain's profit [9]. In the research, demand is assumed as a price-sensitive function, and differentiation is utilized in order to determine the optimal/economic model quantities. In this article, we also investigated the pricing and inventory costs in a multi-product supply chain with a difference that parameters are deterministic.

Fahimnia et al. [10] presented a five-echelon green and closed-loop supply chain consisting of the manufacturer, wholesaler, customer, collection centers, and salvage centers. The aim of this article is to minimize supply chain costs and determine the optimal price for the level of produced carbon dioxide by the supply chain. The objective of our article is to maximize the profit.

Ahmadi-Javid and Hoseinpour [11] designed a multi-product network consisting of the wholesaler, retailer, distribution center, and customer. The objective is to maximize the profit by taking inventory costs into consideration. The location of the distribution center is determined with the aid of the proposed model and sale price is determined following the model solving process. In our article, all the above steps are carried out in a closed-loop supply chain and a separate channel is taken into consideration to sell the product directly to the customer.

Fattahi et al. [12] investigated the components pricing and placement in a two-echelon supply chain consisting of manufacturer and wholesaler. They proposed a mixed-integer linear programming model for a multi-product supply chain over a multi-period horizon by taking flow capacity and inventory system costs into consideration. The difference between this research with our article is associated with supply chain, network design, and model solution. In our article, the model was solved on a small scale and also, metaheuristic genetic algorithms were also utilized on a large scale. However, we have proposed a single-period model Kaya and Urek [13] investigated the location and pricing decision of products with the aid of a nonlinear model. This study is conducted for a chain store in Turkey. Our article not only attempts to propose a model but also determine the optimal price with the aid of differentiation and concepts such as market share and product flow capacity and a separate sale channel is taken into consideration.

Ahmadzadeh and Vahdani [14] provided a single-product and three-echelon close-looped supply chain under possible conditions of uncertainty. The model objective is to maximize the total supply chain profit by taking inventory shortages costs into consideration. The genetic algorithms (GAs), imperialist competitive algorithm (ICA), and the firefly algorithm (FA) were utilized for solving the model. The comparison between these algorithms depicts that FA achieved a better result over a minimum length of time. Conditions of uncertainty are not taken into consideration on our inventory shortage costs but we have considered a multi-product supply chain. In addition, not only did we solve the model on a small scale, but also the genetic algorithm and particle swarm optimization were utilized for large scales.

In another study, location and pricing in a four-echelon close-looped supply chain has been investigated, including supplier, manufacturer, retailer, and recovery center. This study examines the issue of reducing electronic pollution and cell phone reuse. The mathematical model is a multi-objective problem that involves maximizing the profit. This mathematical model has been prepared using the fuzzy method and the Epsilon Constraints method has been used to solve it. In this study, only pricing and location in the closed-loop supply chain have been considered, and inventory and maintenance costs have not been examined, and a

separate channel for direct sales of products has not been considered [11].

Tavakkoli-Moghaddam et al. [15] examined pricing, inventory, and location in a four-echelon closed-chain supply chain, including manufacturer, retailer, and distribution center. In this study, the routing of perishable goods is investigated by considering urban traffic and product expiration time. In this research, an independent channel for selling products directly to customers is not considered.

Another work deals with pricing in a four-echelon close-looped supply chain, including suppliers, manufacturers, retailers, and collection centers. In this mathematical model, profit maximization is discussed [16]. In this study, only the pricing in the closed chain supply chain has been studied and the location, inventory and maintenance costs and separate channels for selling directly to customers have not been studied.

In conclusion, "pricing, inventory, and location", "a separate sale channel for the manufacturer", and "distance sensitive location between the components" are investigated in the previous literature. However, these three topics have not been taken into consideration in a closed-loop supply chain. Hence, these topics are utilized for the first time for modelling and the results are analyzed. A summary of previous literature are presented in Table 1.

3. PROBLEM DEFINITION AND MODELLING

In this article, we proposed a closed-looped supply problem chain that is modelled by taking into account the following topics, simultaneously: "pricing, inventory, and location", "a separate sale channel for the manufacturer", and "distance sensitive location between the components". The three-echelon closed-loop supply chain consists of the manufacturer, retailer, and collection centers .

The manufacturer sells optimal order quantity to the retailer and then, the retailer sells the products to the customers. When the products have no use for the customers, the customer sells them to the collection centers. Afterwards, the optimal quantity of collected products is acquired by the manufacturer for salvage and then, the manufacturer sells the Reman products directly to the customers. Such a process for re-selling the product (a separate sale channel) is proposed for the first time in our closed-loop supply chain model.

Following assumptions are taken into consideration for problem modelling in Figure 1:

1. Each customer can only acquire one product from the retailer.
2. Each customer can sell the used product only to one collection center.
3. The new and Reman products can be replaced.

TABLE 1. Summary of previous literature

Authors names & Published dates	*Sup*	*CLSC*	*Inventory*	*location*	*pricing*	*Ssc*	*Model*
Barry Alan Pasternack (1985) [1]	●	●			Yes	●	LP
Plastria Vanhaverbeke (2008) [4]				●	Yes		MIP
Jiawang Xu and Yunlong Zhu (2011) [6]	●	●	●		Yes		NLP
Fahimnia et al. (2013) [10]	●	●	●	●	Yes		MINLP
Onur Kaya , Busra Urek (2015) [13]	●	●	●	●	Yes		MINLP
Mohammad Fattahi et al. (2015) [12]	●		●	●	Yes		MINLP
Ahmadi-Javid, Hoseinpour (2015) [11]	●		●	●	Yes		MINLP
Shu-San Gan et al. (2016) [2]	●	●			Yes	●	NLP
Chen and Sarker.(2016) [7]	●		●		Yes		NLP
Ahmadzadeh, Vahdani (2017) [14]	●	●	●	●	Yes		MINLP
R. Ghasemy Yaghin (2017) [8]	●		●		Yes		NLP
M. A. Edalatpour, S. M. Al-e-Hashem (2019) [9]			●		Yes		NLP
Atabaki et al. (2019) [5]	●	●		●	Yes		MILP
Raaid Batarfia, et al. (2019) [3]	●		●		Yes	●	NLP
Ahmadi, Hassanzadeh Amin (2019) [17]	●	●		●	Yes		MIP
Tavakkoli-Moghaddam et al. (2021) [15]	●	●	●	●	Yes		MINLP
Ziari,Sheikh Sajadieh (2022) [16]	●	●			Yes		LP
This WORK	●	●	●	●	Yes	●	MINLP

4. The manufacturer sees no difference between the retailers.
5. The manufacturer sees no difference between the customers.
6. Location decision of retailers and collection centers is sensitive to their distance to the customer and construction costs .
7. Collection centers and retailers bear carrying and inventory costs that follow the inventory model of economic order quantity.

3. 1. Sets, Parameters, Variables, And Functions

The sets of retailers, customers, collection centers, and products are presented in Table 2 and mathematical model parameters are given in Table 3. Moreover, mathematical functions used in the mathematical model and problem variable are presented in Tables 4 and 5, respectively.

TABLE 2. Sets

I: Retailers	i=1, 2, …, I
J: Customers	j=1, 2, …, J
L: Collection centers	l=1, 2, …, L
H: Commodities	h=1, 2, …, H

TABLE 3. Parameters

$K_{(h,j)}$	Potential demand for products *h* by customers *j* (retailers)
$k'_{(h,j)}$	Potential demand for products *h* by customers *j* (manufacturer)
k_i	Sensitivity coefficient of selling price of products by retailer *i*
k'	Sensitivity coefficient of selling price of products by the manufacturer
b_1	The replacement rate of the product that the retailer sells
b_2	The replacement rate of the product that the manufacturer sells
$h_{(h,i)}$	Holding cost of products *h* by retailer *i*
$h_{(h,l)}$	holding cost of products *h* by collection center *l*
A_i	Fixed cost of ordering products by retailer *i*
A_l	Fixed cost of ordering products by collection centers
$\varphi_{(h,j)}$	Percentage of consumer products *h* that collection centers purchase from customer *j*
$C_{(h,l)}$	The cost of collecting products *h* by the collection center *l*
Crw_h	Cost per unit of raw materials for the purchasing of products *h*
Cm_h	Cost of production of product *h* by the manufacturer
Cr_h	Cost of reproducing production of product *h* by the manufacturer
F_i	Cost of constructing retail *i*
E_l	Cost of constructing collection center *l*
C_{ij}	Customer distance *j* from retailer *i*
D_{lj}	Distance of customer *j* from the collection center *l*
S_i	Construction cost of retailer *i* (depends on the distance of the retailers)
S_l	Construction cost of collection center *l* (depends on the distance of the retailers)
u	Constant value of demand function

TABLE 4. Mathematical functions

$Dr_{(h,i,j)}$	Retail demand function *i* for product *h* (by customer *j*)
$Dm_{(h,j)}$	Manufacturer demand function for product *h* (by customer *j*)
$Dc_{(h,l,j)}$	Collection center *l* demand function for product *h* (by customer *j*)
Π_{Ri}	Retail profit function *i*
Π_{cl}	Collection center profit function *l*
Π_m	Manufacturer profit function

TABLE 5. Variables

$Pnw_{(h,i)}$	Sale price (Manufacturer) of new product *h* to retailer *i*
$Pn_{(h,i,j)}$	Sale price (retailer *i*) of new product *h* to customer *j*
$Pc_{(h,l,j)}$	Purchase price of used product *h* by the collection center *l* from the customer *j*
$Pf_{(h,l)}$	Purchase price of used product *h* by the manufacture frim the collection center *l*
$Pr_{(h,j)}$	Sale price of recycled pruduct *h* by the manufacturer to the customer *j*
$Qm_{(h,j)}$	The amount of recycled products flow *h* that is sent from the manufacturer to the customer *j*
$Qr_{(h,i)}$	The amount of product flow *h* that is sent from the manufacturer to the retailer *i*
$Qc_{(h,l)}$	The amount of used product *h* that is sent from the customer to the collection center *l*
$D1_{(h,i,j)}$	Market share of product *h* for retailer *i* to customer *j*
$D2_{(h,l,j)}$	Market share of second-hand product *h* from the customer *j* for the collection center *l* to the manufacturer
$D3_{(h,j)}$	Market share of recycled product *h* to customer *j*
$Rp_{(h,j)}$	Amount of second-hand product h sold by customer *j* to the collection center
x_{ij}	= 1 if customer *j* buys a product from retailer *i*, otherwise = 0
w_{lj}	= 1 if customer *j* sells product to the collection center, otherwise = 0
y_i	= 1 if the retailer *i* is constructed, otherwise = 0
θ_l	= 1 if the collection center *l* is constructed, otherwise = 0

3. 2. Modelling Here, the problem is presented with the aid of a mathematical model. Utilized parameters and sets are defined in Tables 1 to 4. This mathematical model is an objective function. For problem modelling, demand functions of the retailer, collection centers, and manufacturer are defined firstly. Next, profit functions for both retailers and collection centers are presented and the optimal sale and purchase prices are achieved through differentiation. Ultimately, manufacturer profit is computed and optimal values are achieved by solving this model.

Demand functions for retailers (1), manufacturer (2), and collection centers (3) are given as follows for customer j:

$$Dr_{(h,i,j)} = K_{(h,j)} - k_i Pn_{(h,i,j)} + b_1 Pr_{(h\,j)} \quad (1)$$

$$Dm_{(h\,j)} = K'_{(h\,j)} - k'\,Pr_{(h\,j)} + b_2 Pn_{(h\,i\,j)} \quad (2)$$

$$Dc_{(h\,l\,j)} = \varphi_{(h\,j)} Pc_{(h\,l\,j)}{}^{u}(K_{(h\,j)} - k_i Pn_{(h\,i\,j)} + b_1\,Pr_{(h\,j)}) \quad (3)$$

Profit function for the retailers is given as follows by taking inventory carrying costs into consideration (which follows the EOQ method):

$$Max\Pi_{Ri} = Dr_{(h\,i\,j)}\left(Pn_{(h\,i\,j)} - Pnw_{(h\,i)}\right) - \left(\frac{h_{(h\,i)}Qr_{(h\,i)}}{2} + \frac{A_i Dr_{(h\,i\,j)}}{Qr_{(h\,i)}}\right) \quad (4)$$

This is a concave function. Hence, the optimal value $Pn_{(h,i,j)}$ can be achieved through differentiation:

$$\frac{d\Pi_{Ri}}{dPn_{(h\,i\,j)}} = 0$$

$$\rightarrow Pn^*_{(h\,i\,j)} = \frac{K_{(h\,j)} + b_1\,Pr_{(h\,j)} + k_i Pnw_{(h\,i)} + (\frac{k_i A_i}{Qr_{(h\,i)}})}{2k_i} \quad (5)$$

Profit function for the collection centers is given as follows by taking inventory carrying costs into consideration (which follows the EOQ method):

$$Max\Pi_{cl} = Dc_{(h\,l\,j)}\left(Pf_{(h\,l)} - Pc_{(h\,l\,j)} - c_{(h\,l)}\right) - \left(\frac{h'_{(h\,l)}Qc_{(h\,l)}}{2} + \frac{Dc_{(h\,l\,j)}A_l}{Qc_{(h\,l)}}\right) \quad (6)$$

This is a concave function. Hence, the optimal value $Pc_{(h,l,j)}$ can be achieved through differentiation:

$$\frac{d\Pi_{cl}}{dPc_{(h\,l\,j)}} = 0$$

$$\rightarrow Pc^*_{(h\,l\,j)} = \frac{-A_l u + Pf_{(h\,l)}Qc_{(h\,l)}u - c_{(h\,l)}Qc_{(h\,l)}u}{Qc_{(h\,l)} + Qc_{(h\,l)}u} \quad (7)$$

The manufacturer profit model is an objective function. The first part includes the revenue achieved by new product sales to the constructed retailers. The second part is the revenue achieved by Reman product sales to the customers. The third part of the objective function is the purchase price of used products from collection centers. The fourth and fifth part of this function denotes the construction costs of retailers and collection centers. Lastly, the sixth and seventh part includes the costs caused by the distance between customers and constructed retailers and collection centers:

$$Max\Pi_m = \sum_{h\in H}\sum_{i\in I} Qr_{(h\,i)}(Pnw_{(h\,i)} - Crw_h - Cm_h) + \sum_{h\in H}\sum_{j\in J} Qm_{(h\,j)}(Pr_{(h\,j)} - Cr_h) - \sum_{h\in H}\sum_{l\in L} Qc_{(h\,l)}Pf_{(h\,l)} - \sum_{i\in I} F_i y_i - \sum_{l\in L} E_l\theta_l - \sum_{i\in I}\sum_{j\in J} S_i C_{(i\,j)}x_{(i\,j)} - \sum_{l\in L}\sum_{j\in J} S_l D_{(l\,j)}w_{(l\,j)} \quad (8)$$

Retailers' market share is included in constraint (9):

$$D1_{(h\,i\,j)} = K_{(h\,j)} - k_i Pn_{(h\,i\,j)} + b_1 Pr_{(h\,j)} \quad \forall h\ i\ j \quad (9)$$

Constraint (10) illustrates the optimal sale price of retailers for the customers that can be achieved through the differentiation of retailers' objective function:

$$Pn^*_{(h\,i\,j)} = \frac{K_{(h\,j)} + b_1\,Pr_{(h\,j)} + k_i Pnw_{(h\,i)} + (\frac{k_i A_i}{Qr_{(h\,i)}})}{2k_i} \quad (10)$$

Constraint (11) illustrates that retailers should purchase less or equal to their market share from the manufacturer for sale.

$$Qr_{(h\,i)} \le \sum_{j\in J} x_{(i\,j)} D1_{(h\,i\,j)} \quad \forall\ i\ h \quad (11)$$

Constraint (12) illustrates that customers should purchase products only from the constructed retailers:

$$\sum_{j\in J} x_{i\,j} \le m y_i \quad \forall i \quad (12)$$

Constraint (13) shows that each customer should purchase the needed product from only one retailer:

$$\sum_{i\in I} x_{i\,j} = 1 \quad \forall j \quad (13)$$

Constraint (14) expresses that the product sale price by retailers should be at least 10% higher than the product purchase price (minimum retailers' profit: 10%):

$$Pn_{(h\,i\,j)} \ge 1{,}1 Pnw_{(h\,i)} \quad \forall h\ i\ j \quad (14)$$

Constraint (15) illustrates the ratio of purchased products by the customers willing to sell to the collection centers:

$$p_{(h\,j)} = \varphi_{(h\,j)} \sum_{i\in I} Dr_{(h\,i\,j)} x_{(i\,j)} \quad \forall h\ j\ R \quad (15)$$

Constraint (16) illustrates the market share of purchasing used products for the collection centers:

$$D2^u_{(h\,l\,j} = PD2Rp_{(h\,j)} \quad \forall h\ l\ j \quad (16)$$

Constraint (17) illustrates that each customer can sell their used product only to one collection center:

$$\sum_{l\in L} w_{l\,j} = 1 \quad \forall j \quad (17)$$

Constraint (18) shows that customer can only sell their products to the constructed collection centers:

$$\sum_{j\in J} w_{l\,j} \le n\theta_l \quad \forall l \quad (18)$$

Constraint (19) is the upper bound on the used product quantity that is sold by the collection centers to the manufacturer. This quantity should be less than or equal to the purchase market share of used products for the collection centers:

$$Qc_{(h\,l)} \le \sum_{j\in J} w_{(l\,j)} D2_{(h\,l\,j)} \qquad \forall h\ l \tag{19}$$

Constraint (20) shows that the sale quantity of the manufacturer's Reman product cannot be more than the product quantity that is purchased from collection centers:

$$\sum_{j\in J} Qm_{(h\,j)} \le \sum_{l\in L} \theta_l Qc_{(h\,l)} \qquad \forall h \tag{20}$$

Constraint (21) illustrates the sale market share of Reman products for the customers:

$$D3_{(h\,j)} = K'_{(h\,j)} - k' Pr_{(h\,j)} + b_2 \sum_{i\in I} Pn_{(h\,i\,j)} x_{(i\,j)} \qquad \forall h\ j \tag{21}$$

Constraint (22) shows that sold quantity of Reman product to the customers should be less than or equal to the manufacturer' sale market share:

$$Qm_{(h\,j)} \le D3_{(h\,j)} \qquad \forall h\ j \tag{22}$$

Constraint (23) guarantees that collection centers will purchase the used products from the customers at an optimal purchase price (optimal purchase price can be achieved through differentiation of profit function by the collection centers):

$$Pc^*_{(h\,l\,j)} = \frac{-A_l u + Pf_{(h\,l)} Qc_{(h\,l)} u - c_{(h\,l)} Qc_{(h\,l)} u}{Qc_{(h\,l)} + Qc_{(h\,l)} u} \tag{23}$$

Constraint (24) illustrates that the sale price of Reman products should be at least 30% less than the new product price:

$$0{,}7 Pn_{(h\,i\,j)} \ge Pr_{(h\,j)} \qquad \forall h\ i\ j \tag{24}$$

4. VALIDATION

4. 1. Model Solving at a Small Scale Firstly, the proposed problem is solved with the aid of the accurate method at a small scale, both for multi-product and single product situations. The problem dimensions are presented in Table 6. Problem parameters are also generated randomly for single product and multi-product (with two products) situations. The problem is solved for all the customers by taking $\varphi_{(h,j)} = 10\%$ into consideration.

The problem is solved with the aid of the accurate method and Lingo software both for multi-product and single product situations. In Table 7, the optimal prices for both multi-product and single product situations are presented. In Table 8, economic order and delivery quantity are presented for each stage and sale/purchase market share are presented for both multi-product and single product situation.

TABLE 6. Specification of exact solution

Example	Retaile (*i*)	Customer b(*j*)	Collection Center (*l*)	Product (*h*)
1	1	1	1	1
2	1	1	1	2

TABLE 7. Optimal prices

Variables	Single product	Multi product	
pnw^*	314.6748	314.6748	270.6984
Pn^*	413.11	413.11	354.8172
Pc^*	22.95323	22.95323	19.62221
Pf^*	88.91764	88.91764	77.40262
Pr^*	289.1770	289.1770	248.3721
z^*	18368.16	31702.42	

TABLE 8. Optimal quantities of products

Variables	Single product	Multi product	
*Qr**	49.1158	49.1158	41.94021
*D1**	49.1158	49.1158	41.94021
*D2**	17.2012	17.2012	13.79525
*Qc**	17.2012	17.2012	13.79525
*Qm**	17.2012	17.2012	13.79525
*D3**	157.1799	157.1799	131.9336

The results achieved by accurately solving the model illustrates that there is a price balance in the model.

Optimal Sale/purchase prices in supply chain components are designed in a way that the sale price will be higher than the product purchase price and each component will acquire fair profit.

In addition to balanced price, the results illustrate that the proposed problem possesses balanced product flow capacity. Supply chain components acquire the product by taking their market share and current costs into consideration and selling the product in the same quantity.

All the above considerations (balanced price and balanced product flow capacity) show that all the connections in the closed-looped supply chain are designed in a way that all the supply chain components can enjoy the highest profit. In other words, the profit does not belong to a particular part of the chain. The total profit of the network in a multi-product situation is higher than a single-product situation and this also proves the mathematical modelling accuracy.

This non-linear mathematical model cannot be solved for large values with the aid of the accurate method. As a result, metaheuristic algorithms are utilized for solving the large model.

4. 2. Proposed Solution for Larger Scales

Considering the non-linearity and high-complexity of the model, the time required to reach a solution increased for medium and large sizes and therefore, we are forced to utilize metaheuristic algorithms. In this article, metaheuristic genetic algorithms (GAs) and particle swarm optimization (PSO) were utilized for the proposed model.

The genetic algorithm is a metaheuristic algorithm that is inspired by organism reproduction and based on Darwin's theory of natural selection and survival of the fittest. This algorithm is a heuristic optimization approach for finding the best solution (best person). This algorithm is capable of solving complex optimization problems at an acceptable speed and accuracy. The algorithm works firstly by creating the initial population with the aid of a stochastic method. Next, the secondary population is created by using cross-sectional and mutation operations and the algorithm compares the chromosomes constantly from these generations to find the best solution.

The structure of the genetic algorithm in this paper is as follows: first, using the roulette cycle, we select the chromosomes and form the initial population randomly. Then the intersection and mutation operations are performed and a secondary population is formed. The intersection and mutation operations are shown in Figures 2 and 3.

Particle swarm optimization (PSO) is another metaheuristic algorithm. This algorithm is inspired by the motion of bird flocks. In this algorithm, each solution is similar to a bird inside the search space with the following parameters: current position (x_i), velocity (v_i), best-known position (p_i) and the best direction of a bird flock movement (Gbest). Using the following method, the birds' velocity is updated. C_1 and C_2 are the cognitive coefficients with the following values, respectively: 0.5 and 1. r_1 and r_2 denote the random numbers in $[1, 2]$ and w is inertia coefficient with a value equal to 0.3. This recursive relationship is defined in terms of velocity and therefore, the velocity's initial value is considered to be 0:

$$V_i = W.V_{i-1} + C_1.rr_1.(G_{Best} - X_i) + C_2.r_2.(P_{Best} - X_i)$$

In standard particle swarm optimization, the initial population value (quantity) is generated randomly. Pbest values (best-known position) and Gbest (best direction of a bird flock movement) are calculated consistently until the termination condition is realized. The velocity and position of birds are updated with the aid of achieved values at each stage. In Table 9, the solutions by metaheuristic algorithm are compared with the aid of the accurate method. RPD mean index is one of the crucial indices for the performance assessment that is also utilized in this research. This index is defined as follows:

$$RPD = \frac{Alg_{sol} - Best_{sol}}{Best_{sol}} \times 100$$

where Agl_{sol} is the objective function solution in the metaheuristic algorithm and $Best_{sol}$ is the objective function solution in the accurate method.

According to this table, the values achieved by objective function in the accurate method (Lingo) is close to metaheuristic algorithm solutions. In the first example and second example, there is a difference of less than 0.01% and 0.16%, respectively (according to the RPD index). We conclude that the proposed mathematical model is highly credible.

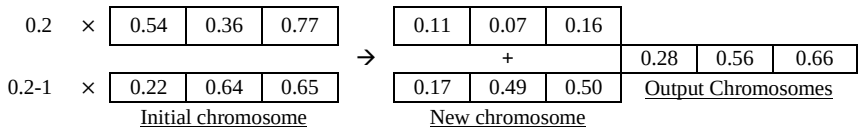

Figure 2. Intersection operations

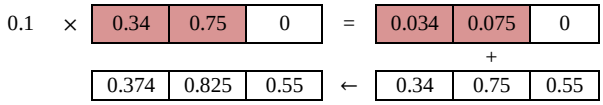

Figure 3. Mutation operations

TABLE 9. Comparing metaheuristics & exact solutions

No.	Lingo	GA	RPD	PSO	RPD
1	18368.16	18366.32	0.01	18366.32	0.01
2	31702.42	31651.77	0.16	31651.77	0.16

However, the accurate method cannot be utilized for problems at a large scale. Hence, we use metaheuristic genetic algorithms (GAs) and particle swarm optimization (PSO). In this regard, 10 different experiments are conducted. The number of retailers is

considered to be between 2 and 12, the number of customers between 2 and 9, the number of collection centers between 2 and 10, and the number of products between 2 and 8. The results achieved by using GA and PSO at medium and large scales are presented in Table 10.

According to the achieved results by GA and PSO algorithms, solving the model using the GA algorithm at medium and large scales (according to RPD index) generated far better solutions than the PSO algorithm in terms of quality. However, PSO functions better than GA in terms of the time needed to find the solution.

5. SENSIVITY ANALYSIS

In this section, the impact of the following parameters is investigated on product flow and price and ultimately, supply chain profit: retailer replacement factor (b_1), price sensitivity coefficient in the retailer (k_i), and purchasing power of customers' used product (u).

The sale market share of the retailer and manufacturer for selling the new and used products to the customer is a ratio of each other's sale price. In other words, an increase in the sale price of a retailer's product will cause an increase in the sale market price of the manufacturer at a certain ratio and vice versa. According to Figures (a-1) to (b-1), an increase in retailer replacement factor and in the impact of manufacturer's price on sale market share of the retailer has caused product's sale market share for the retailer to increase and the customers are more inclined to buy a new product from the retailer. As a result, the retailer acquires the product in higher quantities, and product flow increases in all echelons/levels of the closed-loop supply chain network.

An increase in the product purchase volume in different echelons of the closed-loop supply chain will result in an increase in the optimal purchase/sale price of products in all echelons. Another reason for the increase in the optimal price is that retailer's optimal price has a direct connection to the retailer replacement factor. Increasing this factor will cause an increase in the product sale price to the retailer. Hence, purchase/sale price increases in all other echelons. In Figures 4(a-2) and 4(b-2), it is obvious that used product volume, which is sold (online) directly to the customers, increases the sale market share of the manufacturer. Another reason for the increased demand for purchasing used products is the increased sale price of the new products.

The results of changing sensitivity coefficient parameters in the retailer depict that the retailer reduces the sale price for customer retention if the customer shows higher sensitivity to the product price. Nevertheless, the volume of the acquired product decreases according to retailer function. As a result, all the network echelons reduce the price and the volume of their acquired/sold products. Hence, product flow balance and optimal price are retained (Figures 4c-1, 4d-1, 4c-2, and 4d-2).

According to Figures 4(e-1), 4(f-1), 4(e-2), and 4(f-2), an increase in customers power (purchase price of used product) causes a decline in the product flow and optimal price. Such an event can be attributed to the direct relationship of the market share parameter of collection centers that increases product flow in the whole close-looped supply chain network. Also, due to the inverse relationship between this parameter with product price acquired by the customer, the optimal purchase price of collection centers decrease. Moreover, such an inverse relationship result in the reduction of all optimal prices.

The result of this investigation depicts that increasing retailer replacement factor causes an increase in the optimal product flow and optimal price in all echelons, and it plays a major role in increasing the total profit of

TABLE 10. Solution for large scales

RPD	$TIME_{PSO}$	PSO_{best}	$TIME_{GA}$	GA_{best}	No.
15	27.14	82282.64	41.32	97087.88	1
10	28.18	99110.3	36.39	110784.55	2
13	31.55	226902.66	43.12	263810.89	3
18	27.99	269977.72	44.28	332170.32	4
20	33.90	517905.01	55.22	655377.33	5
3	37.82	1201395.92	57.93	1246158.52	6
25	43.69	1162482.84	69.60	1561082.83	7
19	63.53	2135817.89	159.65	2668196.99	8
40	144.43	3237473.33	370.2	5706453.22	9
37	315.26	3985210.71	424.1	6339803.1	10

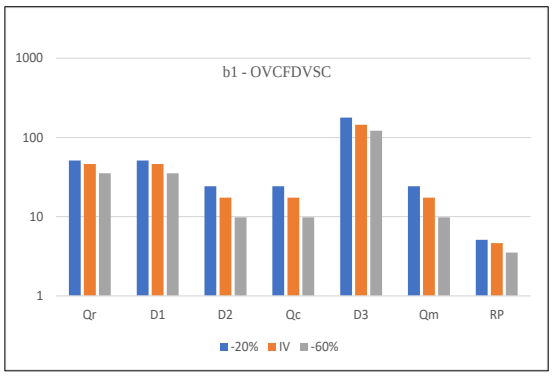

a-1. Optimal values of commodity flow for different values b1 for the first commodity

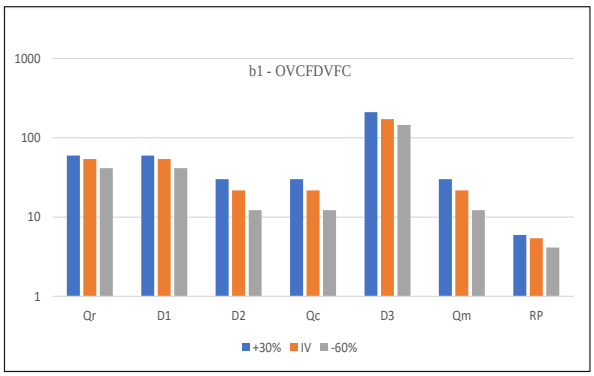

b-1. Optimal values of commodity flow for different values b1 for the second commodity

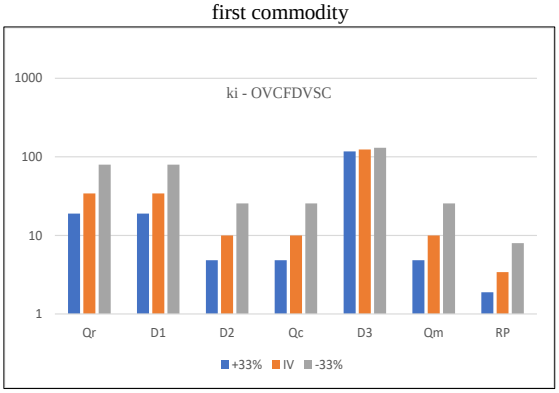

c-1. Optimal values of commodity flow for different values k_i for the first commodity

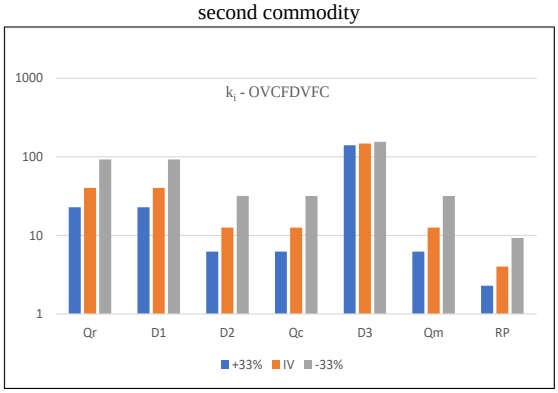

d-1. Optimal values of commodity flow for different values k_i for the second commodity

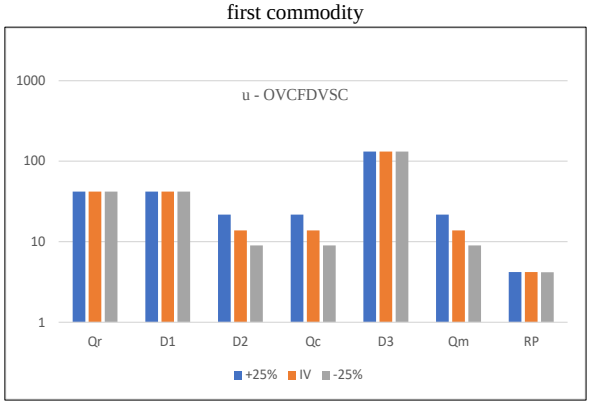

e-1. Optimal values of commodity flow for different values u for the first commodity

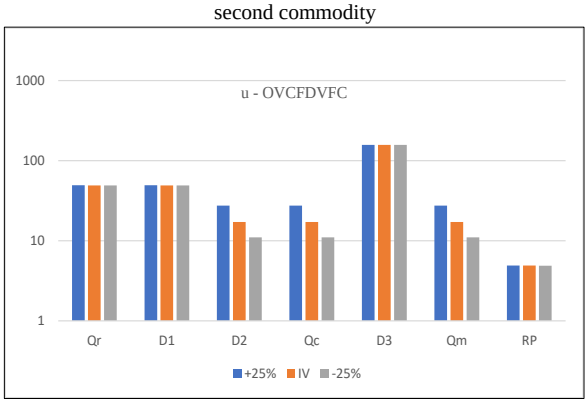

f-1. Optimal values of commodity flow for different values u for the second product

Figures 4. Sensitivity analysis

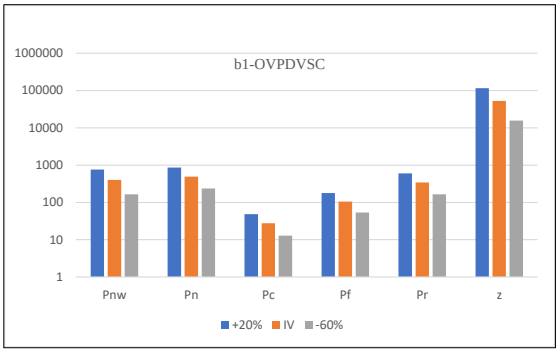

a-2. Optimal values of prices for different values of b1 for the first product

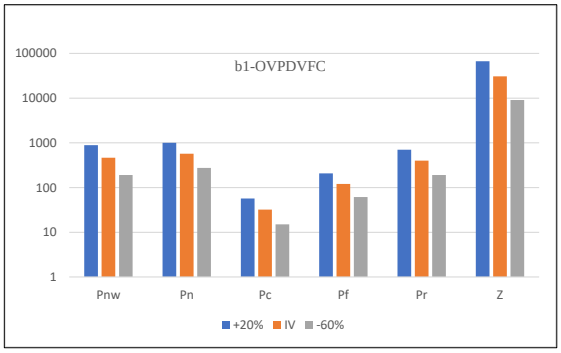

b-2. Optimal values of prices for different values of b1 for the second product

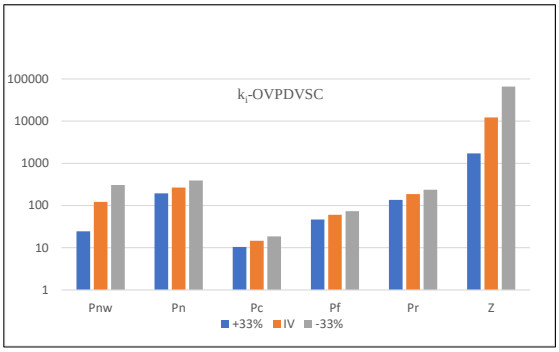

c-2. Optimal values of prices for different values of k_i for the first product

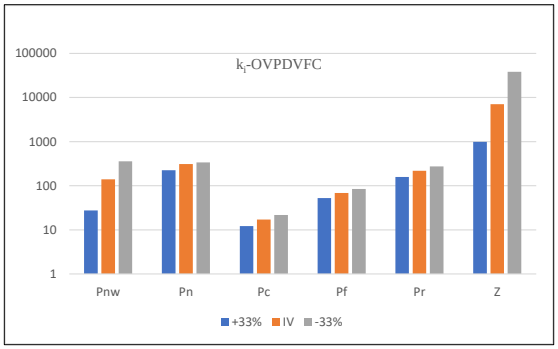

d-2. Optimal values of prices for different values of k_i for the second product

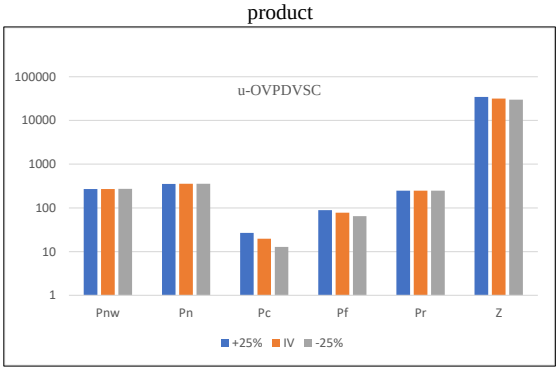

e-2. Optimal values of prices for different values of u for the first product

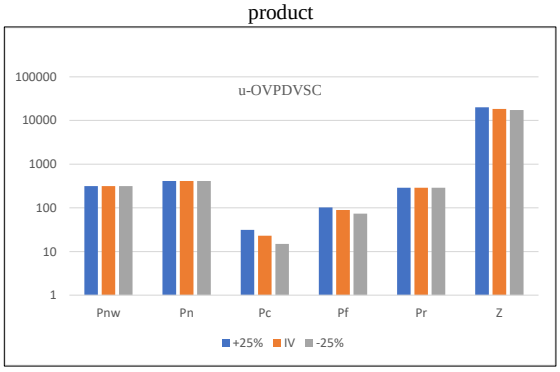

f-2. Optimal values of prices for different values of u for the second product

Figures 4. Sensitivity analysis

the supply chain. However, consumers' price sensitivity factor can reduce the profit of each component and ultimately, reduce the total profit of the closed-loop supply chain. Customer purchasing power also has a huge impact on the balance between products price and products flow.

6. MANAGERIAL INSIGHTS

In this article, the main objective is to design a supply chain with maximized profit. To achieve such a goal, the following strategies are utilized: optimal location of components, sale-purchase optimal pricing, capability to use used products, and capability to re-sell these products directly (online sale) to the customers.

Due to the importance of location and pricing in the creation or development of an economic activity, such as chain stores, this research is designed so that it can be a great help to the industry by preventing irrecoverable costs and resulting in economic growth. In the present article, the following managerial insights are suggested for more use:

1. Using the designed model (in this paper), the location of supply chain components (e.g., sale/purchase branches of a chain store throughout the country) can be determined by taking the population of each region, customers' distance to the sale branches, and collection centers into account.
2. In this research, determining the purchasing/sale price of products so that the most profit is gained by the chain components. Such a matter is one of the biggest concerns of industry owners. In this research, hence, the optimal price of supply chain components can be determined by taking predictions of customer demand into account, which is sensitive to product inventory costs.
3. Other factors that may help increase industry owners' revenue is the ability to reuse the used products by the customers and also, re-selling these products. In this article, collection centers consider a fair sale/purchase price that encourages the customers to sell their used products and creates a motivation to acquire collected products for the manufacturers. Moreover, a separate channel is taken into account for selling Reman products directly from the manufacturer to the customers without the interference of an intermediary.

7. RESULTS AND FUTURE RECOMMENDATIONS

A small numerical example is proposed in order to investigate the mathematical model accuracy and

credibility. Metaheuristic genetic algorithms (GA) and particle swarm optimization (PSO) were utilized to solve the model at a large scale and then, the results were compared with solutions at small scales in the accurate method (through RPD index). Moreover, the performance of both algorithms, PSO and GA, are compared (in terms of time required to reach a solution and RPD index) by changing the number of customers, retailers, collection centers, and the number of products. The result of comparing optimal quantities and time required to reach a solution shows the higher quality of the genetic algorithm compared to particle swarm optimization. In most cases, however, PSO reached a solution over a time, less than GA.

In this model, all the problem and demand parameters are considered deterministic. In future research, the non-deterministic model can be taken into consideration and solved with the aid of algorithms developed for non-deterministic models. In this article, a mathematical model is developed for the problem under the investigation, and carrying and inventory costs are only considered in sale and collection centers through the EOQ method. In the future, different inventory models will be taken into consideration and the best approach will be selected. The following recommendation can be given for future research:

- Considering perishable products or supplements
- Adding route-finding and vehicle type
- Considering multi-objective mathematical models and environmental considerations

8. REFERENCES

1. Pasternack, B.A., "Optimal pricing and return policies for perishable commodities", ***Marketing Science***, Vol. 4, No. 2, (1985), 166-176, https://doi.org/10.1287/mksc.4.2.166
2. Gan, S.-S., Pujawan, I.N. and Widodo, B., "Pricing decision for new and remanufactured product in a closed-loop supply chain with separate sales-channel", ***International Journal of Production Economics***, Vol. 190, (2017), 120-132, https://doi.org/10.1016/j.ijpe.2016.08.016
3. Batarfi, R., Jaber, M.Y. and Glock, C.H" ,.Pricing and inventory decisions in a dual-channel supply chain with learning and forgetting", ***Computers & Industrial Engineering***, Vol. 136, (2019), 397-420, https://doi.org/10.1016/j.cie.2019.07.034
4. Plastria, F. and Vanhaverbeke, L., "Maximal covering location problem with price decision for revenue maximization in a competitive environment", ***OR Spectrum***, Vol. 31, No. 3, (2009), 555-571, https://doi.org/10.1007/s00291-008-0158-z
5. Atabaki, M.S., Khamseh, A.A. and Mohammadi, M., "A priority-based firefly algorithm for network design of a closed-loop supply chain with price-sensitive demand", ***Computers & Industrial Engineering***, Vol. 135, (2019), 814-837, doi. https://doi.org/10.1016/j.cie.2019.06.054
6. Xu, J. and Zhu, Y., "Dynamic pricing model for the operation of closed-loop supply chain system", ***Intelligent Control and Automation***, Vol. 2, No. 4, (2011), 418-423, doi: 10.4236/ica.2011.24048 .
7. Chen, Z. and Sarker, B.R., "Integrated production-inventory and pricing decisions for a single-manufacturer multi-retailer system of deteriorating items under jit delivery policy", ***The International Journal of Advanced Manufacturing Technology***, Vol. 89, No. 5, (2017), 2099-2117, https://doi.org/10.1007/s00170-016-9169-0
8. Yaghin, R.G., "Integrated multi-site aggregate production-pricing planning in a two-echelon supply chain with multiple demand classes", ***Applied Mathematical Modelling***, Vol. 53, (2018), 276-295, https://doi.org/10.1016/j.apm.2017.09.006
9. Edalatpour, M. and Mirzapour Al-e-Hashem, S., "Simultaneous pricing and inventory decisions for substitute and complementary items with nonlinear holding cost", ***Production Engineering***, Vol. 13, No. 3, (2019), 305-315, https://doi.org/10.1007/s11740-019-0088٦-٣
10. Fahimnia, B., Sarkis, J., Dehghanian, F., Banihashemi, N. and Rahman, S., "The impact of carbon pricing on a closed-loop supply chain: An australian case study", ***Journal of Cleaner Production***, Vol. 59, (2013), 210-225, doi. https://doi.org/1/٠,١٠١٦j.jclepro.2013.06.056
11. Ahmadi-Javid, A. and Hoseinpour, P., "Incorporating location, inventory and price decisions into a supply chain distribution network design problem", ***Computers & Operations Research***, Vol. 56, (2015), 110-119, https://doi.org/10.1016/j.cor.2014.07.014
12. Fattahi, M., Mahootchi, M., Govindan, K. and Husseini, S.M.M., "Dynamic supply chain network design with capacity planning and multi-period pricing", ***Transportation Research Part E: Logistics and Transportation Review***, Vol. 81, (2015), 169-202, https://doi.org/10.1016/j.tre.2015.06.007
13. Kaya, O. and Urek, B., "A mixed integer nonlinear programming model and heuristic solutions for location, inventory and pricing decisions in a closed loop supply chain", ***Computers & Operations Research***, Vol. 65, (2016), 93-103, https://doi.org/10.1016/j.cor.2015.07.005
14. Ahmadzadeh, E. and Vahdani, B., "A location-inventory-pricing model in a closed loop supply chain network with correlated demands and shortages under a periodic review system", ***Computers & Chemical Engineering***, Vol. 101, (2017), 148-166, https://doi.org/10.1016/j.compchemeng.2017.02.027
15. Navazi, F., Sazvar, Z. and Tavakkoli-Moghaddam, R., "A sustainable closed-loop location-routing-inventory problem for perishable products", ***Scientia Iranica***, (2021), doi: 10.24200/SCI.2021.55642.4353 .
16. Ziari, M. and Sajadieh, M.S., "A joint pricing and network design model for a closed-loop supply chain under disruption (glass industry)", ***RAIRO-Operations Research***, Vol. 56, No. 1, (2022), 431-444, https://doi.org/10.1051/ro/2022002
17. Ahmadi, S. and Amin, S.H., "An integrated chance-constrained stochastic model for a mobile phone closed-loop supply chain network with supplier selection", ***Journal of Cleaner Production***, Vol. 226, (2019), 988-1003, https://doi.org/10.1016/j.jclepro.2019.04.132

Persian Abstract

چکیده

هدف اصلی از طراحی زنجیره تأمین، افزایش سودآوری است. بدین منظور در این مقاله، یک مدل جدید زنجیره تأمین حلقه بسته‌ی سه سطحی شامل تولیدکننده، خرده‌فروش و مراکز جمع‌آوری ارائه شده است. در این مدل برای اولین بار، با در نظر گرفتن کانالی مجزا و مستقل برای فروش کالاهای بازیافتی، سودآوری تولیدکننده افزایش خواهد یافت. به علاوه، در این مدل زنجیره تأمینِ جدید، مکان‌یابی و موجودی و قیمت‌گذاری کالا نیز در نظر گرفته شده است. سود تولیدکننده با در نظر گرفتن هزینه احداث مراکز خرده‌فروشی و جمع‌آوری کالاهای بازیافتی و در نظر گرفتن ظرفیت جریان کالا و سهم بازار محاسبه خواهد شد. برای حل تابع هدف غیر خطیِ سود تولیدکننده در ابعاد کوچک، از نرم‌افزار لینگو و در ابعاد بزرگ، از الگوریتم‌های فرا ابتکاری ژنتیک و تجمع ذرات استفاده شده است. نتایج حاصل از انجام این پژوهش نشان می‌دهد که طراحی مدل جدید زنجیره تأمین حلقه بسته دارای اعتبار است و مکان‌یابی بهینه‌ی اجزای زنجیره تأمین، پاسخ بهینه‌ی جریان کالاها و قیمت محصولات به درستی انجام شده است. در نتیجه، سودآوری کل شبکه زنجیره تأمین حلقه بسته افزایش یافته است. تحلیل حساسیت مدل ریاضی نیز نشان می‌دهد که این مدل نسبت به پارامترهای ضریب جایگزینی، قیمت و توان قیمت خرید مراکز جمع‌آوری، حساسیت بالایی دارد. همچنین در مقیاس بزرگ، الگوریتم ژنتیک از نظر کیفیت جواب، عملکرد بهتری دارد. اما زمان حل الگوریتم تجمع ذرات بسیار بهتر است. در انتها، با توجه به طراحی مدل جدید زنجیره تأمین حلقه بسته، پیشنهادات کاربردی برای مدیران نیز ارائه شده است.

International Journal of Engineering

Journal Homepage: www.ije.ir

Effect of Suspension System Stiffness on Dynamic Load Action Chassis Multi-purpose Forest Fire Fighting Vehicle

L. Van Van*, C. Hung Phi, N. Thanh Tung

Vinh Long University of Technology Education, 73, Nguyen Hue street, Vinh Long city, Vietnam

P A P E R I N F O

Paper history:
Received 01 April 2022
Received in revised 19 April 2022
Accepted 28 April 2022

Keywords:
Multimaterial Forest Fire Fighting Vehicle
Suspension System
Dynamic Load
Stiffness

A B S T R A C T

Multi-purpose forest fire fighting vehicles include a combination of fire fighting equipment such as a high-pressure water pump, create corridor fire insulation cutting machine, vacuum and high wind speed bowling machine, extinguish the fire sandblast apparatus that is mounted on the URAL 4320 active three axles vehicle. When installing fire fighting equipment on vehicles, increases the load, affecting the vehicle's load distribution, angularity, and stability. Therefore, to ensure structural rigidity, the suspension system is redesigned to increase rigidity. However, alteration of the suspension stiffness will change the dynamic load acting on the chassis. This research presents the results of research on the influence of suspension stiffness on dynamic loads acting on the chassis of a multi-purpose forest fire fighting vehicle. The survey results showed that an increasing the suspension stiffness will increase the dynamic load acting on the chassis, and reduce the durability of the chassis in particular and the details of the vehicle in general. The research outcomes are the basis for evaluating the working life of the chassis in subsequent studies.

doi: *10.5829/ije.2022.35.08b.13*

1. INTRODUCTION

According to statistics, Vietnam has about 10 million hectares of natural and planted forests. In the dry season, the potential risk is very high, leading to thousands of forest fires, causing great economic losses, and destroying the ecological environment of the country. The main method of forest fire fighting is to use rudimentary equipment such as hoes, consequently, the effectiveness of forest fire fighting is not high [1]. The multi-purpose forest fire fighting vehicle manufactured by Vietnam has improved the effectiveness of forest fire fighting, meeting the requirements in the process of fighting forest fires deep, far from water sources and residential areas (Figure 1). When designing and installing forest firefighting equipment on the vehicle, the vehicle's load increases, so the stiffness of the suspension must be increased so that the vehicle does not bevel compared to the original design. However, when changing the suspension stiffness, will affect the dynamic load acting on the chassis and other details on the vehicle, affecting the durability and working life of the part [1-4].

Automobile loads were studied in early automobile vibration research with the aim of reducing dynamic loads, and improving the destructive strength and long-term durability of automobile assemblies and components [5]. When the car moves on the road, there will be dynamic loads that destroy the road [6, 7], on the contrary, the road surface also reacts, causing dynamic loads to increase, tires to be worn, and dynamic safety is lost [8, 9].

When operating, the driver controls the vehicle by 3 actions: acting on the accelerator, brake, and steering wheel; the parameters shown are longitudinal acceleration, horizontal and vertical accelerations. Together with the weight of the vehicle, the above accelerations act on the wheel vertically through the suspension. From the roadside, activation by the bumpy road will cause the wheel to oscillate vertically, generating a dynamic load [5]. The maximum dynamic load will affect the breaking strength, cyclic dynamic loads will affect fatigue life. Dynamic load depends on

*Corresponding Author Institutional Email: vanlv@vlute.edu.vn (L. Van Van)

Please cite this article as: L. Van Van, C. Hung Phi, N. Thanh Tung, Effect of Suspension System Stiffness to Dynamic Load Action Chassis Multi-purpose Forest Fire Fighting Vehicle, ***International Journal of Engineering, Transactions B: Applications***, Vol. 35, No. 08, (2022) 1571-1578

(a)

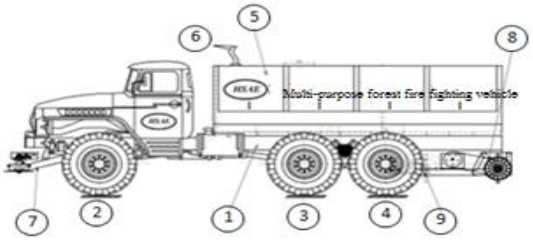

(b)

Figure 1. (a) Multi-purpose forest fire fighting vehicle (b) Overall multi-purpose forest fire fighting vehicle: 1. Vehicle, 2. front drive axle, 3. middle drive axle, 4. rear drive axle, 5. Water pump equipment, fire water tank, 6. water nozzle, 7. Equipment to cut trees, clean garbage, pave the way to create a fire isolation corridor, 8. Equipment to clean grass on the road, 9. Fire-fighting sandblasting equipment [1-3,5]

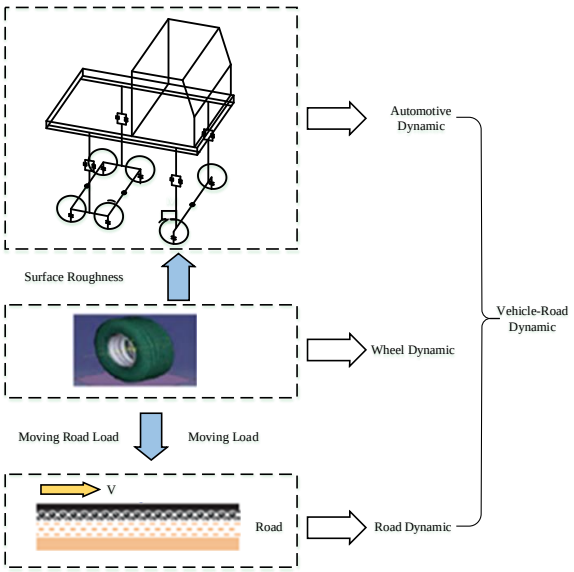

Figure 2. Tire-road interaction

vehicle structure including suspension stiffness, tire stiffness, influence from the roadside, and vehicle speed [10-12]. In order to reduce the dynamic load acting on the car, there are two research directions, namely the study of the suspension system and the study of the influence of the road. The investigtion on the influence of suspension stiffness was studied by the authors [13-16]. Dynamic load studies of multi-purpose forest fire fighting vehicles with research work have experimented to determine the dynamic load when the vehicle goes through the bump [17]. Other research works mainly on conventional vehicles. After being designed, the vehicle's load increases [1]; so to ensure rigidity, the suspension system is designed to increase rigidity to prevent the vehicle from tilting when fully loaded. When changing the suspension stiffness will affect the dynamic load acting on the chassis, Therefore, it is necessary to determine the dynamic load when the vehicle is working in order to serve as a scientific basis for completing the structure of the multi-purpose forest fire fighting vehicle.

2. RESEARCH CONTENT

2. 1. Build a Multi-purpose Forest Fire Fighting Vehicle Model Applying the object separation method, we build a mechanical model of the vehicle. The objects on the vehicle are defined as follows: Object 1 consists of masses that are not suspended on the front axle, symbol m_1; object 2 consists of masses that are not suspended on the middle axle, symbol m_2; object 3 consists of masses that are not suspended on the rear axle, symbol m3; Object 4 is a vehicle with a mass equal to m4, moments of inertia I4zx and I_{4zy}; Object 5 is a driving water pump with a mass equivalent to m5, moments of inertia I5zx, I_{5zy}; Object 6 is a fire sprinkler with a mass equivalent to m6, moments of inertia I_{6zx}, I_{6zy}; Object 7 includes the masses of the front tree cutting devices, symbol m7; Item 8 includes the mass of the grass cleaning equipment, symbol m_8; Object 9 includes the masses of sandblasting hoe equipment, symbol m_9; Object 0 is the line (background object).

To build the model, we have the following assumptions:

- The mass of the car is distributed symmetrically about the longitudinal plane;
- Since vehicles operating on hilly roads with large undulations are the main sources of oscillation excitation, the excitation source from the engine should be ignored;
- Ignore collisions with the elastic lugs of the suspension and wheel separation of the tires.

From the above analysis and construction of vehicle design drawings, we determine the parameters of the model including:

C_{1L}; C_{1R}; C_{2L}; C_{2R}; C_{3L}; C_{3R}: stiffness of the left and right tires of the front, middle and rear axles;

C_{4L}; C_{4R}; C_{5L}; C_{5R}; C_{6L}; C_{6R}: stiffness of left and right suspension elastic of the front, middle and rear axles;

C_{7L}; C_{7R}; C_{8L}; C_{8R}: stiffness of the left and right elastomers of the front and rear racks;

K_{1L}; K_{1R}; K_{2L}; K_{2R}; K_{3L}; K_{3R}: drag coefficient of left and right tires of the front, middle and rear axles;

K_{4L}; K_{4R}; K_{5L}; K_{5R}; K_{6L}; K_{6R}: drag coefficient of left and right suspension elastic of the front, middle and rear axles;

K_{7L}; K_{7R}; K_{8L}; K_{8R}: drag coefficient of left and right front and rear racks;

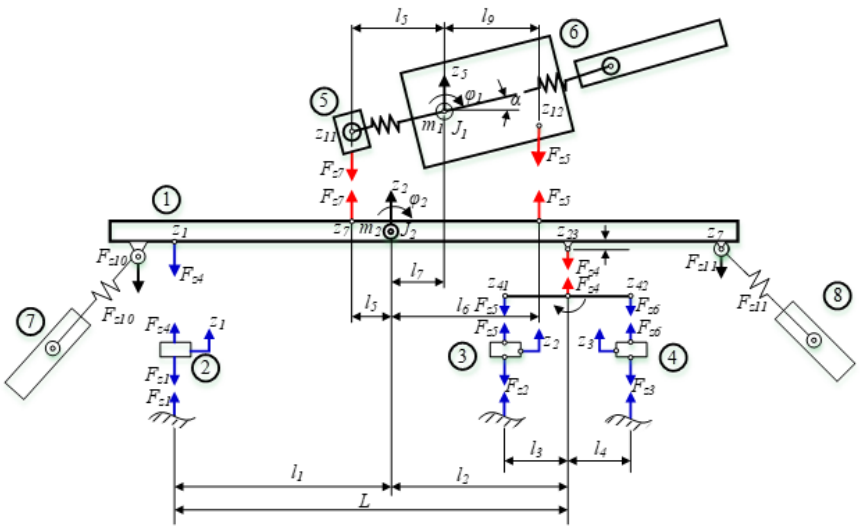

Figure 3. Multi-purpose forest fire fighting vehicle model: 1. Chassis of the vehicle; 2. Front axle; 3. Middle axle; 4. Rear axle; 5. Water pump for fire fighting; 6. Fire sprinkler; 7. Tree cutting structure creates a white corridor; 8. Lawn cleaning machine clears the way

q_{1L}; q_{1R}; q_{2L}; q_{2R}; q_{3L}; q_{3R}: left and right road profiles at the front, middle, and rear wheel;
Mct1: Torque of water pump components and sprinklers;
M_{ct2}: Resistance moment of white tape cutter components;
M_{ct3}: Resistance torque of rear lawn mower components;
M_{ct4}: Resistance moment of sand-generating equipment components.
l_1, l_2: Distance from the center of the vehicle to the center of the front axle and the connection point between the rear springs and the chassis.
l_3, l_4: Distance from the connection point between the rear springs and the chassis to the center of the middle and the rear axle.

2. 2. Set up the System of Equations to Balance the Force on the Vehicle Applying Dalambe's principle to each body whose origin is at the object's static equilibrium position, we have:

2. 2. 1. For the Front Axle The model of separation of objects on the front axle is depicted in Figure 4. Matlab Simulink is applied to solve the front axle force balance equation, the diagram is shown in Figure 5. Matlab Simulink is also applied to solve the force balance equation to determine the dynamic load acting on the chassis through the suspension system (Figure 6).

$$m_1\ddot{z}_1 = -F_{z1L} - F_{z1R} + F_{z4L} + F_{z4R} \quad (1)$$

$$I_{1zy}\ddot{\varphi}_{1zy} = \left(-F_{z1L} + F_{z1R}\right)d_1 + \left(-F_{z4L} + F_{z4R}\right)d_4 \quad (2)$$

2. 2. 2. For The Middle Axle The model of separation of objects on the middle axle is depicted in Figure 6. Matlab Simulink is applied to solve the force

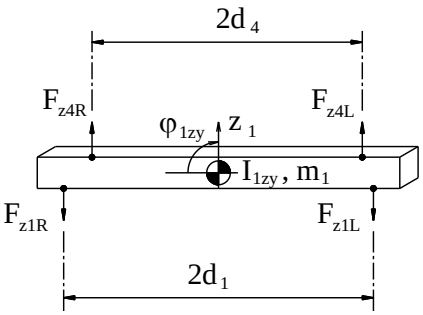

Figure 4. Object separation model of front axle

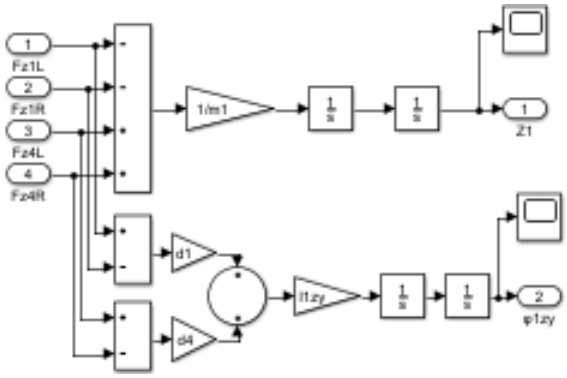

Figure 5. Simulink diagram to solve the front axle force balance equation

balance equation to determine the dynamic load acting on the chassis through the suspension system (Figure 7).

$$m_2\ddot{z}_2 = -F_{z2L} - F_{z2R} + F_{z5L} + F_{z5R} \quad (3)$$

$$I_{2zy}\ddot{\varphi}_{2zy} = \left(-F_{z2L} + F_{z2R}\right)d_2 + \left(-F_{z5L} + F_{z5R}\right)d_5 \quad (4)$$

2. 2. 3. For the Rear Axle The model of separation of objects on the rear axle is depicted in Figure 8. Matlab Simulink is applied to solve the force balance equation to determine the dynamic load acting on the chassis through the suspension system (Figure 9).

$$m_3\ddot{z}_3 = -F_{z3L} - F_{z3R} + F_{z6L} + F_{z6R} \quad (5)$$

$$I_{3zy}\ddot{\varphi}_{3zy} = \left(-F_{z3L} + F_{z3R}\right)d_3 + \left(-F_{z6L} + F_{z6R}\right)d_6 \quad (6)$$

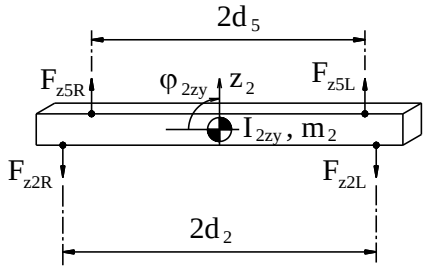

Figure 6. Object separation model of middle axle

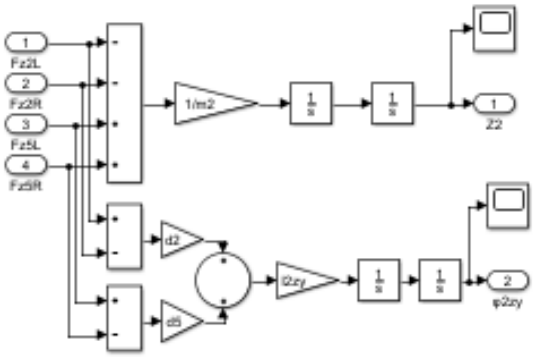

Figure 7. Simulink diagram to solve the middle axle force balance equation

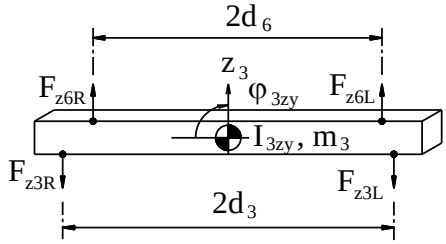

Figure 8. Object separation model of rear axle

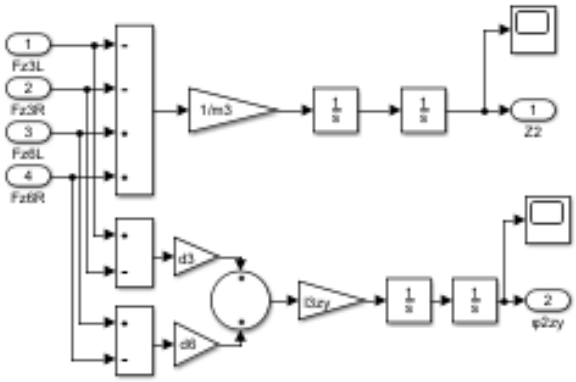

Figure 9. Simulink diagram to solve the rear axle force balance equation

2. 2. 4. For Vehicle Similarly, we can build the object separation model for the vehicle and build the vehicle's force balance equations.

$$m_4\ddot{z}_4 = -F_{z4L} - F_{z4R} + F_{z7L} + F_{z7R} + F_{z8L} + F_{z8R} \quad (7)$$

$$I_{4zx}\ddot{\varphi}_{4zx} = \left(F_{z4L} + F_{z4R}\right)l_1 - \left(F_{z7L} + F_{z7R}\right)l_5 + \left(F_{z8L} + F_{z8R}\right)l_6 \quad (8)$$

$$I_{4zy}\ddot{\varphi}_{4zy} = \left(F_{z4L} - F_{z4R}\right)d_4 + \left(F_{z7L} - F_{z7R}\right)d_6 + \left(F_{z8L} - F_{z8R}\right)d_7 \quad (9)$$

2. 2. 5. For Water Pump Drive Similarly, we can build the object separation model for water pump drive and build the vehicle's force balance equations.

$$m_5\ddot{z}_5 = -F_{z7L} - F_{z7R} + F_{z9} \quad (10)$$

$$I_{5zx}\ddot{\varphi}_{5zx} = \left(F_{z7L} + F_{z7R}\right)l_{12} + F_{z9}l_9 \quad (11)$$

$$I_{5zy}\ddot{\varphi}_{5zy} = \left(-F_{z7L} + F_{z7R}l_{12}\right)d_6 + M_{ct} \quad (12)$$

2 .2. 6. For Sprinklers Similarly, we can build the object separation model for sprinklers and build the vehicle's force balance equations.

$$m_6\ddot{z}_6 = F_{z8L} + F_{z8R} + F_{z9} \quad (13)$$

$$I_{6zx}\ddot{\varphi}_{6zx} = -\left(F_{z8L} + F_{z8R}\right)l_{11} + F_{z9}l_{10} \quad (14)$$

$$I_{6zy}\ddot{\varphi}_{6zy} = \left(-F_{z8L} + F_{z8R}\right)d_7 \quad (15)$$

2. 3. Surveying The Force Balance Model on a Multi-purpose Forest Fire Fighting Vehicle

2. 3. 1. Determine the Parameters of the Model The parameters of the vehicle model are summarized in Table 1 [1, 4].

TABLE 1. Parameters of multi-purpose forest fire fighting vehicle

Order	Technical	Symbol	Unit	Value
1	Front axle mass	m_1	kg	1020
2	Middle axle mass	m_2	kg	1000
3	Rear axle mass	m_3	kg	1000
4	Vehicle mass	m_4	kg	5800
5	Water pump mass	m_5	kg	250
6	Fire sprinkler mass	m_6	kg	1500
7	Stiffness of front wheel tire	C_{L1}	N/m	569964
8	Stiffness of middle wheel tire	C_{L2}	N/m	569964
9	Stiffness of rear wheel tire	C_{L3}	N/m	569964
10	Damping coefficient of front wheel tire	K_{L1}	N.s/m	6497
11	Damping coefficient of middle wheel tire	K_{L2}	N.s/m	6497
12	Damping coefficient of rear wheel tire	K_{L3}	N.s/m	6497
13	The stiffness of front axle suspension without changing stiffness	C_{4B}	N/m	203000
14	The stiffness of middle axle suspension without change stiffness	C_{5B}	N/m	322000
15	The stiffness of rear axle suspension without changing stiffness	C_{6B}	N/m	322000
16	The stiffness of front axle suspension with change stiffness	C_{4A}	N/m	401952
17	The stiffness of middle axle suspension with change stiffness	C_{5A}	N/m	527042
18	The stiffness of rear axle suspension with change stiffness	C_{6A}	N/m	527042
19	Damping coefficient of the front axle	K_4	N.s/m	18900
20	Damping coefficient of middle axle	K_5	N.s/m	18900
21	Damping coefficient of the rear axle	K_6	N.s/m	18900
22	The stiffness of the front bearing	C_7	N/m	203000
23	The stiffness of the rear bearing	C_8	N/m	203000
24	Damping coefficient of the front bearing	K_7	N.s/m	18900
25	Damping coefficient of the rear bearing	K_8	N.s/m	18900

2. 3. 2. Determining the Forest Ground Bump

The purpose of determining the forest ground bump is to serve as an input parameter to determine the dynamic load acting on the chassis. To determine the bump of the forest ground, we must carry out a test. The method of determination is to use the number 2 wheel with an accelerometer sensor to determine the acceleration, then use Dasylab 5.0 software to determine the forest ground elevation.

In order to be able to accurately determine the position of the bumps according to the contour, a Kistler accelerometer must be used, speed sensor V_1, the device that receives and processes measurement data is a computer DEWETRON 3000. During the movement, the vehicle will pull wheel No. 2 rolling on the forest ground, the wheel axle will record the correct forest ground profile and the Kistler sensor will record the acceleration value and transfer it to the computer for processing. Coinstantaneous with the signal of the accelerometer sensor is a signal from the sensor from V_1 to measure the actual moving speed of the vehicle. Thus, at the specified location of the forest ground profile, the bumpy height at that location can be determined.

2. 3. 3. Survey Results of Dynamic Load Assessment

Using Matlab Simulink, we survey and determine the force acting on the chassis when the

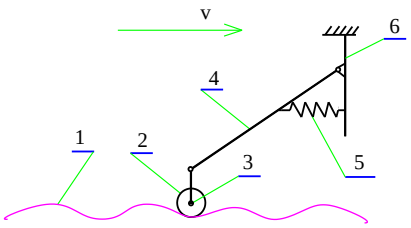

Figure 10. Describe the diagram to determine the bump on the forest ground. *1- Forest ground; 2- wheel 2; 3- Kistler sensor mounting position; 4- link bar; 5- spring; 6- car mount*

Figure 11. Measurement of forest ground bump

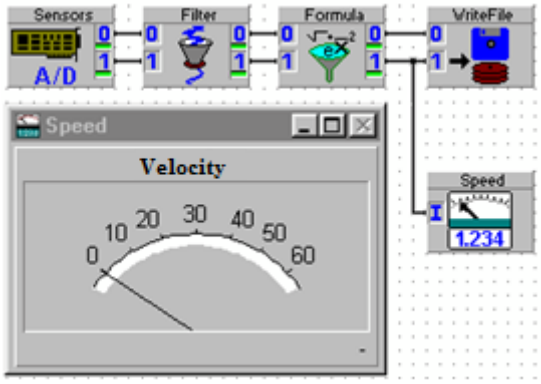

Figure 12. Forest ground measurement program

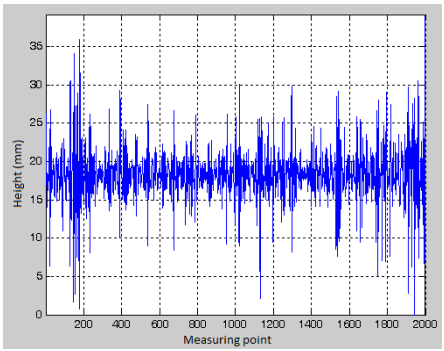

Figure 13. Experimental road surface bump

vehicle moves on the forest road at different moving speeds. In this survey, the author investigates the corresponding suspension stiffness of the base vehicle and the suspension stiffness when it is designed into a forest fire truck to evaluate the dynamic load change. Due to the working characteristics of forest fire trucks with low travel speed [1], the speed of survey vehicles is from 10 km/h to 20 km/h.

When the vehicle is in motion, due to the excitation force of the road surface contour, the dynamic load is applied to the chassis as described in Figures 15 and 16. With a vehicle speed of 10 km/h, the value of the dynamic load acting on the chassis is relatively equal when the suspension stiffness changes. Without changing the suspension stiffness, the maximum dynamic load value on the rear axle is 54833 N, when changing the suspension stiffness, the maximum dynamic load on the rear axle is 58383 N. The maximum dynamic load value when increasing the stiffness is 1.06 times higher than when the hardness is not changed.

When the vehicle speed increases, the excitation force from the road surface causes an increase in dynamic load, making the value of the dynamic load acting on the chassis also increase compared to the case of the vehicle traveling at 10 km/h, described in Figures 16 and 17. With a vehicle speed of 15 km/h, without changing the suspension stiffness, the maximum dynamic load value

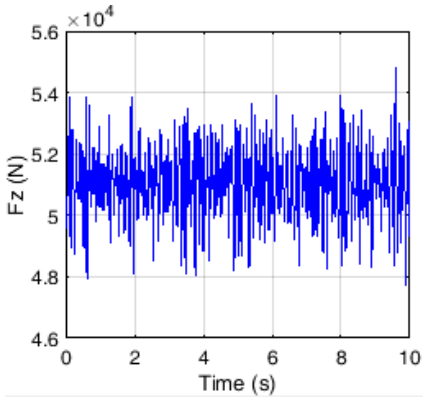

Figure 14. Dynamic load acting on the chassis at the rear axle, v = 10 km/h, C_4 = 203000 N/m, $C_{5,6}$ = 322000 N/m

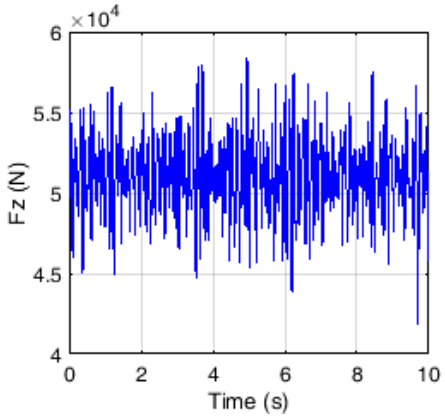

Figure 15. Dynamic load acting on the chassis at the rear axle, v = 10 km/h, C_4 = 401952 N/m, $C_{5,6}$ = 527042 N/m

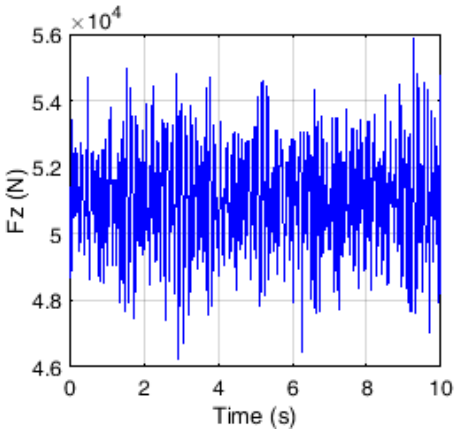

Figure 16. Dynamic load acting on the chassis at the rear axle, v = 15 km/h, C_4 = 203000 N/m, $C_{5,6}$ = 322000 N/m

on the rear axle is 55873 N, with changing the suspension stiffness, the maximum dynamic load on the rear axle is 61912 N. The maximum dynamic load value when increasing the stiffness 1.08 times compared to the original suspension stiffness.

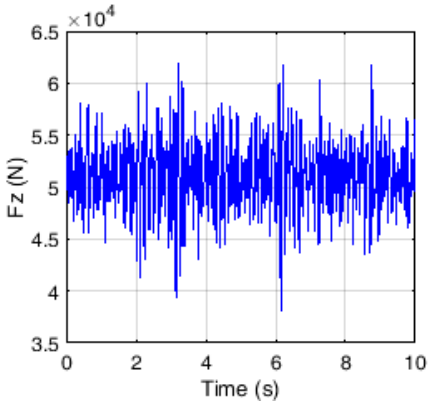

Figure 17. Dynamic load acting on the chassis at the rear axle, v = 15 km/h, C_4 = 401952 N/m, $C_{5,6}$ = 527042 N/m

When the fire fighting vehicle moves at a speed of 20 km/h, without changing the suspension stiffness, the maximum dynamic load value on the rear axle is 58016 N, with changing the suspension stiffness, the maximum dynamic load value on the rear axle is 62225 N. The maximum dynamic load value when increasing the stiffness 1.07 times compared to the original suspension stiffness. The maximum dynamic load acting the chassis without changing and changing the suspension stiffness is summarized in Table 2.

Figures 20 and 21 describe the maximum dynamic load value acting on the chassis at the front and rear axles. The results show that when increasing the suspension stiffness and vehicle movement speed, the dynamic load increases, which is consistent with the laws of physics.

TABLE 2. Maximum dynamic load acting the chassis without changing and changing the suspension stiffness

Vehicle speed	Maximum dynamic load front axle (N)		Maximum dynamic load rear axle (N)	
	C_{1B} = 203000	C_{2B} = 322000	C_{1A} = 401952	C_{2A} = 527042
10 km/h	31960	34109	54833	58383
15 km/h	32603	35654	55873	61912
20 km/h	33405	36251	58016	62225

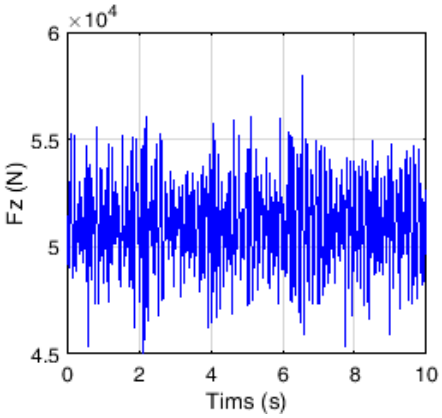

Figure 18. Dynamic load acting on the chassis at the rear axle, v = 20 km/h, C_4 = 203000 N/m, $C_{5,6}$ = 322000 N/m

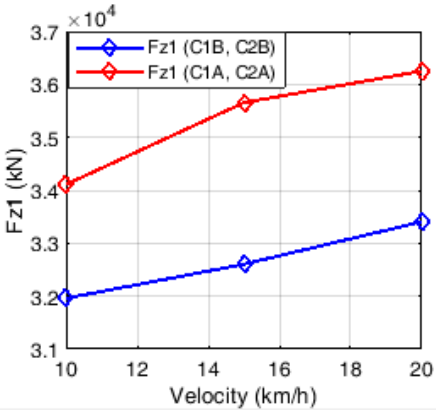

Figure 20. Maximum dynamic load acting on the chassis front axle, v = 10 ÷ 20 km/h

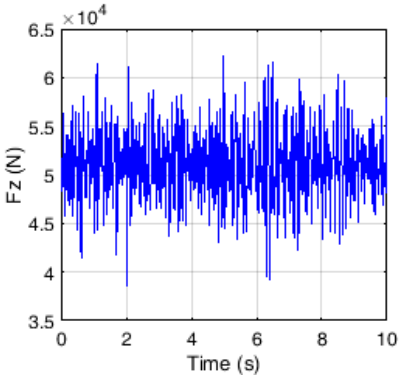

Figure 19. Dynamic load acting on the chassis at the rear axle, v = 20 km/h, C_4 = 401952 N/m, $C_{5,6}$ = 527042 N/m

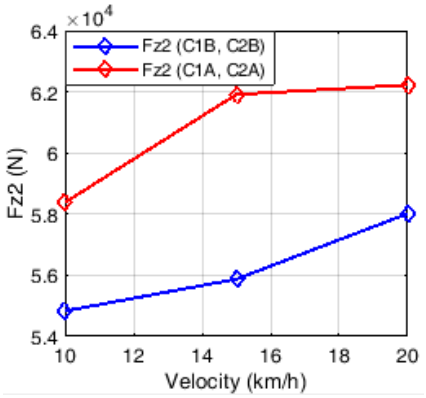

Figure 21. Maximum dynamic load acting on the chassis rear axle, v = 10 ÷ 20 km/h

3. CONCLUSION

The base vehicle URAL 4320 vehicle with permissible payload according to the manufacturer's design is used to make a multi-purpose forest fire truck with enhanced payload, operating on forestry roads with complex terrain. The calculation to determine the force acting on the frame close to the base car to ensure durability when converting the vehicle's features is necessary. The content of the study used the method of separation of objects according to Dalambe's principle and build force balance equations and apply Matlab Simulink to solve. The study will be expanded to fully investigate the operating conditions of the vehicle corresponding to the installation of fire fighting equipment with more uses to improve the effectiveness of forest fire fighting.

4. REFERENCES

1. Duong, T., "Research technology and design and manufacture specialized equipment for forest fire fighting", ***National scientific and Technological Topics KC07***, Vol. 13, (2010), 06-10.
2. Vạn, L.V., "Effect of suspension system stiffness to dynamic load action chassis multi-purpose forest fire fighting vehicle", ***International Journal of Engineering***, ***Transactions B: Applications***, Vol. 35, No. 8, (2022), doi: 10.5829/IJE.2022.35.08B.13.
3. Nguyen, X., "Research dynamics of multi-purpose forest fire fighting vehicle", Doctoral thesis Technology, Vietnam National University of Forestry, (2013),
4. Tung, N., Van, L. and Quang, N., "A survey on the effects of bumpy road on the vibration of multi-purpose forest fire fighting vehicle", ***Engineering Solid Mechanics***, Vol. 9, No. 3, (2021), 291-298, doi: 10.5267/j.esm.2021.3.001.
5. Mitschke, M. and Wallentowitz, H., "Dynamik der kraftfahrzeuge, Springer, Vol. 4, (1972).
6. Thanh Tung, N., "Experimental analysis for determination of longitudinal friction coefficient function in braking tractor semi-trailer", ***International Journal of Engineering, Transactions A: Basics***, Vol. 34, No. 7, (2021), 1799-1803, doi: 10.5829/ije.2021.34.07a.24.
7. Xu, H., He, L. and An, D., "Study on the vehicle dynamic load considering the vehicle-pavement coupled effect", in IOP Conference Series: Materials Science and Engineering, IOP Publishing. Vol. 269, (2017), 012001.
8. Tung, N.T. and Van, L.V., "A study on the effects of tire vertical stiffness on dynamic load of dvm 2.5 truck", in International Conference on Engineering Research and Applications, Springer. (2021), 128-134.
9. Davis, L. and Bunker, J., "In-service testing of heavy vehicle suspensions-background report for the ntc project", (2008).
10. Andreasson, N.P.J., Woodruff, M.G.A. and Modelon, A., "Heavy vehicles modeling with the vehicle dynamics library", (2008).
11. Szurgott, P., Kwasniewski, L. and Wekezer, J.W., "Dynamic interaction between heavy vehicles and speed bumps", in ECMS., (2009), 585-591.
12. Tianjun, Z. and Changfu, Z., "Modelling and active safe control of heavy tractor semi-trailer", in 2009 Second International Conference on Intelligent Computation Technology and Automation, IEEE. Vol. 2, (2009), 112-115.
13. Davis, L. and Bunker, J., "Heavy vehicle suspension testing and analysis-dynamic load sharing", (2009).
14. Li, L., Song, J., He, L., Zhang, M. and Li, H., "Life prediction based on transient dynamics analysis of van semi-trailer with air suspension system", ***Chinese Journal of Mechanical Engineering-English Edition***, Vol. 24, No. 3, (2011), 372.
15. Elischer, M. and BRUZSA, L.L., "Dynamic wheel loads of heavy vehicles–preliminary analysis", ARRB Group Ltd Australia, (2012).
16. Misaghi, S., Nazarian, S. and Carrasco, C., "Impact of truck suspension and road roughness on loads exerted to pavements", The University of Texas, FHWA, El Paso, (2010).
17. Nguyen, T.Q., Le, H.Q., Tran, P.H., Nguyen, X.H. and Van, T.T., "Determination of dynamic loads from the road surface acting on the chassis by experimental methods", in IOP Conference Series: Materials Science and Engineering, IOP Publishing. Vol. 886, (2020), 012008.

Persian Abstract

چکیده

وسایل نقلیه آتش نشانی جنگلی چند منظوره شامل ترکیبی از تجهیزات آتش نشانی مانند پمپ آب فشار قوی، ایجاد دستگاه برش عایق آتش راهرو، دستگاه بولینگ وکیوم و سرعت باد بالا، اطفاء دستگاه سندبلاست آتش نشانی که بر روی URAL 4320 نصب شده است. وسیله نقلیه سه محور فعال هنگام نصب تجهیزات آتش نشانی بر روی وسایل نقلیه، بار را افزایش می دهد و بر توزیع بار، زاویه و پایداری خودرو تأثیر می گذارد. بنابراین، برای اطمینان از استحکام ساختاری، سیستم تعلیق برای افزایش استحکام دوباره طراحی شده است. با این حال، تغییر سفتی سیستم تعلیق باعث تغییر بار دینامیکی بر روی شاسی می شود. این تحقیق نتایج تحقیق در مورد تأثیر سختی تعلیق بر بارهای دینامیکی وارد بر شاسی یک وسیله نقلیه آتش نشانی جنگلی چند منظوره را ارائه می دهد. نتایج بررسی نشان می دهد که افزایش سفتی سیستم تعلیق باعث افزایش بار دینامیکی وارد بر شاسی و کاهش دوام شاسی به طور خاص و جزئیات خودرو به طور کلی می شود. نتایج تحقیق مبنایی برای ارزیابی عمر کاری شاسی در مطالعات بعدی است.

International Journal of Engineering

Journal Homepage: www.ije.ir

A Constraint Programming Approach to Solve Multi-skill Resource-constrained Project Scheduling Problem with Calendars

R. Nikaeen[a,b], A. A. Najafi*[a]

[a] *Faculty of Industrial Engineering, K. N. Toosi University of Technology, Tehran, Iran*
[b] *System Engineering Department, École de technologie supérieure, Montreal, Canada*

PAPER INFO

Paper history:
Received 05 Januarary 2022
Received in revised form 12 April 2022
Accepted 17 April 2022

Keywords:
Multi-skill
Project Scheduling
Constraint Programming
Mathematical Programming

ABSTRACT

The multi-skill resource constrained project scheduling is an important and challenging problem in project management. Two key issues that turn this topic into a challenging problem are the assumptions that are considered to approximate the model to a real-world problem and exact solution approach for the model. In this paper, we deal with this two issues. To consider real-word situations, we take into account calendars specifying time intervals during which the resources are available. We proposed a constraint programming approach to solve the problem exactly. The problem with and without resource calendars are modeled with mathematical programming (MP) and constraint programming (CP). In addition, the performance of CP approach is evaluated by comparing Time-Indexed Model (TIM) and Branch and Price (B&P) approaches. Computational results show that the proposed approach can efficiently solve real-size instances.

doi: *10.5829/ije.2022.35.08b.14*

1. INTRODUCTION

Project scheduling is one of the most influential subjects in project management. Project scheduling consists of finding a scheduling pattern for all the activities and the constraint satisfaction simultaneously in order to optimize an objective function of the problem. In order to consider the realistic features which often occur in project scheduling problem in the real world and approximate the actual problem, many assumptions are taken into consideration in resource constrained project scheduling problem (RCPSP) [1-6]. One of these assumptions which is having an influential effect on executing a project is resource calendar constraint. The calendar constraint plays a significant role in project scheduling problems and has many applications in real-life cases. Recently, some of the investigations focus on project scheduling problems with calendars. Franck et al. [7] addressed the problem of scheduling the activities of a project subject to calendar constraints. They presented efficient algorithms for computing the earliest and latest start and completion times of activities. Kreter et al. [8] extended the RCPSP by the concept of break-calendars by considering the possibility of the absence of renewable resources. Ahmadpour and Ghezavati [9] proposed a new mathematical model for the RCPSP under uncertainty in which the resources are not available at any time.

Each resource in RCPSP masters only one skill to execute an activity and each activity needs one skill to be executed, while in a real situation each resource has one or more skills. When the resources are multi-skill, not only it is important to choose which of the resources to be assigned to each activity but also the skill with which they contribute to each activity [10]; that is called Multi-skill Resource-Constrained Project Scheduling Problem (MS-RPSP). Considering the resources as multi-skill, leads the MS-RCPSP to become more complex than RCPSP [11]. Approaching this problem having another perspective we could consider MS-RCPSP as an extension of RCPSP, because the formulation of RCPSP can be used in order to illustrate a MS-RCPSP, but MS-RCPSP is more complex than RCPSP.

*Corresponding Author Institutional Email: aanajafi@kntu.ac.ir (A. A. Najafi)

Please cite this article as: R. Nikaeen, A. A. Najafi, A Constraint Programming Approach to Solve Multi-skill Resource-constrained Project Scheduling Problem with Calendars, ***International Journal of Engineering, Transactions B: Applications***, Vol. 35, No. 08, (2022) 1579-1587

One of the challenging features in project scheduling problems is finding the optimum allocation of the resources. Using the multi-skill resources brings about advantages such as flexibility in scheduling that causes improvement in productivity, decreasing the idle time of resources, and reducing the labor cost. These advantages caused the researchers to use multi-skill resources in their research. The primary investigations in this field were conducted by Bellenguez-Morineau and Neron [12].

The solution techniques that are used in MS-RCPSP are divided into two categories, heuristic and meta-heuristic approaches besides exact approaches. The articles that have proposed the former category for MS-RCPSP are as follows: Avramidis et al. [13] studied an agent scheduling problem in which each agent has a selected number of skills and the agents are differentiated by the set of call types they can do. The goal is to minimize the total cost of the project. Cai and Li [14] proposed a multi-criteria model to formulate the staff scheduling problem with multiple skills and solved the problem with a meta-heuristic approach. Wongwai and Malaikrisanachalee [15] firstly prioritized the tasks then they allocated the resources to the tasks regarding the priorities created at the former step. In case of inadequate resources an activity cannot be commenced, therefore, the activity uses the resource of other activities with lower priorities. Walter and Zimmermann [16] deals with a multi-skill project scheduling problem and consider the skills as hierarchical levels, and the objective is to minimize the average project team size and satisfy the requirements of the project and the departments. The most important articles which proposed an exact solution for MS-RCPSP are as follows: In the survey by Heimerl and Kolisch [17] the skills are considered as hierarchical levels, therefore, every resource can have a high level of skill that helps them to be able to execute activities faster or in higher quality relative to the other resources. Furthermore, in the investigation by Bellenguez-Morineau and Néron [12] also the skills are considered in hierarchical levels. A review paper was published in the field of MS-RCPSP by De Bruecker et al. [18] that would be useful for the readers.

In this paper, staffing and scheduling problems with multi-skill resources are considered and the resource calendars are added to the problem. As mentioned before, calendar constraints are taken into account in RCPSP because the resource calendar has a significant role in real applications of scheduling problems. This assumption could be more important for MS-RCPSP because in MS-RCPSP each activity needs the set of skills to be executed and these skills must be assigned to one human resource that masters one of the required skills. For each activity, if any of its required resources become unavailable, that activity cannot start until all of its required resources become available. So the MS-RCPSP with calendar constraint is more complex than RCPSP with this assumption. Another contribution of the current research in solution approach is a CP model developed for solving the MS-RCPSP with and without Calendar constraints. Besides the developed CP models, two mathematical models are provided for comparison with the results of CP models.

The rest of this paper is organized as follows: In section 2 the problem is defined mathematically and sets, notations, parameters, and assumptions are explained. The third and fourth sections respectively describe the MP and CP models. In section 5 the experimental results are presented and two models were compared. Finally, in section 6 we conclude the paper and present our perspective of future studies.

2. PROBLEM DESCRIPTION

To describe the problem first consider a project that contains the set A of activities, where each activity has to be processed without preemption to complete the project. The project resources master the set k of skill and each activity needs also one or more skills to be executed, the project is represented by an activity on node network $N = (A, E)$ where E represents the direct successor of the activities, Activities 0 and $n+1$ are dummy and represent the beginning and the end of the project, the network is acyclic and the weight of an arc$(i, j) \in E$ is equal to the processing time of activity i. For executing each of the activities, the set of skills that are needed by that activity must be simultaneously accomplished, the number of these operations are fixed at the project and all of the operations must be executed during the project.

To the best of our knowledge, all researches in MS-RCPSP consider the resources available at any time during the project execution; however, at the real condition sometimes some resources could not be accessed, hence considering the resource calendar will be worthwhile. Off-work days including weekends and holidays are having a significant effect on the project execution time due to the fact that human resources would not be available during these days. The consideration of a resource calendar is necessary for many operative MS-RCPSP applications in which manpower are required.

In fact, each resource has its own specific time calendar during the project. Therefore taking the time calendar into account for each of the resources at the scheduling phase plays a significant role in controlling the budget and executing the project according to the scheduling plan. To diminish the disruptive effect of the off days, it is highly desired to distinguish the interruptible and non interruptible activities. For instance, non-interrupting task such as heating which takes 5 work days cannot be commenced on Thursday morning; hence, to be assured of having it executed

continuously, it has to be started on days between Monday and Thursday.

In this paper mathematical equalities similar to Montoya et al. [19] have been proposed, however, some inequalities have been added to the model for defining calendar for each resource. After defining the mathematical model, the substructure of constraint programming has been drawn out and the CP model is proposed.

2. 1. Problem Statement The sets and parameters that use for the models are listed below:

A	:	The set of activities, i=0,1,…,n+1
R	:	The set of resources, j=1,2,…,$\|R\|$
K	:	The set of skills, k=1,2,…,$\|K\|$
T	:	The set of time periods, t=1,2,…,$\|T\|$
p_i	:	Processing time of activity i
ES_i	:	The earliest start of activity i
LS_i	:	The latest start of activity i
E_i	:	The set of direct successors of activity i
$b_{i,k}$	:	The number of workers mastering skill k needed for performing activity i
RS_j	:	The set of skills that resources j master it
AS_i	:	The set of skills that activity i need it

$TM_{j,t}$ and $w^i_{j,t}$ are considered to define the resource calendar. $TM_{j,t}$ is a binary variable and shows the availability of the resources in each time period and $w^i_{j,t}$ determines the feasibility of assigning resource j to activity i at time period t. For instance, resource 2 at 5th and 6th days of each week is on vacation, so for the t= 1, 2, 3, 4 and 7, $TM_{2,t}$ equals 1. Now, consider that we are at the third day of the project and activity 3 with a processing time of 4 is possible to be executed at time 3, due to the assumption of non-preemptive activities, assignment of resource 2 to activity 3 at time 3 is impossible, because after 2 working days the resource is unavailable, so the value of $w^3_{3,2}$ equals 0.

All resources which are used during the project are renewable which means that, under consideration of the resource calendar, each resource is available after completion of the operation which is assigned to the resource. Requirements of the resources are expressed in a matrix $AS_{i,k}$ and also $O_{j,k}$ and $AL_{i,k,j}$ define the all operation of the project and all doable assignments, respectively. To attain the solution, all the operations must be taken into account but some rows could be optional in the matrix of $AL_{i,k,j}$.

2. 2. Assumptions The list of assumptions that must be enumerated to complete the explanation of our framework are:

- The problem consists of a set of non-pre-emptive activities.
- All resources are non-renewable and each of them could not execute more than one operation at a time.
- The set of skills that are needed by each activity must be executed simultaneously.
- Each resource has a specific calendar and the availability of each resource during the project are different.
- All parameters and variables are considered an integer.

3. MATHEMATICAL PROGRAMMING

We define four binary decision variables: $w^i_{j,t}$ determines the feasibility of assigning resource j to activity i at time t, z_i^t which takes the value 1 if an activity i starts at time t, x_{ij}^t states if worker j starts activity i at time t and y_{ijk} which takes the value 1 if worker j uses skill k to perform activity i. The main elements of the model is as follows:

- **Precedence relationships**

The relation between the activities are represented by Equation (1).

$$\sum_{t=ES_i}^{LS_i} tz_i^t + p_i \le \sum_{t=ES_j}^{LS_j} tz_j^t \quad \forall i \in A \ , \ \forall j \in E_i \tag{1}$$

- **Resource constraint**

Equation (2) states that if each resource is available in the specific time window, it can start an activity at most once, during the time window. Equation (3) ensures that each resource can execute at most one activity at each time period.

$$\sum_{t=ES_i}^{LS_i} x_{ij}^t \le 1 \qquad \forall i \in A \ , \ \forall j \in R \tag{2}$$

$$\sum_{i=1}^{n} \sum_{d=\max\{ES_i, t-p_i+1\}}^{\min\{LS_i, t\}} x_{ij}^d \le 1 \quad \forall j \in R, \ \forall t \in T \tag{3}$$

- **Resource calendar**

Constraints (4-6) guarantees that each resource can carry out each activity just during its specified calendar.

$$\left\lceil \frac{\sum_{d=t}^{t+p_i-1} TM_{j,d}}{p_i} \right\rceil = w_{i,j}^t \quad \forall t \in \mathrm{T},\ \forall i \in A,\ \forall j \in R \tag{4}$$

$$w_{i,j}^t * x_{i,j}^t \le z_i^t \quad \forall t \in \mathrm{T},\ \forall i \in A,\ \forall j \in R \tag{5}$$

$$w_{i,j}^t * x_{i,j}^t + 1 \ge z_i^t + \sum_{\forall k \in AS_{i,k}} y_{i,j,k} \quad \forall t \in \mathrm{T},\ \forall i \in A,\ \forall j \in R \tag{6}$$

- **Simultaneously execution**

A set of skills that was required by an activity was fulfilled by different resources, Equation (7) ensures that all of these skills are simultaneously executed.

$$\sum_{\forall j \in R} x_{i,j,t} = z_i^t * \sum_{\forall k \in K} AS_{i,k} \quad \forall t \in \mathrm{T},\ \forall i \in A \tag{7}$$

- **Resource allocation**

Constarints (8) and (9) state the requirements of each activity are satisfied by allocating the resources to them and each resource executes at most one skill of activity.

$$\sum_{\forall j \in R} y_{i,j,k} = b_{i,k} \quad \forall i \in A,\ \forall k \in RS_j \tag{8}$$

$$\sum_{t=ES_i}^{LS_i} x_{i,j}^t = \sum_{\forall k \in RS_j} y_{i,j,k} \quad \forall i \in A,\ \forall j \in R \tag{9}$$

- **Objective function**

Equation (10) aims to minimize the makespan of the project.

$$\min \quad \sum_{t=ES_{n+1}}^{LS_{n+1}} t * z_{n+1}^t \tag{10}$$

4. CONSTRAINT PROGRAMMING

CP formation started in 1970s and development stages were passed in parallel in US, Germany, and Australia; additionally Sabin and Freuder [20] disregarding previous investigations devised an approach in order to define and solve the problem using a specific language. It is essential to mention that the term "state" which had been used in the paper, defining and declaring the problem does not mean to give the linear mathematic model to the software to be solved; ironically, it means to define the problem in a different (expressive language) way. Expressive language is the most important advantage of CP optimizer and this language is based on the notion of interval variables [21]. The CP optimizer comes up in the artificial intelligence area that investigates Constraint Satisfaction Programming (CSP) and Logic Programming [21]. In the objective function in CP at decision problem, an optimal solution is not of interest; instead, the main goal in the decision problem is to find a feasible solution. CP cannot be counted as a solution algorithm or even a solution methodology; even though CP presents the solution methodology the solution cannot be limited to it; thus, CP cannot be considered as a software to solve the model. To present a correct definition for CP one can say it is a concept like LP and MILP. In CP the term CSP is called for decision variables, in CSP the goal is to find a feasible solution or allocate a series of values of the variables in order to satisfy the constraints and substructures. The significant techniques of CP are propagation and search. Consistency is a key factor for constraint propagation, the consistency warrants every value in a domain to be consistent with every constraint [21]. CP has been proven to be very efficient in solving scheduling problems, the basis of CP is to decrease the domain of the variables, as long as every variable takes a unique value this algorithm uses every constraint in order to reduce the domain of variables, this procedure is fully described in Figure 1. Choosing the variable and branching at the decision tree could have a substantial impact on the computational time.

Combining the MP and CP are useful to achieve the solution faster. The common method to combine CP and mathematical model is to firstly solve the linear relaxation problem and after that use the solution of the relaxation problem for reducing the domain of variables or helping to choose a better branch.

A valuable point about CP is that it can solve every non-linear problem or any problem with discrete variables or with non-convex solution space. The further study in the CP area in scheduling problem [22] are worth to mention.

We propose the CP algorithm as shown in Figure 2.

Sets and parameters are defined through lines 1 to 7 and decision variables are defined through lines 8 to 11. The objective function is to minimize the makespan of the project which was illustrated in line 12. In lines 13-19, the set of skills that was required by an activity was simultaneously executed and activity allocation to resources were considered. The algorithm of alternative and calendar constraints are shown in Figures 3 and 4. Lines 20-22 define the relationship between the activities. Lines 23-26 guarantee that each resource is only able to execute the activity in its time calendar. Lines 27-29 ensure that every resource can execute at most only one skill of activity at a specific time.

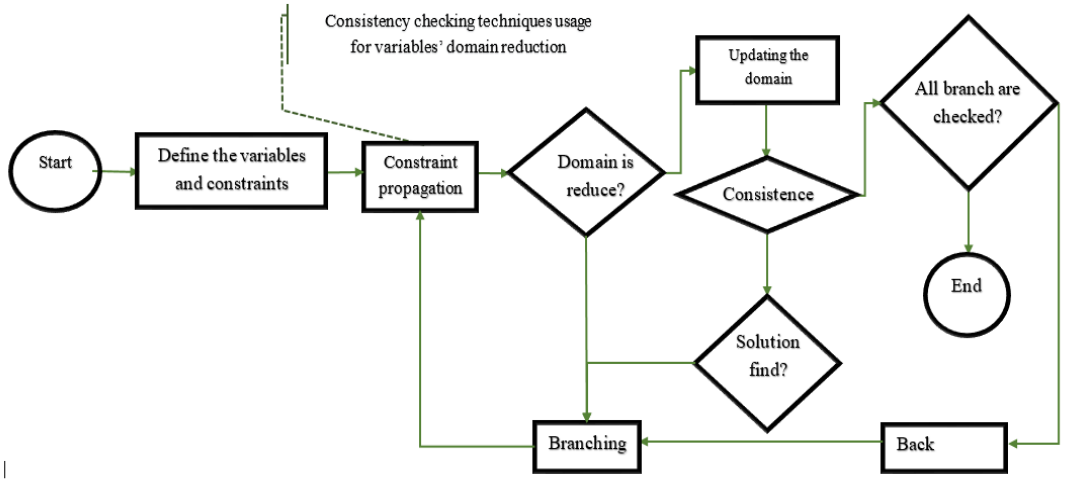

Figure 1. Procedure of CP optimization

```
Input :
1)R : Set of resources
2)A : Set of activity
3)K : Set of skill
4)O : set of Operation
5)AL : set of Allocation
6)Act _Skill : Set of skill that activity needed
7)Res _skill : Set of skill that resource master it
Variable :
8)act −time[A]
9)act −skill −time[O]
10)act −skill −res −time[AL]
11)workers[R]
12)Minimize Max(EndOf (Act −time[A]))
S.T
13)     For i ←1to i ←|A|
14)         For j ←1to j ←|O|
15)             Synchronize(i, j) Act −skill −time[j] where | j.task == r
16)             Alternative(act −skill −time[j]|where j.task == i , (awhere a.ops == o))
17)         End
18)     End
19)End

20)For i, j ←1to i, j ←|A|| A[i][j]==1
21)   EndBeforStart(i, j, 0)
22)End

23)For a ←1to a ←|AL|
24)   ForbidStart(act −skill −res −time(a), calendar(a.res))
25)   ForbidEnd(act −skill −res −time(a), calendar(a.res))
26)End

27)Forj ←1to j ←|R|
28)   NoOverlap(workers( j))
29)End
```

Figure 2. The CP algorithm

5. EXPERIMENTAL RESULTS

In this section, the results of computational experiments are presented. Acquiring the demanded tools to make the desired comparison, the two models are tested and now it is feasible to determine which can be the more successful. The models were both run on an Intel Core i5 duo processor with 8 GHz RAM. The Mathematical model using integer programming was coded in optimization programming language and solved by CPLEX 12.6.

The CP model uses a constraint programming method, it was solved by the Constraint Programming Optimizer included in ILOG optimizers. Since the CP algorithm works upon a set of parameters, Taguchi method is used for optimizing the parameters

To the best of our knowledge, no investigation has considered the calendar constraints for MS-RCPSP. Therfore, for having a better comparison, the problems are solved with MP and CP and the results of solutions were compared.

$n = |RS_r|$

r_j

$= set\ of\ resources\ which\ can\ execute\ the\ activity\ a$

$x\ is\ the\ objective\ fuction$

1) *If interval variable a is present*

2) *c=0;*

3) $r_1 = r^*$;

4) For i=r_1 *to i=*r_n

5) *IF* $x(r_{i+1})$ *is better than* $x(r_i)$

6) $c \leftarrow x(r_{i+1})$

7) else

8) $c \leftarrow x(r_i)$

9) End If

10) End for

11) End If

Figure 3. The algorithm of Alternative

```
A : set of activity
BT : Break time
AV : available
R : set of resources
D_t : set of break time in t'th position
1) For j ← 1 to |R|
2)   For t ← 1 to T
3)       AV[j][t] ← 1
4)   end
5) end
6) For  j ← 1 to |R|
7)  For  z ← to |D|
8)       For  t  ← min{D_z} to max {D_z}
9)            AV[j][t] ← 0
10)     end
11)  end
12) end
13) For  i ← 1 to |A|
14)     For j ← 1 to |R|
15)         If (Σ_{d=t}^{t+p_i−1} TM_{j∈t}) / p_i == 1
16)         endIf
17)   end
18) end
```

Figure 4. The algorithm of calendar constraint

In the next step, for further validation of the solution approach, it is needed to equalize the assumptions of our work with the problem investigated by Montoya et al. [19]. The calendar constraints are relaxed; then the acquired results from the solution of the relaxed problem (which is solved by CP algorithm) were compared with Montoya et al. [19]'s results.

5. 1. Input Data In order to evaluate the proposed methods of MS-RCPSP, the set of instances which was proposed by Montoya et al. [19] are used in this study. The instances involved between 20 and 62 activities, 2 and 15 skills, and 2 and 19 resources. The 271 related instances are divided into three groups (similar to Montoya et al. [19]), the groups are shown in Table 1.

5. 2. Taguchi Method To design an experiment and optimize the parameters based upon the above-specified conditions Taguchi method was used. The statistical approach used here named as Taguchi method considers three conditions, (a) larger the better (b) smaller the better (c) On-target, minimum variation. Taguchi method suggests the matrix of experiments and can get maximum information from a minimum number of experiments and also the best level of each parameter can be acquired for an objective function. Signal-to-noise ratios are used to compute the response of the empirical test. The configuration of the CP package did not employ the default settings and we selected the best options based on Taguchi method, for performing this method three parameters at four levels have been considered as shown in Table 2.

In the orthogonal array the levels corresponding to each control factor are similarly integrated with other factor level; hence, the number of runs to study three parameters at four levels diminish to only 16 instead of 3^4=81 runs. The experimental tests were conducted in a total of sixteen runs to calculate the SNR which is summarized in Table 3.

Figure 5 shows the main plot based upon average values of SNR, the horizontal axis shows the levels and the vertical axis shows the signal of noise ratio, the larger the SNR value, the better the parameter. For the result which is presented in Figure 6, values of the parameters are set to A= low, B=100, C= 1.3.

TABLE 1. Instance category

	Activity	Resource	Skill
Group 1	20-51	5-14	2-8
Group 2	32-62	5-19	9-15
Group 3	22-32	4-15	3-12

TABLE 2. Levels for control factors used in the experiment

Control Factor	Level			
	1	**2**	**3**	**4**
A: inference level	low	basic	medium	extended
B: restart fail limit	50	80	100	150
C: restart growth factor	1.05	1.1	1.3	1.7

TABLE 3. Experimental design with SNR

Ex. Run	A	B	C	SNR	MEAN
1	low	50	1.05	61.9936	1258
2	low	80	1.1	75.7902	6159
3	low	100	1.3	55.9591	628
4	low	150	1.7	79.7577	9725
5	basic	50	1.1	67.7406	2438
6	basic	80	1.05	64.5833	1695
7	basic	100	1.7	71.3098	3677
8	basic	150	1.3	72.3985	4168
9	medium	50	1.3	68.5885	2688
10	medium	80	1.7	74.9108	5566
11	medium	100	1.05	76.9032	7001
12	medium	150	1.1	70.1571	3220
13	extended	50	1.7	75.5499	5991
14	extended	80	1.3	78.7111	8621
15	extended	100	1.1	72.2726	4108
16	extended	150	1.05	80.3206	10376

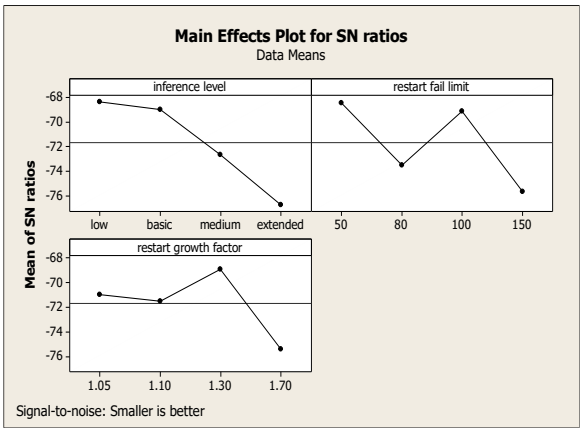

Figure 5. Effect of control factors on CPU time

5. 3. Computational Results For having a better insight into how the CP and MP models are performed, 9 instances that are randomly selected among three groups proposed by Montoya et al. [19] were considered. The results of solving these instances under resource calendar assumption by MP and CP are taken into consideration and data are shown in Table 4. According to the results, it goes without saying that the CPU time of CP is much less than MP. The major point is the number of variables each technique had taken into account; which according to the outcomes the average number of used variables by MP is 57 times bigger than CP. (note: in CP due to the use of "Alternative interval variables", some of the variables do not activate during solving the problem). In general, the net number of the problems in which their optimal solutions had been achieved are more in CP relative to MP and this hypothesis is also valid in all our nine instances. Table 4 shows that the number of the achieved optimal solutions for MP and CP are five and nine respectively.

The prominent point about the CP model is that when the calendar constraints are considered, the CPU time for solving the problem is reduced; with that in constraint propagation technique, the bigger the number of the constraints, the faster the algorithm in reducing the domain of the variables and reaching the solution. This fact is presented in Table 5.

5. 4. Computational Results by Relaxing the Calendar Constraint According to compare our results with the results achieved by Montoya et al. [19], we initially removed the calendar constraint then modeled the problem by CP. The comparison results are shown in Table 6. It can be conspicuously observed in Tables 6 and 7 that CP model outperforms the B&P and TIM in terms of obtained optimal solutions and also a shorter total average CPU time than the TIM and B&P. It is obviously seen that average CPU time of the CP is shorter than other two methods, except for group 2 it is slightly longer than average CPU time of the B&P.

TABLE 4. Comparison of the solutions obtained through MP and CP

Problem number	No. of activities	No. of resources	No. of skills	**CPU time** (in seconds)		**No. of variables**		**No. of constraints**	
				CP	**MP**	**CP**	**MP**	**CP**	**MP**
1	20	13	3	23.25	126.65	287	13212	549	18797
2	22	11	3	12.20	112.28	235	14534	444	26043
3	22	7	3	13.54	65.87	180	11048	334	21572
4	27	10	3	0.34	97.35	397	17537	774	31901
5	32	15	12	0.36	221.59	474	24923	1076	48751
6	32	16	12	0.46	no answer	552	24987	1081	48876
7	51	10	3	2.26	no answer	612	45383	1332	81602
8	62	10	9	46.76	no answer	699	56161	1383	99202
9	62	19	9	135.66	no answer	1328	68254	3055	112301

TABLE 5. Comparison of the solutions obtained by CP with and without assumption of calendars

Problem number	No. of activities	No. of resources	No. of skills	**CPU time** (in seconds)		**No. of variables**		**No. of constraints**	
				CP^1	**CP^2**	**CP^1**	**CP^2**	**CP^1**	**CP^2**
1	22	11	3	85.87	12.20	235	235	112	444
2	22	7	3	174.54	13.54	180	180	94	334
3	27	10	3	0.42	0.341	397	397	162	774

CP^1: CP without assumption of calendars & CP^2: CP with assumption of calendars

TABLE 6. The obtained result of TIM, B&P and CP

	Optimal solution		
	CP	**B&P**	**TIM**
Group 1	84%	43.6%	21.81%
Group 2	77%	66.19%	64.78%
Group 3	63%	51.11%	15.55%

TABLE 7. Average CPU time of TIM and B&P and CP

	Average CPU time (in seconds)		
	CP	**B&P**	**TIM**
Group 1	49.9	148.95	1420.81
Group 2	83.3	57.09	737.32
Group 3	66.75	283.02	1569,21

6. CONCLUSIONS

In this paper, we proposed a constraint programming approach for the multi-skill resource constrained project scheduling problem. In order to improve the problem in terms of consideration of real-world factors, the resource calendars is taken into account. The results showed that the proposed CP outperformed mathematical programming approach. This model can use specialized constraints, such as the synchronize constraint, that can shorten the time of achieving the solution. In addition, the comparison between CP and branch-and-price algorithm with no calendar constraint was made and the results show that the CP model is faster than the branch-and-price algorithm in finding the optimal solution. The CP approach allows us to deal with complex problems and consider the problem concepts by its substructures successively and reach the solution in an aptly short time.

7. REFERENCES

1. Hartmann, S. and Briskorn, D., "An updated survey of variants and extensions of the resource-constrained project scheduling problem", ***European Journal of Operational Research***, Vol. 297, No. 1, (2022), 1-14, https://doi.org/10.1016/j.ejor.2021.05.004
2. Rezaei, F., Najafi, A.A. and Ramezanian, R., "Mean-conditional value at risk model for the stochastic project scheduling problem", ***Computers & Industrial Engineering***, Vol. 142, (2020), 106356, https://doi.org/10.1016/j.cie.2020.106356
3. Niaki, S., Najafi, A.A., Zoraghi, N. and Abbasi, B., "Resource constrained project scheduling with material ordering: Two hybridized meta-heuristic approaches", ***International Journal of Engineering***, ***Transactions C: Aspects,*** Vol. 28, No. 6, (2015), 896-902, doi: 10.5829/idosi.ije.2015.28.06c.10.
4. Khalili, S., Najafi, A.A. and Niaki, S.T.A., "Bi-objective resource constrained project scheduling problem with makespan and net present value criteria: Two meta-heuristic algorithms", ***The International Journal of Advanced Manufacturing Technology***, Vol. 69, No. 1, (2013), 617-626, https://doi.org/10.1007/s00170-013-5057-z
5. Rezaei, F., Najafi, A.A., Ramezanian, R. and Demeulemeester, E., "Simulation-based priority rules for the stochastic resource-constrained net present value and risk problem", ***Computers & Industrial Engineering***, Vol. 160, No., (2021), 107607, https://doi.org/10.1016/j.cie.2021.107607
6. Mollaei, H., Tavakkoli-Moghaddam, R. and Toloie-Eshlaghy, A., "A new multi-objective model for multi-mode project planning with risk", ***International Journal of Engineering***, ***Transactions B: Applications,*** Vol. 31, No. 5, (2018), 770-779, doi: 10.5829/ije.2018.31.05b.12.
7. Franck, B., Neumann, K. and Schwindt, C., "Project scheduling with calendars", ***OR-Spektrum***, Vol. 23, No. 3, (2001), 325-334, http://dx.doi.org/10.1007/PL00013355
8. Kreter, S., Rieck, J. and Zimmermann, J., "Models and solution procedures for the resource-constrained project scheduling problem with general temporal constraints and calendars", ***European Journal of Operational Research***, Vol. 251, No. 2, (2016), 387-403, https://doi.org/10.1016/j.ejor.2015.11.021
9. Ahmadpour, S. and Ghezavati, V., "Modeling and solving multi-skilled resource-constrained project scheduling problem with calendars in fuzzy condition", ***Journal of Industrial Engineering International***, Vol. 15, No. 1, (2019), 179-197, http://dx.doi.org/10.1007/s40092-019-00328-w
10. Afshar-Nadjafi, B., "Multi-skilling in scheduling problems: A review on models, methods and applications", ***Computers & Industrial Engineering***, Vol. 151, (2021), 107004, https://doi.org/10.1016/j.cie.2020.107004
11. Correia, I. and Saldanha-da-Gama, F., A modeling framework for project staffing and scheduling problems, in Handbook on project management and scheduling vol. 1. 2015, Springer.547-564.
12. Bellenguez-Morineau, O. and Néron, E., "A branch-and-bound method for solving multi-skill project scheduling problem", ***RAIRO-operations Research***, Vol. 41, No. 2, (2007), 155-170, http://dx.doi.org/10.1051/ro:2007015
13. Avramidis, A.N., Chan, W., Gendreau, M., L'ecuyer, P. and Pisacane, O., "Optimizing daily agent scheduling in a multiskill call center", ***European Journal of Operational Research***, Vol. 200, No. 3, (2010), 822-832, http://dx.doi.org/10.1016/j.ejor.2009.01.042
14. Cai, X. and Li, K., "A genetic algorithm for scheduling staff of mixed skills under multi-criteria", ***European Journal of Operational Research***, Vol. 125, No. 2, (2000), 359-369, https://doi.org/10.1016/S0377-2217(99)00391-4
15. Wongwai, N. and Malaikrisanachalee, S., "Augmented heuristic algorithm for multi-skilled resource scheduling", ***Automation in Construction***, Vol. 20, No. 4, (2011), 429-445, https://doi.org/10.1016/j.autcon.2010.11.012
16. Walter, M. and Zimmermann, J., "Minimizing average project team size given multi-skilled workers with heterogeneous skill levels", ***Computers & Operations Research***, Vol. 70, (2016), 163-179, https://doi.org/10.1016/j.cor.2015.11.011
17. Heimerl, C. and Kolisch, R., "Scheduling and staffing multiple projects with a multi-skilled workforce", ***OR spectrum***, Vol. 32, No. 2, (2010), 343-368, http://dx.doi.org/10.1007/s00291-009-0169-4
18. De Bruecker, P., Van den Bergh, J., Beliën, J. and Demeulemeester, E., "Workforce planning incorporating skills: State of the art", ***European Journal of Operational Research***, Vol. 243, No. 1, (2015), 1-16, https://doi.org/10.1016/j.ejor.2014.10.038

19. Montoya, C., Bellenguez-Morineau, O., Pinson, E. and Rivreau, D., "Branch-and-price approach for the multi-skill project scheduling problem", ***Optimization Letters***, Vol. 8, No. 5, (2014), 1721-1734, http://dx.doi.org/10.1007/s11590-013-0692-8

20. Sabin, D. and Freuder, E.C., "Contradicting conventional wisdom in constraint satisfaction", in International Workshop on Principles and Practice of Constraint Programming, Springer. (1994), 10-20.

21. Baumgärtner, S., Becker, C., Frank, K., Müller, B. and Quaas, M., "Relating the philosophy and practice of ecological economics: The role of concepts, models, and case studies in inter-and transdisciplinary sustainability research", ***Ecological Economics***, Vol. 67, No. 3, (2008), 384-393, http://dx.doi.org/10.1016/j.ecolecon.2008.07.018

22. Baptiste, P., Le Pape, C. and Nuijten, W., "Constraint-based scheduling: Applying constraint programming to scheduling problems, Springer Science & Business Media, Vol. 39, (2001).

Persian Abstract

چکیده

زمانبندی پروژه منابع محدود چندمهارته یکی از مسائل چالشی و مهم در مدیریت پروژه است. دو موضوع کلیدی این مسئله را چالش برانگیز می‌کند، مفروضاتی که برای تقریب مدل به یک مسئله واقعی در نظر گرفته می‌شود و نیز حل دقیق مسئله. در این مقاله، به این دو موضوع می‌پردازیم. بدین منظور، برای درنظرگیری شرایط دنیای واقعی، تقویم کاری منابع را در مدل وارد می‌کنیم تا روزهای کاری و غیرکاری منابع در مسئله لحاظ شود. همچنین از برنامه‌ریزی محدودیت برای حل دقیق مدل و استخراج جواب بهینه استفاده می‌شود. مسئله با و بدون درنظرگیری تقویم منابع با استفاده از برنامه ریزی‌ریاضی و همچنین برنامه‌ریزی محدودیت مدلسازی می‌شود. همچنین، عملکرد رویکرد برنامه ریزی محدودیت با رویکرد TIM و رویکرد B&P مورد ارزیابی قرار می‌گیرد. نتایج محاسباتی نشان می‌دهد که رویکرد پیشنهادی می‌تواند به طور موثری نمونه‌های با اندازه واقعی را حل نماید.

IJE TRANSACTIONS B: Applications Vol. 35, No. 08, (August 2022) 1588-1598

International Journal of Engineering

Journal Homepage: www.ije.ir

A New Framework for Canny Edge Detector in Hexagonal Lattice

M. Firouzi[a], S. Fadaei*[a], A. Rashno[b]

[a] *Department of Electrical Engineering, Faculty of Engineering, Yasouj University, Yasouj, Iran*
[b] *Department of Computer Engineering, Engineering Faculty, Lorestan University, Khorramabad, Iran*

PAPER INFO

Paper history:
Received 05 March 2022
Received in revised form 25 April 2022
Accepted 27 April 2022

Keywords:
Edge Detection
Square Lattice
Hexagonal Lattice
Hexagonal Gradient

ABSTRACT

Feature extraction is widely used in image processing applications such as face recognition, character recognition, fingerprint identification and medicine. Edge features is among the most important features for such applications. Canny edge detector is the most popular one and has many benefits in comparison with other methods. Since pixels in hexagonal domain have many benefits in comparison with square domain, this paper presents an efficient Canny edge detector in hexagonal domain. The proposed method includes square to hexagonal transformation and edge detection based on a new algorithm. The proposed method has been evaluated on synthetic and real image datasets with different signal to noise ratios (SNRs). Detected edges in synthetic images show that the proposed hexagonal edge detector outperforms existing methods in 44 cases out of 60 cases with respect to figure of merit (FoM). Finally, results of real images demonstrate the superiority of the proposed method in qualitative analysis of sub-images.

doi: *10.5829/ije.2022.35.08b.15*

1. INTRODUCTION

Image processing can be helpful and plays an efficient role to solve problems such as medical field, robot vision, video processing and pattern recognition. To process, save, represent and translate an image, the first step is image sampling. As shown in Figure 1, there are three tessellation schemes with no overlaps and no gaps including hexagons, squares and regular triangles [1, 2]. Other tessellation methods lead to either overlap or gap between adjacent pixels.

Based on Nyquist frequency, a band-limited signal can be reconstructed using its samples if the sampling frequency is equal or greater than twice the highest frequency of the signal. The hexagonal sampling is the best sampling scheme for band-limited 2D signals. In comparison to other methods, it requires fewer samples to reconstruct original signal. Therefore, the hexagonal sampling needs 13.4% lower samples in comparison with square sampling [3].

Lower samples in hexagonal lattice leads to higher efficiency in sampling. The sampling efficiency in hexagonal domain is 90.7% compared with 78.5% in square domain [4]. The sampling efficiency is the ratio of nonzero area spectrums of the signal over the total area of a period of signal spectrum. On the other hand, quantization is inevitable in sampling and it is proven that for a specific resolution of sensors, the quantization error in hexagonal sampling is lower than square one [5, 6]. Another important issue that makes hexagonal lattice better than other grids is the consistent connectivity property. Neighboring pixels of a central pixel have the same distance from that central pixel. This property in hexagonal lattice makes image processing algorithms on this grid simpler and more efficient. For example, the thinning algorithm on this network is simpler because fewer connection modes are involved in the calculations [7-9].

Due to the advantages of hexagonal network, the implementation of image processing algorithms in this

*Corresponding Author Institutional Email: s.fadaei@yu.ac.ir (S. Fadaei)

Please cite this article as: M. Firouzi, S. Fadaei, A. Rashno, A New Framework for Canny Edge Detector in Hexagonal Lattice, ***International Journal of Engineering, Transactions B: Applications***, Vol. 35, No. 08, (2022) 1588-1598

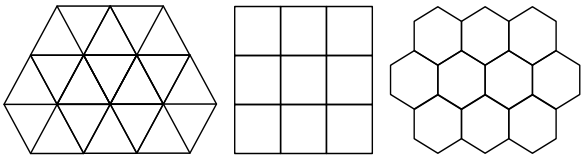

Figure 1. Three tessellation scheme; (a) regular triangles, (b) squares and (c) hexagons

network leads to better results, so researchers try to implement image processing algorithms on hexagonal lattice. A new framework for hexagonal image processing using hexagonal pixel-perfect approximations in subpixel resolution is proposed to convert square pixels to hexagonal one [10]. Hexagonal grid in image processing is studied and its advantages such as higher circular symmetry, equidistant, smaller quantization error, greater angular resolution have been investigated [11]. An approach based on bilinear interpolation was used to convert square image to hexagonal one [12]. A complete study of hexagonal image processing was provided [13, 14]. It was mentioned that arrangement of photoreceptors in the human retina is hexagonal [14]. Image compression based on wavelet was performed on both square and hexagonal images and their performances were compared using two criteria Peak Signal to Noise Ratio (PSNR) and Mean Square Error (MSE). The implementation results showed that compression in hexagonal lattice is better than square one [14].

The construction of symmetric FIR filter banks for image processing on hexagonal lattice was investigated [15]. A new filter was introduced to denoise hexagonal images and it was shown that results in hexagonal lattice is better than square one [16]. Hexagonal lattice provides 13.4 percent fewer samples than square lattice [17]. A new algorithm was proposed to convert square to hexagonal image and it was shown that variable grids occur in Hexagonal Discrete Fourier Transform (HDFT) [17]. Two-dimensional Modulation Transfer Function (MTF) model of hexagonal lattice detector was deduced based on its definition. MTF is the tool widely used to quantify the efficiency of an electro-optical imaging system [18].

A new approach was proposed to design operators for hexagonal image processing and by developing these operators, a framework for obtaining large-scale neighborhood operators and edge maps at different scales was presented [19]. A new addressing for hexagonal imaging was proposed to simplify implementation and keeps all excellent properties of hexagonal grid [20]. An approach for corner detection on hexagonal images presented and it is shown that its accuracy is comparable to corner detectors applied to square images [21]. Essential operators of translation and rotation were applied to hexagonal images [22]. The computational complexity of edge detection on hexagonal image was reduced using an edge map pyramid approach [23]. Several algorithms were presented for uniform image separation based on virtual hexagonal structure are presented [24].

Feature extraction is very helpful in many applications of image processing such as face recognition, character recognition, content-based image retrieval (CBIR), and medical diagnosis [25-29]. Indeed, to reduce the number of required resources to describe an image, feature extraction is done. Edge detection is one of the most important and widely used feature extraction algorithms and several methods such as Middleton, Staunton, Li and Davies have proposed [30-33]. He et al. [34] has converted the image to hexagonal lattice using virtual hexagonal structure method and edge detection was applied to hexagonal image. The edge detection operator was done through three steps: filtering of noise by a bilateral filter, edge detection using Sobel operator and edge thinning using thresholds. Converting from square to hexagonal lattice was implemented and then the edges of hexagonal image was extracted using Canny edge detector [35].

Edge detection on hexagonal and square image was compared and it was proven that the computational complexity of hexagonal lattice is less than square lattice as well as better qualitative performance in hexagonal lattice [30]. Using the finite element framework, a new method to develop multiscale gradient operators in hexagonal lattice is presented [36]. Some binary morphological operators on hexagonal lattice were introduced to manipulate edge detection by Mostafa et al. [37]. The proposed operators by Mostafa et al. [37] showed that combination of 0°, 60° and 120° directional structuring elements on hexagonal grid gives better results than square grid. An approach for hexagonal gradient operators was developed on hexagonal grid within finite element framework [38]. Square lattice was converted to hexagonal domain by two-dimensional to one-dimensional interpolation transformation [39]. Hexagonal image was created from square image using hexagonal deep neural networks [40]. As one of hexagonal advantages, less computational cost of hexagonal Gabor filter in comparison with square one was proven by Varghese and Saroja [41]. Hexagonal domain was developed to use in CNNs with hexagonal convolution defination [42]. Hexagonal lattice was also investigated for better angular symetry, isotropy and consistent connectivity by singular value decomposition definition in hexagonal domain [43]. Finally, bilateral filter was developed for hexagonal edge detection by He et al. [44].

Although hexagonal lattice is the best tessellation scheme, approximately all the edge detection algorithms have been introduced in square lattice. Since the edge

detection plays important role in image processing and its precision and quality can affect results of image processing applications, a hexagonal edge detection method is proposed and investigated in this paper. The proposed hexagonal edge detector is a pure extension of Canny edge detector in square lattice. For this task, images are first transferred from square to hexagonal lattice. Then, gradient magnitude and direction of pixels in hexagonal domain are calculated. Hexagonal level quantization and non-maximum suppression are presented in the next step. Then, thresholds selection and double thresholding are applied to edges. Finally, Edge tracking is done by hysteresis and untrue edges are removed. The organization of this paper is as follows: Section 2 presents Motivation of this research. Proposed method with details is presented in section 3. Implementation results is reported in section 4 and the paper is concluded in section 5.

2. MOTIVATION

Many advantages of image processing applications and operators in hexagonal lattice have been reported in the literature. As stated in our previous framework for hexagonal image processing [10], benefits such as perfect hexagonal shape, accurate intensity level of hexagonal pixels and high resolutions in hexagonal space can be used in real applications. These benefits also revealed that hexagonal lattice has better angular resolution 60 in comparison with 90 in square domain which leads to better edge detection results [10]. Since edge detection operator is among the most significant operators for industrial image processing techniques [34], mentioned advantages of hexagonal lattice motivated us to present an edge detector in this domain. Canny is a conventional edge detector in many applications, therefore a framework for transferring Canny edge detector from square to hexagonal lattice is proposed in this research and referred as hexagonal Canny edge detector.

3. PROPOSED METHOD

In one side, edge detection is an important topic in image processing and among edge detection methods, Canny operator is the most popular one which is widely used in the literature. On the other side, researches have shown that the image processing in hexagonal grid leads to better results than square grid. In this paper, an optimized hexagonal Canny edge detection method is proposed. The flowchart of the proposed method is shown in Figure 2.

Images are first converted to hexagonal grid followed by hexagonal image filtering by a gaussian filter. Then, magnitude and direction of gradients are computed in three axis *x*, *y* and *z*. In the next stage, the non-maximum suppression is applied to the magnitude and direction of gradients. Finally, threshold selection, double thresholding, untrue edge tracking and edge removing are done sequentially to reach edges in hexagonal domain.

3. 1. Square to Hexagonal Transformation

Since the edge processing should be applied to hexagonal image, the square images are first transferred to hexagonal image. To do this, several algorithms have been proposed in the literature. The most significant method is that each square pixel is divided into 7×7 sub-pixels and hexagonal pixels are composed from square sub-pixels [11]. The intensity of sub-pixels is equal to the intensity of the original square pixel. This division leads to a new virtual image, 49 times larger than original image. Finally, each hexagonal pixel is formed from averaging on 56 sub-pixels of the virtual image as shown in Figure 3.

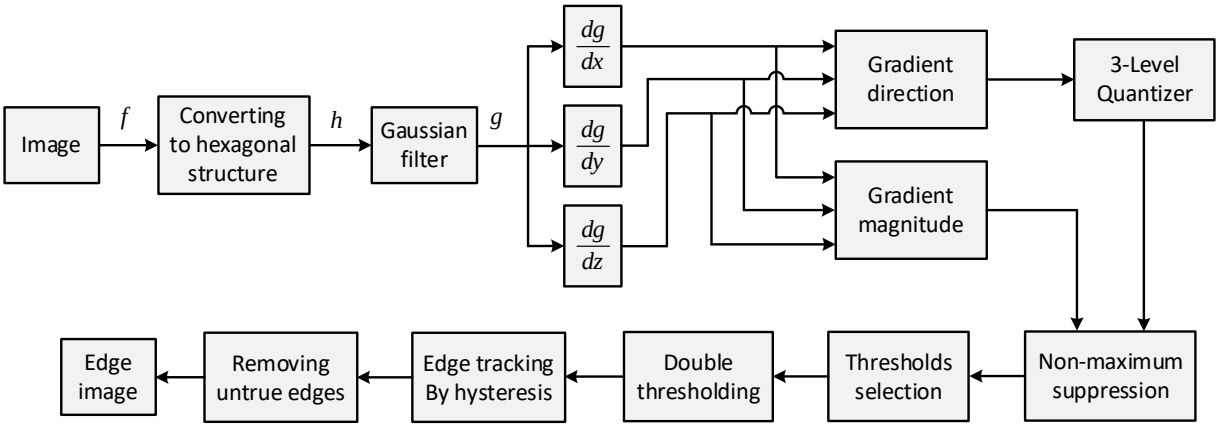

Figure 2. Proposed Canny edge detector in hexagonal domain

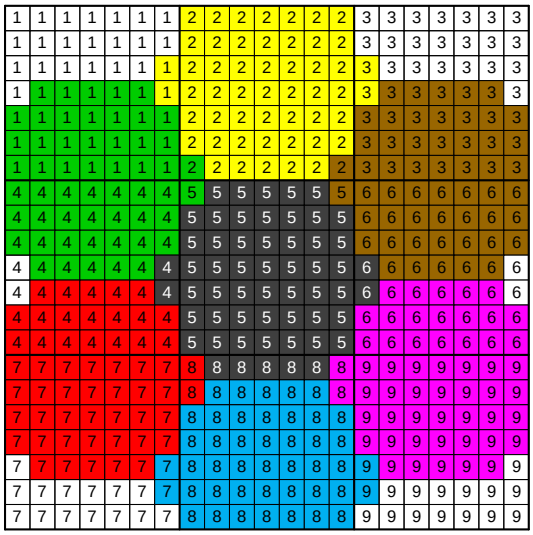

Figure 3. Square to hexagonal image technique [11]

In this research, in order to eliminate noise, the hexagonal image is filtered by a gaussian filter. Gaussian filter size can be varied as 3×3, 5×5, 7×7 and etc. The relation between the size (K) and standard deviation (σ) of gaussian filter is $\sigma = K/6$.

3. 2. Gradient Magnitude and Direction Calculation To determine directional changes of pixel intensities, gradient operation is used. The more changes in the intensity are occurred, the higher gradient values are achieved. Because of the high intensity changes in the edges, the gradient of edge regions is bigger than the uniform regions of the image. Therefore, the gradient is very powerful tool for edge detectors. As depicted in Figure 4a, in square domain, the gradient is a 2D vector with the components given by the derivation in x and y directions. Compared with the square images, the gradient in hexagonal domain is a 3D vector in which its components are obtained from derivation in r, s and t directions (see Figure 4(b)).

To calculate gradient in three directions, kernel matrices shown in Figure 5 are considered. Since the hexagonal image is not in square grid, a platform should be defined to locate hexagonal pixels. Figure 6 shows the proposed platform in which the filled circles are on locations of hexagonal pixels. Indeed, the hexagonal image in Figure 6(a) is mapped to the matrix in Figure 6(b).

As shown in Figure 5, and based on defined platform in Figure 6, the gradient in three directions for the pixel on location (i, j) is computed as:

$$g_r(i,j) = OP_r \times G_n(i,j) \quad (1)$$

$$g_s(i,j) = OP_s \times G_n(i,j) \quad (2)$$

$$g_t(i,j) = OP_t \times G_n(i,j) \quad (3)$$

where OP_r, OP_s, OP_t and $G_n(i,j)$ are defined as:

$$OP_r = \begin{bmatrix} 0 & -2 & 0 \\ -1 & 0 & -1 \\ 0 & 0 & 0 \\ 1 & 0 & 1 \\ 0 & 2 & 0 \end{bmatrix}, OP_s = \begin{bmatrix} 0 & -1 & 0 \\ -2 & 0 & 1 \\ 0 & 0 & 0 \\ -1 & 0 & 2 \\ 0 & 1 & 0 \end{bmatrix}, OP_t = \begin{bmatrix} 0 & 1 & 0 \\ -1 & 0 & 2 \\ 0 & 0 & 0 \\ -2 & 0 & 1 \\ 0 & -1 & 0 \end{bmatrix} \quad (4)$$

$$G_n(i.j) = \begin{bmatrix} 0 & I(i-2.j) & 0 \\ I(i-1.j-1) & 0 & I(i-1.j+1) \\ 0 & 0 & 0 \\ I(i+1.j-1) & 0 & I(i+1.j+1) \\ 0 & I(i+2.j) & 0 \end{bmatrix} \quad (5)$$

where $I(i,j)$ represents the intensity of pixel (i,j). The gradient in directions x and y is:

$$g_r^x(i,j) = g_r(i,j) \times \cos(\beta) \quad (6\text{-a})$$

$$g_s^x(i,j) = g_s(i,j) \times \cos(\beta) \quad (6\text{-b})$$

$$g_t^x(i,j) = g_t(i,j) \times \cos(\beta) \quad (6\text{-c})$$

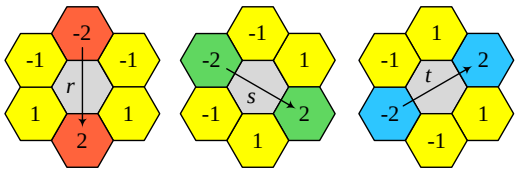

(a) (b) (c)

Figure 5. Gradient calculation in three directions: (a) r, (b) s and (c) t

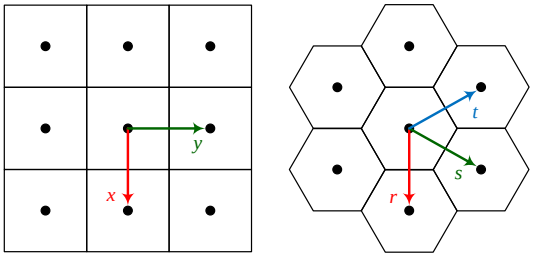

(a) (b)

Figure 4. Gradient directions in: (a) Square and (b) Hexagonal

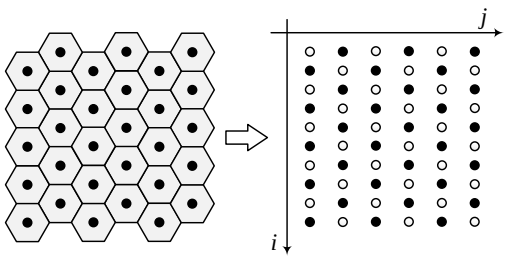

(a) (b)

Figure 6. Platform to locate hexagonal pixels

$$g_r^y(i,j) = g_r(i,j) \times sin(\beta) \quad (6\text{-d})$$

$$g_s^y(i,j) = g_s(i,j) \times sin(\beta) \quad (6\text{-e})$$

$$g_t^y(i,j) = g_t(i,j) \times sin(\beta) \quad (6\text{-f})$$

where β is defined as:

$$\beta = \begin{cases} 0\,, & for\ dierection\ r \\ \pi/3\,, & for\ direction\ s \\ 2\pi/3\,, & for\ direction\ t \end{cases} \quad (7)$$

The resultant vector in x and y directions is:

$$G_x(i,j) = g_r^x(i,j) + g_s^x(i,j) + g_t^x(i,j) \quad (8)$$

$$G_y(i,j) = g_r^y(i,j) + g_s^y(i,j) + g_t^y(i,j) \quad (9)$$

Finally, gradient magnitude and gradient direction of pixel (i,j) are $G_M(i,j)$ and $\theta(i,j)$, respectively, computed as follows:

$$G_M(i,j) = \sqrt{G_x^2(i,j) + G_y^2(i,j)} \quad (10)$$

$$\theta(i,j) = tan^{-1}\big(G_y(i,j)/G_x(i,j)\big) \quad (11)$$

where, θ is the gradient direction matrix.

3. 3. Level Quantization and Non-maximum Suppression Since the direction of gradient has different values, it should be quantized. Based on the Figure 4b, the direction of gradient is quantized into 3 main directions and takes values between $-\pi/2$ and $\pi/2$ added by $\pi/2$ leads to interval $0 \le G_D(i,j) < \pi$. As shown in Figure 7, the quantization is done in three directions demonstrated by red, green and blue arrows.

It is clear in Figure 7, the quantization of direction is calculated as:

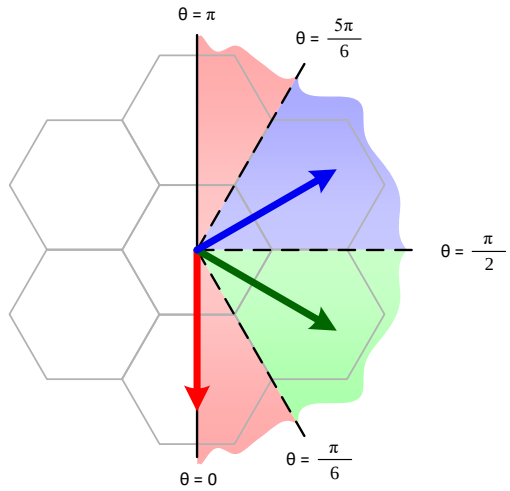

Figure 7. 3-Level direction quantization

$$G_D(i.j) = \begin{cases} 0, & 0 \le \theta(i,j) < \pi/6\ or\ 5\pi/6 \le \theta(i,j) < \pi \\ \pi/3, & \pi/6 \le \theta(i,j) < \pi/2 \\ 2\pi/3, & \pi/2 \le \theta(i,j) < 5\pi/6 \end{cases} \quad (12)$$

where G_D is the quantization of gradient direction matrix. After applying gradient calculation and angle quantization, non maximum suppression is used to select more significant edges which makes edges thinner.

Indeed, non-maximum suppression helps suppressing all gradient values except the local maxima and determines locations with the maximum change of intensity levels. To do this, for direction of the current pixel, if the gradient magnitude of the current pixel is greater than the gradient magnitude of that pixels in the negative and positive gradient directions, the pixel is preserved as edge candidate. Otherwise, the pixel is suppressed.

As shown in Figure 8a, if quantized direction of the central pixel is 0 ($G_D = 0$) and its gradient magnitude is greater than two adjacent gray pixels, the central pixel is used as edge candidate (set to 1), else, the central pixel is removed from edge candidates (set to 0). Figsures 8b and 8c are similar to Figure 8a but for directions $G_D = \pi/3$ and $G_D = 2\pi/3$. Based on defined platform in Figure 6, the edge candidates are determined as follows:

$$E(i,j) = \begin{cases} 1, G_D(i,j) = 0, G_M(i-2,j) < G_M(i,j), \\ \quad G_M(i,j) > G_M(i+2,j) \\ 1, G_D(i,j) = \pi/3, G_M(i-1,j-1) < G_M(i,j), \\ \quad G_M(i,j) < G_M(i+1,j+1) \\ 1, G_D(i,j) = 2\pi/3, G_M(i+1,j-1) < G_M(i,j), \\ \quad G_M(i,j) < G_M(i-1,j+1) \\ 0, Otherwise \end{cases} \quad (13)$$

where, E is the edge candidate matrix.

3. 4. Thresholds Selection and Double Thresholding Thresholding is an important process in a wide range of image processing applications. There are a variety of methods to calculate thresholds such as fixed thresholding, optimal thresholding, Otsu method and etc. In this research, thresholding is done by Otsu method which has better results than other methods because it minimizes intra-class variance or maximizes inter-class variance. Edge detection results depend on two parameters: window size of Gaussian filter and the threshold value. To achieve better results, while the size of window is increased, the value of threshold should be decreased.

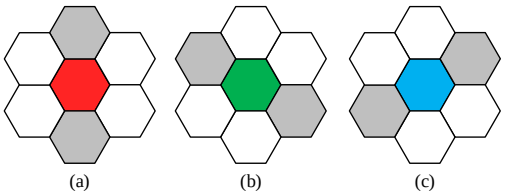

Figure 8. Non-maximum suppression for different directions: (a) $G_D = 0$, (b) $G_D = \pi/3$ and (c) $G_D = 2\pi/3$

After non-maximum suppression and remove some unreal edges, the remaining edge locations have more accurate representation of edges in the image. However, some remained edge pixels are because of noise, diversity of gradient domain value and etc. In order to remove these pixels, double thresholding is used in which two thresholds are defined: T_{low} and T_{high}. If gradient magnitude of an edge pixel is higher than the T_{high}, it is introduced as a strong edge pixel and should certainly be marked as real edge. If gradient magnitude of an edge pixel is lower than the T_{low}, it is removed. If gradient magnitude of an edge pixel is between T_{low} and T_{high}, it is introduced as a weak edge pixel. Since T_{low} and T_{high} are dependent on content of the image, the low and high thresholds should be defined based on the image content. As mentioned before, by inspiring Otsu thresholding method, a threshold can be defined as follows:

$$\sigma_b^2(t) = \sigma^2(t) - \sigma_w^2(t) = w_0(t)\mu_0^2(t) + w_1(t)\mu_1^2(t) - \mu_T^2(t) \quad (14)$$

Which $w_0(t) = \sum_{i=0}^{t-1} p(i)$, $w_1(t) = \sum_{i=t}^{L-1} p(i)$, $\mu_0(t) = \sum_{i=0}^{t-1} ip(i)/w_0(t)$, $\mu_0(t) = \sum_{i=t}^{L-1} ip(i)/w_1(t)$ and $\mu_T = \sum_{i=0}^{L-1} ip(i)$. It is clear that there are L intensity levels. The optimal threshold corresponds to maximum value of $\sigma_b^2(t)$ and is determined as T_{Otsu}. T_{high} and T_{low} defines as below:

$$T_{high} = \frac{7}{8} \times T_{Otsu}\,, \quad T_{low} = \frac{\sqrt{3}}{2} \times T_{high} \quad (15)$$

The coefficients of T_{low} and T_{high} are obtained by supervision.

3. 5. Edge Tracking by Hysteresis And Removing Untrue Edges Remained edges after non-maximum suppression are divided into two groups: strong and weak edges (see Figure 9).

We know that all weak edges are not real edges, as these edges can be extracted from either real edges or noise. To achieve better accuracy, the weak edges extracted form noise should be removed. Usually a weak edge pixel caused by noise is unconnected to a strong edge pixel while true edges are connected. To do this, as shown in Figure 10a, a 6-neighbor set is considered to search for strong edge pixels around weak edge pixel. For weak edge pixel P_c, if one or more pixels of P_1, P_2, … , P_6 are not strong edges, the pixel P_c is removed.

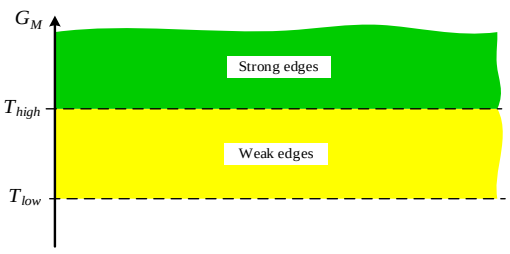

Figure 9. Strong and weak edges

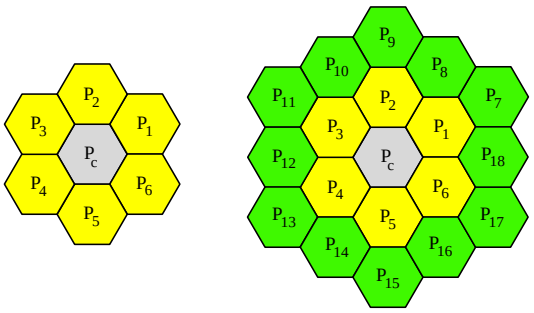

Figure 10. Definition of neighboring in hexagonal lattice: (a) 6-neighbor, (b) 18-neighbor

Finally, to remove edge pixels with no neighbor edges, a new algorithm is proposed. As shown in Figure 10, two neighboring in hexagonal lattice is defined and we have introduced ε_1 and ε_2 as below:

$$\varepsilon_1 = \sum_{i=1}^{6} P_i\,, \quad \varepsilon_2 = \sum_{i=1}^{18} P_i \quad (16)$$

As depicted in Figure 10b, ε_1 and ε_2 are sum of yellow and green pixels, respectively and P_i takes 0 (not edge) and 1 (edge) resulted from previous stage. If $\varepsilon_1 \geq 2$ or $\varepsilon_1/\varepsilon_2 \neq 1$ then the pixel p_c is preserved as edge, otherwise p_c is removed.

4. IMPLEMENTATION RESULTS

To evaluate performance of the proposed method, comparisons have been made between four existing methods and the proposed method. For this task, edge detection results of the proposed method and other methods are reported in synthetic and real images.

4. 1. Edge Detection Results on Synthetic Images For quantitative evaluation, 6 synthetic images horizontal, oriented, curved, square, chess and wave edges are used as shown in Figure 11.

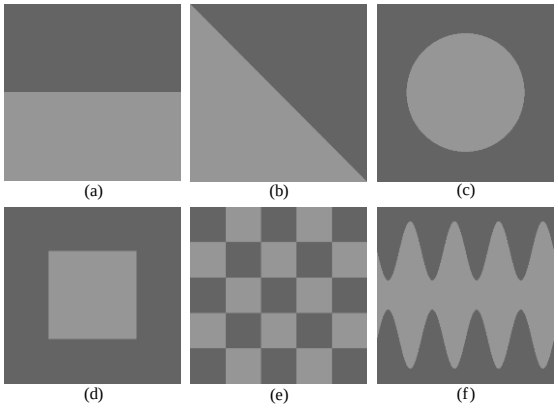

Figure 11. Synthetic images for edge detection evaluation

For synthetic evaluation, Figure of Merit (FoM) is used [39]. FoM considers three important errors including: missing valid edge pixels, failure to localize edge pixels and classification of noise fluctuations as edge pixels. FoM is defined as:

$$\text{FoM} = \frac{1}{\max(I_I, I_A)} \sum_{i=1}^{I_A} \frac{1}{1+\alpha d_i^2} \quad (17)$$

where I_A is the number of detected edge pixels, I_I is the number of ideal edge pixels, d_i is the separation distance of a detected edge point normal to a line of ideal edge points, and α is a scaling factor and usually set to 1/9.

Figure of Merit is normalized to interval [0 1], where 0 shows that none of the edge points were found correctly and 1 shows that all edge points were detected perfectly. To compare the proposed method with the other methods, we consider each synthetic image in Figure 11. It is necessary to mention that FoM criterion can only be used for synthetic images since in these images real edges are known.

To simulate a real environment for quantitative evaluation of all methods, the FoM measure is applied to images with different signal-to-noise ratios (SNRs), where $SNR = A^2/\sigma_n^2$, A is the difference between high and low intensities of synthetic images and σ_n^2 is the variance of noise. To generate synthetic images, A is configured to 50 with SNRs = 10, 20, 30, 40, 50, 60, 70, 80, 90 and 100 for all synthetic images in Figure 11. For each synthetic image and each SNR, 10 sets of test images are generated. In the next step, FoM of each test image is calculated and the FoM of a specific image and SNR is computed by averaging over these 15 test images. Therefore, each FoM is obtained from 10 test images. All test images are $6 \times 15 \times 10 = 900$. FoM results of methods Prewitt [30], He et al. [34], Sonya et al. [39], He et al. [45] and the proposed method applied to 6 synthetic images in 10 mentioned SNRs are shown in Table 1.

Results show that the proposed method has increased accuracy in the majority of cases. The proposed method outperforms other methods in Curved, Chess and Wave edge images over all SNRs. In the Chess edge images, the proposed method outperforms other methods in all SNRs. In the Horizontal, Curved and Wave edge images, the proposed method achieves better accuracy in 9 SNRs out of 10. In the Oriented edge image, the proposed method outperforms other methods in 6 SNRs among 10 ones and in the rest SNRs the FoM of the proposed method is very close to Sonya. Sonya achieves better FoM in 9 SNRs out of 10 on the Square edge image. Therefore, Sonya achieves better accuracy in Square edge image. To sum up, the proposed method outperforms other methods in 44 cases out of 60 (73.33% of cases).

4. 2. Edge Detection on Real Images For further evaluation of the proposed edge detector, 15 real images and 15 images taken from Coil-100 dataset [45] are used as shown in Figure 12.

To compare visually, edge detection results of all methods are shown in Figure 13. In each row, the left image is input image and the others are results of Middleton and Sivaswamy [30], He et al. [34], Sonya et al. [38], He et al. [44] and the proposed method, respectively.

TABLE 1. FoM results for all methods in different SNRs and Synthetic images shown in Figure 11

Image	Method	SNR=10	SNR=20	SNR=30	SNR=40	SNR=50	SNR=60	SNR=70	SNR=80	SNR=90	SNR=100
Horizontal	Proposed	**0.96099**	**0.96390**	**0.96115**	**0.96370**	**0.96561**	**0.96673**	**0.96655**	**0.96606**	0.96610	**0.96744**
	He [44]	0.52438	0.94502	0.95592	0.95671	0.95599	0.95601	0.96074	0.95921	0.96140	0.96243
	Sonya [38]	0.66342	0.95620	0.96072	0.96156	0.96396	0.96624	0.96618	0.96501	**0.97049**	0.96739
	He [34]	0.41895	0.70703	0.69897	0.71551	0.72674	0.71581	0.71994	0.73294	0.71669	0.72526
	Middleton [30]	0.45180	0.93496	0.94372	0.94499	0.94203	0.94205	0.94402	0.94367	0.94427	0.94665
Oriented	Proposed	**0.97649**	**0.98534**	0.98870	0.98998	**0.99100**	0.99114	0.99220	**0.99243**	**0.99282**	**0.99319**
	He [44]	0.69861	0.98127	0.98319	0.98297	0.98576	0.98790	0.99006	0.98794	0.98983	0.98899
	Sonya [38]	0.72752	0.98442	**0.98889**	**0.99073**	0.98935	**0.99164**	**0.99324**	0.99123	0.99203	0.99280
	He [34]	0.59332	0.92251	0.90948	0.92973	0.93646	0.93019	0.94358	0.94004	0.94408	0.94577
	Middleton [30]	0.63586	0.97089	0.97582	0.97832	0.98028	0.97915	0.98278	0.98367	0.98413	0.98484
Curved	Proposed	**0.97255**	**0.97876**	**0.98201**	**0.98278**	0.98335	**0.98393**	**0.98558**	**0.98598**	**0.98584**	**0.98724**
	He [44]	0.67431	0.96834	0.97439	0.98130	**0.98349**	0.98357	0.98310	0.98486	0.98533	0.98499
	Sonya [38]	0.62811	0.96866	0.97686	0.97654	0.97772	0.98017	0.97992	0.97980	0.98029	0.98069
	He [34]	0.48692	0.95903	0.96227	0.97320	0.96093	0.97728	0.97301	0.97934	0.97419	0.97852
	Middleton [30]	0.54296	0.95696	0.96085	0.95960	0.94371	0.97124	0.95502	0.97749	0.96486	0.97253
Square	Proposed	**0.91313**	0.96481	0.97426	0.97581	0.97806	0.97663	0.97694	0.97681	0.97893	0.97794
	He [44]	0.68941	0.97439	0.98017	0.98238	0.98508	0.98395	0.98483	0.98576	0.98631	0.98517

	Sonya [38]	0.71867	**0.98655**	**0.99139**	**0.99322**	**0.99444**	**0.99523**	**0.99676**	**0.99632**	**0.99727**	**0.99782**
	He [34]	0.61212	0.80975	0.81267	0.83886	0.84299	0.85720	0.86391	0.87249	0.87276	0.87786
	Middleton [30]	0.64802	0.96671	0.97003	0.97165	0.97264	0.97274	0.97389	0.97449	0.97520	0.97562
	Proposed	**0.96527**	**0.96924**	**0.97286**	**0.97259**	**0.97329**	**0.97465**	**0.97457**	**0.97609**	**0.97608**	**0.97594**
Chess	He [44]	0.87642	0.96829	0.97070	0.97193	0.97006	0.97081	0.97216	0.97274	0.97228	0.97301
	Sonya [38]	0.90638	0.92554	0.92758	0.92897	0.93165	0.93597	0.94201	0.94233	0.94417	0.94433
	He [34]	0.82936	0.80940	0.81811	0.83242	0.84313	0.84152	0.84751	0.85252	0.85684	0.85611
	Middleton [30]	0.85503	0.95528	0.95925	0.95901	0.96103	0.96088	0.96217	0.96317	0.96255	0.96350
	Proposed	**0.96661**	**0.97076**	**0.97233**	0.97471	**0.97607**	**0.97595**	**0.97710**	**0.97766**	**0.97789**	**0.97819**
	He [44]	0.87631	0.96893	0.97135	**0.97486**	0.97493	0.97235	0.97482	0.97399	0.97467	0.97620
	Sonya [38]	0.87150	0.96694	0.97087	0.97303	0.97471	0.97423	0.97694	0.97652	0.97684	0.97725
Wave	He [34]	0.78957	0.95220	0.94489	0.95508	0.96093	0.96593	0.96248	0.96235	0.97079	0.97147
	Middleton [30]	0.81584	0.96233	0.94929	0.95974	0.96001	0.96851	0.96418	0.95981	0.97223	0.97189

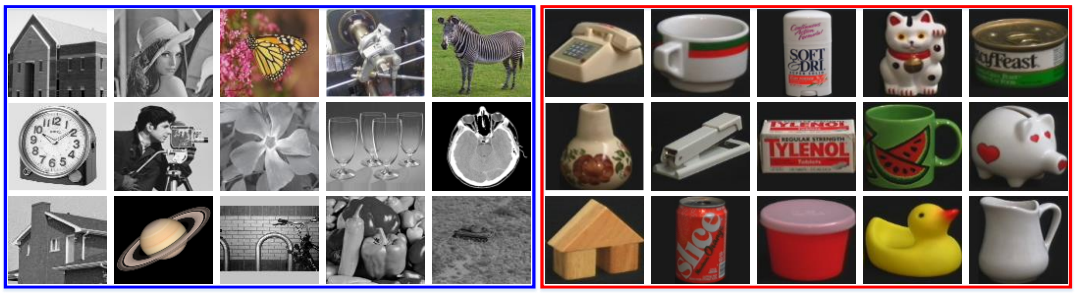

Figure 12. Real images (in blue box) and images from Coil-100 dataset (in red box) for quality evaluation

Figure 13. Edge detection results applied to images in Figure 12

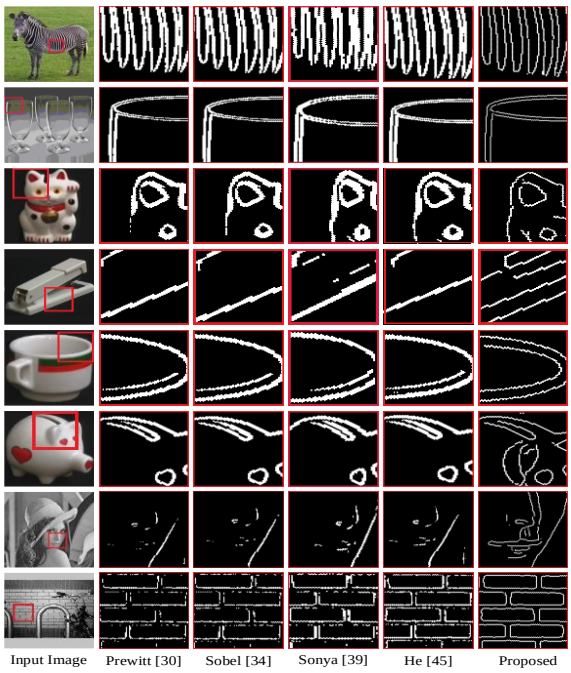

Figure 14. sub-image of 8 real images to illustrate edge detection quality of all methods in details

To illustrate edge detection quality of all methods in details, sub-image of 8 real images are selected and shown in Figure 14. It is obvious that detected edges in the proposed method are more accurate than the other methods. Indeed, the proposed method extracts the edges more accurately and edges are thinner than the other methods.

Edges are identified based on T_{low} and T_{high} thresholds in Equation (15). Pixels lower than T_{low} are excluded from edges and pixels greater than T_{high} are labeled as edge. Pixels between these thresholds are further evaluated in the next steps. Higher values of T_{low} leads to loss real edge pixels and lower values of T_{high} assigns edge label to non-edge pixels. Therefore, redundant edges appeared in images stem from threshold values. In the proposed methods, thresholds have been configured carefully, although even appropriate values of thresholds cannot exclude all redundant edges from edge pixels.

5. CONCLUSION

This paper presented a new edge detector in hexagonal lattice which includes square to hexagonal transformation, gradient magnitude and direction calculation, level quantization, non-maximum suppression, thresholds selection, double thresholding and edge tracking.

To evaluate detected edges, the proposed method was evaluated on two datasets of synthetic and real images. Results showed the superiority of the proposed method quantitatively and qualitatively. Suggested works can be directed toward implementing other image processing algorithms such as, corner detection, object segmentation and image filtering in hexagonal domain.

5. REFERENCES

1. Middleton, L. and Sivaswamy, J., "Hexagonal image processing: A practical approach, Springer Science & Business Media, (2006).
2. Coxeter, H.S.M., "Introduction to geometry", (1961).
3. Petersen, D.P. and Middleton, D., "Sampling and reconstruction of wave-number-limited functions in n-dimensional euclidean spaces", ***Information and Control***, Vol. 5, No. 4, (1962), 279-323, doi: 10.1016/S0019-9958(62)90633-2.
4. Mersereau, R.M., "The processing of hexagonally sampled two-dimensional signals", ***Proceedings of the IEEE***, Vol. 67, No. 6, (1979), 930-949, doi: 10.1109/PROC.1979.11356.
5. Kamgar-Parsi, B., "Evaluation of quantization error in computer vision", ***IEEE Transactions on Pattern Analysis & Machine Intelligence***, Vol. 11, No. 09, (1989), 929-940, doi: 10.1109/34.35496.
6. Kamgar-Parsi, B., "Quantization error in hexagonal sensory configurations", ***IEEE Transactions on Pattern Analysis & Machine Intelligence***, Vol. 14, No. 06, (1992), 665-671, doi: 10.1109/34.141556.
7. Scotney, B., Coleman, S. and Gardiner, B., "Biologically motivated feature extraction using the spiral architecture", in 2011 18th IEEE International Conference on Image Processing, IEEE., (2011), 221-224.
8. Staunton, R.C., "An analysis of hexagonal thinning algorithms and skeletal shape representation", ***Pattern recognition***, Vol. 29, No. 7, (1996), 1131-1146, doi: 10.1016/0031-3203(94)00155-3.
9. Staunton, R., "One-pass parallel hexagonal thinning algorithm", ***IEE Proceedings-Vision, Image and Signal Processing***, Vol. 148, No. 1, (2001), 45-53, doi: 10.1049/cp:19990443.
10. Fadaei, S. and Rashno, A., "A framework for hexagonal image processing using hexagonal pixel-perfect approximations in subpixel resolution", ***IEEE Transactions on Image Processing***, Vol. 30, (2021), 4555-4570, doi: 10.1109/TIP.2021.3073328.
11. Asharindavida, F., Hundewale, N. and Aljahdali, S., "Study on hexagonal grid in image processing", ***Proc. ICIKM***, Vol. 45, (2012), 282-288, doi: 10.1.1.707.7492.
12. He, X., Jia, W. and Wu, Q., "An approach of canny edge detection with virtual hexagonal image structure", in 2008 10th International Conference on Control, Automation, Robotics and Vision, IEEE., (2008), 879-882.
13. Staunton, R.C., "The processing of hexagonally sampled images", ***Advances in Imaging and Electron Physics***, Vol. 119, (2001), 191-265, doi: 10.1016/S1076-5670(01)80088-4.
14. Jeevan, K. and Krishnakumar, S., "Compression of images represented in hexagonal lattice using wavelet and gabor filter", in 2014 International Conference on Contemporary Computing and Informatics (IC3I), IEEE., (2014), 609-613.
15. Jiang, Q., "Fir filter banks for hexagonal data processing", ***IEEE Transactions on Image Processing***, Vol. 17, No. 9, (2008), 1512-1521, doi: 10.1109/TIP.2008.2001401.

16. Nourian, M.B. and Aahmadzadeh, M., "Image de-noising with virtual hexagonal image structure", in 2013 First Iranian Conference on Pattern Recognition and Image Analysis (PRIA), IEEE., (2013), 1-5.
17. Li, X., "Implementation of a simulated display for hexagonal image processing", ***Displays***, Vol. 50, (2017), 63-69, doi: 10.1016/j.displa.2017.09.005.
18. Wang, F., Ni, J. and Guo, R., "Modulation transfer function of an imaging system with a hexagonal pixel array detector", ***Optik***, Vol. 179, (2019), 986-993, doi: 10.1016/j.ijleo.2018.11.035.
19. Gardiner, B., Coleman, S.A. and Scotney, B.W., "Multiscale edge detection using a finite element framework for hexagonal pixel-based images", ***IEEE Transactions on Image Processing***, Vol. 25, No. 4, (2016), 1849-1861, doi: 10.1109/TIP.2016.2529720.
20. Li, X., "Storage and addressing scheme for practical hexagonal image processing", ***Journal of Electronic Imaging***, Vol. 22, No. 1, (2013), 010502, doi: 10.1117/1.JEI.22.1.010502.
21. Liu, S.J., Coleman, S., Kerr, D., Scotney, B. and Gardiner, B., "Corner detection on hexagonal pixel based images", in 2011 18th IEEE International Conference on Image Processing, IEEE., (2011), 1025-1028.
22. He, X., Jia, W., Hur, N., Wu, Q. and Kim, J., "Image translation and rotation on hexagonal structure", in The Sixth IEEE International Conference on Computer and Information Technology (CIT'06), IEEE., (2006), 141-141.
23. Gardiner, B., Coleman, S. and Scotney, B., "Fast edge map pyramids for hexagonal image structures", in 2009 13th International Machine Vision and Image Processing Conference, IEEE., (2009), 41-46.
24. He, X., Wang, H., Hur, N., Jia, W., Wu, Q., Kim, J. and Hintz, T., "Uniformly partitioning images on virtual hexagonal structure", in 2006 9th International Conference on Control, Automation, Robotics and Vision, IEEE., (2006), 1-6.
25. Fadaei, S., Amirfattahi, R. and Ahmadzadeh, M.R., "New content-based image retrieval system based on optimised integration of dcd, wavelet and curvelet features", ***IET Image Processing***, Vol. 11, No. 2, (2017), 89-98, doi: 10.1049/iet-ipr.2016.0542.
26. Duan, Y., Lu, J., Feng, J. and Zhou, J., "Context-aware local binary feature learning for face recognition", ***IEEE transactions on Pattern Analysis and Machine Intelligence***, Vol. 40, No. 5, (2017), 1139-1153, doi: 10.1109/TPAMI.2017.2710183.
27. Fadaei, S., Amirfattahi, R. and Ahmadzadeh, M.R., "Local derivative radial patterns: A new texture descriptor for content-based image retrieval", ***Signal Processing***, Vol. 137, (2017), 274-286, doi: 10.1016/j.sigpro.2017.02.013.
28. Fadaei, S. and Rashno, A., "Content-based image retrieval speedup based on optimized combination of wavelet and zernike features using particle swarm optimization algorithm", ***International Journal of Engineering***, ***Transactions B: Applications***, Vol. 33, No. 5, (2020), 1000-1009, doi: 10.5829/IJE.2020.33.05B.34.
29. Fadaei, S., "New dominant color descriptor features based on weighting of more informative pixels using suitable masks for content-based image retrieval", ***International Journal of Engineering***, ***Transactions B: Applications,*** Vol. 35, No. 8, (2022), doi: 10.5829/IJE.2022.35.08B.01.
30. Middleton, L. and Sivaswamy, J., "Edge detection in a hexagonal-image processing framework", ***Image and Vision Computing***, Vol. 19, No. 14, (2001), 1071-1081, doi: 10.1016/S0262-8856(01)00067-1.
31. Staunton, R.C., "The design of hexagonal sampling structures for image digitization and their use with local operators", ***Image and Vision Computing***, Vol. 7, No. 3, (1989), 162-166, doi: 10.1016/0262-8856(89)90040-1.
32. Li, J., Tang, X. and Jiang, Y., "Comparing study of some edge detection algorithms", ***Information Technology***, Vol. 38, No. 9, (2007), 106-108, doi: 10.1109/ICCCIS51004.2021.9397225.
33. Davies, E., "Circularity—a new principle underlying the design of accurate edge orientation operators", ***Image and Vision Computing***, Vol. 2, No. 3, (1984), 134-142, doi: 10.1016/0262-8856(84)90049-0.
34. He, X., Jia, W., Li, J., Wu, Q. and Hintz, T., "An approach to edge detection on a virtual hexagonal structure", in 9th Biennial Conference of the Australian Pattern Recognition Society on Digital Image Computing Techniques and Applications (DICTA 2007), IEEE., (2007), 340-345.
35. He, X., Li, J., Wei, D., Jia, W. and Wu, Q., "Canny edge detection on a virtual hexagonal image structure", in 2009 Joint Conferences on Pervasive Computing (JCPC), IEEE., (2009), 167-172.
36. Gardiner, B., Coleman, S. and Scotney, B., "Multi-scale feature extraction in a sub-pixel virtual hexagonal environment", in 2008 International Machine Vision and Image Processing Conference, IEEE., (2008), 111-116.
37. Mostafa, K., Chiang, J. and Her, I., "Edge-detection method using binary morphology on hexagonal images", ***The Imaging Science Journal***, Vol. 63, No. 3, (2015), 168-173, doi: 10.1179/1743131X14Y.0000000098.
38. Coleman, S., Scotney, B. and Gardiner, B., "Tri-directional gradient operators for hexagonal image processing", ***Journal of Visual Communication and Image Representation***, Vol. 38, (2016), 614-626, doi: 10.1016/j.jvcir.2016.04.001.
39. Li, X., "Simplified square to hexagonal lattice conversion based on 1-d multirate processing", ***Signal Processing: Image Communication***, Vol. 99, (2021), 116481, doi: 10.1016/j.image.2021.116481.
40. Schlosser, T., Beuth, F. and Kowerko, D., "Biologically inspired hexagonal deep learning for hexagonal image generation", in 2020 IEEE International Conference on Image Processing (ICIP), IEEE., (2020), 848-852.
41. Varghese, P. and Saroja, G.A.S., "Hexagonal image enhancement using hex-gabor filter for machine vision applications", ***Materials Today: Proceedings***, Vol. 56, (2022), 555-558, doi: 10.1016/j.matpr.2022.02.277.
42. Luo, J., Zhang, W., Su, J. and Xiang, F., "Hexagonal convolutional neural networks for hexagonal grids", ***IEEE Access***, Vol. 7, (2019), 142738-142749, doi: 10.1109/ACCESS.2019.2944766.
43. Varghese, P. and Saroja, G.A.S., "Hexagonal image compressionusing singular value decomposition in python", in 2021 2nd International Conference on Advances in Computing, Communication, Embedded and Secure Systems (ACCESS), IEEE., (2021), 211-215.
44. He, X., Wei, D., Lam, K.-M., Li, J., Wang, L., Jia, W. and Wu, Q., "Canny edge detection using bilateral filter on real hexagonal structure", in International Conference on Advanced Concepts for Intelligent Vision Systems, Springer., (2010), 233-244.
45. Nene, S.A., Nayar, S.K. and Murase, H., "Columbia object image library (coil-100)", (1996).

Persian Abstract

چکیده

در پردازش تصویر، پیکسل‌های شش‌ضلعی نسبت به پیکسل‌های مربعی مزایای زیادی دارند. از طرفی استخراج ویژگی در بسیاری از کاربردهای پردازش تصویر از جمله تشخیص چهره، تشخیص کاراکتر، اثر انگشت و پزشکی استفاده می‌شود. آشکارسازی لبه یکی از الگوریتم‌های مهم استخراج ویژگی در تصویر است و لبه‌یاب کنی از معروفترین روش‌های استخراج لبه‌های تصویر است که نسبت به دیگر روش‌ها عملکرد مناسب‌تری دارد. در این مقاله یک الگوریتم لبه‌یابی کنی برای شبکه‌های شش‌ضلعی ارایه شده است. در روش پیشنهادی ابتدا تصویر از حالت مربعی به شش‌ضلعی تبدیل شده سپس الگوریتم لبه‌یابی کنی روی شبکه‌ی شش‌ضلعی تعریف می‌شود. روش پیشنهادی به تصاویر مصنوعی و همچنین تصاویر واقعی با سیگنال به نویزهای مختلف اعمال شده است. بر اساس معیار FoM برای تصاویر مصنوعی، روش پیشنهادی در ٤٤ حالت از ٦٠ حالت، بهتر از دیگر روش‌ها عمل نموده است و نتایج لبه‌یابی روی تصاویر واقعی برتری روش پیشنهادی را نسبت به دیگر روش‌ها نشان می‌دهد.

IJE TRANSACTIONS B: Applications Vol. 35, No. 08, (August 2022) 1599-1607

International Journal of Engineering

Journal Homepage: www.ije.ir

An Experimental Evaluation of Axial Load Bearing Capacity of Belled and Straight Piles Embedded in Sand

S. Goudar*[a], A. Kamatagi[b]

[a] *Department of Civil Engineering, SKSVMACET Lakshmeshwar, Affiliated to VTU, Belagavi, Karnataka, India*
[b] *Department of Civil Engineering, Global Academy of Engineering College Bangalore, Affiliated to VTU, Belagavi, Karnataka, India*

PAPER INFO

Paper history:
Received 22 February 2022
Received in revised form 08 May 2022
Accepted 11 May 2022

Keywords:
Straight Piles
Belled Piles
Dry Sand
Vertical Bearing Capacity
Relative Density
Belled Piles

ABSTRACT

This paper presents the laboratory axial load test results of two different geometries of model aluminum pile groups, such as equal section piles, and enlarged base (Belled) piles embedded in locally available river sand. For belled piles, the enlarged diameter is achieved by providing a 3-degree outer extension angle at the middle of equal section piles to all three L/D ratios. The load versus settlement tests are carried out on 1X1 and 1X2 of both pile groups having a length to diameter ratios (L/D) of 12, 17, and 22. The spacing to diameter (S/D) of 3, 4, and 5 times of D and 3, 4, and 5 times of D_b. (Where D is 31mm equal section outer diameter of model pile and D_b is 46.7mm enlarged base diameter of belled pile respectively). To avoid overlapping stress zone at bottom of piles during application of load. All the tests are conducted in a brick masonry testing tank of 1X1X1m. The vertical load is applied on a single pile and group of both piles by using a 30kN capacity of hydraulic inverted jack, run by a 1HP single phase motor. The load-bearing capacity is evaluated and a comparison is made between straight piles and belled piles. It is observed that the load-carrying capacity is higher in a belled model pile at a lesser L/D ratio. However, the load-carrying capacity increased 40% higher than straight piles, because of the extension angle. In addition, (S/D) and (S/D_b) make significant variations in bearing capacity.

***doi**: 10.5829/ije.2022.35.08b.16*

1. INTRODUCTION

1. 1. General The most common foundations in coastal areas offshore, and waterlogged areas are pile foundations. These foundations are quite commonly subjected to lateral loads and vertical loads, the failure of these foundations is usually due to earthquakes, wind force, and some of the unexpected major impacts from the nature. Often deep foundations are constructed in groups to withstand the structure and the behavior of these groups of piles differs considerably comparing to single piles. However, in the case long piles (Flexible piles) are required to construct deeper in the ground, which requires more usages of concrete as compared to short piles (Rigid piles). Sandy soil, saturated soil deposit and marine clay supporting deep foundations under lateral and vertical loading shows deterioration in rigidity and decreases in shear strength. The problems under such loadings on piles in these soils are formation of gap at pile soil interface, and it develop the pore pressure and retreat of soft soils, causes the measurable deformations and greater bending moments than uniform loading. However, most of the researchers have investigated pile foundations in groups of piles as well as single piles under vertical and lateral loading conditions but a few kinds of literature are reported on the effect of increasing the L/D ratio and most common failures. In this present study, attempts are made to analyze the effect of the L/D (12, 17, and 22) ratio in equal section piles and partially tapered belled piles under vertical load with evaluating critical S/D ratio in both geometry of piles.When the flexible piles are under vertical load the pile resists load through pile-soil interaction and base the resistance. However, when the

*Corresponding Author Email: shivarajkumar.goudar@gmail.com (S. Goudar)

Please cite this article as: S. Goudar, A. Kamatagi, An Experimental Evaluation of Axial Load Bearing Capacity of Belled and Straight Piles Embedded in Sand, ***International Journal of Engineering, Transactions B: Applications***, Vol. 35, No. 08, (2022) 1599-1607

load is acting with some inclination, it is the reason for the decrease in resistance offered by the pile foundations, because of deficiency in the base resistance and the shaft friction.

2. LITERATURE REVIEW

Previous investigations stated that increasing the embedment ratio can increase the load-carrying capacity by creating friction on the surrounding soil and pile surface [1]. Harris and Madabhushi [2] investigated the effect of changing the angle of the under-reamed bulbs on pullout and load-displacement curve in three-dimensional models by varying density of dry sand. They concluded that there is a measurable impact on uplift capacity by varying angles of the under-reamed bulb and it also depends on the state of sand deposit around the pile surface. Arabpanahan et al. [3] have studied and examined the behavioral aspects of five strip foundations keeping width constant and varying the embedment depth in loose sandy soil under vertical loading. They have concluded that increasing the depth to width ratio from 0 to 1.2 causes an increase in load-carrying capacity and axial stiffness for 33 and 23% respectively. The investigations on displacement behavior of belled piles are relatively very less. These piles are having more vertical bearing capacity, due to providing a large bottom surface. Rahman et al. [4]. studied on single and group piles with various L/d ratios and maintaining pile material as same, that is aluminum pile having a hollow tube of 19 mm outside diameter and 0.81 mm wall thickness which was used and the outer diameter was 20 mm with L/d ratio of 20, 30, and 35. The lateral load resistance of a single L/d ratio is 32, and different S/D ratios as 6D and 3D. Khari et al. [5], the model pile group configurations such as 1X2, 1X3, 2X2, 3X3, and 3X2 were selected in two different relative densities of sand. In addition, the pile cap made up of steel plate having a thickness of 0.64 cm was used. For all configurations such as the 1X2 and 2X2 pile groups, in the experimental setup, the model tank of dimension 1x1x1m was used**.** They have concluded that the difference in lateral displacement increased when the relative density increased from 30 to 75% under the same loading condition. Pile to pile interaction is very minimum in 6d ratio in dense sand but sometimes it may be more in a loose state. Soil medium as sand was poured at a height of 0.5 meters into the tank and maintained uniform density, thereafter the lateral load was applied by pulley arrangement with flexible wire attached to the pile cap. Displacements were measured by sensitive dial gauges having a 0.01 mm least count. In the test, one a single pile was tested with L/D ratios of 20, 30, and 35 and obtained the test results as 107N, 196N, and 225N, respectively. As the L/D ratio increases the lateral load, carrying capacity increases in a single pile. In test two having a 2X2 pile group and L/D ratio was kept as constant as 20, but varying S/D ratios as 3d, 4.5d and 6d. The obtained values were 166N, 196N and 225N, respectively. In the third test having a 2X1 pile group again, L/D was kept constant at 20 and S/D as 3d, 4.5d, and 6d the obtained values were 117.2N, 147N, and 166N, respectively. All these test results are compared with theoretical values suggested by and got almost same values. In the 2X2-pile group, the S/D ratio of 3 is 41.63% greater than the 1X2 pile group of S/D of 3. In the 2X2-pile group, the S/D ratio of 4.5 is 33.33% greater than the 1X2-pile group of S/D of 6. In the 2X2-pile group, the S/D ratio of 6 is 35.3% greater than the 1X2 pile group of S/D of 6. Finally, it is observed that the length to diameter ratio takes a major role in increasing the lateral capacity of the single pile and pile group. This investigation helps to study about L/D ratio and S/D ratio. The gap in the research work is the relative density of sand when the cohesive less soil is considered as a soil medium, the relative density takes a major role in the results. On the other hand, the pore water pressure also makes a significant difference in the loading mechanism. Issac and Thomas [6] In this paper the behavior of single model steel and concrete piles subjected to changing inclination loads to failure in cohesion-less soil was investigated. Under various inclination loads, experimental results of the ultimate vertical load-bearing capacity and lateral load-carrying capacity of piles immersed in the sand were plotted. They concluded that the axial load and the lateral capacity of the pile increase with the increase in L/D ratios [7-11]. The circular deep foundations are evaluvated in series of 3D numerical analyses on pile raft pile length, spacing, and pile configurations inorder to evaluate the numerical modeling results of previous investigators. They conclued that soft soil, dense soil, pile spacing, and length of pile are the main parameters used to reduce the settlement and increas in pile contribution ratio. This could be due to an increase in passive resistance with the increase in pile length. Constructing more numbers of piles to increse the performance of foundation sutaible only limited to optimum level further incresing leads to no additinoal benefits in beasring capacities. During the installation of mini pile the excess pore water pressure increase in satureated soil mass around the surface of clay. The excess pore water pressure decreases by increasing over consolidation ratio during installation of mini piles. The axial load capacities of concrete piles are found to be more than that of steel piles. Whereas lateral load capacities of steel piles were found to be more than that of concrete piles furthermore, thousands of researches are completed on the experimental side and theoretical side to examine the loading mechanism and the reason for the failure of deep foundations.

However, very least research was conducted, by considering combined loading with saturated conditions of soil medium to understand the failure mechanism of single and group of piles. These ample literatures are mainly focused on experimental and theoretical investigations of vertically and laterally loaded flexible piles. A few studies were found on belled piles in order to increase the bearing capacity in weak soil. In this present study, trials were made to increase the load-carrying capacity by providing a minimum extension angle at the bottom of the pile. This can be the main reason to reduce the consumption of concrete and avoid the failure of long (flexible piles).

3. MATERIALS AND EXPERIMENTAL SETUP

3. 1. Model Piles The model pile materials and dimensions selected to adhere to similitude laws. Wood et al. [12] and Chandrasekaran et al. [13] proposed the scaling law, based on their scaling laws, and the reference, the dimensions are selected for experimental investigation in the present study. The following flexural rigidity equation used to calculate the field pile parameters.

$$\frac{\text{Em Im}}{Ep\ Ip} = \frac{1}{n^5}$$

where, E_m = modulus of elasticity of model pile, E_p = modulus of elasticity of prototype pile, I_m = moment of inertia of model pile, I_p= moment of inertia of prototype pile and 1/n = scale factor for length.1/10 is fixed as scaling factor for length and $1/10^5$ is adopted as pile flexural rigidity. Aluminum 3mm gauge hollow tube of outer diameter 31mm and inner diameter is 25mm selected as model piles to ensure the prototype pile of 550mm diameter of solid section made-up of reinforced cement concrete having the compressive strength of 25N/mm^2 (M25 grade). Figure 1 shows the prototype piles used for tests.

The length to diameter ratio selected as 12, 17, and 22 to avoid boundary effects and stressed zone in the testing tank. In the present investigation, the model piles are design in order to reduce material consumption during the construction of pile foundations. Generally, the equal section piles (uniform diameter piles) have diameters of 1m, 1.5m, 2m, and 2.5m also with varying lengths of piles in large-scale construction activities. This uniform diameter of piles can consume large-scale concrete material and more space and it can lead to increase in project cost. In order to reduce the material consumption, space, and cost to achieve a higher ultimate bearing capacity a small 3 outer extension angle is adopt at the middle of the equal section piles, it enlarges the pile base diameter. During large-scale constructions, in the low bearing capacity of soils, the enlarged base diameter piles are most suited. In such conditions simply increasing, the length leads to a decrease in the performance of equal section piles. The load versus settlement behavior is observe in three different lengths to diameter ratios and three spacing to diameter ratios are investigated in both straight and belled piles. To ensure the rigidity in the pile cap the mild steel plates having a thickness of 20mm used as pile caps. The threads are provided at all piles top and the same pitch screws are made in pile cap up to 10mm deep, by screwing piles into the pile cap fixity condition is achieved.

Figure 1. Prototype aluminum pile

3. 2. Sand The locally available river sand is used for experiments. Initially, the sand was in wet condition so it completely air-dried and kept in an open atmosphere to ensure complete dry condition. It is

TABLE 1. Model pile parameters

D_s	Alpha (α^0)	(L/D)	D_b (mm)	S/D	Remark
31	3^0	12	46.7	3	Belled Pile
				4	
				5	
		17	53.3	3	
				4	
				5	
		22	59.8	3	
				4	
				5	
31	0^0	12	31	3	Straight piles
				4	
				5	
		17	31	3	
				4	
				5	
		22	31	3	
				4	
				5	

For belled pile, D_b is used, and for straight pile, D is used. α is extension angle, D_b is base diameter and D is outer diameter of equal section pile.

sieved from 600 microns IS sieve to maintain homogeneity, the basic properties of sand were carried out according to IS 2720 (Part 4)-1985 [14] represented in Table 2. Based on the sieve analysis test, the sand is classified as poorly graded sand (SP). Figure 2 shows the particle size distribution curve. The sand bed is prepared by rainfall technique, several trials are made at the laboratory to attain medium dense state, and it is achieved at height of fall of 70cm from the base. In addition, the relative density measured 39.5% at medium dense sand.

3. 3. Test Setup and Procedure The line diagram experimental setup used for axial compression load tests on pile groups is shown in Figure 3. The tests are conducted on prototype piles embedded in sand bed prepared in testing tank build up with brick masonry having dimensions of 1x1x1meters (LxBxH) to ensure there is no boundary effect. The load applied on the pile cap, made up of mild steel having a thickness of 20mm, the piles placed in the testing tank with respect to the center of gravity (CG) of the testing tank and pile cap. A 70% of the tank is filled with sand at the calculated height of fall then piles are carefully placed in a tank and continued sand bed preparation until the top surface of the tank. However, the loading frame designed and constructed in a laboratory, the 10mm thick solid mild steel having a width of 3cm is fixed an arch-shape, which is connected to two parallel "L" shaped angles fixed in the testing tank. Additional care is taken to minimize any deflections during the application of loads to the pile groups. The model piles are fixed to the pile cap by providing the thread system at the top of the pile and respective threads are made in the pile cap at depth of 10mm to ensure rigidity. The load application procedure is as follows, the 30kN capacity of the inverted hydraulic jack is fixed at the center of the arch-type of loading frame and the 1HP single-phase motor is used to operate the jack. The rate of the load is maintained at 1.25mm/min and for every 30-second interval, the dial gauge readings and 30kN capacity of proving ring readings are measured.

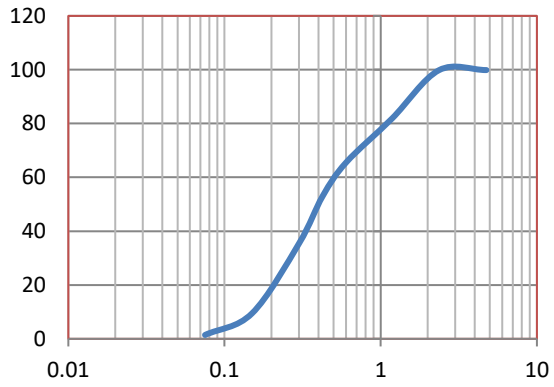

Figure 2. Shows particle size distribution curve

TABLE 2. Physical Properties of Sand

Parameter	Symbol and Unit	Values
Specific gravity	-	2.64
Coefficient curvature	C_c	1.02
Uniformity coefficient	C_u	3.25
Maximum dry density	gr/cm^3	1.81
Minimum dry density	gr/cm^3	1.466
Maximum void ratio (e_{max})	-	0.96
Minimum void ratio (e_{min})	-	0.46
Relative density	%	39.5
Classification	-	SP

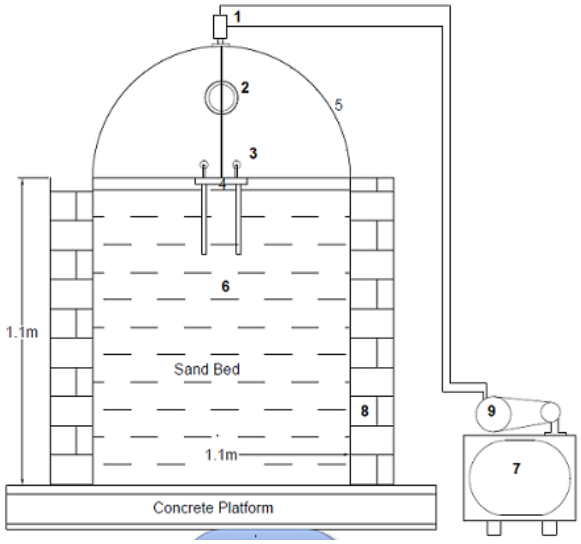

Figure 3. The systematic loading setup line diagram

3. 4. Pile Spacing The group effect is compared between single piles and groups of both belled piles and straight piles. The three different spacing to diameter (S/d) is adopted as 3D, 4D, and 5D. Where D is the outer diameter of 31mm for equal

TABLE 3. Description of loading setup

SL No.	Description	
1	Inverted Hydraulic jack	6. Sand Bed
2	Proving ring	7. 1 Hp Single Phase Mortar
3	Dail Gauge	8. Brick Masonry
4	Pile Cap	9. Oil Tank
5	M.S.Steel Section	

section piles. For belled piles, the S/D ratio is maintained as the same parameters but where D_b is enlarged base diameters 46.7mm to avoid the stress zone in between the pile group. Figure 4. Shows configuration of pile groups Khari et al. [5] they have investigated on twelve model pile groups under monotonic lateral loading. The pile groups configurations as 1 X 2, 1 X 3, 2 X 2, 3 X 3, and 3 X 2 and L/D ratio of 32. All groups of piles placed in loose and dense dry sand. They concluded that 53% higher ultimate lateral load was achieved in increasing s/d ratio from 3 to 6, and increasing number of piles in groups reduced the efficiency of group due to overlapped stress zone. Rollins et al. [15] focused on effect of pile spacing in stiff clay, s/d ratio 3.3, 4.4, and 5.65 times the pile diameter. They found effect of decrease in load carrying capacity by increasing the spacing. The pictorial view of configuration of pile groups is shown in Figure 5. In addition, the pictorial view of configuration of pile groups is depicted in Figure 6.

4. RESULTS AND DISCUSSION

The load-displacement curve is plotted from the test results; the ultimate load is obtained by the tangent intersection method [13, 16-21]. In which initial and final tangent lines are drawn to the load-displacement curves and the point of intersection of this tangent line

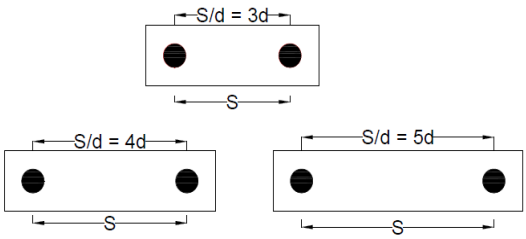

Figure 4. Configuration of pile groups

Figure 5. Pictorial view of configuration of pile groups

Figure 6. Pictorial representation of loading setup

is the ultimate load-carrying capacity (Q_u) also the corresponding settlement of pile for applied load is discussed. In Figure 7 the load versus settlement test conducted to a single belled pile L/D ratio of 12, initially, the curve is straight which means the model pile carries the vertical load. After reaching, the optimum level there is a defalcation in a curve, which indicates settlement of belled pile.

In Figure 7, the length to diameter ratio of 12 is tested and the ultimate load-carrying capacity Q_u is observed as 6.83kg. Comparison of load deflection behavior of single belled piles is shown in Figure 8. In Figure 9, the ultimate load-carrying capacity of a single straight pile is noted as 3.25kg. It is clearly observed that the maximum load observed in the straight piles 1X2 group of piles 3D, 4D, and 5D pile spacing carries load of 5.70Kg, 4.40Kg, and 4.18Kg, respectively, in L/D ratio 12. Whereas, in belled piles, $3D_b$, $4D_b$, and $5D_b$ pile spacing carries the load in the 1X2 group of belled piles as 9.38Kg, 8.06Kg, and 7.03Kg, respectively. As the spacing of piles increases, there is a decrease in the load-carrying capacity of the pile group.

As compared to the belled pile group, the load-carrying capacity is 40% more than that of straight pile groups in 3D and further, increasing the pile spacing there is decrement in load-carrying capacity. It is proved that the load settlement of belled piles were higher than that of straight piles. However, this does not mean that the bearing capacity of belled piles were always higher than those of straight piles, since the method for obtaining bearing capacities of both piles is measured based on extension angle and equal section piles.

The comparison of load deflection behavior of belled pile groups is shown in Figure 10. Comparison of load deflection behavior of belled pile groups for different Qu combination of L/D are illustrated in Figures 11-15.

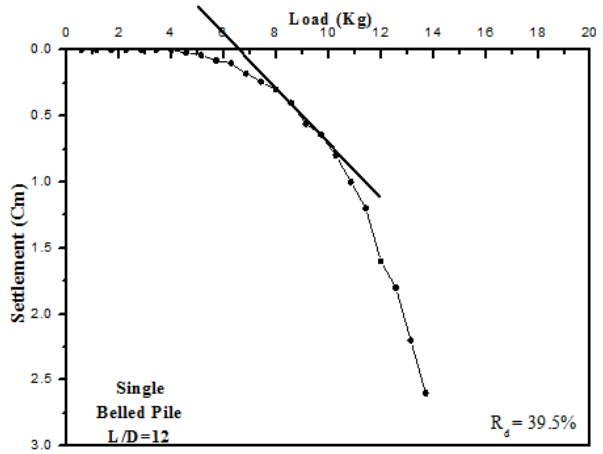

Figure 7. Load deflection behavior of single belled pile (Q_u= 6.83Kg)

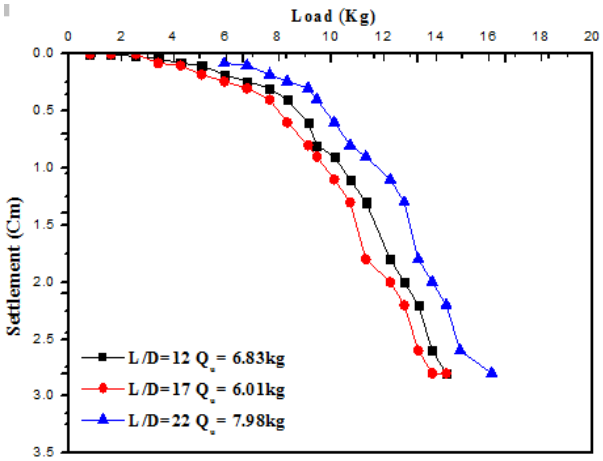

Figure 8. Comparison of load deflection behavior of single belled piles

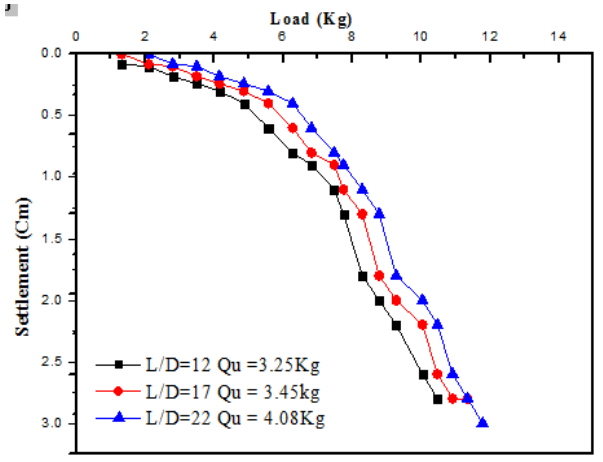

Figure 9. Comparison of load deflection behavior of single straight piles

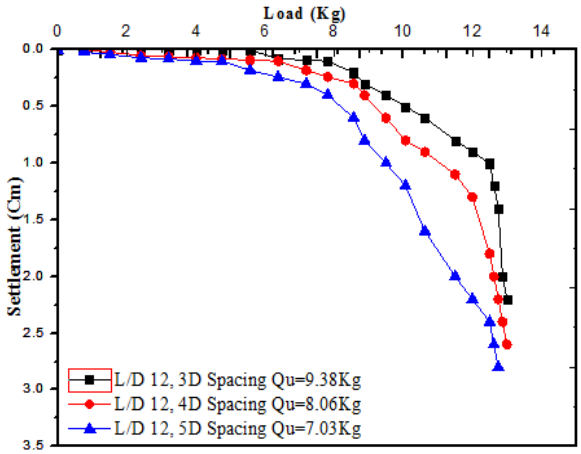

Figure 10. Comparison of load deflection behavior of belled pile groups

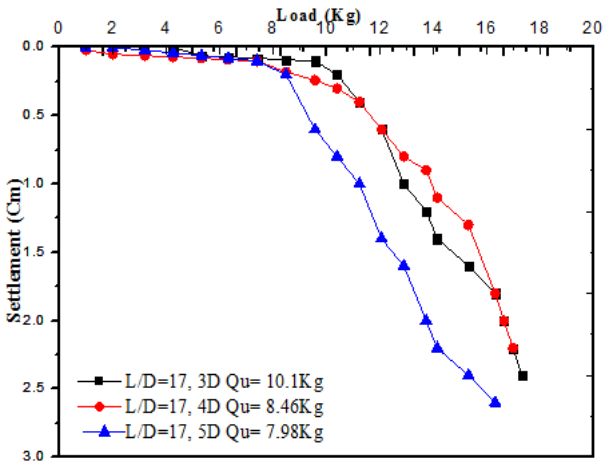

Figure 11. Comparison of load deflection behavior of belled pile groups

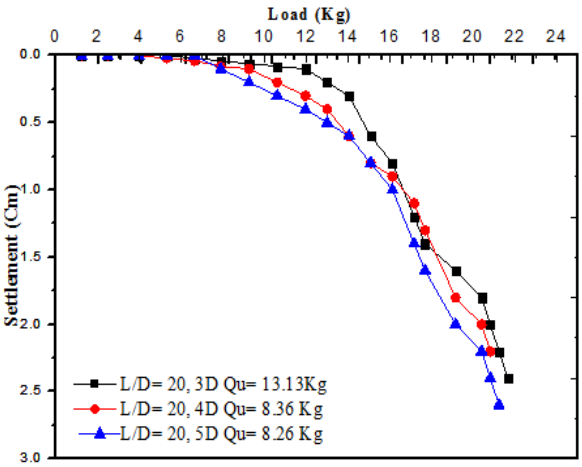

Figure 12. Comparison of load deflection behavior of belled pile groups

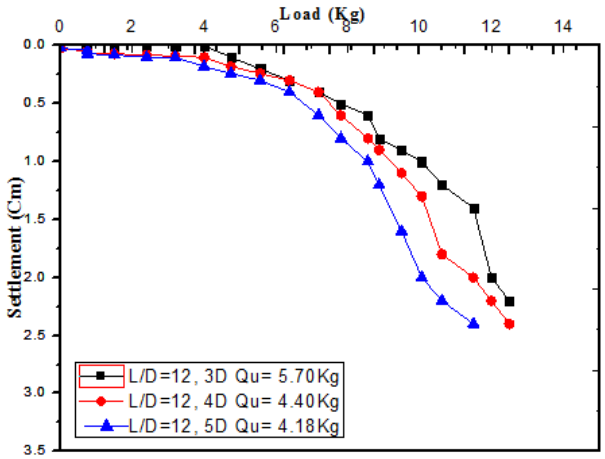

Figure 13. Comparison of load deflection behavior of straight pile groups

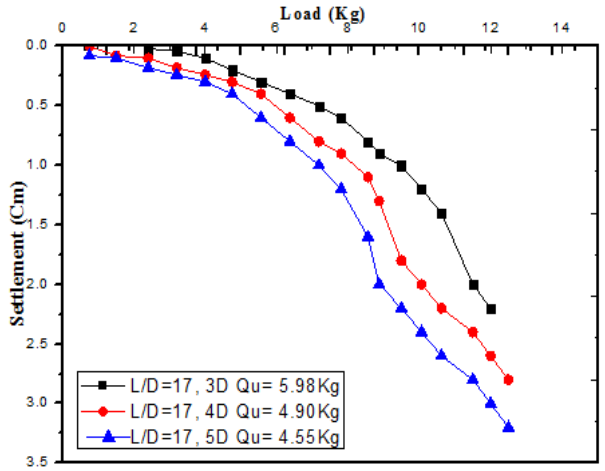

Figure 14. Comparison of load deflection behavior of straight pile groups

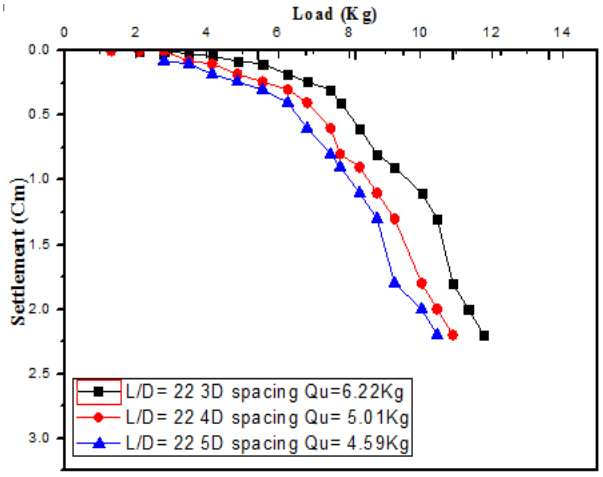

Figure 15. Comparison of load deflection behavior of straight pile groups

TABLE 4. Vertical load carrying capacity of Single and group of both Piles

Sand bed	R_d (%)	L/D	S/D	Q_u (Kg)	Pile Group	Remark
Medium dense sand	39.5	12	-	6.83	1X1	Belled piles
			$3D_b$	9.38	1X2	
			$4D_b$	8.06		
			$5D_b$	7.03		
		17	-	6.01	1X1	
			$3D_b$	10.1	1X2	
			$4D_b$	8.46		
			$5D_b$	7.98		
		22	-	7.28	1X1	
			$3D_b$	13.13	1X2	
			$4D_b$	8.36		
			$5D_b$	8.26		
Medium dense sand	39.5	12	-	3.25	1X1	Straight piles
			3D	5.70	1X2	
			4D	4.40		
			5D	4.18		
		17	-	3.45	1X1	
			3D	5.98	1X2	
			4D	4.90		
			5D	4.55		
		22	-	4.08	1X1	
			3D	6.22	1X2	
			4D	5.01		
			5D	4.59		

R_d is Relative density. Q_u is Ultimate load bearing capacity, L/D Length to diameter ratio and S/D Spacing to Diameter.

5. CONCLUSION

The purpose of this investigation is to attain the higher bearing capacity by reducing the length of pile and finding the optimum pile spacing. Increasing the base diameter of pile by providing small degree of extension angle can increase the benefits. Such piles are suitable for medium dense sand and soft soils with less consumption of concrete. Based on the present experimental work on model belled piles and straight piles in medium dense sand, the following conclusion is stated.

1) It is concluded that, the embedment ratio, pile spacing, and extension angle are the main parameters that affect the vertical load-carrying capacity of belled piles and straight bored piles. In a single belled pile of L/D ratio 12 is achieved bearing

capacity of 25% higher than that of L/D 12 of single straight pile.

2) Compared with equal section pile, the ultimate bearing capacity of single belled pile L/D 12 attains 40% higher than L/D 22 of the equal section pile. Providing a small extension angle of 30 at middle straight pile increases the base diameter lead to an increase load-carrying capacity. So that in equal section pile of L/D 22 the length of pile is more, that means concrete consumption is more in the field.
3) The efficiency of pile group is mainly depending on pile spacing and pile configuration. In the present investigation, the load-carrying capacity of 1X2 belled pile of L/D 12 is 20% greater than 1X2 straight pile of L/D 22 of 5D and $5D_b$ spacing respectively. The spacing between the piles and extended base diameter is directly proportional to the load-bearing capacity of piles.
4) It is clearly proves that the optimum pile spacing in all three L/D ratios is $3D_b$ of 1X2 configurations of belled pile group. The ultimate load carrying capacity Q_u is in increasing order as embedment ratio increases with same $3D_b$ spacing. Further, in $4D_b$ and $5D_b$ the Q_u is similar of $3D_b$. that means increasing the pile spacing the Q_u is linearly horizontal. Based on the laboratory test results the $3D_b$, 3D of belled pile and equal section pile attains the higher values, and there is no further increment in Q_u even increasing the pile spacing.
5) The 3^0 outer extension angle increases the base diameter, as compared to equal section piles, the load-carrying capacity is relatively high in belled piles. In addition, the material consumption is increasing as increasing the L/D ratio but it is more economical and cost-saving method to design belled piles.

6. REFERENCES

1. Bharathi, M. and Dubey, R.N., "Dynamic lateral response of under-reamed vertical and batter piles", ***Construction and Building Materials***, Vol. 158, (2018), 910-920, https://doi.org/10.1016/j.conbuildmat.2017.10.042
2. Harris, D.E. and Madabhushi, G.S.P., "Uplift capacity of an under-reamed pile foundation", ***Proceedings of the Institution of Civil Engineers-Geotechnical Engineering***, Vol. 168, No. 6, (2015), 526-538, http://dx.doi.org/10.1680/jgeen.14.00154
3. Arabpanahan, M., Mirghaderi, S.R., Hosseini, A., Parsa Sharif, A. and Ghalandarzadeh, A., "Experimental–numerical investigation of embedment effect on foundation behavior under vertical loading", ***International Journal of Civil Engineering***, Vol. 17, No. 12, (2019), 1951-1969, https://doi.org/10.1007/s40999-019-00437-y
4. Rahman, M.M., Alim, M.A. and Chowdhury, M.A.S., "Investigation of lateral load resistance of laterally loaded pile in sandy soil, University of Canterbury. Civil and Natural Resources Engineering, (2003).
5. Khari, M., Kassim, K.A. and Adnan, A., "An experimental study on pile spacing effects under lateral loading in sand", ***The Scientific World Journal***, Vol. 2013, (2013), http://dx.doi.org/10.1155/2013/734292
6. Issac, S. and Thomas, S., "A model study on pile behavior under inclined compressive loads in cohesionless soil", ***International Journal of Engineering Research & Technology (IJERT)***, Vol. 4, No. 11, (2015), 166-172S.
7. Khanmohammadi, M. and Fakharian, K., "Evaluation of performance of piled-raft foundations on soft clay: A case study", ***Geomechanics and Engineering***, Vol. 14, No. 1, (2018), 43-50, http://dx.doi.org/10.12989/gae.2018.14.1.043
8. Poulos, H., "Piled raft foundations: Design and applications", ***Geotechnique***, Vol. 51, No. 2, (2001), 95-113.
9. Khanmohammadi, M. and Fakharian, K., "Numerical simulation of soil stress state variations due to mini-pile penetration in clay", ***International Journal of Civil Engineering***, Vol. 16, No. 4, (2018), 409-419, https://doi.org/10.1007/s40999-016-0141-z
10. Leung, Y.F., Klar, A. and Soga, K., "Theoretical study on pile length optimization of pile groups and piled rafts", ***Journal of Geotechnical and Geoenvironmental Engineering***, Vol. 136, No. 2, (2010), 319-330.
11. Khanmohammadi, M. and Fakharian, K., "Numerical modelling of pile installation and set-up effects on pile shaft capacity", ***International Journal of Geotechnical Engineering***, (2017), https://doi.org/10.1080/19386362.2017.1368185
12. Wood, D.M., Crewe, A. and Taylor, C., "Shaking table testing of geotechnical models", ***International Journal of Physical Modelling in Geotechnics***, Vol. 2, No. 1, (2002), 01-13, https://doi.org/10.1680/ijpmg.2002.020101
13. Chandrasekaran, S., Boominathan, A. and Dodagoudar, G., "Group interaction effects on laterally loaded piles in clay", ***Journal of Geotechnical and Geoenvironmental Engineering***, Vol. 136, No. 4, (2010), 573-582, https://doi.org/10.1061/ASCE GT.1943-5606.0000245
14. Code, I.S., "Is 2720 (part 4)-1985 grain size analysis", ***Methods of Test for soil, Indian Standard Code, Bureau of Indian Standard***, Vol., No., doi.
15. Rollins, K.M., Olsen, R.J., Egbert, J.J., Jensen, D.H., Olsen, K.G. and Garrett, B.H., "Pile spacing effects on lateral pile group behavior: Load tests", ***Journal of Geotechnical and Geoenvironmental Engineering***, Vol. 132, No. 10, (2006), 1262-1271, doi: 10.1061/ASCE1090-02412006132:101262.
16. Davisson, M., "High capacity piles", Proceedings, Lecture Series on Innovations in Foundation Construction, Vol. 52, (1972).
17. Vesic, A.S., "Design of pile foundations", ***NCHRP Synthesis of Highway Practice***, No. 42, (1977).
18. Dharmatti, V. and Rakaraddi, G., "An experimental study on vertically loaded driven and cast-in-situ piles", ***Journal of Mechanical and Civil Engineering***, Vol. 11, No. 2, (2014), 43-48.
19. Al-Khazaali, M. and Vanapalli, S.K., "Experimental investigation of single model pile and pile group behavior in saturated and unsaturated sand", ***Journal of Geotechnical and Geoenvironmental Engineering***, Vol. 145, No. 12, (2019), 04019112, https://doi.org/10.3390/app9122435.
20. IS:, Methods for test for soil, determination of consolidation properties. 1986, Bureau of Indian Standards New Delhi.
21. 1, I.P.S., *Indian standard design and construction of pile foundations-code of practice: Concrete piles*. 2010, Bureau of Indian Standards New Delhi.

Persian Abstract

چکیده

این مقاله نتایج آزمایش بار محوری آزمایشگاهی دو هندسه مختلف از گروه‌های شمع آلومینیوم مدل، مانند شمع‌های مقطع مساوی و شمع‌های پایه بزرگ شده (Belled) تعبیه‌شده در شن و ماسه رودخانه‌ای موجود را ارائه می‌کند. برای شمع های زنگ دار، قطر بزرگ شده با ارائه یک زاویه ۳ درجه ای گسترش بیرونی در وسط شمع های بخش مساوی به هر سه نسبت L/D به دست می آید. آزمایش های بار در مقابل نشست بر روی X1۱ و X2۱ هر دو گروه شمع با نسبت طول به قطر 12 (L/D)، ۱۷ و ۲۲ انجام می شود. فاصله تا قطر 3 (S/D)، ٤، و ٥ برابر D و ۳، ٤ و ٥ برابر) .Dbکه در آن 31 D میلی متر قطر خارجی بخش مساوی شمع مدل و Db به ترتیب ٤٦.۷ میلی متر قطر پایه شمع زنگ دار بزرگ شده است). برای جلوگیری از همپوشانی ناحیه تنش در پایین شمع ها در هنگام اعمال بار. تمام آزمایشات در یک مخزن آزمایش سنگ تراشی آجری به ابعاد X1X1۱ متر انجام می شود. بار عمودی بر روی یک شمع و گروهی از هر دو شمع با استفاده از ظرفیت ۳۰ کیلونیوتن جک معکوس هیدرولیک که توسط یک موتور تک فاز HP۱ اجرا می شود اعمال می شود. ظرفیت باربری ارزیابی شده و مقایسه ای بین شمع های مستقیم و شمع های زنگ دار انجام می شود. مشاهده شده است که ظرفیت حمل بار در یک شمع مدل زنگ دار با نسبت L/D کمتر بیشتر است. با این حال، ظرفیت حمل بار ٤٠٪ بیشتر از شمع های مستقیم افزایش یافته است، زیرا زاویه امتداد دارند. علاوه بر این، (S/D)و (S/Db)تغییرات قابل توجهی در ظرفیت باربری ایجاد می کنند.

International Journal of Engineering

Journal Homepage: www.ije.ir

Optimization of Line of Magnetite Recovery from Wet Tailings by Creating Second Medium Intensity Magnetic Field (Case Study: Processing Plant of Gol-e-Gohar Hematite)

M. Hosseini Nasab*[a], R. Rezazadeh[b]

[a] *Mining Engineering Department, University of Sistan and Baluchestan, Zahedan, Iran*
[b] *Mining Engineering, Head of Golgohar's Hematite Factory, Sirjan, Iran*

PAPER INFO

Paper history:
Received 04 September 2021
Received in revised form 15 May 2022
Accepted 19 May 2022

Keywords:
Gol-e-Gohar
Magnetite
Wet Tailing Process
Pulp
Magnetic Separator

ABSTRACT

The primary raw material of the steel industry is iron. This paper aims to optimize magnetite recovery from wet tailings by increasing the iron content in the concentrate of the line. To manage tailings, a Wet Tailing Processing (WTP) line constructed at Gol-e-Gohar Iron Ore Company to recover the magnetite. The dominant crystalline phases in these tailings were quartz, albite, talc, hematite, and calcite. The line feed is 45 microns, which is not suitable for the gravity method. Thus, separation can achieve using only the magnetic method. Because of the high iron content in the tailings, a wet magnetic separator is used. According to the results, the proposed medium-intensity separator and the associated circuit modifications increase iron recovery from 7 to 30 percent; resulting in 150 tons of annual production; preventing loss of iron through concentrator plant tailings, and increasing the Blain number by 50 to 100 units in the hematite plant. Furthermore, water consumption is significantly reduced by replacing old wet tailings of the concentrator plant with new wet tailings as the feed, which is another significant achievement of this research. Instead of fresh water, saline water with flow rate of 250 cubic meters per hour are used.

***doi**: 10.5829/ije.2022.35.08b.17*

NOMENCLATURE

FOB	Free On Board	D80	The 80% passing size

1. INTRODUCTION

In recent years, steel applications have been developed [1-3]. The significant raw material of the steel industry is iron. There are several methods to increase the iron grade of its ore, the most important of which is the magnetic method [4]. In this method, particles containing magnetic properties are affected by magnetic forces [5]. Low-intensity magnetic separators, which comprise one of the most widely employed magnetic separation equipment, in both dry and wet forms, concentrate relatively large and highly magnetic particles [6-8]. Their magnetic field is permanent and is about 1,000 to 2,000 gauss. Low-intensity wet magnetic separators have better efficiency than dry type, and their extracted iron grade reaches to about 70% [6, 7].

Reuse of tailings results in savings cost for dumping and handling of tailing dumps and decreases the pollution of the environment [9].

In general, to produce iron concentrate in Gol-e-Gohar plant, pre-processing stage by the spiral concentrator, wet low and high-intensity magnetic separation and flotation process for desulfurization of the final concentration are performed [10]. Reverse flotation of pyrite is done at pH= 4.5 by 300 g/t potassium amyl xanthate collector with maximum foaming time. The rotation speed of the cylinder, the intensity of the magnetic field, and the degree of crushing are the main factors to effect the iron recovery from the tailings [11].

*Corresponding Author Institutional Email: hosseininasab@eng.usb.ac.ir (M. Hosseini Nasab)

Please cite this article as: M. Hosseini Nasab, R. Rezazadeh, Optimization of Line of Magnetite Recovery from Wet Tailings by Creating Second Medium Intensity Magnetic Field (Case Study: Processing Plant of Gol-e-Gohar Hematite), ***International Journal of Engineering, Transactions B: Applications,*** Vol. 35, No. 08, (2022) 1608-1618

Gol-e-Gohar hematite plant, located in the southeast of Iran (Sirjan), includes 1.2 billion tons of geological reserve and an annual production of 7 million tons of iron ore concentrate. This plant has three separate lines: Line 100 (L1), used for hematite recovery from dry tailings of the concentrator plant; Line 200 (L2), used for magnetite recovery from Wet Tailings Processing (WTP); and Line 300 (Line 3), used to desulfurize the concentrate obtained from the concentrator plant. The tailings from the three lines combine to enter the thickener. Solid pulp concentration can increase using the thickener, and the recovered water re-enters the line.

Hematite is the dominant mineral containing iron in Gol-e-Gohar. Sulfur impurities in the feed, which causes environmental problems in discharging the tailing [12], are due to iron-bearing minerals such as muscovite and biotite. Nearly 67 percent of the iron ore particles in the plant are smaller than 38 microns in diameter. Approximately 80 percent of WTP tailings pass through a screen opening (D_{80}), 70 microns in diameter. The iron ore locked with gangue minerals is observed at the smallest level, and the best degree of liberation under 38 microns is 40 percent. The small size of the feed particles complicates the recovery process [13].

Wet magnetic drums[1] use to extract iron particles from ore, increase efficiency, and obtain higher-quality output[2]. These magnetic drums are classified into three groups: Low-Intensity Magnetic Separators (LIMS) [14-16], Medium-Intensity Magnetic Separators (MIMS) [14], and High-Intensity Magnetic Separators (HIMS) [14, 17].

Wet magnetic drums are composed of a housing[3] (stainless steel[4]) and a cylindrical shell (made of anti-abrasion stainless steel) which generates a constant magnetic field. Magnetic drum separation obtained by the rotation of a cylindrical surface around a permanent magnetic field. Once the feeder releases raw materials onto the roller of the separator, non-magnetic materials move along the typical path and are removed appropriately; in contrast, the iron attracted onto the shell continues to rotate to the last magnetic point and is discharged at the back of the roller [18-20]. Based on working conditions, three types of wet drums can employ: co-current, counter-current, and counter-flow. Advantages of wet magnetic drums include high strength, anti-abrasion stainless steel shell, very high magnetic attraction, automatic separation of iron particles, a permanent magnetic field without a supply source, and various designs with different magnetic field intensities. Wet drums are also helpful in mining industries such as mining iron ore, processing silica, and separating iron particles in mines using wet methods[3].

Extensive research has been conducted on increasing the iron ore grade by magnetic methods in recent years, as mentioned below.

Shao et al. [21] investigated the processing of Esmalon iron ore by magnetic separation method. They obtained a 63% iron grade concentrate and a 65% recovery rate by a low-intensity wet magnetic separator. Zhang et al. [22] developed a novel method for iron recovery from iron ore tailings with pre-concentration followed by magnetization roasting and magnetic separation. In the first stage, they obtained 42% iron grade and 74.43% iron recovery in the size of +74-149 microns and the intensity of 1200 gauss. Then the obtained concentrate was milled, and in the second stage, in the power of 2000 gauss, it resulted in a concentrate with a 62.79 % iron grade and 98.23% iron recovery. Dwari et al. [23] concentrated low-grade iron ore in a low-intensity wet magnetic separator. They obtained a concentrate with 67% iron grade and 90% iron recovery of a particle size distribution smaller than 200 microns [23]. Behnamfard and Khaphaje [24] increased the iron grade of low-grade iron ore in a low-intensity dry magnetic separator and obtained a concentrate with a grade of 47.15% and weight recovery of 68.56%. Behnamfard and Khaphaje [24] used a dry magnetic separator (1000 Gauss) and freshwater to process the Sangan iron ore, not exploit the tailings, and not consider the profitability of their research.

Argimbaev et al. [9] studied chemical composition, the mineral petrography of thin and polished sections, grain size distribution, and physical-mechanical properties of iron-containing tailing of enrichment of combined mining and processing in Kursk magnetic anomaly of Russia. Their research showed that iron-containing tailings of processing plants could find an increased absorption capacity due to the presence of clay minerals in them.

According to Qaredaqi and Rafizadeh [13], the low magnetic sensitivity of fine hematite particles precludes the use of a LIMS. However, Wang et al. [8] showed the use of auxiliary permanent magnets, which are embedded in the main permanent magnets, could capture a wider range and finer particle size in low-intensity magnetic separators.

The most well-known wet magnetic separator is the Jones separator [20]. The HIMS is often used with fine and magnetically weak iron particles [23-27]. The first implementation of the separator dates back to 1972 in Brazil, when it was used to increase the fine-grained hematite content in the feed [18]. In 1996, Shao et al. [21] proved that the dimensions of the particles are relatively insignificant when using a HIMS. However, the high

[1]- Wet cylindrical-magnetic separators

[2] http://www.papkomagnetics.com/product/p2.htm

[3]- A housing is a metallic container or cover for mechanical parts such as filters, bearings, and gears.

[4]- Refers to a group of iron-based alloys containing at least 10.5 percent chromium; the chromium content rarely exceeds 30 percent, while iron grade rarely falls below 50 percent [24].

hematite content in WTP prevents using a HIMS in the studied plant.

To produce iron-containing concentrate in Gol-e-Gohar plant, the iron ore extracted from the mine after initial crushing transfers to a gyratory crusher. Then the materials in the dry autogenous mill are re-crushed, and are sent into the dry magnetic separators after passing through the air classifier, the cyclone, and the two-layer sieve (in a closed circuit with a mill). This step has three outputs. The first output is the final dry concentrate sent to the dry concentrate silo for sale. Cleaner tailing and scavenger concentrate are the middle product of the wet line feed of the plant. Scavenger tailing, as dry tailing, firstly transports by conveyor to the storage silo of dry tailing and then sent to a dry tailing dump.

The objective of this paper is to design an optimal circuit for the WTP line and investigate its efficiency under actual conditions in the plant. Thus, in the following, the WTP line in the plant is described.

The wet tailings of the plant, after being stored in a 2000-ton container, transport from the lower part of the container to the washing drum using a conveyor belt. The separation process requires 60 cubic meters of water per hour. The developed pulp transfer onto the vibrating screen; materials larger than 1.5 mm, comprising a small portion of the materials, are carried out by the conveyor belt. The remaining particles using a pump move to three LIMS: rougher, cleaner, and re-cleaner. In the first stage, iron ore particles separate using a magnetic separator, and the concentrate advances to the second stage. The final tailings developed by the rougher and cleaner separators subsequently move to the tailing thickener. The tailings from the last separator return to the cleaner. The concentrate from the re-cleaner is the final concentration of the plant. The pulp containing iron concentrate separate in three stages and subsequently sent to the filtration stage. Concentrate with an iron content of 69 percent is transferred outside using the conveyor belt. The stages of the process can be summarized as follows:

1. Preventing the formation of lumps
2. Eliminating particles larger than 1.5 mm
3. Three-stage LIMS
4. Dewatering

A schematic representation of the WTP line (L2) is illustrated in Figure 1. The line was created in 2016. Figure 2 presents the input grade at the beginning of Line 2 operations and compares the designed and actual grades. As is shown, by design, iron content was predicted to reach 52 percent; however, actual values do not exceed 46 percent on average, which contributes to the low efficiency of the line.

During its early days, a large number of problems were observed in Line 2, the most significant of which are as follows:

1. Extremely low efficiency (below ten percent)
2. Flawed processing circuit design which is inadequate for the input feed (the old tailing pond in the concentrator plant, briefly described in Section 3)
3. High iron content in the tailings (nearly 40 percent)

These problems caused the line to come to a halt from 23/09/2017 to 14/11/2017.

2. Materials and Methods

Experimental studies carried out with magnetite ore particles less than 45 µm. 80 percent of WTP tailings pass through a screen opening (D_{80}), 70 microns in diameter.

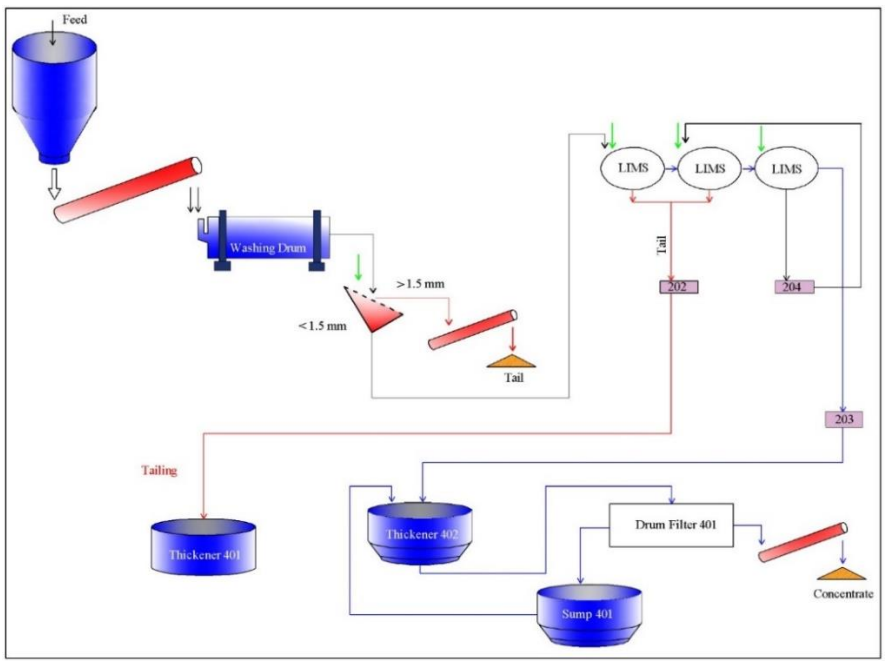

Figure 1. Flowsheet of Line 2 in the plant

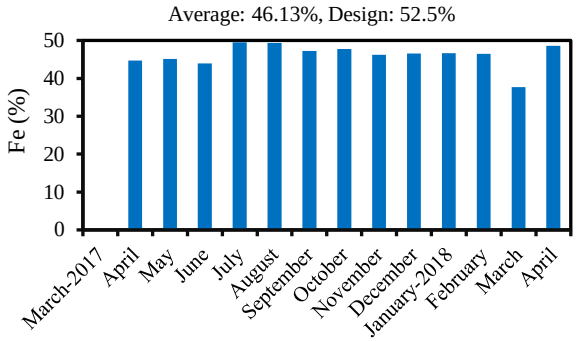

Figure 2. Input iron content for the first two years of line operation

Not only it is not necessary to spend more on crushing, but also by crushing more and reducing D_{80} from 70 to 57 µm, the flotation performance of the coarser-grained feed in all four cases for grades of iron and sulfur in the concentrate, the recovery of non-pyrite iron, and the removal of pyrite will be slightly better. Because of the high iron content in the tailings, a wet magnetic separator had to be used. A sampling of the magnetic separation circuit of the WTP line was done. Samples after drying and dividing were screened then for determining the iron content were analyzed. Iron and sulfur grades in feed, tailing and concentrate, screen analysis for obtaining cumulative percentage smaller than the particular dimensions, and Blain Number in every modified circuit were determined. Finally, calculations of the project profitability were done.

The mineralogical composition of the tailings is shown in Figure 3. The results of XRD analysis revealed that quartz, albite, talc, hematite, calcite, and riebeckite (amphibole) are the dominant crystalline phases (>10%) in these tailings. Magnetite, antigorite, dickite, and dolomite, which are sub-minerals, constitute 2-10% of these tailings. Feldspar, quartz, and calcite were seen in the image prepared using the polarizing light microscope (Model: Zeiss Axioplan-2), and muscovite was formed as a substitute in feldspar (Figure 4).

3. RESULTS AND DISCUSSION

The modifications have done in three steps as follows, which will discuss in more detail later:

Step 1: using the new wet tailings instead of old wet tailings from the concentrator plant as the feed
Step 2: adding the MIMS to the WTP Line
Step 3: adding 2nd MIMS

Step 1: using the new wet tailings instead of old wet tailings from the concentrator plant as the feed

Initially, the wet tailings of the plant, also tailings of the dust collector from the concentrator plant, were accumulated in the tailing pond (old wet tailings). These

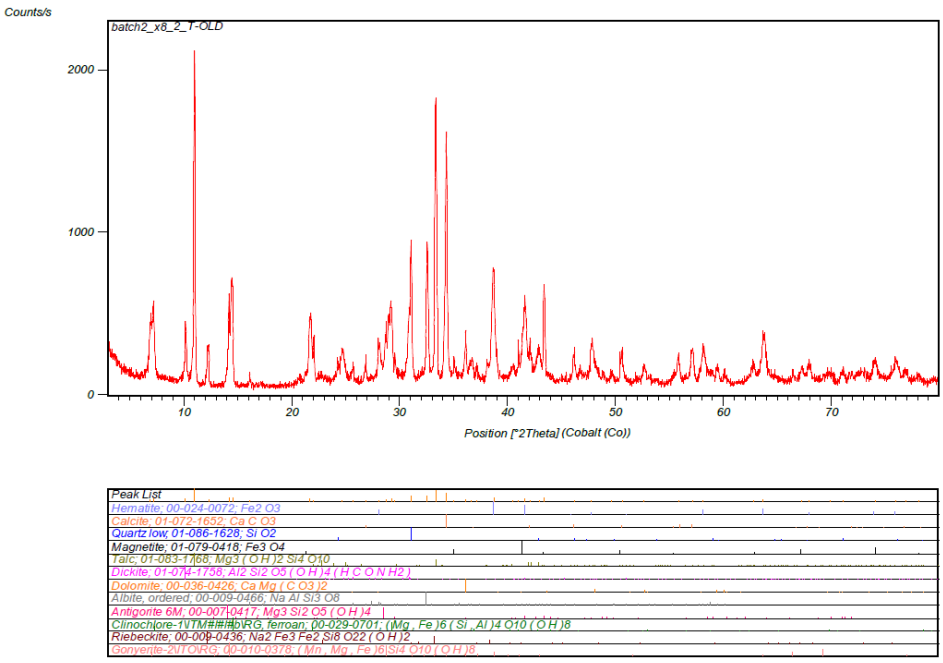

Figure 3. Results of XRD analysis of the tailing sample

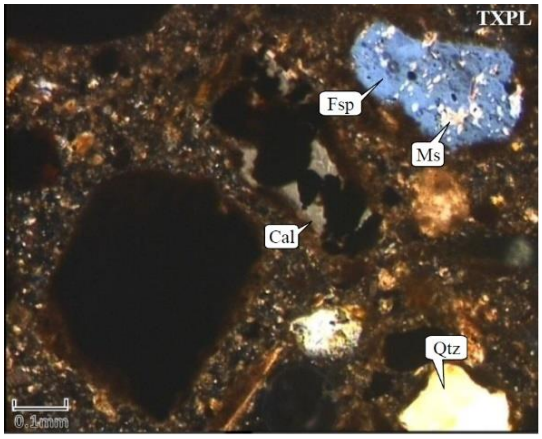

Figure 4. Results of XRD analysis of the tailing sample

tailings were estimated to weigh approximately five million tons; thus, the line was designed to handle a capacity of five million tons of the tailing. In other words, initially, the old wet tailings as the feed were given to the line. However, due to the issues mentioned above and the chemical analysis of the wet tailings (Mixer 102), it was decided that the tailings be fed directly as pulp (Figure 5). The initial modifications mean changing the old tailings to new tailings –the current tailings from the concentrator plant. The new tailings of the concentrator plant are directed as input to the wet tailings line in the concentrator plant (WTP line). In 2017, experimental results from the authors' work showed that iron content in the new wet tailings and FeO content were 26.6 and 9.3 percent, respectively (Figure 6). Therefore, the

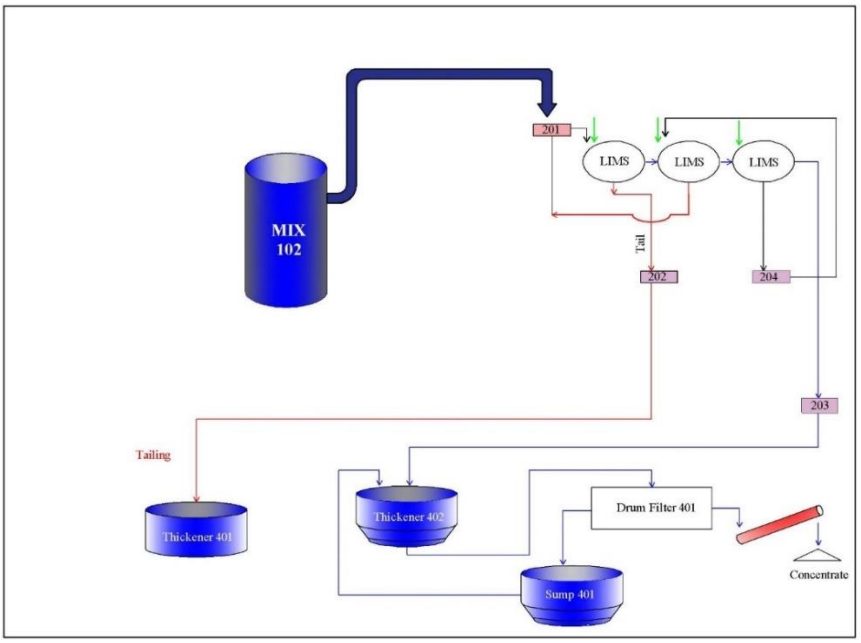

Figure 5. Flowsheet of Line 2 in the hematite plant (after the modifications)

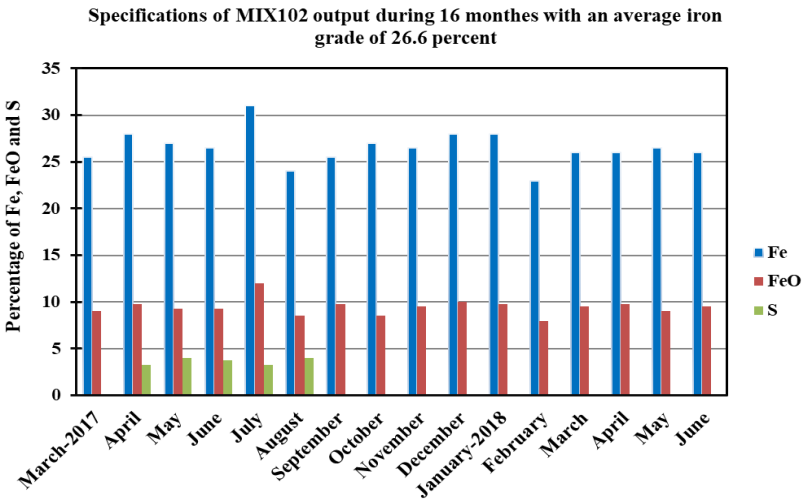

Figure 6. Specifications of the new wet tailings in the concentrator plant (MIX102 output)

TABLE 1. Comparison of Line 2 efficiencies at the initial operation, after the modifications, and by design method

	Percentage of iron in the feed	Cumulative percentage smaller than the X dimensions (%)	Efficiency (%)	Percentage of iron in the concentrate	Percentage of iron in tailings
Before	46.58	7.4	10.7	68.8	45.76
After	47.44	27.2	39.6	68.12	38.57
Design	52.5	40.51	53.39	69.2	41.13

Fe/FeO in the mixer output equals 2.8, which shows the magnetic nature of the load, and that the current circuit of Line 2 is more appropriate for these materials.

Mixer 102 is the new feed to the hematite plant from the wet tailings of the concentrator plant. The tailings collectively known as Mixer 102 tailings are from two sources: the thickener (output of the concentrator plant) and the dust collector.

Table 1 presents the specifications of the old wet tailings (tailing pond) and the new wet tailings (after the modifications).

As stated in Table 1, after doing these modifications, recovery has increased, and the percentage of iron in the tailings has decreased.

A three-dimensional model of the wet and dry tailings (constructed in 2015) showed 24.6 million tons of dry tailings with an iron grade of 37 percent and 3.3 milliontons of wet tailings with an iron grade of 5.42 percent. Further research, however, indicated that the sampling process at the design time had not been representative of the wet tailing deposits. Furthermore, LIMS test results do not lead to adequate efficiency and recovery; the feed with the designed grade constitutes a negligible portion of the deposit.

Advantages of the current pulp in Mixer 102 instead of old tailings are as follows:

1. Increased hourly feeding capacity in Line 200, from 80 to 140 tons.
2. Elimination of critical line equipment (i.e., input hopper[1], input silo conveyor belt, silo, output feeder of the silo, input conveyor belt, washing drum, screen, and an output conveyor belt of the screen)
3. Increased annual production capacity in Line 200, from 170000 to 240000 tons
4. Higher Blain number (from 1000 to 2500)
5. Elimination of line feeding machinery (e.g., excavators, loaders, and trucks)
6. Prevention of material accumulation in the concentration tailing pond
7. Reasonable reduction of tailing grade in Line 200 after processing in the plant (13 percent)
8. Optimized drum filter performance due to higher density and prevention of halts
9. Clearer thickener overflow by preventing the circulation of input materials in the thickener
10. Reduction of water consumption and replacing saline water with fresh water (approximately 250 cubic meters per hour). The fine-grained particles in the dust collector need to be flowed using a fluid; thus, water is used for this purpose. Since the particles required moving toward the tailings, the water inside the mine was used, which has high TDS. Therefore, saline water utilizes for the mixer, and the consumption of fresh water in the hematite plant decreases.
11. Reduction of iron wasted through the tailings

On the other hand, the disadvantages of the current pulp in Mixer 102 instead of old tailings are as follows:

1. Higher sulfur content in the concentrate
2. Five to ten percent reduction of line efficiency

The advantages of the project outweigh its disadvantages; thus, overall, the project is beneficial.

3. 1. Primary Problems of WTP Line after Initial Modifications

Following the modifications, the efficiency issue was somewhat resolved – going from below 10 percent to nearly 30 percent. However, several problems were still outstanding:

1. The high costs associated with the transportation of materials from the tailings pond to the plant using excavators, loaders, and trucks
2. High humidity, lumps in the depot, and transportation problems
3. Blockage in the silo of Line 2 causing fluctuations in the line
4. Extreme sensitivity to the weather, especially rain
5. Issues with the conveyor belt and silo reducing the availability factor[2]of the machinery
6. Limited depot capacity based on the age of the plant (six working years)
7. High (nearly 40 percent) iron content in the tailings as a result of the hematite in the feed

Step 2: adding the MIMS to the WTP Line

After stopping the line, the following modifications applied:

1. The LIMS from the first stage (i.e., the rougher) was replaced with a MIMS
2. Line efficiency increased from 7 to 30 percent. By design, an efficiency of 40 percent had considered;

[1]- A hopper (the funnel) is a temporary silo used to store materials (at the beginning of the production line) in processing plants

[2]- Availability factor of a machine is the amount of time it is operating in a working shift divided by the amount of time in the shift. The ratio usually is smaller than 100 percent due to failures and waiting times.

however, a more than 7 percent achieved in operation.

3. The LIMS tailings from the second stage moved to the first.

Figure 7 presents the secondary modifications applied to the WTP line.

The circuit in Figure 7 operationalized in April of 2019. Currently, nearly half of the pulp obtained from Mixer 102 in the concentrator plant (70 tons per hour) fed to Line 2. The remaining materials are transported to the tailings mixer (Workshop 30 in the old tailing pond), and sent to the new tailing pond. The materials contain almost 30 percent iron and 10 percent FeO. However, due to its fine-grained nature (K80 < 40 microns), a perfect load goes to waste.

A sampling of input feed, concentrate, and tailings is carried out during each working shift and sent to the laboratory unit. Determination of the chemical composition of samples is done by XRF analysis. As shown in Table 2, at the beginning of Line 2 operation, the annual average iron and iron oxide contents are 29.6 and 10.9 percent, respectively. From April to September of 2019, the Blain number, determined by a manometer, is generally rising, which is one of the benefits of doing these modifications. According to Table2, the plant during these months is stable a great extent, and the table's data are acceptable.

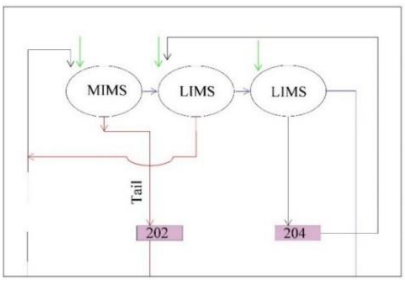

Figure 7. Secondary modifications applied to the WTP line

Using a new MIMS at the beginning of the second stage, instead of LIMS, is due to achieving of maximum hematite recovery. In fact, scavenging of the feed is done at this stage. Therefore, a recommendation was to install a pipeline connecting Mixer 102 in the concentrator plant to Line 2 in the hematite recovery plant to transport the entire output of the mixer to Line 2. Currently, the pulp from concentration enters Sump[1] 201, which is not capable of handling the increase in volume, since a pump cannot be installed underneath it. Therefore, another sump and two pumps (one of which is ready to work) are needed. The pumps feed the pulp as input to the second MIMS. In addition, the concentrate from the second MIMS is fed to the rougher LIMS (second stage). The remaining parts of the line are unchanged (Figure 8). The circuit has been in operation since October of 2020. It should be noted that Sump 401 in Figure 8 is a water sump.

Figure 8 presents the final modifications using two MIMS. Following the modifications, the pulp from Mixer 102 in the concentrator plant with a solid content of 140 tons per hour enters Line 2. Considering an approximate efficiency of 30 percent, during each hour, almost 40 tons of concentrate is produced in Line 2:

$140 \times 0.3 = 42$

which shows an increase of 20 tons per hour in the capacity of Line 2.

3. 2. Economic Analysis of the Final Circuit As mentioned earlier, the final WTP model is shown in Figure 8. An estimation of the required investments is summarized in Table 3.

Additionally, installation and power supply cost 2 and 2.5 billion Rials, respectively. Thus, the entire project requires an initial investment of 18.5 billion Rials. In the following, we describe the revenues generated by the project during its first year of operation.

TABLE 2. The operational status of Line 2 from April to September of 2019

Sample type	WTP								
	F_{200}(Feed)				C_{200}(Concentrate)			T_{200} (Tailing)	
	Iron (%)	FeO (%)	Sulfur (%)	K_{80} (micron)	Iron (%)	Sulfur (%)	Blain Number	Iron (%)	FeO(%)
Annual Average	29.6	10.9	2.6	40	65.2	0.9	2479	11.5	3.1
April	27.3	10	2.24	39	65	0.99	2474	11.1	3.1
May	28.2	10.2	2.36	42	65.8	0.8	2497	11.5	3
June	29.7	9.7	2.37	42	66.4	0.72	2424	14.3	3.1
July	30.2	12	2.85	40	64.3	1.04	2495	10.2	3.2
August	32.4	12.6	3.02	39	64.6	1.03	2507	10.3	2.8

[1]- A pit for collecting sludge or sewage

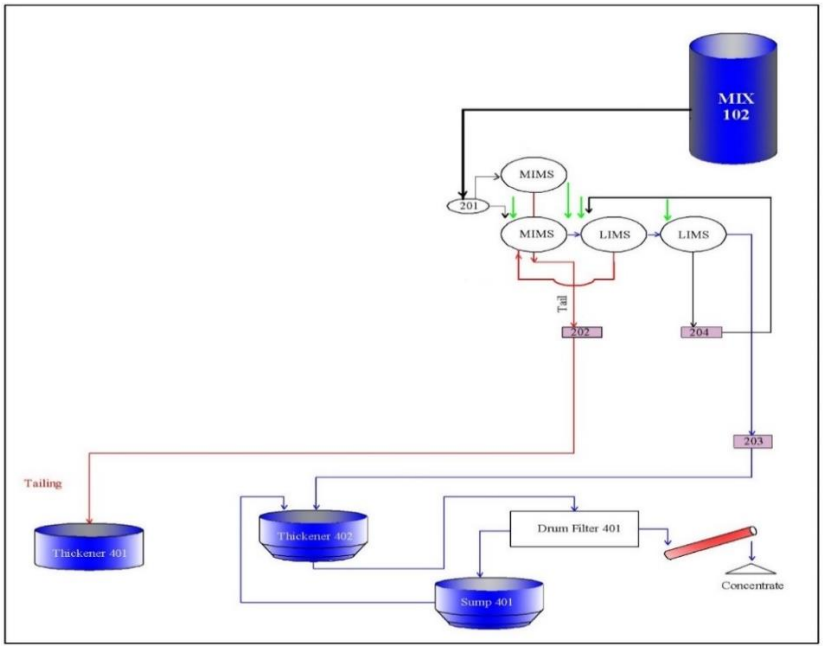

Figure 8. Final circuit of the WTP line to use new wet tailings of concentrator plant

TABLE 3. Investment requirements of the final circuit

Item	Equipment/ Materials	Quantity	Unit Price (Rials)	Total Price (Rials)
1	Piping connecting the concentrator plant to the hematite plant	400 meters	500,000	200,000,000
2	Tailing pipe from the new line to the middle mixer	600 meter	500,000	300,000,000
3	MIMS drum and paraphernalia	2	3500,000,000	7000,000,000
4	Slurry pump	6	1,000,000,000	6,000,000,000
5	New sump	1	500,000,000	500,000,000
	Total cost		14,000,000,000 Rials	

The iron concentrate may be sold either domestically at approved prices or internationally. The two prices are usually different, and the latter achieves easier.

Therefore, an estimated international price is used in our calculations. Assuming that the Free On Board (FOB) price of 65 percent magnetite concentrate is 45 dollars per ton and that shipping costs 10 dollars per ton, each ton will sold with a minimum profit of 35 dollars; which is almost equal to one million Rials.

The profit in selling each ton of FOB concentrate equals 35 dollars or 1,155,000 Rials (excluding production costs). Variable costs for each ton of concentrate include bills by the contractor and energy costs. Because additional workers are not needed, human resource costs are set to zero.

The project requires 300 kWh (based on the number of engines), and 15 kW is used to produce a ton of product. Assuming each kilowatt costs 800 Rials, 12 thousand Rials need for each ton of product. The contractor charges 215,000 Rials per ton of feed; considering a production efficiency of 30 percent, each ton of product needs 715,000 Rials.

Energy costs for each ton of concentrate: 12,000 Rials

Contractor bills for each ton of product: 715,000 Rials

As a result, the net profit from selling each ton of concentrate produced by Line 2 is 428,000 Rials.

The project increases Line 2 production capacity by 20 tons per hour. In 2019, the line operated for 8133 hours. By assuming the 7500 work hours per month, the increased annual production from the project is at least 150 thousand tons. Thus, annual net profits (excluding initial investments) can reach to 64 billion Rials (over 5 billion Rials each month).

An overview of the calculations is given in Table 4: By considering investment costs, the project begins to yield profits after four months. This rate of profitability is significant from an economic point of view.

3. 3. Project Profitability for the Contractor

The increase in line production also results in higher profits for the contractor. This matter can serve as an

TABLE 4. An overview of the calculations of the project profitability

Item	Price (Rials)
Initial investment	18,500,000,000
Profit of exporting each ton of concentrate (FOB)	1,485,000
Transportation and storage costs for each ton of concentrate	330,000
Energy costs for each ton of concentrate	12,000
Contractor bills for each ton of production	715,000
Net profit from each ton of concentrate	1,485,000 – (330,000 + 12,000 + 715,000) = 428,000
Increased production capacity in Line 2	20 × 7500 = 150,000 tons
Annual profits of the project (excluding initial investment costs)	150,000 × 428,000 ~ 64,000,000,000 Rials

incentive to delegate the execution of the project to a contractor. Pertinent calculations have summarized in Table 5:

Thus, annual net profit (excluding initial investment) equals 97 billion (over 8 billion each month) Rials. By considering investment costs, the project after three months yield profits.

Therefore, the present study, which was somewhat similar to the research of Behnamfard and Khaphaje [24] increased the iron content economically from 47.15% to 68.12%, while reducing the iron grade in the tailings to 38.57%. However, this amount of iron in the tailings is a significant amount that, in the future, with further research, should decrease.

According to the promising results of the present research, the following cases are recommended to produce suitable iron concentrate for the steel industry from the tailings of the Gol-e-Gohar processing plant:

- Complementary studies of flotation, especially from an electrochemical perspective (Effect of E_h and oxidation rates) in the efficiency of desulfurization operations of both hematite and magnetite concentrate of Gol-e-Gohar Iron Ore Complex
- Dephosphorization studies of hematite concentrate by flotation due to the relatively high amount of phosphorus (>0.05%) in the concentrate produced in this study

TABLE 5. A summary of the calculation of the project profitability for the contractor

Item	Price (Rials)
Initial investment	18,500,000,000
Profit from each ton of product	715,000
Operational costs incurred by the contractor for each ton of product in Line 2 (more than current production)	65,000
Net profit from developing each ton of concentrate in Line 2	715,000 – 65,000 = 650,000
Annual profit of executing the project (excluding initial investment)	150,000 × 650,000 ~ 97,000,000,000 Rials

4. CONCLUSION

This study optimized the line of magnetite recovery from wet tailings by creating a second medium intensity magnetic field. The main results of this research are summarized as follows:

Based on the presented calculations, the optimization is economically feasible and profitable. The reformation made was associated with some other advantages, as stated below:

1. An increase in150 tons in the annual production to achieve new production thresholds
2. Preventing loss of iron in the form of tailing from the concentrator plant
3. Preventing loss of water in the form of tailing from the concentrator plant and recovering a portion of that water in the hematite plant
4. An increase in 50 to 100 units in the product's Blain number. The Blain number in Line 2 equals 2500 cm^2/g instead of 850 and 1450 cm^2/g in Lines 1 and 3, respectively. Moreover, the value is 1450 – 1500 cm^2/g for the hematite plant. Increasing the hourly production rate by 20 tons nearly doubles production capacity in Line 2. This amount is added to the production of 150 tons per hour with an approximate Blain number of 1500 cm^2/g. By calculating the weight ratios, an overall increase of at least 100 units obtained. However, in contrast to iron grade, the increase in the Blain number cannot calculate using a weight ratio (since the value does not directly relate to K_{80}). Nevertheless, the number expected to be 50 to 100 units larger.

Note that the calculations performed pessimistically; for instance, Line 2 operated for 8133 hours in 2019; however, the value has assumed to be 7500 hours; thus, a lower bound on the profits of these optimizations is determined.

5. REFERENCES

1. Abbasian, A., Ravangard, A., Hajian Nia, I. and Mirzamohammadi, S., "Investigation of microstructure and mechanical properties of newly developed advanced high strength

trip steel", ***International Journal of Engineering, Transaction C: Aspects***, Vol. 35, No. 3, (2022), 567-571, doi: 10.5829/IJE.2022.35.03C.09.

2. Ahadi Akhlaghi, I., Kahrobaee, S., Sekhavat, M., Norouzi Sahraei, H. and Akhlaghi Modiri, F., "Application of artificial neural network and multi-magnetic nde methods to determine mechanical properties of plain carbon steels subjected to tempering treatment", ***International Journal of Engineering, Transaction A: Basics***, Vol. 34, No. 4, (2021), 919-927, doi: 10.5829/IJE.2021.34.04A.18.
3. Gapsari, F., Hidayatia, N., Setyarini, P., Alan, M.P., Subagyo, R. and Andoko, A., "Hydroxyapatite coating on stainless steel 316l using flame spray technique", ***International Journal of Engineering, Transaction B: Applications***, Vol. 34, No. 2, (2021), 493-499, doi: 10.5829/IJE.2021.34.02B.22.
4. David, D., Larson, M. and Li, M., "Optimising western australia magnetite circuit design", ***Proceedings of the Metallurgical Plant Design and Operating Strategies, Perth***, (2011).
5. Xiong, D., Lu, L. and Holmes, R., Developments in the physical separation of iron ore: Magnetic separation, in Iron ore. 2015, Elsevier.283-307.
6. Bulatovic, S. and Salter, R., High intensity conditioning—a new approach to improving flotation of mineral slimes, in Processing of complex ores. 1989, Elsevier.169-181.
7. Wyslouzil, H., "The production of high grade iron ore concentrates using flotation columns", ***Skillings' Mining Review(USA)***, Vol. 86, No. 37, (1997), 4-8.
8. Wang, F., Zhang, S., Zhao, Z., Gao, L., Tong, X. and Dai, H., "Investigation of the magnetic separation performance of a low-intensity magnetic separator embedded with auxiliary permanent magnets", ***Minerals Engineering***, Vol. 178, (2022), 107399, doi: 10.1016/j.mineng.2022.107399.
9. Argimbaev, K., Ligotsky, D., Mironova, K. and Loginov, E., "Investigations on material composition of iron-containing tails of enrichment of combined mining and processing in kursk magnetic anomaly of russia", ***International Journal of Engineering, Transaction A: Basics***, Vol. 33, No. 7, (2020), 1431-1439, doi: 10.5829/IJE.2020.33.07A.31.
10. Amin Saravari, A.S. and Shayanfar, S., "Desulfurization of iron ore concentrate using a combination of magnetic separation and reverse flotation", ***Journal of Chemical Technology and Metallurgy***, Vol. 56, No. 5, (2021), 1002-1110.
11. Panahi, E., Abdollahzadeh, A., Sam, A., Jahani, M., Moghaddam, M.Y. and Mehrani, A., "Desulfurization of hematitic concentrate of iron ore of the gol-e-gohar mine using reverse flotation method", ***Techincal Rep***, (2012).
12. Dehghani, F., Khosravi, R., Pazoki, A., Kebe, M., Jahanian, R., Siavoshi, H. and Ghosh, T., "Application of magnetic separation and reverse anionic flotation to concentrate fine particles of iron ore with high sulfur content", ***Physicochemical Problems of Mineral Processing***, Vol. 58, (2022), doi: 10.37190/ppmp/145420.
13. Qaredaqi, M. and Rafizadeh, A., "Application of different wet high intensity magnetic separators in gole-gohar mine".
14. Tripathy, S.K., Singh, V. and Suresh, N., "Prediction of separation performance of dry high intensity magnetic separator for processing of para-magnetic minerals", ***Journal of The Institution of Engineers (India): Series D***, Vol. 96, No. 2, (2015), 131-142, doi: 10.1007/s40033-015-0064-x.
15. Stener, J.F., Carlson, J.E., Pålsson, B.I. and Sand, A., "Evaluation of the applicability of ultrasonic velocity profiling in conditions related to wet low intensity magnetic separation", ***Minerals Engineering***, Vol. 62, (2014), 2-8, doi: 10.1016/j.mineng.2013.08.005.
16. Stener, J.F., Carlson, J.E., Sand, A. and Pålsson, B.I., "Internal flow measurements in pilot scale wet low-intensity magnetic separation", ***International Journal of Mineral Processing***, Vol. 155, (2016), 55-63, doi: 10.1016/j.minpro.2016.08.008.
17. Padmanabhan, N. and Sreenivas, T., "Process parametric study for the recovery of very-fine size uranium values on super-conducting high gradient magnetic separator", ***Advanced Powder Technology***, Vol. 22, No. 1, (2011), 131-137. https://doi.org/10.1016/j.apt.2010.09.013
18. Wasmuth, H.-D. and Unkelbach, K.-H., "Recent developments in magnetic separation of feebly magnetic minerals", ***Minerals Engineering***, Vol. 4, No. 7-11, (1991), 825-837.
19. Svoboda, J., "The effect of magnetic field strenght on the efficiency of magnetic separation", ***Minerals Engineering***, Vol. 7, No. 5-6, (1994), 747-757, https://doi.org/10.1016/0892-6875(94)90104-X
20. Wills, B.A., "Mineral processing technology: An introduction to the practical aspects of ore treatment and mineral recovery, Elsevier, (2013).
21. Shao, Y., Veasey, T. and Rowson, N., "Wet high intensity magnetic separation of iron minerals", ***Magnetic and Electrical Separation***, Vol. 8, (1970), doi: 10.1155/1996/34321.
22. Zhang, X., Han, Y., Sun, Y., Lv, Y., Li, Y. and Tang, Z., "An novel method for iron recovery from iron ore tailings with pre-concentration followed by magnetization roasting and magnetic separation", ***Mineral Processing and Extractive Metallurgy Review***, Vol. 41, No, 2, (2020), 117-129. https://doi.org/10.1080/08827508.2019.1604522
23. Dwari, R.K., Rao, D.S. and Reddy, P.S.R., "Magnetic separation studies for a low grade siliceous iron ore sample", ***International Journal of Mining Science and Technology***, Vol. 23, No. 1, (2013), 1-5, https://doi.org/10.1016/j.ijmst.2013.01.001
24. Behnamfard, A. and Khaphaje, E., "Beneficiation of a low-grade iron ore by combination of wet low-intensity magnetic separation and reverse flotation methods", ***Journal of Mining and Environment***, Vol. 10, No. 1, (2019), 197-212, doi: 10.22044/JME.2018.7392.1595.
25. Svoboda, J. and Fujita, T., "Recent developments in magnetic methods of material separation", ***Minerals Engineering***, Vol. 16, No. 9, (2003), 785-792, https://doi.org/10.1016/S0892-6875(03)00212-7
26. Makhula, M.J., "Beneficiation of fine ores using the longi wet high magnetic separator", Ph.D. Dissertation, University of the Witwatersrand, Faculty of Engineering and the Built Environment, School of Chemical and Metallurgical Engineering, (2014),
27. Tripathy, S.K., Banerjee, P. and Suresh, N., "Separation analysis of dry high intensity induced roll magnetic separator for concentration of hematite fines", ***Powder Technology***, Vol. 264, (2014), 527-535. https://doi.org/10.1016/j.powtec.2014.05.065

Persian Abstract

چکیده

مهمترین ماده خام صنعت فولاد، آهن است. هدف این مقاله، بهبود بازیابی مگنتیت از باطله‌های تر، با افزایش محتوای آهن در کنسانتره خط است. برای مدیریت باطله‌ها، خط فرآوری باطله تر (WTP) برای بازیابی مگنتیت، در مجتمع سنگ آهن گل‌گهر ایجاد شد. مهمترین فازهای کریستاله در این باطله‌ها، کوارتز، آلبیت، تالک، هماتیت و کلسیت بودند. ابعاد خوراک خط، ٤٥ میکرون بود که برای استفاده از روش ثقلی مناسب نیست. بنابراین، جداسازی فقط با استفاده از روش مغناطیسی می‌تواند انجام شود. بدلیل محتوای بالای آهن در باطله‌ها، جداکننده مغناطیسی تر استفاده شد. بر اساس نتایج، جداکننده شدت متوسط پیشنهادی و اصلاحات مربوط به مدار، بازیابی آهن را از ۷ به ۳۰ درصد افزایش داد که ۱۵۰ تن تولید سالیانه بدست آمد؛ مانع هدر رفتن آهن از طریق باطله‌های کارخانه تغلیظ شد و عدد بلین را در کارخانه هماتیت به میزان۵۰ تا ۱۰۰ واحد افزایش داد. بعلاوه، با جایگزینی باطله‌های تر قدیمی کارخانه تغلیظ با باطله‌های تر جدید به عنوان خوراک، مصرف آب بطور قابل توجهی کاهش یافت که دستاورد مهم دیگر این تحقیق است؛ در هر ساعت، ۲۵۰ مترمکعب آب شور به جای آب شیرین استفاده می‌شود.

International Journal of Engineering

Journal Homepage: www.ije.ir

Improving Punching Shear in Flat Slab by Replacing Punching Shear Reinforcement by Ultrahigh Performance Concrete

H. Y. Talib*, N. H. A. Al-Salim

Civil Engineering Department, College of Engineering, Babylon University, Iraq

P A P E R I N F O

Paper history:
Received 01 March 2022
Received in revised form 15 April 2022
Accepted 22 April 2022

Keywords:
Flat Slab
Punching Shear
Shear Reinforcement Steel
Ultra High Performance Concrete
Steel Fiber

A B S T R A C T

Extensive studies have focussed on the issue of the failure of punching shear in flat slabs and ways to strengthen it internally, externally and the importance of this structure (flat slab), and the danger of punching shear failure in the areas of connection of the column - slab. Therefore, this study was based on strengthening the bearing capacity of the flat slab to failure of punching shear with high-performance concrete (UHPC); because it is expensive, so it is not feasible to use it for the whole slab. Therefore, the aim of the study was to replace reinforcement punching shear with UHPC and to determine its optimal use in the shear area. Six samples of flat slabs reinforced with maximum flexural steel loaded with a column in the middle, four forms of UHPC casting instead of shear reinforcement and at two different depths were used. The results showed an improvement in the punching shear strength of the sample cast with UHPC instead of punching shear reinforcement (ACI 318-19) and with all thickness of the slab, it to arrived twice compared to reference sample (NSC) with reinfored flexural steel only. This is the perfect application for the UHPC. It was also noted that casting UHPC with half the thickness of the slab does not give good results compared to those casting with all thicknesses, despite doubling the distance of the UHPC from all faces of the column; but it changes the failure pattern and keeps it away from the danger areas near the unwanted columns.

***doi**: 10.5829/ije.2022.35.08b.18*

1. INTRODUCTION

Flat slab is structure supported by a column without beam. It is a widely used for its many benefits, including: reducing the construction cost in order to reduce the amount of materials used in construction and reduce the work of molds and faster construction and ease the work of flexural reinforcement, reducing the height of the building and thus reducing the loads, ease of setting up of services, reduction in finishing material and flexibility in the arrangement of partitions [1].

There are downsides to use flat slab which are: high shear stresses at slab-column connections may cause punching shear failure, increase in the vertical deflections and the structure has a relatively lesser stiffness under lateral loading [2].

Punching shear failure is considered unwanted failure and defined by Moe [3] as the failure of a concrete slab directly under a concentrated load that occurs when a concrete plug is pushed out of the slab. The pushed-out plug takes the shape of a cone with a top area at least equal to the loading area.

Therefore, many researchers have used methods to strengthening the failure of the punching shear and increase the punching shear capacity in flat plat slabs including an shear stirrups, or use of column heads, drop panels, increased thickness [4, 5], shear heads [6, 7], or shear studs [8, 9]. It is also possible to external strengthening and restore resistance of steel bolts [10, 11], steel bars [12], steel plates [13], fiber reinforced polymer (FRP) sheets or strips [14-17], the combination of FRP sheets and steelbolts [18], FRP strips as through-depth shear stirrups [19, 20]. The normal and hybrid concrete specimens are shown in Figure 1.

Ultra-high-performance concrete (UHPC) is cementitious material is a special and modern type of

*Corresponding Author Institutional Email: hussein.talap.engh363@student.uobabylon.edu.iq (H. Y. Talib)

Please cite this article as: H. Y. Talib, N. H. A. Al-Salim, Improving Punching Shear in Flat Slab by Replacing Punching Shear Reinforcement by Ultrahigh Performance Concrete, ***International Journal of Engineering, Transactions B: Applications,*** Vol. 35, No. 08, (2022) 1619-1628

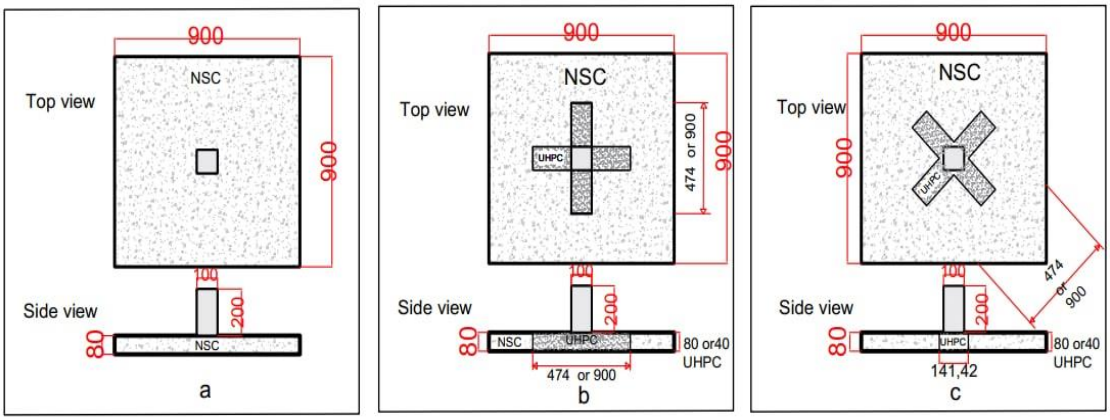

Figure 1. Specimen layout:**(a)** normal concrete NSC or Sh.R.N **(b)** hybrid concrete 187-PF or 400-PC **(c)** hybrid concrete 187-XF or 400-XC (Note: all dimensions in (mm))

concrete, its components differ slightly from one country to another according to the availability of its ingredients and the method of production and maturation [21] amazing mechanical properties, high energy absorption, ductility, permeability and durability. Steel fiber added to improve durability and tensile strength [22].

By reviewing the literature and applications used UHPC and after studying their engineering properties, it was found that the tensile strength of this type of concrete is good and equal to (2.5-3) of the tensile strength of ordinary concrete. This may be due to its high resistance to compression, as the proportionality is direct between the resistance to pressure and tensile strength, in addition to the presence of steel fiber. For these reasons, the idea for this study was formed. There are many applications for high performance concrete (UHPC) such as on-site casting or as an injected material in bridge decks [23], bridge connections [24], strengthening of existing structure [25] and thin slab [26]. There are researchers who used ultra-high performance concrete (UHPC) to strengthen the slab as partial or total use and with different parametric study such as: Harris [27] made an experimental study of (12) unreinforced flat slab model, it was made of a material (UHPC) with different thicknesses and dimensions of the loading plate, and after tests, it was found that the punching shear failure in slab of thickness (51mm) and the shear-flexure failure in slabs thickness 64 and 74 mm; it finally ended the punching shear capacity can be anticipated using updated equations from ACI318-2 instead of the effective depth, the slab thickness is used.

Joh et al. [28] examined five unreinforced flat slabs made of (UHPC) with fixed ends, with investigated variables casting and curing methods. Equations were used by Harris [27] and Graddy et al. [29] to compare the capacities of the slabs that failed in the punching shear to the expected value. whilst the expected strength was compared to Park et al. [30] values of the slabs that failed in flexure. The formula introduced by Graddy et al. [29] overestimated the results while the results were very close to Harris's [27].

Moreillon [31] the researcher studied many variables as fibre volume ratio, reinforcement arrangement, reinforcement ratio and thickness of slabs. the punching shear and flexural strength, they increase by increasing the percentage of fiber steel for the same reinforcement and thickness of the slab, and the strain decreases at the maximum load by increasing the fiber content, reinforcing steel has a greater effect with thicker plates. The researcher concluded a model for calculating the punching shear for plates (UHPC).

Aaleti et al. [32] used waffle bridge deck thickness 200mm, a 150 mm by 200 mm steel plate was used to apply the load to the deck cell between the ribs. Punching shear failure seen at an angle 45, the shear ability obtained by 2.3 is approximately from what can be calculated from the ACI code proposed from Harris [27].

Zohrevand et al. [33] conducted a practical study of hybrid flat plates (NSC/UHPC) with full or half depth and slabs (UHPC) complete with different reinforcement ratio for two groups (1.8% and 0.6%). In slabs with reinforcement ratio (1.8%) that failed to shear the punching as well as the slab full UHPC, as for the slabs with the reinforcement ratio (0.6%) it failed with a composite shear-flexural failure. The hybrid slabs with full UHPC depth had a failure load of 70% (at 1.8%) and 45–66% at (0.6%) more than the reference slab.

Few studies have dealt with on punching shear in flat slab with UHPC, and because it is an expensive material, it is used with normal concrete as a hybrid concrete and what distinguishes this study is that no one searched for the replaceing punching shear reinforcement by ultrahigh performance concrete and obtaining the optimal and economical use (UHPC) in the areas where the column contacts the slab.

2. MATERIAL PROPERTIES

It is necessary to know the physical and chemical properties and the source of all materials used in the composition of concrete, for both types normal and ultra-high performance concrete.

2. 1. Cement Portland limestone cement (CEM II/A-L- 42.5 R) was the type of cement used in this study. Manufactured in Iraq known as (Karasta) and obtained from the local markets, respect to (IQS No. 5/1984) limitations [34].

2. 2. Fine Aggregate (Sand) Natural local sand correspond to the limits of Iraq specification (IQS No.45/1984) [35], used in NSC.

2. 3. Coarse Aggregate (Gravel) Local material maximum size of 14 mm of which correspond to the Iraqi specifications No.45/1984 [35], used in NSC.

2. 4. Fine Aggregate (Extra Fine) Natural fine aggregate imparted was used as natural sand in UHPC just fine sand that was sieved by (600 μm sieve) [35], used in UHPC.

2. 5. Silica Fume Produce from MASTER BUILDERS SOLUTIONS company MBCC Group Silica fume is an extremely fine powder was used in UHPC [36].

2. 6. Steel Fiber Micro steel fibers (type WSF0213) available in the market were used in this research to produce UHPC This sort of steel fibers was made by a company in Jiangxi Province. It is utilized in the present study with length 13mm and aspect ratio (Lf/Df) = 65 and volume fraction (Vf =1.5%).

2. 7. Admixtures (Super Plasticizer) A Super plasticizer used throughout this study for UHPC was "Sika ViscoCrete 5930-L", ViscoCrete 5930-L was made by Sika Company, ASTM C494 05 [37].

2. 8. Mixing Water Tap water has been used for casting and curing all the slab specimens.

2. 9. Reinforcing Steel In this paper, deformed steel bars of two different diameters were used, the ultimate and yielding strength of the diameter (6 and 10 mm) bar were determined by testing method [38]. Table 1 summarized the reinforcing steel ultimate and yielding strength.

3. EXPERIMENTAL WORK

Six specimen, each of them designed as square flat slabs with dimensions (900 * 900 mm) and thickness (80 mm)

TABLE 1. Result of Reinforcing Steel

ϕ (mm)	Fy (MPa)	Fu (MPa)
6	420	448
10	545	626.45

and a square column in the center of the slab with dimensions (100 * 100 mm) and height (200 mm) and the column is reinforced with 4 Ø 10mm according to ACI-318M-19 code chapters 10, 10.6 and 10.7 [39] and three bars shear reinforcement (stirrups) Ø 6mm as show in Figure 2. The flexural reinforcing factor was installed for each slab and according to ACI-318M-19 code chapters 8, 8.6 and 8.7 [39], and we used the largest percentage (ρmax) for the purpose of studying the punching shear failure. The cover in all directions equal 15mm according to ACI-318M-19 term 20.5.1 [39] and effective depth 55mm. This study included three parameters (Investigated variables): (1) shape of UHPC (2) depth of UHPC, and (3) the presence or absence of reinforcement of the punching shear. Two slabs was made entirely from NSC one of which contains the reinforcement of the punching shear Figure 1a. The rest of the models of hybrid concrete in different shapes for UHPC Figures 1(b) and 1(c). Reinforcement steel of flexural and punching shear is shown in Figure 2.

The first specimen name NSC (normal strength concrete), the two specimen name Sh.RN (normal strength concrete with reinforcement shear punching)

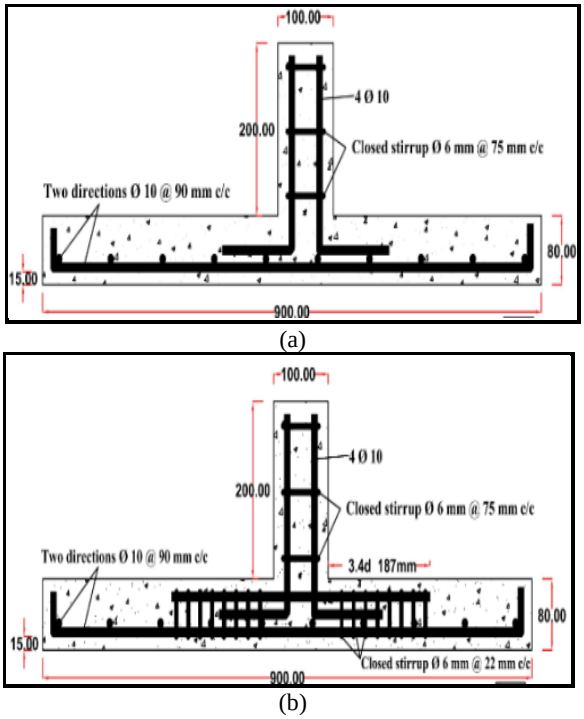

Figure 2. (a) Reinforcement Steel of Flexural (b) Reinforcement Steel of Flexural and Punching Shear

designed according Figure R8.7.6(d) in ACI-318M-19 code [38] Figure 3. The third specimen name 187-PF(187 equal 3.4d) [39], where P: plus shape UHPC F:full depth, 4th specimen 187-XF(X: multiplication sign shape of UHPC F: full depth), 5th specimen name 400-PC (Arm length plus shape same amount of UHPC used in the third model for the half thickness of the slab in the face of compression), 6th specimen name 400-XC (the same 5th model rotated at angle 45).

All samples were reinforced with the above-mentioned details shown in Figure 2(a). One model had reinforcement with punching shear, the details of which are shown in Figure 2(b). This model was poured and thefirst model was cast with ordinary concrete as a reference for comparison. Since UHPC is an expensive material, this study relied on strengthening the punching shear by replacing the same area of the shear reinforcement steel, which is in plus shape of the length of each arm equal to 3.4d Figure 2(b) and equal to 187 mm because the effective depth is 55 mm and the same shape UHPC was rotated at an angle of 45 in the fourth model. As for the model Fifth, the same amount of UHPC in the third model was used to half the thickness of the slab in the compression face of slab, and the sixth model was rotated the fifth model at an angle of 45. The UHPC was not placed in the tension face because it does not give the desired results as mentioned in literature [40].

3. 1. Specimen Preparation and Casting The molds were prepared from plywood of the necessary dimensions, and a pre-prepared reinforcing steel mesh was placed and covered from the mold with plastic spacers. Table 2 summarized the components and proportions NSC and is designed according to ACI-211.1 the aim of the concrete strength (f'c) for all slabs was (23 MPa) at age of 28 days. Table 3 states the components and proportions UHPC and were designed according to ACI PRC-239-18: Ultra-High Performance Concrete [41], as well as we made experimental mixtures to reach the compressive strength of 122Mpa at age of 28 days, these numbers were taken from an average of three cylinders for each mixture, (100*200mm) for UHPC and (150*300mm) for NSC.

Mixing Procedure of NSC by electrical horizontal mixer rotary drum of (0.09 m³), while UHPC was mixed by manually controlled electric mixer used as in Figure 4. A work plan has been developed for casting UHPC and NSC in the hybrid samples at the same time and the steel mold of UHPC is withdrawn and compacted at the same time also to prevent cold joints as in Figure 4. the columns were casted the next day used NSC.

3. 2. Test Setup and Procedure The specimen were prepared and cleaned after the end of the curing stage after 28 days and paint it white to make it easier to notice cracks during and after testing. A simple support

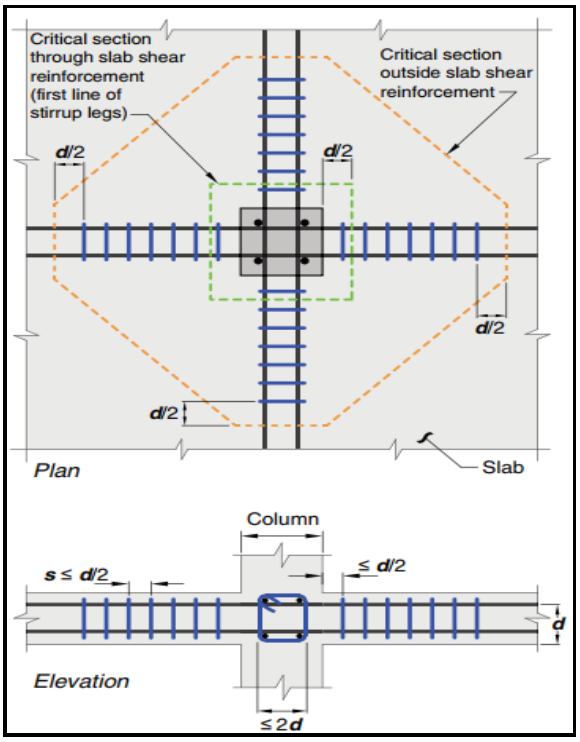

Figure 3. Reinforcement steel of punching shear according ACI318-19 code [38]

TABLE 2. Details of Mix Proportions

W/C =0.58	Cement	Coarse Aggregate	Fine Aggregates	Water
Weight (kg)	368	900	850	213

TABLE 3. Trail Mixes Proportion of UHPC

No. of Mix	1	2	3 (Selected)
Cement (kg/m³)	975	1000	1000
Fine sand (kg/m³)	1050	1050	1050
Micro silica fume (kg/m³)	230	245	255
Steel fiber % by volume	2	2	2
water/(cement+silicafume)	0.19	0.17	0.155
Superplasticizer % by weight of cementitious material	4.25	4.5	5
***fc'* (28 days) MPa**	85.63	105	122

for the slab was used, represented by a pre-prepared steel frame, and it was placed in test device with a capacity of (600 kN). The protocol loading that was used to load the slabs is to transfer the axial load from the column to the slab after placing a cap over the column to prevent local failures, we placed the load sensor (load cell) and placed a bearing plates between them as shown in Figure 5.

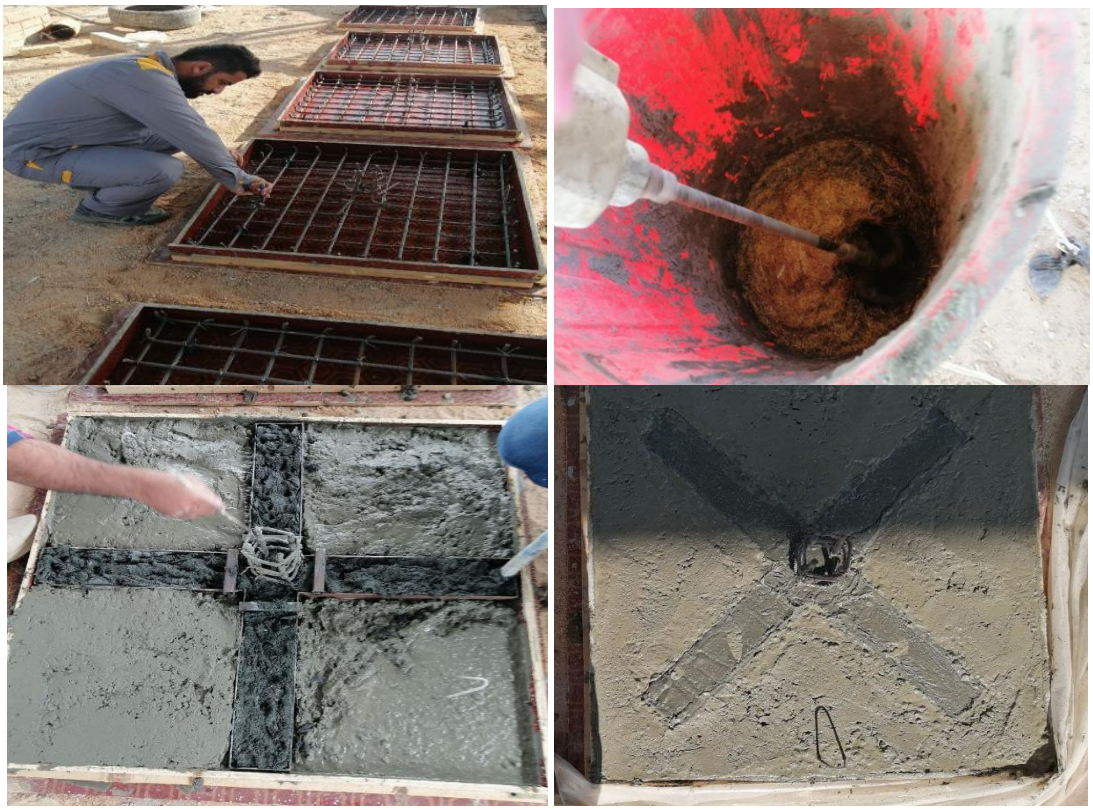

Figure 4. Specimen Preparation and Casting

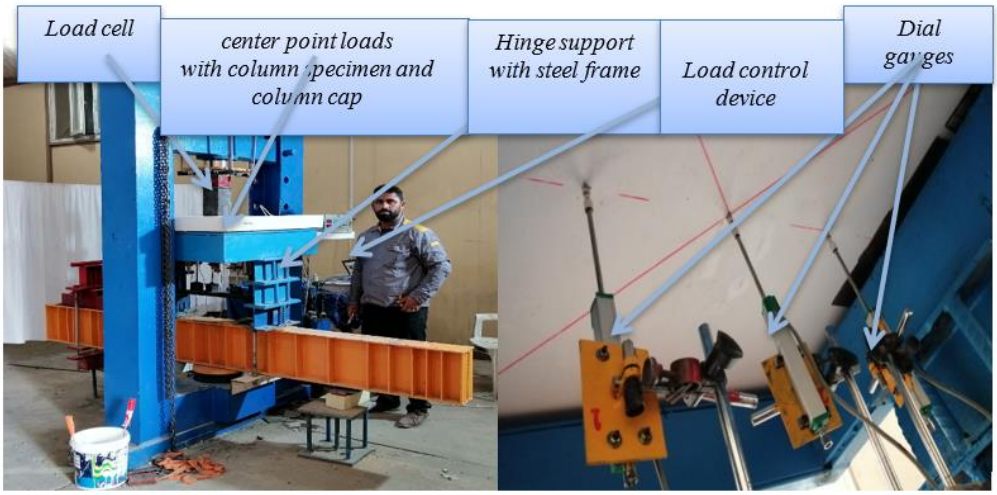

Figure 5. Test setup

We followed a constant load rate for all models, and dial cauges a number of three, one in the middle and two with the average distance between the center and the edge on each side, as shown in Figure 5. After preparing all the test instruments, we started loading and recording data (load, deflection, cracks pattren , and cracks location) and indicating the development of cracks.

4. EXPERIMENTAL RESULTS AND DISCUSSIONS

4. 1. Estimating Punching Shear Capacity The punching shear of slabs can be calculated based on ACI 318-19 as in Equation (1). It should be noted that this model has limitations on compressive strength which should not exceed 69 MPa. This limitation is ignored in

this study since this model is applied for UHPC slabs which have fc significantly larger than 69 MPa.

$$Vc = 0.33\lambda s \sqrt{fc}, u * b_o d$$
$$\lambda s = \sqrt{\frac{2}{1+0.004d}} \leq 1 \quad (1)$$

where fc,u: compressive strength for NSC or UHPC bo: critical punching perimeter at a distance of d/2 from the column face and λs: size effect modification factor.
Kadhim et al. [42] proposed Equation (2). model to calculate the perimeter of failure. It is established that the failure of the punching shear occurs outside UHPC and this applies to our study except in slab 400-XC where the failure occurred during UHPC.

$$b_o = \max\left(\frac{4(c=d)}{4L}\right) \quad (2)$$

After estimating the shear capacity with the modified model of the code as in the Table 4 and after comparing with the practical estimation, we notice that the percentage of difference is good for the references slabs. As for 187-PF and 187-XF, the percentage difference is greater, and this may be due to combined shear-flexural behavior. As for samples 400-PC and 400-XC it cannot be guessed according to Kadhim et al. [42] because of the failure within the region of UHPC or because of the failure of the flexural.

From the foregoing, we conclude that the code equation is very conservative, and we also recommend suggesting a new mathematical model or an modify to the code equation in order to be inclusive of all forms UHPC and not just for regular shapes.

4. 2. Failure Modes All models were designed to fail in punching shear, so we used the largest percentage of flexure reinforcement, general description of the evolution of cracks, at early stages of loading, all tested flat slabs were free from cracks and responded in an elastic manner at low load levels. The deflection was proportion to the applied loads. Subsequently, with increasing load, more cracks were developed and we noticed that in the sample consisting of ordinary concrete NSC (pure punching). We note that the first crack appeared at distance d/2 from the face of the column and with the continuation of the loading, the diagonal cracks appeared, the cracks developed and their width increased, and then the oceanic dredgers appear. As for Sh.RN the failure of punching shear occurs earlier compared to the flexural failure whose features are not complete in this model, the failure of the punching shear in this model proves what the code predicts at a distance d/2 from the end of the punching shear reinforcement. In the two models made of normal concrete, we notice the delay in the appearance of the first crack compared to the rest of the models made of hybrid concrete, where (for NSC 31% of the ultimate load) and (for Sh RN 35% of the ultimate load).

In the 187-PF model, it occurs Punching failure and the diagonal cracks where the first crack appeared in the connection NSC & UHPC and parallel to the first crack, cracks began to appear with the progression of the load and other cracks perpendicular to the previous one, and then the cracks developed and became diagonal towards the corners of the slab, and the last crack appeard in the tension face in the Figure 6(c).

In the 187-XF model, it occurs punching failure and the diagonal cracks too, great similarity between this slab and the previous sample to a large extent in the development of the cracks and the value of the first crack (25% and 26% compared to the the ultimate load and perhaps the only difference in the ultimate load.

In samples strengthen punching shear according to code distance (Sh.RN,187-PF &187-XC), failure occurs at a distance of approximately d/2 from the ends. a circular or redial crack occurs away from the column in the tension face of the slab in the two models (187-XC & 400-PC). Isolation occurs between NSC & UHPC in 400-PC and we can say that this form of UHPC strengthening made the slab fail with flexural failure (diagonal cracks or yield lines) in this model. In all the hybrid models in the face of tension, we notice the crack almost at the limits of the UHPC region , except in the 400-XC model, the failure occurs at a distance equal to the column side in all UHPC directions, as shown in Figure 6.

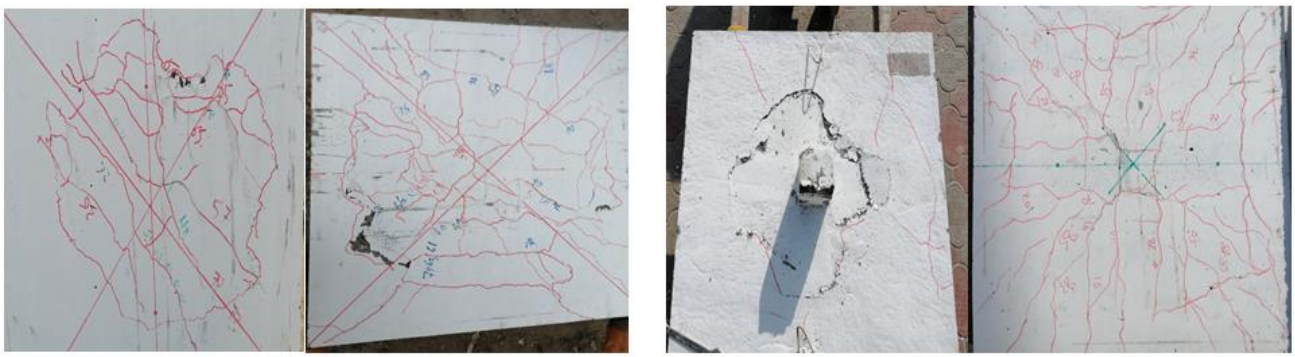

Tension face (a) Tension face (b) Compression face Tension face (c)

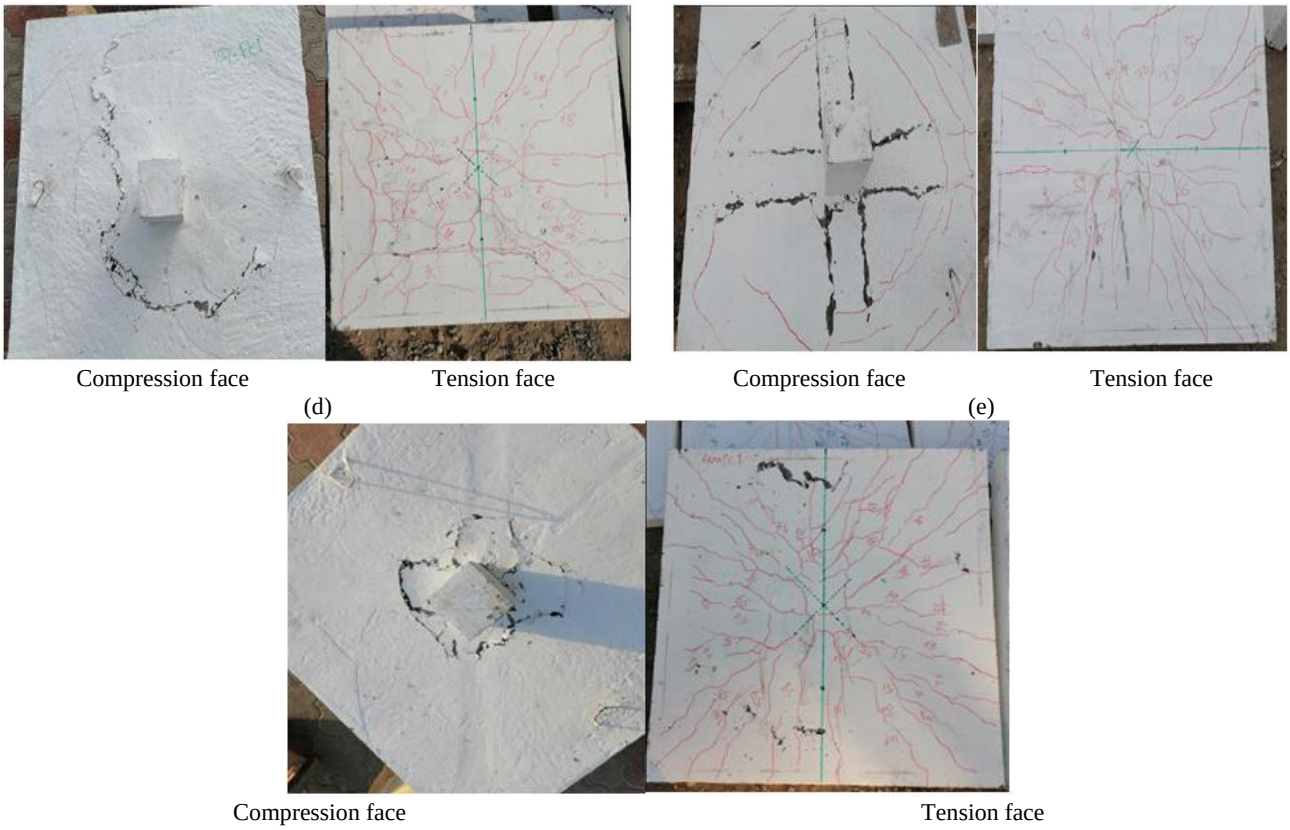

Figure 6. Failure Mode For All Specimens (a) NSC (b) Sh.RN (c) 187-PF (d) Specimen 187-XF (e) 400-PC (f) 400-XC

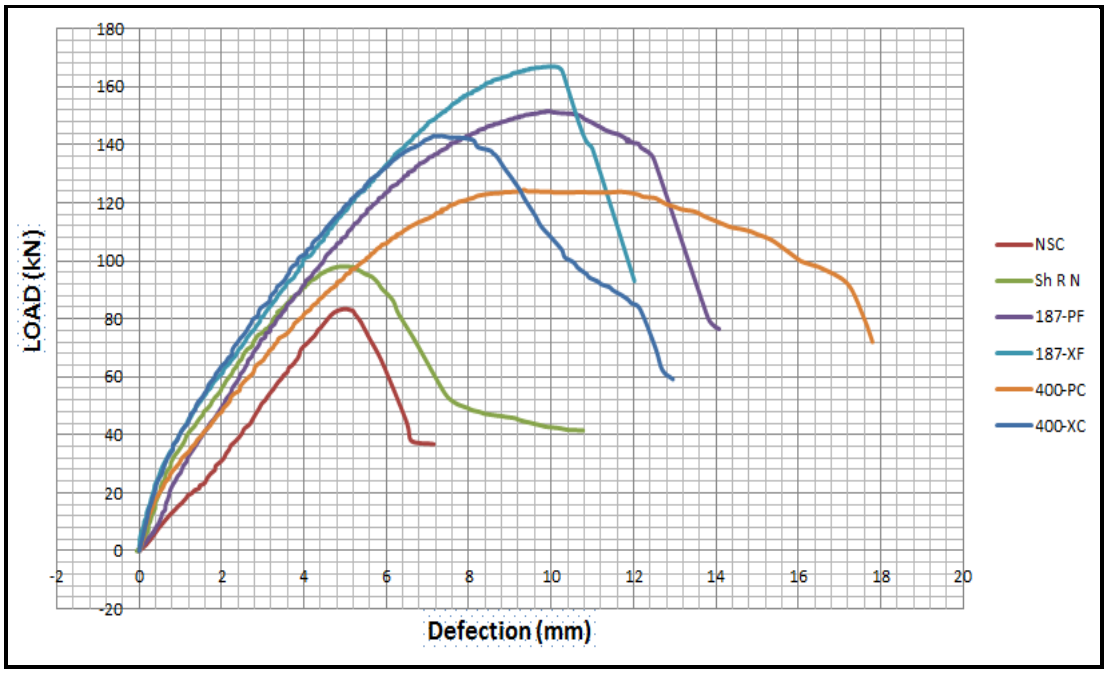

Figure 7. Load-Center Deflaction Curves of Specimens

TABLE 4. Result of Specimen

Specimen	First crack (KN)	Ultimate load (KN)	Ultimate deflection mm	Shear capacity (kN) ACI 318-19	Vexp./Vnum.	Failure type
NSC	26	83.5	4.98	58.45	1.42	P
Sh RN	35	98	5.03	72.24	1.35	P
187-PF	38	151.5	9.94	90.9	1.66	P+F
187-XF	44	167	9.94	103.54	1.61	P+F
400-PC	30	124	8.34	----	----	F
400-XC	36	143	7.31	----	----	P+F

where p: punching failure F: Flexure failure

4. 3. Load-Deflection Response Generally, there was insignificant deflection at the first stage of loading representing the uncrack stage, however, the deflection increased after the formation of the first flexural crack in the slab.

All curves were drawn in one figure for ease of observation of the results and comparison between them in terms of ultimate load, deflection and area under the curve, from Figure7 (load-deflection curves) and Table 4 we observe the failure of the brittle and sudden punching shear for the model without the shear reinforcement

The models with UHPC total depth of slab gave a high punching shear bearing capacity that reached twice the resistance of the reference model and 70% of the model containing the punching shear reinforcement. The models with UHPC half thickness of the slab gave not high results to strength shear in 70% of the normal concrete model, but it change of failure pattern and contains energy absorbed after failure(post punching capacity) and which increase by increasing ratio steel fiber in UHPC.

The improvement of punching resistance after being proven by this practical study was compatible and supported by a theoretical study in the finite element method using the (ABAQUS) program by Kadhim et al. [42] and Sousa et al. [43] as shown in Figures 8 and 9.

The two above researchers used an expirmental study for the same as Zohrevand et al. [33] to compare with

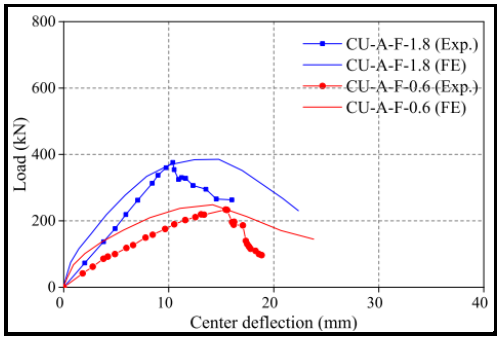

Figure 8. Validation Study: Load- Central Deflection [42]

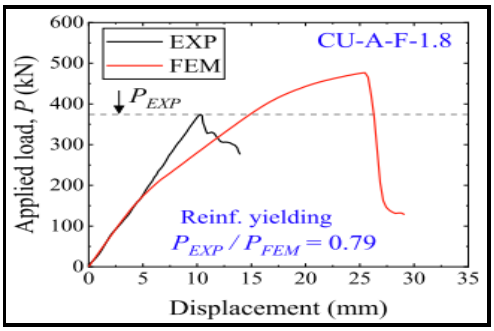

Figure 9. Validation Study: Load- Central Deflection [43]

their theoretical study and they reached theoretical results with a small coefficient of change. They proved that using UHPC is a viable solution to strengthen the flat slab, and this is consistent with the conclusion of present study.

5.CONCLUSIONS

Six square samples of flat plate slabs with central bearing of a column model consisting of normal concrete, this slab consisting from normal concrete or hybrid concrete (normal and high-performance concrete) to be tested the capacity of punching shear with the stability of the quantity of high-performance concrete with a change in its depth or shape. After the experimental study, the following conclusions were summarized:

1. The models with UHPC total depth of slab gave a high punching shear bearing capacity that reached twice the resistance of the reference model and 70% of the model containing the punching shear reinforcement.
2. The models with UHPC half thickness of the slab gave not high results to strength shear , but it change of failure pattern and contains energy absorbed after failure(post punching capacity).
3. We notice the crack at the limits of the UHPC region, except in the 400-XC model, the failure occurs at a distance equal to the column side in all UHPC directions so there is no need to use it.

4. Post punching capacity is the residual strength of slab may be measured as the load after punching failure at whose the load-deflection response tends to flatten and which increase by increasing ratio steel fiber in UHPC.
5. Hybrid slabs composed of NC and UHPC often fail the punching and flexural compound due to high initial stiffness and ductility of the UHPC.
6. Replacing the reinforcement shear with another strengthening is an important point that designers resort to in areas of rebar engagement.
7. From theoretical punching shear capacities, we conclude that the code equation (ACI318-19) is very conservative, and we also recommend suggesting a new mathematical model or an modify to the code equation in order to be inclusive of all forms UHPC and not just for regular shapes.
8. Since the sample rotated at an angle 45 gave the best results, so this study suggests that the position of the shear reinforcement should be studied at an angle 45 from what the code places.

6. REFERENCES

1. Dovich, L.M., "Lateral response of nonseismically detailed reinforced concrete flat slab structures", University of Michigan, (1994),
2. Ramana, N.V., Gnaneswar, K., Sashidhar, C. and Kumar, T.N., "Behavior of high performance concrete two way slabs in punching shear", ***International Journal of Science and Advanced Technology***, Vol. 2, No. 3, (2012), 122-126, doi.
3. Moe, J., "Shearing strength of reinforced concrete slabs and footings under concentrated loads, Portland Cement Association, Research and Development Laboratories, (1961).
4. Broms, C.E., "Shear reinforcement for deflection ductility of flat plates", ***ACI Structural Journal***, Vol. 87, No. 6, (1990), 696-705, doi.
5. Bloem, D.L. and Delevante, O.L., "Building code requirements for reinforced concrete", ***ACI Journal***, Vol. 1, No., (1970), 77, doi.
6. Andersson, J.L., "Punching of concrete slabs with shear reinforcement: Kungliga tekniska högskolans handlingar", (1963).
7. Corley, W.G. and Hawkins, N.M., "Shearhead reinforcement for slabs", in Journal Proceedings. Vol. 65, (1968), 811-824.
8. Dilger, W.H. and Ghali, A., "Shear reinforcement for concrete slabs", ***Journal of the Structural Division***, Vol. 107, No. 12, (1981), 2403-2420, doi.
9. Mokhtar, A.-S., Ghali, A. and Dilger, W., "Stud shear reinforcement for flat concrete plates", in Journal Proceedings. Vol. 82, No. Issue, (1985), 676-683.
10. El-Salakawy, E.F., Polak, M.A. and Soudki, K.A., "New shear strengthening technique for concrete slab-column connections", ***Structural Journal***, Vol. 100, No. 3, (2003), 297-304.
11. Adetifa, B. and Polak, M.A., "Retrofit of slab column interior connections using shear bolts", ***ACI Structural Journal***, Vol. 102, No. 2, (2005), 268.
12. Hassanzadeh, G. and Sundquist, H., "Strengthening of bridge slabs on columns", ***Nordic Concrete Research-Publications-***, Vol. 21, No., (1998), 23-34, doi.
13. Ebead, U. and Marzouk, H., "Fiber-reinforced polymer strengthening of two-way slabs", ***Structural Journal***, Vol. 101, No. 5, (2004), 650-659.
14. Harajli, M. and Soudki, K., "Shear strengthening of interior slab–column connections using carbon fiber-reinforced polymer sheets", ***Journal of Composites for Construction***, Vol. 7, No. 2, (2003), 145-153.
15. Johnson, G.P. and Robertson, I.N., "Retrofit of slab-column connections using cfrp", in 13th world conference on earthquake engineering, Vancouver, BC, Canada, paper. (2004).
16. Beiram, A. and Al-Mutairee, H., "Effect of using waste rubber as partial replacement of coarse aggregate on torsional strength of square reinforced concrete beam", ***International Journal of Engineering, Transactions B: Applications***, Vol. 35, No. 2, (2022), 397-405, doi: 10.5829/ije.2022.35.02b.16.
17. Esfahani, M.R., Kianoush, M.R. and Moradi, A., "Punching shear strength of interior slab–column connections strengthened with carbon fiber reinforced polymer sheets", ***Engineering Structures***, Vol. 31, No. 7, (2009), 1535-1542, https://doi.org/10.1016/j.engstruct.2009.02.021
18. Harajli, M., Soudki, K. and Kudsi, T., "Strengthening of interior slab–column connections using a combination of frp sheets and steel bolts", ***Journal of Composites for Construction***, Vol. 10, No. 5, (2006), 399-409, https://doi.org/10.1061/(ASCE)1090-0268(2006)10:5(399)
19. Sissakis, K. and Sheikh, S.A., "Strengthening concrete slabs for punching shear with carbon fiber-reinforced polymer laminates", ***ACI Structural Journal***, Vol. 104, No. 1, (2007), 49.
20. Erdogan, H., Zohrevand, P. and Mirmiran, A., "Effectiveness of externally applied cfrp stirrups for rehabilitation of slab-column connections", ***Journal of Composites for Construction***, Vol. 17, No. 6, (2013), 04013008, doi: 10.1061/(ASCE)CC.1943-5614.0000389.
21. Muteb, H.H. and Hasan, D.M., "Ultra-high-performance concrete using local materials and production methods", in IOP Conference Series: Materials Science and Engineering, IOP Publishing. Vol. 870, (2020), 012100.
22. Hashim, A. and Ali, A., "Structural behavior of reinforced concrete horizontally curved box beam with opening", ***International Journal of Engineering,Transactions A: Basics***, Vol. 35, No. 4, (2022), 774-783, doi: 10.5829/ije.2022.35.04a.17.
23. Honarvar, E., Sritharan, S., Matthews Rouse, J. and Aaleti, S., "Bridge decks with precast uhpc waffle panels: A field evaluation and design optimization", ***Journal of Bridge Engineering***, Vol. 21, No. 1, (2016), 04015030, https://doi.org/10.1061/(ASCE)BE.1943-5592.0000775
24. Haber, Z.B. and Graybeal, B.A., "Lap-spliced rebar connections with uhpc closures", ***Journal of Bridge Engineering***, Vol. 23, No. 6, (2018), 04018028, https://doi.org/10.1061/(ASCE)BE.1943-5592.0001239
25. Afefy, H.M. and El-Tony, E.-T.M., "Punching shear resistance of strengthened reinforced concrete interior slab–column connections using ultra-high-performance strain-hardening cementitious composite material", ***Advances in Structural Engineering***, Vol. 22, No. 8, (2019), 1799-1816, https://doi.org/10.1177/1369433218823841
26. Lampropoulos, A.P., Duncan, J.N. And Tsioulou, O.T., "Punching shear resistance of uhpfrc", in 20th Congress of IABSE, New York City 2019: The Evolving Metropolis–Report, International Association for Bridge and Structural Engineering (IABSE Vol. 114, (2019), 867-872.
27. Harris, D.K., "Characterization of punching shear capacity of thin uhpc plates", Virginia Tech, (2004),
28. Joh, C., Hwang, H. and Kim, B., "Punching shear and flexural strengths of ultra high performance concrete slabs", ***High***

Performance Structures and Materials IV, Vol. 97, (2008), 97-106.

29. Graddy, J.C., Kim, J., Whitt, J.H., Burns, N.H. and Klingner, R.E., "Punching-shear behavior of bridge decks under fatigue loading", ***Structural Journal***, Vol. 99, No. 3, (2002), 257-266, doi.
30. Park, H., "Model-based optimization of ultra high performance concrete highway bridge girders", Massachusetts Institute of Technology, (2003),
31. Moreillon, L., "Shear strength of structural elements in high performance fibre reinforced concrete (HPFRC)", Université Paris-Est, (2013),
32. Aaleti, S., Petersen, B. and Sritharan, S., *Design guide for precast uhpc waffle deck panel system, including connections*. 2013, United States. Federal Highway Administration.
33. Zohrevand, P., Yang, X., Jiao, X. and Mirmiran, A., "Punching shear enhancement of flat slabs with partial use of ultrahigh-performance concrete", ***Journal of Materials in Civil Engineering***, Vol. 27, No. 9, (2015), 04014255, https://doi.org/10.1061/(ASCE)MT.1943-5533.0001219
34. Specification, I.S., "No. 5/1984, portland cement", Central Organization for Standardization & Quality Control (COSQC), Baghdad, Iraq, (1984).
35. specification No, I., "Natural sources for gravel that is used in concrete and construction", (1984).
36. ASTM, "C1240-04 standard specification for the use of silica fume as a mineral admixture in hydraulic cement concrete, mortar and grout", in American Society for Testing and Materials.
37. ASTM, "C494-05, standard specification for chemical admixtures for concrete", in American Society for Testing and Materials.
38. ASTM, D., "6751-15a standard specification for biodiesel fuel blend stock (b100) for distillate fuels", in American Society for Testing and Materials. (2015).
39. Committee, A., "Building code requirements for structural concrete (aci 318-08) and commentary, American Concrete Institute. (2008).
40. Shwalia, A.S.I., Al-Salim, N.H.A. and Al-Baghdadi, H.M., "Enhancement punching shear in flat slab using mortar infiltrated fiber concrete", ***Civil Engineering Journal***, Vol. 6, No. 8, (2020), 1457-1469, doi: 10.28991/cej-2020-03091560.
41. ACI, "Prc-239-18: Ultra-high performance concrete", (2018).
42. Kadhim, M.M., Saleh, A.R., Cunningham, L.S. and Semendary, A.A., "Numerical investigation of non-shear-reinforced uhpc hybrid flat slabs subject to punching shear", ***Engineering Structures***, Vol. 241, (2021), 112444, https://doi.org/10.1016/j.engstruct.2021.112444
43. de Sousa, A.M., Lantsoght, E.O., Genikomsou, A.S., Krahl, P.A. and Mounir, K., "Behavior and punching capacity of flat slabs with the rational use of uhpfrc: Nlfea and analytical predictions", ***Engineering Structures***, Vol. 244, (2021), 112774, https://doi.org/10.1016/j.engstruct.2021.112774

Persian Abstract

چکیده

مطالعات گسترده ای بر روی موضوع شکست برش پانچ در دال های مسطح و راه های استحکام بخشی داخلی، خارجی و اهمیت این سازه (دال تخت) و خطر شکست برشی پانچ در نواحی اتصال ستون متمرکز شده است. – دال بنابراین، این مطالعه مبتنی بر تقویت ظرفیت باربری دال تخت در برابر شکست برش پانچ با بتن با کارایی بالا (UHPC) بود. چون گران است، بنابراین استفاده از آن برای کل دال امکان پذیر نیست. بنابراین، هدف از این مطالعه جایگزینی برش پانچ آرماتور با UHPC و تعیین استفاده بهینه از آن در ناحیه برشی بود. شش نمونه دال مسطح تقویت شده با حداکثر فولاد خمشی بارگذاری شده با ستون در وسط، چهار فرم ریخته گری UHPC به جای آرماتور برشی و در دو عمق متفاوت استفاده شد. نتایج نشان داد که مقاومت برشی پانچ نمونه ریختگی با UHPC به جای آرماتور برشی پانچ (ACI 318-19)بهبود یافته و با تمام ضخامت دال، در مقایسه با نمونه مرجع (NSC)با فولاد خمشی مسلح شده، دو برابر شده است. فقط. این برنامه عالی برای UHPC است. همچنین اشاره شد که ریخته‌گری UHPC با نصف ضخامت دال در مقایسه با ریخته‌گری با تمام ضخامت‌ها، علیرغم دوبرابر شدن فاصله UHPC از تمام وجوه ستون، نتایج خوبی را به همراه ندارد. اما الگوی شکست را تغییر می دهد و آن را از مناطق خطرناک نزدیک ستون های ناخواسته دور نگه می دارد.

IJE TRANSACTIONS B: Applications Vol. 35, No. 08, (August 2022) 1629-1640

International Journal of Engineering

Journal Homepage: www.ije.ir

Experimental and Statistical Investigations on Alccofine Based Ternary Blended High-performance Concrete

B. Sankar*, P. Ramadoss

Department of Civil Engineering, Puducherry Technological University, Puducherry, India

PAPER INFO

Paper history:
Received 30 April 2022
Received in Revised form 15 May 2022
Accepted 20 May 2022

Keywords:
Alccofine
High-Performance Concrete
Ternary Blended Concrete
Synergy Assessment
Empirical Models
Silica Fume

ABSTRACT

This paper investigates the potential benefits of Ternary blended High-performance concrete containing Silica fume (SF) and Alccofine (AL) as partial cement replacements. The experimental program contains a total of 14 mixes with a water to binder ratio of 0.4 and varying percentages (0-20%) of Silica fume and Alccofine both as binary and ternary blended. Fresh and hardened properties of concrete were evaluated based on slump, compressive strength, flexural strength, split tensile strength and water absorption tests. Ternary mixes containing SF and AL increased concrete compressive strength by 14-27% and tensile strength by 26-43% compared to the reference mix. Rise in early strength development for all the ternary blended mixes is attributed to the presence of highly reactive alccofine. Higher replacement of Alccofine more than 10% led to a steady decrease in strength due to dilution effect, whereas for silica fume, the strength dilution was gradual beyond 15% replacement. Denser particle packing reduced water absorption in ternary mixes. A mix containing 15% SF and 5% AL showed 65.7% reduction in water absorption compared to reference mix. Synergy assessment were done for all the ternary mixes, peak result was obtained for a mixture containing 10% SF and 10% AL. Based on the experimental data, empirical models were developed and compared with the existing codes and earlier researches. Empirical models proposed in this study have the least Integral Absolute Error (IAE) of 0.47% and 1.55% in predicting flexural strength and split tensile strength based on compressive strength of concrete.

doi: *10.5829/ije.2022.35.08b.19*

1. INTRODUCTION

In recent years, there is a steady growth in the consumption of concrete due to growing population and rapid modernization. Due to the increased demand, there is a continual depletion of natural resources that forms the key constituents of the cement industry. On the other hand, improper disposal of industrial by-products has reported landfill problems causing adverse effects on the environment [1, 2]. Some of these industrial by-products have cementitious values and are being used as partial cement replacements. Supplementary cementitious materials (SCMs) such as Fly ash (FA), Silica fume (SF), Metakaolin (MK), Alccofine (AL), Rice husk ash (RHA) and ground granulated blast-furnace slag (GGBS) are rich in silica and alumina content essential for the strength development of concrete [3, 4].

Modern concrete has to grow along with the fast-growing world and has to serve bigger purposes beyond strength criterion i.e. early strength development and durability. High-performance concrete (HPC) is predominantly being used in high-rise buildings, bridges and marine structures where erection time and durability are critical factors [5]. The mentioned conditions can be fulfilled by three methods 1) by using special types of cement, which has high production cost and are therefore not suitable for most cases 2) steam curing, where implementation might be quite tedious in actual field practices 3) using mineral admixtures. Eventhough numerous studies have reported the benefits of using SCMs in concrete, incorporating higher dosages of SCMs in binary form can often lead to negative side effects such as dilution of strength and extended setting time [6, 7]. One possible way to overcome such disadvantages is to

*Corresponding Author Institutional Email: samkarboomibalan180@pec.edu (B. Sankar)

Please cite this article as: B. Sankar, P. Ramadoss, Experimental and Statistical Investigations on Alccofine Based Ternary Blended High-performance Concrete, ***International Journal of Engineering, Transactions B: Applications***, Vol. 35, No. 08, (2022) 1629-1640

use combinations of mineral admixtures subjected to demand, where the potential synergy between two different SCMs can be explored [8, 9].

The packing density of concrete can have a huge influence on strength and durability. Using mineral admixtures with varying particle sizes can result in denser matrix. In the case of ultrafine silica fume (about 100 times finer than cement), the wide size gap was filled by incorporating metakaolin (finer than cement and coarser than SF) which further improved concrete microstructure [10]. On the other hand, increasing particle packing densities reduces void gaps and brings out the excess water present in the pores for the lubrication of binder particles [11], highly essential for HPC where lower water to binder ratio is adapted.

Several researchers have pointed out the effectiveness of ternary blending (cement + two different SCMs). Ahmed et al. [12] studied chloride ion penetration in concrete mixes and observed a significant decrease in average charge passed for a mix containing ternary blend of 25% FA and 10% SF compared to corresponding binary blend. Jung et al. [13] reported that ternary blending of SCMs can be a suitable alternative to type IV cement in preventing thermal cracks caused due to high heat of hydration. Murthi et al. [14] studied the effect of nanomaterials in the early strength development of ternary blended concrete. In the case of fly ash known for its long-term mechanical and durability properties, it has shortcomings such as poor early strength development, which can be overcome by adding finer materials such as silica fume, metakaolin [15, 16].

Alccofine-1203 is an ultra-fine form of slag produced as a result of controlled granulation process. It has been well documented that this low calcium silicate-based admixture is highly reactive and eco-friendly. Even though several studies have reported the effects of using alccofine in binary form [17, 18]; Only fewer studies have been carried out with alccofine as a ternary additive in cement concrete, particularly in HPC. A replacement of 10% alccofine in fly ash-based geopolymer resulted in increased load-carrying capacity in compression [19]. Soni et al. [20] reported increased particle packing due to the addition of fly ash and alccofine, and increased early strength development powered by alccofine's high reactivity.

In view of the aforementioned knowledge about the past studies, this present study aims to investigate the effects of adding silica fume and alccofine both in binary and ternary form on the mechanical and durability aspects of HPC. Synergy assessment is done for all the ternary mixes in compression, flexural and split tensile strength. From the results obtained through experimental works, empirical relations have been formulated to predict flexural and split tensile strength based on compressive strength. Finally, a cost-based analysis is carried out to examine the economical deviations with strength and durability of concrete.

2. RESEARCH SIGNIFICANCE

The concrete industry is now wide awake of the limiting raw materials for construction. Combinations of SCMs provide superior workability, strength and durability, which are essential for High strength concrete structures where frequent repair and rehabilitation is a major setback considering economic, environmental and exertion levels. Despite the vast numbers of research published and growing interest in ternary blended concrete, limited information has been documented on the interaction between SCMs and synergy evaluation. This study emphasizes on the performance comparison of a new blended cement in HPC containing two ultrafines SF and AL, both in binary and ternary forms. Empirical relations from the existing codes to predict tensile strength based on compression tends to deviate more in the case of combinations of SCMs, not just in the case of this study, but rather in most ternary mixes from previous researchers. Hence re-evaluation of empirical relations is necessary for SCM replaced concrete.

3. EXPERIMENTAL PROGRAM

The following methodology discussed in this section has been tailored to attain the objectives of the proposed study.

3. 1. Material Properties Ordinary Portland cement of 53-grade with a 28-day compressive strength of 54.5 Mpa and specific gravity of 3.12 confirming to IS 12269-2013 [21], is used as cementing material for all the mixes. Silica fume is a superior ultrafine mineral admixture now available in markets everywhere and was obtained from Astrra Chemicals Pvt Ltd complying with ASTM C1240 [22]. Alccofine-1203 is an ultra-fine form of GGBS processed through controlled granulation, are highly reactive in nature. The particles have irregular shapes with sizes mostly falling under the range of 4-10 µm. The particle size distribution of OPC, SF and AL are shown in Figure 1. Chemical compositions and tested physical properties of OPC, SF and AL are mentioned in Tables 1 and 2, respectively. Manufactured sand confirming to zone II sieve passing percentage of IS: 383-1970 [23] is used as fine aggregate for all the mixes. Fine aggregate has the specific gravity of 2.67, fineness modulus of 2.72 and water absorption of 0.96% at an interval of 24 h. Crushed granite rock of size not less than 12.5 mm is used as coarse aggregate. Coarse aggregate has the specific gravity of 2.7, fineness modulus of 6.67

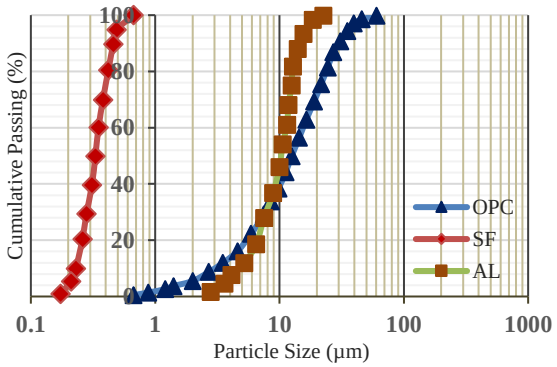

Figure 1. Particle size distribution of OPC, SF and AL

TABLE 1. Chemical composition of OPC,SF and Al (%)

Chemical composition	OPC	SF	AL
SiO_2	21.07	92.06	21-23%
Al_2O_3	5.54	0.48	5-5.6%
CaO	64.26	0.4	61-64%
Fe_2O_3	5.16	2.11	3.84.4%
MgO	0.86	0.63	0.81.4%
K_2O	0.37	1.24	-
P_2O_5	0.33	0.02	-
LOI	1.54	2.54	-

TABLE 2. Physical properties of OPC, SF and AL

	OPC	SF	AL
Specific gravity	3.1	2.63	2.9
Specific surface area (cm^2/g)	-	18800	12000
Bulk density (kg/m^3)	1550	600	820
Standard consistency (%)	27.4	-	-
Setting time (min)			
Initial	110	-	-
Final	300	-	-

and water absorption of 0.70% at an interval of 24 h. Sulfonated Naphthalene Formaldehyde based high range water reducer confirming to IS: 9103-1999 [24] and ASTM C494 [25] with a specific gravity of 1.2 ± 0.05 is used as superplasticizer.

3. 2. Mix Proportioning and Preparation of Specimens A total of 14 mixes were proportioned using guidelines and specifications recommended by ACI 211.4R-93 [26]. Four binary mixes with both SF and AL with replacement levels of 5-20% and five ternary mixes with a maximum replacement of 15% and 20% were prepared. For all the mixes fine aggregate content is reduced corresponding to the volume change from the addition of SCMs. Superplasticizer content was varied by weight of cementitious materials in order to ensure the desired workability, with a slump not less than 75 mm. The mixture proportions used in this experimental program are summarized in Table 3. Concrete was carefully mixed in a tilting type mixer machine and placed in cubical moulds of size 100 mm x 100 mm x 100 mm, cylindrical moulds of size 100 mm x 200 mm and prism moulds of size 100 x 100 mm x 500 mm. For every mix, 3 Numbers of specimens were cast. The specimens after de-moulding were allowed for curing in a laboratory controlled environment.

TABLE 3. Mixture proportioning of Binary and Ternary blended concrete

Mix No.	Mix	C, Kg	SF, Kg	AL, Kg	W, Kg	FA, Kg	CA, Kg	SP (%)
M1	Control	450	-	-	179	669	1099	-
M2	SF-5	427.5	22.5	-	179	629	1099	0.5
M3	SF-10	405	45	-	179	589	1099	0.5
M4	SF-15	382.5	67.5	-	179	549	1099	0.5
M5	SF-20	360	90	-	179	509	1099	0.5
M6	AL-5	427.5	-	22.5	179	640.5	1099	0.75
M7	AL-10	405	-	45	179	612.1	1099	0.75
M8	AL-15	382.5	-	67.5	179	583.6	1099	0.75
M9	AL-20	360	-	90	179	555.1	1099	0.75
M10	SF-5, AL-10	382.5	22.5	45	179	572.1	1099	0.85
M11	SF-10, AL-5	382.5	45	22.5	179	560.5	1099	0.85
M12	SF-15, AL-5	360	67.5	22.5	179	520.5	1099	0.85
M13	SF-10, AL-10	360	45	45	179	532.1	1099	0.85
M14	SF-5, AL-15	360	22.5	67.5	179	543.6	1099	0.85

3. 3. Testing Methods To determine the workability of fresh concrete, slump test was performed in accordance with ASTM C143 [27]. Compression testing machine with a maximum load-carrying capacity of 3000 kN is used to test cube samples. Split tensile strength test was conducted in a Universal testing machine to determine the indirect tensile strength of concrete as per specifications of ASTM C 496-90 [28]. Flexural strength test was performed as per the specifications of ASTM C78 [29] using a three-point loading system. Samples were taken after curing at a temperature of 27±2ºC (90-95% Relative Humidity) and surface dried before testing. Sample preparation and testing are shown in Figure 2.

4. RESULTS AND DISCUSSION

The results of mechanical and durability properties obtained from the tested samples of binary and ternary blended concrete are discussed in this section.

4. 1. Workability of Concrete Workability is a paramount fresh concrete property to measure the ease in mixing, transporting and placing concrete without much segregation, bleeding, loss of materials and energy consumption, while maintaining homogeneity. Addition of different SCM shows distinct effect on the workability of concrete. In this study, three different superplasticizer dosages were used for SF concrete, AL concrete and Ternary blended concrete to attain a slump not less than 75 mm. Addition of SF increased workability due to its fine and spherical shaped particles, whereas slump degradation was observed significantly for higher dosages of AL. Ternary mixes containing SF and AL provided better slump with a homogeneous and cohesive mixture. Slump values for all the mixes in this present study are mentioned in Figure 3.

Figure 2. Sample preparation and testing

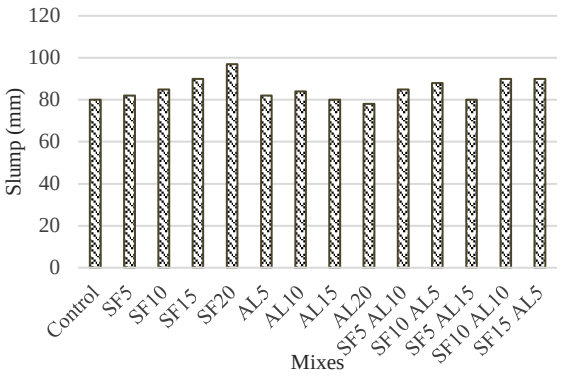

Figure 3. Slump values of the Mixes

4. 2. Mechanical Properties of Concrete

4. 2. 1. Compressive Strength The compressive strength results of tested cube samples are presented in Figure 4. Tests were performed on four curing ages of 7, 14, 28 and 45 days for all the mixes. Replacement of cement with SF in the control mix significantly increases the compressive strength, Figure 5(a) shows the improvement in the strength of SF replaced concrete mixes for different curing ages. The silica-rich SF reacts with portlandite to produce additional C-S-H gel which progressively densifies the matrix resulting in increased strength [30]. AL replacement with cement rapidly increased strength due to its highly reactive components, maximum value was observed for a 10% replacement. Figure 5(b) shows improvement in the strength of AL replaced HPC mixes for different curing ages. For SF binary concrete a maximum strength increment of 20.8% was attained for 15% replacement at 28-day period, after which there is a gradual decrease in the strength primarily due to dilution effect. For AL binary concrete, a maximum strength increment of 17.9% was observed for a 10% replacement, after which a significant dropdown in the strength was noticed. In the case of both SF and AL the strength increments and decrements are in

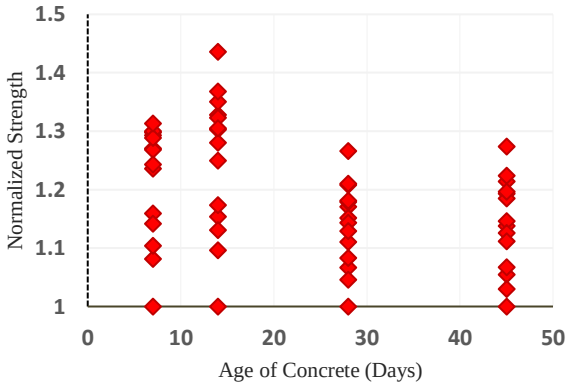

Figure 4. Strength Improvement of concrete in compression

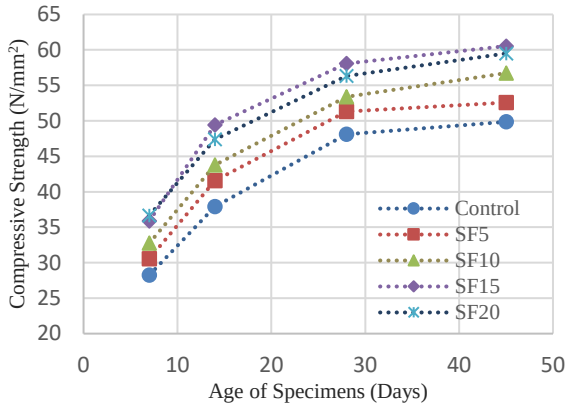

(a)

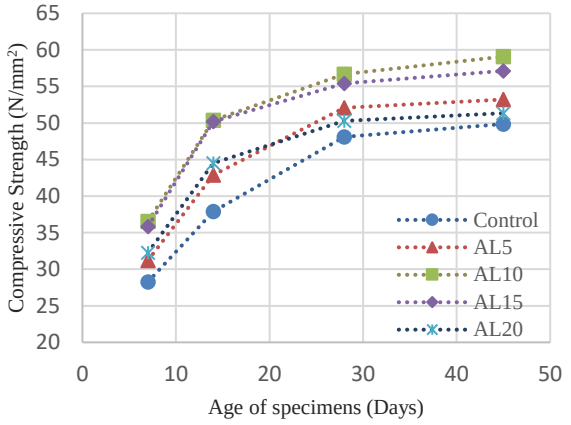

(b)

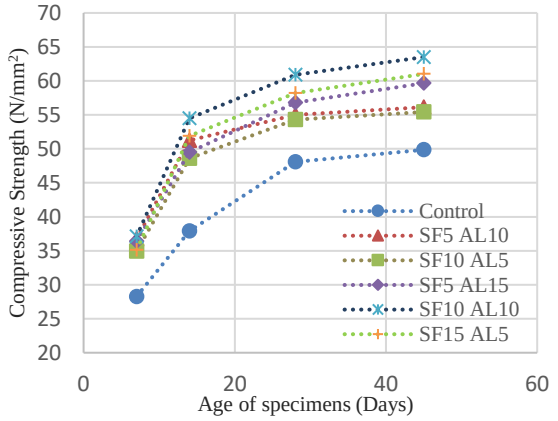

(c)

Figure 5. Compressive strength test results (a) SF blended concrete (b) AL blended concrete (c) Ternary blended concrete

compliance with their corresponding pozzolanicity and dilution effect. AL contains highly active silica and calcium content which results in rapid crystallization and hardening essential for early strength development, but on the negative side, a significant decrement is observed for mixes containing higher dosages due to dilution of hydration products. Dilution rate for SF concrete is much less compared to AL concrete, for M5 concrete containing 20% SF, only a 3.3% strength decrement was observed to that of M4 containing 15% SF. Compressive strength of Ternary blended mixes M10, M11, M12, M13 and M14 were enhanced by 14.3%, 12.8%, 18%, 26.6 and 20.9% to that of the reference mix M1.

The 28-day compressive strength increment of 10%SF + 10% AL from the current study is higher compared to 10% strength increment from 10% RHA + 10% MK [31], 17.7% strength increment from 10% AL + 20% FA [32] and 7.15% strength increment from 30% Bagasse ash + 1.5% Nano silica [14]. Ternary mixes showed better performance in compression compared to binary mixes from the current study as well as from similar studies conducted by Biswas et al. [33] and Bhanja et al. [34], where SF binary mixes provided a maximum strength increment of 15% and 23.6% for 12% and 20% replacement of SF.

Ternary blending of SF and AL has positive interaction in terms of compressive strength. Higher replacement of AL is made possible with the addition of SF. Figure 5(c) shows the variation in strength with SF & AL dosage and curing age of ternary mixes. Figure 4. depicts the improvement in early strength compared to the later age strength of ternary blended concrete, mainly due to the presence of highly reactive AL. Even though, the dormant SF and AL components resulting from higher dosages will provide strength in later ages of concrete through ettringite formation, for early ages the dilution effect is less in ternary blended mixes compared to binary SF and AL mixes. Increase in the strength of ternary blended HPC is attributed to the presence of synergy between SF and AL.

4. 2. 2. Flexural Strength The flexural strength of all the mixes is tested for a 28-day curing period and the results are shown in Figure 6. From the results, it is evident that the flexural strength of SF and AL blended binary concrete follows a similar course with the results of compressive strength and the results are in good agreement with earlier researches [35, 36]. Addition of pozzolanic materials into the concrete mix reduces calcium hydroxide concentration through the formation of secondary C-S-H gel, which then solidifies the interfacial bond between aggregates and paste in the matrix. Stronger the interfacial bond higher the flexural strength and resistance towards crack propagation. SF binary concrete increased the flexural strength furthermore compared to AL binary concrete.

M4 and M7 concrete with SF 15% and AL 10% showed increment in flexural strength of 30% and 26.2% in reference to the control mix M1. Ternary blended mixes M12, M13 and M14 with 20% replacement by weight of cement showed an increment of 25.8%, 43.1% and 31.9% compared to M1. Similar studies containing ternary blended mixes provided 10.69% increment in

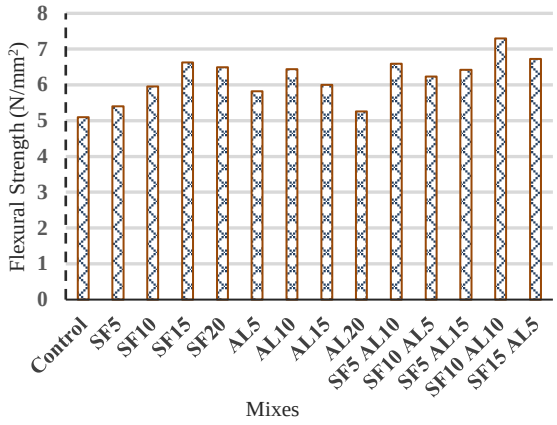

Figure 6. Comparison of flexural strength test results

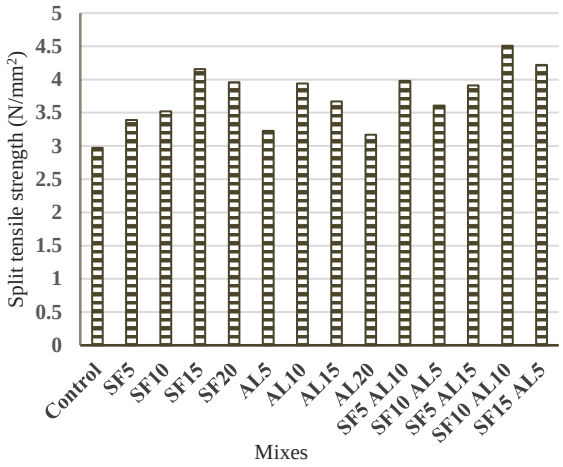

Figure 8. Comparison of Splitting tensile strength test results

flexural strength resulting from 10% AL + 20% FA [32] and 31.2% increment resulting from 10% SF + 10% MK [10]. In the case of previous studies and the current study, ternary mixes provided better results in flexure compared to binary mixes. Mix containing a combination of 10% SF and 10% AL provided the maximum result. Failure modes of the samples in flexure are shown in Figure 7(b). Synergy was observed in all the ternary mixes with an increase in flexural values compared to their corresponding binary mix.

4. 2. 3. Split Tensile Strength Even though concrete is purely designed to withstand compressive stresses, some tensile stresses may also develop due to temperature gradient, shrinkage and indirect tensile loads. Hence it is necessary to measure the tensile stress carrying capacity of the concrete elements. Figure 8 shows the split tensile strength (STS) test results at a curing period of 28 days, for all the mixes in the present study. From the results, it can be seen that, as the pozzolanic material content is escalated a significant improvement can be seen in both binary and ternary mixes with respect to control mixes. Similar to flexure strength, an increase in splitting tensile strength can be achieved through aggregate and matrix bond. Results of the splitting tensile strength test are in similar trends with the compressive strength values, the failure modes of the samples are shown in Figure 7(a).

(a) (b)

Figure 7. Failure modes a) Split tensile test b) Flexure test

Tensile strength increases with an increase in SF content up to 15%, after which, due to inadequate hydration products bond between matrix and aggregate weakens. M4 showed a tensile strength increment of 40% with reference to M1. Similarly, for AL binary mixes, STS increases up to a 10% replacement level after which powdered squashing is detected due to delayed crystallization and lack of hydration products. An increment in tensile strength of 32.6% for M7 is observed in reference to M1. In ternary blended concretes, dilution due to SF is balanced to some extent with the lime content present in AL, similarly, an increase in active silica content of SF made use of the Calcium oxide content in AL to produce effective C-S-H products. Ternary mixes M10 and M11 with 15% total replacement showed increments of 34% and 21.5% compared to M1. Ternary mixes M12, M13 and M14 with 20% total replacement showed increment of 31.6%, 51.8% and 42% compared to M1, which indicates its superiority over 16% increment from blending of 10% AL & 20% FA [32], 16.6 % increment resulting from 30% FA + 6% SF replacement [37] and 7.6% increment from 30% Bagasse ash + 1.5% Nano silica [14].

4. 3. Water Absorption Percentage water absorption is the measurer of water absorbed by hardened concrete when immersed in water having temperature of 23ºC for a period of 48 hours, to that of oven-dried concrete sample for 24 hours. The test was carried out in a 100 X 100 mm cube sample taken out after 28 days of curing. Water absorption in concrete is a major durability

test method, which is an indirect indicator of surface and internal pores. An increase in water absorption can damage the cover area of concrete and adversely affect the internal reinforcement [38]. Test has been carried out for all binary and ternary mixes and the results are compared in Figure 9. From the figure, a significant difference can be observed in the values for binary and ternary blended HPC. Binary mixes containing SF showed lower water absorption compared to AL binary mixes. Increase in alccofine percentage beyond 15% tends to increase water absorption, maybe due to the occupation of porous water in the AL particles. For SF binary mixes maximum and minimum decrement was observed for M5 and M1 with a percentile of 55.8 and 10.5. For AL binary mixes, maximum and minimum decrement was observed for M7 and M9 with a percentile of 52 and 4.9. In binary mixes, SF blended concrete prevents water absorption better than AL concrete. Ternary blended mixes M13 and M14 showed the lowest water absorption with a decrement of 64.6% and 65.7% compared to the control mix.

In general, the mechanical and durability properties of concrete have a higher correlation. Addition of SF and AL densifies the matrix through the reduction of pores which in turn reduces the ingress of water. The densification of pores is associated with the formation of secondary C-S-H crystals. The variation in the values of strength and water absorption for varying admixture proportions can be better ascertained from Figure 10. The graph shows similar trends with the work carried out by Al-Amoudi et al. [39] where an increase in strength resulted in reduced water penetration of plain and blended concretes.

4. 4. Empirical Relations Empirical relations are necessary to determine the strength properties of concrete in the absence of another or inapplicability to perform the test [40, 41]. Standard codes and numerous researches have established empirical relations for normal/High strength concrete [42-50]. In this study, empirical relations to predict flexural and split tensile strength of HPC based on compressive strength are developed. From the tested results, it is observed that more data are inconsistent with the models proposed by standard codes and earlier studies, especially for ternary blended concrete. A similar observation has been pointed out by Abdul and Wong [51]. Hence re-evaluation of empirical relations is necessary for SCM replaced concrete both in binary and ternary forms. Empirical relations are developed in such a way that the deviation between experimental values and predicted values are much lesser, measured in terms of Integral Absolute Error (IAE).

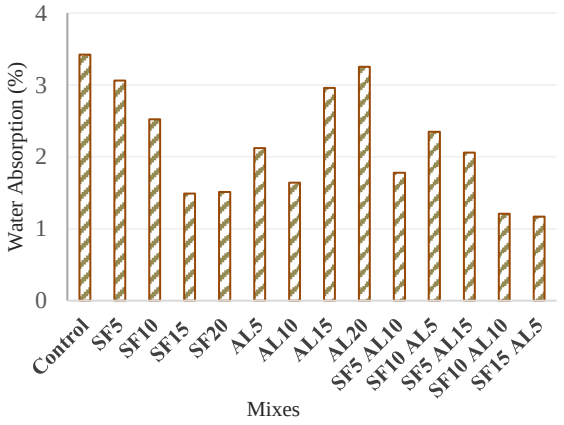

Figure 9. Influence of Binary and Ternary mixes on Water absorption

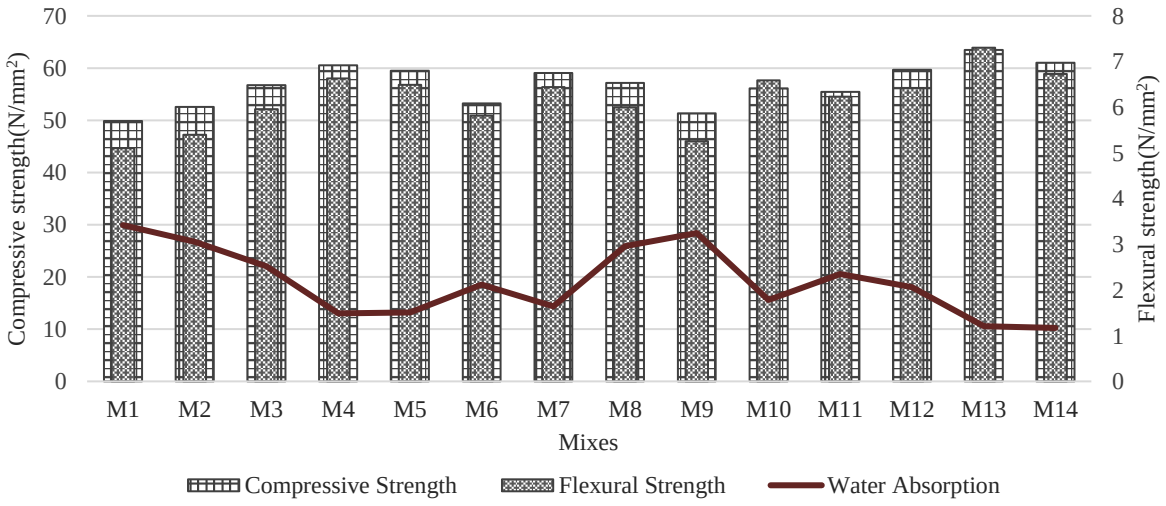

Figure 10. Comparative analysis of strength and durability

$$\text{IAE} = \frac{\sum(Q-P)}{\sum P} \times 100\% \quad (1)$$

where Q is the experimental value and P is the predicted value. Figure 11 shows the predicted values of flexural strength based on formulas proposed by various researchers and codes using compressive strength values from the current study. A general agreement is made on 0.5 as the power value to predict flexural strength with respect to compressive strength. From the figure, large deviations of predicted values from the experimental results are noticeable. The line of best fit indicates the power value of 1.54 due to the rise in the values of ternary blended concrete.

Even though the line of best fit has the maximum prediction accuracy, a formula has been proposed in agreement with the codal practices which has the least IAE of 0.47%. The proposed empirical relation for flexure strength is in close relation with ACI 363-92 (IAE = 2.07%) and Mindess et al. [34] (IAE = 2.33%). Table 4 displays the flexure strength prediction formulas and their corresponding IAE.

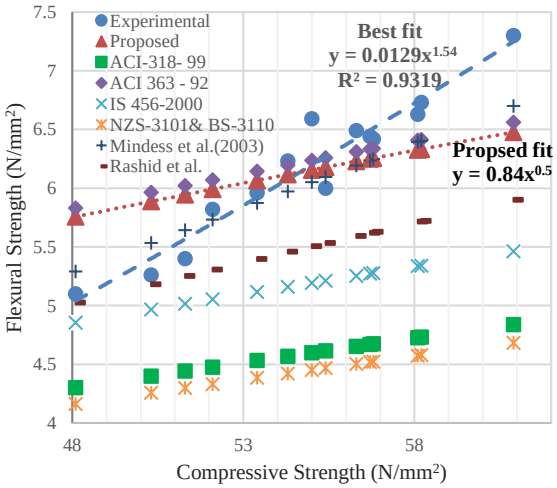

Figure 11. Relationship between Compressive strength and Flexural strength

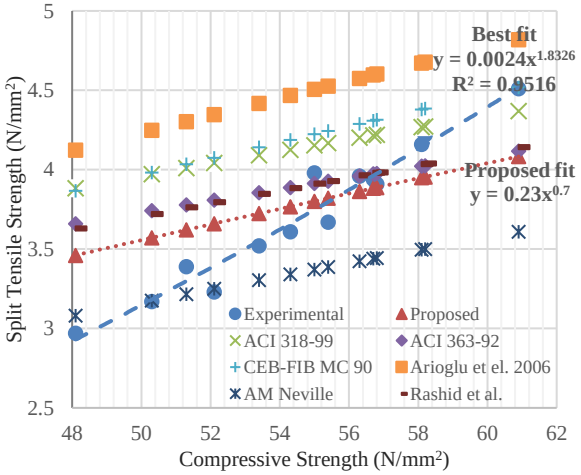

Figure 12. Relationship between Compressive strength and Split tensile strength

The predicted values of split tensile strength based on compressive strength from the current study using formulas proposed by various codes and researches are shown in Figure 12. The line of best fit has the power value of 1.83 unlike the more popular 0.5 and 0.66. This deviation in predicted values is majorly due to SCM replacement, especially in ternary forms where the positive interactions gave rise to higher strength values than that of binary mixes. The proposed empirical relation between STS and compression strength follows a power value of 0.7 with the least IAE of 1.55%. The proposed empirical relation for STS is in close relation with ACI 363-92 (IAE = 4.62%) and Rashid et al. [35] (IAE = 4.56%). Table 5 displays the STS prediction formulas and their corresponding IAE.

TABLE 4. Empirical relations between Compressive strength and Flexural strength

Code of practice/Researchers	Empirical Relation	Integral Absolute Error (IAE) %
ACI 318-99	$f_r = 0.62(f_c')^{0.5}$	25.65
ACI 363-92	$f_r = 0.94(f_c')^{0.5}$	2.07
IS 456-2000	$f_r = 0.7(f_c)^{0.5}$	16.06
NZS - 3101 & BS - 3110	$f_r = 0.6(f_c)^{0.5}$	28.05
Mindess et al. (2003)	$f_r = 0.11(f_c)$	2.33
Rashid et al. (2002)	$f_r = 0.42(f_c')^{0.68}$	11.04
Proposed	$f_r = 0.83(f_c)^{0.5}$	0.47

f_c – cube compressive strength, f_c' – cylinder compressive strength. Cylinder compressive strength assumed to be 0.8 times of cube compressive strength.

TABLE 5. Empirical relations between Compressive strength and Split tensile strength

Code of practice/Researchers	Empirical Relation	Integral Absolute Error (IAE) %
ACI 318-99	$f_{sp} = 0.56(f_c')^{0.5}$	11.02
ACI 363-92	$f_{sp} = 0.59(f_c')^{0.5}$	4.62
CEB - FIB MC 90	$f_{sp} = 0.3(f_c)^{0.66}$	12.86
Arioglu et al. (2006)	$f_{sp} = 0.32(f_c)^{0.66}$	20.38
AM Neville	$f_{sp} = 0.23(f_c)^{0.67}$	9.94
Rashid et al. (2002)	$f_{sp} = 0.47(f_c')^{0.56}$	4.56
Proposed	$f_{sp} = 0.23(f_c)^{0.7}$	1.55

f_c – cube compressive strength, f_c' – cylinder compressive strength. Cylinder compressive strength assumed to be 0.8 times of cube compressive strength.

4. 5. Synergy Assessment of Ternary HPC Mixes

Banthia et al. [52] have defined synergy as an increase in performance of the concrete mixture containing two materials to that of the combined individual performance of the material. Synergy assessment in fundamental mechanical properties is rarely discussed in past researches. In the case of ternary blended concrete, an assessment of synergy is necessary to evaluate the combined effect of cementitious materials, since two different SCMs are being used together. A formula has been worked out to evaluate synergy between SCMs in ternary mixes for compression, split tension and flexure.

$$\text{Synergy} = \frac{f_{(a+b)}}{[f_a + f_b]} - 0.5 \quad (2)$$

where f is the strength of concrete in compression, split tension and flexure, a and b are percentages of SCMs used. The synergy equation estimates the combined effect of SCMs with respect to binary concrete, a positive value indicates the increased performance of ternary mix over two separate binary mixes.

Significant positive synergy is observed in early age compressive strength for all the ternary mixes. Ternary mix containing AL 10% + SF 5% and SF 10% + AL 5% showed zero synergy in later age strength of 28 and 45 days. In mixes M12, M13 and M14, only a slight increment in synergy is observed, and no negative synergy was noticed for any of the mixes in compression. Synergy values for ternary mixes in compression are shown in Figure 13. Mix 11 with SF 10% + AL 5% provided the least synergy in split tensile and flexure strength. Mix 13 with SF 10% + AL 10% provided a maximum of 8%, 10% and 9% increment in compression, split tensile and flexural strength synergy values. Figure 14 shows the synergy values of ternary mixes under indirect tensile stresses.

4. 6. Cost Analysis of SCM Replaced HPC

Cost analysis of SCM replaced HPC with respect to normal concrete can help contractors and customers better understand the additional benefits from the marginal cost increments. The increment spent for durability and strength will improve the service life of structures and can minimize the frequent repair cost due to the ingress of harmful agents. The cost of production of 1 m^3 of concrete for all the mixes from the current study is mentioned in Table 6. The unit prices taken as reference for all the raw materials are from the current market price (in Indian National Rupees, INR) of 2022, especially pertaining to Indian regions. The strength and durability increments of SCM concrete at the cost of small cost increments can be seen in Figure 15.

From the figure, a significant difference in the production cost is visible for SCM replaced concrete, with M5 having a higher cost in binary mix whereas M12 shows a higher cost for the ternary mix. All the SCM replaced mixes show increased production cost values compared to the control mix. The cost increment range varies from 2.23% to 9.7%, whereas the strength

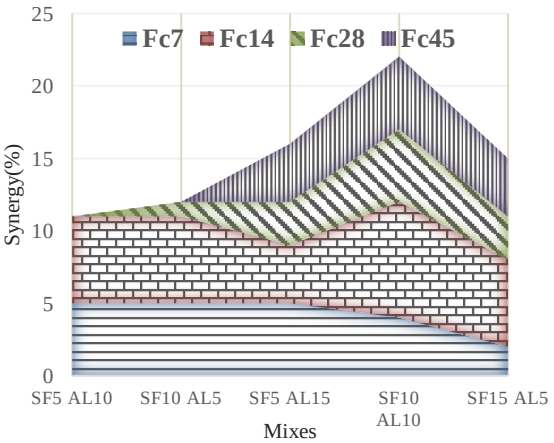

Figure 13. Synergy in Compressive strength

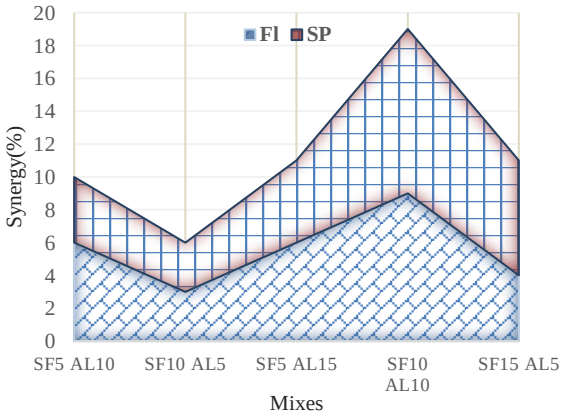

Figure 14. Synergy in Flexure and Split tensile strength

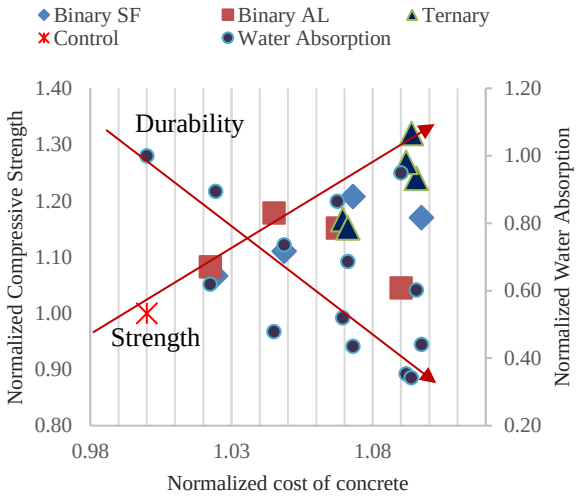

Figure 15. Cost analysis in terms of Durability and Strength

TABLE 6. Production cost of Binary and Ternary blended concrete

Mix Grade															
Material	**Unit Price per kg (INR*)**	**M1**	**M2**	**M3**	**M4**	**M5**	**M6**	**M7**	**M8**	**M9**	**M10**	**M11**	**M12**	**M13**	**M14**
OPC	8	3600	3420	3240	3060	2880	3420	3240	3060	2880	3060	3060	2880	2880	2880
SF	16	-	360	720	1080	1440	-	-	-	-	360	720	1080	720	360
AL	18	-	-	-	-	-	405	810	1215	1620	810	405	405	810	1215
FA	1.05	702.4	660.4	618.4	576.4	534.4	672.5	642.7	612.7	582.8	600.7	588.5	546.5	558.7	570.7
CA	0.7	769.3	769.3	769.3	769.3	769.3	769.3	769.3	769.3	769.3	769.3	769.3	769.3	769.3	769.3
Mixing Water	0.02	3.58	3.58	3.58	3.58	3.58	3.58	3.58	3.58	3.58	3.58	3.58	3.58	3.58	3.58
Electricity	-	600	600	600	600	600	600	600	600	600	600	600	600	600	600
Total (INR)	-	**5675.33**	**5813.3**	**5951.3**	**6089.3**	**6227.3**	**5870.4**	**6065.6**	**6260.7**	**6455.7**	**6203.6**	**6146.4**	**6284.4**	**6341.6**	**6398.7**

*INR – Indian National Rupee

increment varies from 5% to 32%. Previous researches in ternary blended concrete involving cost analysis in terms of strength shows cost variation of 0.85% to 1.025% with strength variation of 0.975% to 1.12% [31], whereas in this study a significant difference can be observed while comparing cost range and strength range. For an equal cost, ternary mixes M12, M13, and M14 showed better mechanical and durability performance compared to binary mixes M5 and M9.

5. CONCLUSIONS

Based on the results from experimental works and statistical analysis, the following conclusions can be drawn.

1. An attempt has been made to study the effects of ternary blending of SF and AL on the workability, mechanical and durability properties of HPC. Workability of ternary mixes were improved naturally to some extent due to ultrafine SF with rounded particle shape, in addition, superplasticizer was used to achieve a workable mix.
2. Binary SF mix M4 with 15% SF provided a maximum increment of 20.8% in compression, 30% in flexure and 40% in splitting tensile strength tests. After which dilution occurs gradually due to loss of hydration products. Binary AL mix M7 with 10% AL provided a maximum increment of 17.9% in compression, 26.2% in flexure, and 32.6% in splitting tensile strength. Components of AL are highly reactive, evident from its high early age strength development. Similarly, the dilution rate of AL is much greater than SF, hence higher replacement levels are not recommended.
3. Ternary blended mixes showed improved load carrying capacity due to microstructural development through secondary C-S-H formation. All ternary mixes provided greater strength values compared to their binary counterparts. A mix containing SF 10% and AL 10% attained a maximum result of 26.6% in compression, 43.1% in flexure and 51.8% in splitting tensile strength.
4. No negative synergy was observed for any of the ternary mixes, however, mixes M10 and M11 exhibited zero synergy in later ages of 28 and 45 days compressive strength. Mix M11 and M13 showed the lowest and highest synergy in flexure and split tensile strength.
5. Higher replacement levels of SCMs, more than 20% total replacement should be explored since the dilution effect is less in ternary blended concrete compared to binary blend.
6. SF and AL densify the concrete, preventing harmful agents from entering through the pores. Water absorption test carried out in this study gave the lowest value for a mix containing SF 15% and AL 5%.
7. Empirical formulas from existing codes and previous researches to predict tensile strength from compression strength shows deviation in case of combinations of SCMs, the power value increases above 1 than the widely accepted 0.5. Hence re-evaluation of empirical relations is necessary for ternary blended concrete with the inclusion of a factor for synergy between the corresponding SCMs.

8. The new empirical relation proposed has the least Integral Absolute Error of 0.73% in predicting flexural strength and 1.55% in predicting split tensile strength.
9. Performance variation in ternary blended concrete is significantly greater compared to cost variation, hence will increase service life and reduce maintenance cost for structures in the long run.

6. REFERENCES

1. Khan, M. I.., Lynsdale, C. J., and Waldron, P., "Porosity and strength of PFA/SF/OPC ternary blended paste" ***Cement and Concrete Research,*** Vol. 30, No. 8, (2000), 1225-1229. doi: 10.1016/S0008-8846(00)00307-0.
2. Sagar, B., and Sivakumar, M. V. N., "An Experimental and Analytical Study on Alccofine Based High Strength Concrete," ***International Journal of Engineering, Transactions A: Basics*****,** Vol. 33, No. 4 (2020), 530-538. doi: 10.5829/IJE.2020.33.04A.03.
3. Mehta, P. K., "Pozzolanic and Cementitious By-Products in Concrete - Another Look," ***ACI Special Publication*** 114, (1989), 1-44.
4. Habert, G., "Assessing the environmental impact of conventional and green cement production". In *Eco-efficient construction and building materials*, Woodhead Publishing, (2014), 199-238, doi: 10.1533/9780857097729.2.199.
5. Neville A. and Aïtcin, P. C. "High performance concrete - An overview," ***Materials and Structures/Materiaux et Constructions*****.** 1998. doi**:** 10.1007/bf02486473.
6. Thomas, M. D. A., Shehata, M. H.,. Shashiprakash, S. G D. S. Hopkins, and Cail, K., "Use of ternary cementitious systems containing silica fume and fly ash in concrete," ***Cement and Concrete Research***, Vol, 29, No. 8, (1999), 1207-1214. doi: 10.1016/S0008-8846(99)00096-4.
7. Sankar. B., and Ramadoss, P., "Review on fiber hybridization in ternary blended high-performance concrete," ***Materials Today: Proceedings***, Vol. 45, (2021), 4919-4924. doi: 10.1016/j.matpr.2021.01.366.
8. Kavyateja, B. V., Jawahar, J. G., and Sashidhara, C. "Durability performance of self compacting concrete incorporating alccofine and fly ash," ***International Journal of Engineering, Transactions B: Applications***, Vol. 33, No. 8 (2020), 1522-1528. doi: 10.5829/ije.2020.33.08b.10.
9. Yurdakul, E. Taylor, P. C. Ceylan, H. and Bektas, F. "Effect of Water-to-Binder Ratio, Air Content, and Type of Cementitious Materials on Fresh and Hardened Properties of Binary and Ternary Blended Concrete," ***Journal of Materials in Civil Engineering,*** Vol. 26, No. 6, (2014), 04014002-11, doi: 10.1061/(asce)mt.1943-5533.0000900.
10. Chu, S. H.., Chen, J. J., Li, L. G., Ng, P. L. and. Kwan, A. K. H,. "Roles of packing density and slurry film thickness in synergistic effects of metakaolin and silica fume," ***Powder Technology,*** Vol. 387, (2021), 575-583, doi: 10.1016/j.powtec.2021.04.029.
11. Chen, J. J. Ng, P. L,.. Chu, S. H.,. Guan G. X,. and. Kwan, A. K. H,. "Ternary blending with metakaolin and silica fume to improve packing density and performance of binder paste," ***Construction and Building Materials,*** Vol. 52 (2020), 119031, doi: 10.1016/j.conbuildmat.2020.119031.
12. Ahmed, M. S,. Kayali, O., and Anderson, W., "Evaluation of Binary and Ternary Blends of Pozzolanic Materials Using the Rapid Chloride Permeability Test," ***Journal of Materials in Civil Engineering,*** Vol. 21, No. 9 (2009), 446-453, doi: 10.1061/(asce)0899-1561(2009)21:9(446).
13. Jung, S. H,. Choi Y. C., and Choi, S,. "Use of ternary blended concrete to mitigate thermal cracking in massive concrete structures—A field feasibility and monitoring case study," ***Construction and Building Materials.,*** Vol, 137, (2017), 208-215, doi: 10.1016/j.conbuildmat.2017.01.108.
14. Murthi, P,. Poongodi, K., Awoyera, P. O., Gobinath, R., and Saravanan, R., "Enhancing the Strength Properties of High-Performance Concrete Using Ternary Blended Cement: OPC, Nano-Silica, Bagasse Ash," ***Silicon,*** Vol. 12, No. 8, (2020), 1949-1956, doi: 10.1007/s12633-019-00324-0.
15. Khalil, E. A. B,. and Anwar, M., "Carbonation of ternary cementitious concrete systems containing fly ash and silica fume," ***Water Science***, Vol. 29, No. 1, (2015), 36-44., doi: 10.1016/j.wsj.2014.12.001.
16. Shehata, M. H., and Thomas, M. D. A., "Use of ternary blends containing silica fume and fly ash to suppress expansion due to alkali-silica reaction in concrete," ***Cement and Concrete Research,*** Vol. 32, No. 3, (2002), 341-349. doi: 10.1016/S0008-8846(01)00680-9.
17. Narasimha Reddy, P., and Ahmed Naqash, J. , "Effect of alccofine on mechanical and durability index properties of green concrete," ***International Journal of Engineering, Transactions C: Aspects***, Vol. 32, No. 6, (2019), 813-819. doi: 10.5829/ije.2019.32.06c.03.
18. Reddy, A. N., and Meena, T., "An experimental investigation on mechanical behaviour of eco-friendly concrete," In *IOP Conference Series: Materials Science and Engineering*, vol. 263, No. 3, IOP Publishing, (2017). doi: 10.1088/1757-899X/263/3/032010.
19. Bhushan Jindal, B. "Development of High Strength Fly Ash based Geopolymer Concrete with Alccofine," ***IOSR Journal of Mechanical and Civil Engineering,*** (2016), 55-58, doi: 10.9790/1684-15010010155-58.
20. Soni, D., Kulkarni, S., and Parekh, V., "Experimental Study on High-Performance Concrete with Mixing of Alccofine and Fly Ash," ***Indian Journal of Research,*** Vol. 3, No. 4, (2013), 84-86.
21. Bureau of Indian Standards (BIS), "IS 12269: 2013 Ordinary Portland Cement , 53 grade specification," *Indian Stand.*, 2013.
22. ASTM 192, "Standard Specification for Silica Fume Used in Cementitious Mixtures," *Annu. B. ASTM Stand. 1–7*, Vol. 04, (2002), 1-8.
23. B. of I. S. (BIS), "IS 383: 1970 Specification for Coarse and Fine Aggregates from Natural Sources for Concrete," *Indian Stand.*, 1970.
24. B. of Indian Standards, "IS 9103: 1999, Specification for Concrete Admixtures BIS," *Bur. Indian Stand. Delhi*, 1999.
25. ASTM C494-99, "C494 - 99 Standard Specification for Chemical Admixtures for Concrete," *ASTM Int.*, Vol. 04, (2013), 1-9.
26. ACI Committee 211, "ACI 211.4R-93 Guide for Selecting Proportions for High-Strength Concrete with Portland Cement and Fly Ash," ***Manual Concrete Practical, ACI Material Journal***, Vol. 90, No. 3, (1993), 272-283.
27. ASTM C143/C143M, "Standard Test Method for Slump of Hydraulic-Cement Concrete," *ASTM C143*, No. 1, (2015), 1-4, doi: 10.1520/C0143.
28. ASTM C496/C496M − 17, "Standard Test Method for Splitting Tensile Strength of Cylindrical Concrete Specimens ASTM C-496," *ASTM International*, no. March 1996, (2011), 1-5,
29. ASTM, "Astm C78/C78M -18:," *Stand. Test Method Flexural Strength Concr. (Using Simple Beam with Third-Point Loading) ASTM Int. USA*, vol. 04.02, (2002), 1-3.
30. P. Ramadoss, "Combined effect of silica fume and steel fiber on the splitting tensile strength of high-strength concrete,"

International Journal of Civil Engineering, Vol. 12, No. 1, 96-103, (2014).

31. R. A. Khan and M. Haq, "Long-term mechanical and statistical characteristics of binary- and ternary-blended concrete containing rice husk ash, metakaolin and silica fume," ***Innovative Infrastructure Solutions,*** Vol. 5, No. 2 (2020), 1-14. doi**:** 10.1007/s41062-020-00303-0.
32. B. Sagar and S. M.V.N, "Mechanical and Microstructure Characterization of Alccofine Based High Strength Concrete," ***Silicon,*** Vol. 14, No. 3, (2022), 795-813. doi: 10.1007/s12633-020-00863-x. 14, no. 3
33. Biswas, R., Rai, B., and Samui, P., "Compressive strength prediction model of high-strength concrete with silica fume by destructive and non-destructive technique," ***Innovative Infrastructure Solutions,*** Vol. 6, No. 2, (2021), 1-14, doi: 10.1007/s41062-020-00447-z.
34. Bhanja, S., and Sengupta, B., "Investigations on the compressive strength of silica fume concrete using statistical methods," ***Cement and Concrete Research,*** Vol. 32, No. 9, (2002), 1391-1394, doi: 10.1016/S0008-8846(02)00787-1.
35. Ramadoss, P., and Nagamani, K., "Tensile strength and durability characteristics of high-performance fiber reinforced concrete," ***Arabian Journal for Science & Engineering*** *(Springer Science & Business Media BV)*, 33 (2008), 307-319.
36. Reddy, P. N., and Naqash, J. A., "Development of high early strength in concrete incorporating alccofine and non-chloride accelerator," ***SN Applied Sciences,*** Vol. 1, No. 7, (2019), 1-11, doi: 10.1007/s42452-019-0790-z.
37. Hariharan, A. R., Santhi, A. S., and Mohan., Ganesh, G., "Statistical model to predict the mechanical properties of binary and ternary blended concrete using regression analysis," ***International Journal of Civil Engineering,*** Vol. 13, No. 3, (2015), 331-340.
38. Parrott, L. J., "Water absorption in cover concrete," ***Materials and Structures,*** Vol. 25, No. 5, (1992), 284-292. doi: 10.1007/BF02472669.
39. Baghabra Al-Amoudi O. S., Al-Kutti, W. A., Ahmad, S., and Maslehuddin, M., "Correlation between compressive strength and certain durability indices of plain and blended cement concretes," ***Cement and Concrete Composites,*** Vol. 31, No. 9, (2009), 672-676, doi: 10.1016/j.cemconcomp.2009.05.005.
40. Perumal, R., "Correlation of compressive strength and other engineering properties of high-performance steel fiber-reinforced concrete," ***Journal of Materials in Civil Engineering***, Vol. 27, No. 1, (2015), 04014114, doi: 10.1061/(ASCE)MT.1943-5533.0001050.
41. Ramadoss, P., and Prabath, N. V. N., "Engineering Properties and Prediction of Strength of High-Performance Fibre Reinforced Concrete using Artificial Neural Networks," ***Electronic Journal of Structural Engineering,*** Vol. 21, (2021), 76-90.
42. Cagley, J. R.., *et al.*, "Building Code Requirements for Structural Concrete (ACI 318-99)".
43. ACI, "Report on High-Strength Concrete Reported by ACI Committee 363," *ACI 363R-92*, 1992.
44. "NZS-3101-1-and-2 "New Zealand Concrete Structures Standards"2006.
45. British Standards Institution, "Bs 8110-1:1997," *Br. Stand. Inst. London*, No. 1, 1997.
46. Sidney Mindess, D., Francis Young, J., "Concrete Second Edition," *Pearson Educ. Inc. Up. Saddle River, NJ 07458*, 2003.
47. Rashid, M. A., Mansur, M. A.., and Paramasivam, P., "Correlations between Mechanical Properties of High-Strength Concrete," ***Journal of Materials in Civil Engineering,*** Vol. 14, No. 3 (2002), 230-238, doi: 10.1061/(asce)0899-1561(2002)14:3(230).
48. CEB-FIP, *Model Code 2010*. 2010.
49. Arioglu, N., Canan Girgin, Z., and Arioglu, E., "Evaluation of ratio between splitting tensile strength and compressive strength for concretes up to 120 MPa and its application in strength criterion," ***ACI Materials Journal,*** Vol. 103, No. 1 (2006), 18-24., doi: 10.14359/15123.
50. Neville, A. M., Properties of Concrete, 4th Edition. 2011.
51. Abdul R.., and Wong, H., "Re-evaluation of strength and stiffness relationships for high-strength concrete," ***Asian Journal of Civil Engineering (Building and Housing),*** Vol. 5, No. 1-2, (2004), 85-99.
52. Banthia, N., Majdzadeh, F., Wu, J., and Bindiganavile, V., "Fiber synergy in Hybrid Fiber Reinforced Concrete (HyFRC) in flexure and direct shear," ***Cement and Concrete Composites***, Vol. 48 (2014), 91-97. doi: 10.1016/j.cemconcomp.2013.10.018.

Persian Abstract

چکیده

این مقاله به بررسی مزایای بالقوه بتن سه‌گانه با کارایی بالا ترکیبی حاوی دوده سیلیس (SF)و آلکوفین (AL)به عنوان جایگزین‌های جزئی سیمان می‌پردازد. برنامه آزمایشی در مجموع شامل ۱٤ مخلوط با نسبت آب به اتصال دهنده ۰.٤ و درصدهای متفاوت (۰–۲۰٪) دوده سیلیس و آلکوفین هر دو به صورت دوتایی و سه تایی است. خواص تازه و سخت شده بتن بر اساس اسلامپ، مقاومت فشاری، مقاومت خمشی، مقاومت کششی شکافته و جذب آب مورد ارزیابی قرار گرفت. مخلوط های سه تایی حاوی SF و AL مقاومت فشاری بتن را ۱٤–۲۷٪ و مقاومت کششی را ۲٦–٤۳٪ در مقایسه با مخلوط مرجع افزایش دادند. افزایش استحکام اولیه برای همه مخلوط های سه تایی به وجود آلکوفین بسیار واکنش پذیر نسبت داده می شود. جایگزینی بیشتر از آلکوفین بیش از ۱۰٪ منجر به کاهش مداوم در استحکام به دلیل اثر رقیق شد، در حالی که برای دوده سیلیس، رقت استحکام به تدریج فراتر از جایگزینی ۱۵٪ بود. بسته بندی ذرات متراکم باعث کاهش جذب آب در مخلوط های سه تایی می شود. مخلوطی حاوی ۱۵ درصد SF و ۵ درصد AL 65.7 درصد کاهش جذب آب را در مقایسه با مخلوط مرجع نشان داد. ارزیابی هم افزایی برای تمام مخلوط های سه تایی انجام شد، نتیجه اوج برای مخلوطی حاوی ۱۰٪ SF و ۱۰٪ AL به دست آمد. بر اساس داده‌های تجربی، مدل‌های تجربی تهیه و با کدهای موجود و تحقیقات قبلی مقایسه شد. مدل های تجربی ارائه شده در این مطالعه دارای کمترین خطای مطلق انتگرال 0.47% (IAE) و ۱.۵۵٪ در پیش بینی مقاومت خمشی و مقاومت کششی شکافته بر اساس مقاومت فشاری بتن هستند.

IJE TRANSACTIONS B: Applications Vol. 35, No. 08, (August 2022) 1641-1650

International Journal of Engineering

Journal Homepage: www.ije.ir

Improved Performance Analysis of Single-phase Line Start Synchronous Reluctance Motor Derived from Induction Motor

M. Chaudhari*, A. Chowdhury

Department of Electrical Engineering, Sardar Vallabhbhai National Institute of Technology, Surat, Gujarat, India

P A P E R I N F O

Paper history:
Received 12 August 2021
Received in revised form 03 May 2022
Accepted 22 May 2022

Keywords:
Barrier
Parametric Analysis
Motor Efficiency
Finite Element Analysis

A B S T R A C T

Energy efficiency is an essential aspect of motor technologies. The replacement of conventional Single Phase Induction Motor (SPIM) by Permanent Magnet Synchronous Motor (PMSM), Synchronous Reluctance Motor (SynRM), or Switched Reluctance Motor (SRM) for energy-efficient operation leads to high capital expenses. This paper presents a cost-effective design method to improve the efficiency of the existing SPIM. It implements a novel idea by transforming it to Line Start Synchronous Reluctance Motor (LS-SynRM). A rotor of 0.5 HP, SPIM is successfully redesigned using finite element analysis (FEA). A comprehensive parametric sensitivity analysis in terms of barrier position and width focused on the work. Moreover, introducing a permanent magnet in the rotor barrier has also been investigated. Parametric analysis determines the optimum size of the permanent magnet. However, the best-fit significant rotor parameters have been estimated. Results revealed substantial improvement in the performance of derived LS-SynRM and Permanent Magnet Assisted LS-SynRM (PMaLS-SynRM).

***doi**: 10.5829/ije.2022.35.08b.20*

NOMENCLATURE

ψ	Flux linkages	P_{cu}	Copper losses
β	Winding dislacement between auxiliary and main winding	P_{core}	Core losses
α	Turns ratio	P_{core-s}	Stator core loss
m	Number of phases	I_L	Line current
p	Number of poles	I_m	Main winding current
L_d	Direct axis inductance	I_a	Auxiliary winding current
L_q	Quadrature axis inductance	**Greek Symbols**	
T_e	Electromagnetic torque	η	Efficiency
T_{cage}	Cage torque	**Subscripts**	
T_{rel}	Reluctnce torque	d	Direct axis
P_{mech}	Mechanical output power	q	Quadrature axis
P_{elect}	Electrical input power		

1. INTRODUCTION

Single-phase induction motors (SPIM) have widespread applications. However, there is growing interest in energy-efficient motors like PMSMs, SRMs, and SynRMs, although it incurs a cost to the user [1]. Many research studies reported in the literature attempted to improve the performance of induction motors in terms of

*Corresponding Author Institutional Email: mandar.chaudhari@ges-coengg.org (M. Chaudhari)

Please cite this article as: M. Chaudhari and A. Chowdhury, Improved Performance Analysis of Single-phase Line Start Synchronous Reluctance Motor Derived from Induction Motor, ***International Journal of Engineering, Transactions B: Applications***, Vol. 35, No. 08, (2022) 1641-1650

the introduction of slits in the teeth, magnetic wedges, use of nanomaterial, and high-grade steel to reduce the losses [2-5]. Although these methods improve efficiency, it also leads to increased manufacturing difficulties added with material cost. However, PMSMs, SRMs, and SynRMs, although energy-efficient, line-starting capability is still under investigation.

The option of single-phase operation of three-phase induction motors has also been investigated [6, 7] to retrieve the benefits of three-phase IM. The research reported by Chaudhari and Fernandes [8] also considers the same principle for PMSM with a reduction in thirty percent output. The work presented by Gwoździewicz and Zawilak [9] uses skewed stator slots to enhance the performance; however, it reduces noise with trivial improvements in the performance. However, the availability of high-density permanent magnets for PMSM motors at low cost is a significant concern.

The motors like SRM and SynRM [10, 11] have superior features compared with PMSM, like reduced cost and better performance. However, their line starting ability is still a research interest.

The absence of rotor bars and permanent magnets makes the SRM rugged in construction and efficient. However, it demands the converter and rotor position sensors for operation [12, 13], increasing complexity and cost. Line starting with a simple diode rectifier [14] significantly compromises the efficiency.

In synchronous motors like SynRM, the current induced in the rotor at synchronism is absent. It leads to negligible rotor copper loss resulting inefficient operation. As SynRMs are realized by replacing SPIM rotors [15-23], efficient performance is obtained at a reduced cost than the PMSM. The energy density and performance are better for these motors than induction motors [15]. The new rotor design [16] further improves the polyphase operation performance. The analytical investigations into line start single phase SynRM using rotating field theory [22], and symmetrical components analysis in transient and steady-state is presented [17].

Self-starting single-phase SynRM with barriers and with cage bars designed and analyzed by Gu and Zhou [19]. The operation of a single-phase cage rotor reluctance motor with a variable capacitor is presented by Obe and Oje [20], considering speed error signal as feedback. However, an additional control circuit in the feedback loop and the variable capacitor increases the system cost. Recently, Ganesan and Chokkalingam [21] developed line start single-phase synchronous reluctance motor records 6% increase in efficiency than SPIM. Aghazadeha et al. [23] compared the permanent magnet assisted SynRM (PMaSynRM) with SynRM without PM. It has superior performance in terms of torque profile. However, all of these analyses use the newly manufactured rotor to improve performance. Moreover, adding active material in motor structure or replacing the motor with energy-efficient motor results in increased cost.

This literature review reveals comparatively less attention to the online operation of single-phase SynRM. However, the attention given to improve the efficiency of SPIM without manufacturing a new rotor is scant. A novel concept reported in this paper considers these research gaps. It derives LS-SynRM from the existing SPIM rotor itself. The investigation of optimum barrier dimensions is determined through parametric analysis. The parameters such as placement of the barrier, its width, and rib dimensions were examined. The conversion of SPIM to LS-SynRM, without the requirement for additional material and little modification cost, is an economically viable option. In addition, considering the advantages of high-density permanent magnets, the effect of adding pieces of permanent magnets in the rotor is investigated. The performance, in this case, is compared for varying lengths of the magnets. The performed analysis also determines the best-fit magnet configuration with improved efficiency for the PMaLS-SynRM.

In section 2, a brief introduction of line start SynRM is given in this paper. In section 3 proposed design procedure of line start, SynRM is described. Section 4 deals with single-phase 0.5HP motor simulation in Ansys Maxwell for rated load condition and FEM-based sensitivity analysis of rotor structures for different parameters with simulation results such as synchronizing capability, torque, losses, and efficiency. The conclusion is given in section 5.

2. SINGLE PHASE LINE START SYNCHRONOUS RELUCTANCE MOTOR

The stator structure is kept the same for the proposed conversion of SPIM to LS-SynRM. The main and auxiliary windings displaced through 90° in space. Two capacitors, starting and running, are connected in the circuit. The starting capacitor is connected with auxiliary winding through a centrifugal switch to start the machine directly online. A low-value run capacitor is left in the auxiliary winding for better performance.

The starting torque (T_{cage}) developed by the rotor cage makes the motor line start while the reluctance torque (T_{rel}) maintains synchronism [18].

The flux linkage equations in the d-q reference frame for FEM analysis [24] and flux linkages along the dq axis are stated in Equation (1).

$$\begin{bmatrix} \psi_d \\ \psi_q \end{bmatrix} = \begin{bmatrix} \cos\theta & \sin\theta \\ -\sin\theta & \cos\theta \end{bmatrix} \begin{bmatrix} 1 & 0 \\ 0 & 1/\alpha \end{bmatrix} \begin{bmatrix} 1 & \cos\beta \\ 0 & \sin\beta \end{bmatrix} \begin{bmatrix} \psi_{as} \\ \psi_{bs} \end{bmatrix} \quad (1)$$

where α indicates auxiliary to main winding turns ratio and β represents winding displacement between auxiliary

and main winding and ψ_{as}, ψ_{bs} is flux linkages of stator *'a'* phase and stator *'b'* phase respectively.
The current in d-q frame is also given in Equations (2) and (3):

$$i_d = i_a \cos\theta + i_b\left[\cos\theta.\cos\beta+\alpha.\sin\theta.\sin\beta\right] \quad (2)$$

$$i_q = i_a \sin\theta - i_b\left[-\sin\theta.\cos\beta+\alpha.\cos\theta.\sin\beta\right] \quad (3)$$

Knowing the flux linkages and currents, the inductances along the direct and quadrature axis are given by-

$$L_d = \frac{\psi_d}{i_d} \quad (4)$$

$$L_q = \frac{\psi_q}{i_q} \quad (5)$$

Then equation for electromagnetic torque can be expressed as follows:

$$T_e = T_{cage} + T_{rel} \quad (6)$$

$$T_e = \frac{m}{2}\frac{p}{2}\frac{L_m}{L_r}L_m i_d + \frac{m}{2}\frac{p}{2}\left(L_d - L_q\right)i_d i_q \quad (7)$$

where,
T_e - Electromagnetic torque
L_m - Magnetizing inductance
p - Number of Poles
m - Number of phases
L_d, L_q - Direct axis and quadrature axis inductance
i_d, i_q - Direct axis and quadrature axis current

The steady state efficiency is calculated by the ratio of output mechanical power (P_{mech}) and input electrical power (P_{elect}).

$$\eta = \frac{P_{mech}}{P_{elect}} = \frac{P_{mech}}{P_{mech}+P_{cu}+P_{core}+\ other\ losses} \quad (8)$$

where P_{mech} is calculated as Equation (9):

$$P_{mech} = (Torque)\times(angular\ speed) \quad (9)$$

While friction, windage losses are assumed to be 1.2% and stray losses are considered 1% of output power. The addition of copper losses (P_{cu}), core losses (Pcore), and other losses computes total loss.

Total copper loss is the summation of auxiliary and main winding copper loss and rotor copper loss. Total core losses include stator and rotor core loss. Consequently, Equation (10) determines the input electrical power.

$$P_{elect} = (P_{mech}) + (P_{cu}) + (P_{core}) + (other\ loss) \quad (10)$$

Other loss includes friction, windage losses and stray losses.

3. PROPOSED DESIGN PROCEDURE

3. 1. Design Method A new LS-SynRM design aims to replace an existing single-phase IM subjected to two aspects. Firstly, it has to have line-starting and successful synchronization. Second, the motor should have higher or equal torque and higher efficiency at a steady-state than the existing single-phase IM. The FE analysis considers the FB design and its effect on performance and motor parameters. The parametric design variables considered for analysis are barrier position, barrier width, and PM size. The evaluated efficiency and torque are then compared with base SPIM. The design steps undertaken prescribed in Figure 1. The

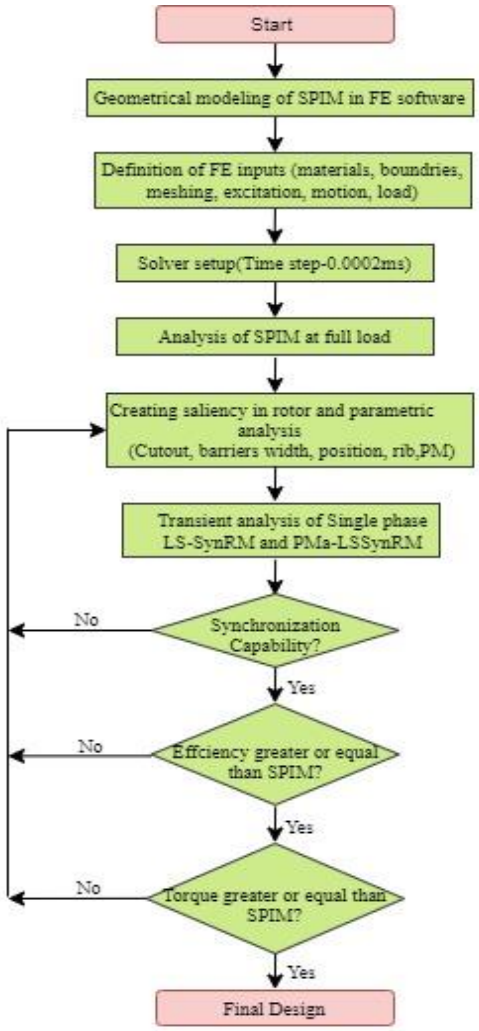

Figure 1. Design and analysis procedure

base SPIM first analyzed at rated load condition. The modified rotor with barriers has been exanined with various barrier and PM dimensions as described in Figures 2(a) and 2(b). Each of the examined model was checked for synchronization ability, efficiency and torque. The model that satisfies above three criterions were compared. The model satisfying set criterions and higher efficiency than SPIM designated as best fit model.

3. 2. Simulation Model The motor models with structural dimensions are realized using ANSYS Maxwell™ FE analysis software. The material used for the rotor cage is aluminum, while the stator winding conductors are of copper. The half-section automatic adaptive mesh models, as shown in Figure 3, are generated considering the memory requirements. The mesh elements generated were 6742 for SPIM and that for LS-SynRM was 6824. The external excitation circuit is coupled with a voltage of single-phase 230V.

4. RESULTS AND DISCUSSION

The relative performance presented in this section is for SPIM, LS-SynRM, and PMaLS-SynRM.

4. 1. Base Motor Analysis A single-phase induction motor (SPIM) is used as a base motor for comparative analysis in this study. Rated as 230V, 50 Hz, 0.5HP, 1440 rpm, capacitor start-capacitor run induction motor modeled in software as shown in Figure 4. The starting and running capacitor values were 70 µF and 15 µF, respectively. The constructive parameters have been specified in Table 1.

The transient performance analysis of torque, speed, mechanical power output and losses have been analyzed under full load conditions. Figure 5 shows the significant performance characteristics. The evaluated core loss, stator copper losses, and rotor copper losses are 31.72W, 33.1W, and 22.9W, respectively, with the mechanical power developed as 387.83W. The full load torque developed was 2.55N-m at a speed of 1447rpm, where the efficiency noted was 80.12%. The other losses calculated are 2.2 percent of rated output power.

4. 2. LS-SynRM Motor Analysis

4. 2. 1. Parametric Sensitivity Analysis for Barrier Positions and Width The total 24 models, including six width sizes for each of the four barrier positions, are created and analyzed. The width was varied from 2mm to 7mm in a step of 1mm, and the barrier positions from the rotor center were varied from 15mm to 30mm in a step of 5mm. However, the rib width of 0.5mm was maintained. Among 24 models, only 12 models can synchronize at full load, while the

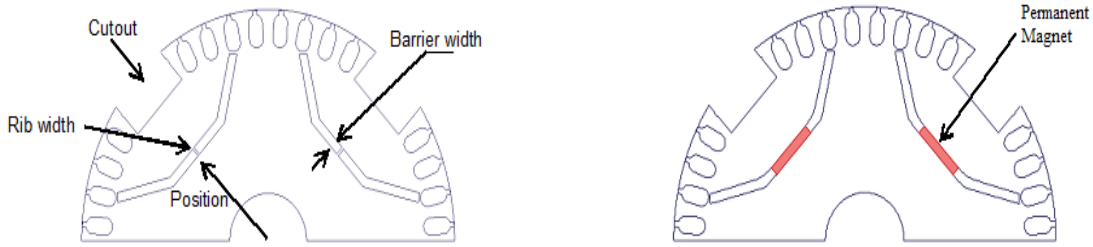

(a) LS-SynRM (b) PMaLS-SynRM

Figure 2. Rotor structures

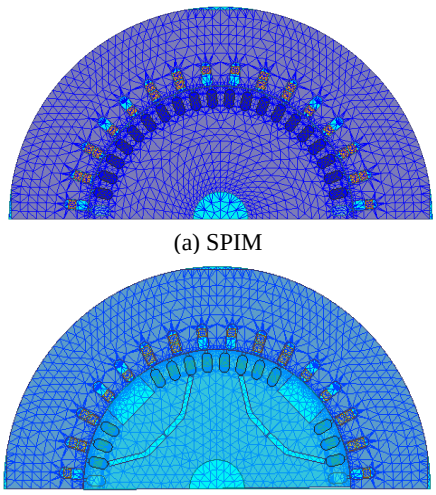

(a) SPIM

(b) LS-SynRM

Figure 3. Mesh models (a) SPIM and (b) line start SynRM

TABLE 1. Geometrical dimensions of SPIM

Parameter	Dimension	Parameter	Dimension
Stator outer diameter	152mm	Rotor outside diameter	91.4mm
Bore Diameter	92mm	Number of stator slots	32
Stack Length	48.8mm	Number of rotor slots	44
Air gap length	0.35mm	Number of poles	4

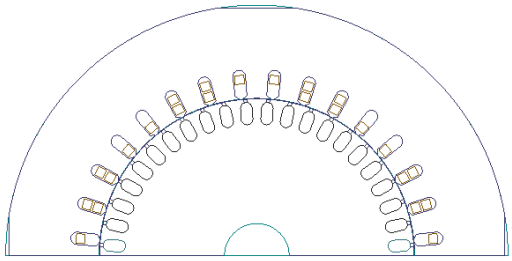

Figure 4. Single phase induction motor 2D geometry

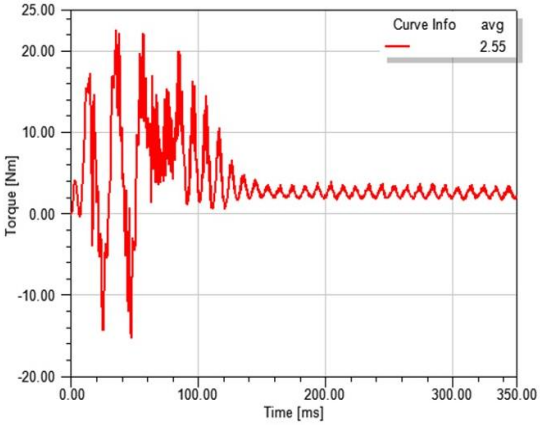

(a) Torque

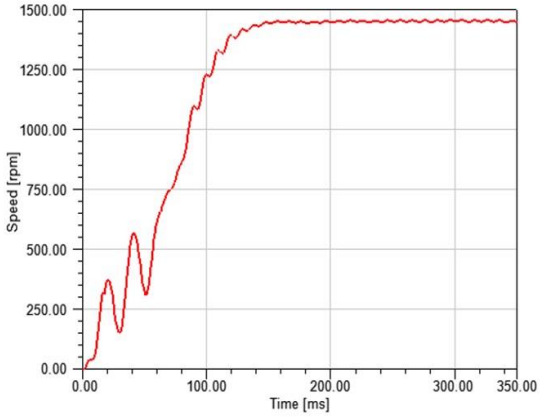

(b) Speed

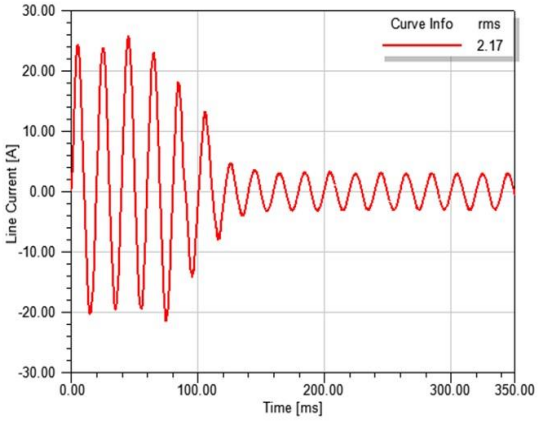

(c) Line Current

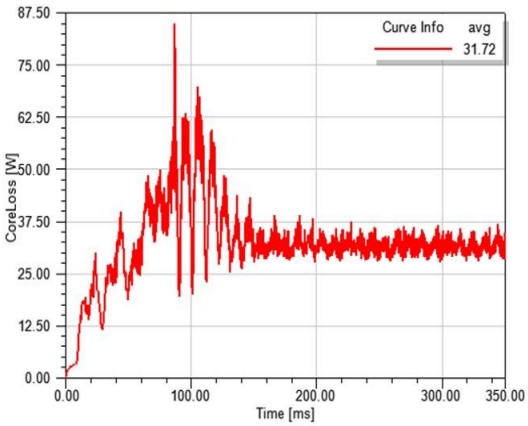

(d) Core loss

Figure 5. Performance results of single phase induction motor

other models are unable to develop required reluctance torque at full load. It is due to the fact that the synchronization capability depends on the developed reluctance torque.

It has been observed that the barrier width of 2mm leads to synchronization for each barrier position. Figure 6 describes the torque, efficiency, and total loss variations concerning the barrier positions.

Compared to the 25mm barrier position, the evaluated torque is highest at 15mm at a 3% decrease in efficiency. It is due to an increase of 16.96% in copper losses in the case of a 15 mm barrier position. The increase in the pulsating toque also leads to higher core losses. For the 25 mm barrier position, the highest efficiency of 82.04% with a mechanical power output of 393.67 W (higher than SPIM due to an increase in the speed of LS-SynRM) has been recorded.

Figure 7 shows the reluctance torque for barrier width 2mm and position of 25mm. The average torque was 2.5 Nm. The copper and core losses noted in this case were 42.42W and 35.5W, respectively. The better reluctance torque of 2.48Nm, as shown in Figure 7, has also been observed with the reduction in torque pulsation.

4. 2. 2. Performance without Rib Considering the better performance at a barrier position of 25mm and width 2mm, the performance without a rib, as shown in Figure 8, has also been investigated. The significant reduction of 15% in torque ripples, as shown in Figure 9(a), has been recorded compared to a barrier with rib. However, the settling time, in this case, found increased, as shown in Figure 9(b). Also, a reduction of 2% in the total losses increases the efficiency by 0.4%. The average torque developed remains consistent in both cases with and without barrier rib.

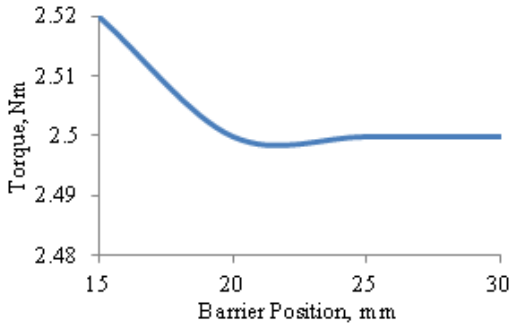

(a) Torque plot

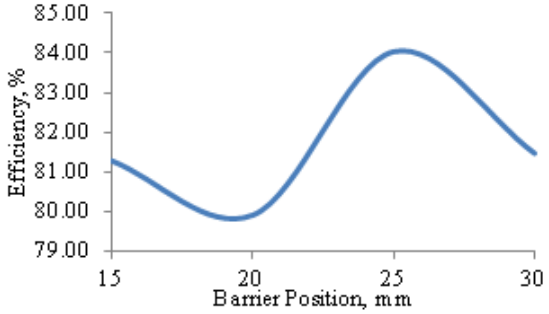

(b) Efficiency

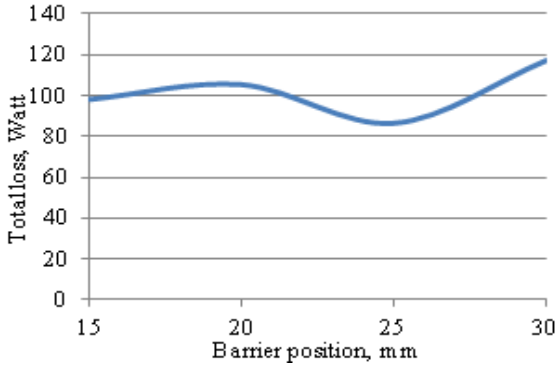

(c) Total loss

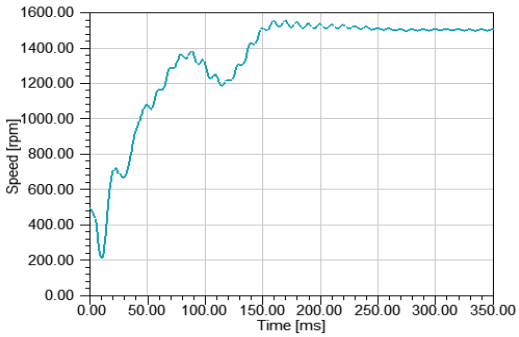

(d) Speed plot for 25mm barrier position

Figure 6. Performance plots with respect to barrier positions for 2mm width

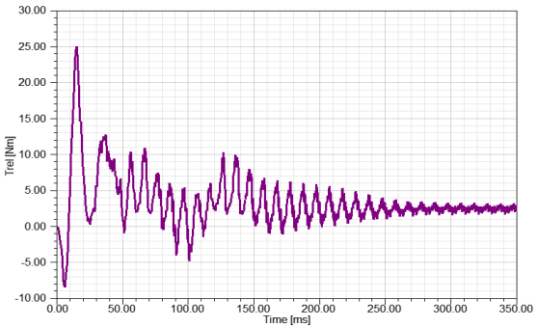

Figure 7. T_{rel} for barrier width 2mm and position of 25mm

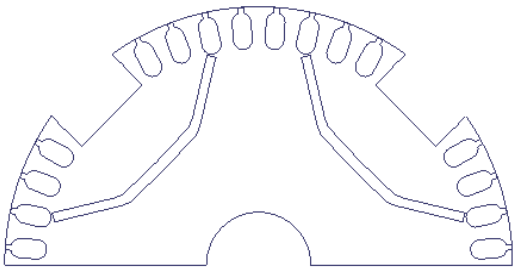

Figure 8. Barrier without rib

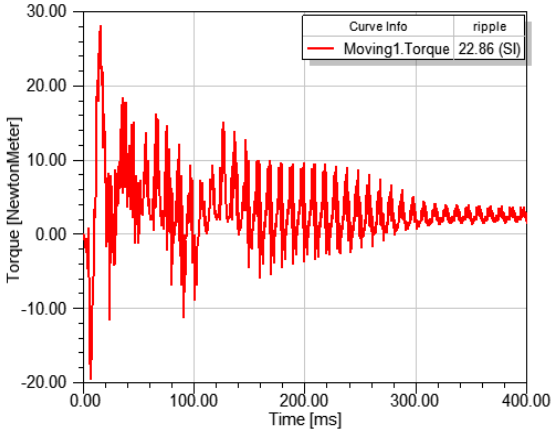

(a) Torque

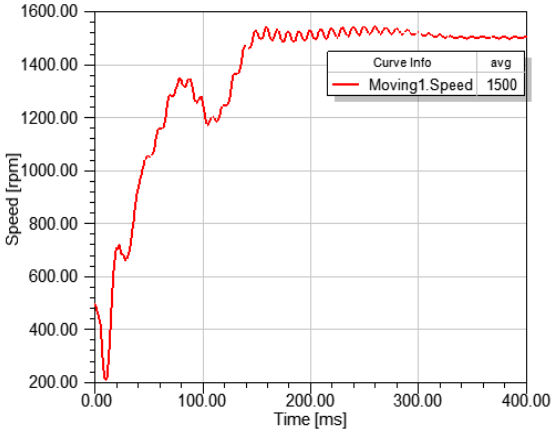

(b) Speed

Figure 9. Plots of torque and speed for zero rib width

4. 2. 3. PM assisted LS-SynRM (PMaLS-SynRM) Considering better performance with the introduction of permanent magnets (PM) [25], further investigations have been carried out with PMs in the rotor barrier. A NdFe30 PM type was used to analyze the same barrier position and width without rib, as shown in Figure 2(b). However, models with different sizes of PMs in the barrier analyzed for overall performance. Table 2 describes the results.

It has been observed that there is an increase in the efficiency with the length of PM. It was least for a length of 4mm and maximum for a length of 12mm. It is due to the reduction of the line current and the subsequent decrease in the copper losses. It has also been inferred from Figure 10, that the torque ripples increase with the length of the PM. However, the developed torque was consistent in all the designated cases for analysis.

Table 3 describes the analysis of stator and rotor core losses. The stator and rotor core losses decrease with the increase in PM length. However, the significant contributor to the core losses is the stator. These results are also consistent with the main and auxiliary winding current findings. The main winding current for the PM size of 12 mm is the lowest in all investigated cases.

Figure 11 demonstrates the torque and speed variation plots for PMaLS-SynRM. It is observed that the early synchronization(250ms) is achieved in the case of PMaLS-SynRM compared with LS-SynRM (325ms).

Figure 12 shows the speed plot under variable loading pattern for the best fit PMaLS-SynRM. At point 'a', the load torque is 1.8N-m (75% of rated load). However, it has increased to 2.4Nm (100% load, point 'b') at 400ms. The motor took 70ms to synchronize after the sudden dip (at point 'b').

TABLE 2. Performance of PMaLS-SynRM as function of size of PM

Barrier Position (mm)	PM size (mm)	P_{mech} (W)	P_{elect} (W)	I_L (A)	P_{cu} (W)	P_{core} (W)	Other loss (W)	Total loss (W)	Efficiency (%)
	4.00	396.31	485.15	2.21	43.67	36.45	8.72	88.84	81.69
15.00	8.00	397.96	482.10	2.15	40.50	34.89	8.76	84.14	82.55
	12.00	396.52	477.72	2.11	38.12	34.36	8.72	81.20	83.00
	4.00	394.93	482.24	2.18	43.67	34.95	8.69	87.31	81.90
20.00	8.00	395.08	477.87	2.13	40.14	33.95	8.69	82.79	82.68
	12.00	398.86	479.86	2.13	38.61	33.61	8.77	81.00	83.12
	4.00	400.32	479.48	2.12	37.48	32.87	8.81	79.16	83.49
25.00	8.00	393.00	469.49	2.09	35.38	32.47	8.65	76.49	83.71
	12.00	401.12	477.51	2.14	34.96	32.61	8.82	76.39	84.00
	4.00	393.62	483.70	2.19	44.86	36.56	8.66	90.08	81.38
30.00	8.00	397.68	481.82	2.13	40.14	35.25	8.75	84.14	82.54
	12.00	396.15	476.36	2.09	37.32	34.17	8.72	80.21	83.16

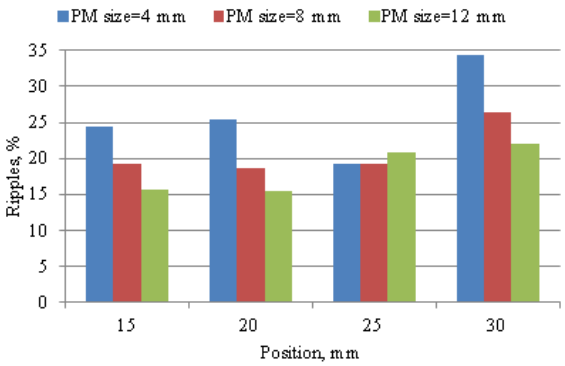

Figure 10. Torque ripple as a function of PM position and size

The comparative efficiency curves of LS-SynRM and PMaLS-SynRM at different loadings are shown in

TABLE 3. Losses in PMaLS-SynRM

Barrier Position (mm)	PM length (mm)	I_m (A)	I_a (A)	P_{core-S} (W)	P_{core-R} (W)
	4.00	1.80	1.36	32.56	3.88
15.00	8.00	1.63	1.36	31.25	3.64
	12.00	1.49	1.36	30.87	3.48
	4.00	1.80	1.36	31.10	3.85
20.00	8.00	1.61	1.36	30.38	3.57
	12.00	1.52	1.36	30.27	3.34
	4.00	1.45	1.36	29.52	3.35
25.00	8.00	1.31	1.36	29.29	3.18
	12.00	1.28	1.36	29.40	3.21
	4.00	1.86	1.36	32.47	4.09
30.00	8.00	1.61	1.36	31.66	3.59
	12.00	1.44	1.36	30.90	3.27

Figure 13. Both of these motors operate at the highest efficiency under full load. However, the efficiency of PMaLS-SynRM is 2% more than the LS-SynRM.

4. 3. Comparative Analysis Table 4 presents the performance comparison of the three motors, viz. SPIM, LS-SynRM, PMaLS-SynRM. The PMaLS-SynRM has the highest efficiency of 84 %, which is 4% more than the base SPIM. The significant reduction(60% compared with base SPIM) in the copper loss in PMaLS-SynRM is also evident in this case. The core loss is also decreased in this case, although it is more compared with the base SPIM. However, the torque performance registered by all these three motors was the consistent and comparative analysis of the three motors is described in Table 4. It is observed that the torque developed by the three motors is nearly equal.

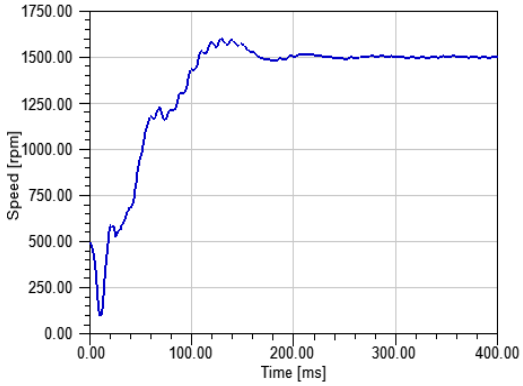

(a) Speed

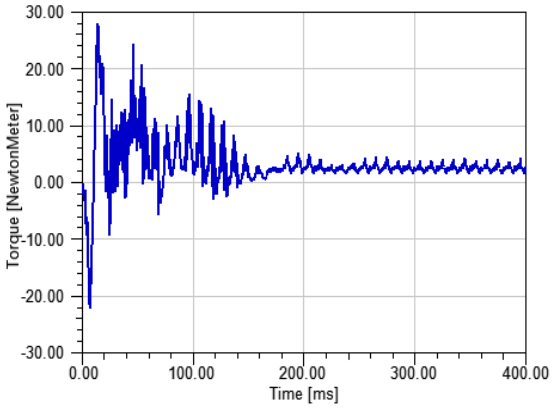

(b) Torque

Figure 11. Speed and torque plot for best fit PM size

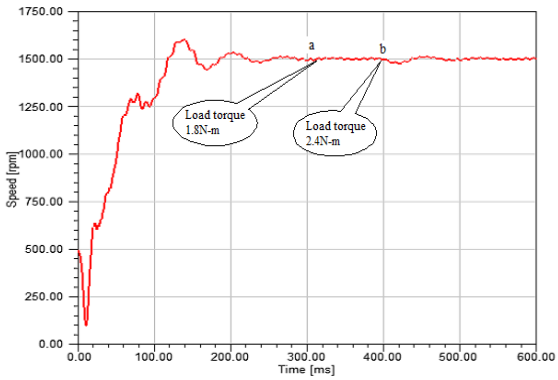

Figure 12. Speed transients at different load conditions

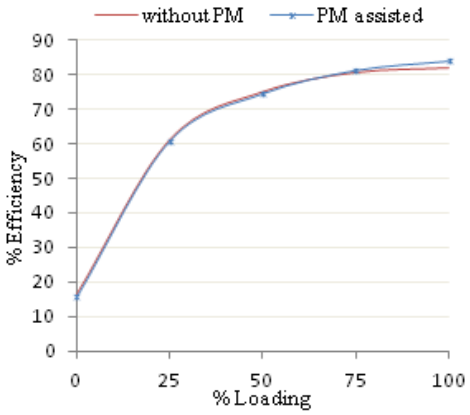

Figure13. Efficiency plot

The analysis of the active material requirement in the motor reveals that PMaLS-SynRM requires 10% less material than the base SPIM.

The techno economic comparison also reveals the proposed conversion is still better option for efficiency improvement. Considering the current pricing, the average cost of 0.5hp SPIM is 74 USD, and the proposed conversion cost of the motor is 90 USD, including the cost of permanent magnets. Assuming flat 12 hours of daily motor operation and an energy rate of 0.106 USD per unit, the energy cost evaluated was 214.4 USD/Year and 204.5 USD/Year for SPIM and proposed PMaLS-SynRM. The proposed conversion will thus lead to energy saving of 10 USD/Year even for such a low power rated machine due to enhanced efficiency (4%). The significantly less payback time of 1.5 years thus leads to an attractive solution instead of replacing conventional SPIM with high-cost PMSM.

TABLE 4. Comparative results for three investigated motors

Parameter	SPIM	Ls-SynRM	PmaLS-SynRM
Torque (Nm)	2.5	2.55	2.55
Speed (rpm)	1447	1500	1500
Core loss (Watts)	31.72	35.2	32.51
Copper loss (Watts)	56	42.32	34.96
Efficiency (%)	80.05	82.04	84
Magnetic material(pu.)	0.86	0.78	0.8
Aluminum(pu.)	0.13	0.1	0.1

5. CONCLUSION

The results of parametric design to convert the existing SPIM to LS-SynRM to enhance the overall performance have demonstrated that the barrier position and their width significantly affect the motor performance. The 25 mm barrier position and 2mm width have resulted in an efficiency of 82.04% for LS-SynRM, along with the reduction in torque pulsations. The best-fit barrier without a rib has further improved the performance in terms of efficiency and torque ripples. The rise of 0.4% efficiency has been recorded for the same motor.

However, the insertion of a permanent magnet in the barrier largely affected the overall motor performance. The efficiency noted, in this case, was maximum and is 84.04 % for the 12mm PM size. The significant rise of 4% in efficiency compared with the base motor has been evident in this case. It has also been observed that the efficiency increases significantly with the PM size at the cost of slightly inferior torque performance. It indicates the trade-off between the efficiency and ripples for selecting optimum PM dimensions.

The analysis through these extensive simulations has revealed that the conversion of existing SPIM is a better and more cost-effective option for performance improvement than the replacements. However, the PMaLS-SynRM is a suitable motor for constant speed applications.

6. REFERENCES

1. De Almeida, A.T., Ferreira, F.J. and Baoming, G., "Beyond induction motors—technology trends to move up efficiency", in 49th IEEE/IAS Industrial & Commercial Power Systems Technical Conference, IEEE., (2013), 1-13.
2. Yetgin, A.G. and Turan, M., "Efficiency optimization of slitted-core induction motor", ***Journal of Electrical Engineering***, Vol. 65, No. 1, (2014), 60, doi: 10.2478/jee-2014-0009.
3. Verucchi, C., Ruschetti, C., Giraldo, E., Bossio, G. and Bossio, J., "Efficiency optimization in small induction motors using magnetic slot wedges", ***Electric Power Systems Research***, Vol. 152, (2017), 1-8, doi: 10.1016/j.epsr.2017.06.012.
4. Ganesan, L.J., Jeyadevi, S. and Selvaraj, D.E., "Energy efficient single phase induction motor", (2013), doi: 10.1049/cp.2013.2222.
5. Ghosh, P.K., Sadhu, P.K., Basak, R. and Sanyal, A., "Energy efficient design of three phase induction motor by water cycle algorithm", ***Ain Shams Engineering Journal***, Vol. 11, No. 4, (2020), 1139-1147, doi: 10.1016/j.asej.2020.01.017.
6. Alolah, A. and Badr, M., "Starting of three-phase reluctance motors connected to a single phase supply", ***IEEE Transactions on Energy Conversion***, Vol. 7, No. 2, (1992), 295-301, doi: 10.1109/60.136224.
7. Badr, M. and Alolah, A., "Transient analysis of three phase reluctance motors fed from a single phase supply", ***IEE Proceedings-Electric Power Applications***, Vol. 142, No. 2, (1995), 104-112, doi: 10.1049/ip-epa:19951702.
8. Chaudhari, B. and Fernandes, B., "Performance of line start permanent magnet synchronous motor with single-phase supply system", ***IEE Proceedings-Electric Power Applications***, Vol. 151, No. 1, (2004), 83-90, doi: 10.1049/ip-epa:20030849.
9. Gwoździewicz, M. and Zawilak, J., "Single-phase line start permanent magnet synchronous motor with skewed stator", ***Power Electronics and Drives***, Vol. 1, (2016), doi: 10.5277/PED160212.
10. Salehinai, S., Afjei, E., Hekmati, A. and Aghazadeh, H., "Design procedure of an outer rotor synchronous reluctance machine for scooter application", ***International Journal of Engineering, Transactions C: Aspects*** Vol. 34, No. 3, (2021), 656-666, doi: 10.5829/ije.2021.34.03c.10.
11. Siadatan, A., Rafiee, M. and Afjei, E., "Design, construction and comparison of a sensorless driver circuit for switched reluctance motor", ***International Journal of Engineering, Transactions A: Basics*** Vol. 27, No. 1, (2014), 143-156, doi: 10.5829/idosi.ije.2014.27.01a.17.
12. Stephenson, J. and Jenkinson, G., "Single-phase switched reluctance motor design", ***IEE Proceedings-Electric Power Applications***, Vol. 147, No. 2, (2000), 131-139, doi: 10.1049/ip-epa: 20000176.
13. Higuchi, T., Fiedler, J.O. and De Doncker, R., "On the design of a single-phase switched reluctance motor", in IEEE International Electric Machines and Drives Conference, 2003. IEMDC'03., IEEE., (2003), 561-567.
14. Yoneoka, Y. and Akatsu, K., "An optimized design of high-efficiency switched reluctance motor with single-phase input operation", in 2011 International Conference on Electrical Machines and Systems, IEEE., (2011), 1-6.
15. Qi, F., Scharfenstein, D., Weiss, C., Müller, C. and Schwarzer, U., "Motor handbook".
16. Kostko, J., "Polyphase reaction synchronous motors", ***Journal of the American Institute of Electrical Engineers***, Vol. 42, No. 11, (1923), 1162-1168, doi: 10.1109/JoAIEE.1923.6591529.
17. Finch, J. and Lawrenson, P., "Asynchronous performance of single-phase reluctance motors", in Proceedings of the Institution of Electrical Engineers, IET. Vol. 126, (1979), 1249-1254.
18. Chang, S., "An analysis or unexcited synchronous capacitor motors", ***Transactions of the American Institute of Electrical Engineers***, Vol. 70, No. 2, (1951), 1978-1982, doi: 10.1109/EE.1952.6437948.
19. Gu, K. and Zhou, E., "Calculation and analysis for a new type of single-phase reluctance motor", ***Electric Machines and Power Systems***, Vol. 15, No. 3, (1988), 163-176, doi: 10.1080/07313568808909329.
20. Obe, E. and Ojo, O., "Line-start performance of single-phase synchronous reluctance motor with controlled capacitor", ***IEE Proceedings-Electric Power Applications***, Vol. 152, No. 4, (2005), 967-976, doi: 10.1049/ip-epa:20055208.
21. Ganesan, A.u. and Natesan Chokkalingam, L., "Single-phase direct-on-line synchronous motor for a specific application in comparison with an induction motor", ***International Transactions on Electrical Energy Systems***, Vol. 29, No. 4, (2019), e2809, doi: 10.1002/etep.2809.
22. Finch, J. and Lawrenson, P., "Synchronous performance of single-phase reluctance motors", in Proceedings of the Institution of Electrical Engineers, IET. Vol. 125, (1978), 1350-1356.
23. Aghazadeh, H., Afjei, E. and Siadatan, A., "Comprehensive design procedure and manufacturing of permanent magnet assisted synchronous reluctance motor", ***International Journal of Engineering, Transactions C: Aspects*** Vol. 32, No. 9, (2019), 1299-1305, doi: 10.5829/ije.2019.32.09c.10.

24. Miller, T.J., "Single-phase permanent-magnet motor analysis", ***IEEE Transactions on Industry Applications***, No. 3, (1985), 651-658, doi: 10.1109/TIA.1985.349722.

25. Parivar, H. and Darabi, A., "An improvement on slot configuration structure of a low-speed surface-mounted permanent magnet synchronous generator with a wound cable winding", ***International Journal of Engineering, Transactions C: Aspects***, Vol. 34, No. 9, (2021), doi: 10.5829/ije.2021.34.09c.01.

Persian Abstract

چکیده

بهره وری انرژی یک جنبه ضروری از فن آوری های موتور است. جایگزینی موتور القایی تک فاز معمولی (SPIM)با موتور سنکرون مغناطیس دائم (PMSM)، موتور رلوکتانس سنکرون (SynRM)یا موتور رلوکتانس سوئیچ شده (SRM)برای عملکرد کارآمد انرژی منجر به هزینه های سرمایه ای بالایی می شود. این مقاله یک روش طراحی مقرون‌به‌صرفه برای بهبود کارایی SPIM موجود ارائه می‌کند. این ایده جدید را با تبدیل آن به موتور عدم تمایل همزمان شروع خط (LS-SynRM)پیاده سازی می کند. روتور ۰.۵ اسب بخار، SPIM با موفقیت با استفاده از تجزیه و تحلیل المان محدود (FEA)دوباره طراحی شد. تجزیه و تحلیل حساسیت پارامتریک جامع از نظر موقعیت مانع و عرض متمرکز بر کار. علاوه بر این، معرفی یک آهنربای دائمی در مانع روتور نیز مورد بررسی قرار گرفته است. تجزیه و تحلیل پارامتری اندازه بهینه آهنربای دائمی را تعیین می کند. با این حال، بهترین تناسب پارامترهای روتور قابل توجه تخمین زده شده است. نتایج بهبود قابل توجهی را در عملکرد LS-SynRM مشتق شده و LS-SynRM با کمک مغناطیس دائمی نشان داد.

IJE TRANSACTIONS B: Applications Vol. 35, No. 08, (August 2022) 1651-1661

International Journal of Engineering

Journal Homepage: www.ije.ir

Analytical Solution of Electromagnetic Force on Nanofluid Flow with Brownian Motion Effects Between Parallel Disks

E. Tayari[a], L. Torkzadeh[a], D. Domiri Ganji*[b], K. Nouri[a]

[a] *Department of Mathematics, Faculty of Mathematics, Statistics and Computer Sciences, Semnan University, Semnan, Iran*
[b] *Department of Mechanical Engineering, Babol Noushirvani University of Technology, Babol, Iran*

PAPER INFO

Paper history:
Received 31 March 2022
Received in revised form 07 May 2022
Accepted 20 May 2022

Keywords:
Akbari-Ganji's Method
Brownian Motion
Electromagnetic Force
Hardy Multiquadric Function
Nanofluid Flow
Radial Basis Function

ABSTRACT

The innovation of the present paper is the analytical study of Brownian motion effects on nanofluid flow and electromagnetic force between parallel disks with a heat source. Nanoparticle effects on nondimensional temperature field and velocity of fluid flow were analyzed using Akbari-Ganji's Method and radial basis function approximation based on Hardy multiquadric function. Akbari-Ganji's Method (AGM) is a strong analytical method that solves any linear and nonlinear differential equation with any degree of variables. Radial basis functions is an approximation method for analyzing functions and equations at high degrees, especially when it is necessary to apply the interpolation problem for scattered data on irregular geometry. The results signified that the maximum difference between AGM and RBF methods, for nondimensional horizontal velocity on CuO nanofluid at $Sq = 1$ and $\eta = 0$ is 0.2251 and the minimum difference for the nondimensional vertical velocity of Al_2O_3 nanofluid at $\eta = 0$ is equal to 0.0018. Also, the effects of the Hartmann number (Ha) on nondimensional horizontal and vertical velocities field for Al_2O_3 nanoparticles at $\eta = 0$ have a slight difference from the other Hartmann values using the AGM method. The maximum of nondimensional horizontal velocities at $\eta = 0$ and $Ha = 8$ is equal to 1.9354.

***doi**: 10.5829/ije.2022.35.08b.21*

NOMENCLATURE

a	Compressed parameter	μ_f	viscosity of fluid (kg/m.s)
k	thermal conductivity (W/m. K)	μ_{static}	effective viscosity of the component static (kg/m.s)
B	magnetic field	$\mu_{Brownian}$	effective viscosity of Brownian motion part (kg/m.s)
B_0	primary magnetic field	μ_{eff}	effective viscosity (kg/m.s)
S	heat source	F	electromagnetic force (N)
S_0	primary heat source	Pr_f	electromagnetic force (N)
H	place of the plate (m)	Sq	squeeze number $\left(a\frac{H^2}{2v_f}\right)$
u, v	vlosity components	Ha	hartmann number $\left(H.B_0.\sqrt{\frac{\sigma_f}{\mu_f}}\right)$
x, y	coordinates (m)	ϕ	nanofluid volume fraction
r_j	euclidean norm	d_s	particle diameter (m)
x_j	centers of radial base function	ρ_{nf}	density of nanofluid (kg/m3)
Ψ	polynomial	ρ_f	density of fluid (kg/m3)
N	number of the distinct points at RBF	ρ_s	density of nanoparticles (kg/m3)
λ_j	interpolation coefficient at RBF	σ_{nf}	electrical conductivity of nanofluid (s/m)
ϵ	shape parameter	σ_f	electrical conductivity of fluid (s/m)
T	temperature (K)	σ_s	electrical conductivity of nanoparticles (s/m)

*Corresponding Author Institutional Email: torkzadeh@semnan.ac.ir (L. Torkzadeh), mirgang@NIT.ac.ir (D. Domiri Ganji)

Please cite this article as: E. Tayari, L. Torkzadeh, D. Domiri Ganji, K. Nouri, Analytical Solution of Electromagnetic Force on Nanofluid Flow with Brownian Motion Effects Between Parallel Disks, ***International Journal of Engineering, Transactions B: Applications***, Vol. 35, No. 08, (2022) 1651-1661

θ	nondimensional temperature	k_{nf}	thermal conductivity of nanofluid (W/m.K)
$\vec{J}$	electric current	k_f	thermal conductivity of fluid (W/m.K)
k_s	thermal conductivity of nanoparticles (W/m. K)	**Subscripts**	
k_{static}	effective thermal conductivity of the component static (W/m. K)	nf	nanofluid
$k_{Brownian}$	effective thermal conductivity of Brownian motion part (W/m. K)	s	solid
k_{eff}	effective thermal conductivity (W/m.K)	f	fluid
μ_{nf}	viscosity of nanofluid (kg/m.s)	eff	effective

1. INTRODUCTION

Electromagnetic effects on a nanofluid with squeezing flow and Brownian motion effects between two parallel disks have been analytically investigated. Squeezing flow is used in industrial applications such as metallurgy, magnetic hydrodynamic (MHD) generators [1], and petroleum industries. Asefi et al. [2] examined the hydromagnetic flow of a micropolar fluid on a tensile sheet with unstable properties. Also, they investigated the conduction heat transfer numerically with ununiformed heat sources. Ravindran et al. [3] studied the effects of chemical reaction, heat generation, and absorption on unstable MHD flow. This process takes place on top of a vertical cone with ununiformed mass transfer. Motahar [4] studied the effect of entropy production on the magnetic hydrodynamic magnetic flow of a nanofluid in a vertical channel. Asgari and Tariverdilo [5] studied the flow of the MHD boundary layer of an Oldroyd-B fluid in the vicinity of the vertical stretching sheet. They used a non-thermal flux to define the equilibrium energy relation. Han et al. [6,7] studied the significance of Hall current and Joule heating on the dynamics of Darcy–Forchheimer peristaltic flow of Rabinowitsch fluid and also studied partial slips and temperature Jumps of a nanofluid flow over a stretched or shrinking surface. Rashidi et al. [8] studied the modeling and analysis of sensitivity and thermal conductivity of water-based ethylene glycol nanofluids with alumina nanoparticles. Alagumalai et al [9] studied conceptual analysis framework development to understand barriers to nanofluid commercialization. Nouri et al. [10, 11] and Dadsetadi et al. [12] analytically and numerically investigated the system of fractional differential equations based on the hybrid functions. Pourziaei Araban et al. [13] numerically surveyed a cavity with heat source using the lattice Boltzmann method based on the D3Q19 model and compared with experimental results.

In the present study, a combination of squeezing flow with Brownian motion effects and electromagnetic force is modeled to improve the thermal field between two parallel disks with a heat source. All numerical implementations and executions have been done by Maple software to investigate the nondimensional temperature and velocity field due to nanoparticle effects and a heat source between two parallel disks with electromagnetic boundary conditions, alongside hardware configuration: Core (TM) i3-7130U CPU @ 2.70 GHz 2.71 GHz 4GB RAM. First, with the similarity transformation, the governing equations with partial differential equations (PDE) transform to a set of nonlinear ordinary differential equations (ODE). These equations are simulated according to their boundary conditions with AGM and RBF based on Hardy multiquadric (MQ) function. Finally, to study more precisely, the Hartmann number, the squeeze number, and the heat source parameter between two parallel disks have been investigated.

2. PROBLEM DEFINITION

According to Figure 1, if we consider the bottom disk at $z = 0$, the upper disk is located at $z = 2H\sqrt{(1-at)}$. H is a place of the plate at $z = 0$. a is a compressed parameter that at $a > 0$, referred two plates were compressed until $t = {}^{1}/_{a}$ and so, at $a < 0$, two plates separated from each other. In this case, the general governing equations on physics of the problem are as follows:

$$\vec{\nabla}.\vec{V} = 0 \tag{1}$$

$$\rho\frac{\partial\vec{V}}{\partial t} = -\vec{\nabla}\vec{p} + \mu\nabla^2\vec{V} + \vec{F} \tag{2}$$

$$\frac{\partial T}{\partial t} = \frac{k}{\rho C_p}\nabla^2 T + \frac{S}{\rho C_p}T \tag{3}$$

Here, μ is the dynamic viscosity, ρ is the fluid density, k is the thermal conductivity coefficient and S is a heat source that is defined as follows [14].

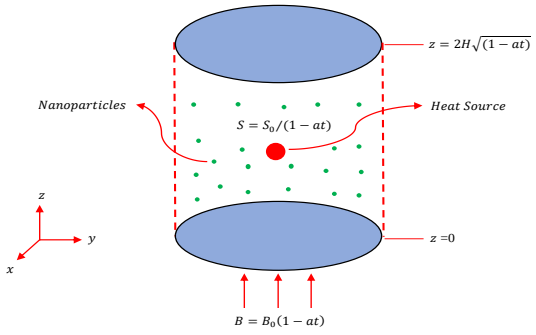

Figure 1. Schematic diagrams of MHD nanofluid flow that compressed between two limited parallel disks

$$S = {S_0}/{(1 - at)} \quad (4)$$

A magnetic field $\vec{B}$ applied perpendicular to the disk plates goes downwards. Of course, the magnetic Reynolds number is very small and the induced magnetic field is also neglected. So, a magnetic field is defined as follows:

$$\vec{B} = B\vec{e}_y, \;\; B = B_0(1 - at) \quad (5)$$

The electric current $\vec{J}$ and the magnetic field $\vec{B}$ created the electromagnetic force $\vec{F}$ defined as follows:

$$\vec{J} = \sigma[\vec{V} \times \vec{B}]$$
$$\vec{F} = \vec{J} \times \vec{B} = \sigma[\vec{V} \times \vec{B}] \times \vec{B} \quad (6)$$

We replaced expressions (4), (5), and (6) in momentum and energy equations for the 2D unsteady flow of a nanofluid. So, the following results are obtained [15]:

$$\frac{\partial u}{\partial x} + \frac{\partial v}{\partial y} = 0 \quad (7)$$

$$\rho_{nf}\left(\frac{\partial u}{\partial t} + u\frac{\partial u}{\partial x} + v\frac{\partial u}{\partial y}\right) = -\frac{\partial p}{\partial x} + \mu_{nf}\left[\frac{\partial^2 u}{\partial x^2} + \frac{\partial^2 u}{\partial y^2}\right] - \sigma_{nf}B^2 u \quad (8)$$

$$\rho_{nf}\left(\frac{\partial v}{\partial t} + u\frac{\partial v}{\partial x} + v\frac{\partial v}{\partial y}\right) = -\frac{\partial p}{\partial y} + \mu_{nf}\left[\frac{\partial^2 v}{\partial x^2} + \frac{\partial^2 v}{\partial y^2}\right] \quad (9)$$

$$\frac{\partial T}{\partial t} + u\frac{\partial T}{\partial x} + v\frac{\partial T}{\partial y} = \frac{k_{nf}}{(\rho c_p)_{nf}}\left[\frac{\partial^2 T}{\partial x^2} + \frac{\partial^2 T}{\partial y^2}\right] + \frac{S}{(\rho c_p)_{nf}}T \quad (10)$$

The boundary conditions for governing equations according to present physics are expressed as follows:

$$v = v_w = {dh}/{dt} = {-aH}\Big/{\sqrt{(1 - at)}}$$
$$at \;\; y = h(t)$$
$$\frac{\partial u}{\partial y} = 0 \quad at \quad y = 0 \quad (11)$$
$$\frac{\partial T}{\partial y} = 0 \quad at \quad y = 0$$

Some of the governed equations should be changed for modeling the nanofluid because of changes in the fluid thermal conductivity, density, heat capacitance, and electrical conductivity, some of the governed equations should be changed. Thermo-physical nanofluid properties except for density, which is obtained by Boussinesq approximation, are assumed invariant and are given in Table 1 [16].

The electrical conductivity is written as [17]:

$$\frac{\sigma_{nf}}{\sigma_f} = 1 + \frac{3\left(\frac{\sigma_s}{\sigma_f} - 1\right)\phi}{\left(\frac{\sigma_s}{\sigma_f} + 2\right) - \left(\frac{\sigma_s}{\sigma_f} - 1\right)\phi} \quad (12)$$

The effect of density at the reference temperature is given by:

$$\rho_{nf} = (1 - \phi)\rho_f + \phi\rho_s \quad (13)$$

and the heat capacitance of nanofluid can be given as follows [18]:

$$(\rho c_p)_{nf} = (1 - \phi)(\rho c_p)_f + \phi(\rho c_p)_s \quad (14)$$

The effective thermal conductivity of the component static entities and a Brownian motion part due to micromixing in suspensions were introduced by Koo and Kleinstreuer [19] as follows:

$$k_{eff} = k_{static} + k_{Brownian} \quad (15)$$

The component static based on Maxwell's classical correlation significantly impacts the effective thermal conductivity.

$$k_{static} = \left(1 + \frac{3\left(\frac{k_s}{k_f} - 1\right)\phi}{\left(\frac{k_s}{k_f} + 2\right) - \left(\frac{k_s}{k_f} - 1\right)\phi}\right)k_f \quad (16)$$

Koo [20] obtained a particle's Brownian motion via simulating Stokes' flow around a nano-particle and combined the interaction between nano-particles and the temperature effect. So, the Brownian motion part is presented as follows:

$$k_{Brownian} = 5 \times 10^4 \phi\rho_f c_{p,f}\sqrt{\frac{k_s T}{\rho_s d_s}}\,\mathrm{g}'(T, \phi, d_s) \quad (17)$$

Li [21] developed the g′ function with particle diameter, temperature, and volume fraction.

$$\mathrm{g}'(T, \phi, d_s) = (-26.5933 - 0.4038\ln(d_s) - 33.3517\ln(\phi) - 1.9158\ln(\phi)\ln(d_s) + 0.0642\ln(d_s)^2)\ln(T) + (48.4034 - 9.7878\ln(d_s) + 190.2456\ln(\phi) + 10.9285\ln(\phi)\ln(d_s) - 0.7201\ln(d_s)^2) \quad (18)$$

TABLE 1. Thermo-physical properties of water and nanoparticles [16]

Material	ρ $(kg/m\text{^}3)$	$C_P(J/KgK)$	K (W/mK)	$\mu \times 10^6$ (Nsm^{-2})	σ (Sm^{-1})
Pure water	997.10	4179	0.613	855	0.05
Copper oxide (Cuo)	6500	540	18	-	5.96×10^7
Alumina (Al2O3)	3970	765	25	-	3.69×10^7

The effective viscosity of the static and a Brownian motion part due to micromixing in suspensions was introduced by Koo and Kleinstreuer [16] as follows:

$$\mu_{eff} = \mu_{static} + \mu_{Brownian} = \mu_{static} + \frac{k_{Brownian}}{k_f} \times \frac{\mu_f}{Pr_f} \quad (19)$$

The viscosity of the nanofluid containing a dilute suspension of small rigid spherical particles is given by the Brinkman model [18] as:

$$\mu_{static} = \frac{\mu_f}{(1-\phi)^{2.5}} \quad (20)$$

For the partial differential Equations 7-10, we introduce the following similarity parameters [22]:

$$\eta = \frac{y}{H\sqrt{1-at}}$$
$$u = \frac{ax}{2(1-at)} f'(\eta)$$
$$v = -\frac{aH}{2\sqrt{1-at}} f(\eta) \quad (21)$$
$$\theta = \frac{T}{T_H}$$

By replacing these parameters in the main equations, the dimensionless equations are as follows:

$$\left(\frac{\mu_{eff}}{\mu_f}\right) f^{(4)} - Sq\left(\frac{\rho_{nf}}{\rho_f}\right) \left[\eta f^{(3)} + 3f'' + f'f'' - ff^{(3)}\right] - Ha^2\left(\frac{\sigma_{nf}}{\sigma_f}\right) f'' = 0 \quad (22)$$

$$\left(\frac{k_{eff}}{k_f}\right)\theta'' - PrSq\left(\frac{(\rho c_p)_{nf}}{(\rho c_p)_f}\right)[f-\eta]\theta' + S\theta = 0 \quad (23)$$

The boundary conditions for the non-dimensional momentum and energy equations are presented as follows:

$$f(0) = 0,\ f''(0) = 0,\ f(1) = 1,\ f'(1) = 0, \quad (24)$$

$$\theta(1) = 1, \quad \theta'(0) = 0 \quad (25)$$

Here, *Ha* is the Hartmann number, *Sq* is the squeeze number, *Pr* is the Prandtl number and *S* is the heat source parameter. So, the parameters presented are as follows:

$$Ha = HB_0\sqrt{\frac{\sigma_f}{\mu_f}} \quad (26)$$

$$Sq = \frac{aH^2}{2\upsilon_f} \quad (27)$$

$$Pr = \frac{\mu_f(\rho c_p)_f}{\rho_f k_f} \quad (28)$$

$$S = \frac{S_0 H^2}{k_f} \quad (29)$$

3. SIMULATION METHODOLOGY

3. 1. Radial Basis Function Approximation The approximate method of the Radial Basis Functions (RBF) is an efficient tool for analyzing functions and equations at high degrees, especially when it is necessary to apply the interpolation problem for scattered data on an irregular geometry [23]. The general form of the radial base function is presented as follows:

$$\Phi[\![(r]\!]_j) = \Phi(\|x - x_j\|),\ \ \Phi:\ \mathcal{R}^d \to \mathcal{R} \quad (30)$$

Here, $r_j = \|x - x_j\|$ is a Euclidean norm, and $x_j, x \in \mathcal{R}^d$. Also, x_j is the center of radial base functions. The interpolation of the radial basis functions is presented as follows:

$$u(x) = \sum_{j=1}^{N} \lambda_j \Phi(\|x - x_j\|) \quad (31)$$

If exist *N* distinct points $\{x_j\}_{j=1}^{N}$ and values $\{f_j\}_{j=1}^{N}$ such as these points are given, so, coefficients λ_j are specified using the interpolation condition as follows:

$$u(x_j) = f_j, \quad j = 0,1 \dots, N \quad (32)$$

Approximation of function $u(x)$ can be written as a linear combination of the *N* radial basis function as follows:

$$u(x) = \sum_{j=1}^{N} \lambda_j \Phi_j(x) + \Psi(x) \quad (33)$$

Also, the above approximation can be written without adding Ψ polynomials. In the present study, the radial basis function based on Hardy multiquadric (MQ) is presented as follows:

$$\Phi_j(x) = \sqrt{r_j^2 + \epsilon^2} \quad (34)$$

Here, ϵ, is a shape parameter that significantly affects on the accuracy of the answer [24, 25].

3. 2. Application of RBF For the application of RBF based on Hardy multiquadric (MQ) on governing equations of the present problem, the general form of the nondimensional momentum and energy equations are considered as follows:

$$f^{(4)} = F(\eta, f, f', f'', f^{(3)})$$
$$\theta'' = \Theta(\eta, \theta, \theta', f) \quad (35)$$

The boundary conditions for governing equations of the present problem are presented as follows:

$$f(0) = 0,\ f''(0) = 0,\ f(1) = 1,\ f'(1) = 0,\ \theta(1) = 1, \quad \theta'(0) = 0. \quad (36)$$

Radial basis function based on Hardy multiquadric (MQ) for nondimensional momentum and energy equations are presented as follows:

$$f(\eta) = \sum_{i=0}^{N} w_i \varphi_i(\eta)$$
$$\theta(\eta) = \sum_{i=0}^{M} v_i \varphi_i(\eta) \quad (37)$$

Also, the *pth* derivation of the nondimensional f function is represented as follows:

$$\frac{d^P f(\eta)}{d\eta^P} = \frac{d^P}{d\eta^P}\left(\sum_{i=0}^{N} w_i \varphi_i(\eta)\right)$$
$$= \sum_{i=0}^{N} w_i (d^P \varphi_i(\eta)/d\eta^P) \quad (38)$$
$$= \sum_{i=0}^{N} w_i h_i^{[p]}(\eta)$$

Nondimensional θ is represented according to Equation (38), so, with applied the Equations (37) and (38) into Equation (35):

$$\sum_{i=0}^{N} w_i h_i^{[4]}(\eta) = F\begin{pmatrix}\eta, \sum_{i=0}^{N} w_i \varphi_i(\eta), \sum_{i=0}^{N} w_i h_i^{[1]}(\eta),\\ \sum_{i=0}^{N} w_i h_i^{[2]}(\eta), \sum_{i=0}^{N} w_i h_i^{[3]}(\eta)\end{pmatrix} = 0$$
$$\sum_{i=0}^{M} v_i h_i^{[2]}(\eta) = \Theta\begin{pmatrix}\eta, \sum_{i=0}^{M} v_i \varphi_i(\eta), \sum_{i=0}^{M} v_i h_i^{[1]}(\eta),\\ \sum_{i=0}^{N} w_i \varphi_i(\eta)\end{pmatrix} \quad (39)$$

Set the residual (39) equal to zero at the set of collocation points η_j as follows:

$$\sum_{i=0}^{N} w_i h_i^{[4]}(\eta_j) - \mathrm{F}\begin{pmatrix}\eta_j, \sum_{i=0}^{N} w_i \varphi_i(\eta_j), \sum_{i=0}^{N} w_i h_i^{[1]}(\eta_j),\\ \sum_{i=0}^{N} w_i h_i^{[2]}(\eta_j), \sum_{i=0}^{N} w_i h_i^{[3]}(\eta_j)\end{pmatrix} = 0$$
$$\sum_{i=0}^{M} v_i h_i^{[2]}(\eta_j) - \Theta\begin{pmatrix}\eta_j, \sum_{i=0}^{M} v_i \varphi_i(\eta_j), \sum_{i=0}^{M} v_i h_i^{[1]}(\eta_j),\\ \sum_{i=0}^{N} w_i \varphi_i(\eta_j)\end{pmatrix} = 0 \quad (40)$$

Then, for solving *M+N-4* nonlinear equations, we set the boundary conditions (36) as follows:

$$f(0) = \sum_{i=0}^{N} w_i \varphi_i(0) = 0,$$
$$f''(0) = \sum_{i=0}^{N} w_i h_i^{[2]}(0) = 0,$$
$$f(1) = \sum_{i=0}^{N} w_i \varphi_i(1) = 1,$$
$$f'(1) = \sum_{i=0}^{N} w_i h_i^{[1]}(1) = 0, \quad (41)$$
$$\theta(1) = \sum_{i=0}^{M} v_i \varphi_i(1) = 1,$$
$$\theta'(0) = \sum_{i=0}^{M} w_i h_i^{[1]}(0) = 0.$$

Equations (40) and (41) are represented the *M+N+2* nonlinear equations and unknowns, and with solving these equations, w_i and v_i are obtained. So, by substituting w_i and v_i at Equations (37), f and θ are obtained.

3. 3. Application of Akbari-Ganji's Method

This method has been presented by Akbari-Ganji and applied by many researchers [26-30]. For the application of AGM to the nondimensional momentum and energy equations, the detail of these equations are considered as follows:

$$F(\eta) = \left(\frac{\mu_{eff}}{\mu_f}\right) f^{(4)} - Sq\left(\frac{\rho_{nf}}{\rho_f}\right)[\eta f^{(3)} + 3f'' + f'f'' - ff^{(3)}] - Ha^2\left(\frac{\sigma_{nf}}{\sigma_f}\right) f'' = 0$$
$$\Theta(\eta) = \left(\frac{k_{eff}}{k_f}\right)\theta'' - PrSq\left(\frac{(\rho c_p)_{nf}}{(\rho c_p)_f}\right)[f - \eta]\theta' + S\theta = 0 \quad (42)$$

Total answers with constant coefficients for nondimensional momentum and energy equations are considered as follows:

$$f(\eta) = a_0.\eta^0 + a_1.\eta^1 + a_2.\eta^2 + a_3.\eta^3 + a_4.\eta^4 + a_5.\eta^5,$$
$$\theta = b_0.\eta^0 + b_1.\eta^1 + b_2.\eta^2 + b_3.\eta^3. \quad (43)$$

Equation (43) sustituted into governing Equations (42) and considered boundary conditions as follows:

$$f(0) = 0,\ \frac{d^2 f}{d\eta^2}(0) = 0,$$
$$f(1) = 1,\ \frac{df}{d\eta}(1) = 0, \quad (44)$$
$$\theta(1) = 1,\ \frac{d\theta}{d\eta}(0) = 0$$

Since the proposed problem engaged with four trial functions which contain ten constant coefficients and this geometry has six equations according to Equation (44) and created four additional equations in the following order:
$F(0) = 0, F(1) = 0, \Theta(0) = 0, \Theta(1) = 0.$
So by utilizing the above procedures, we have obtained a set of polynomials containing ten equations and ten constants which by solving them we would be able to obtain Equation (43). By substituting obtained constant coefficients from mentioned procedures, Equation (43) could easily be yielded nondimensional momentum and energy equations, respectively as follows:

$$f(\eta) = -0.4816\eta^5 + 0.4631\eta^3 + 1.0184\eta$$
$$\theta(\eta) = 0.1902\eta^3 + 0.2699\eta^2 + 0.5399 \quad (45)$$

3. 4. Differential Transform Method (DTM)

Basic definitions and operations of differential transformation are introduced as follows. Differential transformation of the function $f(\eta)$ is defined as follows:

$$F(k) = \frac{1}{k!}\left.\frac{d^k f(\eta)}{d\eta^k}\right|_{\eta=\eta_0} \quad (46)$$

In Equation (46), $f(\eta)$ is the original function and *F (k)* is the transformed function which is called the *T* -function (it is also called the spectrum of the $f(\eta)$ at $\eta = \eta_0$, in the *k* domain). The differential inverse transformation of *F* (*k*) is defined as:

$$f(\eta) = \sum_{k=0}^{\infty} F(k)(\eta - \eta_0)^k \quad (47)$$

By combining Equations (46) and (47) $f(\eta)$ can be obtained:

$$f(\eta) = \sum_{k=0}^{\infty} \left[\frac{d^k f(\eta)}{d\eta^k}\Big|_{\eta=\eta_0}\right] \frac{(\eta-\eta_0)^k}{k!} \quad (48)$$

Equation (48) implies that the concept of the differential transformation is derived from Taylor's series expansion, but the method does not evaluate the derivatives symbolically. However, relative derivatives are calculated by an iterative procedure that is described by the transformed equations of the original functions. From the definitions of Eqautions (46) and (47), it is easily proven that the transformed functions comply with the basic mathematical operations shown below. In real applications, the function $f(\eta)$ in Equation (48) is expressed by a finite series and can be written as:

$$f(\eta) = \sum_{k=0}^{N} F(k)(\eta-\eta_0)^k \quad (49)$$

Equation (49) implies that $f(\eta) = \sum_{k=N+1}^{\infty} F(k)(\eta-\eta_0)^k$ is negligibly small, where *N* is series size. Theorems to be used in the transformation procedure, which can be evaluated from Equations (46) and (47), are given by Sheikholeslami and Domairry Ganji [31]. Also, refer to the same reference to solve the model with DTM.

3. 5. Validation for Analytical Methods The comparison and verification between the simulation of the nondimensional velocity profile of CuO-water multiphase fluid flow and the Differential Transformation Method (DTM) by Sheikholslami and Domiri Ganji. [31] is represented in Figure 2. This figure shows the velocity profiles are close together and according to the physical condition of the problem, there is good accuracy between the Akbari-Ganji's Method (AGM) and Radial Basis Function approximation (RBF) based on Hardy multiquadric (MQ) function and DTM [31].

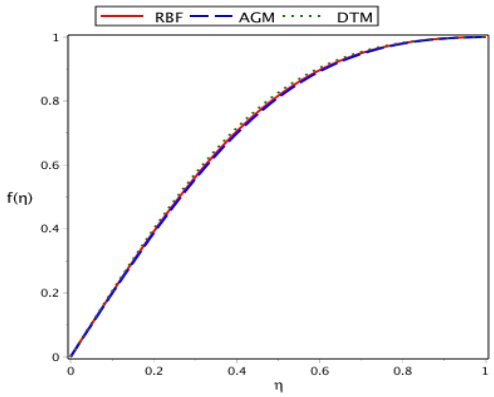

Figure 2. Comparison of the nondimensional velocity profile of CuO-water multiphase fluid flow (present work) and DTM for previous work ([31]) at $S = -1$, $Pr = 6.2$, $Ha = 8$, and $Sq = 1$.

Table 2, represented the numerical comparison between the Akbari-Ganji's Method (AGM), Radial Basis Function approximation (RBF) based on Hardy multiquadric (MQ) function, and Differential Transformation Method (DTM) as shown in Figure 2.

4. RESULTS AND DISCUSSION

In this research, Brownian motion with heat source effects between parallel disks on nondimensional velocity and temperature fields are illustrated. Also, electromagnetic force effects on squeezing flow between parallel disks are surveyed. Figure 3 is represented the effect of squeeze number on nondimensional velocity and temperature profiles of copper oxide (CuO) nanoparticles. The velocity and temperature profiles are depicted using Akbari-Ganji's Method (AGM) and Radial Basis Function approximation (RBF) based on Hardy multiquadric (MQ) function. At the AGM method, the vertical velocity of nanofluid flow is increased with increasing squeeze number, and with extending more than $Sq = 1$, the concavity of the diagrams is close to each other and almost coincides. But at a squeeze number more than $Sq = 1$, the vertical velocity profile of nanofluid flow is slightly reduced. At the RBF method, the vertical velocity of the nanofluid is increased with the enhancement of the squeeze number. The graphs converge and the vertical velocity of the nanoparticles is not changed significantly because the graphs are matched together.

The numerical values of nondimensional velocity and temperature of CuO nanoparticles are illustrated at AGM and RBF (MQ) methods and the numerical difference ($|\Delta| = |\mathrm{AGM} - \mathrm{RBF}|$) between them in Tables 3-5.

TABLE 2. Numerical comparison between AGM, RBF, and DTM for nondimensional velocity profile of CuO-water multiphase fluid flow at $S = -1$, $Pr = 6.2$, $Ha = 8$, and $Sq = 1$

η	RBF	AGM	DTM [31]
0.0	0	0	0
0.1	0.1984	0.1964	0.2033
0.2	0.3871	0.3834	0.3962
0.3	0.5566	0.5518	0.5683
0.4	0.6994	0.6943	0.7116
0.5	0.8116	0.8072	0.8225
0.6	0.8933	0.8900	0.9014
0.7	0.9477	0.9457	0.9526
0.8	0.9800	0.9791	0.9821
0.9	0.9957	0.9955	0.9962
1.0	1	1	1

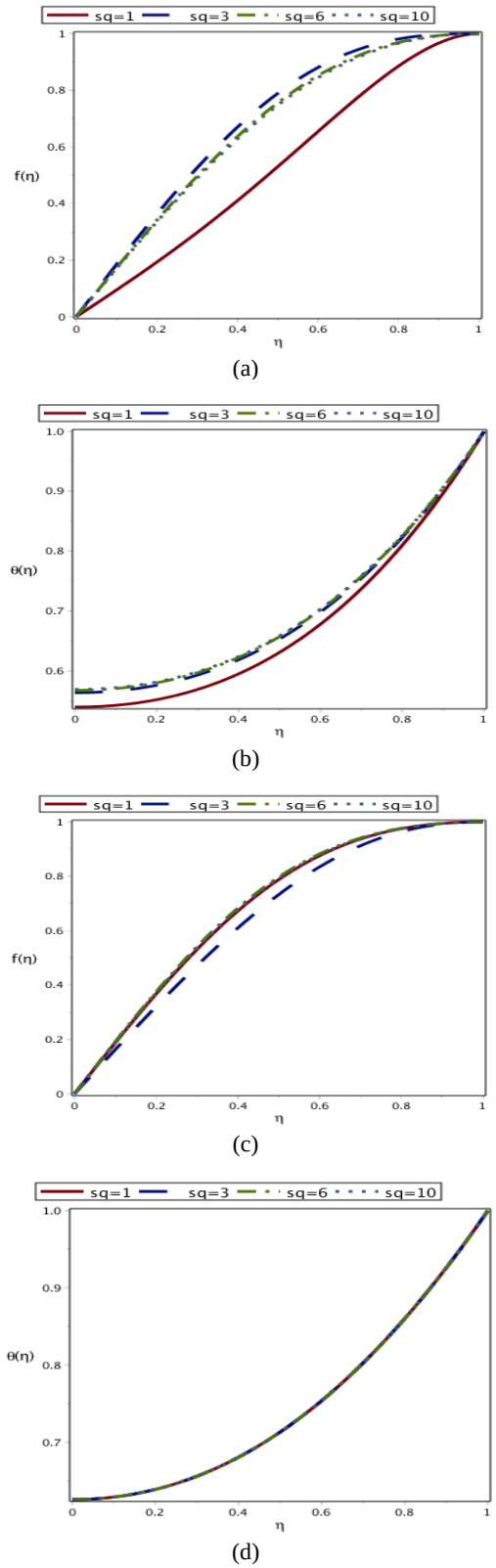

Figure 3. Comparison between AGM (a,b) and RBF (c,d) for effects of squeeze number on dimensionless vertical velocity and temperature profile for CuO-water multiphase fluid flow at $S = -1$, $Pr = 6.2$ and $Ha = 1$

TABLE 3. Numerical comparison of vertical velocity between AGM and RBF for CuO-water multiphase fluid flow at $Ha = 1, S = -1, Pr = 6.2, Sq = 3$.

	f		
η	AGM	RBF(MQ)	|Δ|
0.0	0	0	0
0.1	0.1850	0.1629	0.0221
0.2	0.3628	0.3215	0.0413
0.3	0.5265	0.4718	0.0547
0.4	0.6702	0.6104	0.0598
0.5	0.7894	0.7330	0.0564
0.6	0.8810	0.8350	0.0460
0.7	0.9445	0.9126	0.0319
0.8	0.9816	0.9643	0.0173
0.9	0.9973	0.9920	0.0053
1.0	1	1	1

TABLE 4. Numerical comparison of horizontal velocity between AGM and RBF for CuO-water multiphase fluid flow at $Ha = 1, S = -1, Pr = 6.2, Sq = 3$.

	f'		
η	AGM	RBF(MQ)	|Δ|
0.0	1.8623	1.6372	0.2251
0.1	1.8257	1.6142	0.2115
0.2	1.7182	1.5501	0.1681
0.3	1.5463	1.4507	0.0956
0.4	1.3209	1.3135	0.0074
0.5	1.0571	1.1310	0.0739
0.6	0.7745	0.9031	0.1286
0.7	0.4971	0.6463	0.1492
0.8	0.2531	0.3913	0.1382
0.9	0.0751	0.1695	0.0944
1.0	0	0	0

These Tables are shown at $Sq = 3$ and $\eta = 0$, the maximum difference in horizontal velocity is 0.2251 and the minimum difference at $\eta = 0.9$ is 0.0053. Also, the nondimensional temperature at $\eta = 0.3$ and $\eta = 0.4$ has a maximum difference of 0.0627 and the minimum difference at $\eta = 0.9$ is equal to 0.0213.

Figure 4 represents the effects of squeeze number on nondimensional vertical velocity and temperature profile for Al_2O_3-water multiphase fluid flow using AGM and RBF (MQ) at $S = -1$, $Pr = 6.2$, and $Ha = 1$.

This figure has depicted the same behavior as CuO-water multiphase fluid flow; however, there is no

TABLE 5. Numerical comparison of temperature between AGM and RBF for CuO-water multiphase fluid flow at $Ha = 1, S = -1, Pr = 6.2, Sq = 3$.

	θ		
η	**AGM**	**RBF (MQ)**	**$\|\Delta\|$**
0.0	0	0	0
0.1	0.1850	0.1629	0.0221
0.2	0.3628	0.3215	0.0413
0.3	0.5265	0.4718	0.0547
0.4	0.6702	0.6104	0.0598
0.5	0.7894	0.7330	0.0564
0.6	0.8810	0.8350	0.0460
0.7	0.9445	0.9126	0.0319
0.8	0.9816	0.9643	0.0173
0.9	0.9973	0.9920	0.0053
1.0	1	1	1

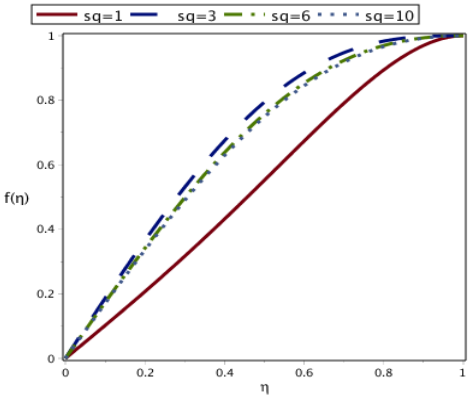

(a)

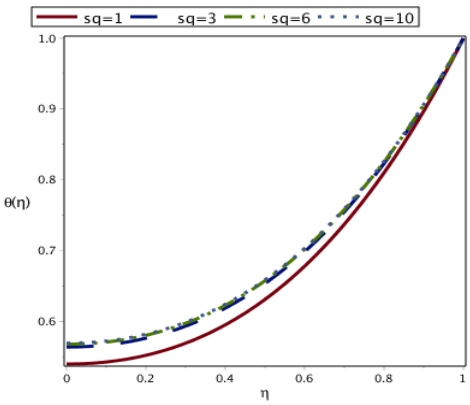

(b)

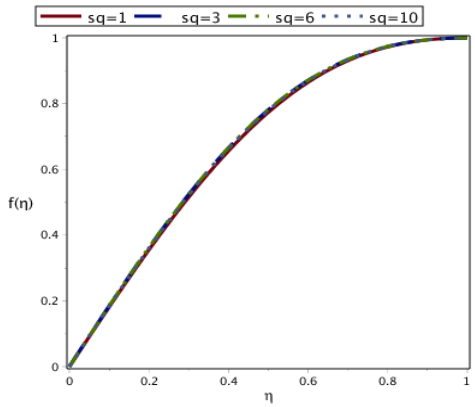

(c)

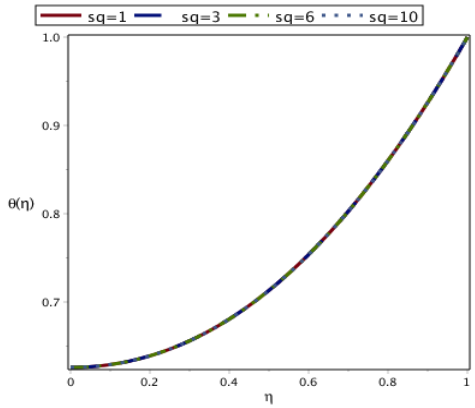

(d)

Figure 4. Comparison between AGM(a,b) and RBF (c,d) for effects of squeeze number on dimensionless vertical velocity and temperature profile for Al2O3-water multiphase fluid flow at S=−1, Pr=6.2, and Ha=1.

significant change with increasing the squeeze number on this nanofluid in the RBF method.

Figure 5 investigated the effect of the Hartmann number on Alumina (Al_2O_3)-water multiphase fluid flow using AGM and RBF methods. With an increase in the Hartmann number, the nanofluid's nondimensional horizontal and vertical velocities are increased using the AGM method. Except for $Ha = 0$, the graphs converged together and the heat transfer didn't change by increasing the Hartmann number. With increasing Hartmann number, the nondimensional horizontal and vertical velocities of nanofluid are increased, the graphs converged together, and the heat transfer didn't change using the RBF method.

Figure 6 illustrated the effect of the Prandtl number on the nondimensional temperature profiles of Al_2O_3 and CuO nanofluids using the AGM method. According to this figures., maximum values for nondimensional temperature profile were at $Pr = 2$.

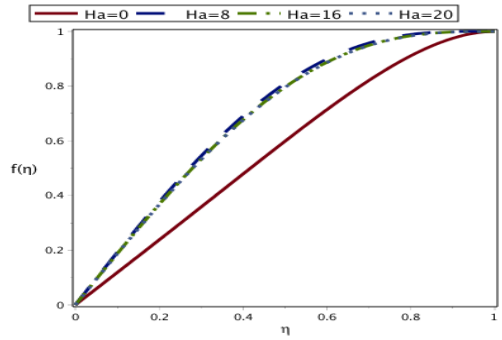

(a)

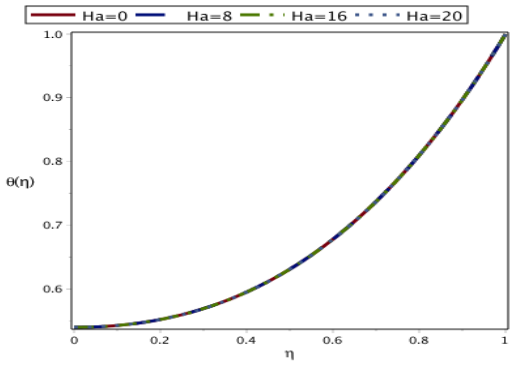

(b)

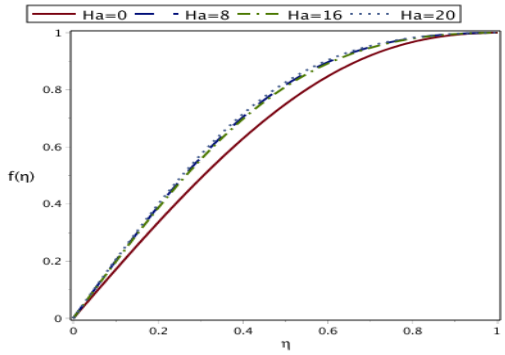

(c)

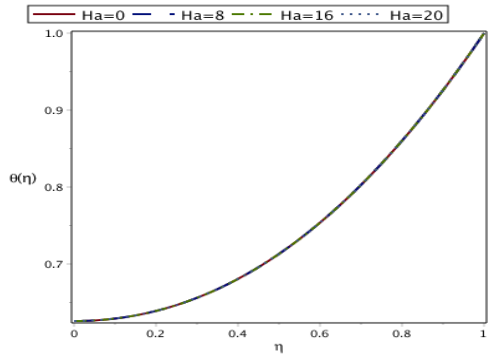

(d)

Figure 5. Comparison between AGM (a,b) and RBF (c,d) for effects of Hartman number on dimensionless vertical velocity and temperature profile for Al2O3-water multiphase fluid flow at S=−1, Pr=6.2, and Sq=1

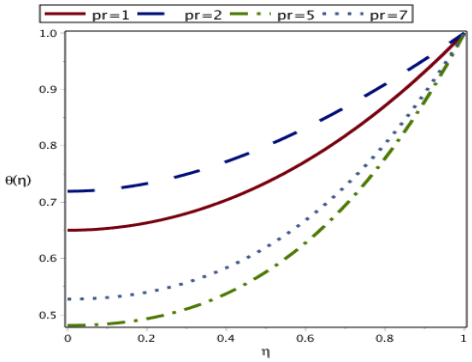

Alumina (Al_2O_3)

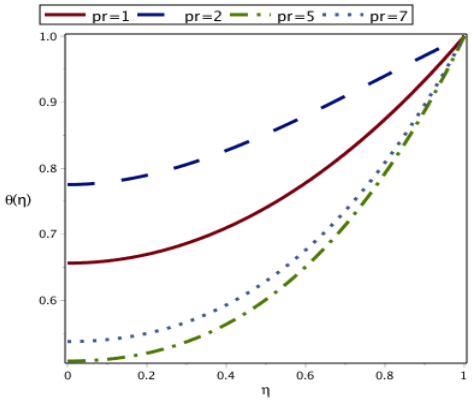

Copper oxide (CuO)

Figure 6. Comparison between Al2O3 and CuO nanoparticles for effects of Prandtl number on dimensionless temperature profile at S=−1, Sq=1, and Ha=1.

Figure 7 shows the residual error function graph for the Al_2O_3 nanoparticle because there is no exact solution in this geometry, we obtain the residual error function using the RBF method.

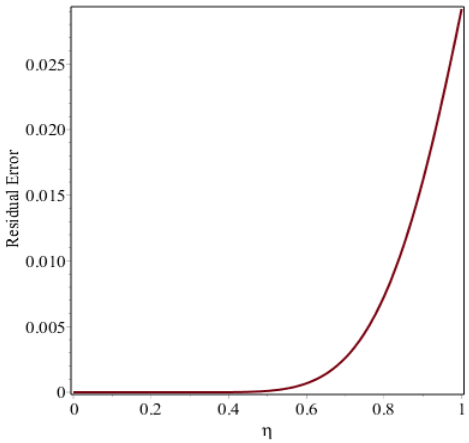

Figure 7. Graph of residual error function using RBF method on velocity profile for Al_2O_3-water multiphase fluid flow at $S = -1$, $Pr = 6.2$, and $Sq = 1$.

5. CONCLUSION

In the present study, squeezing flow with Brownian motion effects on nondimensional vertical, horizontal velocity, and temperature profiles were surveyed between parallel disks with a heat source. Also, for simulating the nanoparticle effects on nondimensional temperature fields and velocity profiles were used the Akbari-Ganji's Method (AGM) and Radial Basis Function approximation (RBF) were based on Hardy multiquadric (MQ) function. We investigated Al_2O_3 and CuO nanoparticle's effects on nondimensional velocity and temperature fields between parallel disks with a heat source and electromagnetic force. Finally, some of the main points are summarized:

- The effects of squeezes number on nondimensional horizontal and vertical velocity and temperature field for Al_2O_3 and CuO nanoparticles have a similar behaviour using the AGM method.
- With increasing the squeezes number on Al_2O_3 and CuO nanofluid flow, the nondimensional temperature field did not change using the RBF method.
- The minimum difference between AGM and RBF methods for nondimensional vertical velocities field at $\eta = 0.9$ and $Ha = 8$.
- The effects of the Hartmann number on nondimensional vertical velocities field for Al_2O_3 nanoparticles at $\eta = 0$ have a slight difference from the other Hartmann values using the AGM method.
- Also, increasing the Prandtl number for Al_2O_3 and CuO nanoparticles in AGM and RBF methods, decreased the nondimensional temperature field, which has the minimum difference between AGM and RBF methods at $Pr = 1$, $\eta = 0.9$ is equal to 0.0019.

6. REFERENCES

1. Hosseinzadeh, Kh., Alizadeh, M., and Ganji, D. D., "Hydrothermal Analysis on MHD Squeezing Nanofluid Flow in Parallel Plates by Analytical Method," ***International Journal of Mechanical and Materials Engineering***, Vol. 15, No. 8 (2020). https://doi.org/ 10.1186/s40712-018-0089-7
2. Asefi, M., Molavi, H., Shariaty-Niassar, M., babaee Darband, j., Nemati, N., Yavari, M., and Akbari, M., "An Investigation on Stability, Electrical and Thermal Characteristics of Transformer Insulating Oil Nanofluids," ***International Journal of Engineering, Transactions A: Basics,*** Vol. 29, No. 10, (2016), 1332-1340. https://doi.org/0.5829/idosi.ije.2016.29.10a.02
3. Ravindran, R., Ganapathirao, M., Pop, I., "Effects of Chemical Reaction and Heat Generation/Absorption on Unsteady Mixed Convection MHD Flow Over A Vertical Cone With Non-Uniform Slot Mass Transfer," ***International Journal of Heat and Mass Transfer,*** Vol. 73, (2014), 743-751. https://doi.org/ 10.1016/j.ijheatmasstransfer.2014.02.053
4. Motahar, S., "A Neural Network Approach to Estimate Non-Newtonian Behavior of Nanofluid Phase Change Material Containing Mesoporous Silica Particles, " ***International Journal of Engineering, Transactions B: Applications,*** Vol. 34, No. 08, (2021), 1974-1981. https://doi.org/10.5829/ije.2021.34.08b.18
5. Asgari, M., Tariverdilo, S., "Investigating The Seismic Response of Structural Walls Using Nonlinear Static and Incremental Dynamic Analyses, " ***International Journal of Engineering, Transactions B: Applications,*** Vol. 30, No. 11, (2017), 1691-1699. https://doi.org/10.5829/ije.2017.30.11b.09
6. Han He, Ji., Mostapha, Doaa R., "Insight into the Significance of Hall Current and Joule Heating on the Dynamics of Darcy–Forchheimer Peristaltic Flow of Rabinowitsch Fluid, " ***Journal of Mathematics,*** (2021) Article ID 3638807. https://doi.org/10.1155/2021/3638807
7. Han He, Ji., Abed Elzam., N. Y., "Insights into partial slips and temperature Jumps of a nanofluid flow over a stretched or shrinking surface, "***Journal of Energies***, Vol. 14, No. 20, (2021), 6691. https://doi.org/10.3390/en14206691
8. Rashidi, M. M., Alhuyi Nazari, M., Mhariq, I, Ali, N,"Modeling and Sensitivity Analysis of thermal Conductivity of Ethylene Glycol-Water Based Nanofluids with Alumina Nanoparticles, " ***Computations & Experiments on Dynamics of Complex Fluid & Structure***, (2022) 1-8. https://doi.org/10.1007/s40799-022-00567-4
9. Alagumalai, A., Qin, C., Vimal, K.E.K., Solomin, E., Yang, L., Zhang, P., Otanicar, T., Kasaeian, A., Chamkha, A.J., Rashidi, M.M. and Wongwises, S., "Conceptual Analysis Framework Development to Understand Barriers of Nanofluid Commercialization, "***Journal of Nano Energy***, Vol. 92, (2022), 106736. https://doi.org/ 10.1016/j.nanoen.2021.106736
10. Nouri, K., Nazari, M., and Torkzadeh, L., "Numerical Approximation of The System of Fractional Differential Equations with Delay and Its Applications," ***The European Physical Journal Plus***, Vol. 135, No. 3, (2020) 1-14. https://doi.org/10.1140/epjp/s13360-020-00351-6
11. Nouri, K., Baleanu, D., and Torkzadeh, L., "Study on Application of Hybrid Functions To Fractional Differential Equations," ***Iranian Journal of Science and Technology*, Transactions A: Science**, Vol. 42, No. 4, (2018), 1343-1350. https://doi.org/ 10.1007/s40995-017-0224-y
12. Dadsetadi, S., Nouri, K., and Torkzadeh, L., "Solvability of Some Nonlinear Integro-Differential Equations of Fractional Order Via Measure of Noncompactnes," ***The Pure and Applied Mathematics,*** Vol. 27, No. 1, (2020), 13-24. https://doi.org/10.7468/jksmeb.2020.27.1.13
13. Pourziaei Araban. H., Alinejad, J., Peiravi, M. M., and Domairry Ganji, D., "3D Numerical Simulation of Cavity with Bottom Heat Source for Ra-Nu Correlation," ***Transport Phenomena Nano Micro Scales***, (2021). https://doi.org/10.1140/epjp/s13360-020-00351-6
14. Eringen, A., "Theory of Micropolar Fluids," ***Journal of Mathmatics,*** Vol. 16, No. 1, (1966), 1-18.
15. Mustafa, M., Hayat, T., and Obaidat, S., "On Heat And Mass Transfer in The Unsteady Squeezing Flow Between Parallel Plates," ***Meccanica***, Vol. 47, No. 7, (2012), 1581-1589. https://doi.org/ 10.1007/s11012-012-9536-3
16. Koo, J., and Kleinstreuer, C., "Laminar Nanofluid Flow in Micro heat-Sinks," ***International Journal of Heat and Mass Transfer***, Vol. 48, No. 7, (2005), 2652-2661. https://doi.org/ 10.1016/j.ijheatmasstransfer.2005.01.029
17. Salehi, S., Nori, A., Hosseinzadeh, Kh., and Ganji, D. D., "Hydrothermal Analysis Of MHD Squeezing Mixture Fluid Suspended By Hybrid Nanoparticles Between Two Parallel Plates," ***Case Studies in Thermal Engineering***, Vol. 21, (2020) 100650. https://doi.org/ 10.1016/j.csite.2020.100650

18. Zhang, B., Song, Z., and Mao, W., "A Novel Wake Energy Reuse Method to Optimize The Layout For Savonius-Type Vertical Axis Wind Turbines," ***Energy***, Vol. 121, No. 7, (2017), 341-355. https://doi.org/ 10.1016/j.energy.2017.01.004
19. Koo, J., and Kleinstreuer, C., "Viscous Dissipation Effects In Micro Tubes And Micro Channels," ***International Journal of Heat and Mass Transfer,*** Vol. 47, No. 7, (2004), 3159–3169. https://doi.org/ 10.1016/j.ijheatmasstransfer.2004.02.017
20. Koo, J., "Computational Nanofluid Flow and Heat Transfer Analyses Applied to Microsystems," (Ph.D. thesis), NC State University, Raleigh, NC, (2004).
21. Li, J., "Computational Analysis of Nanofluid Flow in Micro Channels With Applications to Micro-Heat Sinks And Bio-MEMS," (Ph.D. thesis), NC State University, Raleigh, NC, (2008).
22. Singh, K., Rawat, S. K., and Kumar, M., "Heat and Mass Transfer on Squeezing Unsteady MHD Nanofluid Flow between Parallel Plates with Slip Velocity Effect," ***Journal of Nanoscience***, (2016). https://doi.org/ 0.1155/2016/9708562
23. Cheng, A. H. D., Golberg, M. A., Kansa, E. J., and Zammito, G., "Exponential Convergence And H-C Multiquadric Collocation Method For Partial Differential Equations," ***Numerical Methods Partial Differential Equations***, Vol. 19, No. 1, (2003), 571-594. https://doi.org/ 10.1002/num.10062
24. Elansari, M., Ouazar, D., and Cheng, A. H. D., "Boundary Solution of Poisson's Equation Using Radial Basis Function Collocated on Gaussian Quadrature Nodes," ***Communications in Numerical Methods in Engineering***, Vol. 17, No. 7, (2001), 455-464. https://doi.org/ 10.1002/cnm.419
25. Haq, S., Hussain, A., and Uddin, M., "On The Numerical Solution of Nonlinear Burgers-Type Equations Using Meshless Method Of Lines," ***Applied Mathematics and Computation***, Vol. 218, No. 1, (2012), 6280-6290. https://doi.org/ 10.1016/j.amc.2011.11.106
26. Peiravi, M. M., Alinejad, J., Domairry Ganji, D., and Maddah, S., "Numerical Study of Fins Arrangement and Nanofluids Effects on Three-Dimensional Natural Convection in The Cubical Enclosure," ***Transport Phenomena Nano Micro Scales***, Vol. 7, No. 2, (2019), 97-112. https://doi.org/ 10.22111/TPNMS.2019.4845
27. Peiravi, M. M., and Alinejad, J., "Hybrid Conduction, Convection, and Radiation Heat Transfer Simulation in A Channel with Rectangular Cylinder," ***Journal of Thermal Analysis and Calorimetry,*** Vol. 140, No. 6, (2020), 2733-2747. https://doi.org/ 10.1007/s10973-019-09010-0
28. Peiravi, M. M., Alinejad, J., Domairry Ganji, D., and Maddah, S., "3D Optimization of Baffle Arrangement in A Multi-Phase Nanofluid Natural Convection Based on Numerical Simulation," ***International Journal of Numerical Methods for Heat and Fluid Flow***, Vol. 30, No. 5, (2019), 2583-2605. https://doi.org/ 10.1108/HFF-01-2019-0012
29. Alinejad, J., Peiravi, M. M., "Numerical analysis of secondary droplets characteristics due to drop impacting on 3D cylinders considering dynamic contact angle," ***Meccanica***, Vol. 55, No. 10, (2020), 1975-2002. https://doi.org/ 10.1007/s11012-020-01240-z
30. Domairry Ganji, D., Peiravi, M. M., and Abbasi, M., "Evaluation of The Heat Transfer Rate Increases in Retention Pools Nuclear Waste," ***International Journal of Nano Dimension***, Vol. 6, No. 4, (2015), 385-398.
31. Sheikholeslami, M, Domairry Ganji, D., "Nanofluid Flow and Heat Transfer Between Parallel Plates Considering Brownian Motion Using DTM, " ***Computer Methods in Applied Mechanics and Engineering,*** 283, (2015), 651-663. https://doi.org/10.1140/epjp/s13360-020-00351-6

Persian Abstract

چکیده

نوآوری مقاله حاضر بررسی تحلیلی اثرات حرکت براونی بر جریان نانوسیال و نیروی الکترومغناطیسی بین دیسک‌های موازی با منبع حرارت است. اثرات نانوذرات بر میدان دمایی بی‌بعد و سرعت جریان سیال با استفاده از روش اکبری گنجی و تقریب تابع پایه شعاعی بر اساس تابع چند مربعی هاردی تحلیل شده است. روش اکبری گنجی یک روش تحلیلی قوی است که هر معادله دیفرانسیل خطی و غیرخطی را با هر درجه ای از متغیرها حل می‌کند. توابع پایه شعاعی یک روش تقریبی برای تجزیه و تحلیل توابع و معادلات در درجات بالا است، به ویژه زمانی که لازم است مسئله درون یابی برای داده‌های پراکنده در هندسه نامنظم اعمال شود. نتایج نشان داد که حداکثر تفاوت بین روش‌های اکبری گنجی و تابع پایه شعاعی برای سرعت افقی بی‌بعد روی نانوسیال CuO در $Sq = 1$ و $\eta = 0$ برابر ۰.۲۲۵۱ و حداقل تفاوت برای سرعت عمودی بی‌بعد نانوسیال Al_2O_3 در $\eta = 0$ برابر با ۰.۰۰۱۸ است. . همچنین اثرات عدد هارتمن بر میدان سرعت‌های افقی و عمودی بی‌بعد برای نانوذرات Al_2O_3 در $\eta = 0$ تفاوت جزئی با سایر مقادیر هارتمن با استفاده از روش AGM دارد. حداکثر سرعت های افقی بی‌بعد در $\eta = 0$ و $Ha = 8$ برابر با ۱.۹۳۵٤ است.

IJE TRANSACTIONS B: Applications Vol. 35, No. 08, (August 2022) 1662-1673

International Journal of Engineering

Journal Homepage: www.ije.ir

Optimal Sizing of Battery Energy Storage System in Commercial Buildings Utilizing Techno-economic Analysis

A. Ashabi[a], M. M. Peiravi*[b], P. Nikpendar[c], S. Salehi Nasab[d], F. Jaryani[e]

[a] *UM Power Energy Dedicated Advanced Centre (UMPEDAC), University of Malaya, Kuala Lumpur, Malaysia*
[b] *Department of Mechanical Engineering, Technical and Vocational University (TVU), Tehran, Iran*
[c] *Department of Mechanical Engineering, Babol Noshirvani University of Technology, Babol, Iran*
[d] *Department of Computer Engineering, Lorestan University, Khorramabad, Iran*
[e] *Faculty of Computer Science and Information System, Universiti Teknologi Malaysia*

PAPER INFO

Paper history:
Received 19 March2022
Received in revised form 11 May 2022
Accepted 20 May 2022

Keywords:
Battery Sizing
Benefit-Cost Ratio
Payback Period
Peak Shaving
Techno-economic Analysis

ABSTRACT

Finding the correct battery size is important to the project's financial success. Many studies utilize complicated simulations to identify the optimal battery size. It is also difficult to reuse the outcomes of such optimization in other projects. In this paper, by introducing the factor β as the energy to power ratio, a simple techno-economic model is proposed to allow a quick evaluation of the feasibility of a building-integrated battery energy storage system (BI-BESS) and can apply to all commercial buildings that use the same tariff structure and is independent on the building load profile. Because the battery's energy and power are coupled, defining β allows both metrics to be addressed, resulting in high accuracy. For validating the results, the load profile from a commercial building based on Malaysia's tariff structure is used, and the optimal size of the battery is obtained from the proposed techno-economic model with the help of a Benefit-cost ratio (BCR) and simple iterative model for peak shaving. The results reveal that after finding the optimal BCR=1.08, the optimal battery size is achieved at 66.84 kWh. However, considering the market interests in the payback period, the economic feasibility of installing BESS is evaluated at BCR= 1.7, which is higher than our results. Hence, the impact of battery cost reduction is assessed.

***doi**: 10.5829/ije.2022.35.08b.22*

NOMENCLATURE

$BESS$	battery energy storage system	RTE	Round trip efficiency of BESS
P_{BESS}	Required power for BESS (kW)	N_{days}	Number of working days per year
E_{BESS}	Required energy for BESS (kWh)	Deg	Degradation efficiency of the battery
ΔE	Shifted energy of peak shaving (kWh)	η_{inv}	Efficiency of the inverter
ΔP	Shaved power of peak shaving (kW)	P_{inv}	Power rating of the inverter (kW)
DoD	Depth of discharge	Δr	Peak to the off-peak cost difference
D_{rate}	Charging/discharging rate	C_{energy}	Energy cost of BESS
$P_{L,i}$	Load power (kW)	C_{power}	Power cost of BESS
$E_{D,i}$	Discharged energy of battery (kWh)	C_{tot}	Total cost of BESS
$E_{max,i}$	Maximum energy of battery (kWh)	C_{opex}	Operational cost of BESS
β	Energy to power ratio (kWh/kW)	BCR	Benefit-cost ratio
MD	Maximum demand charge (USD/kW)	PV_{rate}	total yearly revenue of the project
R	Revenue of the project	PP	Payback period
R_{kWh}	Revenue of load shifting	K	Proposed parameter for total battery storage costs
R_{MD}	Annual revenue of demand cost reduction		

*Corresponding Author Institutional Email: Mohsenpeiravi@gmail.com (M. Peiravi)

Please cite this article as: A. Ashabi, M. M. Peiravi, P. Nikpendar, S. Salehi Nasab, F. Jaryani, Optimal Sizing of Battery Energy Storage System in Commercial Buildings Utilizing Techno-economic Analysis, ***International Journal of Engineering, Transactions B: Applications***, Vol. 35, No. 08, (2022) 1662-1673

1. INTRODUCTION

The utilization of energy storage systems (ESS) is becoming an emerging trend in recent years mainly due to the increasing development of smart grids related technologies introduced by Hassan [1], Alhajj Hassan et al. [2] and Jain et al. [3]. For a long time, battery storage was mostly used for starting engines, a few emergencies backup, portable devices, etc. Lithium-based batteries revolutionized the landscape by providing improved energy efficiency and density, as well as longer shelf life, quick charge and discharge, and other benefits. Energy storage devices can assist lower consumer power costs, increasing grid flexibility, and promoting renewable energy integration [4, 5]. One of the most notable benefits of implementing a Battery Energy Storage System (BESS) in buildings is the ability to minimize bill expenses through peak shaving and load shifting strategies. However, when using BESS, determining the correct battery size is a key challenge. Since oversizing battery consideration can result in early investments that threaten the project's economic benefit, under-sizing can put greater strain on batteries and shorten the BESS's overall life. In this manner, Kumar and Biswas [6] have determined the optimal battery.

Many complicated strategies for optimal BESS size have been discussed in recent years. Lange et al. [7], and Chua, Lim, and Morris [8] identified the battery and algorithm parameters; the authors suggested a real-time peak shaving control technique and an optimization procedure. Englberger et al. [9] provided a two-step technique for developing the linear optimizer with extensive modelling of non-linear effects on the battery. Martins et al. [10] presented research on linear optimization in MATLAB using a dual simplex method for peak shaving in commercial buildings based on maximum yearly peaks while accounting for power costs, energy prices, and battery degradation costs. However, all of the discussed publications are restricted to improving storage systems based on historical data from certain commercial load patterns.

There has been a substantial amount of research dedicated to managing BESS charging/discharging in order to reduce total energy costs [11-13]. However, the high cost of BESS is frequently the limiting factor in such projects' financial feasibility, and BESS sizing is the first problem to be addressed in such projects.

The load profile and tariff structure will also need to be examined in terms of financial viability. Previously, researchers presented many iterative simulations or optimization tools to study the feasibility of building-integrated BESS. However, the building load profile and tariff structure vary from case to case, and there is a lack of consensus on the efficacy of BESS in lowering building energy expenditures.

Some articles examined the economic viability of energy storage projects using various metrics such as Payback Period (PP), Internal Rate of Return (IRR), and Net Present Value (NPV) by positioning the battery at the maximum point of peak in load profiles. Uddin et al. [14] used BESS and generators; they suggested a decision-tree-based peak shaving method for islanded microgrids. To determine the project's economic viability, the payback period and net profit are calculated. However, there is a lack of battery parameters considered for battery sizing. In recent research conducted by Tsai et al. [15], they determined the appropriate size of the battery using HOMER software's techno-economic simulation and assessed the project's viability using economic methods such as internal rate of return (IRR) and net present value (NPV). Several economic approaches may be used to assess the viability of adopting BI-BESS, but determining the most realistic method that does not require complex calculations has proven difficult.

There is a need to find a simpler solution to allow a quick preliminary evaluation of the feasibility of the BI-BESS project. Instead of relying on optimization; there should be some underlying relationship between the various design parameters for a BI-BESS project such that a techno-economic model can be built to better understand the feasibility of such project for the given constraints that are attempted in this project.

In this study, a techno-economic model is provided to assess the economic feasibility of a Building-Integrated Battery Energy Storage System (BI-BESS) in commercial projects. The practicality of a BI-BESS, especially in commercial buildings to lower bill costs, may be examined by specifying the energy to power ratio ($\beta = \Delta E/\Delta P$) as a single parameter in a techno-economic model, with the aid of a benefit-cost ratio (BCR) as an important economic tool, and a simple iterative model for battery sizing. The proposed approach is described and proven using MATLAB simulation based on a real-world building load profile. Finally, for checking the feasibility of the project based on market interests, the payback period calculation is considered to check the return of investments based on market interests. The main contributions of this study, which make this study original, are listed briefly in the following:

- Proposing a novel techno-economic model for checking the economic possibility of a BESS project in commercial buildings.
- Defining a new parameter ($\beta = \Delta E/\Delta P$) as a single parameter in the proposed model that coupled energy and power of the peak shaving.
- Using β in techno-economic analysis to find the effective parameters in optimal battery sizing.
- Applying the results on the actual load profile to validate the achievements from the proposed method.

- Considering the market interests in the results and assessing the importance of BESS cost reduction in different future scenarios.

In the following, the overview of BI-BESS and the related cost and revenue parameters will be discussed in section 2. In section 3, the proposed research method will be presented. In section 4, the results of implementing the proposed model in the actual commercial load profile will be assessed and finally, the conclusion would be stated in section 5.

2. BACKGROUND

In this section, basic concepts of using battery energy storage systems in buildings, as well as related cost and revenue considerations are briefly described.

2. 1. Building-integrated BESS Through peak shaving and load shifting, a building-integrated BI-BESS has the ability to minimize a building's energy consumption bill. However, the BESS size must be changed based on the load profile and the building's tariff system to guarantee that the BI-BESS project is economically viable. Figure 1 depicts the process of sizing BI-BESS for commercial load profiles while taking economic aspects into account.

2. 2. Load Shifting and Peak Shaving To reduce a business building's overall electricity bill, BI-BESS can perform two key purposes. The first is to minimize the building's highest consumption, which is known as peak shaving, and the second is to shift energy from peak to off-peak hours, which is known as load shifting. Peak shaving saves money on power bills by lowering maximum demand (MD) rates, but load shifting saves money by lowering peak-to-off peak kWh costs.

Figure 2 demonstrates the concept of peak shaving in a load of a typical building for peak shaving. A threshold power ($P_{threshold}$) is first specified. The BESS will subsequently discharge anytime the load exceeds the $P_{threshold}$ to reduce the higher load depicted by the shaded portion of the curve.

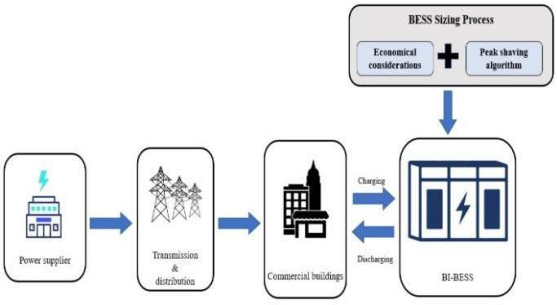

Figure 1. Schematic representation of BI-BESS sizing for commercial buildings

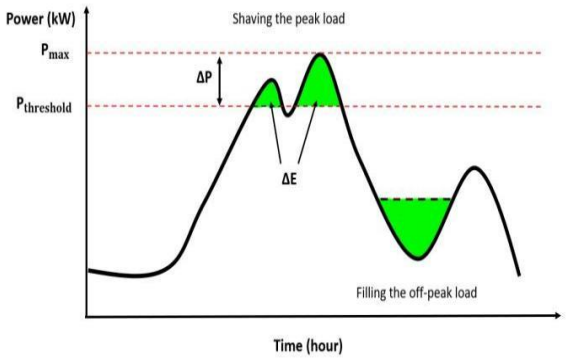

Figure 2. Typical building load profile with peak shaving and load shifting operations

The peak power shaved by the BESS is represented by ΔP, and the energy required to achieve the peak shaving is represented by ΔE. Because peak shaving typically occurs during peak hours, the energy ΔE will be subject to peak hour kWh price as well. Energy cost savings owing to load shifting can be realized if the BESS delays the recharging of this ΔE energy to the off-peak time. This means that load shifting will be an inherent feature of peak shaving, allowing for both a decrease in maximum demand (MD) charges and a reduction in peak to off-peak kWh costs to be achieved at the same time.

2. 3. Technical Considerations of BI-BESS The BESS must dispatch energy comparable to peak shaving energy ΔE to accomplish peak shaving. This peak shaving energy must then be restored by recharging the BESS before the next discharge round from the BESS is required. It is necessary to comprehend the BESS's authorized charging/discharging cycle each day as well as the depth of discharge (DoD). With the revenue from load shifting, the BESS should discharge only during peak hours and recharge only during off-peak hours. With 1 charging/discharging cycle per day assumed, the BESS energy capacity will be a function of ΔE and DoD as follows:

$$E_{BESS} \geq \frac{\Delta E}{DoD} \quad (1)$$

On the other hand, the required power of the BESS is determined by the peak shaving power (ΔP), hence the BESS should be configured to deliver equal or greater power than ΔP. The power of a BESS is limited by its energy capacity and discharge rate (D_{rate}). If the BESS's energy capacity is insufficient to compensate for the high power, the D_{rate} may be excessively high, damaging the battery and reducing its lifespan. The power constraint equation of the BESS can be rewritten for maximum D_{rate} as:

$$D_{rate} \times E_{BESS} \geq \Delta P \quad (2)$$

Then:

$$E_{BESS} \geq \frac{\Delta P}{D_{rate}} \quad (3)$$

By comparing Equations (1) and (3), it is possible to determine that the charge-discharge rate as well as the depth of discharge, will influence the size of the BESS. The total energy of the battery can be calculated by combining the energy and power limits stated as follows:

$$E_{BESS} = max\left(\frac{\Delta E}{DoD}, \frac{\Delta P}{D_{rate}}\right) \quad (4)$$

This means that for a particular peak shaving power and energy requirement, the BESS's minimum energy capacity should be chosen as the largest of the two battery size formulae generated from the two restrictions.

2. 4. Economic Considerations of BI-BESS The economic advantage of peak shaving divides into two categories: the first is the price savings by lowering maximum demand, and the second is load shifting. The annual income obtained by the lowering of MD charges may be computed over a period of 12 months as follows:

$$R_{MD} = \Delta P \times C_{MD} \times \text{Deg} \times \eta_{inv} \times 12 \left[\frac{USD}{kW.month}\right] \quad (5)$$

where ΔP is the peak power shaved in kW, C_{MD} are MD charges imposed by the utility in USD/kW, Deg is the degradation of BESS per unit, and η_{inv} is the efficiency of the BESS per unit. On the other hand, the annual revenue generated from kWh cost saving due to the peak-to-off peak load shifting, R_{kWh} can be calculated as follows:

$$R_{kWh} = \Delta E \times \Delta r \times RTE \times N_{days} \left[\frac{USD}{year}\right] \quad (6)$$

where ΔE is the energy shifted from peak to off-peak, RTE is round trip efficiency of the battery system, N_{days} is the number of days where the peak-to-off peak load shifting is performed in a year and Δr is the difference in price from the peak and off-peak hours. The total revenue from a BI-BESS project then be calculated as the sum of R_{MD} and R_{kWh}. The change in ΔP affects the benefit of maximum demand saving, while the change in ΔE affects the revenue for the arbitrage.

Operational expense is one of the cost elements that influence overall revenue. It is connected to the size of the battery and should be factored into overall income. This operating cost comprises insurance, system management, service contract, maintenance, and administrative charges, which are determined as follows:

$$C_{opex} = \Delta P \times C_{opex-unit} \left[\frac{USD}{year}\right] \quad (7)$$

where $C_{opex-unit}$ is the operational costs in USD/kW-year and C_{opex} is the total annual operating costs in USD/year. The total revenue based on ΔP and ΔE is defined as:

$$R_{tot} = \Delta P \left(C_{MD} \times Deg \times \eta_{inv} - C_{opex-unit}\right) + \Delta E \left(\Delta r \times RTE\right) \quad (8)$$

The battery and a bidirectional DC/AC inverter that serves as the interface between the DC battery and the AC grid are the two primary cost components of a BESS. The total cost of the BESS based on battery and inverter costs is as follows:

$$C_{tot} = \left(C_{energy} \times E_{BESS}\right) + \left(C_{power} \times P_{inv}\right) \quad (9)$$

where C_{tot} is the total cost of BESS, C_{energy} energy cost of BESS in USD/kWh, E_{batt} the size of BESS in kWh, C_{power} is power cost of BESS in USD/kW and P_{inv} is the power rating of the BESS in kW. As previously stated, the BESS's power is proportional to its energy and D_{rate}. The total cost of BI-BESS may be reduced to a simple function of BESS energy as follows:

$$C_{tot} = \left(C_{energy} + \left(D_{rate} \times C_{power}\right)\right) \times E_{BESS} \quad (10)$$

By defining K as:

$$K = C_{energy} + \left(D_{rate} \times C_{power}\right) \quad (11)$$

That means the total cost of the BI-BESS can be expressed as $K \times E_{BESS}$.

After replacing the E_{BESS} in the total cost equation, the total cost of BESS is presented as:

$$C_{tot} = K \times max\left(\frac{\Delta E}{DoD}, \frac{\Delta P}{D_{rate}}\right) \quad (12)$$

3. PROPOSED TECHNO-ECONOMIC METHOD

The proposed model is explained in this section based on the β variable. Since the battery's energy and power are linked, specifying this variable allows the sizing and economic calculation of the battery to be discussed using both parameters, resulting in more accurate conclusions at the end. The flowchart, as shown in Figure 3 is divided into three sections: economic analysis, peak shaving algorithm, and battery sizing. In terms of economic computation, the BCR is used after defining and adding basic parameters related to the tariff structure and a specific lithium Ion battery, and the BCR against the graph achieves the best result. The simple peak shaving using an iterative approach was presented to graph the ΔE against β with the help of the ratio of ΔE to ΔP. Finally, the optimal β can reveal the best battery size for the particular building by comparing the two graphs from an economic and peak shaving analysis.

3. 1. Energy to Power Ratio ΔP may be thought of as a design parameter, whereas ΔE is a function of ΔP and the load profile of the building. β variable is provided

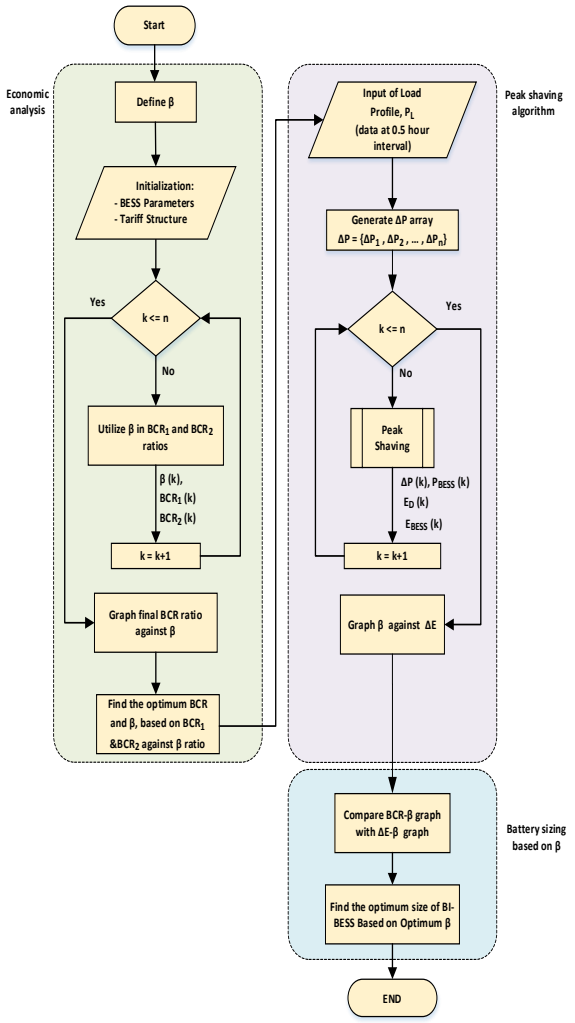

Figure 3. Proposed Techno-economic model for optimal battery sizing

here as a ratio of ΔE to ΔP to allow a techno-economic method to analyze the economic feasibility of the BI-BESS project as follows:

$$\Delta E = \beta \times \Delta P \tag{13}$$

A new formula for the total cost may be produced by substituting the specified ΔE equation into Equation (12):

$$C_{tot} = K \times [max\left(\frac{\beta}{DoD}, \frac{1}{D_{rate}}\right) \times \Delta P] \tag{14}$$

Similarly, by swapping ΔE into Equation (8), the total yearly revenue is redefined as follows:

$$R_{tot} = [(\beta \times \Delta r \times \text{RTE}) + (C_{MD} \times \text{Deg} \times \eta_{inv} - C_{opex-unit})] \times \Delta P \tag{15}$$

The β is the load profile characteristics, all other parameters are fixed values, and ΔP is the sole variable in these equations. When ΔP rises, the overall revenue rises as well. On the other side, the overall cost will increase as well. It follows that there should be an ideal value of ΔP at which the economic gain of the BI-BESS is maximized.

3. 2. Benefit-cost Ratio The Benefit-cost ratio (BCR) is calculated by dividing the entire income by the total cost of the project defined by Cotter [16]. A BCR larger than one indicates that the project will be profitable, but a BCR less than one indicates that the project will result in a loss. The idea of BCR is used to analyze the BI-BESS project in this case. It is vital to highlight that the project's revenue is seen to be recurring yearly throughout the project's life, whilst the project's cost is thought to be spent at the start of the project. The yearly revenue and expense must be examined over a variety of time frames. It is necessary to determine the overall length of the project as well as the discount rate for each year to estimate the appropriate BCR. In this way, it is required to consider the discount rate parameter in the total benefit-cost ratio. The discount rate is the interest rate paid by commercial banks and other financial institutions on short-term loans obtained from the Federal Reserve Bank. The interest rate used in BCR analysis to assess the present value of future cash flows is referred to as the discount rate by Shively and Galopin [17]. For calculating the present value of annual revenue, the following multiplication factor can be utilized:

$$PV_{rate} = \left[\frac{1-(1+r)^{-n}}{r}\right] \tag{16}$$

where n is the total years of the project, r is the discount rate of a specific area based on the market, and PV_{rate} is the total yearly revenue during the life of the project. By adding the discount rate into the BCR, the ratio will change as:

$$BCR = \frac{Rtot \times PV_{rate}}{Ctot} \tag{17}$$

Based on the total cost equation that consists of two ratios, the BCR should be evaluated in BCR_1 and BCR_2, which means the BCR is considered based on power and energy constraints. By considering whole costs and revenue consideration in the formula above, the total benefit-cost ratio will be expressed as:

$$BCR_1 = \frac{(\beta \times \Delta r \times RTE \times N_{days}) \times PV_{rate}}{\frac{k \cdot \beta}{DoD}} + \frac{[(C_{MD} \times Deg \times \eta_{inv} \times 12) - C_{opex}] \times PV_{rate}}{\frac{k \cdot \beta}{DoD}} \tag{18}$$

and

$$BCR_2 = \frac{(\beta \times \Delta r \times RTE \times N_{days}) \times PV_{rate}}{\frac{k}{D_{rate}}} + \frac{[(C_{MD} \times Deg \times \eta_{inv} \times 12) - C_{opex}] \times PV_{rate}}{\frac{k}{D_{rate}}} \tag{19}$$

The minimum of the two equations above may be used to display BCR versus β graph. This is the BCR of

a BI-BESS project based on a certain tariff structure and BESS technology, irrespective of the building load profile. The overall BCR for the BI-BESS should be the lowest of the two ratios:

$$BCR = \min(BCR_1, BCR_2) \quad (20)$$

Observing Equations (18) and (19), it is evident thatBCR_1 is an inverse function of β and BCR_2 is a linear function of β. As a result, a typical graph of both BCRs against β will look like Figure 4:

There exists an optimal β location where the total BCR is maximized, which is supplied by the intersection point of BCR_1 and BCR_2. By checking the two equations it is clear that there are two parameters that can affect the optimum point of β:

$$\beta_{opt} = \frac{DOD}{D_{rate}} \quad (21)$$

It's important to note that once the tariff structure and BESS technology are in place, the BCR-graph is no longer changeable. Because it is not affected by the load profile of the building, the same graph will apply to all buildings that employ the same tariff and BESS technology in the future. This tool may also be used to determine how specific elements, such as BESS cost reduction and MD fee revisions, influence the potential economic gain from a BI-BESS project.

3. 3. Iterative Model for Peak Shaving The battery size graph of the techno-economic technique can be employed with the help of a peak shaving iterative model and a peak shaving iterative model. For this iterative model, the 1-day load profile data from a commercial building in Malaysia is modeled in MATLAB using the data from the commercial building. Based on the Malaysian electricity supplier[1], the MD is calculated every 30 minutes, then the load profile data should be given every 30 minutes intervals, resulting in i = 48 data points for the load profile in a single day. The peak shaving power will be iteratively varied to determine the battery size, and the corresponding battery size will be computed. This project employs 100 iterations.

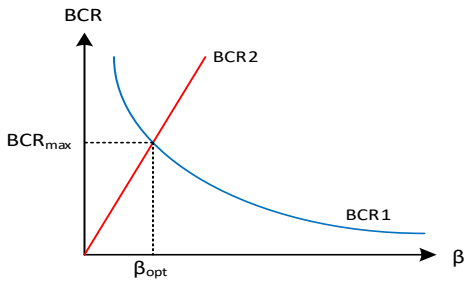

Figure 4. Typical BCR against β plot

[1] https://www.tnb.com.my/commercial-industrial/pricing-tariffs1

After selecting a peak shaving power (ΔP_1), the appropriate threshold power ($P_{threshold1}$) can be determined. The simulation will then determine the operation of the BESS for each of the load profile data points from i = 1 to i = 48. The load profile data has been reorganized so that i=1 denotes the commencement of the peak hour when the BESS discharge procedure is expected to start. This means that data at i=48 will be the last point of the off-peak hour at which battery charging should stop. This captures the battery charging-discharging cycle inside the 48 data points, which is critical for confirming that the battery energy can be fully replenished during off-peak hours before the next discharging cycle begins.

At any point in (i), the algorithm will first determine if the point is in the peak or off-peak hour. If the data point falls during the peak hour, the peak shaving algorithm's "battery discharge" operation will be called; otherwise, the peak shaving algorithm's "battery charging" operation will be invoked. The size of the battery $E_{BESS(1)}$ required for the selected peak shaving power (ΔP_1) will be determined based on the results, and the related E_{BESS} will be calculated. The process is then repeated for the next peak shaving power (ΔP_k) with the $E_{BESS}(k)$ determined using the same technique described above for each iteration. The β to attain the ΔE can be plotted after k = n iterations.

"Battery Discharging" and "Battery Charging" are the two sections of the Peak Shaving algorithm used in the iterative approach. It will be necessary to request the former during peak hours, and it will be necessary to request the latter during off-peak hours. The load profile power $P_{L,i}$ is compared with the threshold power $P_{threshold,i}$. If the load power is higher than the threshold power, the battery will discharge at a power $P_{BESS,i} = P_{L,i} - P_{threshold,i}$.

$$P_{BESS,i} = P_{L,i} - P_{threshold,i} \quad (22)$$

Because the battery must be recharged during off-peak hours, it is necessary to determine the amount of energy that has been drained by the battery. The discharged energy at point-i should be updated in the following manner, assuming that both the charging and discharging efficiency of the battery stay constant.

$$E_{D,i+1} = E_{D,i} - \frac{0.5 * P_{BESS,i}}{\sqrt{RTE}} \quad (23)$$

Given that the BESS has the same charging and discharging power capabilities, the peak power required for recharging the battery will be equal to the peak shaving power (ΔP) required. The greatest amount of energy that may be acquired through this recharging power will be as follows for data points taken at 30-minute intervals:

$$E_{max,i} = \sqrt{RTE} * 0.5 * \Delta P \quad (24)$$

If the drained energy for the battery at point-i exceeds the $E_{max,i}$, the battery shall recharge at full power. Otherwise, the battery should be recharged at a lower power level merely to help compensate for the lost energy. The battery power and discharge energy may be computed using the following conditions:

$$if\ E_{D,i} < -E_{max,i}$$
$$then$$
$$P_{BESS,i} = \Delta P$$
$$E_{D,i+1} = E_{D,i} + E_{max,i}$$
$$else\ if\ E_{D,i} < 0\ then$$
$$P_{BESS,i} = \frac{-E_{D,i}}{0.5*\sqrt{RTE}}$$
$$E_{D,i+1} = 0$$

The simulation will produce time-series data for battery power (P_{BESS}) and discharged energy (E_D), which will be used in further calculations. For battery size, it is necessary to guarantee that the energy discharged during peak hours can be adequately recharged during off-peak hours; otherwise, the BESS would have a net loss of energy after each charging-discharging cycle, making the operation unfeasible. i.e. E_D (48) = 0 can be verified as the final point of the discharged energy array by evaluating the final point of the discharged energy array and confirming that it is zero. Figure 5 shows the total process of battery charging/discharging in the proposed iterative method.

3. 4. Battery Sizing Utilizing Optimum β

Finding the maximum value of each time-series data allows for determining the maximum battery power and maximum drained energy. Finally, the energy constraint and power constraint may be used to calculate the minimal BESS size in kWh and BESS power as follows:

$$E_{BESS} = \max\left(\frac{\max(abs(E_D))}{DoD}, \frac{\Delta P}{D_{rate}}\right) \quad (25)$$

Note that the absolute value of E_D is considered here due to the negative value of discharged energy. Once the E_{BESS} is decided, the whole process is then repeated with a different peak shaving power ΔP(k+1) and so on, up to ΔP(N). This iterative process will generate the N numbers of ΔP value chosen. Finally, the curve of β against ΔE can be plotted. After plotting the β against ΔE and fixing the achieved value of optimum β from the economic calculation, the optimum size of the battery can be calculated.

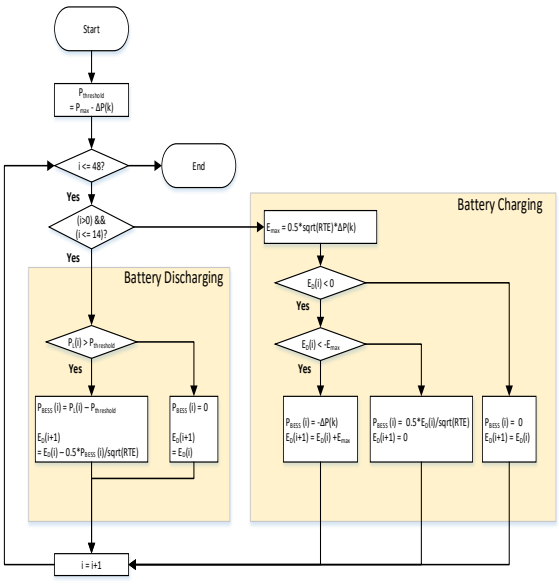

Figure 5. Battery charging/discharging process of the iterative method

4. RESULTS AND DISCUSSION

Here, the results of the techno-economic technique for commercial buildings are examined in detail, with the help of MATLAB program. In addition, the effective parameters of the techno-economic approach are addressed in greater detail. The results and outputs of the ratios are analyzed in the context of commercial buildings in Malaysia, and all cost estimations and tariff structures are based on the country's tariff system. Despite the fact that the cost of batteries and associated considerations would fluctuate over time, the interest rate for the first 10 years of the BESS project has been set at 3%, based on the market's interest in having an accurate layout. Final considerations are given to the influence of market interests on the payback duration of the project. Also, a detailed analysis of the cost reduction estimation and its impact on the entire profits of the project's overall benefits is included.

4. 1. Economic Considerations Utilizing β in Commercial Tariff Structure

To check the techno-economic model's applications, it must clarify parameters included in BCR1 and BCR2. The energy tariff structure summarized in Table 1; which is based on the tariff structured by Tenaga Nasional Berhad (TNB), the sole utility company in Peninsular Malaysia TNB 2021[1]. Tariff structures have been selected here for this study, based on the commercial medium-voltage C2 Tariff.

In terms of battery technology, Lithium-Ion batteries (LiB) with the following parameters mentioned in Table 2 have been selected Asian Development Bank [18, 19].

It should be noted that since the specific project is being evaluated in accordance with Malaysia's tariff system, the costs of BESS components are being obtained from vendors in Malaysian marketplaces due to the lack of battery manufacturers in the country. Some of the real prices are determined at a higher level than the manufacturer's price lists, taking into account shipping and other additional expenditures.

[1] https://www.tnb.com.my/commercial-industrial/pricing-tariffs1

TABLE 1. Electricity tariff rates for Commercial Buildings in Malaysia (C2 Tariff)

Parameters	Values
Maximum Demand Charge (C_{MD})	10.72 (USD/kW)
Peak Hour kWh Charges ($C_{rate\,peak}$)	0.09 (USD/kWh)
Off-Peak Hour kWh Charge ($C_{rate\,off-peak}$)	0.06 (USD/kWh)
Difference from off-peak hours to peak hours costs (Δr)	0.03 (USD/kWh)

TABLE 2. Techno-economic parameters of BESS

Parameters	Values
BESS Energy Cost (C_{energy})	363.37 (USD/kWh)
BESS Power Cost (C_{power})	242.25 (USD/kWh)
BESS Operational Costs (C_{opex})	12.11 (USD/kW-year)
Round-trip efficiency of the battery (RTE)	90%
Efficiency degradation of BESS (Deg)	5%
The efficiency of the inverter (η_{inv})	97.5 %
Depth of discharge for 3000 cycles (DoD)	80%
The discharge rate of the battery per cycle (D_{rate})	0.5 (C)
Present value rate for the total life of the project (PV_{rate})	8.53
Total number of working days in a year (N_{days})	250
Proposed unit of power and energy costs of the battery (k)	484.495

As explained before, the BCR can be evaluated by Equation (20) which consists of BCR_1 and BCR_2. By calculating discussed parameters, it is possible to find the ratios of BCR for commercial customers in Malaysia:

$$BCR_1 = \frac{[(\beta \times 0.03 \times 0.9 \times 250)\,] \times 8.53}{\frac{484.495 \times \beta}{0.8}} + \frac{[(10.72 \times 0.95 \times 97.5 \times 12) - 12.11] \times 8.53}{\frac{484.495 \times \beta}{0.8}} = 0.095 + \frac{167.65}{\beta}$$

and

$$BCR_2 = \frac{[(\beta \times 0.03 \times 0.9 \times 250)] \times 8.53}{\frac{484.495}{0.5}} + \frac{[(10.72 \times 0.95 \times 97.5 \times 12) - 12.11] \times 8.53}{\frac{484.495}{0.5}} = (0.059 \times \beta) + 104.79$$

As the β is the only variable in the two ratios, simply changing its value in BCR_1 and BCR_2, the final graph is achieved, and the maximum point of β that evaluated at 1.6. Figure 6 shows the final BCR against β for Commercial buildings in Malaysia. The result shows that the maximum benefit-cost ratio of the project is based on the optimum energy to power ratio achieved at 1.08.

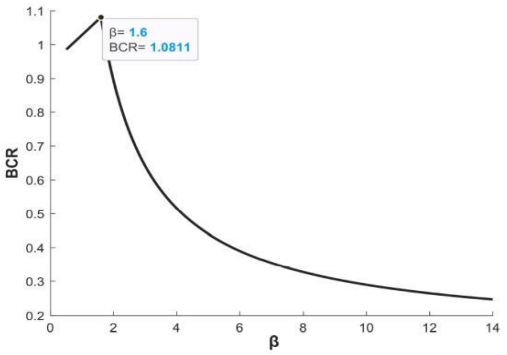

Figure 6. BCR against β in Commercial buildings

4. 2. Battery Sizing Utilizing Optimum β in Commercial Buildings In this section, the results of the economic calculation's optimum β are compared to the commercial building's suggested battery sizing, which employs the iterative method of peak shaving. Peak shaving takes into account a commercial building's 1-day load profile. Peak hours in Malaysia last 14 hours, from 8 a.m. to 10 p.m. The minimum peak shaving indicates that the threshold line is close to peak power. The power and energy of the battery will increase as the threshold line is moved to the mean of the load. The load profile is derived from the one-day load profile of the commercial building, which has a maximum power of 740.66 kW and a mean power of 382.17 kW. By running MATLAB with the proposed peak shaving algorithm, the size of the battery for different threshold considerations is shown in Figure 7:

The number of threshold considerations is determined by the algorithm's required accuracy. By increasing the number of thresholds, the total number of battery sizing considerations increase as shown in Figure 8. For commercial load profiles, the graph of β versus ΔE can show the different sizes of batteries over each fixed

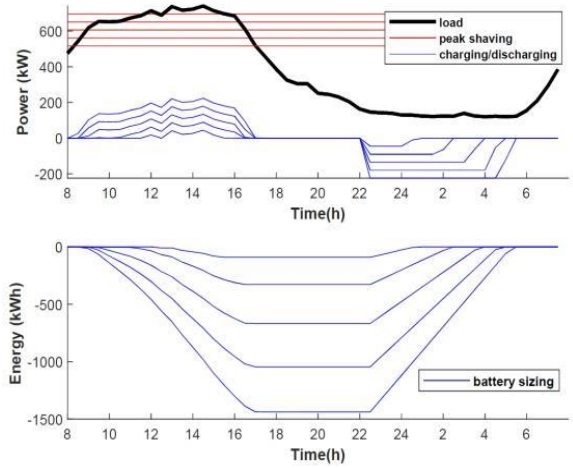

Figure 7. Battery sizing: 1-day of Commercial load profile based on an iterative method

threshold consideration. As is obvious, increasing the size of the battery increases the amount of energy saved in a load profile. Nonetheless, as previously discussed, it is critical to assess the project's economic feasibility to determine the optimal battery size.

In economic terms, the maximum β in total BCR in commercial buildings shown in Figure 6 is fixed at 1.6. By determining the optimum β from the economic calculation in Figure 8, the feasible size of the battery in β=1.6 is specified at 66.84 kWh, representing the best feasible battery size consideration for that specific commercial load profile. The BCR against the β graph can be plotted by taking the minimum of the previously explained Equations (18) and (19). This represents the BCR of a BI-BESS project under a specific tariff structure, and BESS technology is solely a function of DoD and Drate, which is dependent on the BESS technology selected.

According to several manuals from battery manufacturers, the DoD in batteries is considered to be 80% and the Drate to be 0.5 C. By plugging them into Equation (26), the fixed β can be calculated as follows:

$$\beta_{opt} = \frac{DOD}{D_{rate}} = \frac{0.8}{0.5} = 1.6$$

that is independent of the building load profile and will apply to all buildings that are using the same tariff and BESS technology. The result from the Final BCR against β in Figure 6 shows that based on optimum β, the BCR is fixed at 1.08, which means it is economically feasible to use BESS in commercial buildings in Malaysia and the investments will be compensated during the life of the project.

There are some related studies conducted by Rosati et al. [20], Yan et al. [21] and Mayyas et al. [22] they have developed technoeconomic models to find the best size of the battery utilizing different economical tools. Comparing the results of this study with mentioned research proves the simplicity and applicability of our research on all other commercial buildings without huge initial data from the load of buildings.

In addition, it is required to check the feasibility of the project based on market interest to ensure the return of investments in this project is still beneficial in comparison with market interest investments. In this case, the market interest factor as a crucial element for planning and installing the project will be discussed in the next session.

4. 3. Finding the Feasibility of BI-BESS in the Marketplace Utilizing the Payback Period The feasibility of the project depends on the BCR calculation. Whenever the BCR is evaluated more than 1, it means that there are some economic benefits to using BESS in the project and the total economic benefit of the project will be more than the total initial investments. Figure 9 shows the feasibility area of the BCR−β graph. The result shows that it is economically possible to employ BESS in commercial buildings in Malaysia, and the investments will be repaid during the 10 years of the project's life consideration. However, by considering the impact of the payback period in the marketplace, the desired payback period in Malaysia considers less than 5 years which impacts the total BCR calculation. That means the project with more than mentioned period is not interesting enough to be planned.

The payback period is a simple useful tool that calculates the total required payback period consideration of the project based on the ratio of total cost per total revenue:

$$PP = \frac{C_{tot}}{R_{tot}}[year] \quad (26)$$

By defining the payback period as PP, the total revenue can consider as follows:

$$R_{tot} = \frac{C_{tot}}{PP}[year] \quad (27)$$

Regarding the benefit-cost ratio in Equation (17), the total BCR for 10 years of consideration can be represented as follows:

$$BCR = \frac{R_{tot} \times PV_{10}}{C_{tot}} \quad (28)$$

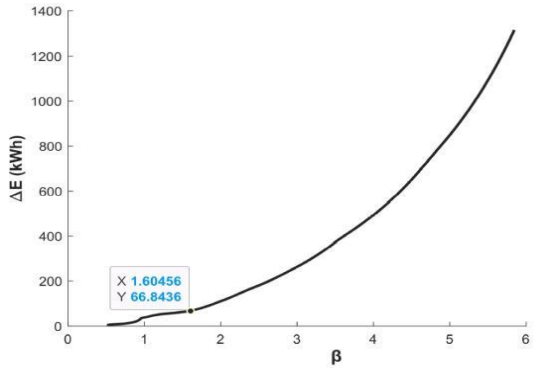

Figure 8. The optimum size of the battery based on β in the commercial load profile

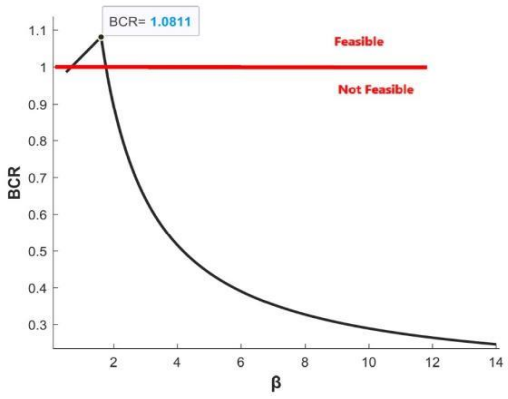

Figure 9. Feasibility area of BCR

where PV_{10} is the present value rate for 10 years life span consideration of the BI-BESS project. After replacing total revenue in Equation (28), the benefit-cost ratio can be defined as Equation (29) where the benefit-cost ratio is defined as the ratio of the present value of the project for 10 years of consideration, and PP is the desired payback period.

$$BCR = \frac{PV_{10} \times \left(\frac{C_{tot}}{PP}\right)}{C_{tot}} = \frac{PV_{10}}{PP} \quad (29)$$

Considering the 3% rate of return from the market and 10 years for the lifespan of BESS the present value rate based on Equation (16) is evaluated as 8.53. The benefit-cost ratio based on Equation (29) can be evaluated:

$$BCR = \frac{PV_{10}}{PP} = \frac{8.53}{5} = 1.7$$

Comparing the new calculated BCR based on market interest with the achieved one at 1.08, the result shows that however, the evaluated BCR for the commercial building is more than 1, and using BI-BESS demonstrates economic benefit for the project, but the result is less than the market expectation.

4. 4. The Impact of Cost Reduction on the Feasibility of the Project While the costs of lithium-ion technologies have dropped dramatically since their commercialization, their adoption will be influenced by both their costs and trends in alternative battery technologies. We explore the principles of the cost drop witnessed for lithium-ion technologies to better understand prior improvements and inform plans to further develop electrochemical storage technologies. Once it comes to determining the feasibility of a project, the price of the battery and inverter can have a significant influence on the project's viability. In upcoming years, as it is estimated by Mongird et al. [19], the cost of BESS will decrease by around half of the present value. Considering the cost reduction for different scenarios, the new benefit-cost ratio for commercial buildings is shown in Figure 10:

Since the maximum BCR is less than 1.7, it is clear that even with a 25 percent cost reduction, installing BESS in commercial buildings will remain unattractive to Malaysian investors, despite the cost reduction.

As a consequence of the predicted 40 percent cost reduction in the approaching years, the BCR would be larger than 1.7, indicating that using BI-BESS for commercial buildings will be profitable for investors when considering market interests. Since the value of β is the same before and after the cost reduction, the size of the battery remains unchanged. In this example, the BCR improves dramatically as a result of cost reduction, highlighting the relevance of cost reduction in enhancing a project's viability.

Aside from the study's findings, Figure 11 demonstrates the significance of BESS cost reduction in

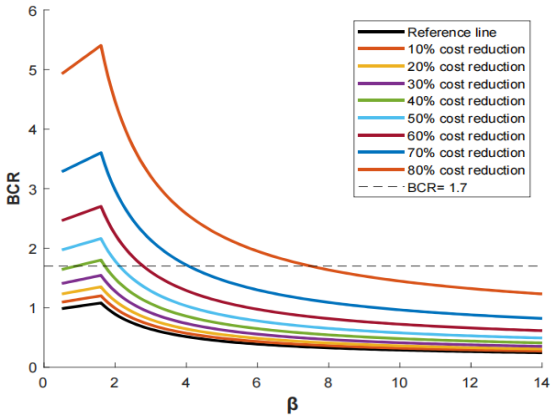

Figure 10. BCR against β in commercial buildings before and after cost reductions

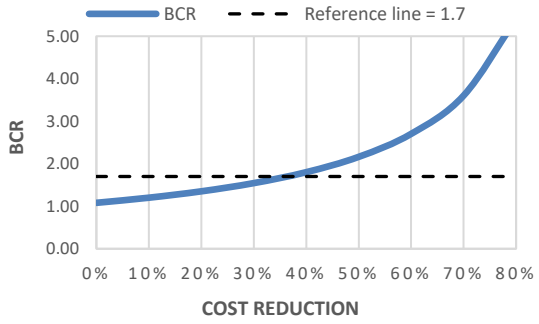

Figure 11. The impact of cost reduction on BCR

the project's overall profit. In this situation, many scenarios were explored to determine the best BESS cost reduction for the overall profit of the project. As is obvious, the project will be considered beneficial after around 40% cost reduction. Many experts assessed a cost decrease of 50 to 60% by Cole et al. [23]. Based on the present market position and various cost-cutting estimates, this should happen soon.

5. CONCLUSION

The current study developed a techno-economic model to assess the viability of commercial building-integrated BESS. Because the energy and power attributes of a BESS are interrelated, an energy-to-power factor ($\beta = \Delta E/\Delta P$)) was merged into a single metric allowing both metrics to be addressed, resulting in high accuracy. A Benefit-Cost Ratio (BCR) versus β relationship was created to describe the tariff structure and BESS parameters independently of the building load profile. By modeling a real-world building load profile in MATLAB, the suggested technique was detailed and validated. The summary of the critical results is represented as follows:

- The assessed β from economic calculation was established at 1.6 by charting the BCR- β ratio.
- The final $\Delta E - \beta$ ratio was obtained via the peak shaving approach by calculating different battery sizing from the 1-day load profile of a commercial building in Malaysia.
- After comparing two graphs from the proposed model's economic and technical parts, the optimum size of the battery was determined to be 66.84 kWh.
- Based on the BCR-β graph, the maximum BCR was achieved at 1.08 which means it is economically feasible to install BESS for peak shaving in commercial buildings.
- Considering market interests for the initial investments and economic calculations, the desired payback period in Malaysia considered 5 years that impacted the BCR calculation, and the critical BCR was evaluated at 1.7
- Different BESS cost reduction scenarios were evaluated to check the improvement of the profitability of the project.
- Finally, the findings demonstrated that once the tariff structure and BESS technology are determined, the proposed techno-economic analysis will apply to all buildings.

6. REFERENCES

1. Hassan, F.A., "Multi-criteria approach and wind farm site selection analysis for improving power efficiency", ***Journal of Human, Earth, and Future***, Vol. 1, No. 2, (2020), 60-70, doi: 10.28991/hef-2020-01-02-02.
2. Hassan, F.A., Mahmoud, M. and Almohammed, O.A., "Analysis of the generated output energy by different types of wind turbines", ***Journal of Human, Earth, and Future***, Vol. 1, No. 4, (2020), 181-187, doi: 10.28991/hef-2020-01-04-03.
3. Jain, S., Khandelwal, P. and Agarwal, P., "Use of blockchain technology in energy banking and electricity markets", ***HighTech and Innovation Journal***, Vol. 2, No. 3, (2021), 179-186, doi: 10.28991/hij-2021-02-03-03.
4. Abbasi, M., Sharafi Miyab, M., Tousi, B. and Gharehpetian, G.B., "Using dynamic thermal rating and energy storage systems technologies simultaneously for optimal integration and utilization of renewable energy sources", ***International Journal of Engineering, Transations A: Basics***, Vol. 33, No. 1, (2020), 92-104, doi: 10.5829/ije.2020.33.01a.11.
5. Sagar, G. and Debela, T., "Implementation of optimal load balancing strategy for hybrid energy management system in dc/ac microgrid with pv and battery storage", ***International Journal of Engineering***, Vol. 32, No. 10, (2019), 1437-1445, doi: 10.5829/ije.2019.32.10a.13.
6. Kumar, A. and Biswas, A., "Techno-economic optimization of a stand-alone photovoltaic-battery renewable energy system for low load factor situation-a comparison between optimization algorithms", ***International Journal of Engineering, Transations A: Basics***, Vol. 30, No. 10, (2017), 1555-1564, doi: 10.5829/ije.2017.30.10a.17.
7. Lange, C., Rueß, A., Nuß, A., Öchsner, R. and März, M., "Dimensioning battery energy storage systems for peak shaving based on a real-time control algorithm", ***Applied Energy***, Vol. 280, (2020), 115993, doi: 10.1016/j.apenergy.2020.115993.
8. Chua, K.H., Lim, Y.S. and Morris, S., "Energy storage system for peak shaving", ***International Journal of Energy Sector Management***, (2016), doi: 10.1108/IJESM-01-2015-0003.
9. Englberger, S., Hesse, H., Kucevic, D. and Jossen, A., "A techno-economic analysis of vehicle-to-building: Battery degradation and efficiency analysis in the context of coordinated electric vehicle charging", ***Energies***, Vol. 12, No. 5, (2019), 955, doi: 10.3390/en12050955.
10. Martins, R., Hesse, H.C., Jungbauer, J., Vorbuchner, T. and Musilek, P., "Optimal component sizing for peak shaving in battery energy storage system for industrial applications", ***Energies***, Vol. 11, No. 8, (2018), 2048, doi: 10.3390/en11082048.
11. Abdullah, W.S.W., Osman, M., Ab Kadir, M.Z.A., Verayiah, R., Ab Aziz, N.F. and Rasheed, M.A., "Techno-economics analysis of battery energy storage system (bess) design for virtual power plant (vpp)–a case study in malaysia", ***Journal of Energy Storage***, Vol. 38, (2021), 102568, doi: 10.1016/J.EST.2021.102568.
12. Mirhoseini, P. and Ghaffarzadeh, N., "Economic battery sizing and power dispatch in a grid-connected charging station using convex method", ***Journal of Energy Storage***, Vol. 31, (2020), 101651, doi: 10.1016/J.EST.2020.101651.
13. de Mattos Affonso, C. and Kezunovic, M., "Technical and economic impact of pv-bess charging station on transformer life: A case study", ***IEEE Transactions on Smart Grid***, Vol. 10, No. 4, (2018), 4683-4692, doi: 10.1109/TSG.2018.2866938.
14. Uddin, M., Romlie, M., Abdullah, M., Tan, C., Shafiullah, G. and Bakar, A.H.A., "A novel peak shaving algorithm for islanded microgrid using battery energy storage system", ***Energy***, Vol. 196, (2020), 117084, doi: 10.1016/j.energy.2020.117084.
15. Tsai, C.-T., Ocampo, E.M., Beza, T.M. and Kuo, C.-C., "Techno-economic and sizing analysis of battery energy storage system for behind-the-meter application", ***IEEE Access***, Vol. 8, (2020), 203734-203746, doi: 10.1109/ACCESS.2020.3036660.
16. Cotter, T.S., "Engineering managerial economic decision and risk analysis: Economic decision-making and risk analysis, Springer Nature, (2021).
17. Shively, G. and Galopin, M., "An overview of benefit-cost analysis", (2013).
18. Kim, D.K., Yoneoka, S., Banatwala, A.Z. and Kim, Y.-T., "Handbook on battery energy storage system", Asian Development Bank: Manila, Philippines, (2018).
19. Mongird, K., Viswanathan, V.V., Balducci, P.J., Alam, M.J.E., Fotedar, V., Koritarov, V.S. and Hadjerioua, B., *Energy storage technology and cost characterization report*. 2019, Pacific Northwest National Lab.(PNNL), Richland, WA (United States).
20. Rosati, A., Facci, A.L. and Ubertini, S., "Techno-economic analysis of battery electricity storage towards self-sufficient buildings", ***Energy Conversion and Management***, Vol. 256, (2022), 115313, doi: 10.1016/j.enconman.2022.115313.
21. Yan, X., Zhang, X., Chen, H., Xu, Y. and Tan, C., "Techno-economic and social analysis of energy storage for commercial buildings", ***Energy Conversion and Management***, Vol. 78, (2014), 125-136, doi: 10.1016/j.enconman.2013.10.014.
22. Mayyas, A., Chadly, A.A., Khaleel, I. and Maalouf, M., "Techno-economic analysis of the li-ion batteries and reversible fuel cells as energy-storage systems used in green and energy-efficient buildings", ***Clean Energy***, Vol. 5, No. 2, (2021), 273-287, doi: 10.1093/ce/zkab009.
23. Cole, W., Frazier, A.W. and Augustine, C., *Cost projections for utility-scale battery storage: 2021 update*. 2021, National Renewable Energy Lab.(NREL), Golden, CO (United States).

Persian Abstract

چکیده

یافتن سایز مناسب باتری در موفقیت مالی پروژه اهمیت بسزایی دارد. بسیاری از تحقیقات از شبیه سازی های بسیار پیچیده برای تعیین بهترین سایز باتری استفاده می کنند. همچنین، استفاده مجدد از خروجی این بهینه سازی در پروژه های دیگر نیز بسیار دشوار است. در این مقاله با معرفی فاکتور β به عنوان رابط انرژی در ضریب توان، مدل تکنو اکونومیک ساده ای ارائه شده که ارزیابی سریع سیستم ذخیره انرژی باتری به صورت یکپارچه را ممکن می سازد و همزمان میتوان آن را برای تمامی ساختمان های تجاری با تعرفه ی یکسان ،بدون در نظر گرفتن پروفایل مصرفی ساختمان ها بکار برد. از آنجا که انرژی و توان باتری در کنار هم قرار گرفته اند، با تعیین β هر دو معیار مورد مطالعه قرار گرفته و در نتیجه دقت محاسبات نیز افزایش می یابد. برای اعتبار سنجی نتایج، نمایه مصرف انرژی یک ساختمان تجاری براساس ساختار تعرفه مالزی در نظر گرفته شده و اندازه ی بهینه ی باتری با استفاده از مدل تکنو اکونومیک پیشنهادی، و با در نظر گرفتن نسبت سود به هزینه (BCR) و با به کار گیری یک مدل تکرار شونده ی بسیار ساده برای مدیریت اوج بار محاسبه شده است. نتایج نشان می دهند با یافتن بهینه BCR=1.08، مناسبترین سایز باتری ٦٦٨٤ kWh است. اگرچه با در نظر گرفتن نرخ بهره بازار در دوره ی بازپرداخت، ارزش اقتصادی نصب و راه اندازی پروژه برابر با BCR=1.7 ارزیابی می شود که بسیار بالاتر از نتایج می باشد. به این ترتیب تاثیر ناشی از کاهش هزینه باتریب در آینده نیز ارزیابی شده است.

AIMS AND SCOPE

The objective of the International Journal of Engineering is to provide a forum for communication of information among the world's scientific and technological community and Iranian scientists and engineers. This journal intends to be of interest and utility to researchers and practitioners in the academic, industrial and governmental sectors. All original research contributions of significant value focused on basics, applications and aspects areas of engineering discipline are welcome.

This journal is published in three quarterly transactions: Transactions A (Basics) deal with the engineering fundamentals, Transactions B (Applications) are concerned with the application of the engineering knowledge in the daily life of the human being and Transactions C (Aspects) - starting from January 2012 - emphasize on the main engineering aspects whose elaboration can yield knowledge and expertise that can equally serve all branches of engineering discipline.

This journal will publish authoritative papers on theoretical and experimental researches and advanced applications embodying the results of extensive field, plant, laboratory or theoretical investigation or new interpretations of existing problems. It may also feature - when appropriate - research notes, technical notes, state-of-the-art survey type papers, short communications, letters to the editor, meeting schedules and conference announcements. The language of publication is English. Each paper should contain an abstract both in English and in Persian. However, for the authors who are not familiar with Persian, the publisher will prepare the latter. The abstracts should not exceed 250 words.

All manuscripts will be peer-reviewed by qualified reviewers. The material should be presented clearly and concisely:

- *Full papers* must be based on completed original works of significant novelty. The papers are not strictly limited in length. However, lengthy contributions may be delayed due to limited space. It is advised to keep papers limited to 7500 words.
- *Research* notes are considered as short items that include theoretical or experimental results of immediate current interest.
- *Technical notes* are also considered as short items of enough technical acceptability with more rapid publication appeal. The length of a research or technical note is recommended not to exceed 2500 words or 4 journal pages (including figures and tables).

Review papers are only considered from highly qualified well-known authors generally assigned by the editorial board or editor in chief. Short communications and letters to the editor should contain a text of about 1000 words and whatever figures and tables that may be required to support the text. They include discussion of full papers and short items and should contribute to the original article by providing confirmation or additional interpretation. Discussion of papers will be referred to author(s) for reply and will concurrently be published with reply of author(s).

INSTRUCTIONS FOR AUTHORS

Submission of a manuscript represents that it has neither been published nor submitted for publication elsewhere and is result of research carried out by author(s). Presentation in a conference and appearance in a symposium proceeding is not considered prior publication.

Authors are required to include a list describing all the symbols and abbreviations in the paper. Use of the international system of measurement units is mandatory.

- On-line submission of manuscripts results in faster publication process and is recommended. Instructions are given in the IJE web sites: www.ije.ir-www.ijeir.info
- Hardcopy submissions must include MS Word and jpg files.
- Manuscripts should be typewritten on one side of A4 paper, double-spaced, with adequate margins.
- References should be numbered in brackets and appear in sequence through the text. List of references should be given at the end of the paper.
- Figure captions are to be indicated under the illustrations. They should sufficiently explain the figures.
- Illustrations should appear in their appropriate places in the text.
- Tables and diagrams should be submitted in a form suitable for reproduction.
- Photographs should be of high quality saved as jpg files.
- Tables, Illustrations, Figures and Diagrams will be normally printed in single column width (8cm). Exceptionally large ones may be printed across two columns (17cm).

PAGE CHARGES AND REPRINTS

The papers are strictly limited in length, maximum 8 journal pages (including figures and tables). For the additional to 8 journal pages, there will be page charges. It is advised to keep papers limited to 3500 words.

Page Charges for Papers More Than 8 Pages (Including Abstract)	
For International Author ***	**$55 / per page**
For Local Author	**100,000 Toman / per page**

AUTHOR CHECKLIST

- Author(s), bio-data including affiliation(s) and mail and e-mail addresses).
- Manuscript including abstracts, key words, illustrations, tables, figures with figure captions and list of references.
- MS Word files of the paper.

International **J**ournal of **E**ngineering, P.O. Box 13145-1659, Tehran, I.R. Iran
Materials and Energy Research Center, 5 Ahuramazda St., Alvand Ave., Argentina Sq., Tehran, Islamic Republic of Iran
www.merc.ac.ir - www.emerc.ac.ir

THOMSON REUTERS

WEB OF SCIENCE

Scopus®

CAS®
A DIVISION OF THE
AMERICAN CHEMICAL SOCIETY

Google
Scholar